RESEARCH PAPERS

Constructal Design of Cooling Channel in Heat Transfer System by Utilizing Optimality of Branch Systems in Nature

Xiaohong Ding[1]

Department of Mechanical Engineering,
University of Shanghai for Science and
Technology,
Shanghai 200093, China
e-mail: xhding @vip.citiz.net

Koetsu Yamazaki

Department of Human & Mechanical Systems
Engineering,
Kanazawa University,
Kanazawa 920-1192 Japan

There are similarities between the morphology of branch systems in nature and the layout of cooling channel in heat transfer system in engineering. The branch systems in nature always grow in such a way that approximate global optimal performances can be achieved. By utilizing the optimality of branch systems in nature, an innovative layout design methodology of cooling channel in heat transfer system is suggested in this paper. The emergent process of branch systems in nature is reproduced according to their common growth mechanisms. Branches are grown under the control of a so-called nutrient density so as to make it possible for the distribution of branches to be dependent on the nutrient distribution. The growth of branches also satisfies the hydrodynamic conditions and the minimum energy loss principle. If the so-called nutrient density in the generation process of branch systems is referred to as the heat energy in a heat transfer system, the distribution of branches is responsible for the distribution of cooling channels. Having similar optimality of branch systems in nature, the constructed cooling channel can be designed flexibly and effectively in any shape of perfusion volume to be cooled adaptively to very complex thermal boundary conditions. The design problems of both a conductive cooling channel and a convective cooling channel are studied, and the layouts of two-dimensional and three-dimensional cooling channels are illustrated. The cooling performances of the designed heat transfer systems are discussed by the finite element method analysis and are compared with the results designed by other conventional design methods. [DOI: 10.1115/1.2426357]

Keywords: layout optimization, cooling channel, heat transfer, branch system, constructal theory

1 Introduction

The research frontier of heat transfer systems is being pushed in the direction of smarter and more effective distribution of cooling channels in order to meet the developing requirements, for example, the miniaturization, high speed, high density of electronic packages, and the high-precision productions by injection molding process. There is no doubt that the layout of a cooling channel impacts greatly on the cooling performance of a heat transfer system, thus the optimum layout design problem of cooling channels has attracted considerable attention during the past 2 decades. However, the most widely adopted cooling channel is the straight parallel cooling channel, and related research work is focused on the optimum spacing of the cooling channels [1–4]. It is noted that the straight parallel cooling channel has some major drawbacks, for example, great pressure drop and nonuniform temperature distribution of the whole system. In recent years, a remarkable layout design method termed constructal theory has been suggested by Bejan [5]. Its basic design principle is that better global performance of a heat transfer system is achieved when the thermal resistances are minimized, i.e., when the thermodynamic imperfection is distributed in space optimally [5]. It results in a tree-like network, in which every single geometric detail is determined theoretically. The constructal theory was first proposed in a problem of pure heat conduction [6,7], and was extended subsequently to design the layout of convective fins [8] and fluid flow [9–11].

Recently, some new styles of tree-like heat transfer systems, such as multi-scale structure and tree-shaped networks with loops, have been developed by the constructal theory [12,13].

On the other hand, computer modeling and visualization of branch systems in nature, such as lungs, vascular tissues, botanical trees (canopies, roots, leaves), etc., have emerged as a vibrant area of interdisciplinary research, attracting the efforts of biologists and doctors. The first geometrical computer model of a tree-like body has been proposed by Honda [14], in which the model is described by a relatively few parameters of branch angle and relative ratio of branch length. Since then, much related research has appeared in both botanical tree and animal vascular systems [15–18]. Although the morphologies and the growth environments of various branch systems in nature are different and their growth mechanisms are unknown in detail, the geometric forms (sizes, shapes, and topologies) of branch systems in nature can be considered to be resulted from such common growth principles that they must provide the easiest way for the current to flow through the whole network. As a result, the branch systems in nature always show an approximate global optimal performance that can minimize the costs of construction and maintenance of the fluid transportation system under the restraints of a growth environment [19].

It is noted that there are similarities between the branch systems in nature and the engineering systems and structures, because shapes and structures spring from the struggle for better functional performance in both nature and engineering. Thus, it can be expected that optimum layout of the cooling channel in a heat transfer system would be obtained by the generation method based on the growth mechanism of branch systems in nature. Actually, the

---

relationship of layout pattern between the branch systems in nature and engineering systems and structures has been revealed by some recent research. From the engineering point of view, the results of the constructal theory for designing the layout of heat transfer system have shown that the thought of the objective and constraints principle used in engineering is also the growth mechanism of natural flow systems [5]. In contrast, based on a growing and branching tree model, we have succeeded in optimum design of stiffener layout patterns for plate and shell structures to achieve minimum compliance and maximum natural frequency [20,21].

In this paper, an innovative layout design methodology of cooling channels in the heat transfer system by utilizing the optimality of branch systems in nature is suggested. The method is based on such essential characteristics of branch systems in nature that branches can grow by adapting themselves automatically to the growth environments in order to achieve a better global functional performance, such as the maximum absorption of nutrition or sunlight in plants and the intelligent blood distribution of a vascular system in the animal body. Because there are similarities between the branch systems in nature and heat transfer systems in engineering, it can be expected that optimum layout of the cooling channel in the heat transfer system would be obtained by utilizing the generation method based on the growth mechanism of branch systems in nature. First, the common optimality and growth mechanisms of branch systems in nature are studied, and a reproduction approach of the emergent process of branch systems is proposed. Branches are grown under the control of a so-called nutrient density so as to make it possible that the distribution of branches is dependent on the nutrient distribution. The growth of branches also satisfies the hydrodynamic conditions and the minimum energy loss principle. Then, the generation method of branch systems in nature is applied to the layout design problem of a heat transfer system. If the so-called nutrient density in the generation process of the branch system is referred to as the heat energy in a heat transfer system, the distribution of branches is responsible for the distribution of cooling channels. Because the simulated branch system can grow adaptively corresponding to the nutrient distribution, the cooling channel can be constructed adaptively under the control of the heat energy so as to make it possible to achieve comparative uniform temperature distribution of the whole heat transfer system. Having similar optimality of branch systems in nature, the constructed cooling channel can be designed flexibly and effectively in any shape of perfusion volume to be cooled adaptively to very complex thermal boundary conditions. The design problems of both a conductive cooling channel and a convective cooling channel are studied, and the layouts of two-dimensional and three-dimensional cooling channels are illustrated. The cooling performances of the designed cooling channels are discussed by the finite element method (FEM) analysis and are compared with the results designed by other conventional design methods.

2 Reproduction of Emergent Process of Branch Systems in Nature

It is necessary to reproduce the emergent process of branch systems in nature in order to apply their optimality to engineering design. As shown in Fig. 1, a fluid transportation branch system between a point M and a finite-size volume V is to be reproduced, in which Q_0 is the total volumetric flow through the point M, and Q_i is the volumetric flow at any point belonging to the volume V.

2.1 Growth Mechanism. A typical fluid transportation branch system in nature which has the most common essential characteristics is: (1) a dichotomous hierarchical branch system; (2) a network over all the specified perfusion space; (3) a system with minimum energy loss; (4) a flow system satisfied the hydrodynamic constraints of fluid pressure and flow; and (5) a network grown adaptively to the local growth environment. In order to
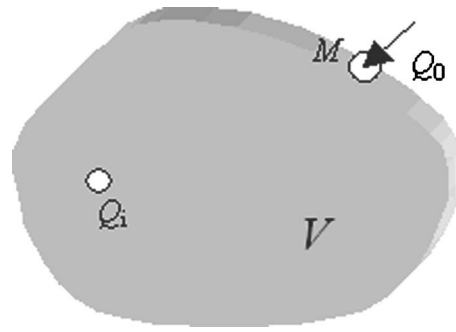
Fig. 1 A fluid flow between a point and a finite-size volume

reproduce the emergent process of such a branch system, a certain nutrient density is supposed in advance to distribute over all the specified perfusion space, which can be considered as the water or fertilizer distribution in the soil when the root system of a plant grows. Then, a dichotomous hierarchical branch system, geometries of which are shown in Fig. 2, begins to grow from seed (point M in Fig. 1) and extends over all the specified perfusion space (the finite-size volume V in Fig. 1) by the restraints of minimum energy loss and the hydrodynamic conditions. Branches grow adaptively according to the local growth environment, i.e., toward the higher nutrient space similar to the hydrotropism in the root system of a plant. Thus, the distribution of branches is dependent on the distribution of the initial nutrient density in order to absorb nutrition as much as possible. As a result, during the generation process of the branch system, the average nutrient density decreases and the nutrient distribution over the perfusion space tends to be uniform. The prerequisites to construct such a fluid transportation branch system are described as follows:

1. Branching law stands for the relationship of radii between the parent branch and the daughter branches, which is adopted at every bifurcation point. For a dichotomous branch system, it is formulated by the following Eq. (1)

$$r_0^\lambda = r_1^\lambda + r_2^\lambda \tag{1}$$

where r_0, r_1, and r_2 are radii of the parent branch and the daughter branches, respectively, as shown in Fig. 2. The bifurcation exponent, λ, is physiologically reasonable when it is in the range of $2 \le \lambda \le 3$ [17]. Murray's law shows when $\lambda = 3$ the energy loss for transporting material throughout the whole network is made minimum.
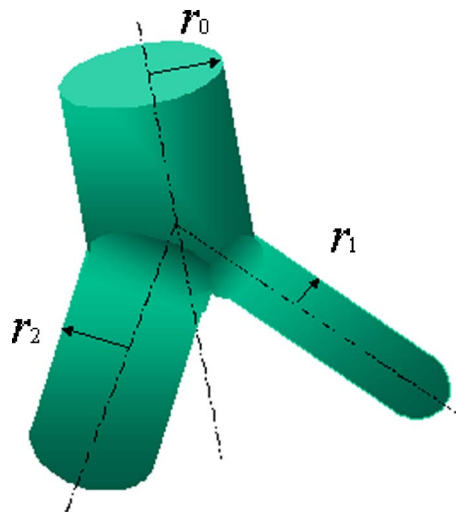
Fig. 2 Geometry of a dichotomous branch system

2. Growing law relates to the growing direction and the growing velocity of a new branch, which is assumed to be dependent on the local nutrient distribution (adaptive growth). A new terminal site is always positioned at the point with the highest nutrient density in the local growth space around the grown branches. If there is more than one point having the highest nutrient density in the local growth space, it is selected by a pseudo-random number sequence (PRNS).

3. The hydrodynamic conditions are assumed so that each terminal branch has the same flow and pressure to bathe the whole perfusion space evenly. Such hydrodynamic characteristics are similar to that of arterial vascular systems in the human body [17]. The branches are assumed to be cylinders. Flows in the branches are assumed as fully developed laminar flow, which obey Poiseuille's law formulated by the following Eq. (2)

$$Q = \frac{\pi r^4}{8\nu} \frac{\Delta P}{l} \qquad (2)$$

where Q is the volumetric flow rate; ΔP is the pressure drop; r and l are the radius and the length of the vessel; and ν is the dynamic viscosity of the fluid.

4. The criterion of optimality is defined in terms of the functional structure of the branch system, which is the volume of the whole branch system [22] in the suggested model. So the branch system is designed in such a way that the volume of it is minimized

$$V = \sum_{i=1}^{n} r_i^2 l_i \rightarrow \min \qquad (3)$$

where r_i, l_i are the radius and the length of branch i; and n is the total number of branches.

According to the above prerequisites, the branch system can be grown under the control of the nutrient density, and by satisfying the hydrodynamic conditions, as well as the minimum energy loss principle. The growth process stops when the average nutrient density in the perfusion space cannot be decreased anymore. It implies that no more branches can be grown in the perfusion space because of lack of either nutrition or fluid pressure.

2.2 Simulation Results.

2.2.1 Branch Systems Generated on Circular Perfusion Areas.
First, branch systems are generated on some circular perfusion areas to show the characteristics of the simulated branch systems and to discuss some influence factors introduced in the generation method.

2.2.1.1 Emergent process of branch system.
Figures 3(a)–3(d) show the emergent process of a two-dimensional branch system generated on a circular perfusion area, in which the numbers of branches in the growth process are 501, 1001, 2001, and 6743, respectively. The initial nutrient density is distributed uniformly. Murray's law is adopted as the branching law, i.e., the bifurcation exponent λ in the law is assumed to be 3. The PRNS is selected as 2 when a new terminal site is located in the local growth space. The local growth space ratio (LGSR) is set as 1/25, which will be discussed later. The final number of branches is 6743. If the circular perfusion area is considered as a plate with the thickness of 1/14 of its radius, the branch volume fraction, i.e., the ratio of the branch volume to the whole plate volume, is 1.56%.

Figures 4(b)–4(d) show the emergent process of a two-dimensional branch system generated on a circular perfusion area distributed with nonuniform nutrient density. The nutrient distribution is shown in Fig. 4(a), in which the circular perfusion area is divided symmetrically into four parts, and two diagonal parts are assigned with the same nutrient densities. The ratio of the lower nutrient density to the higher nutrient density is assumed to
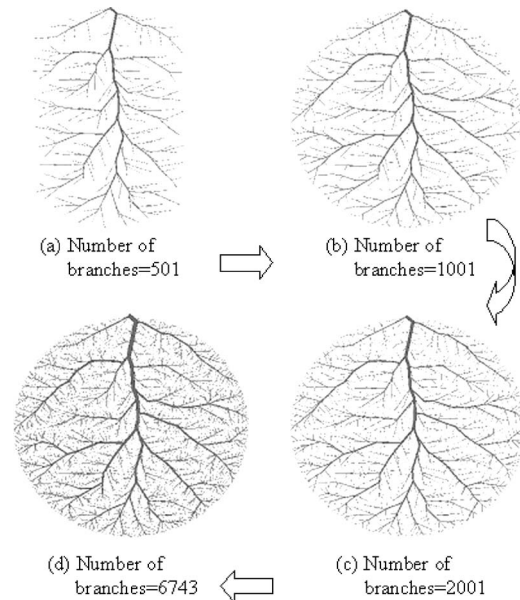
Fig. 3 Emergent process of a branch system generated on a circular perfusion area with uniform nutrient density

be 0.6. Murray's law is adopted as the branching law as well. The PRNS and the LGSR are selected as 4 and 1/25, respectively. The final number of branches is 5583, and the branch volume fraction is 1.50% which is calculated under the same assumption as Fig. 3.

As shown in Figs. 3 and 4, the following essential characteristics of the simulated branch systems can be found:

1. The simulated branch systems can fill up the whole specified spaces and the distributions of branches are dependent on the assigned distribution of nutrient densities. It is obvious that the distribution density of branches is almost uniform in the case of uniformly distributed nutrient density (Fig. 3(d)), while the distribution densities of branches generated on the higher and the lower nutrient density areas are distinctly
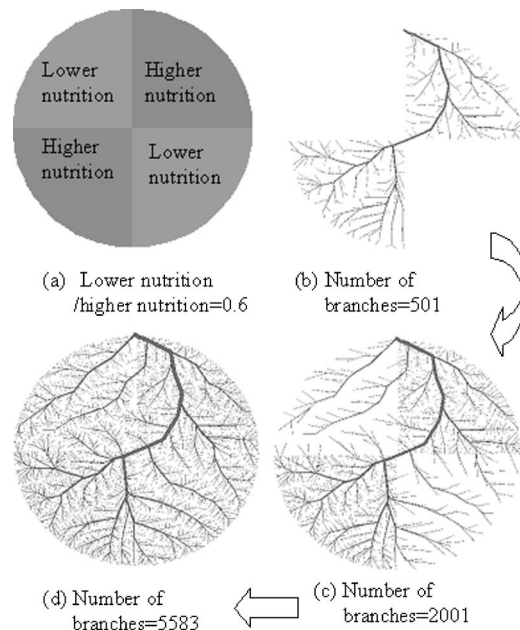

Fig. 4 Emergent process of a branch system generated on a circular perfusion area with nonuniform nutrient density
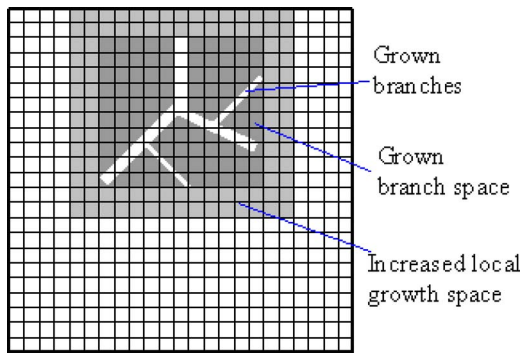
Fig. 5 Local growth space in two-dimensional perfusion area

(a) LGSR=4/75(8/150)
(Branch volume fraction =0.56%, Number of branches=1071)

(b) LGSR=7/150
(Branch volume fraction =1.55%, Number of branches=6653)

(c) LGSR=1/25(6/150)
(Branch volume fraction =1.60%, Number of branches=6953)

(d) LGSR=2/75(4/150)
(Branch volume fraction =1.95%, Number of branches=9023)

Fig. 6 Branch systems resulted from different local growth space ratios (LGSR)

different in the case of nonuniformly distributed nutrient density (Fig. 4(d)). Consequently, the nutrient density is the most important factor impacted on the morphology of the simulated branch system. This characteristic can be considered to be responsible for the adaptive growth characteristics of branch systems in nature, for example, the hydrotropism of a root system of the plant, and the phototropism of a tree branch system.

2. During the growth process of the branch system generated on the area with the uniformly distributed nutrient density (Fig. 3), a trunk grows first, and some boughs grow spreading the whole perfusion area at very initial period. However, a number of twigs finally grow. On the other hand, in the case of the nonuniformly distributed nutrient density (Fig. 4), a trunk, boughs, and some twigs grow on the higher nutrition density area at first, and boughs spread the lower nutrition density area latterly. Finally, a number of twigs grow spreading the whole perfusion area.

3. The simulated branch system has both thicker and thinner size levels, which can be considered to be responsible for the characteristics of a fluid transportation branch system in nature that the thicker branches convey a long-distance material transportation, and the thinner ones exchange material with the environment.

By comparing with the essential characteristics of branch systems in nature, it can be said that the simulated branch systems are qualitatively similar to the branch systems in nature.

2.2.1.2 Branch systems resulted from different local growth space ratios. The new terminal site at each growth step can be selected only in the local growth space, which is similar to the growth mechanism of a root branch system of a plant that the distal branches have sentience of the local growth environment for extending new branches. The local growth space is described as a rectangular area in a two-dimensional branch system, which is the grown branch space adding to the increased local growth space. The grown branch space illustrated as the dark gray area in Fig. 5 is a space including all the grown branches, while the increased local growth space illustrated as the light gray area in Fig. 5 includes a few unit elements in up, down, left, and right directions. In order to grow branches evenly in all directions, the increased numbers of unit elements along all directions are assumed to be the same. New terminal sites cannot be selected beyond the local growth space. The parameter of the local growth space is defined as LGSR, which is the ratio of n_i/n_t, where n_i is the increased unit element number along one direction in the increased local growth space, and $n_t=\max(n_{tx}, n_{ty})$, in which n_{tx} and n_{ty} are the total unit element numbers of the whole growth space along the horizontal and the vertical directions.

Figure 6 shows the branch systems resulted from different LGSR, in which the LGSR is set as: (a) 4/75, (b) 7/150, (c) 1/25, and (d) 2/75, respectively. The PRNS is set as 6 and Murray's law
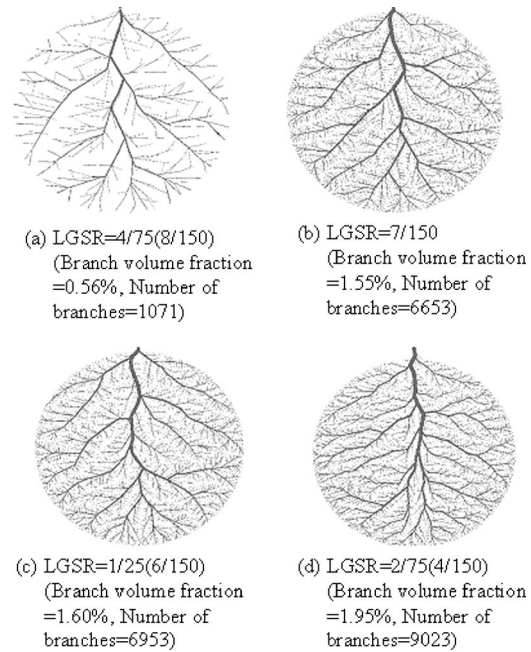
is adopted. It is found that the branch volume fractions increase by decreasing the value of LGSR, which are 0.56%, 1.55%, 1.60%, and 1.95%, respectively. And a similar changing tendency is found for the total number of segments. The branches are long and straight in the case of larger LGSR (Figs. 6(a) and 6(b)), while they are short and curved in the case of smaller LGSR (Figs. 6(c) and 6(d)). It is noted that too large LGSR results in too thin and too long branches (Fig. 6(a)), which induce a very great viscous resistance and pressure consumption. As a result, new branches may not be grown in some areas because of lack of pressure drop, and the branch system consists of too small a number of branches. Therefore, the LGSR cannot be selected too large, similar to the fact that the distal branches of a root system in a plant cannot detect too large a growth environment for extending new branches.

2.2.1.3 Branch systems resulted from different pseudo-random number sequences. The morphology of a branch system is impacted by the position of the new terminal site at each growth step. However, a new terminal site is selected on where the nutrient density is highest in the local growth space. Therefore, if there is more than one point having the highest nutrient density in the local growth space, different PRNSs for locating the new terminal site must result in different topologies of branch systems. Figure 7 shows the branch systems resulted from different PRNSs, in which the PRNS is set as: (a) 4, and (b) 8, respectively. The LGSR is set as 1/25 and Murray's law is adopted. By comparing with Figs. 3(d) and 6(c), where the PRNSs are set as 2 and 6, respectively, it can be found that different topologies are formed because of different PRNSs. However, the essential characteristics of these branch systems are similar and the branch volume fractions for all cases are also very close. This characteristic of the simulated branch systems is similar to branch systems in nature that branches extend themselves randomly under the control of the adaptive growth rules, but the basic characteristics of each kind of branch system in nature are very alike because of the same genetic factors.

2.2.1.4 Branch systems resulted from different branching laws. The topology of a branch system is also dependent on the bifurcation exponent, λ, governing the shrinkage of radii from

(a) PRNS=4
(Branch volume
fraction =1.58%)

(b) PRNS=8
(Branch volume
fraction =1.59%)

Fig. 7   Branch systems resulted from different pseudo random number sequences (**PRNS**)

parent to daughter segments. It is noted again that $2 \leq \lambda \leq 3$ is indicated by some experimental measurements and is considered reasonable by most of the researchers.

Figure 8 shows the branch systems resulted from different bifurcation exponents, in which λ is set as: (*a*) 2.5, and (*b*) 3.5, respectively. The PRNS and the LGSR are set as 6 and 1/25. By comparing with Fig. 6(*c*), w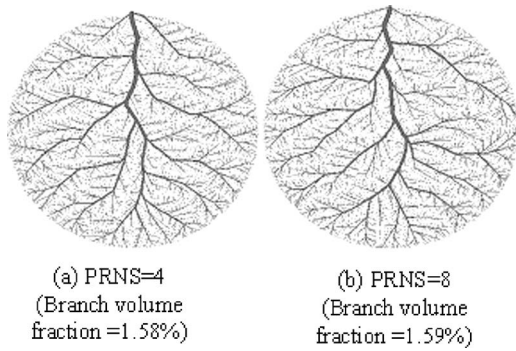here λ is set as 3.0 (Murray's law), it is found that different topologies are formed because of the different bifurcation exponents λ. It is obvious that a smaller value of λ results in larger cross sections of big segments as compared to small ones, while the difference of cross-sectional areas between the larger and the smaller segments decreases when λ increases. On the other hand, different values of λ have a distinct impact on the distribution of flow velocity and the pressure profile from root segment to terminal segments. Moreover, it is noted from the simulation results that the branch volume fraction of λ =3.0 is smallest among three cases, i.e., Murray's law results in the branch system with the smallest volume.

2.2.2 Branch Systems Generated in Several Perfusion Spaces With Different Shapes. Figure 9(*a*) shows a rectangular perfusion area assigned with a complex distribution of the nutrient density, in which the rectangular area is divided into six equal parts, and the higher and the lower nutrient densities are assigned alternately. The ratio of the lower nutrition to the higher nutrition is set as 0.6. The corresponding simulated branch system is shown in Fig. 9(*b*), in which the LGSR and the PRNS are set as 1/50 and 6, and Murray's law is adopted. It is found that the branch system can fill up the whole rectangular perfusion areas as well, even if there are corners. And it is obvious that the distribution densities of branches on the higher and the lower nutrition density areas are distinctly different. If the rectangular perfusion area is considered as a plate with the thickness of 3/100 of its long edge length, the branch volume fraction of the system is 1.60%.

Figure 10 shows a branch system generated in a half spherical

(a) λ =2.5
(Branch volume
fraction =2.11%)

(b) λ=3.5
(Branch volume
fraction =1.69%)
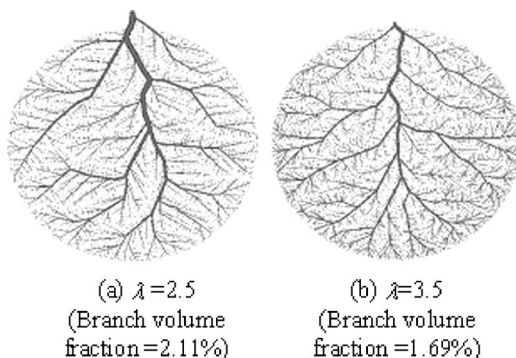
Fig. 8   Branch systems resulted from different branching laws
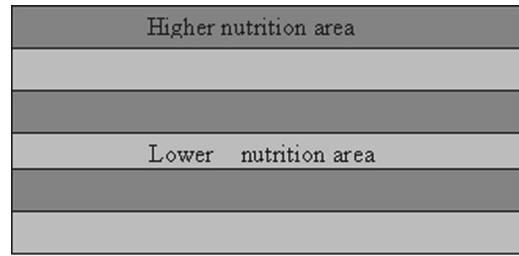
(a) Nonuniformly distributed nutrient density
(Lower nutrition/higher nutrition = 0.6)
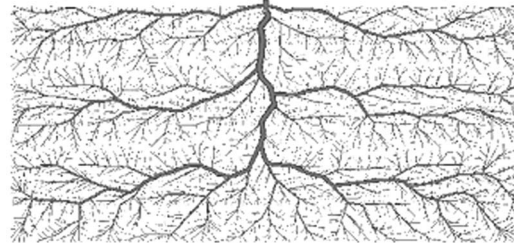
(b) Simulated branch system
(Branch volume fraction =1.60%)

Fig. 9   Branch system generated on a rectangular perfusion area with nonuniformly distributed nutrition density

surface perfusion space, in which: (*a*) shows the three-dimensional image; (*b*) shows the front view; and (*c*) shows the bottom view. The LGSR and the PRNS are set as 1/100 and 6, and Murray's law is adopted. The initial nutrient densities are distributed uniformly. It is found that the main characteristics of the three-dimensional branch system are similar to that of the two-dimensional branch system.

In conclusion, it is said that the suggested generation method can grow branch systems to fill up any specified perfusion area

(a) Three-dimensional image
(Branch volume fraction=0.53%,
Number of branches=2103)

(b) Front view   (c) Bottom view
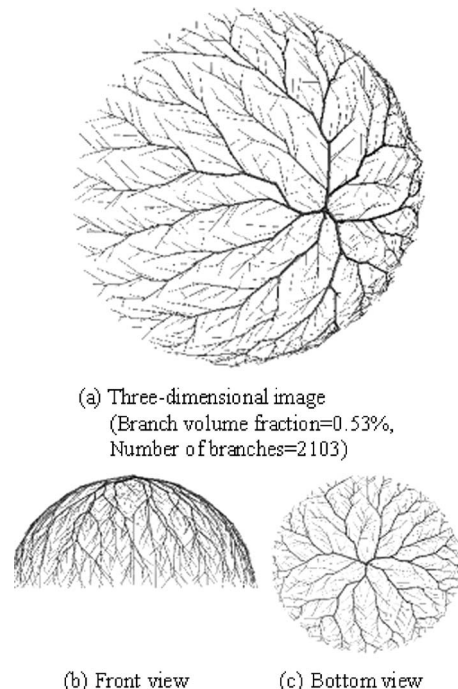
Fig. 10   Branch system generated in a half spherical surface

adaptively to the arbitrarily distributed initial nutrition densities. And the generated branch systems are qualitatively similar to the branch systems in nature.

3 Layout Design of Cooling Channel in Heat Transfer System

In a uniform composition material, the heat energy is a function of temperature. If the concept of the so-called nutrient density in the generation process of branch systems is referred to as the heat energy in a heat transfer system, and the material dealt with is assumed to be a uniform composition, the growth process of branches can be considered as an adaptive growth of the cooling channel according to the local temperature. Thus it is possible to apply the generation method based on the growth mechanism of branch systems in nature to the layout design of cooling channel in heat transfer systems.

3.1 Conductive Cooling Channel Design. A conductive cooling channel is an insert made of a high thermal conductivity material in a background matrix, which is made of a low thermal conductivity material. The ratio of the thermal conductivity of the high-conductivity material (k_p) to the low-conductivity material (k_0) is usually assumed to be $k=k_p/k_0 \gg 1$ so as to make it possible to remove the heat generated in the matrix through the conductive cooling channel. The layout design of the conductive cooling channel is to decide the optimum distribution of the finite amount of material k_p in the matrix such that the temperature distribution of the whole volume can be made as uniform as possible. The problem is worth studying because of the engineering applications such as the smaller and smaller electronic package dimensions. The miniaturization makes the convective cooling impractical, because the ducts through which the coolant must flow take up too much space.

A plate is considered as the finite-size volume to be cooled. A natural branch-like conductive cooling channel is constructed by the generation method based on the growth mechanisms of branch systems in nature, the cross section of which is assumed to be a rectangle with the same thickness as the plate. The width of the channel, however, is assumed to be the same as the diameter of the corresponding segment in the simulated branch system.

First, a circular plate with the ratio of the thickness to the diameter of 0.01 is considered. The plate is assumed to be made of glass-reinforced polymer, the thermal conductivity of which is set as $k_0=0.2$ W/mK. The layout of the conductive cooling channel is based on the original branch system shown in Fig. 6(c), in which some branches with smaller cross sections are omitted. The cooling channel is assumed to be made of copper, the thermal conductivity of which is set as $k_p=400$ W/mK. Thus, the ratio of the thermal conductivities of the high-conductivity material (k_p) to the low-conductivity material (k_0) is $k=k_p/k_0=2000.0$. It is noted that the original branch system is generated under a uniformly distributed nutrient density, so the distribution of volumetric heat-generating rate in the background matrix is correspondingly assumed to be uniform, which is $q'''=10^5$ W/m^3. The temperature at the heat sink located at the boundary is set as $T_{min}=10°$C. The whole structure is insulated from the environment.

Figure 11(a) shows the FEM model created by several imaged CT scan slides by the image-based structural analysis software VOXELCON, in which the channel volume fraction is 9.71%. Figure 11(b) shows the temperature field of the whole plate, in which the lighter color stands for the higher temperature and the darker one stands for the lower temperature. The maximum temperature is $T_{max}=38.85°$C. The nondimensional global volume-to-point resistance, which is defined as the ratio $\Delta \tilde{T}=(T_{max}-T_{min})k_0/(q'''A)$ (A is the area of the plate) is 0.0074.

Next, the temperature field of a circular plate with a natural branch-like conductive cooling channel under a nonuniformly distributed volumetric heat-generating rate is analyzed. The geomet-

(a) FEM model
(Channel volume
fraction=9.71%)

(b) Temperature field
T_{max}=38.85°C

Fig. 11 FEM model and temperature field of a circular plate with a natural branch-like conductive cooling channel under uniform heat-generating rate

ric and material parameters are assumed to be the same as that of Fig. 11. The conductive cooling channel is based on the original branch system shown in Fig. 4(d), in which the circular area was divided into symmetrical four parts, and two diagonal parts were assigned with the same nutrient densities. The ratio of the lower nutrient density to the higher nutrient density was assumed to be 0.6. According to its generation conditions, the distribution of the volumetric heat-generating rate over the circular plate is set to be identical to that of the nutrient density (the same location and the same ratio), as shown in Fig. 12(a). The higher heat-generating rate illustrated as the darker color in Fig. 12(a) is set as $q'''_h=10^5$ W/m^3, while the lower one illustrated as the lighter color in Fig. 12(a) is set as $q'''_l=0.6 \times 10^5$ W/m^3. The other analysis thermal parameters are identical to that adopted in Fig. 11. Figures 12(a) and 12(b) show the FEM model with the channel volume fraction 6.95%, and the temperature field of the whole plate with the maximum temperature $T_{max}=40.09°$C. The nondimensional global volume-to-point resistance $\Delta \tilde{T}$ is 0.0096, where $q'''=(q'''_h+q'''_l)/2$.

3.2 Convective Cooling Channel Design. A convective cooling channel means the heat generated in the matrix is removed by a flow of coolant. A flat plate or a curved shell is considered, inside of which a natural branch-like convective cooling channel is constructed. As similar to that done for the conductive cooling channel, the layout of a convective cooling channel is based on a certain corresponding original branch systems generated by the method based on the growth mechanisms of branch systems in nature. In order to make the coolant flow through the channel, the convective cooling channel is assumed as a circular pipe, the diameter of which is assumed to be identical to that of the corre-

(a) FEM model
(Channel volume
fraction=6.95%)

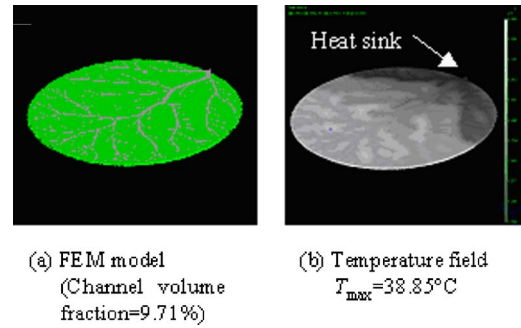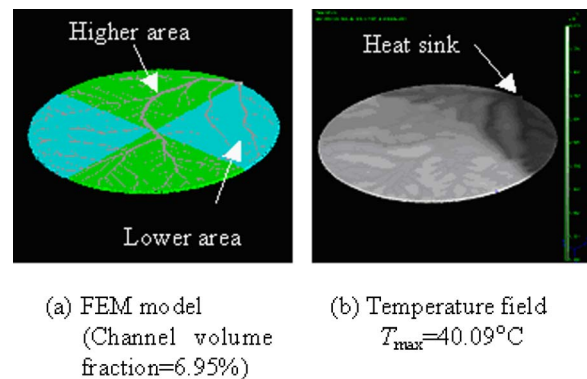(b) Temperature field
T_{max}=40.09°C

Fig. 12 FEM model and temperature field of a circular plate with a natural branch-like conductive cooling channel under nonuniform heat-generating rate

Fig. 13 Analysis model of a circular plate with a convective cooling channel

Table 1 Analysis parameters of a plate applied a uniform heat flux

Thermal conductivity (beryllium–copper alloy)	$k=260.0$ W/mK
Heat transfer coefficient (forced air convection)	$h=500.0$ W/m^{2}K
Heat flux (uniform distribution)	$q=5.0 \times 10^5$ W/m^2
Temperature at inlet	$T_{min}=20.0\,°$C
Volumetric flow at inlet	$Q=8 \times 10^{-5}$ m^3/s

sponding segment in the original simulated branch system. The heat generated in the matrix is due to a certain distributed heat flux applied on the surface of the plate or shell.

Actually, this problem is a transient heat conduction problem between the solid and the coolant in the pipe. However, because our prime goal here is to confirm the heat conduction efficiency of the heat transfer system with a natural branch-like convective cooling channel, the problem is simplified as a steady-state heat conductive problem, which can be dealt with by the image-based structural analysis software VOXELCON. However, it is necessary to consider the energy balance in the system responsible for the fluid convection. Because the temperature of coolant becomes higher and higher by passing through the cooling channel from inlet to outlet, the energy balance due to the fluid convection can be approximately considered as the distribution change of the temperatures at the channel wall, which can be formulated by the following Eq. (4) [23]

$$\Delta T_{wi} = \frac{q l_i}{\rho_c C_c r_i u_{ci}} \qquad (4)$$

where q is the heat flux applied uniformly on the upper half part of the pipe; ρ_c and C_c are the density, and the specific heat of coolant, respectively, and u_{ci} is the average velocity of coolant through branch i, which is dependent on the branching law (Eq. (1)) and is given by

$$u_{ci} \propto r_i^{\lambda-2} \qquad (5)$$

Equation (5) implies if the bifurcation exponent $\lambda=2$, the average velocity of coolant throughout the whole network keeps constant; and if the bifurcation exponent $\lambda>2$, the average velocity of coolant becomes slower and slower by flowing through the successive branch generations. It is noted when Murray's law ($\lambda=3$) is adopted, the ratio of average velocity of coolant through the parent branch to that through the daughter branch is simply proportional to the ratio of their radii. In conclusion, if the volumetric flow and the temperature at inlet are specified, the temperature at each segment wall can be determined by Eq. (4).

In the following design examples, the matrix is assumed to be made of beryllium–copper alloy, the thermal conductivity of which is set as $k=260$ W/mK. The coolant flowed through the cooling channel is assumed as water at $20\,°$C, the viscosity of which is 10^{-3} Pa s.

First, a circular plate with a branch-like convective cooling channel in its middle plane is considered. The thickness of the plate is assumed to be 1/14 of its radius. As shown in Fig. 13, a uniformly distributed heat flux is applied on the top surface of the plate, the bottom surface is insulated from the environment, and the circumference is on the forced air convection. The analysis parameters are summarized in Table 1.

Figure 14 shows the FEM models and temperature fields of three circular plates with branch-like convective cooling channels resulted from different branching laws. The branch-like convective cooling channels in the heat transfer systems are constructed

based on the corresponding branch systems shown in Figs. 8(a), 6(c), and 8(b), in which the bifurcation exponents λ are 2.5, 3.0, and 3.5, respectively. The left part of Fig. 14 shows the middle planes of the FEM models, in which the channel volume fractions are 1.77% for $\lambda=2.5$, 1.28% for $\lambda=3.0$, and 1.32% for $\lambda=3.5$, respectively. The right part of Fig. 14 shows the temperature fields that are scaled by the maximum temperature $T_{max}=44.67\,°$C among the three cases. The maximum temperatures are $T_{max}=44.67\,°$C for $\lambda=2.5$, $T_{max}=33.94\,°$C for $\lambda=3.0$, and T_{max}
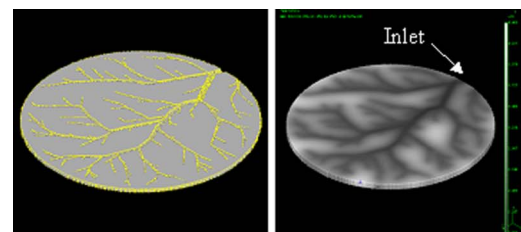
Channel volume
fraction =1.77%
FEM model

$T_{max}=44.67\,°$C
Temperature field

(a) $\lambda=2.5$
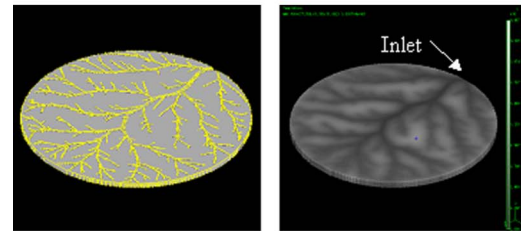
Channel volume
fraction =1.28%
FEM model

$T_{max}=33.94\,°$C
Temperature field

(b) $\lambda=3.0$
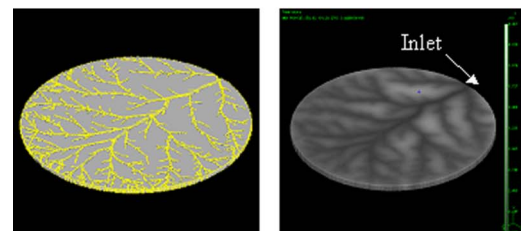
Channel volume
fraction =1.32%
FEM model

$T_{max}=34.20\,°$C
Temperature field

(c) $\lambda=3.5$

Fig. 14 FEM models and temperature fields of heat transfer systems with branch-like convective cooling channels resulted from different branching laws

Channel volume
fraction=1.26%
(a) FEM model

T_{max}=32.55°C
(b) Temperature field
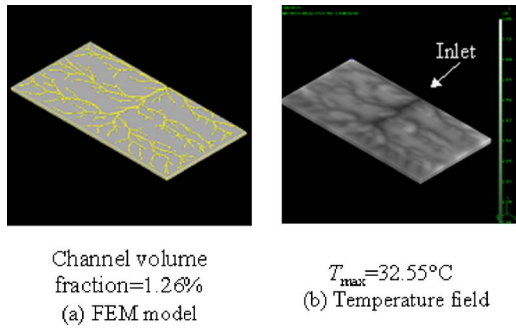
Fig. 15 FEM model and temperature field of heat transfer system with branch-like convective cooling channel applied non-uniformly distributed heat flux

=34.20°C for λ=3.5, respectively. It is easy to find that the case of λ=3.0 results in the most uniform temperature distribution and the most nonuniform one is the case of λ=2.5. It is noted that the volumes of the convective cooling channels from small to large are put in order as λ=3.0, 3.5, and 2.5, which is the same sequence with the uniformities of temperature distributions. The nondimensional global thermal conductance defined as the ratio $\tilde{C}=qA/[(T_{max}-T_{min})kR]$ (A and R are the area applied with heat flux, and the radius of the circular plate, respectively) is 21.66 for λ=3.0, which is 1.77 times of that of λ=2.5, and 1.02 times of that of λ=3.5. If the pressure drops in bends are ignored, the pressure drop ΔP between the inlet and the outlet of each branch-like convective cooling channel can be evaluated approximately by the Poiseuille's law (Eq. (2)), in which the terminal volumetric flow at each outlet is assumed with the same value. The nondimensional resistance $\Delta \tilde{P}=\Delta PV/(8\nu Q)$, where V is the total volume of the cooling channels, is 5.52×10^4 for λ=3.0, which is 1.07 times of that of λ=2.5, and 0.75 times of that of λ=3.5. It is found that although the pressure consumption in the case of λ=2.5 is a little smaller than that in the case of λ=3.0, λ=3.0 results in much greater global thermal conductance and more uniform temperature distribution. As a result, Murray's law is the most effective branching law for constructing the branch-like convective cooling channel system. The reason is that Murray's law is derived from such principle that the energy loss due to the viscous friction throughout the whole network is minimum, which provides the easiest way for the coolant to pass.

Figure 15 shows the middle plane of the FEM model and temperature field of a rectangular plate with the aspect ratio of 0.5 and the ratio of the thickness to the short edge length of 3/50. The branch-like convective cooling channel is constructed based on the branch system shown in Fig. 9(b), in which the channel volume fraction is 1.26% by omitting some branches with smaller cross sections, as shown in Fig. 15(a). The analysis parameters are identical to that listed in Table 1, except the distribution of the heat flux and the volumetric flow at the inlet. The heat flux is distributed on the top surface with the same distribution as the nutrient density illustrated in Fig. 9(a), in which the stronger and the weaker heat fluxes are assumed as q_h=5.0×10⁵ W/m² and q_l=3.0×10⁵ W/m², respectively, and the volumetric flow at the inlet is assumed to be Q=6×10⁻⁵ m³/s. As shown in Fig. 15(b), the maximum temperature is 32.55°C. The nondimensional global thermal conductance defined as the ratio $\tilde{C}=qA/[(T_{max}-T_{min})kL]$ (L is the length of the rectangular plate) is 7.36, where $q=(q_h+q_l)/2$, and the nondimensional resistance $\Delta \tilde{P}$ is 5.61×10⁴.

Figure 16 shows a half spherical surface shell model with the ratio of the thickness to the inner radius of 1/14. A branch-like convective cooling channel with the channel volume fraction 0.42% is constructed inside the shell, which is based on the origi-
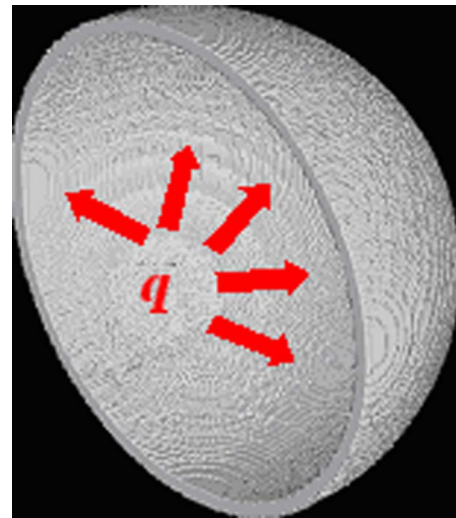
Fig. 16 Analysis model of a spherical surface shell with a branch-like convective cooling channel

nal branch system generated on the condition of the uniformly distributed nutrient density shown in Fig. 10. As shown in Fig. 16, a uniform heat flux, q=5.0×10⁴ W/m², is applied on the inner surface of the spherical shell, and its outer surface is on the forced air convection with the heat transfer coefficient h=500 W/m²K. The volumetric flow at the inlet is assumed to be Q=1.5×10⁻⁵ m³/s, and the temperature at the inlet of the cooling channel is assumed to be T_{min}=20.0°C. Figure 17(a) shows the FEM model of the cooling channel, and the temperature field of the whole structure is illustrated in Fig. 17(b), in which the maximum temperature is T_{max}=28.64°C. The nondimensional global thermal conductance defined as the ratio $\tilde{C}=qA/[(T_{max}-T_{min})kR]$ (A and R are the area and the radius of the inner spherical surface shell) is 6.49, and the nondimensional resistance $\Delta \tilde{P}$ is 4.79×10⁴.

As shown in the above design examples, it is said that the suggested design method can design the effective layout of the cooling channels in the matrix with any shape adaptively to very complex thermal boundary conditions.

3.3 Comparison With Cooling Channel Designed by Conventional Method. In order to validate the effectiveness of the suggested generation method, the cooling performances between the natural branch-like cooling channel designed by the suggested generation method and the horizontal–vertical tree-like cooling channels constructed by the constructal theory proposed by Bejan

(a) FEM model of channel
(Channel volume fraction
=0.42%)

(b) Temperature field
T_{max}=28.64°C
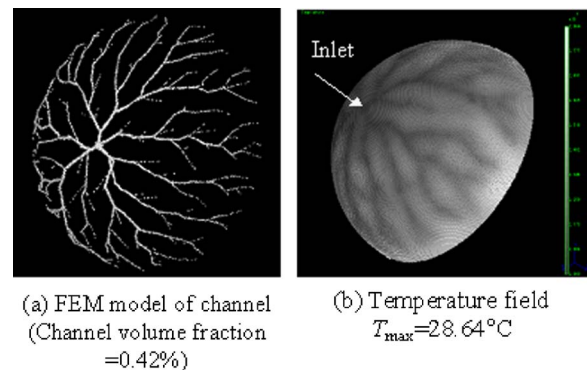
Fig. 17 FEM model and temperature field of a spherical shell with branch-like convective cooling channel
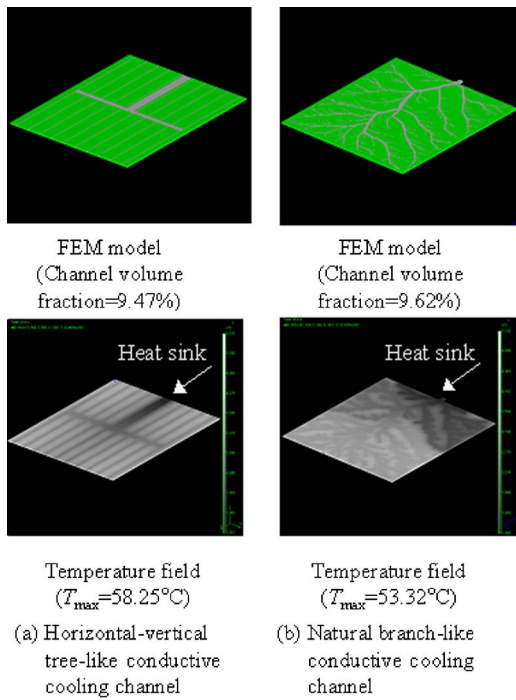
Fig. 18 Comparison of horizontal–vertical tree-like and natural branch-like conductive cooling channel

Fig. 19 Comparison of horizontal–vertical tree-like and natural branch-like convective cooling channel

[5] are compared.

The unique principle of the constructal theory for designing the conductive cooling channel is: every portion of the given volume can have its shape optimized such that its resistance to heat flow is minimum [5]. By utilizing this principle, the cooling channel is determined in a sequence of steps consisting of shape optimization and subsequent construction.

Figure 18(a) shows the FEM model and the corresponding temperature field of a square plate with a horizontal–vertical tree-like conductive cooling channel until second construction. The ratio of the thermal conductivities of the high-conductivity material to the low-conductivity material is assumed to be $k=k_p/k_0=3333.33$. The volumetric heat-generating rate is set as $q'''=10^5$ W/m^3, and is uniformly distributed over the whole plate. The shape of the plate is derived from the sequence of shape optimization and construction by the constructal theory, and the ratio of the thickness to the edge length is set as 0.01. The temperature at the heat sink is set as $T_{min}=10°$C, and the whole structure is insulated from the environment. As shown in Fig. 18(a), the channel volume fraction, i.e., the k_p material in which the whole allocated volume is 9.47%, and the maximum temperature is $T_{max}=58.25°$C. The nondimensional global volume-to-point resistance $\Delta \tilde{T}$ is 0.0048.

According to the geometries of the horizontal–vertical tree-like conductive cooling channel, a corresponding branch system is generated on a square perfusion area applied a uniformly distributed nutrient density, in which the design parameters, PRNS and LGSR, are set as 6 and 6/125, respectively. And Murray's law is adopted. Figure 18(b) shows the FEM model and the corresponding temperature field. Compared to the corresponding horizontal–vertical tree-like conductive cooling channel in Fig. 18(a), the channel volume fraction is 9.62%, and the maximum temperature is $T_{max}=53.32°$C which is a little lower. The nondimensional global volume-to-point resistance $\Delta \tilde{T}$ is 0.0043, which is 0.89 times that of the corresponding horizontal–vertical tree-like conductive cooling channel. It is found that both conductive cooling channels can achieve good cooling performances. However, it should be noted that it is just because the thermal boundary conditions are very simple (uniformly distributed heat-generating rates), the
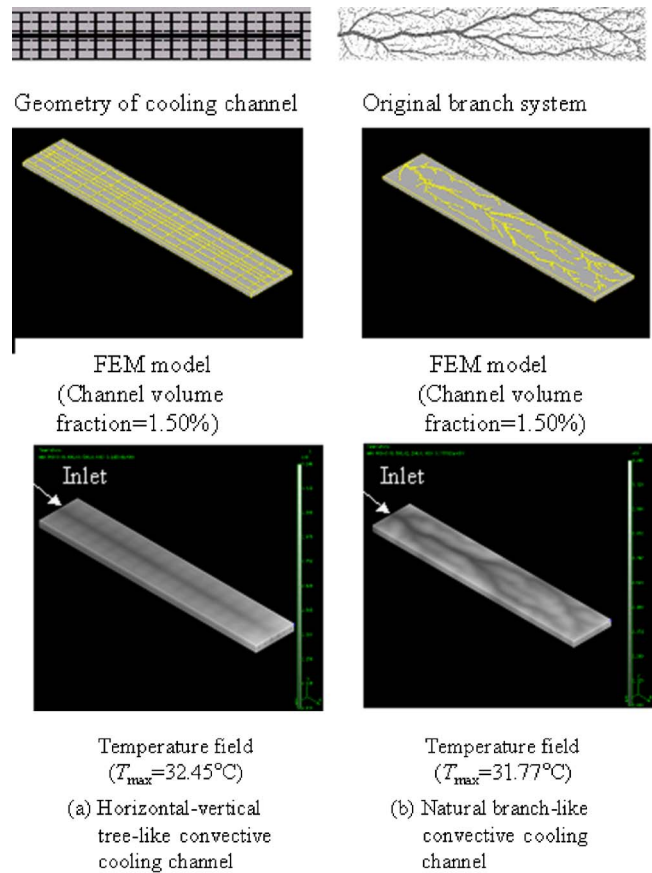
simple and regular distributed conductive cooling channel, i.e., the horizontal–vertical tree-like conductive cooling channel, is available and effective. If the heat-generating rate is applied nonuniformly, it is difficult for the constructal theory to design effective conductive cooling channel, while the flexible natural branch-like conductive cooling channel can be designed adapting to the arbitrary complex thermal boundary conditions. Moreover, because the shape of the design volume to be cooled is a result of shape optimization in the construction process when the constructal theory is adopted, it cannot be changed arbitrarily and be defined in advance. However, the shape of the design volume can be defined in advance and the natural branch-like conductive cooling channel can be designed to fill up the volume with any shape by the suggested generation method. Therefore, it can be said that the suggested generation method is more powerful for designing the conductive cooling channel and the designed cooling channel can remove the heat generated in the matrix effectively.

Figure 19 shows a comparison of the horizontal–vertical tree-like convective cooling channel and the natural branch-like convective cooling channel. The design objectives of the horizontal–vertical tree-like convective cooling channel are that the overall thermal conductance $qA/(T_{max}-T_{min})$ is maximum and the pumping power ΔP is minimum. As shown in the upper part of Fig. 19(a), the designed horizontal–vertical tree-like convective cooling channel until second construction consisted of 16×2 first constructions, each of which includes 3×2 elemental volumes. It is found that the finally constructed shape of the volume to be cooled is a slender rectangle. If the thickness of the plate is assumed to be 3/100 of its long length of the rectangle, the channel volume fraction is 1.50%. The heat flux, $q=5.0 \times 10^5$ W/m^2, is assumed to be uniformly distributed on the top surface of the

rectangular plate, the bottom surface is insulated from the environment, and the circumference of the plate is on the forced air convection with the heat transfer coefficient of h =500.0 W/m^{2}K. The volumetric flow at inlet Q is set as 2 $\times 10^{-5}$ m^3/s. If the volumetric flow of coolant at each outlet is assumed to be kept constant in order to bathe the whole volume evenly, the volumetric flow through each segment can be evaluated according to the continuity conditions that must be fulfilled by an incompressible flow through any bifurcation. The middle part of Fig. 19(a) shows the middle plane of the FEM model of the horizontal–vertical tree-like convective cooling channel, and the bottom part of Fig. 19(a) shows the temperature field of the plate, in which the maximum temperature is $T_{\max}$=32.45 °C. Thus, the nondimensional overall thermal conductance $\widetilde{C}=qA/[(T_{\max}-T_{\min})kB]$ (B is the width of the rectangular plate) is 18.52. It is found that hot spots (parts in lighter color) are concentrated on the tip edge of the plate far away from the inlet. The volumetric flow through each terminal channel is 1.04×10^{-7} m^3/s, and the nondimensional resistance $\Delta \widetilde{P}$ is 8.98×10^4.

A natural branch-like convective cooling channel is constructed under the same geometrical parameters as the horizontal–vertical tree-like convective cooling channel. The upper part of Fig. 19(b) shows the original branch system, in which the design parameters, PRNS and LGSR, are set as 6 and 6/125, respectively and Murray's law is adopted.

The middle part of Fig. 19(b) shows the middle plane of the FEM model, the channel volume fraction is identical to that of the horizontal–vertical tree-like convective cooling channel and the bottom part of Fig. 19(b) shows the temperature field of the structure under the same thermal boundary conditions as the horizontal–vertical tree-like convective cooling channel, in which the maximum temperature is $T_{\max}$=31.77 °C. Compared to the horizontal–vertical tree-like convective cooling channel, the maximum temperature of the natural branch-like convective cooling channel is a little lower, and the nondimensional overall thermal conductance $\widetilde{C}$ is 1.06 times greater. It can be found that the positions of the maximum temperatures for two types of convective cooling channels are the same, which are the vertexes of the rectangles far away from the inlets of coolant. The volumetric flow through each terminal channel is 1.05×10^{-7} m^3/s, which is close to that of the horizontal–vertical tree-like convective cooling channel, but the nondimensional resistance $\Delta \widetilde{P}$ is only 0.61 times that of the horizontal–vertical tree-like convective cooling channel. This is because the natural branch-like convective cooling channel is derived from the principle of minimum energy loss, which can provide much easier access for the current to flow through the network and results in much smaller pressure consumption. Moreover, as similarly noted for the conductive cooling channel design, the horizontal–vertical tree-like convective cooling channel has two major disadvantages that induce difficulties in the practical design problems, that is, the shape of the volume to be cooled cannot be specified in advance and it is difficult to design an effective cooling channel when complex thermal boundary conditions are specified.

4 Related Problems

The suggested design method of branch-like cooling channels is available not only because of the flexible design property and excellent cooling performances of the heat transfer systems with such types of cooling channels, but also because it has developed some innovative techniques, for example, metal stereolithography technology, to make it possible to fabricate such complex branch-like cooling channels. The metal stereolithography technology is an approach for manufacturing injection mold that including complex caves [24]. The technique utilizes a laser to solidify the physical model layer by layer from metal powder. Each new layer bonds to the previous, creating a solid object when complete.

It is necessary to collect coolant and guide it out of the system in a practical heat transfer system with a natural branch-like convective cooling channel, which is a topic of further study. The problem can be solved by several approaches, one of which is to apply a counterpart of the constructed cooling channel, as done in some branch systems in nature, such as the cardiovascular system in the human body. It is expected that the natural branch-like convective cooling channel system performs its heat energy transfer functions by using a double-tree branch structure, in which the cold coolant is pumped in and distributed to all parts of the volume to be cooled through one branch system, and then collected through another counterpart branch system, with a higher temperature.

5 Conclusions

This paper suggested an innovative layout design methodology of engineering systems and structures by utilizing optimality of branch systems in nature. As an example, the layout design problem of cooling channels in heat transfer systems has been studied, in which a conductive cooling channel and a convective cooling channel have been dealt with. The natural branch-like cooling channels can be grown adaptively under the control of local temperature so as to make it possible to achieve good cooling performance and they can be designed flexibly in any specified shape of perfusion volume to be cooled adaptively to very complex thermal boundary conditions. The effectiveness and validity of the suggested design method have been confirmed by some numerical examples and by comparisons of cooling performances with cooling channel systems resulted from other conventional design methods. It is expected that the suggested method can be applied to some more practical engineering design problems, such as cooling channels in injection molds, heat sinks in electronic packages, and so on.

References

[1] Ledezma, G. A., and Bejan, A., 1997, "Optimal Geometric Arrangement of Staggered Vertical Plates in Natural Convection," ASME J. Heat Transfer, **119**, pp. 700–708.
[2] Rocha, L. A. O., and Bejan, A., 2001, "Geometric Optimization of Periodic Flow and Heat Transfer in a Volume Cooled by Parallel Tubes," ASME J. Heat Transfer, **123**, pp. 233–239.
[3] Chen, S., and Liu, Y., 2002, "An Optimum Spacing Problem for Three-by-Three Heated Elements Mounted on a Substrate," Heat Mass Transfer, **39**(1), pp. 3–9.
[4] Kobus, C. J., and Oshio, T., 2005, "Development of a Theoretical Model for Predicting the Thermal Performance Characteristics of a Vertical Pin-Fin Array Heat Sink Under Combined Forced and Natural Convection with Impinging Flow," Int. J. Heat Mass Transfer, **48**(6), pp. 1053–1063.
[5] Bejan, A., 2000, *Shape and Structure, from Engineering to Nature*, Cambridge University Press, Cambridge, UK.
[6] Bejan, A., 1997, "Constructal-Theory Network of Conducting Paths for Cooling a Heat Generating Volume," Int. J. Heat Mass Transfer, **40**, pp. 799–816.
[7] Almogbel, M., and Bejan, A., 1999, "Conduction Tree With Spacing at the Tips," Int. J. Heat Mass Transfer, **42**, pp. 3739–3756.
[8] Bejan, A., and Dan, N., 1999, "Constructal Tree of Convective Fins," ASME J. Heat Transfer, **121**, pp. 675–682.
[9] Bejan, A., and Errera, M. R., 2000, "Convective Tree of Fluid Channels for Volumetric Cooling," Int. J. Heat Mass Transfer, **43**, pp. 3105–3118.
[10] Wechsatol, W., Lorente, S., and Bejan, A., 2002, "Optimal Tree-Shaped Networks for Fluid Flow in a Disc-Shaped Body," Int. J. Heat Mass Transfer, **45**(25), pp. 4911–4924.
[11] Gosselin, L., and Bejan, A., 2005, "Tree Networks for Minimal Pumping Power," Int. J. Therm. Sci., **44**(1), pp. 53–63.
[12] Silva, A. K., and Bejan, A., 2005, "Constructal Multi-Scale Structure for Maximal Heat Transfer Density in Natural Convection," Int. J. Heat Fluid Flow, **26**(1), pp. 34–44.
[13] Wechsatol, W., Lorente, S., and Bejan, A., 2005, "Tree-Shaped Networks with Loops," Int. J. Heat Mass Transfer, **48**(3–4), pp. 573–583.
[14] Honda, H., 1971, "Description of Form of Trees by the Parameters of Tree-

Like Body: Effects of the Branching Angle and the Branch Length on the Shape of the Tree-Like Body," J. Theor. Biol., **31**, pp. 331–338.

[15] Takenaka, A., 1994, "A Simulation Model of Tree Architecture Development Based on Growth Response to Local Light Environment," J. Plant Research, **107**(3), pp. 321–330.

[16] Takaki, R., and Kitaoka, H., 1999, "Virtual Construction of Human Lung," Forma, **14**(4), pp. 309–313.

[17] Schreiner, W., and Karch, R., 2000, "Constrained Constructive Optimization of Arterial Tree Models," *Scaling in Biology*, J. H. Brown, and G. B. West, eds., Oxford University Press, Oxford, UK, Inc., pp. 145–165.

[18] Schreiner, W., Karch, R., Neumann, M., Neumann, F., Szawlowski, P., and Roedler, S., 2005, "Optimized Arterial Trees Supplying Hollow Organs," Med. Eng. Phys., **28**(5), pp. 416–429.

[19] Lararbera, M., 1990, "Principles of Design of Fluid Transport Systems in Zoology," Science, **249**(8), pp. 992–1000.

[20] Ding, X., and Yamazaki, K., 2004, "Stiffener Layout Design for Plate Structures by Growing and Branching Tree Model (Application to Vibration-Proof Design)," Struct. Multidiscip. Optim., **26**, pp. 99–110.

[21] Ding, X., and Yamazaki, K., 2005, "Growth Technique of Stiffener Layout Pattern for Plate and Shell Structures to Achieve Minimum Compliance," Eng. Optimiz., **37**(3), pp. 259–276.

[22] Wang, Z., Zhao, M., and Yu, Q., 2001, "Modeling of Branching Structures of Plants," J. Theor. Biol., **209**, pp. 383–394.

[23] Ding, X., 2004, "Topology Design Optimization for Structures by Adaptive Growth Method—Learning from Branch Systems in Nature," Ph.D. dissertation, Kanazawa University, Kanazawa, Japan.

[24] Yoneyama, T., et al., 2001, "Cooling Enhance and High-Precision of Injection Moulding Process Based on Powder Molding Mould With Cooling Channel Built-in," J. Jpn. Soc. Precis. Eng., **67**(12), pp. 1991–1995 (in Japanese).

Laminar Forced Convection From a Circular Cylinder Placed in a Micropolar Fluid

F. M. Mahfouz

Mechanical Power Department,
Faculty of Engineering,
Menoufia University,
Shebin-Elkom, Egypt
e-mail: fmahfouz64@hotmail.com

In this paper laminar forced convection associated with the cross-flow of micropolar fluid over a horizontal heated circular cylinder is investigated. The conservation equations of mass, linear momentum, angular momentum and energy are solved to give the details of flow and thermal fields. The flow and thermal fields are mainly influenced by Reynolds number, Prandtl number and material parameters of micropolar fluid. The Reynolds number is considered up to 200 while the Prandtl number is fixed at 0.7. The dimensionless vortex viscosity is the only material parameter considered in this study and is selected in the range from 0 to 5. The study has shown that generally the mean heat transfer decreases as the vortex viscosity increases. The results have also shown that both the natural frequency of vortex shedding and the amplitude of oscillating lift force experience clear reduction as the vortex viscosity increases. Moreover, the study showed that there is a threshold value for vortex viscosity above which the flow over the cylinder never responds to perturbation and stays symmetric without vortex shedding. Regarding drag coefficient, the results have revealed that within the selected range of controlling parameters the drag coefficient does not show a clear trend as the vortex viscosity increases. [DOI: 10.1115/1.2426360]

Keywords: cylinder, micropolar fluid, vortex shedding, material parameter, forced convection

1 Introduction

The problem of heat convection and hydrodynamics associated with fluid flow over a circular cylinder has received great attention both theoretically and experimentally. The works of Eckert and Soehngen [1], Dennis et al. [2], Collins and Dennis [3], Honji and Taneda [4], Chun and Boehm [5], and Karniadakis [6] are only examples. Mach attention has been paid to the problem not only due to its fundamental aspects but also to its importance in many practical engineering applications. These applications include nuclear reactors, heat exchangers, hot wires, steam pipes, and offshore structures. Moreover, the interaction between a circular cylinder and its surrounding viscous stream is a good model problem for studying both heat convection and hydrodynamics associated with fluid flow over bluff bodies.

In many practical applications certain non-Newtonian fluids are used as working medium. These fluids, which include, for example, ferro liquids, colloidal fluids, heterogeneous mixtures, exotic lubricants, animal blood, most slurries, and some liquids with polymer additives have microstructure and therefore do not follow the Newtonian fluid flow theory. In order to explore and understand the behavior of such fluids there were relentless efforts to establish new fluid theory. These efforts were finally crowned by developing the theory of microfluids. The micropolar fluid theory, which is a subclass of microfluids theory, has been formulated by Eringen [7] and others. This theory takes into account the local effects arising from microstructure and micromotions of the fluid elements. Micropolar fluids can support surface and body couples which are not present in the theory of Newtonian fluids. The extension of micropolar fluids theory to deal with thermomicropolar fluids has been given by Eringen [8].

The volume of previous studies on both flow and heat convection problems related to micropolar fluid is relatively small. The applications of micropolar fluid mechanics have been thoroughly reviewed by Arimen et al. [9]. In the last 2 decades there has been escalated interest in the theoretical studies related to heat convection in micropolar fluids. These studies, however, mostly focused on heat convection in boundary layer flows, such as those over flat plates and along vertical cylinders. Gorla [10] investigated the heat transfer characteristics of a micropolar boundary layer in a cross flow over the nonisothermal circular cylinder. Lien et al. [11] analyzed free convection micropolar boundary layer flow about a horizontal permeable cylinder at a nonuniform thermal condition. Hassanien et al. [12] investigated combined convection on a vertical slender cylinder. The axisymmetric thermal boundary layer of a micropolar fluid on a cylinder was solved by Gorla [13] while the mixed convection in an axisymmetric stagnation flow of micropolar fluid on a vertical cylinder was studied by Mohammedien et al. [14]. Hassanien and Salama [15] studied the flow and heat transfer of a micropolar fluid in an axisymmetric stagnation flow on a cylinder while Gorla and Takhar [16] studied the unsteady mixed convection boundary layer flow of a micropolar fluid near the lower stagnation point on a cylinder. The magnetohydrodynamic convective micropolar fluid flow has been considered by Mansour et al. [17] and Rahman and Sattar [18]. Mansour et al. [17] studied heat and mass transfer in magnetohydrodynamic flow of micropolar fluid on a circular cylinder with uniform heat and mass flux while Rahman and Sattar [18] studied magnetohydrodynamic convective micropolar fluid flow past a continuously moving vertical porous plate in the presence of heat generation/absorption.

The aforementioned studies are mostly based on the solutions of boundary layer equations. Such solutions are invalid in the regions of flow separation as that resulting in the cylinder wake. Needless to say that these solutions cannot trace the vortex shedding from the cylinder surface and can not predict the resulting oscillating heat transfer and hydrodynamic forces. It is well known that as the flow Reynolds number exceeds a threshold value (about 40 in Newtonian fluids) the vortices detach alternately and periodically from the upper and lower sides of the

cylinder, forming the well known Karman vortex street. The process of vortex shedding results in an oscillating flow in the vicinity of the cylinder which increases the heat transfer rate as compared with the case of nonvortex shedding. Moreover, the process of vortex shedding results in oscillating lift and drag forces acting on the cylinder surface. In response to these oscillating forces the cylinder may experience vibrations. These vibrations, though it may have positive effect on enhancing heat transfer, can cause structural fatigue and, in certain circumstances, can lead to drastic failure of the structure.

The lack of the information about the effect of vortex shedding on both heat transfer and hydrodynamics associated with micropolar fluid flow over cylinders was the motivation for this study. To the author's knowledge, this is the first study that focuses on the vortex shedding process in case of micropolar fluids. The study considers the effect of Reynolds number and material parameters on vortex shedding, hydrodynamic forces, and forced convection associated with the cross flow of micropolar fluids over horizontal circular cylinder. In order to predict the vortex shedding process the full governing equations are considered and solved accurately using the Fourier spectral method.

2 Problem Formulation

In the problem considered, a circular isothermal cylinder of radius c is placed horizontally in an impulsively started uniform cross stream of micropolar fluid of temperature T_∞. The cylinder surface temperature is kept constant at T_s ($T_s > T_\infty$). The micropolar fluid flow is assumed laminar, incompressible, and two dimensional. The viscous dissipation and microrotation heat conduction are also assumed negligible. In polar coordinates (r', θ), where θ is measured counterclockwise from the rearmost point on the cylinder surface and under the above assumptions the conservation equations of motion and energy in terms of the vorticity, stream function, microrotation, and temperature can be expressed as

$$\frac{\partial \zeta'}{\partial \tau} = \left(\frac{\mu + K_v}{\rho}\right)\nabla^2 \zeta' + \frac{1}{r'}\frac{\partial \psi'}{\partial r'}\frac{\partial \zeta'}{\partial \theta} - \frac{1}{r'}\frac{\partial \zeta'}{\partial r'}\frac{\partial \psi'}{\partial \theta} - \frac{K_v}{\rho}\nabla^2 \sigma \quad (1)$$

$$\zeta' = -\nabla^2 \psi' \quad (2)$$

$$\frac{\partial \sigma}{\partial \tau} = \frac{\gamma}{\rho j}\nabla^2 \sigma + \frac{1}{r'}\frac{\partial \psi'}{\partial r'}\frac{\partial \sigma}{\partial \theta} - \frac{1}{r'}\frac{\partial \sigma}{\partial r'}\frac{\partial \psi'}{\partial \theta} + \frac{K_v}{\rho j}(\zeta' - 2\sigma) \quad (3)$$

$$\frac{\partial T}{\partial \tau} = \frac{k}{\rho c_p}\nabla^2 T + \frac{1}{r'}\frac{\partial \psi'}{\partial r'}\frac{\partial T}{\partial \theta} - \frac{1}{r'}\frac{\partial T}{\partial r'}\frac{\partial \psi'}{\partial \theta} \quad (4)$$

where

$$\nabla^2 = \frac{\partial^2}{\partial r'^2} + \frac{1}{r'}\frac{\partial}{\partial r'} + \frac{1}{r'^2}\frac{\partial^2}{\partial \theta^2}$$

K_v, j, and γ are the vortex viscosity, micro-inertia density, and spin-gradient viscosity; τ is the time; ρ is the density; μ is the viscosity coefficient; k is the thermal conductivity; c_p is the specific heat; ζ' is the vorticity; ψ' is the stream function; T is the temperature; and σ is the component of microrotation vector whose direction of rotation is in the $r' - \theta$ plane.

In order to solve the governing Eqs. (1)–(4), initial and boundary conditions are needed. The boundary conditions to be satisfied are the no-slip, impermeability, and isothermal conditions on the cylinder surface together with the uniform free stream conditions very far away from the cylinder surface. The initial and boundary conditions can be expressed as
$\tau \leq 0$:
at $r' = c$

$$\frac{\partial \psi'}{\partial \theta} = 0, \quad \frac{\partial \psi'}{\partial r'} = 0, \quad \zeta' = 0, \quad \sigma = 0, \text{ and } T = T_s \quad (5a)$$

and at $r' > c$

$$\frac{\partial \psi'}{r' \partial \theta} = 0, \quad \frac{\partial \psi'}{\partial r'} = 0, \quad \zeta' = 0, \quad \sigma = 0, \text{ and } T = T_\infty \quad (5b)$$

$\tau > 0$:
at $r' = c$

$$\psi' = \frac{\partial \psi'}{\partial \theta} = 0, \quad \frac{\partial \psi'}{\partial r'} = 0, \quad \sigma = \zeta'/2, \text{ and } T = T_s \quad (5c)$$

and as $r' \rightarrow \infty$

$$\frac{\partial \psi'}{r' \partial \theta} \rightarrow U \cos \theta, \quad \frac{\partial \psi'}{\partial r'} \rightarrow U \sin \theta,$$

$$\zeta' \rightarrow 0, \quad \sigma \rightarrow 0, \text{ and } T \rightarrow T_\infty \quad (5d)$$

For microrotation, σ, the boundary conditions adopted here are similar to those used by Gorla [13]. That is at the cylinder surface the microrotation is taken equal to mean flow rotation (i.e., one-half the vorticity) while far away from the cylinder surface the microrotation is assigned zero value.

The dimensionless forms of the above equations are obtained by introducing the following dimensionless variables

$$r = \frac{r'}{c}, \quad t = \frac{U\tau}{c}, \quad \psi = \frac{\psi'}{Uc}, \quad \zeta = -\zeta'\frac{c}{U}, \quad M = \sigma\frac{c}{U},$$

$$D = \frac{K_v}{\mu}, \quad B = \frac{j}{c^2}, \quad \lambda = \frac{\gamma}{c^2\mu}, \text{ and } \phi = \frac{T - T_\infty}{T_s - T_\infty} \quad (6)$$

Using the above variables in Eqs. (1)–(4) and using modified polar coordinates ($\xi, \theta, \xi = \ln r$) results in

$$e^{2\xi}\frac{\partial \zeta}{\partial t} = \frac{2(1 + D)}{\text{Re}}\nabla^2\zeta + \frac{\partial \psi}{\partial \xi}\frac{\partial \zeta}{\partial \theta} - \frac{\partial \zeta}{\partial \xi}\frac{\partial \psi}{\partial \theta} + \frac{2D}{\text{Re}}\nabla^2 M \quad (7)$$

$$e^{2\xi}\zeta = \nabla^2\psi \quad (8)$$

$$e^{2\xi}\frac{\partial M}{\partial t} = \frac{2\lambda}{\text{Re }B}\nabla^2 M + \frac{\partial \psi}{\partial \xi}\frac{\partial M}{\partial \theta} - \frac{\partial M}{\partial \xi}\frac{\partial \psi}{\partial \theta} - \frac{2D}{\text{Re }B}(\zeta + 2M)e^{2\xi} \quad (9)$$

$$e^{2\xi}\frac{\partial \phi}{\partial t} = \frac{2}{\text{Re Pr}}\nabla^2\phi + \frac{\partial \psi}{\partial \xi}\frac{\partial \phi}{\partial \theta} - \frac{\partial \phi}{\partial \xi}\frac{\partial \psi}{\partial \theta} \quad (10)$$

where $\text{Re} = 2\rho Uc/\mu$ is the Reynolds number and $\text{Pr} = \mu/\rho\alpha$ is the Prandtl number.

The initial and boundary conditions (5) based on the new variables can be expressed as
$t \leq 0$:
at $\xi = 0$

$$\psi = \frac{\partial \psi}{\partial \theta} = \frac{\partial \psi}{\partial \xi} = 0, \quad M = 0, \text{ and } \phi = 1 \quad (11a)$$

at $\xi > 0$

$$e^{-\xi}\frac{\partial \psi}{\partial \theta} = 0, \quad e^{-\xi}\frac{\partial \psi}{\partial \xi} = 0, \quad \zeta = 0, \quad M = 0, \text{ and } \phi = 0 \quad (11b)$$

$t > 0$:
at $\xi = 0$

$$\psi = \frac{\partial \psi}{\partial \theta} = \frac{\partial \psi}{\partial \xi} = 0, \quad M = \zeta/2, \text{ and } \phi = 1 \quad (11c)$$

as $\xi \rightarrow \infty$

$$e^{-\xi}\frac{\partial \psi}{\partial \theta} \rightarrow \cos \theta, \quad e^{-\xi}\frac{\partial \psi}{\partial \xi} \rightarrow \sin \theta, \quad \zeta \rightarrow 0, \quad M \rightarrow 0, \text{ and } \phi \rightarrow 0 \quad (11d)$$

3 Method of Solution

The method of solution is based on approximating the stream function, vorticity, microrotation, and temperature using Fourier series expansion. The approach is similar to that used by Badr and Dennis [19] and Mahfouz and Badr [20]. The dimensionless stream function ψ, vorticity ζ, microrotation M, and temperature ϕ are approximated as

$$\psi(\xi,\theta,t) = \frac{1}{2}F_0(\xi,t) + \sum_{n=1}^{N} [f_n(\xi,t)\sin(n\theta) + F_n(\xi,t)\cos(n\theta)]$$
(12a)

$$\zeta(\xi,\theta,t) = \frac{1}{2}G_0(\xi,t) + \sum_{n=1}^{N} [g_n(\xi,t)\sin(n\theta) + G_n(\xi,t)\cos(n\theta)]$$
(12b)

$$M(\xi,\theta,t) = \frac{1}{2}R_0(\xi,t) + \sum_{n=1}^{N} [r_n(\xi,t)\sin(n\theta) + R_n(\xi,t)\cos(n\theta)]$$
(12c)

$$\phi(\xi,\theta,t) = \frac{1}{2}H_0(\xi,t) + \sum_{n=1}^{N} [h_n(\xi,t)\sin(n\theta) + H_n(\xi,t)\cos(n\theta)]$$
(12d)

where F_0, f_n, F_n, G_0, g_n, G_n, R_0, r_n, R_n, H_0, h_n, and H_n are the Fourier coefficients and N represents the number of terms considered in the Fourier series. Substitution of ψ, ζ, M, and ϕ defined in Eqs. (12a)–(12d) in Eqs. (7)–(10) results in the following set of differential equations

$$\frac{\partial^2 F_0}{\partial \xi^2} = e^{2\xi} G_0$$
(13a)

$$\frac{\partial^2 f_n}{\partial \xi^2} - n^2 f_n = e^{2\xi} g_n$$
(13b)

$$\frac{\partial^2 F_n}{\partial \xi^2} - n^2 F_n = e^{2\xi} G_n$$
(13c)

$$e^{2\xi}\frac{\partial G_0}{\partial t} = \frac{2(1+D)}{\text{Re}} \frac{\partial^2 G_0}{\partial \xi^2} + S_0$$
(14a)

$$2e^{2\xi}\frac{\partial g_n}{\partial t} = \frac{4(1+D)}{\text{Re}}\left(\frac{\partial^2 g_n}{\partial \xi^2} - n^2 g_n\right) + nF_n\frac{\partial G_0}{\partial \xi} - nG_n\frac{\partial F_0}{\partial \xi} + S_{n1}$$
(14b)

$$2e^{2\xi}\frac{\partial G_n}{\partial t} = \frac{4(1+D)}{\text{Re}}\left(\frac{\partial^2 G_n}{\partial \xi^2} - n^2 G_n\right) - nf_n\frac{\partial G_0}{\partial \xi} + ng_n\frac{\partial F_0}{\partial \xi} + S_{n2}$$
(14c)

$$e^{2\xi}\frac{\partial R_0}{\partial t} = \frac{2\lambda}{\text{Re } B} \frac{\partial^2 R_0}{\partial \xi^2} + K_0$$
(15a)

$$2e^{2\xi}\frac{\partial r_n}{\partial t} = \frac{4\lambda}{\text{Re } B}\left(\frac{\partial^2 r_n}{\partial \xi^2} - n^2 r_n\right) + nF_n\frac{\partial R_0}{\partial \xi} - nR_n\frac{\partial F_0}{\partial \xi} + K_{n1}$$
(15b)

$$2e^{2\xi}\frac{\partial R_n}{\partial t} = \frac{4\lambda}{\text{Re } B}\left(\frac{\partial^2 R_n}{\partial \xi^2} - n^2 R_n\right) - nf_n\frac{\partial R_0}{\partial \xi} + nr_n\frac{\partial F_0}{\partial \xi} + K_{n2}$$
(15c)

$$e^{2\xi}\frac{\partial H_0}{\partial t} = \frac{2}{\text{Re Pr}} \frac{\partial^2 H_0}{\partial \xi^2} + Z_0$$
(16a)

$$2e^{2\xi}\frac{\partial h_n}{\partial t} = \frac{4}{\text{Re Pr}}\left(\frac{\partial^2 h_n}{\partial \xi^2} - n^2 h_n\right) + nF_n\frac{\partial H_0}{\partial \xi} - nH_n\frac{\partial F_0}{\partial \xi} + Z_{n1}$$
(16b)

$$2e^{2\xi}\frac{\partial H_n}{\partial t} = \frac{4}{\text{Re Pr}}\left(\frac{\partial^2 H_n}{\partial \xi^2} - n^2 H_n\right) - nf_n\frac{\partial H_0}{\partial \xi} + nh_n\frac{\partial F_0}{\partial \xi} + Z_{n2}$$
(16c)

where S_0, S_{n1}, S_{n2}, K_0, K_{n1}, K_{n2}, Z_0, Z_{n1}, and Z_{n2} are all easily identifiable functions of ξ and t. Equations (13a)–(13c), (14a)–(14c), (15a)–(15c), and (16a)–(16c) define $(8N+4)$ differential equations that have to be solved simultaneously at every time step to get the flow, microrotation, and thermal fields. The initial and boundary conditions for all functions present in Eqs. (13)–(16) are deduced from Eq. (11) and can be expressed as

$t \leq 0$:

at $\xi = 0$

$$F_0 = F_n = f_n = \partial F_n/\partial \xi = \partial f_n/\partial \xi = \partial F_0/\partial \xi = 0,$$

$$R_0 = R_n = r_n = 0, \quad H_0 = 2, \text{ and } H_n = h_n = 0$$
(17a)

and at $\xi > 0$

$$e^{-\xi}[\partial F_0/\partial \xi, F_n, \partial F_n/\partial \xi] = 0, \quad f_n = \partial f_n/\partial \xi = 0,$$

$$G_0 = G_n = g_n = R_0 = R_n = r_n = 0, \text{ and}$$

$$H_0 = H_n = h_n = 0$$
(17b)

$t > 0$:

at $\xi = 0$

$$F_0 = F_n = f_n = \partial F_n/\partial \xi = \partial f_n/\partial \xi = \partial F_0/\partial \xi = 0, \quad R_0 = \frac{-G_0}{2},$$

$$R_n = \frac{-G_n}{2}, \quad r_n = \frac{-g_n}{2}, \quad H_0 = 2, \text{ and } H_n = h_n = 0$$
(17c)

and as $\xi \to \infty$

$$e^{-\xi}[\partial F_0/\partial \xi, F_n, \partial F_n/\partial \xi] \to 0,$$

$$e^{-\xi}f_n \to \delta_{1,n}, e^{-\xi}\partial f_n/\partial \xi \to \delta_{1,n}, G_0, G_n, g_n, R_0, R_n, r_n$$
$$\to 0 \text{ and } H_0, H_n, h_n \to 0$$
(17d)

Integrating both sides of Eq. (13a) with respect to ξ between $\xi = 0$ and $\xi = \infty$ and using the boundary conditions in Eq. (17) gives the following integral condition

$$\int_0^{\infty} e^{2\xi} G_0 \, d\xi = 0$$
(18a)

Similarly, multiplying both sides of Eqs. (13b) and (13c) by $e^{-n\xi}$ and integrating from $\xi = 0$ to $\xi = \infty$ and using boundary conditions (17), one can obtain the following integral conditions

$$\int_0^{\infty} e^{(2-n)\xi} g_n \, d\xi = 2\delta_{1,n}$$
(18b)

$$\int_0^{\infty} e^{(2-n)\xi} G_n \, d\xi = 0$$
(18c)

where $\delta_{1,n} = 1$ if $n = 1$ and $\delta_{1,n} = 0$ if $n \neq 1$.

The above integral conditions are used at every time step to calculate the values of the functions G_0, g_n, and G_n on the cylinder surface ($\xi = 0$). These functions are then used to compute ac-
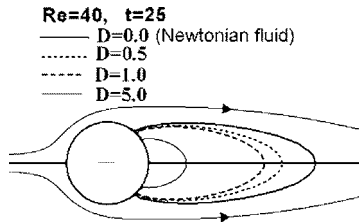
Fig. 1 Wake length for the case of Re=40, *t*=25 and at different values of vortex viscosity *D*

Fig. 2 Time development of wake length for the case of Re =40 and comparison with Collins and Dennis [3] and Honji and Taneda [4]

curately the vorticity distribution on the cylinder surface. The first condition Eq. (18*a*) is essential to ensure the periodicity of the pressure on the surface. The rest of the details of the method of solution and the numerical treatment is similar to that used in Badr and Dennis [19] and Mahfouz and Badr [20] and will not be repeated here for the sake of brevity.

4 Results and Discussion

The governing equations along with boundary conditions are solved in order to give the details of both flow and thermal fields. The main controlling parameters beside the classical ones (Re and Pr) are the dimensionless micropolar material parameters. These are the parameter D which characterizes the vortex viscosity; the parameter λ which characterizes the spin gradient viscosity; and the parameter B which characterizes the microinertia density. The close scrutiny of Eqs. (7) and (9) shows that the parameter D represents a direct link between the flow field and microrotation field. The other two dimensionless material parameters λ and B appear only in microrotation Eq. (9). This means that the effect of these two parameters is expected not to be as significant as the effect of parameter D. For this reason and for the sake of brevity only the influence of the vortex viscosity is considered. The parameter D is selected in the range from 0 to 5 while the other two material parameters λ and B are assigned a value of 1. The Reynolds number is varied up to 200 while the Prandtl number is fixed at 0.7.

4.1 Wake Flow and Vortex Shedding. With the start of computation, the flow commences impulsively over the cylinder surface. As time goes on the flow separates from the upper and lower surfaces of the cylinder, forming two pair of vortices behind the cylinder. For Reynolds numbers less than a certain value (about 40 for Newtonian fluids), the flow over the cylinder remains stable and remains horizontally symmetric with respect to the cylinder axis. The two generated symmetric vortices remain attached behind the cylinder and the wake length continues to grow with time until the quasi-steady state condition is almost reached at late times. The wake length, L is the length (divided by cylinder radius) of the separated wake measured along the line $\theta=0$ from the rearmost point of the cylinder to the end of the recirculating region.

Figure 1 shows the wake length L and the two symmetric vortices at late time ($t=25$) for the case of Re=40 and at different values of dimensionless vortex viscosity D. The figure clearly shows that as the parameter D increases the wake length clearly decreases. It can also be observed that as the parameter D increases, the point of flow separation from upper and lower surfaces moves further downstream which is more pronounced for
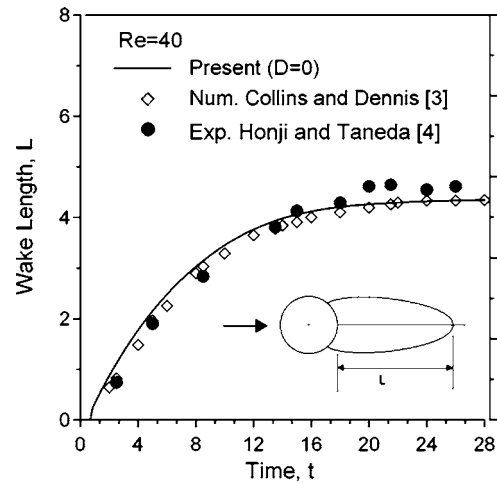
the case of $D=5$. The effect of increasing vortex viscosity seems similar to the effect of decreasing Reynolds number, that is to say that the flow becomes more viscous as the vortex viscosity increases.

Figure 2 shows the time development of the wake length for the case of steady symmetric flow of a Newtonian fluid ($D=0$) at Re=40. Also shown in the same figure are the numerical and experimental results of Collins and Dennis [3] and Honji and Taneda [4], respectively. The figure shows very good agreement with numerical results at both initial and late times, while the comparison with the experimental results is very good up to time $t=18$ and reasonable for $t>18$. Further rigorous testing of the method of solution can be found in the works of Mahfouz and Badr [20,21].

As the Reynolds number exceeds a certain value the flow in the cylinder wake becomes unstable and vortices are shed alternately and periodically from the upper and lower sides of the cylinder, forming the well known Karman vortex street. In the present numerical treatment, in order to excite the Karman vortex street the flow is intentionally disturbed by rotationally oscillating the cylinder for only one complete cycle. The amplitude and duration of the cycle were selected in order to trigger the vortex shedding as rapidly as possible without causing any longtime effects. The frequency of vortex shedding, f_0, is computed from frequency analysis of the time record of lift coefficient.

The dimensionless frequency of vortex shedding is known as Strouhal number ($S_0=2cf_0/U$). The Strouhal number depends not only on the Reynolds number (as in case of Newtonian fluids) but also on the material parameters of micropolar fluid. The numerical results for Strouhal number at various values of Re and D are displayed in Table 1. The table shows that the Strouhal numbers for the cases of Newtonian fluids ($D=0$) at Re=50, 100, and 200 are 0.134, 0.16, and 0.18, respectively. These computed values of S_0 are in a very good agreement with the corresponding experimental results of Roshko [22], numerical results of Jordon and Fromm [23], and numerical results of Mahfouz and Badr [20]. While for micropolar fluid the table shows clearly that as the

Table 1 Calculated values of Strouhal number at different values of Re and *D*

Re	50				100				200			
D	0.0	0.1	0.5	2.0	0.0	0.5	1.0	5.0	0.0	0.1	1.0	2.0
S_0	0.134	0.130	—	—	0.160	0.156	0.120	—	0.180	0.170	0.165	0.145
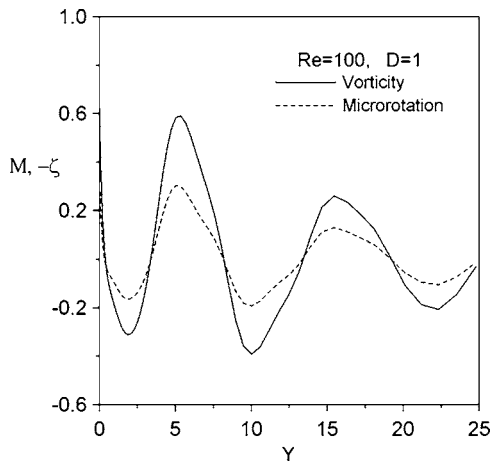
Fig. 3 Variation of microrotation M, and vorticity $-\zeta$ in the cylinder wake along the rear axis ($\theta=0$)

Fig. 4 Time variation of lift coefficient for the case Re=50 and D=0, 0.1, 0.5, and 2

vortex viscosity increases the frequency of vortex shedding decreases. The void (dashed) entries in the table mean that the flow will be steady symmetric (i.e., no vortex shedding) at very large time.

The variation of dimensionless microrotation M which characterizes the microelements rotation, σ, as well as the variation of dimensionless vorticity $-\zeta$ which characterizes the mean flow rotation ζ' in the cylinder wake along the rear axis ($\theta=0$) is shown in Fig. 3 for the case of Re=100, D=1, and at t=150. The figure shows that both M and $-\zeta$ fluctuate along the rear axis due to vortex shedding with decaying amplitude as a result of viscous diffusion. Also the figure clearly shows that almost at all points M is one-half that of $-\zeta$ which means that micro-elements are rotating at the mean flow local rotating velocity. Here it should be realized that both σ and ζ' are scaled in the same way in Eq. (6).

4.2 Flow Hydrodynamics. For the case of symmetric flow only the drag force exists while the lift force vanishes as a result of equally opposing forces acting on upper and lower sides of the cylinder. With the development of periodic shedding of vortices the flow in the cylinder wake becomes unsteady and asymmetric. The periodic shedding of vortices leads to periodic time variation in lift and drag forces. The lift and drag coefficients are defined as $C_D=F_D/c\rho U^2$ and $C_L=F_L/c\rho U^2$, where F_D and F_L are the drag and lift forces exerted on a unit length of the cylinder. In terms of Fourier coefficients the drag and lift coefficients can be expressed as

$$C_D = \frac{2\pi}{\mathrm{Re}}\left[(1+D)\left(g_1 - \frac{\partial g_1}{\partial \xi}\right) + D\left(r_1 - \frac{\partial r_1}{\partial \xi}\right)\right]_s \quad (19a)$$

and

$$C_L = -\frac{2\pi}{\mathrm{Re}}\left[(1+D)\left(G_1 - \frac{\partial G_1}{\partial \xi}\right) + D\left(R_1 - \frac{\partial R_1}{\partial \xi}\right)\right]_s \quad (19b)$$

The time averaged drag coefficient is determined as

$$\bar{C}_D = \frac{1}{t_2 - t_1}\int_{t_1}^{t_2} C_D \, dt \quad (20)$$

where the time period between t_1 and t_2 covers a good number of cycles of vortex shedding.

Figure 4 shows the time variation of lift coefficient for the case of Re=50 and D=0, 0.1, 0.5, and D=2. The figure shows clearly that as the parameter D increases the amplitude of lift coefficient decreases. The lift coefficients for cases D=0.0 and D=0.1 oscillate with almost constant amplitude, which reflects the persistent nature of vortex shedding for these two cases. For higher values of D=0.5 and D=2 the amplitude of lift coefficient is no longer constant but rather continuously decaying with time, expectedly reaching to zero value at large time. The rate of continuous decaying of C_L, once it starts at a threshold value of D, is getting faster as the value of D increases as shown in the figure, where that rate for D=2 is faster than that at D=0.5. The full diminishing of lift forces at large times means that the flow eventually became steady symmetric. Based on Table 1 and Fig. 4, it can be inferred that the increase of vortex viscosity beyond a threshold value may lead to a decrease in the flow response to the perturbation with tendency of the flow to be symmetric (i.e., no vortex shedding) at large times. In this study however, no attempts are made to find the exact value of D (at certain Re) at which the flow at large time becomes steady symmetric. This finding is important asfar as the vortex shedding and separation control is concerned. The closer the behavior of the fluid to the micropolar fluid the weaker the possibility of vortex shedding.

The results of time averaged drag coefficient are displayed in Table 2. It can be seen from the table that in some cases for which the value of D is less than one, the drag coefficient is less than that for Newtonian fluids, especially at Re=200. As the parameter D exceeds one the drag coefficient increases, exceeding that for Newtonian fluids. However, the above conclusion cannot be generalized and the results for time averaged drag coefficient do not show a certain clear trend within the range selected for controlling parameters.

Table 2 Calculated values of time averaged drag coefficient at different values of Re and D

Re		50				100				200		
D	0.0	0.1	0.5	2.0	0.0	0.5	1.0	5.0	0.0	0.1	1.0	2.0
$\bar{C}_D$	1.84	1.86	1.06	2.37	1.51	1.52	1.21	1.414	1.220	1.188	1.188	1.255

Fig. 5 Variation of $\overline{Nu}$ with Re and comparison with the correlation of Knudsen and Katz [24] and Hatton et al. [25]

Fig. 6 Time variation of mean Nusselt number at Re=200, Pr =0.7, and at different values of D
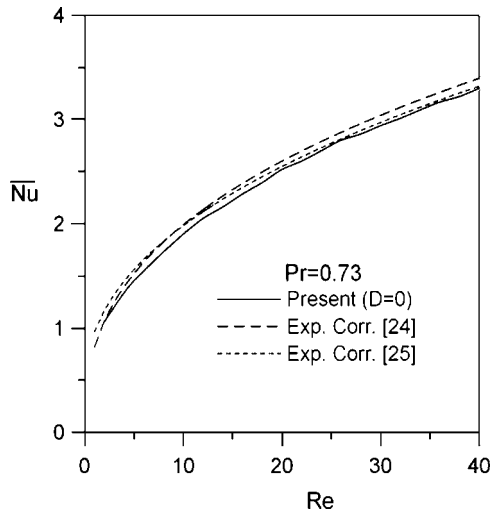
4.3 Heat Transfer Results. Immediately following the impulsive flow motion over the constant temperature cylinder surface, the heat transfer rate gets very high values as a result of heat conduction through a very thin thermal layer. In the early time stages, the fast development of the thermal layer resulted in drastic decrease in heat transfer in a relatively short time. After that short time the thermal layer is almost developed and heat transfer tends to assume almost a steady value if the flow is still not disturbed. Once the flow is disturbed the vortex shedding process starts and causes flow unsteadiness near the cylinder surface. Such unsteadiness causes an enhancement in mean heat convection in comparison with the steady symmetric situation. In order to quantify the heat transfer results let us define the surface local and mean Nusselt numbers

$$ \mathrm{Nu} = \frac{2q'c}{k(T_s - T_\infty)} \quad \text{and} \quad \overline{\mathrm{Nu}} = \frac{1}{2\pi}\int_0^{2\pi} \mathrm{Nu}\, d\theta \tag{21} $$

where q' is heat transfer per unit area given by $q' = -k\,\partial T/\partial r'|_{r'=c}$. From the above definitions and using Eq. (12d), one can deduce the following relations for local Nusselt number and for mean Nusselt number

$$ \mathrm{Nu} = -2\left(\frac{\partial \phi}{\partial \xi}\right)_s = -\left(\frac{\partial H_0}{\partial \xi}\right)_s - 2\left[\sum_1^N \frac{\partial H_n}{\partial \xi}\cos(n\theta)\right. $$

$$ \left. + \frac{\partial h_n}{\partial \xi}\sin(n\theta)\right]_s \tag{22a} $$

and

$$ \overline{\mathrm{Nu}} = -\left(\frac{\partial H_0}{\partial \xi}\right)_{\xi=0} \tag{22b} $$

The time-averaged Nusselt number is obtained from

$$ \overline{\overline{\mathrm{Nu}}} = \frac{1}{t_2 - t_1}\int_{t_1}^{t_2} \overline{\mathrm{Nu}}\, dt \tag{23} $$
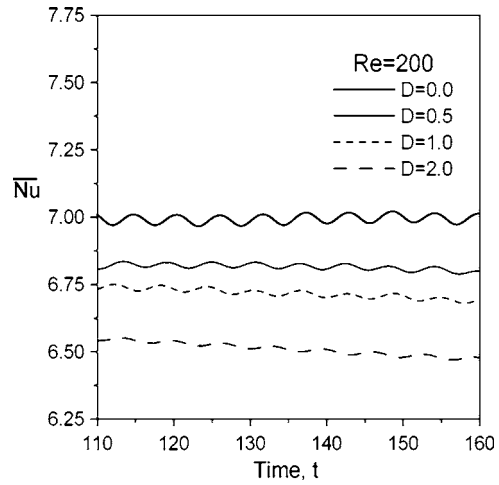
Figure 5 shows the steady mean Nusselt number $\overline{Nu}$ distribution for the case of symmetric Newtonian ($D=0$) low Reynolds numbers ($1 < \mathrm{Re} < 40$) fluid flow at a value of Pr=0.73. Shown also in the same figure for the purpose of comparison are the experimental correlation due to Knudsen and Katz [24] and Hatton et al. [25]. The latter correlation, which is developed for mixed convection, is reduced for the case of forced convection and the correction factor for temperature has been taken as one. The comparison with these two correlations, as shown in the figure, is very good with maximum difference less than 7% in the case of comparison with the former and less than 10% in the case of comparison with the latter.

Figure 6 shows the late time variation of surface mean Nusselt number $\overline{Nu}$ for the unsteady flow for the case of Re=200, Pr =0.7, and $D=0$, 0.5, 1, 5. The figure shows that $\overline{Nu}$ fluctuates around a mean value and the amplitude of these fluctuations is more pronounced for smaller values of D ($D=0$ and $D=0.5$), while at bigger values of D the amplitude of fluctuation becomes smaller. The frequency of fluctuation is twice the frequency of vortex shedding. It can also be observed from the figure that the time-averaged value of $\overline{Nu}$ is getting markedly smaller as D increases. The numerical results of time averaged Nusselt number $\overline{\overline{Nu}}$ for the cases considered in this study are listed in Table 3. The table shows that as D increases $\overline{\overline{Nu}}$ decreases. The reduction of $\overline{Nu}$ which means reduction in heat transfer is consistent with the previous results for natural convection from plates, and circular and elliptic cylinders placed in micropolar fluids [see Ref. [26,27]]. So in general, it can be concluded that the heat convection (forced or natural) in micropolar fluids is smaller in comparison with that in Newtonian fluids.

Shown in Fig. 7 are the local Nusselt number, Nu distributions for the unsteady flow for the case of Re=100, Pr=0.7, $D=0$, 0.5, 1, 5, and at late time $t=150$. The figure shows that Nu distributions for micropolar fluid are similar to that of Newtonian fluid ($D=0$). The figure shows that for all distributions Nu gets its maximum value at the front stagnation point which is located at $\theta=180$ (for symmetric flow), or in its vicinity (for asymmetric

Table 3 Calculated values of time averaged Nusselt number at different values of Re and D

Re		50				100				200		
D	0.0	0.1	0.5	2.0	0.0	0.5	1.0	5.0	0.0	0.1	1.0	2.0
$\overline{\overline{Nu}}$	3.796	3.758	3.378	3.313	5.325	5.233	4.412	4.325	6.98	6.79	6.69	6.49
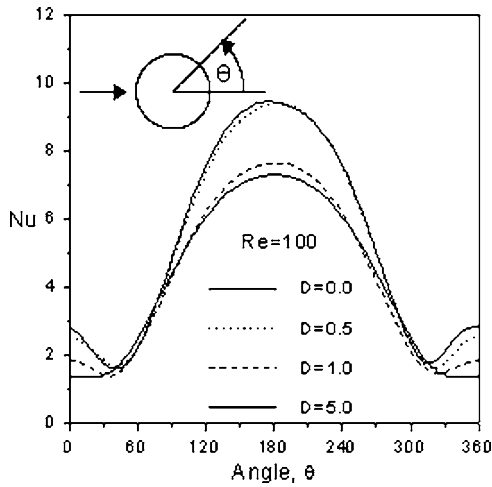
Fig. 7 Distribution of surface local Nu at Re=100, Pr=0.7, t =200, and at different values of D

Fig. 9 Temperature distribution in the wake of the cylinder along line $\theta=0$

flow resulting from vortex shedding). At the stagnation point the thermal layer is minimum, which results in maximum heat rate at that point. The Nu then decreases due to thermal boundary layer growth in the direction of flow on upper and lower sides of the cylinder until it gets its minimum value near the rearmost point of the cylinder ($\theta=0$). In the rear region and as a result of vortex shedding the heat transfer rate and Nu assumes fluctuating and relatively higher values as compared with steady cases (not shown here). The figure also shows clear reduction in Nusselt number at almost all points of the surface as the dimensionless vortex viscosity D increases. The reduction in Nu at almost all points at the surface means the reduction of mean values of $\overline{Nu}$ as the vortex viscosity increases. The decrease of local values of Nu as vortex viscosity increases may be explained in the light of surface vorticity distributions shown in Fig. 8 for the same cases and at the same time. Higher values of surface vorticity at the same location (same θ) means higher flow velocity gradient (i.e., higher convection) near the surface which results in higher heat transfer (i.e., higher Nu). With the increase of the vortex viscosity the flow becomes more viscous and the low velocity gradient near the wall results in low convection currents and therefore low local heat transfer as shown in Fig. 7. The maximum heat transfer rate at the front stagnation point is not controlled by flow velocity gradient,
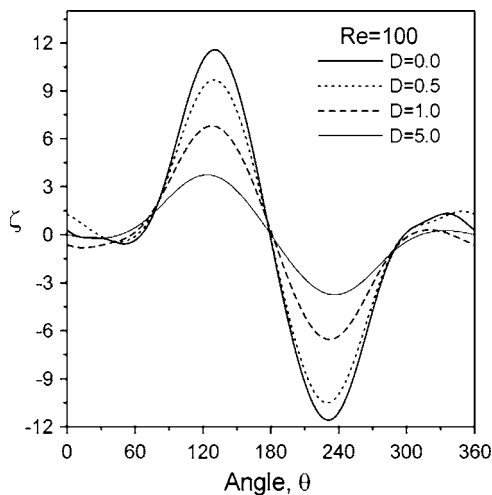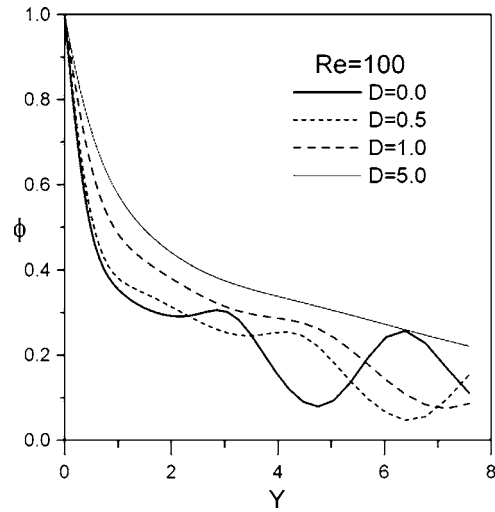
which is zero (and so the vorticity) at that point, but rather controlled by the thickness of the thermal layer which is minimum at that point.

Figure 9 shows the dimensionless temperature distribution in the wake of the cylinder along the rear axis ($\theta=0$) at time of t =150 and for the case of Re=100, Pr=0.7, and $D=0$, 0.5, 1, 5. The figure shows that the temperature decreases in the wake for all cases, expectedly reaching the value of unheated fluid very far away from the cylinder ($\phi=0$). The figure shows clearly that for the cases of $D=0$, 0.5, and 1 the temperature fluctuates during its decrease while for the case of $D=5$ it monotonically decreases. These distributions of temperature again confirm the results shown in Table 1 that the wake flow is characterized by vortex shedding for the cases of $D=0$, 0.5, 1 while for the case of D =5 the symmetric wake flow without vortex shedding is reached at that time. The temperature distributions as shown in the figure tell that as the value of D increases the temperature gradient at the surface decreases, declaring a smaller local heat transfer rate and accordingly, as shown in Fig. 7, smaller Nu as D increases.

Figure 10 shows both the flow field, represented by streamlines and the thermal field, represented by contour plots of isotherm patterns for the case of Re=50 and at time $t=200$ and at four values of D, namely, $D=0.0$, 0.1, 0.5, and $D=2$. The flow is disturbed in the four cases at $t=30$. The figure shows that for the value of $D=0.0$ and 0.1 (Figs. 10(*a*) and 10(*b*)) the streamlines and isotherms reflect the asymmetry of the flow which is persistently characterized by vortex shedding which is clear in time variation of lift coefficient (see Fig. 3). For a larger value of D =0.5 (Fig. 10(*c*)) the streamlines and isotherms are about to be symmetric while for a much larger value of $D=2$ (Fig. 10(*d*)) the perturbation effect is already damped and the flow and thermal fields became fully symmetric. The dashed isotherm contour line in the Fig. 10 (right) represents the isotherm of $\phi=0.1$ which can be considered as a qualitative indicator of the thickness of the thermal layer. The figure clearly shows that the dashed contour encloses a wider loop around the cylinder as D increases, which indicates that the thermal layer around the cylinder gets thicker as the value of D increases. A thicker thermal layer means smaller temperature gradient near the cylinder surface and in turn smaller heat transfer rates.

5 Conclusions

This paper investigated forced convection and hydrodynamic forces associated with the flow of micropolar fluids over a horizontal circular cylinder. The effect of Reynolds number and ma-

Fig. 8 Distribution of surface vorticity at Re=100, Pr=0.7, t =200, and at different values of D

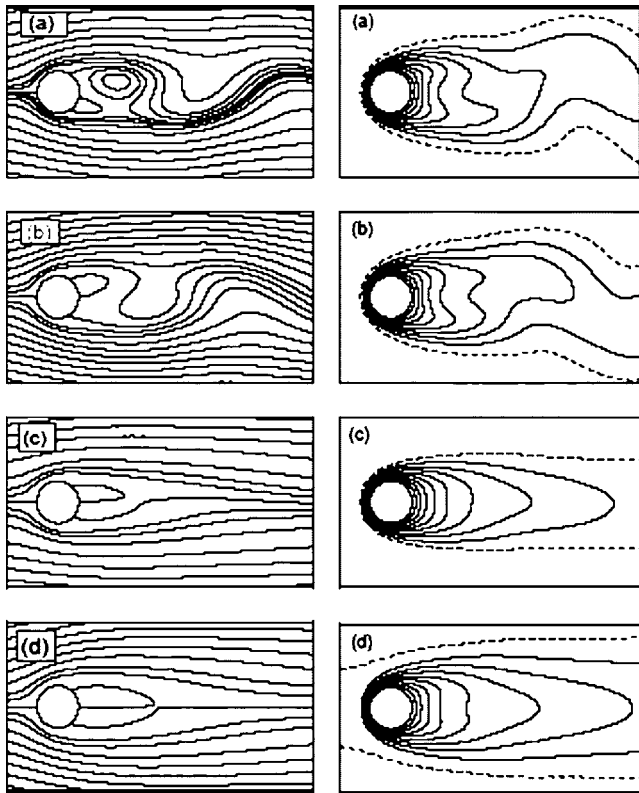**Fig. 10 Streamline patterns (left) and isotherm patterns (right) for the case of Re=50, t=200: (a) D=0.0; (b) D=0.1; (c) D=0.5; and (d) D=2**

terial parameters of micropolar fluid is considered in this study. The Reynolds number is considered up to 200. The vortex viscosity is the only material parameter considered in this study and is selected in the range from 0 to 5. The results have shown a remarkable decrease in mean heat transfer rate as the vortex viscosity increases. Similarly, the natural vortex shedding frequency decreases as the vortex viscosity increases. The amplitude of oscillating lift force also experiences a clear reduction as the vortex viscosity increases. The study showed that there is a threshold value for vortex viscosity above which the flow over the cylinder resists any flow perturbation and gets back its symmetry without vortex shedding. Moreover, the study has revealed that the drag coefficient does not show a clear trend within the selected range of vortex viscosity.

Nomenclature

B = material parameter characterizes microinertia
c = cylinder radius
C_D = drag coefficient
$\overline{C_D}$ = time averaged drag coefficient
C_L = lift coefficient
c_p = specific heat
D = material parameter characterizes vortex viscosity
F_D = drag force per unit length of the cylinder
F_L = lift force per unit length of the cylinder
K_v = vortex viscosity
k = thermal conductivity
j = micro-inertia density
L = dimensionless wake length ($=L'/c$)
M = dimensionless microratation
Nu, $\overline{\text{Nu}}$ = local and average Nusselt numbers
$\overline{\overline{\text{Nu}}}$ = time averaged Nusselt number

r' = radial coordinate
r = dimensionless radial coordinate (r'/c)
t = dimensionless time
T = temperature
U = free stream velocity
Y = the distance from the cylinder ($=r-1$)

Greek Symbols

α = thermal diffusivity
ϕ = dimensionless temperature
ρ = density
ξ = modified radial coordinate ($=\ln r$)
γ = spin gradient viscosity
λ = material parameter characterizes spin gradient viscosity
μ = viscosity coefficient
σ = microrotation in r', θ plane (or the microrotation vector component normal to r', θ plane)
τ = time
θ = angular coordinate
ψ', ψ = stream function, dimensionless stream function
ζ', ζ = vorticity, dimensionless vorticity

Subscripts

s = at cylinder surface
∞ = very faraway from the cylinder surface

References

[1] Eckert, E. R. G., and Soehngen, E., 1952, "Distribution of Heat Transfer Coefficient Around Circular Cylinders in Cross Flow at Reynolds Numbers from 20 to 500," J. Heat Transfer, **74**, pp. 343–347.

[2] Dennis, S. C. R., Hudson, J. D., and Smith, N., 1968, "Steady Laminar Forced Convection from a Circular Cylinder at low Reynolds Numbers," Phys. Fluids, **11**(5), pp. 933–940.

[3] Collins, W. M., and Dennis, S. C. R., 1973, "Flow Past an Impulsively Started Circular Cylinder," J. Fluid Mech., **60**(1), pp. 105–127.

[4] Honji, H., and Taneda, S., 1969, "Unsteady Flow Past a Circular Cylinder," J. Phys. Soc. Jpn., **27**, pp. 1688–1698.

[5] Chun, W., and Boehm, R. F., 1989, "Calculation of Forced Flow and Heat Transfer Around a Cylinder in Cross Flow," Numer. Heat Transfer, Part A, **15**, pp. 101–122.

[6] Karniadakis, G. E., 1988, "Numerical Simulation of Forced Convection Heat Transfer from a Cylinder in Crossflow," Int. J. Heat Mass Transfer, **31**(1), pp. 407–418.

[7] Eringen, A. C., 1966, "Theory of Micropolar Fluids," J. Math. Mech., **16**(1), pp. 1–18.

[8] Eringen, A. C., 1972, "Theory of Thermomicrofluids," J. Math. Anal. Appl., **38**, pp. 480–496.

[9] Ariman, T., Turk, M. A., and Sylvester, N. D., 1973, "Microcontinuum Fluid Mechanics, A Review," Int. J. Eng. Sci., **11**, pp. 905–930.

[10] Gorla, R. S. R., 1984, "Heat Transfer Characteristics of a Micropolar Boundary Layer in a Crossflow Over a Non-isothermal Circular Cylinder," Int. J. Eng. Sci., **22**(1), pp. 47–55.

[11] Lien, F.-S., Chen, T.-M., and Chen, C.-K., 1990, "Analysis of a Free-Convection Micropolar Boundary Layer about a Horizontal Permeable Cylinder at a Non-uniform Thermal Condition," ASME J. Heat Transfer, **112**, p. 504–506.

[12] Hassanien, I. A., Mansour, M. A., and Gorla, R. S. R., 1994, "Combined Convection on a Vertical Slender Cylinder in a Micropolar Fluid," Waerme-Stoffuebertrag., **29**, pp. 355–359.

[13] Gorla, R. S. R., 1995, "Axisymmetric Thermal Boundary Layer of a Micropolar Fluid on a Cylinder," Int. J. Eng. Sci., **23**, pp. 401–407.

[14] Mohammedien, A. A., Gorla, R. S. R., and Hassanien, I. A., 1996, "Mixed Convection in an Axisymmetric Stagnation Flow of Micropolar Fluid on a Vertical Cylinder," Acta Mech., **114**, pp. 139–149.

[15] Hassanien, I. A., and Salama, A. A., 1997, "Flow and Heat Transfer of a Micropolar Fluid in an Axisymmetric Stagnation Flow on a Cylinder," Energy Convers. Manage., **38**(3), pp. 301–310.

[16] Gorla, R. S. R., and Takhar, H. S., 1991, "Unsteady Mixed Convection Boundary Layer Flow of a Micropolar Fluid Near the Lower Stagnation Point on a Cylinder," Int. J. Eng. Fluid Mech., **4**(3), pp. 337–347.

[17] Mansour, M. A., El-Hakiem, M. A., and El Kabeir, S. M., 2000, "Heat and Mass Transfer in Magnetohydrodynamic Flow of Micropolar Fluid on a Circular Cylinder with Uniform Heat and Mass Flux," J. Magn. Magn. Mater., **220**, pp. 259–270.

[18] Rahman, M. M., and Sattar, M. A., 2006, "Magnetohydrodynamic Convective Flow of a Micropolar Fluid Past a Continuously Moving Vertical Porous Plate in the Presence of Heat Generation/Absorption," ASME J. Heat Transfer, **128**(2), pp. 142–152.

[19] Badr, H. M., and Dennis, S. C. R., 1985, "Time-Dependent Viscous Flow Past an Impulsively Started Rotating and Translating Circular Cylinder," J. Fluid Mech., **158**, pp. 447–488.

[20] Mahfouz, F. M., and Badr, H. M., 2000, "Flow Structure in the Wake of a Rotationally Oscillating Cylinder," ASME J. Fluids Eng., **122**, pp. 290–301.

[21] Mahfouz, F. M., and Badr, H. M., 2000, "Forced Convection from a Rotationally Oscillating Cylinder Placed in a Uniform Stream," Int. J. Heat Mass Transfer, **43**(17), pp. 3093–3104.

[22] Roshko, A., 1954, "On the Development of Turbulent Wakes from Vortex Streets," NACA Rep. No. 1191.

[23] Jordon, S. K., and Fromm, J. E., 1972, "Oscillatory Drag, Lift and Torque on a Circular Cylinder in a Uniform Flow," Phys. Fluids, **15**(3), pp. 371–376.

[24] Knudsen, J. D., and Katz, D. L., 1958, *Fluid Dynamics and Heat Transfer*, McGrow-Hill, New York.

[25] Hatton, A. P., James, D. D., and Swire, H. W., 1971, "Combined Forced and Natural Convection with Low Speed Air Flow over Horizontal Cylinders," J. Fluid Mech., **42**, pp. 17–31.

[26] Mahfouz, F. M., 2003, "Transient Free Convection from a Horizontal Cylinder Placed in a Micropolar Fluid," Heat Mass Transfer, **39**, pp. 455–462.

[27] Mahfouz, F. M., 2004, "Natural Convection from an Elliptic Tube with Major Axis Horizontal and Placed in Micropolar Fluid," Int. J. Heat Mass Transfer, **47**(6–7), pp. 1413–1422.

Performance of Phase Change Materials in a Horizontal Annulus of a Double-Pipe Heat Exchanger in a Water-Circulating Loop

J. R. Balikowski
Graduate Student
Mechanical and Aerospace Engineering,
School of Engineering,
State University of New York at Buffalo,
Buffalo, NY 14214-3078

J. C. Mollendorf
Professor of Mechanical
and Aerospace Engineering
School of Engineering,
State University of New York at Buffalo,
Buffalo, NY 14260-4400;
Professor of Physiology and Biophysics
School of Medicine,
State University of New York at Buffalo,
Buffalo, NY 14214-3078,
and
Center for Research and Education in Special
Environments,
State University of New York at Buffalo,
Buffalo, NY 14214-3078
e-mail: molendrf@buffalo.edu

Phase change materials (PCMs) are used in applications where temperature regulation is important because they absorb and release a large amount of energy at a fixed temperature. In the experimental part of this investigation, PCM was placed in the annular region of a double-pipe heat exchanger with water circulated in the inside pipe. Experiments were performed in which the PCM would absorb (charge) and then release (discharge) energy at various temperatures and water flows. Two materials, Climsel 28 (C28) by Climator and microencapsulated Thermasorb 83 (TY83) by Outlast Technologies, were each tested in smooth and spined annuli to observe which configuration facilitated heat transfer. The latent heats and thermal conductivities of C28 and TY83 are 126 kJ/kg *and* 186 kJ/kg *and* 0.6 W/m/°C *and* 0.15 W/m/°C, *respectively. The experimental data were analyzed to verify which PCM transferred more heat. The effect of different water flow rates on the heat transfer rate was also examined. In the theoretical part of this investigation, heat transfer theory was applied to C28 in the smooth-piped heat exchanger in order to better understand the phase change process. The presence of spined fins in the phase change material accelerated charging and discharging due to increased fin contact with the outer layers of the PCM. The spined heat exchanger charged and discharged in* 180 min *and* 120 min, *respectively, whereas the temperature in the smooth heat exchanger remained below the fully charged/fully discharged asymptote by about* 3°C *and thus failed to fully charge or fully discharge. Also, higher water flows increased heat transfer between the PCM and water. TY83 in the spined heat exchanger transferred more heat and did it faster than C28 in the spined heat exchanger. The heat transfer rate from the water to TY83 while charging was 25% greater during the transient period than in C28. While discharging, the heat transfer from TY83 to the water was about 20% greater than in C28. There was generally good agreement (±1.5°C) between theory and experimental data of C28 in the smooth-piped heat exchanger in terms of the trends of the temperature responses. The differences are expected to be a result of approximations in boundary conditions and uncertainties in how the temperature variation of the specific heat is formulated.* [DOI: 10.1115/1.2426359]

Keywords: latent heat, phase change material, PCM, micro encapsulation, annular flow

Introduction

Phase change materials (PCMs) provide an alternative thermal storage mechanism to the usual inherent sensible heat capacity of materials. They store large amounts of energy using less volume and their isothermal behavior is useful in applications like the transportation of temperature-sensitive materials and temperature stabilization in electronic equipment. PCMs are available as inorganic or organic materials. Table 1 shows a comparison of the properties for one inorganic PCM named C28 (sodium sulphate) and one microencapsulated, organic PCM named TY83 (octadecane). Generally, inorganic PCMs have larger latent heats and thermal conductivities than organic PCMs [1]. However, inorganic PCMs can remain in liquid form when cooled below their melting point, a phenomenon called supercooling. Organic PCMs do not exhibit supercooling, but they take longer to charge due to their low thermal conductivities.

Previous studies have demonstrated the need for heat transfer enhancement to improve the performance of PCMs. A few studies

have focused their attention on PCM stored in a horizontal cylindrical annulus. Liu et al. [1] studied the performance of stearic acid around an electrical heating rod with external spiral fins. These fins improved heat conduction and natural convective heat transfer throughout the PCM. The effective thermal conductivity was increased by a factor of up to three. Zhang and Faghri [2] concluded internal longitudinal fins on an inner pipe transporting air enhanced heat transfer more than placing the fins within the annulus. The fins increased the convective heat transfer coefficient for an otherwise low conducting fluid. Parametric studies of a temperature transforming model of the PCM linked to the heat transfer from the air inside the internally finned tube demonstrated that the increase of fin width, height, and number accelerated the melting rate of the PCM. Ismail et al. [3] performed a numerical and experimental study of solidification of a PCM around a vertical axially finned isothermal cylinder. The fin geometry and annular space were varied to find a compromise between heat transfer enhancement and loss of available storage capacity.

Previous theoretical studies have simulated the phase change process in horizontal annuli. Zhang and Faghri [4] solved the temperature distribution of n-octadecane in a cylindrical annulus with water transported in a smooth inner tube. To avoid introducing errors, they coupled the solution of forced convection heat

Table 1 Physical properties of C28 and TY83

	C28	TY83
Phase change temperature, T_m (°C)	28	28.3
Phase change temperature range, $T_1 - T_2$ (°C)	18–38	27.2–29.4
Latent heat, L (kJ/kg)	126	186
Density, ρ (g/cm³)	1.44	0.80 (solid)
		0.77 (liquid)
Specific heat, c_p (kJ/kg/°C)	3.6	2.16
Thermal conductivity, k (W/m/°C)	0.5–0.7	0.15

transfer inside the tube and heat conduction in the annulus rather than using Nusselt number correlations assuming fully developed flow. Ng et al. [5] numerically studied the domination of natural convective heat transfer in the melting of n-octadecane by heating the inner wall of a cylindrical annulus isothermally. Cross-sectional isotherms showed the melt region expanded uniformly in the radial direction at the initial stage. Thereafter, an upward energy flow caused by buoyancy resulted in nonuniform melting at the top of the annulus. Khillarkar et al. [6] adapted Ng's model but investigated two type of annuli described as "square external tube with a circular tube inside" and "circular external tube with a square tube inside," with the inner wall, outer wall, or both walls heated isothermally. The effect of heating both walls isothermally was the same as heating the inside wall and outside wall separately until the melt regions interacted and melting accelerated. Xin and Yinping [7] ignored natural convective heat transfer altogether and formulated the problem for the unsteady one-dimensional heat conduction equation for PCM within cylindrical and spherical walls. They identified thermal conductivity, specific heat, latent heat, density, and temperature difference of the annular walls as factors influencing heat transfer enhancement. In the theory section, a conduction model similar to Ref. [7] was formulated and solved numerically and compared to experimental data to better understand the physics of the phase change process. Also, the goal of the experimental investigation was to determine which of the two PCMs introduced in Table 1 transferred more heat and did it faster in smooth-piped and spined heat exchangers under various charging/discharging and flow conditions.

Experimental Protocol

Figure 1 is a schematic of the experimental setup. Water was circulated through insulated poly vinylchloride (PVC) tubing using a 24 V gear pump manufactured by Enginegear (model no. GP-301). The water temperature was regulated by a thermoelectric cooler (TEC) with dual heating/cooling modes manufactured
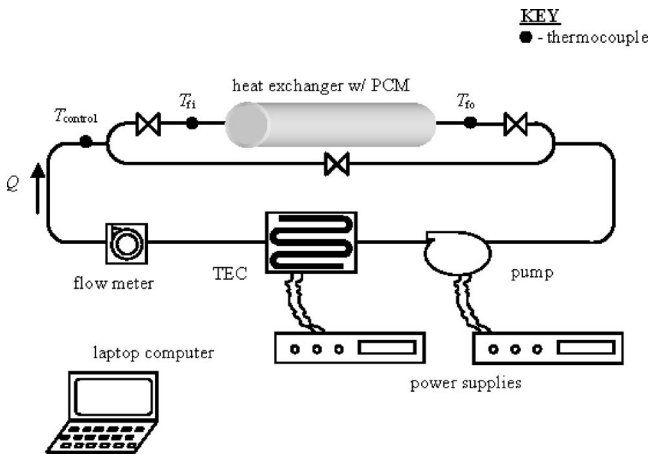
Fig. 2 Cross section of the smooth double-pipe heat exchanger at $x = \frac{l}{2}$

KEY
1 – water
2 – copper pipe, 1/2" ID - 5/8" OD
3 – PCM
4 – Plexiglas, 3/2" ID - 2" OD
5 – vulcanized rubber, 1/4" thickness
6 – ambient air
● - thermocouple

by TE Tech (model no. LC-120). These two components were operated by separate dc power supplies. The two PCMs, Climsel 28 and Thermasorb 83, were charged and then discharged at a fixed water flow rate. The chosen charge/discharge temperature pairings were 30/26°C, 32/24°C, and 34/22°C, respectively. Tests were performed for each pairing at water flow rates of 1 L/min, 2 L/min, and 3 L/min. These flows were chosen based on physiological data from testing in the CRESE laboratory of divers wearing tube suits. Altogether, these nine tests were performed for four PCM-heat exchanger configurations: Climsel 28 in the smooth-piped heat exchanger, Climsel 28 in the spined heat exchanger, Thermasorb 83 in the smooth-piped heat exchanger, and Thermasorb 83 in the spined heat exchanger.

Figure 2 shows a cross section schematic of the smooth double-pipe heat exchanger used in the experimental investigation. The PCM was packed between the copper pipe transporting water and a Plexiglas tube shrouded with vulcanized rubber. There were two heat exchangers built for these experiments: one utilized a smooth inner copper pipe and the other a spined inner copper pipe shown in Fig. 3. Both pipes had smooth inner surfaces and the same wall thickness and inside diameter. The "spined" tube is made by He-atron Inc. using the Thermek process. The tube inside and outside diameters are about 0.49 in. and 0.63 in., respectively. The curved fins are about 0.6 in. long, about 0.08 in. wide at the base, and

KEY
● - thermocouple

Fig. 1 Experimental setup of water-circulating loop with the double-pipe heat exchanger storing PCM

Fig. 3 Photograph of the spined copper pipe used as the inner tube in the double-pipe heat exchanger

about 0.032 in. thick. There are about 25 fins (spines) per one spiral revolution and about 170 revolutions on the tube used.

A Dell Inspiron 8100 laptop computer and National Instruments data acquisition system (model no. FP-1000) were used to record flow and temperature data at 15 s intervals. At the beginning of the experiment, the water bypassed the smooth-piped heat exchanger containing C28 until the water flow was established and thermocouple T_{control} reached the desired charging temperature set by the TEC software. Then, the bypass valve was closed while the valves surrounding the heat exchanger were opened, allowing the heated water to flow through the heat exchanger. Once the outermost thermocouple (T_0 in Fig. 2) reached steady state, it was assumed the PCM was fully charged and ready to discharge. Then the valves surrounding the heat exchanger were closed while the bypass valve was opened, allowing water to once again bypass the heat exchanger until T_{control} reached the desired discharge temperature set by the TEC software. Immediately, the bypass valve was closed while the heat exchanger valves were opened so that cooled water flowed through the heat exchanger. Throughout the experiment, T_0 was monitored until it reached steady state and data recording was ended. Tests of each charge/discharge temperature pairing and corresponding flows were completed for the smooth-piped heat exchanger containing C28. Experiments were then done using the spined heat exchanger with a fresh sample of C28 for repeated testing following the same protocol. Finally, both heat exchangers were cleaned and refilled with TY83 for testing using the same procedures as for C28. The estimated accuracy of the calibration of the flow meter and thermocouples is about ±5%. The resulting accuracy of the inference of the heat transfer is about ±10%. The estimated accuracy of the time and length measurements is about ±0.1 s and ±0.10 in., respectively.

Theory

Theoretical analysis of either C28 or TY83 in the spined heat exchanger is very difficult due to the extremely complex geometry of the spiral wound spines. Also, theoretical analysis of TY83 in the smooth configuration is complicated by the microencapsulation of TY83. Therefore, it was decided to experimentally compare the smooth and spined configurations and analyze the temperature distribution of C28 in the smooth heat exchanger only. It is expected that the main parameters in the smooth-piped heat exchanger analysis will exhibit the same trends as the spined configuration, but with a faster charge/discharge time due to the large surface area of the spined heat exchanger.

The equations and thermophysical properties are presented for solving for the temperature distribution of C28 in the smooth-piped heat exchanger. Later, the temperature distribution will be compared with the values of T_0 in Fig. 2. The formulation of the problem for the temperature distribution in Region 3 of Fig. 2 is

$$\frac{\partial^2 T}{\partial r^2} + \frac{1}{r}\frac{\partial T}{\partial r} = -\frac{q_s}{k} = \frac{\rho c_p(T)}{k}\frac{\partial T}{\partial t} \tag{1}$$

$$k\frac{\partial T}{\partial r}\bigg|_{r=r_i} = h[T(r_i,t) - T_{fm}] \tag{2}$$

$$k\frac{\partial T}{\partial r}\bigg|_{r=r_o} = q'' \tag{3}$$

$$T(r,0) = T_{\text{init}} \tag{4}$$

Following the work done in Ref. [7], the internal heat source was defined in Eq. (1) as a transient term with temperature-dependent specific heat, expressed as

$$q_s = -\rho c_p(T)\frac{\partial T}{\partial t} \tag{5}$$

It is noted that C28 is a mixture of PCM and water with a low concentration of water. Its density, thermal conductivity, and base specific heat (defined as a constant value when the temperature of C28 is not within the melting temperature range) are the following mass-averaged properties from Inaba et al. [8], expressed as

$$\rho = c_m\rho_{C28} + (1 - c_m)\rho_{\text{H}_2\text{O}} \tag{6}$$

$$k = c_m k_{C28} + (1 - c_m)k_{\text{H}_2\text{O}} \tag{7}$$

$$c_{p,\text{base}} = c_m c_{p,C28} + (1 - c_m)c_{p,\text{H}_2\text{O}} \tag{8}$$

When C28 begins changing phase, it absorbs or releases large amounts of heat. This is manifested by a large increase in specific heat when the temperature is within the phase change temperature limits. The specific heat was modeled as an exponential function adapted from Inaba et al. [9] that is centered around the phase change temperature, expressed as

$$c_p = c_{p,\text{base}} + a \exp - \left(b\frac{T(r,t) - T_m}{T_2 - T_m}\right)^2 \tag{9}$$

where T_1 is the low phase change temperature limit; T_2 is the high phase change temperature limit; and T_m is the phase change temperature. The amplitude a is expressed as

$$a = \frac{2b}{\sqrt{\pi} \text{ erf } b}\frac{L}{T_2 - T_1} \tag{10}$$

where b is a constant that determines the width of the curve, as shown in Fig. 4 for $b=2.3$. The properties within the boundary conditions must also be specified. The boundary condition represented by Eq. (2) reflects the physical fact that the convective heat transfer of the flowing water equals the conductive heat transfer through the PCM at the boundary formed by $r=r_i$. The thermal effect of the copper pipe was ignored in this analysis due to its low thermal resistance. The mean water temperature at the midsection was approximated by the average of the inlet and outlet water temperatures of the heat exchanger (see Fig. 1)

$$T_{fm}(t) = \frac{T_{fi}(t) + T_{fo}(t)}{2} \tag{11}$$

The method of computing the convective heat transfer coefficient depends on the type of flow, as indicated by the Reynolds number. The range of Reynolds numbers for these experiments was 1665 to 6262. If $\text{Re}_b < 2300$, then the flow was taken to be laminar, and the following correlation for thermal entrance regions from Ref. [10] is expressed as

$$\text{Nu}_r = \frac{2r_i\bar{h}}{k} = 3.66 + \frac{0.19(\text{Re}_b \text{ Pr}_b d/l)^{0.8}}{1 + 0.117(\text{Re}_b \text{ Pr}_b d/l)^{0.467}} \tag{12}$$

for $0.1 < \text{Re}_b \text{ Pr}_b d/l < 10^4$. If $\text{Re}_b > 2300$, then the flow was taken to be turbulent, and the following correlation for low Reynolds numbers from Ref. [10] is expressed as

$$\text{Nu}_b = \frac{2r_i\bar{h}}{k} = 0.012(\text{Re}_b^{0.87} - 280)\text{Pr}_b^{0.4} \tag{13}$$

where Re_b and Pr_b are dimensionless parameters that depend on the fluid and heat transfer properties of water. The ranges of applicability for Re_b and Pr_b are $2300 < \text{Re}_b < 5 \times 10^6$ and $1.5 < \text{Pr}_b < 500$, respectively.

The outer wall of the double-pipe heat exchanger was not perfectly insulated. The boundary condition represented by Eq. (3) reflects the physical fact that the conductive heat transfer through the PCM equals a prescribed heat flux at the boundary formed by $r=r_o$. Using a quasi-steady approximation, the prescribed heat flux is expressed as
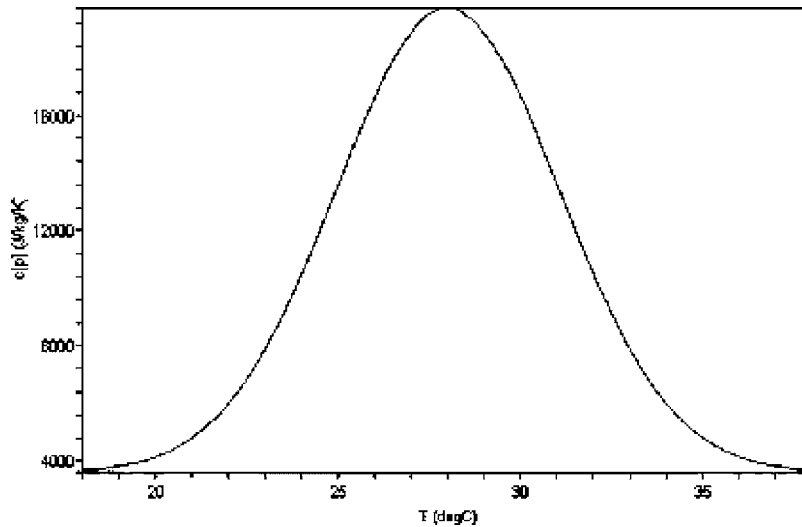
Fig. 4 Specific heat of C28 within the phase change temperature limits for *b* = 2.3, adapted from Ref. [9]

$$q'' = \frac{T_\infty - T_0(t)}{2\pi r_o l R_t} \tag{14}$$

where R_t is the sum of the conductive resistances in the Plexiglas and vulcanized rubber and the convective resistance of quiescent ambient air (see Fig. 1 for a definition of subscripts)

$$R_t = \frac{\ln r_{45}/r_o}{2\pi l k_4} + \frac{\ln r_{56}/r_{45}}{2\pi l k_5} + \frac{1}{2\pi r_{56} l h_6} \tag{15}$$

The initial condition in Eq. (4) is assumed to be the average of three thermocouple readings at $t=0$, or

$$T_{init} = \frac{T_i(0) + T_m(0) + T_0(0)}{3} \tag{16}$$

Equations (1)–(4) and the parameters defined by Eqs. (5)–(16) constitute a second-order, nonlinear, partial differential equation. This was solved numerically using the well-known PDSOLVE/NUMERIC software in MAPLE. This amounts to a second-order (in space and time) centered, implicit finite difference scheme (Crank–Nickolson). A study of grid independence was done and the resulting precision of the computed temperatures is better than 0.001 °C.

Results and Discussion

Figure 5 shows the measured temperature response of C28 in the smooth-piped heat exchanger charging to 34 °C at 2 L/min

water flow. As expected, thermocouple T_i indicated the highest temperature throughout the experiment due to its location on the heated pipe. Thermocouples T_m and T_0 indicated increasingly lower temperatures than T_i because their locations are further away from the heated pipe. Initially, there is a large rise in T_i due to the low thermal conductivity of solid C28. This is because more energy is absorbed by the innermost layer of C28 than transferred to the neighboring layer. Near the melting point, the rise in temperature is slowed by phase change. This is because energy is being used to break chemical bonds in the PCM rather than raise its temperature. The same behavior is observed in T_m and T_0. Initially, there is a large temperature difference between T_i and the other thermocouple readings due to the low thermal conductivity of solid C28. When C28 melts and the liquid phase appears, the effective thermal conductivity increases due to the presence of natural convection heat transfer. Thus more heat is being transferred to the outer layers and the temperatures T_m and T_0 "catchup" to the temperature T_i. Finally, T_i reaches steady state when approaching the temperature of the flowing water inside the copper pipe. As seen in Fig. 5, the experiment was run for over 4 h without T_m and T_0 reaching the temperature of 34 °C of the flowing water. Clearly, heat transfer enhancement would be desirable for the PCM to charge more quickly.

It is well known that the use of extended surfaces increases the surface areas of pipes and thus increases heat transfer. Figure 6 shows the difference between the temperature T_0 of C28 in
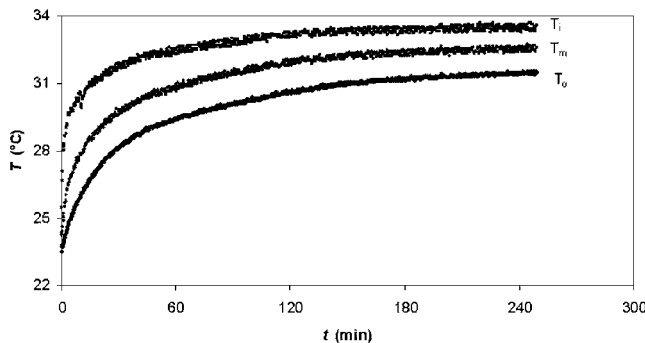

Fig. 5 Temperature response of thermocouples located in region 3 of Fig. 3 for C28 charging in the smooth-piped heat exchanger to 34 °C at 2 L/min water flow
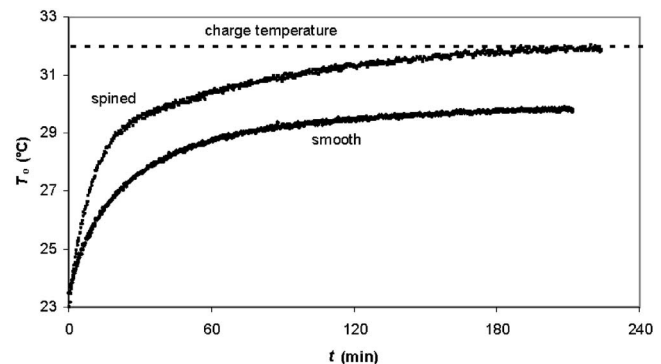

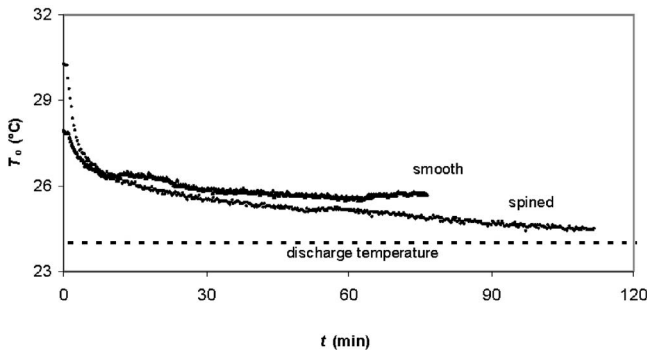**Fig. 6 Comparison of T_0 in the smooth-piped and spined heat exchangers for C28 charging to 32 °C at 2 L/min water flow**

Fig. 7 Comparison of T_0 in the smooth-piped and spined heat exchangers for TY83 discharging to 24°C at 1 L/min water flow

Fig. 9 Comparison of time-averaged q for C28 and TY83 charging to 30°C at 3 L/min water flow in the spined heat exchanger

smooth-piped and spined heat exchangers charging to 32°C at 2 L/min water flow. It is observed that T_0 in the spined heat exchanger reaches the charging temperature represented by the dashed line in Fig. 6, but reaches steady state at a lower temperature in the smooth design. From Fig. 6, it can be seen that during charging the spined heat exchanger reached 29°C and 30°C about 45 min and 195 min sooner than the smooth-piped heat exchanger, respectively. Figure 7 shows the difference between T_0 for TY83 in smooth-piped and spined heat exchangers discharging to 24°C at 1 L/min water flow. It is observed that T_0 in the spined heat exchanger came closer to achieving the discharging temperature than in the smooth-piped heat exchanger. From Fig. 7, it can be seen that during discharging the spined heat exchanger reached 26°C and 25.5°C about 10 min and 30 min sooner than the smooth-piped heat exchanger, respectively. The presence of spined fins accelerated charging and discharging due to increased fin contact (surface area) with the outer layers of the PCM. Therefore, it is advantageous to use the spined design to fully charge or discharge in a timely manner because emergency situations would require a fast response time.

Figure 8 demonstrates that both PCMs reach the charging temperature of 30°C at about the same time. Figure 9 shows that the heat transfer rate during the transient period from the water to TY83 is about 25% greater than the heat transfer from the water to C28 under the same conditions. Figure 10 shows that both PCMs reach the discharging temperature of 24°C at the same time for 3 L/min water flow. The lag (upward bulge) in the thermal response of C28, seen in Fig. 10, is due to its relatively wide phase change temperature range (18–38°C, Table 1) compared with the relatively narrow phase change temperature range (27.2–29.4°C, Table 1) of TY83. Moreover, Fig. 11 shows that the heat transfer from TY83 to the water is about 20% greater than the heat transfer

from C28 to the water while discharging occurs. It can be concluded that TY83 transfers more heat and does it faster than C28 for both charging and discharging.

The effect of three water flow rates on the heat transfer rate was also examined. Figure 12 shows an increase in heat transfer rate with increasing water flow for TY83 in the spined heat exchanger. If higher flows than 3 L/min were tested, it is expected that the heat transfer rate would increase further due to the increase in the mass flow rate of water; however, there may be an overall energy penalty for doing this.

Figures 13 and 14 show a comparison between theory and experimental data (T_0) for C28 in the smooth-piped heat exchanger. There was generally good agreement (±1.5°C) between theory and experimental data for C28 in the smooth-piped heat exchanger in terms of the trends of the temperature responses. It is suggested that the assumptions made in the boundary condition

Fig. 10 Comparison of T_0 for C28 and TY83 discharging to 24°C at 3 L/min water flow in the spined heat exchanger
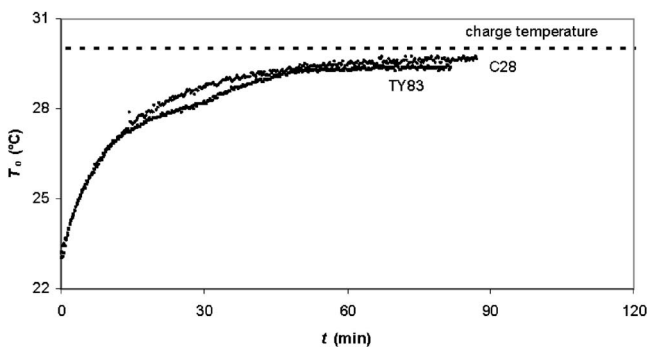

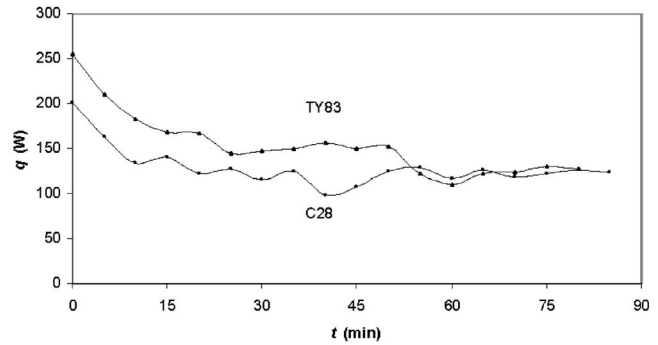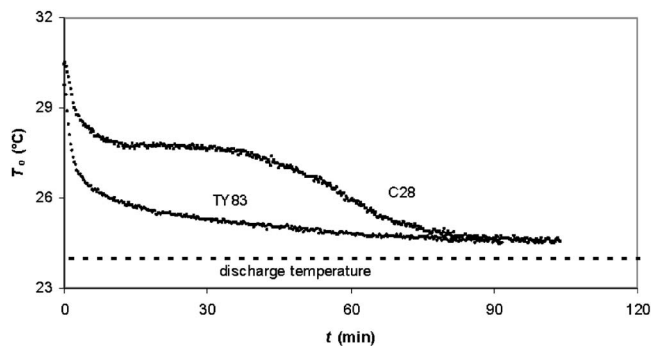**Fig. 8 Comparison of T_0 for C28 and TY83 charging to 30°C at 3 L/min water flow in the spined heat exchanger**
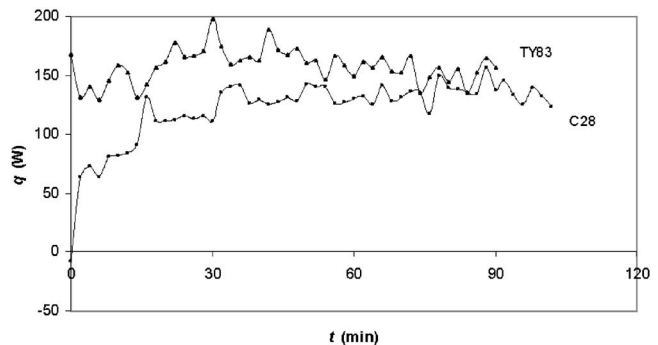

Fig. 11 Comparison of time-averaged q for C28 and TY83 discharging to 24°C at 3 L/min water flow in the spined heat exchanger
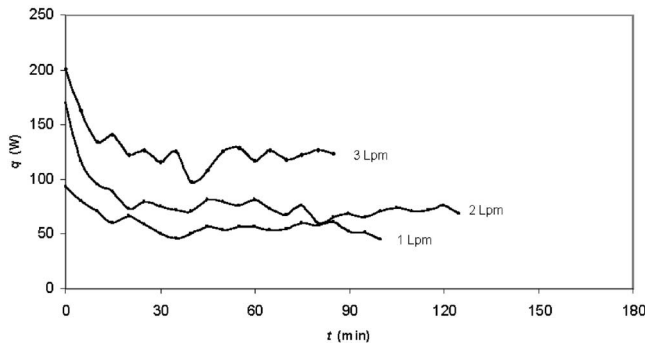
Fig. 12 Time-averaged q for three water flows in the spined heat exchanger with TY83 charging to 30°C

formulations and uncertainties in how to define the specific heat are responsible for the differences. For instance, h in the boundary condition represented by Eq. (2) is approximate due to the limitations of the Nusselt number correlations represented by Eqs. (12)
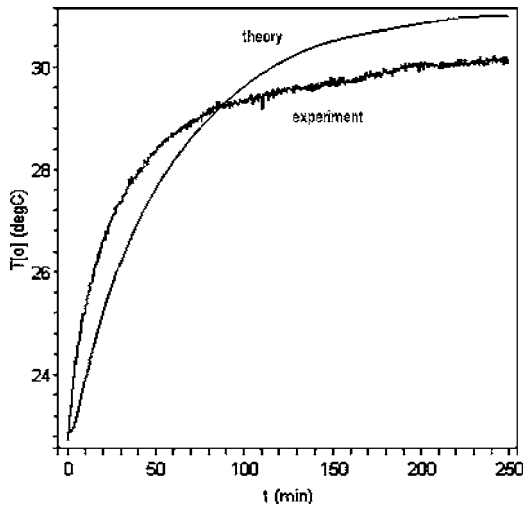

Fig. 13 Comparison of theory and experimental data of T_0 for C28 in the smooth-piped heat exchanger charging to 32°C at 3 L/min water flow
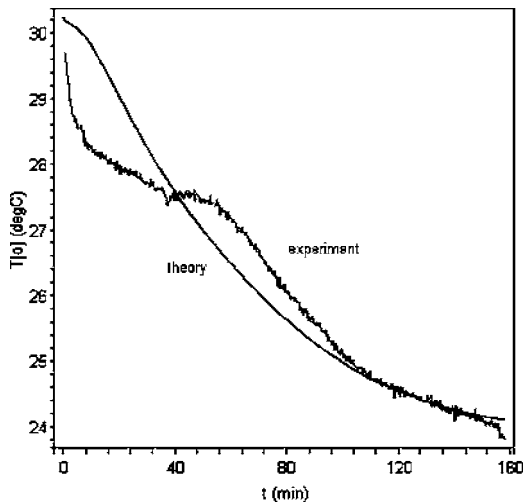
Fig. 14 Comparison of theory and experimental data of T_0 for C28 in the smooth-piped heat exchanger discharging to 24°C at 3 L/min water flow

Fig. 15 Predicted theoretical distribution of temperature in the radial direction for various times with C28 in the smooth-piped heat exchanger charging to 32°C at 3 L/min water flow

and (13). The Nusselt number correlation represented by Eq. (12) is accurate when the inner surface of the copper pipe is at a constant temperature. However, a constant surface temperature was never achieved in any of the experiments. The Nusselt number correlation represented by Eq. (13) is accurate for fully developed turbulent flow. However, the double-piped heat exchanger is not long enough for this type of flow to occur. Also, T_{fm} is approximated in Eq. (2) as the average of the inlet and outlet water temperatures in the heat exchanger. This assumes a linear temperature distribution along the length of the heat exchanger. The use of a log mean temperature difference (LMTD) would have been more appropriate but the impracticality of measuring the inner surface temperature of the copper pipe midsection precluded its use. An attempt to approximate T_i as this surface temperature resulted in random or undefined h values in the data analysis. This randomness was caused by the fluctuating temperature difference of the flowing water, $T_{fi} - T_{fo}$, which resulted in fluctuating LMTD values. These fluctuations are expected to be the result of accumulated system noise. The undefined h values occurred whenever one of the water temperatures T_{fi} or T_{fo} was less than the surface temperature T_i while the PCM was charging or whenever one of the water temperatures T_{fi} or T_{fo} was greater than T_i while the PCM was discharging. These conditions yielded a negative number in the argument of the log function, which causes the LMTD to be undefined. The boundary condition in Eq. (3), which is calculated from the resistance model in Eq. (16), is also approximate. Equation (16) is expected to be accurate for the uninsulated midsection, yet it ignores insulated sections that precede and follow it.

There is also uncertainty in how to define the specific heat within the phase change temperature range. There is room for other interpretations of the shape and fullness of the curve seen in Fig. 4. The specific heat could be more or less concentrated or could be unsymmetrical as found in Ref. [9] from differential scanning calorimeter (DSC) measurements. A specific heat curve that is symmetrical about the phase change temperature was introduced in the "Theory" section based on the success that Hu and Zhang [11] had using square and sine waves that were symmetrical around the melting point.

Equations (1)–(4) were also used to predict the radial distribution of temperature for various times, as seen in Fig. 15 when C28

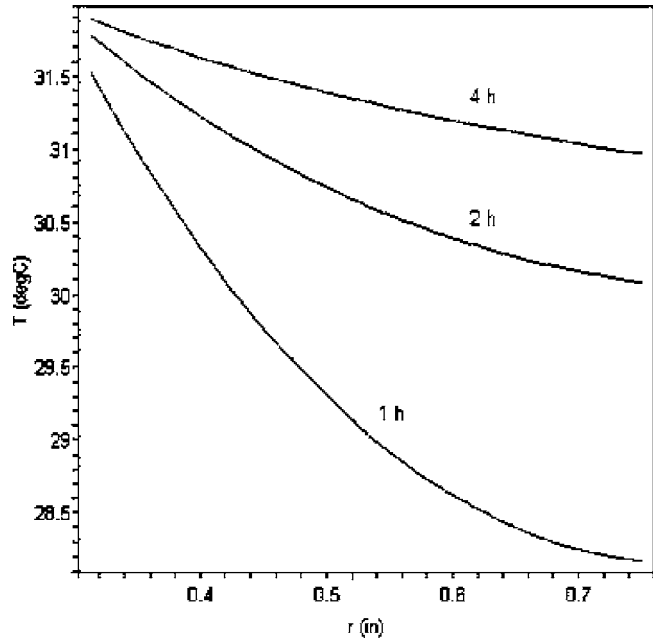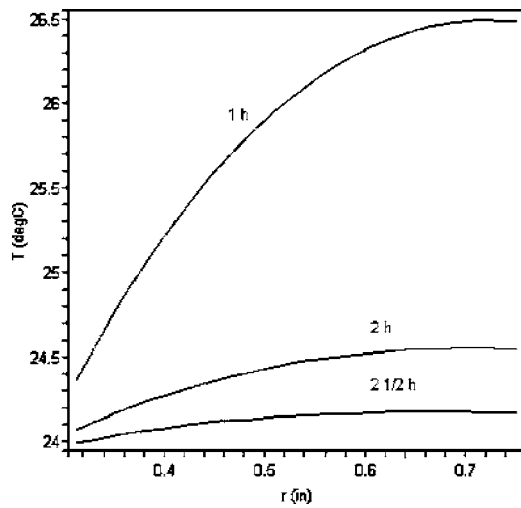**Fig. 16 Predicted theoretical distribution of temperature in the radial direction for various times with C28 in the smooth-piped heat exchanger discharging to 24°C at 3 L/min water flow**

is charging and in Fig. 16 when C28 is discharging in the smooth-piped heat exchanger. Figure 15 shows a decrease in temperature as the distance from the heated copper pipe increases. As time increases, the magnitude of the temperature gradient defined as $(T_0 - T_i)/(r_o - r_i)$ decreases as the temperature of the outermost PCM particles reaches the temperature of the heated copper pipe. Figure 16 shows an increase in temperature as the distance from the cooled copper pipe increases. As time increases, the temperature gradient defined as $(T_0 - T_i)/(r_o - r_i)$ decreases as the temperature of the outermost PCM particles reaches the temperature of the cooled copper pipe.

Results of the experiments for other charge/discharge temperatures and water flow pairings are reported in the appendix of Balikowski [12]. Because of the quite specific and limited range of conditions considered, it is not meaningful to generalize the results in terms of nondimensional parameters. Nevertheless, for reference purposes, it is noted that the three flows considered (1 L/min, 2 L/min, and 3 L/mins) correspond to Reynolds numbers of about 2000, 4000, and 6000, respectively; and typical times (60 min, 120 min, and 180 min) correspond to Fourier numbers of 3.4, 6.8, and 10.2, respectively. It is further noted that a reasonable characteristic heat transfer rate, for nondimensional scaling, would be proportional to the latent heat. This approximate scaling can be seen in the trends in Figs. 9 and 11.

Conclusions

The goal of this experimental investigation was to compare two PCMs in smooth-piped and spined heat exchangers for various charging/discharging and flow conditions. It was found that the presence of spined fins accelerated charging and discharging due to increased fin contact with the outer layers of the PCM. Higher water flows increased heat transfer between the PCM and water. However, it is cautioned that there may be an overall energy penalty for using higher flows. TY83 in the spined heat exchanger transferred more heat and did it faster than C28 in the spined heat exchanger. Both materials charged fully at about the same time, but the heat transfer rate from the water to TY83 during the transient period was 25% greater than the heat transfer rate from the water to C28. Likewise, both materials discharged fully at about the same time, but the heat transfer from TY83 to the water was about 20% greater than the heat transfer from C28 to the water.

There was generally good agreement (±1.5°C) between theory and experimental data of C28 in the smooth-piped heat exchanger in terms of the trends of the temperature responses. The differ-

ences between theory and experimental data are expected to be a result of approximations in boundary conditions and uncertainties in how to define the specific heat.

Acknowledgment

Nomenclature

a = amplitude, J/kg/°C
b = arbitrary constant
c_m = mass concentration of C28
c_p = specific heat, J/kg/°C (see Eq. (9))
d = inner diameter of copper pipe, m
$\bar{h}$ = average convective heat transfer coefficient, W/m²/°C
k = thermal conductivity, W/m/°C
l = length of heat exchanger, m
L = latent heat, J/kg
Nu = Nusselt number (see Eqs. (12) and (13))
Pr = Prandtl number
q = total heat transfer rate, W
q_s = internal heat source, W/m³
q'' = heat flux, W/m²
Q = volumetric flow, m³/s
r = radius, m
R_t = total resistance, K/W
Re = Reynolds number
t = time, s
T = temperature, °C
T_m = phase change temperature, °C
T_1 = low phase change temperature limit, °C
T_2 = high phase change temperature limit, °C

Greek Letters

ρ = density, kg/m³

Subscripts

b = bulk
fi = fluid (water) inlet
fm = fluid (water) midsection
fo = fluid (water) outlet
init = initial
i = inner surface
m = midpoint
o = outer surface
T = constant temperature
∞ = ambient

References

[1] Liu, Z., Sun, X., and Ma, C., 2005, "Experimental Investigations on the Characteristics of Melting Processes of Stearic Acid in an Annulus and Its Thermal Conductivity Enhancement by Fins," Energy Convers. Manage., **46**(6), pp. 959–969.

[2] Zhang, Y., and Faghri, A., 1995, "Heat Transfer Enhancement in Latent Heat Thermal Energy Storage System by Using the Internally Finned Tube," Int. J. Heat Mass Transfer, **39**(15), pp. 3165–3173.

[3] Ismail, K. A. R., Alves, C. L. F., and Modesto, M. S., 2001, "Numerical and Experimental Study on the Solidification of PCM around a Vertical Axially Finned Isothermal Cylinder," Appl. Therm. Eng., **21**(1), pp. 53–77.

[4] Zhang, Y., and Faghri, A., 1995, "Semi-analytical Solution of Thermal Energy Storage System With Conjugate Laminar Forced Convection," Int. J. Heat Mass Transfer, **39**(7), pp. 717–724.

[5] Ng, K. W., Gong, Z. X., and Mujumdar, A. S., 1998, "Heat Transfer in Free Convection-Dominated Melting of a Phase Change Material in a Horizontal Annulus," Int. Commun. Heat Mass Transfer, **25**(5), pp. 631–640.

[6] Khillarkar, D. B., Gong, Z. X., and Mujumdar, A. S., 2000, "Melting of a Phase Change Material in Concentric Horizontal Annuli of Arbitrary Cross-

section," Appl. Therm. Eng., **20**(10), pp. 893–912.

[7] Xin, W., and Yinping, Z., 2002, "Solid-Liquid Phase Change Heat Transfer Enhancement Analysis in Cylindrical and Spherical Walls," J. Enhanced Heat Transfer, **9**, pp. 109–115.

[8] Inaba, H., Myoung-Jun, K., and Akihiko, H., 2004, "Melting Heat Transfer Characteristics of Microencapsulated Phase Change Material Slurries With Plural Microcapsules Having Different Diameters," J. Heat Transfer, **126**(4), pp. 558–565.

[9] Inaba, H., Dai, C., and Horibe, A., 2003, "Natural Convection Heat Transfer of Microemulsion Phase Change Material Slurry in Rectangular Cavities Heated From below and Cooled From above," Int. J. Heat Mass Transfer, **46**(23), pp.

4427–4438.

[10] Kakac, S., and Yener, Y., 1995, *Convective Heat Transfer*, 2nd ed., CRC Press, Boca Raton, FL, pp. 291–294.

[11] Hu, X., and Zhang, Y., 2002, "Novel Insight and Numerical Analysis of Convective Heat Transfer Enhancement With Microencapsulated Phase Change Material Slurries: Laminar Flow in a Circular Tube With Constant Heat Flux," Int. J. Heat Mass Transfer, **45**(15), pp. 3163–3172.

[12] Balikowski, J. R., 2005, "The Feasibility of a Fuel Cell/Phase Change/ Thermoelectric System for Free Swimming Diver Thermal Protection," M.S. thesis, University at Buffalo, Buffalo, NY.

Porous Medium Interconnector Effects on the Thermohydraulics of Near-Compact Heat Exchangers Treated as Porous Media

K. Sumithra Raju
Ph.D. Student

Arunn Narasimhan[1]
Assistant Professor
e-mail: arunn@iitm.ac.in

Heat Transfer and Thermal Power Laboratory,
Department of Mechanical Engineering,
Indian Institute of Technology Madras
Chennai, Tamil Nadu 600036, India

A novel approach of treating near-compact heat exchangers (NCHX) (surface to volume ratio, $\alpha = 100-300 \text{ m}^2/\text{m}^3$ with hydraulic diameter $D_M \sim 6$ mm) as a "global" porous media, whose thermohydraulic performance is being influenced by the presence of "local" tube-to-tube porous medium interconnectors, connecting the in-line arrangement of tubes ($D = 2$ mm) having square pitch of $X_T = X_L = 2.25$, is investigated in this study using numerical methods. The thermohydraulics of the global porous media (NCHX) are characterized by studying the effect of transverse thickness (δ) and permeability (represented by Da_i) of the local metal foam type porous medium interconnectors on the global heat transfer coefficient (Nu) and nondimensional pressure drop (ξ). The fluid transport in the porous medium interconnectors is governed by the Brinkman–Darcy flow model while the volume averaged energy equation is used to model energy transport, with the tube walls kept at constant temperature and exchanging heat with the cooling fluid having $Pr = 0.7$ under laminar flow ($10 < Re < 100$). For the chosen NCHX configuration, ξ and Nu increases for an increase in Re and also with an increase in the thickness (δ) of the interconnecting porous medium. However, as the local Darcy number (Da_i) of the interconnecting porous medium increases, the ξ decreases but the Nu increases. Treating the heat exchanger as a global porous media this result translates to an increase in the ξ and Nu as the global permeability (represented by Da_g) decreases, where the decrease in Da_g is because of either an increase in δ or a decrease in Da_i. Separate correlations predicting ξ and Nu as a function of Re and Da_g (which in turn is correlated to δ and Da_i) have been developed for the chosen NCHX configuration, both of which predict the numerical data with $\pm20\%$ accuracy. [DOI: 10.1115/1.2427074]

Keywords: forced convection, porous medium, metal foams, tube banks, porous fins, permeability, heat transfer enhancement, heat exchangers

1 Introduction

Use of porous medium in a forced convection configuration has become one of the most effective enhancement techniques in recent years [1–4] due to the wide engineering and industrial applications in microporous enhanced heat exchangers [5], electronic cooling using metal foams, heat pipes, and solar collectors. In typical forced convection applications, however, the pressure penalty of the porous medium usage may be high and hence the demand for enhanced heat transfer payback is also higher: for instance cooling of airborne radar electronics using porous medium enhanced cold plates [5] is restricted by the pump power, which is a premium in the aircraft that houses the electronics.

The alternate is to explore forced convection configuration with a partially filled porous medium region coexisting with a region without the porous medium. This design promises a heat transfer enhancement of comparable magnitude while incurring lesser global pressure-drop. For instance, recently, Hadim [6] reported that the use of porous substrate enhances heat transfer of equal magnitude with less pressure drop when compared to the fully filled

porous medium case in a channel using fluid of $Pr = 10$ as a cooling medium. Alkam and Al-Nimr [7] studied numerically the use of porous substrates in a double pipe heat exchanger. Kiwan and Al-Nimr [8] introduced a novel method that enhance heat transfer from a given surface using porous fins and compared the thermal performance of porous fins with that of solid fins. It is found that using porous fins equal in overall size and shape when compared to a conventional solid fin, enhances the convection performance.

Recently, numerical investigations by Mohamad [9] reveals that the optimum porous medium thickness of about 60% of channel height is better for heat transfer enhancement in a heat exchanger fitted with fully filled or partially filled porous medium. Laminar flow of air was considered in his study and the form-drag term is found to be not important for $Da < 10^{-4}$. Bogdan and Mohmmad [10] introduced heat transfer augmentation technique in a pipe using porous substrates and studied the effect of porous medium thickness and its properties. Results are compared with clear (of porous medium) fluid solution. Angirasa [11] showed experimentally that the heat transfer augmentation with metallic fibrous materials and the porous block of lower porosity have lower thermal resistance and higher heat transfer rates. Kuznetsov [12] proposed analytical solution for the fluid flow and heat transfer effects for steady fully developed fluid flow in a partially filled porous medium parallel-plates channel. This solution accounts for the boundary and form effects and considers a stress-jump boundary

Table 1 Values of constants in Eq. (9) taken from experimental values found in literature

S No.	Reference	Permeability (K_i, m^2)	Porosity (Φ)	k_{eff}
1	[5]	4.44×10^{-10}	0.58	85.69
2	[34]	4.44×10^{-9}	0.8	40.82
3	[35]	4.44×10^{-8}	0.95	10.22

condition at the porous-fluid interface. Further analytical studies of forced convection in other partly porous configuration are given in more detail [13]. Faghri and Rao [14] studied the effect on pressure drop and heat transfer by equipping the tubes with unconnected longitudinal solid fins in inline tube banks for various Pr and it was found that the finned tube do not enhance heat transfer.

With the above literature serving as a relevant background, the idea of tube-to-tube porous medium interconnectors as a means of heat transfer enhancement in a cross flow, near-compact heat exchanger (NCHX) ($\alpha = 100-300$ m^2/m^3 with hydraulic diameter $D_M \sim 6$ mm [15]) with inline arrangement of tubes ($d=2$ mm) is investigated in this paper. The porous medium connecting the tubes in the longitudinal flow direction are of metal foam type (properties given in Table 1) and the effect of their thickness and permeability on heat transfer enhancement of the NCHX is studied in detail.

2 Physical Model and Boundary Conditions

A schematic of the physical model of cross flow, near compact heat exchanger with aligned tubes interconnected by porous medium fins is shown in Fig. 1(a). The porous medium fins are employed only in the longitudinal direction (Fig. 1(b)). The thick-
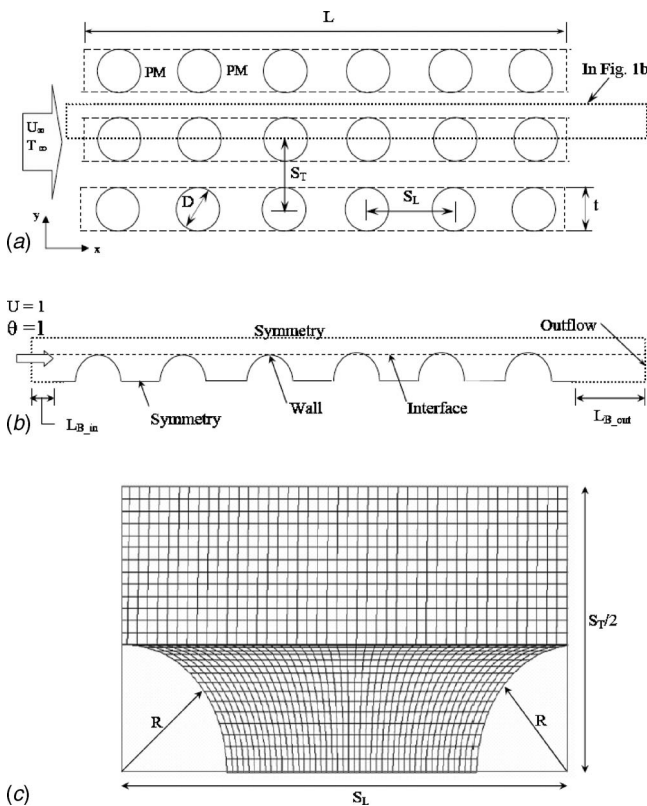

Fig. 1 Problem configuration: (a) schematic of the problem, (b) boundary conditions and computational domain, and (c) grid used

ness (t, m) of porous medium fins shown in Fig. 1(a) is equal to the diameter of the tube, although in the numerical simulation, this is the parameter of study (varies from 0 to $S_T/2$). The governing equations in dimensional and dimensionless form are as follows.

Mass conservation equation

$$\frac{\partial u}{\partial x} + \frac{\partial v}{\partial y} = 0 \qquad (1a)$$

$$\frac{\partial U}{\partial X} + \frac{\partial V}{\partial Y} = 0 \qquad (1b)$$

Momentum conservation equation in x-direction

$$\rho\left(u\frac{\partial u}{\partial x} + v\frac{\partial u}{\partial y}\right) = -\frac{\partial p}{\partial x} + \lambda_1\mu\left(\frac{\partial^2 u}{\partial x^2} + \frac{\partial^2 u}{\partial y^2}\right) + \lambda_2\frac{\mu}{K}u \qquad (2a)$$

$$\left(U\frac{\partial U}{\partial X} + V\frac{\partial U}{\partial Y}\right) = -\frac{\partial P}{\partial X} + \frac{\lambda_1}{\text{Re}_D}\left(\frac{\partial^2 U}{\partial X^2} + \frac{\partial^2 U}{\partial Y^2}\right) + \lambda_2\frac{U}{\text{Re}_D\text{Da}^2} \qquad (2b)$$

Momentum conservation equation in y-direction

$$\rho\left(u\frac{\partial v}{\partial x} + v\frac{\partial v}{\partial y}\right) = -\frac{\partial p}{\partial y} + \lambda_1\mu\left(\frac{\partial^2 v}{\partial x^2} + \frac{\partial^2 v}{\partial y^2}\right) + \lambda_2\frac{\mu}{K}v \qquad (3a)$$

$$\left(U\frac{\partial V}{\partial X} + V\frac{\partial V}{\partial Y}\right) = -\frac{\partial P}{\partial Y} + \frac{\lambda_1}{\text{Re}_D}\left(\frac{\partial^2 V}{\partial X^2} + \frac{\partial^2 V}{\partial Y^2}\right) + \lambda_2\frac{V}{\text{Re}_D\text{Da}^2} \qquad (3b)$$

Energy conservation equation

$$\rho c_p\left(u\frac{\partial T}{\partial x} + v\frac{\partial T}{\partial y}\right) = k_e\left(\frac{\partial^2 T}{\partial x^2} + \frac{\partial^2 T}{\partial y^2}\right) \qquad (4a)$$

$$\left(U\frac{\partial \theta}{\partial X} + V\frac{\partial \theta}{\partial Y}\right) = \frac{1}{\text{Pr}_e\text{Re}_D}\left(\frac{\partial^2 \theta}{\partial X^2} + \frac{\partial^2 \theta}{\partial Y^2}\right) \qquad (4b)$$

The nondimensional form of each conservation equation (1b), (2b), (3b), and (4b) is obtained by using the nondimensional variables listed in the Nomenclature.

The above conservation equations are solved for both clear (of porous medium) fluid flow and porous medium flow by setting the parameters λ_1 and λ_2 as one and zero, respectively, in clear fluid zone and μ_{eff}/μ and unity respectively, in the porous medium zone so that Eqs. (2b) and (3b) automatically satisfy the porous-fluid zone interface condition (see Fig. 1) detailed in the following section. The effective thermal conductivity used in Eq. (4b) is calculated using

$$k_e = (1 - \phi)k_s + \phi k_f \qquad (5)$$

where the symbols are explained in the nomenclature.

Periodic boundary conditions [16] for simplifying the computational domain similar to that of the present problem (Fig. 1(a)) could be considered. However, the flow field in the present problem cannot be periodically thermally fully developed even though it could be hydrodynamically fully developed. This is due to the presence of the porous medium, which results in a nonperiodic diffusion dominated flow domain. However, owing to the symmetry of the domain, Fig. 1(a), the flow through the tubes bank can be simulated accurately by calculating the flow through the half section of one row in the direction of flow as shown in Fig. 1(b). To complete the problem formulation, the following boundary conditions are used in location as shown in Fig. 1(b).

The hot fluid flowing inside the tube is modeled to be at constant wall temperature (θ_w). No slip boundary condition is assumed adjacent to the wall and both the components of velocity (U, V) are set to zero. Since the flow is laminar and steady, $\partial U/\partial Y = V = \partial\theta/\partial Y = 0$ can be imposed in the mid plane between two rows and axes (line joining the tube centers) as shown in Fig.

1(b), while at the inlet to the channel, a known uniform velocity field is assumed. Since, the location of velocity inlet can affect the numerical solution of the given computational domain, sufficient buffer length has been provided at the inlet ($L_{B\text{-in}}$) such that flow should be uniform (U_∞, θ_∞) without thermal "back" diffusion at the inlet. There is no thumb rule for deciding the length of the buffer zone and it can only be determined by a trial and error method. The buffer zone length provided in the problem is computed for the maximum mass flow rate (Re=100) and are kept same for all the other lower flow rates. At the exit, the flow is made to be fully developed by imposing $\partial U / \partial X = V = \partial T / \partial X = 0$, a requirement met by an additional buffer length ($L_{B\text{-out}}$) provided at the exit between the last cylinder and the exit.

In order to accommodate a possible interface discontinuity in the diffusion flux of momentum and heat, respectively, the appropriate boundary condition at the interface between a porous medium and clear fluid flow section (see Fig. 1(b)), has been the point of interest of many researchers. In a series of pioneering analytical studies, Vafai and Thiyagaraja [17], Vafai and Kim [18,19] have explored several interface boundary conditions, which was later extended in the analytical studies of Kuznetsov [13]. In recent reviews, the merits and demerits of such interface boundary conditions and their validity are discussed in detail by Alazmi and Vafai [20,21]. We adopt here, the boundary conditions proposed by Ochoa-Tapia and Whitaker [22] for partially filled porous medium configurations, namely

$$U_f|_{\text{CF}} = U_f|_{\text{PM}} \qquad (6)$$

$$\mu_{\text{eff}} \frac{dU_f}{dY}\bigg|_{\text{PM}} - \mu_f \frac{dU_f}{dY}\bigg|_{\text{CF}} = \beta \frac{\mu_f}{\text{Da}} U_f|_{\text{interface}} \qquad (7)$$

$$\theta|_{\text{CF}} = \theta|_{\text{PM}} \qquad (8)$$

$$k_{\text{eff}} \frac{d\theta}{dY}\bigg|_{\text{PM}} = k_f \frac{d\theta}{dY}\bigg|_{\text{CF}}. \qquad (9)$$

In Eq. (7), β, as explained in Ochoa-Tapia and Whitaker [23], is an adjustable coefficient of the order one, which depends on the porous medium properties and, hence, has to be predetermined from individual experiments. Following the procedure in Ref. [23], in the present work we set the coefficient β to zero as experimentally determined β value for the metal foam porous media ($K \leq 10^{-7}$, listed in Table 1) is not available. As a result of $\beta=0$, when Eq. (7) is used as interface boundary condition, Eqs. (2b) and (3b) retain their Brinkman extended Darcy differential formulation of the momentum statement inside the porous layer, allowing for continuity of velocity and shear stress at the fluid-porous layer interface and a no-slip condition on the solid wall. Similar explanation is consistent with the use of Eqs. (8) and (9) as interface boundary condition for solving the volume averaged energy equation, Eq. (4b). This procedure was used earlier by other researchers like Hadim [6], Lundgren [24] and Abh-Hijleh and Al-Nimr [25], for similar partial porous medium filled configurations.

3 Computational Domain and Validation

The above problem is solved using numerical methods, employing the finite volume method to discretise the set of partial differential equations, Eqs. (1)–(4). Implicit, second order upwind solver is used with the velocity and pressure coupling achieved by the SIMPLE algorithm. The convergence criterion (difference between the results of two successive iterations) for the continuity residual is set as 10^{-3}, momentum equation as 10^{-6}, and for the energy equation as 10^{-9}. Since the work reports the heat transfer coefficient and involves a porous medium where diffusion effects could become dominant, the convergence criterion used for the energy equation is much more stringent. The grid independence study, using the following nondimensional numbers

(a)

(b)

(c)
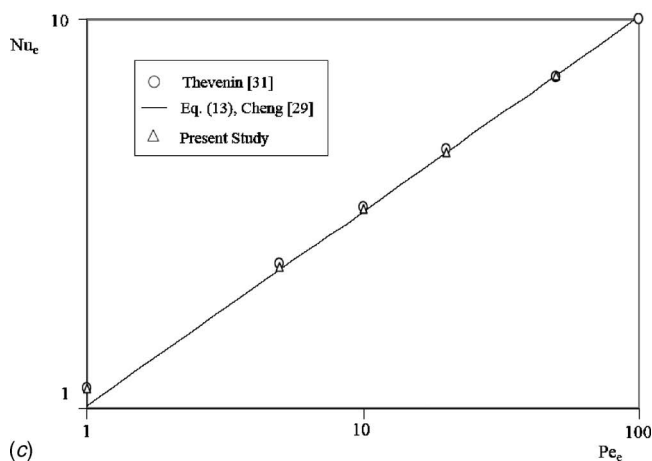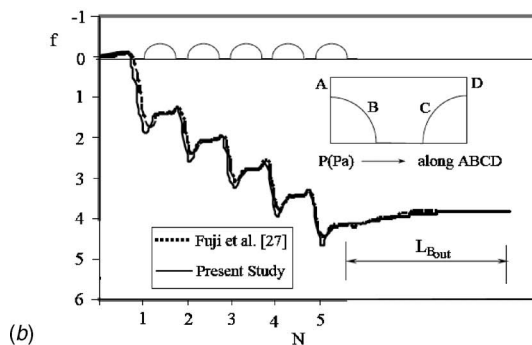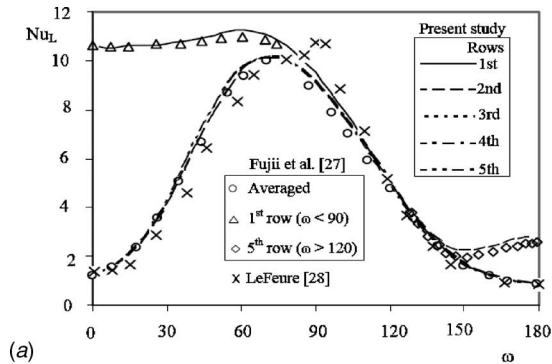
Fig. 2 Validation of numerical method: (a) Nu_{local} versus ω for flow around cylinders, (b) dimensionless longitudinal pressure distribution of the tube for flow over bank of five tubes, and (c) validation of porous medium model used: variation of Nu with Pe for cylinder embedded in porous medium

$$\text{Re} = U_m D / \nu \quad \text{Eu} = \Delta P / 0.5\rho U_m^2 N \quad \text{Nu}_f = qD / A(T_W - T_{bn})k_f N \qquad (10)$$

where the symbols are explained in nomenclature, are conducted for four successive grid levels (5368, 9764, 11,586, and 16,488) at Re=100 for flow over a tube bank (Fig. 1). When the error between two successive levels of grid refinement is less than 1% for both the Euler and the Nusselt number, a suitable grid size is chosen for all the subsequent computation work. The quadrilateral uniform grid in both x and y direction with 11,586 nodes used over the numerical domain of Fig. 1(b) is shown in part in Fig. 1(c), which is the cut view between two successive cylinders of Fig. 1(a). Further details are available in Ref. [26].

The present numerical model has been validated for flow over the tube banks and flow past a cylinder embedded with porous medium. Figure 2(a) shows the distribution of the local Nusselt

Fig. 3 Local dimensionless velocity U variation with Y at x $=0.01125$ for Re$=10$

Fig. 4 Streamlines for the tube bank arrangement with interconnecting PM thickness $\delta = D = 0.45$ and $K_i = 4.4 \times 10^{-10}$. (a) Re $= 10$ and (b) Re$=100$.

number around each of the five tubes in the angle ω direction with $X_T = X_L = 1.5$. The abscissa is the angle ω from the front upstream stagnation point of each tube. The ordinate is the local Nusselt number defined as

$$\text{Nu}_L = q''D/(T_W - T_{bn})k_f \tag{11}$$

The representative temperature difference is taken as the difference between the wall temperature (T_W) and the bulk mean temperature (T_{bn}) at minimum flow cross sectional area. Results for Nu$_L$ from the present study is compared with that of the numerical simulation results of Fujii et al. [27] and LeFeuvre [28] for Re $=120$ and Pr$=0.7$. The comparison is good as seen from Fig. 2(a) and it is evident that the shape of the distribution of Nu$_L$ is the same for all the results and the peak occurs at $\omega = 70$ deg. The distribution of the Nu$_L$ for the first ($\omega < 90$ deg) and fifth row of tubes in the direction of flow ($\omega > 120$ deg) also compare well with the value predicted by Fujii et al. [27].

Figure 2(b) shows dimensionless pressure distribution f along the path ABCD for Re$=120$. The dimensionless pressure distribution defined as

$$f = (p_{\text{in}} - p)/0.5\rho U_m^2 \tag{12}$$

The solid and dashed lines in Fig. 2(b) correspond to the present study and Fujii et al. [27], respectively. After the fifth cylinder sufficient buffer length has been provided such that the outflow b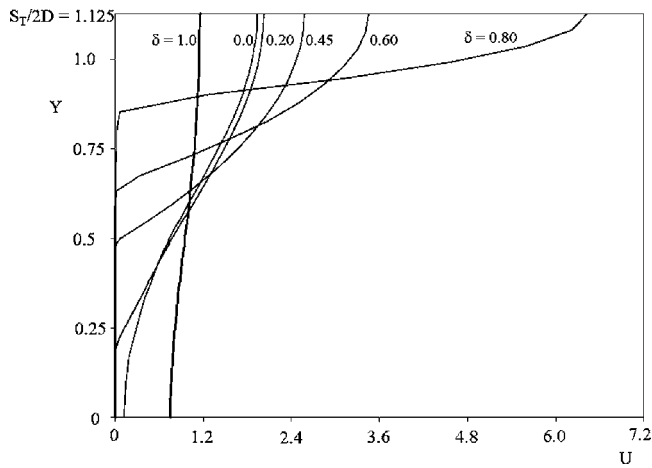oundary condition does not affect the pressure distribution along the above-mentioned path. The pressure distribution of the present study agrees well with that of Fujii et al. [27]. Figure 2(c) shows the plot between the mean effective Nusselt number Nu$_e$ over a cylinder against effective Peclet number Pe$_e$

$$\text{Nu}_e = 1.015 \, \text{Pe}^{0.5} \tag{13}$$

The solid line in Fig. 2(c) shows the analytical solution [29] in Eq. (13) as correlated by Nield and Bejan [30]. The numerical results from the present study with Da$=1 \times 10^{-6}$ and porosity ϕ $=0.9$ has good agreement with Eq. (13) and with the results reported in Ref. [31].

4 Hydrodynamic Results and Discussions

Figure 3 illustrates the local velocity profiles at midplane of the present configuration (see Fig. 1) for Re$=10$, for all the interconnector thickness ($0 < \delta < 1.0$). The PM interconnector is having a permeability $K_i = 4.4 \times 10^{-10}$ m^2, porosity of $\phi = 0.58$, and solid thermal conductivity $k_s = 202$ W/mK, resembling an aluminium metal foam (Table 1). It is observed that the fluid flow through porous medium is negligible for $\delta \leqslant 0.8$, where the fluid flow is
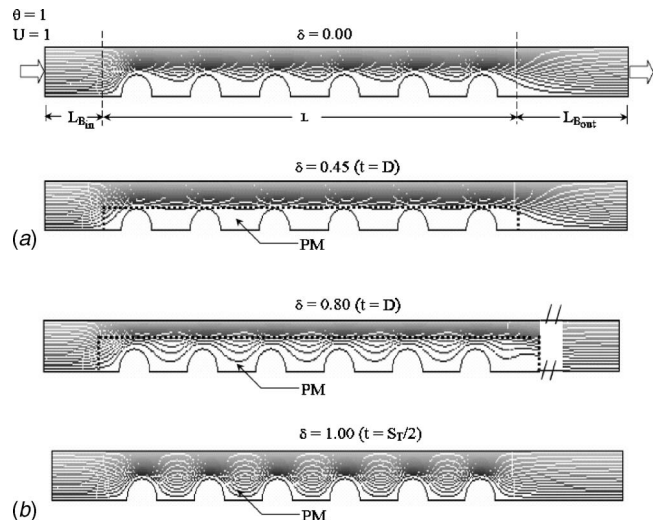
mainly through the gap between the PM interconnector and the top symmetry. For the fully filled porous medium ($\delta = 1.0$) case, due to the bulk damping caused by the PM, the viscous effects are confined near to the wall region resulting in almost flat velocity profile. A similar effect was also observed by Hadim [6].

Figures 4(a) and 4(b) show, for identical interconnector PM, the streamlines for Re$=10$ and Re$=100$, in the chosen computational domain with six cylinders, Fig. 1(b), for the several porous medium inter connector thicknesses, $0 < \delta < 1$. From the parallel horizontality of the entry and exit streamlines in Figs. 4(a) and 4(b) it is clear that for all of the δ including the CF case, $(0 < \delta < 1)$ the buffer zone length (L_B) chosen at the entry and exit of the computational domain is sufficient to meet the outflow and the velocity inlet boundary condition as discussed in the previous section. Even though flow through the interconnector jutting out transversely into the longitudinal flow exists when $\delta > 0.45$, most of the flow passes through the clear fluid channel (gap between the PM interconnector and the top symmetry line). This is the reason for the nominal increase in the overall pressure drop (ΔP/L) until $\delta < 0.45$ and the marked increase in $\Delta P/L$ versus U_∞ once $\delta > 0.45$ in Figs. 5(a) and 5(b). Further, as seen in Fig. 5(a), the $\Delta P/L$ for $\delta = 0.2$ (bottom most curve marked with "$\times$" symbols) is less than that of the CF case (second continuous curve from the bottom) because the presence of the PM interconnector negates pressure-losses due to the originally existing recirculation in the CF case (see top picture in Figs. 4(a) and 4(b)). The insignificant pressure drop increase for $\delta = 0.45$ when compared with the CF case can also be attributed to the same reasoning, in this situation, the increase in pressure drop caused by the PM interconnector is just counterbalanced by the magnitude of the now absent pressure-drop increase caused by the recirculation behind all tubes in the CF configuration. Once the PM interconnector juts transversely in to the flow ($\delta > 0.45$) pressure drop increased markedly (other curves in Figs. 5(a) and 5(b)) and reaches a maximum as expected when the channel is entirely filled with the porous medium (Fig. 5(b)).

To explain the effect of PM interconnector thickness and permeability on the overall pressure drop, a nondimensional pressure drop (ξ) term is defined as

$$\xi = (\Delta P/L)/(\rho U_\infty^2/2D) \tag{14}$$

which is different from the one used in Eq. (10) for validation. The nondimensional plot between ξ and Re for several PM interconnector thickness δ, is shown in Fig. 6(a). The bottom most and

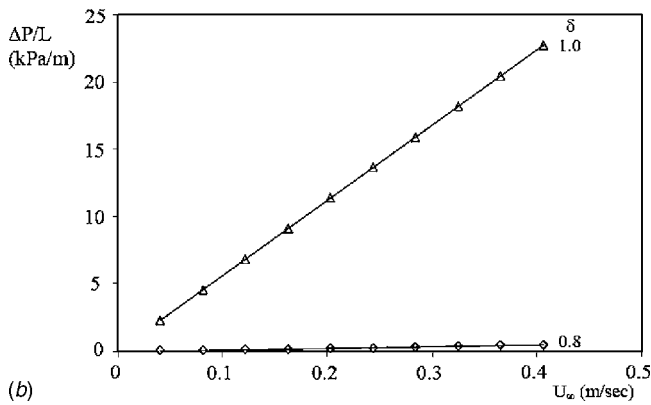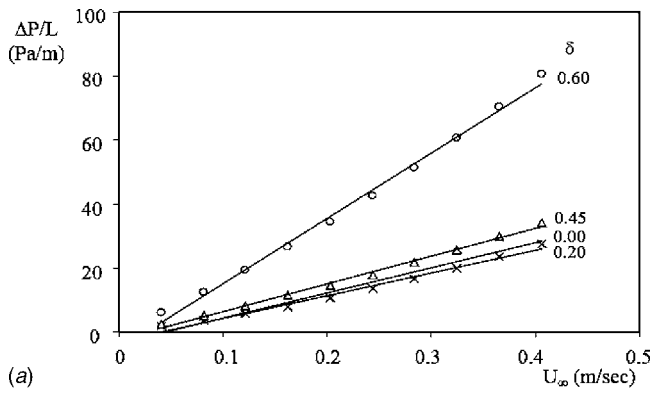(a)

(a)

(b)

Fig. 5 Variation of pressure drop with average velocity (a) 0 ≤ δ ≤ 0.6 and (b) δ=0.8 and 1.0

(b)

Fig. 6 (a) Effect of δ on ξ versus Re for K_i=4.4×10⁻¹⁰ and (b) effect of δ and K_i on ξ versus Re

the top most curves correspond to the CF (δ=0) and the fully PM filled (δ=1) case, respectively. As Re→100, ξ→1 for cases with δ<0.45, suggesting the pressure drop is balanced now by the U^2 term, i.e., the flow around the tube banks is departing from the laminar flow regime. In other words, one can still interpret the departure from the laminar regime in such (tube bank) situations using the criterion for departure from laminar regime as tube diameter based Re>100, even though the tubes are connected by porous medium. However, as the interconnecting PM juts into the flow (δ>0.45), the nondimensional pressure drop increase and shows no trend of approaching 1 (ΔP comparable to U_m^2 drag) at Re∼100. This suggests that although the oncoming upstream flow can be nonlaminar (transition or turbulent flow), once it passes through the PM zone, it is yet to become either turbulent or form drag dominated flow(ΔP∼U_m^2) drag. This observation corroborates the conclusion arrived through experiments in Ref. [15] and also suggests that one must no longer use the tube diameter based Re to characterize the flow.

Figure 6(b) depicts the effect of local permeability (K_i) on nondimensional pressure drop (ξ), for various PM interconnector thicknesses (δ) and for the Re range (10–100) tested. The ξ value increases as K_i decreases for a particular δ because the resistance to fluid flow increases as K_i decreases, which in turn results in higher ΔP until δ≤0.8. For the δ→1 the interconnector permeability effect is significant: lower the K_i higher the overall ΔP as the viscous drag of the PM itself becomes many times larger than the drag imposed by the tube bank (compare the ordinate values for the CF curve in Fig. 6(a) to that of the curve with δ=1 in Fig. 6(b)).

To develop a correlation for the overall all pressure drops (ξ) and the average Nusselt number, the above NCHX is modelled as a "global" porous medium [15] with the interconnector porous medium identified as a "local" PM, whose properties (φ,K_i) in-

fluence the global PM properties (K_g), and hence, the global heat transfer enhancement. To correlate the nondimensional pressure drop a global Darcy number Da_g has been introduced and defined as
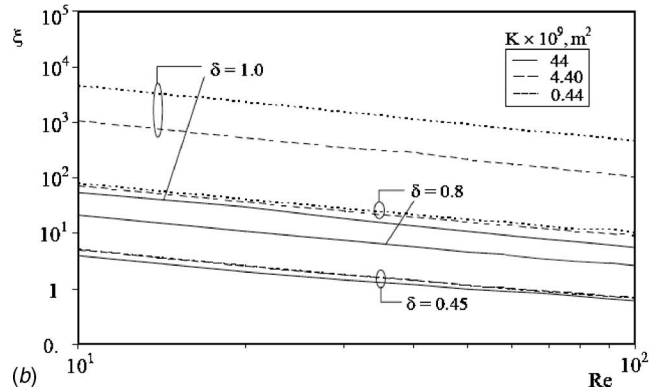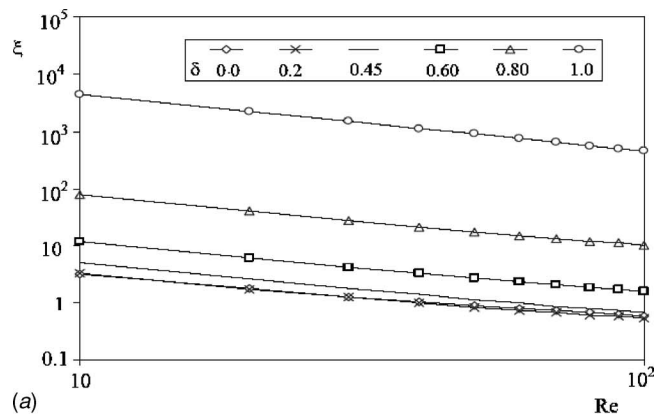
$$Da_g = K_g^{0.5}/D \quad (15)$$

where K_g, m², is the global permeability of the heat exchanger computed from a Darcy law, viz.

$$\Delta P/L = \mu U/K_g \quad (16)$$

curve-fit of the overall pressure-drop (ΔP/L,Pa/m) and the average velocity (U,m/s) data for the flow over the heat exchanger tube banks (the curve fit is shown in Fig. 5). The above Eq. (16) takes the same functional form of the correlations given by Zukauskas [32] for flow over the tube bank and compares with the existing correlation for clear fluid flow over the tube banks, when Da_g=1, with the CF configuration treated as a limiting porous medium (see Refs. [15,33] for more details). For invariant heat exchanger geometry, the global permeability K_g in Eq. (16) is only a function of the PM interconnector thickness (δ) and permeability (K_i,m²). Therefore, the global Darcy number Da_g can be correlated to a local PM interconnector permeability based Darcy number Da_i (=$K_i^{0.5}/D$), the PM interconnector thickness δ. Using the curve-fit of Fig. 5 for all the three cases of K_i listed in Table 1, a general correlation for Da_g can be given as

$$Da_g = C_1\left[\left(\frac{2\delta}{\delta+1}\right)Da_i + C_2(1-\delta)\right] \quad (17)$$

In Eq. (17), C_1 and C_2 are constants which subsume the effect of porosity (φ) and other geometrical parameters (D,S_T,S_L) of the heat exchanger that affect the overall longitudinal pressure drop. In the present paper, these are fixed values of 1 and 0.34, as the
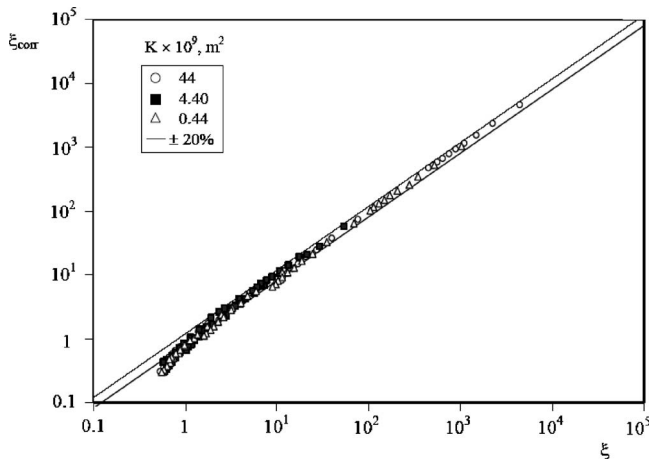
Fig. 7 Parity plot for data versus proposed ξ correlation, Eq. (15)

NCHX geometry is invariant. Further, in the limit when $\delta=0$, Eq. (17) predicts a global Darcy number for the NCHX model without porous medium (i.e., $Da_g = C_1 \times C_2 = Da_{CF} = 0.34$). In other words, Da_{CF}, the Darcy number for NCHX without interconnecting PM is calculated using K_g, obtained from the Darcy fit, Eq. (16), of the data with $\delta=0$ (one curve above the bottom-most curve in Fig. 5(a)). In the other limit when $\delta=1$, Eq. (17), predicts a global Darcy number obtained from the Darcy fit, Eq. (16), of the top most curve in Fig. 5(b). However, this global Da_g ($=C_1 \times Da_i$, from Eq. (17), when $\delta=1$) is not equal to the local Da_i in the limit of $\delta=1$ because of the presence of the tube banks themselves, which cause the global permeability to decrease even further. The correlated Da_g Eq. (17) predicts data obtained from the numerical simulations within $\pm 18\%$ accuracy.

Using Eqs. (14), (10), and (17), Eq. (16) can be expressed in nondimensional form as

$$\xi = 2\,\mathrm{Re}^{-1}\mathrm{Da}_g^{-2} \qquad (18)$$

a form similar to that used in earlier studies [9,15], when the form-drag component of the porous medium model is neglected. Figure 7 shows the parity plot between the non-dimensional pressure-drop results predicted from Eq. (18) used together with the correlation in Eq. (17) and the numerical simulation results. Equation (18), together with the correlation in Eq. (17), predicts the numerical simulation pressure-drop results within $\pm 20\%$ accuracy.

## 5 Heat Transfer Results and Discussion

Figures 8(a) and 8(b) displays the isotherms for the problem domain corresponding to Re=10 and Re=100, respectively. It can be observed that the temperature of the zone in between the tubes approach the value of θ_w, once the tubes are connected by the PM with high thermal conductivity (compare, the case of $\delta=0$ with $\delta \neq 0$ in Figs. 8(a) and 8(b)). The increase in heat transfer area between the fluid and the hot tube wall because of the presence of the PM interconnector results in an increase in the heat transfer to the fluid for fixed tube wall temperature. This enhancement effect is present even though there is less flow (forced convection) in the PM interconnector zone as observed from Figs. 3 and 4. Further, this enhancement effect exists even for situations when $\delta \leq 0.45$, because the flow above the PM zone would still wash over larger surface area with higher average temperature close to θ_w (the PM interconnector zones between tubes). However, because of large heat transfer area provided by the PM interconnector, the fluid bulk temperature T_b (defined at a cross section in the fluid region above the PM interconnector zone) approaches θ_w much sooner before it reaches the final tubes, towards the exit of the system
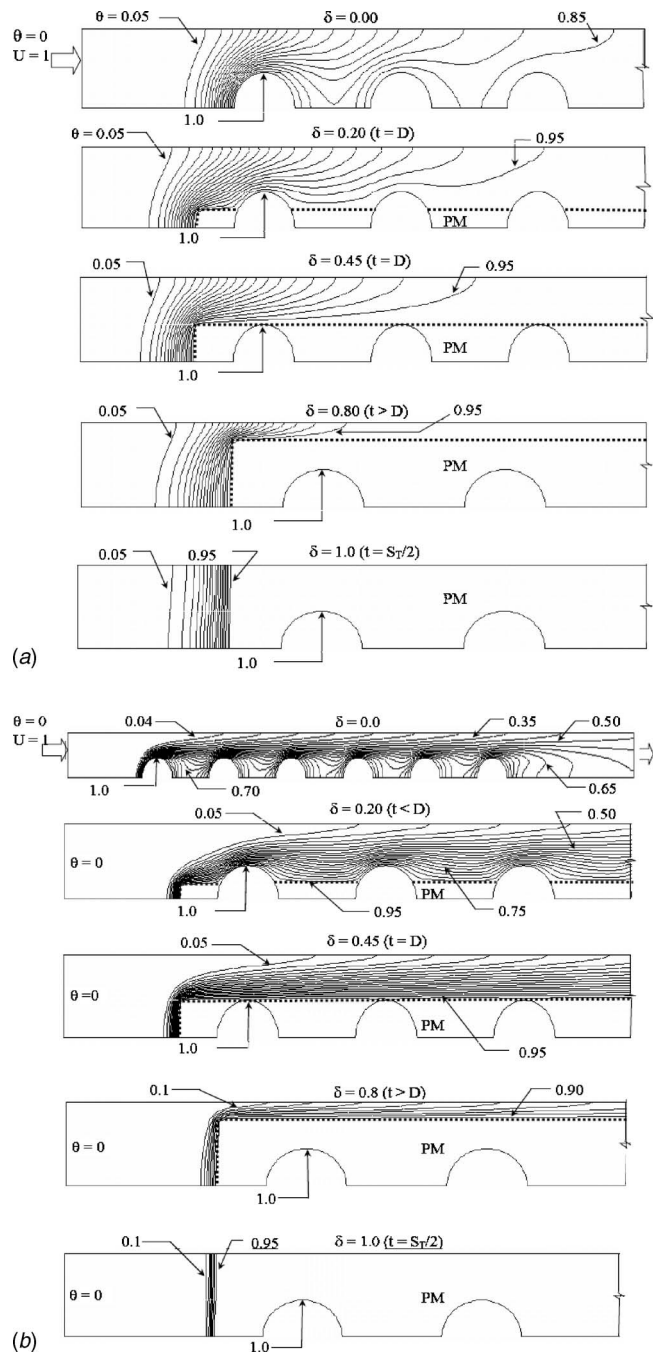
Fig. 8 Isotherms for the tube bank arrangement with interconnecting porous medium thickness $\delta=D$ and $K_i = 4.4 \times 10^{-10}$. (a) Re=10 and (b) Re=100.

(along x-direction in Fig. 1). This reduces the heat transfer between the final tubes (in our case, last three tubes) and the fluid. This effect is seen in Figs. 8(a) and 8(b) and seeps into the flow over the upstream tubes as $\delta \to 1$.

The plot between the average Nusselt number and Re, defined in Eq. (10), for Pr=0.7, is shown in the Fig. 9. The representative temperature difference in the Nu_f is taken as the difference between the wall temperature (θ_w) and the average of the cross-section area and flow weighted bulk mean temperature (θ_b) at the inlet and the exit plane. The bottom most and the top most curve in Fig. 9 correspond to the CF flow case ($\delta=0$) and the fully filled PM case ($\delta=1$), respectively. Further, as Re$\to$10, $\mathrm{Nu}_f \to 1$ for all the δ values including the CF flow ($\delta=0$) because of the fluid
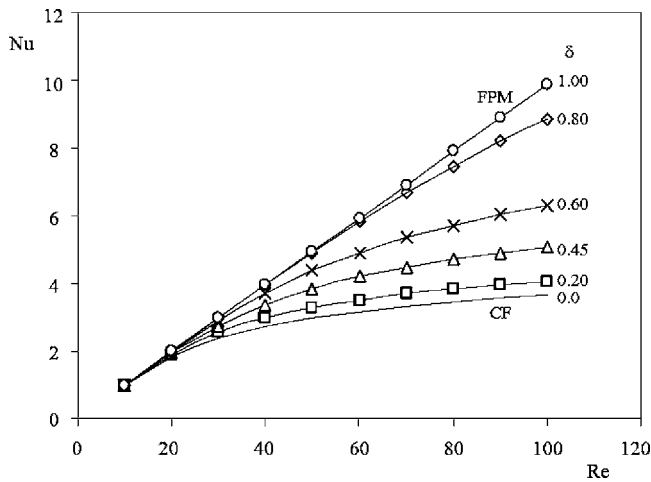
Fig. 9 Effect of δ on Nu versus Re for $K_i = 4.4 \times 10^{-10}$
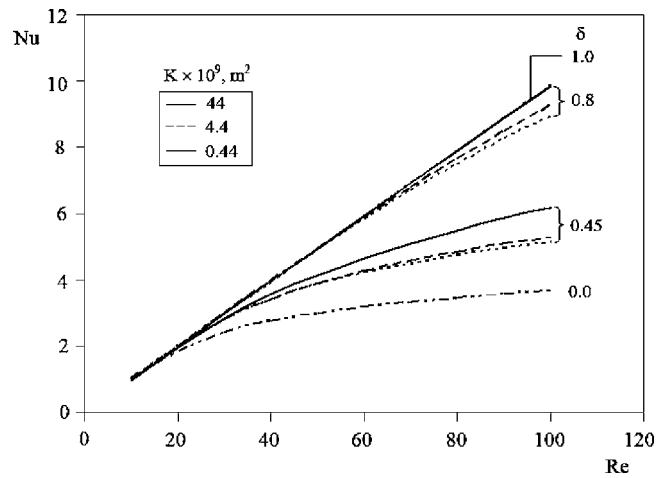
Fig. 11 Nu versus Re for several interconnecting porous medium permeabilities

temperature reaches an asymptotic maximum value ($\sim \theta_w$) irrespective of the porous medium solid material. When Re$\rightarrow$100, Nu$_f$ for the case of δ=0 is about 3.67 and for δ<0.45, Nu$_f$ is greater than the 3.67, which suggests that heat transfer enhancement can be achieved even for δ<0.45 because of the increased heat transfer surface area provided by the PM interconnector, an effect not observed in Ref. [14] when the gap between the tubes is made of unconnected solid fins.

Figures 10(a) and 10(b) show the velocity and temperature profiles at the exit for δ=0.45 and Re=100, for different permeabilities of the interconnector PM. As limiting cases of the interconnector PM, velocity and temperature profiles when $K_i = K_{CF}$ (i.e., the tube bank case in Fig. 1, without the interconnecting PM) and when $K_i \rightarrow 0$ (i.e., when the interconnecting fin is almost a solid) are also included in these figures. It can be observed from the Fig.

(a)

(b)
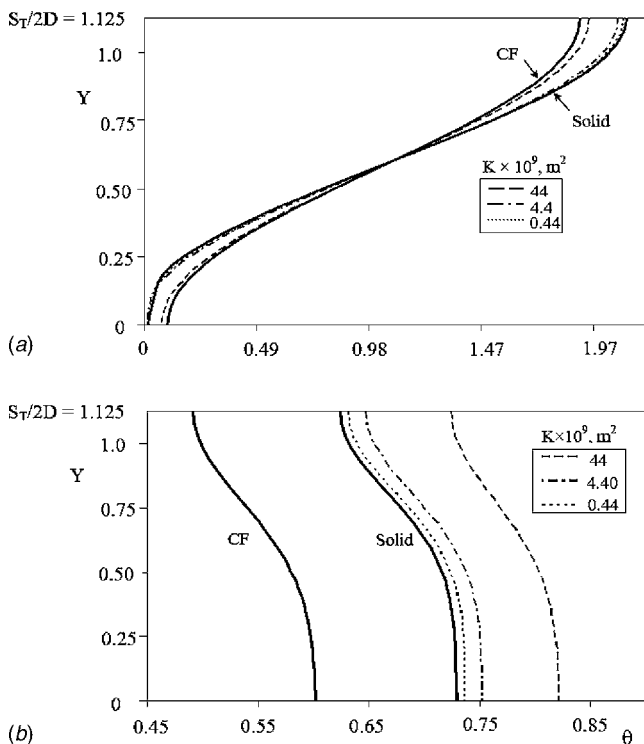
Fig. 10 For several local permeabilities K_i, at Re=100 and δ=0.45. (a) Velocity and (b) temperature profiles at the exit.

10(a) that the local velocity profiles for these limiting cases of K_i "bound" the velocity profiles for other K_i values of the interconnector PM. As expected, the $K_i \rightarrow 0$ case (i.e., when the interconnecting fin is almost a solid) registers for the local velocity value, the lowest inside the PM zone ($\delta \leq 0.45$) and highest out of the PM zone, because of the imposed mass conservation across the flow control volume. Likewise, the $K_i = K_{CF}$ case (i.e., the tube bank case in Fig. 1, without the interconnecting PM) yields the opposite effect. The velocity profiles for the rest of the K_i values moves from near the $K_i = K_{CF}$ case values towards the $K_i \rightarrow 0$ case.

Figure 10(b) displays the corresponding temperature profiles at the exit for the cases discussed in Fig. 10(a). The extreme left curve is for the limiting case of $K_i = K_{CF}$ (i.e., the tube bank case in Fig. 1, without the interconnecting PM). The bulk temperature at the exit for this case is the lowest. The other limiting case when the $K_i \rightarrow 0$ case (i.e., when the interconnecting fin is almost a solid) results in all of the cooling fluid to flow over the tube banks connected with the almost solid fins, resulting in an improved forced convection effect. For fixed wall temperature θ_w of the tubes, this results in a higher local fluid temperature because more heat is drawn from the isothermal tubes. When the K_i takes values other than these two bounding values, the local temperature is influenced by a combination of effects. For $K_i = 4.4 \times 10^{-8}$ m^2 (highest value of the three metal foam matrix tested), first because of the presence of the metal matrix and high porosity, the local heat transfer area around each of the isothermal tubes is increased. Second, as seen from Fig. 10(a), the flow inside the PM zone for this K_i value is close to that of case (i.e., higher than for the rest of the K_i values) resulting in a higher degree of forced convection effect in the PM zone. Because of the combination of these two effects, in this case of $K_i = 4.4 \times 10^{-8}$ m^2, maximum heat is drawn from the tubes when compared to the other cases, resulting in the highest local temperatures registered in Fig. 10(b).

From the results of Fig. 10 it is clear that the exit bulk temperature of the domain in Fig. 1 increases for a fixed δ, when K_i of the interconnector PM increases. For a fixed tube wall temperature, this results in a decrease in the temperature difference ($\theta_w - \theta_b$) used in the definition of the overall Nu in Eq. (10). On the other hand, the average heat flux q/A in the overall Nu definition in Eq. (10) also increases for increase in θ_b, as explained in the above paragraph. The combination of these two effects results in an increase in the overall Nu, as K_i increases for a fixed δ of the interconnecting PM. This result is presented in Fig. 11, as the variation of overall Nusselt number with Re for different K_i and δ values of the PM interconnector. The top and bottom most curves are for δ=1.0 (FPM) and δ=0.0 (CF), respectively. For FPM (δ

Fig. 12 Parity plot for the Nu data and correlation, Eq. (17)

=1.0) case there is no significant variation observed in Nu irrespective of K_i, because the cooling fluid approaches the maximum temperature of the domain (θ_w) just after the entry itself, irrespective of the K_i used. Hence, the temperature difference ($\theta_w - \theta_b$) and heat flux remains almost constant in Eq. (10) and results in no variation in Nu.

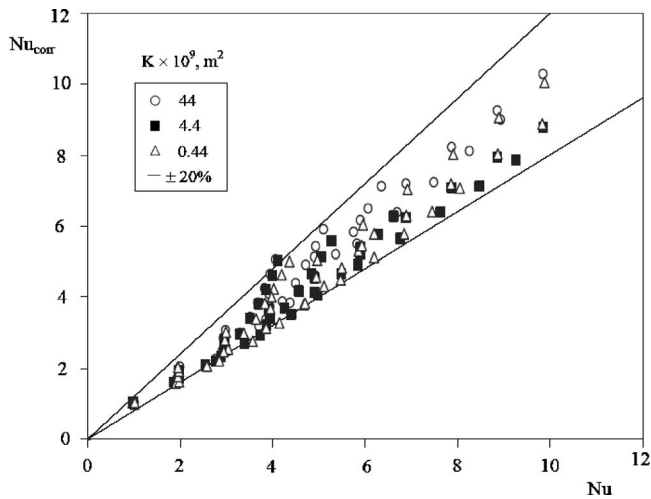For the chosen NCHX configuration (Fig. 1) with the PM interconnectors (Table 1) made of aluminium foam having k_s =202 W/mK, the overall Nu in Fig. 11 is correlated with Re and the global Darcy number defined in Eq. (17) as

$$\text{Nu} = 0.1\text{Re}^{(1-0.5\text{Da}_g)} + \text{Da}_g \tag{21}$$

Equation (21) predicts an increase in the overall Nu as Re increases irrespective of the interconnector PM configuration. As discussed earlier (paragraph below Eq. (17)), $\text{Da}_g = \text{Da}_{CF}$ when δ =0 and $\text{Da}_g \rightarrow \text{Da}_i$ when δ=1. It can be seen that from Eq. (21), results consistent with existing literature [30] are obtained at these limits. The parity plot in Fig. 12 shows that the above correlation Eq. (21) predicts the overall average Nusselt number data within ±20% accuracy.

6 Conclusions

In this work, treatment of NCHX as a global porous medium, whose thermohydraulic performance (heat transfer coefficient, Nu, and pressure drop, ξ) is being influenced by the presence of local tube-to-tube porous medium interconnectors, connecting the in-line arrangement of tubes is studied using numerical methods.

The tubes of the NCHX are kept in inline arrangement having square pitch of $X_T = X_L = 2.25$ and are maintained at constant wall temperature, with the cross flow of Pr=0.7 maintained in the laminar flow ($10 < \text{Re} < 100$). The influence of the permeability ($10^{-8} < K_i < 10^{-10}$, m²) and thickness of the metal foam type porous media, used as interconnectors between successive tubes (D=2 mm), on the NCHX (surface to volume ratio, α =100–300 m²/m³ with hydraulic diameter $D_M \sim 6$ mm) has been studied.

The overall NCHX Nu was found to decrease with an increase in the local interconnecting porous medium permeability (represented as Da_i), for all partially filled porous medium interconnector ($0 < \delta < 0.8$) in the present configuration for all the Re tested. No significant effect of Da_i was observed in the range of $10^{-8} < K_i < 10^{-10}$, m², on the overall heat transfer (Nu), when the porous medium interconnector fills entirely the region around the tube bank (i.e., when δ=1). Also, irrespective of the value of Da_i, when δ=1, the variation of Nu with Re is found to be linear.

For the NCHX configuration chosen in the present problem, the nondimensional pressure drop and heat transfer coefficient (ξ and Nu) values increase for an increase in the cross flow Re and also with an increase in the thickness (δ) of the tube-to-tube interconnecting porous medium. However, as Da_i increases, the ξ decreases but the Nu increases. When the NCHX is viewed as a global porous medium this result is interpreted as an increase in the ξ and Nu as the global NCHX permeability (represented by Da_g) decreases. As Da_g is related to δ and Da_i (through Eq. (17)), the decrease in Da_g is shown to be because of either an increase in δ or a decrease in Da_i, both properties of the interconnecting porous medium. An overall energy gain (pump power/heat transfer) of the present system (Fig. 1) can also be made. For instance with δ=0.45, the present system is found to be 1.4 times that of the system without the porous medium inter-connectors.

Separate correlations predicting ξ and Nu as a function of Re and Da_g (which in turn is correlated to δ and Da_i) have been developed for the chosen NCHX configuration, both of which predict the numerical data with ±20% accuracy. The design engineer can use these correlations as useful tools to predict the performance of such a heat exchanger used in this study.

Nomenclature

A = surface area of the tube, πD, m²
A_1 = minimum cross sectional area between tube to tube, m²
C_F = clear fluid domain, Fig. 1
D = diameter of the tube, m
Da = Darcy number, $K^{0.5}/D$
f = dimensionless pressure drop, Fig. 2, Eq. (12)
k = thermal conductivity, W/mK
K = permeability, m²
L = length of the tube bank, m
L_B = length of the buffer zone length, m
N = number of rows in the tube bank
NCHX = near compact heat exchangers
Nu_e = average effective Nusselt number over the tube, Eq. (13)
Nu = average Nusselt number, Eq. (10)
p = pressure, Pa
PM = porous medium domain, Fig. 1
p_{in} = pressure at inlet, Pa
P = dimensionless pressure $p/(\rho U_\infty^2)$
Pe_e = Peclet number, $U_\infty D/\alpha_e$
Pr_e = effective Prandtl number, $\nu/[k_e/(\rho c_p)_f)]$
ΔP = global longitudinal pressure drop across the tube bank
q = total heat transfer, W
q'' = local heat flux, W/m²
R = radius of the tube, m, Fig. 1
Re_m = Reynolds number, $U_m D/\nu$
Re_D = Reynolds number, $U_\infty D/\nu$
S_L = longitudinal tube pitch, Fig. 1, m
S_T = transverse tube pitch, Fig. 1, m
T = temperature, $[\theta(T_W - T_\infty) + T_\infty]$
T_W = wall temperature, K
T_b = bulk mean temperature, K
T_∞ = free-stream temperature, Fig. 1, K
u = x direction local and seepage speed in CF and PM zones, Fig. 1, m/s
U = dimensionless velocity in x direction, u/U_∞
U_∞ = free stream velocity, Fig. 1, m/s
U_m = average velocity at minimum cross section, Fig. 1, m/s
v = y direction local and seepage speed in CF and PM zones, Fig. 1, m/s
V = dimensionless velocity in y direction, v/U_∞

x, y = space coordinates
X = dimensionless distance in x direction, x/D
X_L = dimensionless longitudinal tube pitch, S_L/D, Fig. 1
X_T = dimensionless transverse tube pitch, S_T/D, Fig. 1
Y = dimensionless distance in y direction, $y/(D)$

Greek Symbols

α = thermal diffusivity, m^2/s
δ = dimensionless transverse porous medium thickness, t/S_n, Fig. 1
ϕ = porosity of the interconnecting PM, Table 1
θ = dimensionless temperature, $(T - T_{in})/(T_W - T_{in})$
μ = dynamic viscosity, N s/m^2
ν = kinematic viscosity, m^2/s
ρ = density, kg/m^3
ξ = non-dimensional pressure drop, Eq. (14)
ω = angle on the tube surface

Subscripts

b = bulk
e = effective porous medium property
f = fluid property
g = global properties
i = interconnector porous medium properties
n = normal, local
s = solid property
t = thickness

References

[1] Lage, J. L., and Narasimhan, A., 2000, "Porous Media Enhanced Forced Convection Fundamentals and Applications," *Handbook of Porous Media*, K. Vafai, ed., Marcel Dekker, New York, Vol. 8, pp. 357–394.

[2] Jung, Y. M., and Sung, J. K., 2005, "A Novel Methodology for Thermal Analysis of a Composite System Consisting of a Porous Medium and an Adjacent Fluid Layer," ASME J. Heat Transfer, **127**, pp. 648–656.

[3] Sheng, C. T., 2006, "Convective Heat Transfer in a Rectangular Channel Filled With Sintered Bronze Beads and Periodically Spaced Heated Blocks," ASME J. Heat Transfer, **128**, pp. 453–464.

[4] Angirasa, D., 2002, "Forced Convective Heat Transfer in Metallic Fibrous Materials," ASME J. Heat Transfer, **124**, pp. 739–745.

[5] Lage, J. L., Narasimhan, A., Porneala, D. C., and Price, D. C., 2004, "Experimental Study of Forced Convection Through Microporous Enhanced Heat Sinks," *Emerging Technologies and Techniques in Porous Media*, D. B. Ingham et al., eds., Kluwer, Dordrecht, Vol. 28, pp. 433–452.

[6] Hadim, A., 1994, "Forced Convection in a Porous Channel With Localized Heat Sources," ASME J. Heat Transfer, **116**, pp. 465–472.

[7] Alkam, M. K., and Al-Nimr, M. A., 1999, "Improving the Performance of Double-Pipe Heat Exchangers by Using Porous Substrates," Int. J. Heat Mass Transfer, **42**, pp. 3609–3918.

[8] Kiwan, S., and Al-Nimr, M. A., 2001, "Using Porous Fins for Heat Transfer Enhancement," ASME J. Heat Transfer, **123**, pp. 790–795.

[9] Mohamad, A. A., 2003, "Heat Transfer Enhancements in Heat Exchangers Fitted With Porous Media Part I: Constant Wall Temperature," Int. J. Therm. Sci., **42**, pp. 385–395.

[10] Bogdan, I. P., and Mohamad, A. A., 2004, "An Experimental and Numerical Study on Heat Transfer Enhancement for Gas Heat Exchanger Fitted With Porous Media," Int. J. Heat Mass Transfer, **47**, pp. 4939–4952.

[11] Angirasa, D., 2002, "Experimental Investigation of Forced Convection Heat Transfer Augmentation With Metallic Fibrous Materials," Int. J. Heat Mass Transfer, **45**, pp. 919–922.

[12] Kuznestov, A. V., 1997, "Influence of the Stress Jump Condition at the Porous-Medium/Clear-Fluid Interface on a Flow at a Porous Wall," Int. Commun. Heat Mass Transfer, **24**, pp. 401–410.

[13] Kuznestov, A. V., 2000, "Analytical Studies of Forced Convection in Partly Porous Configuration," *Handbook of Porous Media*, K. Vafai, ed., Marcel Dekker, New York, Vol. 6, pp. 269–312.

[14] Faghri, M., and Rao, N., 1987, "Numerical Computation of Flow and Heat Transfer in Finned and Unfinned Tube Banks," Int. J. Heat Mass Transfer, **30**, pp. 363–372.

[15] Wilson, L., Narasimhan, A., and Venkateshan, S. P., 2004, "Turbulent Flow Hydrodynamic Experiments in Near-Compact Heat Exchanger Models With Aligned Tubes," ASME J. Fluids Eng., **126**, pp. 990–996.

[16] Patankar, S. V., Liu, C. H., and Sparrow, E. M., 1977, "Fully Developed Flow and Heat Transfer in Duct Having Streamwise-Periodic Variation of Cross-Sectional Area," ASME J. Heat Transfer, **99**, pp. 180–186.

[17] Vafai, K., and Thiyagaraja, R., 1987, "Analysis of Flow and Heat Transfer at the Interface Region of a Porous Medium," Int. J. Heat Mass Transfer, **30**, pp. 1391–1405.

[18] Vafai, K., and Kim, S. J., 1990, "Fluid Mechanics of the Interface Region between a Porous Medium and a Fluid Layer—An Exact Solution," Int. J. Heat Fluid Flow, **11**, pp. 254–256.

[19] Vafai, K., and Kim, S. J., 1990, "Analysis of Surface Enhancement by a Porous Substrate," ASME J. Heat Transfer, **112**, pp. 700–706.

[20] Alazmi, B., and Vafai, K., 2000, "Analysis of Variants Within the Porous Media Transport Models," ASME J. Heat Transfer, **122**, pp. 303–326.

[21] Alazmi, B., and Vafai, K., 2001, "Analysis of Fluid Flow and Heat Transfer Interfacial Conditions Between a Porous Medium and a Fluid Layer," Int. J. Heat Mass Transfer, **44**, pp. 1735–1749.

[22] Ochoa-Tapia, J. A., and Whitaker, S., 1995, "Momentum Transfer at the Boundary Between a Porous Medium and a Homogeneous Fluid-I. Theoretical Development," Int. J. Heat Mass Transfer, **38**, pp. 2635–2646.

[23] Ochoa-Tapia, J. A., and Whitaker, S., 1995, "Momentum Transfer at the Boundary Between a Porous Medium and a Homogeneous Fluid-II. Comparison With Experiments," Int. J. Heat Mass Transfer, **38**, pp. 2647–2655.

[24] Lundgren, T. S., 1972, "Slow Flow Through Stationary Random Beds and Suspensions of Spheres," J. Fluid Mech., **51**, pp. 273–299.

[25] Abu-Hijleh, B. A., and Al-Nimr, M. A., 2001, "The Effect of Local Inertial Term on the Fluid Flow in Channels Partially Filled With Porous Material," Int. J. Heat Mass Transfer, **44**, pp. 1565–1572.

[26] Sahu, K. D., 2005, "Heat Transfer Augmentation in a Near Compact Heat Exchanger Using Porous Medium Fins," M.Tech. thesis, IIT Madras, Chennai.

[27] Fujii, M., and Fujii, T., 1984, "A Numerical Analysis of Laminar Flow and Heat Transfer of Air in an In-line Tube Bank," Numer. Heat Transfer, Part A, **7**, pp. 89–102.

[28] LeFeuvre, R. F., 1973, "Laminar and Turbulent Forced Convection Processes Through In-Line Tube Banks," Imperial College London, Mech. Eng., Dept., HTS/74/5.

[29] Cheng, P., 1982, "Mixed Convection About a Horizontal Cylinder and a Sphere in a Fluid Saturated Porous Medium," Int. J. Heat Mass Transfer, **25**, pp. 1245–1247.

[30] Nield, D. A., and Bejan, A., 1999, *Convection in Porous Media*, 2nd ed., Springer-Verlag, New York.

[31] Thevenin, J., and Sadaoui, D., 1993, "About Enhancement of Heat Transfer Over a Circular Cylinder Embedded in a Porous Medium," Int. Commun. Heat Mass Transfer, **22**, pp. 295–304.

[32] Zukauskas, A. A., 1987, "Convective Heat Transfer in Cross Flow," *Handbook of Single Phase Convective Heat Transfer*, S. Kakaç, R. K. Shah, and W. Aung, eds., Wiley, New York, Chap. 6.

[33] Lage, J. L., Krueger, P. S., and Narasimhan, A., 2005, "Protocol for Measuring Permeability and Form Coefficient of Porous Media," Phys. Fluids, **17**(8), p. 088101.

[34] Boomsma, K., and Poulikakos, D., 2002, "The Effects of Compression and Pore Size Variations on the Liquid Flow Characteristics in Metal Foams," ASME J. Fluids Eng., **124**, pp. 263–272.

[35] Calmidi, V. V., and Mahajan, R. L., 2000, "Forced Convection in High Porosity Metal Foams," ASME J. Heat Transfer, **122**, pp. 557–565.

Luben Cabezas-Gómez[1]

Departamento de Engenharia Mecânica,
Escola de Engenharia de São Carlos,
Universidade de São Paulo,
Av. Trabalhador São-carlense, 400 - Centro,
CEP 13566-590, São Carlos, SP, Brazil
e-mail: lubencg@sc.usp.br

Hélio Aparecido Navarro

Departamento de Estatística, Matemática Aplicada
e Computação,
Instituto de Geociências e Ciências Exatas,
Universidade Estadual Paulista "Júlio de
Mesquita Filho,"
Av. 24-A, 1515, Cx. P 178,
CEP 13506-700, Rio Claro, SP, Brazil
e-mail: helio@rc.unesp.br

José Maria Saiz-Jabardo

Escuela Politécnica Superior,
Universidad de la Coruña,
Mendizábal s/n Esteiro,
15403 Ferrol, Coruña, Spain
e-mail: mjabardo@cdf.udc.es

Thermal Performance of Multipass Parallel and Counter-Cross-Flow Heat Exchangers

A thorough study of the thermal performance of multipass parallel cross-flow and counter-cross-flow heat exchangers has been carried out by applying a new numerical procedure. According to this procedure, the heat exchanger is discretized into small elements following the tube-side fluid circuits. Each element is itself a one-pass mixed-unmixed cross-flow heat exchanger. Simulated results have been validated through comparisons to results from analytical solutions for one- to four-pass, parallel cross-flow and counter-cross-flow arrangements. Very accurate results have been obtained over wide ranges of NTU (number of transfer units) and C^* (heat capacity rate ratio) values. New effectiveness data for the aforementioned configurations and a higher number of tube passes is presented along with data for a complex flow configuration proposed elsewhere. The proposed procedure constitutes a useful research tool both for theoretical and experimental studies of cross-flow heat exchangers thermal performance.
[DOI: 10.1115/1.2430719]

1 Introduction

A number of methods have been applied to the design and analysis of heat exchangers. These approaches include the so-called ε-NTU method, the logarithmic-mean temperature difference (MTD) and those based on the Mueller and Roetzel charts [1]. Kays and London [2] listed some arguments in favor of the ε-NTU method as compared with the MTD method. One of the most significant arguments is that the ε-NTU solution is straightforward in performance prediction for rating problems as compared to the MTD approach, which requires successive approximations. As a general rule, ε-NTU relations are very useful for heat exchangers rating and design [2,3]. Sekulic et al. [1] argued that continuing efforts to design more efficient and compact heat exchangers to operate under specific conditions may require ε-NTU formulas not reported in the literature. They carried out a comprehensive review of methods for the determination of ε-NTU expressions for two-fluid heat exchangers with simple and complex flow arrangements. The available methods were divided into the following categories: analytical, approximate, curve fitting, numerical, matrix formalism, and those based on the heat exchanger configuration properties.

Recently, Pignotti and Shah [4] discussed some methods for the development of ε-NTU expressions for heat exchangers with complex flow arrangements. Among these methods, the following are worth mentioning: the Domingos' rules [5], the chain rules, and the rules for heat exchangers with one of the fluids mixed. By using these procedures, Pignotti and Shah [4] were able to develop ε-NTU relations for 18 new flow arrangements. Shah and Pignotti [6] looked over complex flow arrangements to relate them to simple forms with available solutions either exact or approximated. They raised effectiveness relations for tubular cross-flow heat exchangers with seven different flow arrangements that could be manufactured out from the same six-row tube bundle. Bacliç [7] presented a list of closed-form expressions for the effectiveness of new flow arrangements of compact heat exchangers.

Studies by Taborek [8], Bacliç [7], and Stevens et al. [9] dealing with the evaluation of the heat exchanger effectiveness of multipass parallel and counter-cross-flow configurations are worth mentioning. Recently Chen et al. [10] used the procedure proposed by [9] in the determination of a closed form of the effectiveness of a four-row counter-cross-flow heat exchanger.

The state of the art in the development of ε-NTU data for cross-flow heat exchangers presented in the preceding paragraphs has revealed the need of further research and analysis. The present paper reports results of an ongoing investigation of heat exchanger simulation through a methodology proposed in a previous paper [11]. The focus in this case is multipass cross-flow heat exchangers. Initially, the modeling and solution procedures are outlined, followed by the proposed algorithm validation by comparison to available analytical expressions for the effectiveness. Finally, results for standard and complex multipass cross-flow arrangements are analyzed and discussed.

2 Modeling and Numerical Procedure

The proposed procedure aims at the determination of the thermal effectiveness of cross-flow heat exchangers through a numerical procedure. A summary of this procedure will be developed in the present section. One of the main applications of cross-flow heat exchangers is in processes involving air as the external fluid. Serpentine tube-fin heat exchangers are among those heat exchangers. In what follows, air will be implicitly assumed to be the external fluid, though the conclusions and results could be extended to any fluid.

In the development of the heat transfer model, the following assumptions have been made regarding the heat exchanger as a whole: (i) steady state, (ii) negligible heat transfer with the surroundings, (iii) no heat sources either in the fluids or in the heat exchanger walls, (iv) the tube fluid is considered mixed, (v) trans-
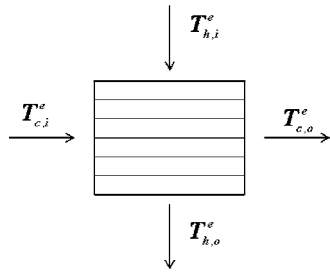
Fig. 1 Fluid element illustration

port properties of the fluids and heat transfer coefficients are assumed constant, and (vi) no phase changes occur in both fluid streams.

The procedure consists of the following basic steps: (i) division of the heat exchanger in finite, three-dimensional, control volumes herein designated by "elements," each element being itself a "mixed-unmixed" cross-flow heat exchanger; (ii) solution of the set of governing equations for each element; and (iii) step-by-step solution of governing equations of subsequent elements along each circuit of the in tube fluid.

A schematic illustration of a typical element is shown in Fig. 1. It can be noted that this is a cross-flow heat exchanger with the tube fluid being mixed and the external unmixed. The tube fluid will be considered as the hot one for analysis purposes. The number of elements along the tube fluid circuit must be sufficiently high so that their size will generally be small, and, as a result, the flow rate of the external fluid will be very small compared to that of the fluid tube (see Fig. 2(a), point 6). Thus, the thermal capacity (specific heat times the mass flow rate) of the external fluid will be significantly smaller than that of the fluid tube, that is, $C_c^e \ll C_h^e$, where the subscripts h and c stand for hot and cold, whereas the superscript e designates the element. Since the elements are small mixed-unmixed crossflow heat exchangers fulfilling the above condition for C_c and C_h, their thermal effectiveness can be approximated by the following expression:

$$\Gamma^e = \frac{\Delta T_c^e}{T_h^e - T_{c,i}^e} = 1 - e^{-(UA)^e / C_c^e} \tag{1}$$

where U is the overall heat transfer coefficient, A is the outer total heat exchanger area, and T_h^e is the average tube fluid temperature in the element, given by

$$T_h^e = 0.5(T_{h,i}^e + T_{h,o}^e) \tag{2}$$

Equations (3) and (4) for the outlet element temperatures, can be obtained by combining Eqs. (1) and (2) with those corresponding to the energy balances in each fluid,

$$T_{c,o}^e = \frac{B + 2(1 - \Gamma^e)}{2 + B} T_{c,i}^e + \frac{2\Gamma^e}{2 + B} T_{h,i}^e \tag{3}$$

$$T_{h,o}^e = \frac{2 - B}{2 + B} T_{h,i}^e + \frac{2B}{2 + B} T_{c,i}^e \tag{4}$$

where $B = C_c^e \Gamma^e / C_h^e$. More detailed information regarding the derivation of the above set of equations can be found in [11]. It must be noted at this point that the thermal effectiveness of the elements, Γ^e, is constant throughout the heat exchanger since the elements are chosen of equal size.

The solution of the governing equations for the set of elements that make up the whole heat exchanger can be accomplished by a marching procedure; a description of it is shown in the block diagrams of Figs. 2(a) and 2(b). Further details of the numerical procedure can be found in [11]. Though the diagrams of Fig. 2 are

1.1 Read a heat exchanger geometry from input file
1.2 Read NTU, C^*
1.3 Choose $C_{min} = (C_c$ or $C_h)$
1.4 Define $T_{c,i}$, $T_{h,i}$ and UA
1.5 Compute $(UA)^e$ according to

$$(UA)^e = \frac{UA}{N_e N_t N_r}$$

1.6 Compute C_c^e and C_h^e
  If $C_{min} = C_c$

$$C_c^e = \frac{UA}{NTU \cdot N_e N_t} \quad \text{and} \quad C_h^e = \frac{UA}{NTU \cdot C^* N_c}$$

  If $C_{min} = C_h$

$$C_c^e = \frac{UA}{NTU \cdot C^* N_e N_t} \quad \text{and} \quad C_h^e = \frac{UA}{NTU \cdot N_c}$$

1.7 Compute temperature distribution iteratively
  Compute initial temperature distribution according to Algorithm in Fig. 2(b)

  Compute initial mean temperature $T_{new} = \frac{1}{N_t N_e} \sum_{e,r,N_r} T_{c,o}^e$

  Do

   $T \leftarrow T_{new}$
   Compute temperature distribution (Fig. 2b).

   Compute mean temperature $T_{new} = \frac{1}{N_t N_e} \sum_{e,r,N_r} T_{c,o}^e$

  While $\dfrac{|T_{new} - T|}{T} < Tolerance$

1.8 Compute effectiveness of heat exchanger

  $T_{c,o} = \dfrac{1}{N_t N_e} \sum_{e,r,N_r} T_{c,o}^e$

  $T_{h,o} = \dfrac{1}{N_c} \sum_{each\ last\ circuit\ element} T_{h,o}^e$

  Compute total heat exchanged using equations:
   $q = -C_h(T_{h,o} - T_{h,i})$ and $q = C_c(T_{c,o} - T_{c,i})$
  Compute ε using by definition

(*a*)

2.1 Compute Γ^e using Eq. (1)
2.2 Compute temperatures following circuiting
  For 1 to N_c
   While not (end of a circuit)
    Compute $T_{c,o}^e$, $T_{h,o}^e$, using Eqs. (3 and 4).
    Go to next element
    Update temperatures for cold and hot fluids sides
   End While
  End For

(*b*)

Fig. 2 (*a*) Diagram of the numerical procedure and (*b*) diagram of the temperature distribution algorithm

self-explanatory, some comments must be made regarding the proposed procedure in order to make some aspects of it clearer to the reader:

- It must be stressed that the aim of the present study is to raise (ε, NTU) or other relationships for heat exchangers of known geometry and flow configuration of both fluids.
- The assumed input parameters are the NTU of the heat exchanger, and one of the two following pairs: C^* and C_{min} or C_c and C_h.
- Since (ε, NTU) relations are independent on the inlet temperatures of both fluids, they are arbitrarily assumed.
- The size of each element and associated parameters, such as $(UA)^e$, C_h^e and C_c^e, and NTU^e can be determined from the assumed number of elements, N_e, and the number of tubes and tube rows of the heat exchanger, N_t and N_r. The number of elements must be chosen so that $C_{min}^e = C_c^e \le C_h^e$, where the cold fluid is assumed to be the unmixed external fluid, as noted before.
- The element effectiveness, Γ^e, can then be determined from Eq. (1).
- The first element is the one at the fluid tube entrance. For a parallel flow configuration, the inlet temperatures of both
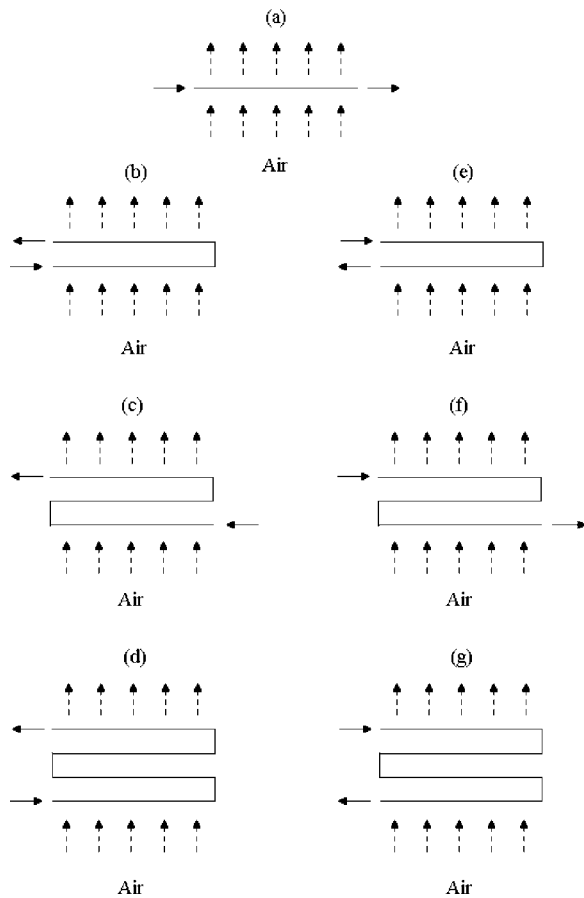
Fig. 3 Schematic representation of the heat exchangers used for the validation of the proposed algorithm: (a) $G_{1,1}$, (b) $G_{2,1}^p$, (c) $G_{3,1}^p$, (d) $G_{4,1}^p$, (e) $G_{2,1}^c$, (f) $G_{3,1}^c$, and (g) $G_{4,1}^c$

fluids are known and the exit temperatures can be obtained from Eqs. (3) and (4). By applying a similar procedure to the succeeding elements along the path of the tube fluid, the corresponding exit temperatures can be determined, allowing for the heat exchanger temperature mapping. The average exit temperatures of both fluids can then be determined.

- The inlet temperature of the external fluid (cold) in the first element is not known in the case of a counterflow configuration. This temperature must be assumed so that an iterative procedure must be followed in the determination of the temperature distribution, as suggested in the diagram of Fig. 2(a). The proposed convergence criterion is given in terms of the average outlet temperature of the external (cold) fluid.
- The thermal effectiveness of the heat exchanger, ε, corresponding to the assumed heat exchanger NTU value, can then be determined.

3 Validation of the Algorithm

In order to validate the proposed algorithm, a comparison to results obtained from theoretical relations from the literature has been carried out. The geometry of the heat exchangers considered for comparison purposes is shown in Fig. 3. These are cross-flow configurations of 1–4 tube rows, designated by $G_{i,j}^k$. The superscript k designates either the set of heat exchangers known as "parallel cross-flow," in which case $k \equiv p$, or the "counter-cross-flow," $k \equiv c$. The first subscript, i, stands for the number of passes of the tube fluid, and j for the number of rows per tube fluid passes. The heat exchangers of Fig. 3 include a "pure cross-flow" heat exchanger, designated by $G_{1,1}$, and those of two, three, and four passes, with one row per pass, parallel and counter-cross-flow

heat exchangers, designated, respectively, by $G_{i,1}^p$ and $G_{i,1}^c$ with i varying from 1 to 4. Table 1 presents the set of theoretical relations for the thermal effectiveness of the heat exchanger configurations of Fig. 3 [2,8,12]. The thermal effectiveness of the parallel flow and counter flow heat exchangers are also displayed in Table 1 as they are the limit of both cross-flow configurations when the number of passes of the tube fluid is sufficiently high. The effectiveness determined from the Table 1 relations are designated by ε_{th}. Comparisons have been made in the following ranges: $0 \le C^* \le 1$, and $0 \le NTU \le 10$. Values of C^* and NTU have been varied at intervals of 0.1, starting at 0. The comparison parameter adopted in the present study is the "relative error" of the algorithm with respect to the results from the Table 1 relations, defined as

$$\lambda = \left| \frac{\varepsilon - \varepsilon_{th}}{\varepsilon_{th}} \right| 100 \tag{5}$$

where ε is the algorithm computed effectiveness.

Table 2 presents the maximum relative errors obtained for the different configurations of Fig. 3 in the aforementioned ranges of C^* and NTU. It can be noted that the obtained errors are rather small for all cases, with upper limits being of the order of $10^{-04}\%$ and $10^{-06}\%$, respectively, for the counter-cross-flow and parallel cross-flow arrangements. These are rather small errors to be considered significant for any practical purpose. As a general rule, the parallel cross-flow arrangement errors are lower than the counter-cross-flow errors. This trend probably is related to the iterative procedure required in counter-cross-flow as compared to its counterpart arrangement. However, this does not mean that the effectiveness computation is not accurate in all cases. Considering the four passes, counter-cross-flow arrangement, for conditions (C^* and NTU) corresponding to the maximum relative error, $1.2 \times 10^{-4}\%$ according to Table 2, effectiveness values from simulation and Eq. (16) are equal to 0.996189 and 0.996188, respectively. This minimal difference implies that, even for an iteratively computed effectiveness, as for the counter-cross-flow arrangements, the results are very accurate.

Comparisons to other geometries and arrangements have been performed and can be found in a previously published paper [11]. All the comparisons carried out under the present investigation have produced rather small errors, confirming the adequacy of the proposed algorithm in predicting the thermal effectiveness of heat exchangers of complex geometry.

4 Other Geometries and Flow Arrangements

Given the satisfactory results obtained from the proposed algorithm in the validation procedure, the following step is to apply it in the analysis of two important problems in the heat exchangers literature, namely, the effect of the number of tube passes (or rows) in cross-flow configurations, and the (ε, NTU) performance in complex flow arrangements.

4.1 Effect of the Number of Tube Passes. The relations of Table 1 for cross-flow arrangements are limited to four tube passes (or rows). There are no known theoretical relations for the thermal effectiveness available for arrangements with a higher-than-six number of tube passes. The general practice has been to assume the relations for pure parallel flows and counterflows, as these are the limit arrangements when the number of tube passes tends to infinity. However, this practice might lead to significant errors in the thermal effectiveness determination. Table 3 has been raised in order to determine the order of magnitude of these errors. The actual effectiveness in this table ε, evaluated by applying the proposed algorithm, is compared to the effectiveness from either the parallel flow or the counterflow arrangements $\varepsilon_{th,\infty}$, for cross-flows with a higher number of tube passes ($N_r \ge 4$). The range and increment intervals of C^* and NTU considered in the development of Table 3 are the same as those of Table 2. Table 3 results are presented in terms of the maximum and the average relative errors, the latter defined as

Table 1 ε-NTU relationships for multipass parallel cross-flow and counter-cross-flow configurations (Eqs. (9), (13), and (17) from [2]; Eqs. (10)–(12) from [12]; Eqs. (14)–(16) from [8,12])

N_r	Side of C_{min}	Relation	Equation
		Pure cross-flow	
1	A	$\varepsilon_A = 1 - e^{-(1 - e^{\mathrm{NTU}_A C_A^*})/C_A^*}$	(9)
		Multipass parallel cross-flow	
2	A	$\varepsilon_A = \left(1 - \dfrac{K}{2}\right)\left(1 - e^{-2K/C_A^*}\right), \ K = 1 - e^{-\mathrm{NTU}_A(C_A^*/2)}$	(10)
3	A	$\varepsilon_A = 1 - \left(1 - \dfrac{K}{2}\right)^2 e^{-3K/C_A^*} - K\left[1 - \dfrac{K}{4} + \dfrac{K}{C_A^*}\left(1 - \dfrac{K}{2}\right)\right]e^{-K/C_A^*}$ $K = 1 - e^{-\mathrm{NTU}_A(C_A^*/4)}$	(11)
4	A	$\varepsilon_A = 1 - \dfrac{K}{2}\left(1 - \dfrac{K}{2} + \dfrac{K^2}{4}\right) - K\left(1 - \dfrac{K}{2}\right)\left(1 + 2\dfrac{K}{C_A^*}\left(1 - \dfrac{K}{2}\right)\right)e^{-2K/C_A^*} - \left(1 - \dfrac{K}{2}\right)^3 e^{-4K/C_A^*}$ $K = 1 - e^{-\mathrm{NTU}_A(C_A^*/4)}$	(12)
	Parallel flow heat exchanger	$\varepsilon = \dfrac{1 - e^{-\mathrm{NTU}_A(1 + C_A^*)}}{1 + C_A^*}$	(13)
		Multipass counter-cross-flow	
2	A	$\varepsilon_A = 1 - \left[\dfrac{K}{2} + \left(1 - \dfrac{K}{2}\right)e^{2K/C_A^*}\right]^{-1}, \ K = 1 - e^{-\mathrm{NTU}_A(C_A^*/2)}$	(14)
3	A	$\varepsilon_A = 1 - \left\{\left(1 - \dfrac{K}{2}\right)^2 e^{3K/C_A^*} + \left[K\left(1 - \dfrac{K}{4}\right) - \left(1 - \dfrac{K}{2}\right)\dfrac{K^2}{C_A^*}\right]e^{K/C_A^*}\right\}^{-1}$ $K = 1 - e^{-\mathrm{NTU}_A(C_A^*/3)}$	(15)
4	A	$\varepsilon_A = 1 - \left\{\dfrac{K}{2}\left(1 - \dfrac{K}{2} + \dfrac{K^2}{4}\right) + K\left(1 - \dfrac{K}{2}\right)\left[1 - 2\dfrac{K}{C_A^*}\left(1 - \dfrac{K}{2}\right)\right]e^{2K/C_A^*} + \left(1 - \dfrac{K}{2}\right)^3 e^{4K/C_A^*}\right\}^{-1}$ $K = 1 - e^{-\mathrm{NTU}_A C_A^*/4}$	(16)
∞	Counter-flow heat exchanger	$\varepsilon = \dfrac{1 - e^{-\mathrm{NTU}_A(1 - C_A^*)}}{1 - C_A^* e^{-\mathrm{NTU}_A(1 - C_A^*)}}$	(17)

Fluid A mixed, Fluid B unmixed, $C_A^* = 1/C_B^*$, $\varepsilon_B = \varepsilon_A C_A^*$, $\mathrm{NTU}_B = \mathrm{NTU}_A C_A^*$, $C_A^* = C_A/C_B$

$$\lambda_{avg} = \frac{1}{N}\sum_1^N \left|\frac{\varepsilon - \varepsilon_{th,\infty}}{\varepsilon_{th,\infty}}\right|100 \quad (6)$$

where N is the number of data points considered in the evaluation of the particular flow arrangement. An overview of Table 3 allows one to draw the following general conclusions:

- The first arrangement for both cross-flow configurations is the one with four tube passes. As expected, the errors are rather high attaining the order of 3.1%, with an average of

Table 2 Maximum relative error as a function of the number of tube rows

N_r	Geometry	$C_{min} = C_{air}$	$C_{min} = C_t$
1	$G_{1,1}$ versus Eq. (9)	1.1×10^{-6}	1.4×10^{-6}
2	$G_{2,1}^p$ versus Eq. (10)	8.7×10^{-7}	9.0×10^{-7}
3	$G_{3,1}^p$ versus Eq. (11)	6.2×10^{-7}	8.9×10^{-7}
4	$G_{4,1}^p$ versus Eq. (12)	6.3×10^{-7}	8.0×10^{-7}
2	$G_{2,1}^c$ versus Eq. (14)	2.6×10^{-5}	1.4×10^{-5}
3	$G_{3,1}^c$ versus Eq. (15)	5.7×10^{-5}	2.4×10^{-5}
4	$G_{4,1}^c$ versus Eq. (16)	1.2×10^{-4}	3.8×10^{-5}

0.6%, for the parallel cross-flow arrangement, and 6.7% and average of 1.5%, for the counter-cross-flow arrangement.

- The maximum and average errors diminish with the number of tube passes. Negligibly small deviations are attained for a number of tube passes of the order of 50, though, for practical purposes, this number could be much smaller, as the results of Table 3 clearly indicate.
- The errors found in counter-cross-flow arrangements are significantly higher than their parallel cross-flow counterparts. In fact, whereas the latter arrangement presents a maximum error of the order of 0.2% ($C_{min} = C_t$) for eight tube passes, the maximum deviation in the case of the counter-cross-flow arrangement is of the order of 2.1%. The latter figure is, by no means, negligible.

It has been a common practice to assume that the thermal effectiveness of a cross-flow heat exchanger with more than six tube passes can be approximated by either the pure parallel or the pure counterflow arrangements for industrial applications [8]. The analysis of Table 3 data demonstrates that this is not the case, at least for the counter-cross-flow arrangements in heat exchangers with high NTU and C^* values (not shown in Table 3). Bes [13] has also called attention to this fact. He found out that the absolute error between his proposed analytical relation for a counter-cross-

Table 3 Comparison between simulation results and pure parallel and counter flow solutions from Eqs. (13) and (17), respectively

| N_r | Geometry | Average relative error (%) and maximum relative error (%) | |
		$C_{\min}=C_{\text{air}}$	$C_{\min}=C_t$
4	$G^p_{4,1}$	$0.2, 1.4$	$0.6, 3.1$
5	$G^p_{5,1}$	$7.4\times10^{-2}, 0.34$	$0.2, 1.2$
6	$G^p_{6,1}$	$3.8\times10^{-2}, 0.16$	$0.1, 0.6$
7	$G^p_{7,1}$	$2.8\times10^{-2}, 0.12$	$0.06, 0.3$
8	$G^p_{8,1}$	$1.9\times10^{-2}, 9.2\times10^{-2}$	$0.04, 0.2$
9	$G^p_{9,1}$	$1.6\times10^{-2}, 7.4\times10^{-2}$	$0.03, 0.1$
10	$G^p_{10,1}$	$1.2\times10^{-3}, 5.9\times10^{-2}$	$0.02, 0.08$
20	$G^p_{20,1}$	$3.2\times10^{-3}, 1.5\times10^{-2}$	$0.003, 0.01$
50	$G^p_{50,1}$	$5.1\times10^{-4}, 2.4\times10^{-3}$	$0.0005, 0.002$
100	$G^p_{100,1}$	$1.3\times10^{-4}, 5.9\times10^{-4}$	$0.0001, 0.0006$
4	$G^c_{4,1}$	$1.5, 6.7$	$1.4, 6.7$
5	$G^c_{5,1}$	$1.0, 4.7$	$0.9, 4.7$
6	$G^c_{6,1}$	$0.7, 3.5$	$0.7, 3.5$
7	$G^c_{7,1}$	$0.5, 2.7$	$0.5, 2.7$
8	$G^c_{8,1}$	$0.4, 2.1$	$0.4, 2.1$
9	$G^c_{9,1}$	$0.3, 1.7$	$0.3, 1.7$
10	$G^c_{10,1}$	$0.26, 1.4$	$0.2, 1.4$
20	$G^c_{20,1}$	$0.06, 0.37$	$0.06, 0.4$
50	$G^c_{50,1}$	$0.01, 0.06$	$0.01, 0.06$
100	$G^c_{100,1}$	$0.002, 0.01$	$0.002, 0.01$

flow arrangement of 20 tube passes and Eq. (17), for NTU>5, tends to 2.5%. For a similar flow arrangement, according to the present approach, the maximum relative error is of the order of 0.4%, for $C^* \geq 0.7$ and NTU>5. This is a figure significantly lower than that found by Bes [13], but still too high to be neglected. It could be argued that these errors are rather low for practical purposes. However, if one considers that in design analysis, the effectiveness is known and the NTU value must be determined from it in order to evaluate the product UA, this conclusion might be questionable. In fact, it has been pointed out in a previous paper [11] that a very small error in the effectiveness can lead to NTU errors of more than one order of magnitude higher in the range of high values of NTU. For example, it can be shown that for a heat exchanger of 1 tube pass, $C^*=0.5$, and NTU=5, an effectiveness error of 0.1% leads to an error of the order of 4.0% in the NTU value. Thus caution must be exercised in applying simplified (ε, NTU) relations in order to prevent incurring larger errors than expected.

Effectiveness data for five to ten tube passes have been determined by applying the proposed algorithm and can be found in Tables 4 and 5 for parallel cross-flow and counter-cross-flow configurations. It must be noted that effectiveness data for flow arrangements of more than six tube passes have not been published thus far in the open literature. The effectiveness of the limit configurations of pure parallel and pure counterflow has also been included in the last column of each table as a reference. The effectiveness considered in these tables is the so-called P temperature effectiveness, defined as

$$P = \frac{\Delta T_c}{T_{h,i} - T_{c,i}} = \frac{T_{c,o} - T_{c,i}}{T_{h,i} - T_{c,i}} \tag{7}$$

The P effectiveness of Tables 4 and 5 is given in terms of NTU and the R parameter, defined as

$$R = \frac{C_c}{C_h} \tag{8}$$

The following conclusions can be drawn from the effectiveness data of Tables 4 and 5:

- The effectiveness of parallel cross-flow and counter-cross-

flow configurations tends to that of the pure parallel and pure counterflow, respectively, as the number of tube passes increases.

- It is interesting to note that the effectiveness varies differently with the number of tube passes in the parallel cross-flows and counter-cross-flows. The effectiveness increases with the number of tube passes in the counter-cross-flow configuration with the limit value (rounded off to four decimals) being attained at different number of passes depending on the values of R and NTU.
- For the parallel cross-flow arrangement, the effectiveness alternates between larger and lower than the limit values depending on the number of tube pass. It can be noted that for an even number of passes, the effectiveness is higher than the limit, whereas for an odd number the effectiveness is lower. In any case, the difference from the limit effectiveness diminishes with the number of tube passes.

4.2 Heat Exchanger of Complex Flow Configuration. The proposed algorithm has been applied to the evaluation of the thermal effectiveness of different cross-flow arrangements in the preceding sections. The obtained results have been scrutinized both to check for their precision through comparisons to available theoretical relations and to raise trends associated to the relationship of thermal effectiveness and the cross-flow configurations. A different heat exchanger with a complex flow arrangement will be considered in the present section. A schematic representation of this heat exchanger is shown in Fig. 4. The flow arrangement has been suggested by Guo et al. [14] as being the one with the best thermal effectiveness among three other configurations: the pure cross-flow, the one-pass cross-flow with four tube rows, and the two-pass counter-cross-flow, the last one corresponding to the flow arrangement of Fig. 3(e). The motivation to address this particular geometry is twofold: to raise effectiveness data for a complex geometry not available in the literature by applying the proposed algorithm and to discuss the results by Guo et al. [14] as compared to those for the four-pass counter-cross-flow configuration from the present investigation.

Curves, not available in the literature, of the thermal effectiveness for the configuration of Fig. 4 versus NTU for several values

Table 4 Thermal effectiveness *P* values for parallel cross-flow arrangement considering five, six, seven, eight, nine, and ten rows, with one tube each

R	NTU	Thermal Effectiveness P						
		Multipass cross-parallel-flow						Parallel-flow
		Five passes	Six passes	Seven passes	Eight passes	Nine passes	Ten passes	
0.2	0.2	0.1778	0.1778	0.1778	0.1778	0.1778	0.1778	0.1778
0.2	0.5	0.3761	0.3760	0.3760	0.3760	0.3760	0.3760	0.3760
0.2	1.0	0.5827	0.5826	0.5825	0.5825	0.5825	0.5824	0.5824
0.2	2.0	0.7587	0.7584	0.7582	0.7581	0.7580	0.7580	0.7577
0.2	5.0	0.8317	0.8316	0.8315	0.8314	0.8314	0.8314	0.8313
0.2	10.0	0.8333	0.8333	0.8333	0.8333	0.8333	0.8333	0.8333
0.5	0.2	0.1728	0.1728	0.1728	0.1728	0.1728	0.1728	0.1728
0.5	0.5	0.3520	0.3519	0.3519	0.3518	0.3518	0.3518	0.3518
0.5	1.0	0.5187	0.5184	0.5183	0.5182	0.5181	0.5181	0.5179
0.5	2.0	0.6348	0.6344	0.6342	0.6340	0.6339	0.6338	0.6335
0.5	5.0	0.6665	0.6664	0.6664	0.6664	0.6664	0.6664	0.6663
0.5	10.0	0.6668	0.6666	0.6667	0.6667	0.6667	0.6667	0.6667
1.0	0.2	0.1649	0.1649	0.1649	0.1648	0.1648	0.1648	0.1648
1.0	0.5	0.3164	0.3163	0.3162	0.3162	0.3162	0.3161	0.3161
1.0	1.0	0.4332	0.4330	0.4328	0.4327	0.4326	0.4326	0.4323
1.0	2.0	0.4919	0.4915	0.4914	0.4912	0.4912	0.4911	0.4908
1.0	5.0	0.5004	0.4998	0.5000	0.5000	0.5000	0.5000	0.5000
1.0	10.0	0.5017	0.4996	0.5001	0.5000	0.5000	0.5000	0.5000
1.5	0.2	0.1134	0.1134	0.1134	0.1134	0.1134	0.1134	0.1134
1.5	0.5	0.2263	0.2263	0.2262	0.2262	0.2262	0.2262	0.2262
1.5	1.0	0.3250	0.3248	0.3247	0.3247	0.3246	0.3246	0.3244
1.5	2.0	0.3866	0.3863	0.3862	0.3860	0.3860	0.3859	0.3857
1.5	5.0	0.4005	0.3997	0.4000	0.3997	0.4000	0.3999	0.3999
1.5	10.0	0.4024	0.3992	0.4002	0.3999	0.4000	0.4000	0.4000
3.0	0.2	0.0585	0.0585	0.0585	0.0585	0.0585	0.0585	0.0585
3.0	0.5	0.1217	0.1218	0.1217	0.1217	0.1217	0.1217	0.1216
3.0	1.0	0.1843	0.1842	0.1842	0.1842	0.1842	0.1842	0.1841
3.0	2.0	0.2331	0.2329	0.2328	0.2328	0.2328	0.2327	0.2326
3.0	5.0	0.2502	0.2495	0.2498	0.2496	0.2498	0.2499	0.2497
3.0	10.0	0.2526	0.2488	0.2505	0.2497	0.2502	0.2499	0.2500
7.0	0.2	0.0255	0.0255	0.0255	0.0255	0.0255	0.0255	0.0255
7.0	0.5	0.0544	0.0544	0.0544	0.0544	0.0544	0.0544	0.0544
7.0	1.0	0.0852	0.0852	0.0852	0.0852	0.0852	0.0852	0.0851
7.0	2.0	0.1124	0.1124	0.1124	0.1123	0.1123	0.1123	0.1123
7.0	5.0	0.1248	0.1245	0.1247	0.1246	0.1246	0.1246	0.1246
7.0	10.0	0.1264	0.1242	0.1254	0.1247	0.1251	0.1249	0.1250

of C^* are shown in Fig. 5. Results for limited ranges of C^* and NTU are also presented in Table 6. Values of the thermal effectiveness are presented in this table for the configuration of Fig. 4 and the four-pass counter-cross-flow configuration, Fig. 3(*g*), not considered by Guo et al. [14] in their analysis. Data for the pure counterflow arrangement have also been included in Table 6 for comparison purposes. The table covers the following ranges of C^* and NTU: $0.1 \leq C^* \leq 1.0$; and $2 \leq NTU \leq 12$. A quick glance at Table 6 allows one to clearly devise some trends regarding differences between the considered flow configurations. The following list of conclusions can be drawn from these trends:

- Initially, it can be noted that the effectiveness of the four-pass counter-cross-flow configuration, Fig. 3(*g*), is higher than that of Fig. 4 for certain ranges of C^* and NTU.
- As expected, the thermal effectiveness increases with NTU for both configurations. However, the effectiveness of the Fig. 3(*g*) arrangement is higher for low NTU values, the difference diminishing with NTU.
- The effectiveness of the Fig. 3(*g*) arrangement is higher over the whole range of NTU for the C^* values of 0.2 and 0.4. However, for higher values of C^* a crossover is noted at a given NTU. The crossover NTU diminishes with C^*.
- The thermal effectiveness of both configurations tend to that of the pure counterflow configuration for lower values of C^* and high values of NTU, as should be expected. It is interesting to note that the best performance of the Fig. 4 configuration with respect to that of Fig. 3(*g*) occurs at high C^* and NTU values, for which the errors with respect to the

pure counterflow are higher (see shadow areas in Table 6). The more uniform temperature difference along the heat exchanger for this configuration at high values of C^* and NTU, as suggested by [14], could explain the above trend.
- However, it must be stressed that the conclusions by Guo et al. [14] with respect to the thermal performance of the Fig. 4 configuration are limited to the flow arrangements considered for comparison in their paper. These conclusions cannot be generalized as the data of Table 6 clearly demonstrate.

The results from Table 6 make clear that the choice of any flow configuration should not be limited to the theoretical characteristics of the heat exchanger. Parameters such as the allowed pressure drop and heat transfer coefficients should also be considered in design and rating of a heat exchanger along with manufacturing and durability aspects [6].

As a final remark, it must be emphasized that the results from the proposed algorithm regarding the configuration of Fig. 4 are complementary to the experimental ones by Guo et al. [14] by extending the performance data to wider ranges of C^* and NTU. These results also demonstrate the extent to which the algorithm of the present investigation can be applied.

5 Conclusions

The developed algorithm for the determination of the thermal effectiveness of multipass parallel and counter-cross-flow configurations has been validated against available theoretical relations,

Table 5 Thermal effectiveness P values for counter-cross-flow arrangement considering five, six, seven, eight, nine, and ten rows, with one tube each

R	NTU	Thermal Effectiveness P						
		Multipass cross-counter-flow						Counter-flow
		Five passes	Six passes	Seven passes	Eight passes	Nine passes	Ten passes	
0.2	0.2	0.1782	0.1782	0.1782	0.1782	0.1782	0.1782	0.1782
0.2	0.5	0.3806	0.3807	0.3807	0.3807	0.3807	0.3807	0.3807
0.2	1.0	0.6046	0.6047	0.6048	0.6049	0.6049	0.6049	0.6050
0.2	2.0	0.8302	0.8306	0.8310	0.8311	0.8312	0.8313	0.8317
0.2	5.0	0.9832	0.9839	0.9842	0.9845	0.9847	0.9848	0.9853
0.2	10.0	0.9992	0.9994	0.9995	0.9996	0.9996	0.9996	0.9997
0.5	0.2	0.1738	0.1738	0.1738	0.1738	0.1738	0.1738	0.1738
0.5	0.5	0.3620	0.3621	0.3622	0.3622	0.3622	0.3622	0.3623
0.5	1.0	0.5637	0.5640	0.5642	0.5643	0.5644	0.5645	0.5647
0.5	2.0	0.7710	0.7720	0.7727	0.7732	0.7735	0.7737	0.7746
0.5	5.0	0.9477	0.9506	0.9524	0.9535	0.9543	0.9549	0.9572
0.5	10.0	0.9882	0.9913	0.9930	0.9940	0.9946	0.9950	0.9966
1.0	0.2	0.1666	0.1666	0.1666	0.1666	0.1667	0.1667	0.1667
1.0	0.5	0.3330	0.3331	0.3331	0.3332	0.3332	0.3332	0.3333
1.0	1.0	0.4984	0.4988	0.4992	0.4993	0.4995	0.4996	0.5000
1.0	2.0	0.6609	0.6626	0.6637	0.6644	0.6648	0.6652	0.6667
1.0	5.0	0.8123	0.8183	0.8221	0.8246	0.8264	0.8277	0.8333
1.0	10.0	0.8661	0.8772	0.8847	0.8898	0.8935	0.8963	0.9091
1.5	0.2	0.1142	0.1142	0.1142	0.1142	0.1142	0.1142	0.1142
1.5	0.5	0.2347	0.2348	0.2348	0.2348	0.2348	0.2349	0.2349
1.5	1.0	0.3610	0.3612	0.3614	0.3615	0.3616	0.3616	0.3618
1.5	2.0	0.4902	0.4911	0.4916	0.4920	0.4922	0.4924	0.4932
1.5	5.0	0.6092	0.6120	0.6137	0.6148	0.6156	0.6162	0.6186
1.5	10.0	0.6465	0.6501	0.6523	0.6537	0.6548	0.6555	0.6586
3.0	0.2	0.0587	0.0587	0.0587	0.0587	0.0588	0.0588	0.0588
3.0	0.5	0.1241	0.1241	0.1241	0.1241	0.1241	0.1241	0.1241
3.0	1.0	0.1954	0.1955	0.1956	0.1956	0.1956	0.1956	0.1957
3.0	2.0	0.2683	0.2685	0.2687	0.2688	0.2689	0.2689	0.2691
3.0	5.0	0.3239	0.3243	0.3246	0.3247	0.3249	0.3249	0.3253
3.0	10.0	0.3326	0.3327	0.3328	0.3329	0.3329	0.3329	0.3330
7.0	0.2	0.0256	0.0256	0.0256	0.0256	0.0256	0.0256	0.0256
7.0	0.5	0.0549	0.0549	0.0549	0.0549	0.0549	0.0549	0.0549
7.0	1.0	0.0875	0.0875	0.0875	0.0875	0.0875	0.0875	0.0875
7.0	2.0	0.1201	0.1201	0.1202	0.1202	0.1202	0.1202	0.1202
7.0	5.0	0.1410	0.1410	0.1411	0.1411	0.1411	0.1411	0.1415
7.0	10.0	0.1428	0.1428	0.1428	0.1428	0.1428	0.1428	0.1428

with accurate results. In addition, the algorithm has been applied to different, complex cross-flow arrangements, providing new thermal effectiveness data. The conclusions from the present investigation could be summarized as follows:

1. The common practice of approximating the thermal effectiveness of the parallel cross-flow and counter-cross-flow arrangements for a large number of tube passes for the limit configurations of pure parallel and pure counterflows might lead to non-negligible errors. Care should be exercised in applying this simplification.
2. The thermal effectiveness of the multipass cross-flow configurations varies differently with the number of tube passes. In the counter-cross-flow configuration, the effectiveness increases tending to that of the limit configuration of pure counterflow. The effectiveness alternates in the case of the parallel cross-flow arrangement though tending progressively to that of the pure parallel flow.
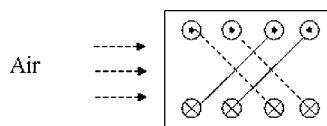

Fig. 4 Schematic representation of the configuration studied experimentally in [14] and simulated in this paper (× and • signs indicates that fluid flows into or out of the paper, respectively)

3. The thermal effectiveness of the complex configuration proposed by Guo et al. [14], shown in Fig. 4, is higher than that of the four pass counter-cross-flow one in the range of higher values of C^* and NTU, not being amenable to generalizations to other conditions.

Nomenclature

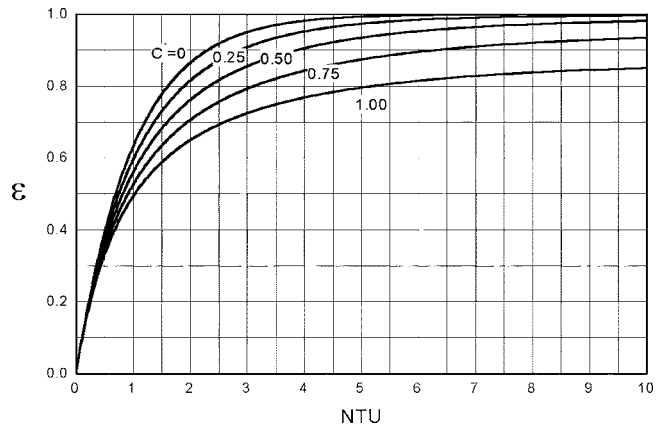A = exchanger outer total heat transfer area, m^2

Fig. 5 Effectiveness-NTU graphic for configuration shown in Fig. 4 for C_{max} mixed and C_{min} unmixed

Table 6 Heat exchanger effectiveness values for three configurations: Fig. 4 configuration, Fig. 3(g) configuration, and the pure counterflow configuration

| C* | NTU | Heat Exchanger Effectiveness | | | | |
| | | $C_{min}=C_{air}$ | | $C_{min}=C_t$ | | Pure counter flow |
		Figure 4 configuration	Four pass counter cross-flow	Figure 4 configuration	Four pass counter cross-flow	
0.2	2	0.8252	0.8293	0.8258	0.8294	0.8317
0.2	5	0.9785	0.9819	0.9799	0.9825	0.9853
0.2	8	0.9958	0.9969	0.9968	0.9976	0.9987
0.2	9	0.9974	0.9981	0.9982	0.9987	0.9994
0.2	10	0.9982	0.9987	0.9989	0.9992	0.9997
0.2	11	0.9988	0.9991	0.9994	0.9996	0.9999
0.2	12	0.9991	0.9993	0.9996	0.9997	0.9999
0.4	2	0.7830	0.7899	0.7838	0.7900	0.7945
0.4	5	0.9527	0.9591	0.9551	0.9606	0.9695
0.4	8	0.9835	0.9860	0.9863	0.9886	0.9950
0.4	9	0.9874	0.9890	0.9902	0.9919	0.9973
0.4	10	0.9900	0.9910	0.9928	0.9940	0.9985
0.4	11	0.9918	0.9923	0.9945	0.9954	0.9992
0.4	12	0.9930	0.9932	0.9958	0.9964	0.9996
0.6	2	0.7389	0.7473	0.7395	0.7474	0.7539
0.6	5	0.9130	0.9211	0.9155	0.9230	0.9411
0.6	8	0.9554	0.9583	0.9594	0.9628	0.9833
0.6	9	0.9619	0.9635	0.9664	0.9688	0.9889
0.6	10	0.9666	0.9671	0.9714	0.9731	0.9926
0.6	11	0.9700	0.9696	0.9753	0.9763	0.9951
0.6	12	0.9725	0.9715	0.9782	0.9788	0.9967
0.8	2	0.6939	0.7028	0.6942	0.7029	0.7109
0.8	5	0.8593	0.8674	0.8609	0.8688	0.8957
0.8	8	0.9060	0.9082	0.9089	0.9118	0.9518
0.8	9	0.9138	0.9144	0.9173	0.9188	0.9619
0.8	10	0.9197	0.9190	0.9236	0.9240	0.9696
0.8	11	0.9241	0.9223	0.9285	0.9279	0.9757
0.8	12	0.9274	0.9247	0.9323	0.9310	0.9804
1.0	2	0.6490	0.6578	0.6490	0.6578	0.6667
1.0	5	0.7952	0.8020	0.7952	0.8020	0.8333
1.0	8	0.8373	0.8384	0.8373	0.8384	0.8889
1.0	9	0.8445	0.8442	0.8445	0.8442	0.9000
1.0	10	0.8499	0.8483	0.8499	0.8483	0.9091
1.0	11	0.8539	0.8514	0.8539	0.8514	0.9167
1.0	12	0.8570	0.8537	0.8570	0.8537	0.9231

B = constant, $C_c^e \Gamma^e / C_h^e$, dimensionless
C = heat capacity rate, W/K
C^* = heat capacity rate ratio, C_{min}/C_{max}, dimensionless
N = number of data points
N_c = number of tube fluid circuits
N_e = number of elements per tube
N_r = number of rows in the heat exchanger
N_t = number of tubes per row
NTU = number of transfer units, UA/C_{min}, dimensionless
P = temperature effectiveness, $(T_{c,o}-T_{c,i})/(T_{h,i}-T_{c,i})$, dimensionless
q = heat transfer rate, W
R = temperature ratio, $(T_{h,i}-T_{h,o})/(T_{c,o}-T_{c,i})$, dimensionless
T = temperature, K
U = overall heat transfer coefficient, W/(m²K)

Greek Symbols
ε = conventional heat exchanger effectiveness, q/q_{max}, dimensionless
λ = relative error
Γ = dimensionless parameter defined by Eq. (1)

Subscripts
∞ = infinite

air = air side
avg = average
c = cold fluid side of heat exchanger or fluid circuit
e = element
h = hot fluid side of heat exchanger
i = inlet conditions or number of tube fluid passes
j = number of rows per tube fluid passes
max = maximum value
min = minimum value
new = new value
o = outlet conditions
r = row
t = tube fluid side of heat exchanger
th = theoretical

Superscripts
c = overall counter cross-flow configuration
e = element
k = designates either c or p superscripts
p = overall parallel cross-flow configuration

References
[1] Sekulic, D. P., Shah, R. K., and Pignotti, A., 1999, "A Review of Solution Methods for Determining Effectiveness-NTU Relationships for Heat Exchangers with Complex Flow Arrangements," Appl. Mech. Rev., **52**(3), pp. 97–117.

[2] Kays, W. M., and London, A. L., 1998, *Compact Heat Exchangers*, McGraw-Hill, New York.

[3] Wang, C.-C., Webb, R. L., and Chi, K.-Y., 2000, "Data Reduction for Air-Side Performance of Fin-and-Tube Heat Exchanger," Exp. Therm. Fluid Sci., **21**, pp. 218–226.

[4] Pignotti, A., and Shah, R. K., 1992, "Effectiveness-Number of Transfer Units Relationships for Heat Exchanger Complex Flow Arrangements," Int. J. Heat Mass Transfer, **35**, pp. 1275–1291.

[5] Domingos, J. D., 1969, "Analysis of Complex Assemblies of Heat Exchangers," Int. J. Heat Mass Transfer, **12**, pp. 537–548.

[6] Shah, R. K., and Pignotti, A., 1993, "Thermal Analysis of Complex Cross-Flow Exchangers in Terms of Standard Configurations," Eur. J. Oper. Res., **115**, pp. 353–359.

[7] Baclic, B. S., 1990, "ε-NTU Analysis of Complicated Flow Arrangements," *Compact Heat Exchangers: A Festschrift*, A. L. London, A. D. Kraus, R. K. Shah, and D. E. Metzger, eds., Hemisphere, Washington, DC, pp. 31–90.

[8] Taborek, J., 1983, "Charts for Mean Temperature Difference in Industrial Heat Exchanger Configuration," *Heat Exchanger Design Handbook*, E. W. Schlünder, ed., Hemisphere, Washington, DC, Chap. 1.5.

[9] Stevens, R. A., Fernandez, J., and Woolf, J. R., 1957, "Mean-Temperature Difference in One, Two, and Three-Pass Crossflow Heat Exchangers," Trans. ASME, **79**, pp. 287–297.

[10] Chen, T. D., Conklin, J. C., and Baxter, V. D., 1998, "Comparison of Analytical and Experimental Effectiveness of Four-Row Plate-Fin-Tube Heat Exchangers With Water, R-22 and R-410A," ASME Winter Annual Meeting, Anaheim.

[11] Navarro, H. A., and Cabezas-Gomez, L., 2005, "A New Approach for Thermal Performance Calculation of Cross-Flow Heat Exchangers," Int. J. Heat Mass Transfer, **48**, pp. 3880–3888.

[12] ESDU 86018, 1991, "Effectiveness-NTU Relations for the Design and Performance Evaluation of Two-Stream Heat Exchangers," Engineering Science Data Unit 86018 with Amendment, London ESDU International plc, pp. 92–107.

[13] Bes, Th., 1996, "Thermal Performance of Codirected Cross-Flow Heat Exchangers," Heat Mass Transfer, **31**, pp. 215–222.

[14] Guo, Z.-Y., Zhou, S.-Q., Li, Z.-X., and Chen, L.-G., 2002, "Theoretical Analysis and Experimental Confirmation of the Uniformity Principle of Temperature Difference Field in Heat Exchanger," Int. J. Heat Mass Transfer, **45**, pp. 2119–2127.

A New Approach to Numerical Simulation of Small Sized Plate Heat Exchangers With Chevron Plates

Sanjeev Jain
e-mail: sanjeevj@mech.iitd.ac.in

Aniruddha Joshi[1]

Department of Mechanical Engineering,
Indian Institute of Technology,
Hauz Khas,
New Delhi-110016, India

P. K. Bansal
Department of Mechanical Engineering,
The University of Auckland,
Auckland, New Zealand

A numerical and experimental study of heat transfer and fluid flow in a single pass counter flow plate heat exchanger with chevron plates has been presented in this paper. CFD analysis of small sized plate heat exchanger was carried out by taking the complete geometry of the heat transfer surface and more realistic hydrodynamic and thermal boundary conditions. A cold channel with two chevron plates and two halves of hot channels on either side having flat periodic boundaries was selected as the computational domain. The numerical model was validated with data from experiments and empirical correlations from literature. Heat transfer and pressure drop data were obtained experimentally with water as the working fluid, in the Reynolds number range 400–1300 and the Prandtl number range 4.4–6.3. [DOI: 10.1115/1.2430722]

1 Introduction

Plate heat exchangers (PHEs) are used in a variety of chemical, process, and power industries over a broad range of temperatures due to their compactness, ease of maintenance, flexibility, and favorable thermal-hydraulic characteristics. The chevron (or herringbone) design is the most commonly used surface pattern in PHEs. Inclination angle, corrugation shape, amplitude and wavelength, plate thickness, etc. are important design parameters for these plates. The plates are closely packed at an angle to form cross-corrugated passages that exhibit high heat transfer rates with comparatively low pressure drops. This geometry is also used in other heat (and mass) exchangers such as rotary regenerators and evaporative cooling pads. The cross corrugation assures channel gap while improving the plate stiffness and allowing the fluids to flow very close to each other. Each plate has four corner ports with flow distribution areas in addition to the main heat transfer surface.

Numerical simulation of plate heat exchangers (PHEs) is an important tool to better understand the fundamental mechanisms, the flow patterns, swirl flows, and their effects on the heat transfer and pressure drop. It helps in faster development of new products by simulating the effect of various design parameters. Some of the previous numerical works on PHEs assumed the computational domain either as a unit cell [1–4] or one complete channel [5–8]. In the former approach, the plate is considered to be a repeating unit cell with periodic boundary conditions (generally fully developed flow). However, in the latter, a channel (either hot or cold) formed between two consecutive plates has been considered for simulation. Further, few studies [5,6] have also assumed one plate to be flat to keep the geometry simple. Uniform wall temperature or uniform heat flux at the plate (in many cases both are not constant and also not known *a priori*) are the typical thermal boundary conditions selected in almost all cases. None of these approaches actually correspond to what happens in a real plate heat exchanger.

Fully developed flow approximations can be assumed to be valid in the central region of a large PHE, away from the inlet. However, in small PHEs, these assumptions may not be valid for most of the region, because the flow is developing at the entry and the central region of the plate, where the direction of flow changes. Further, this developing region is not negligible in comparison to the fully developed region. The uniform wall temperature/heat flux thermal boundary conditions adopted by researchers are also not a true representation of the reality, where the shape of the corrugation pattern creates a complex three-dimensional flow field, causing the temperature and heat flux to vary along the plate [7]. To overcome these drawbacks, the smallest geometry that simulates the complete heat exchanger with actual temperature distribution and heat transfer coefficients needs to be analyzed. Since the alternate plates are stacked at an angle forming cross-corrugated passages, two plates with both the fluids have to be included in the geometry.

The present work, therefore, considered a cold channel (with two corrugated plates on either side) and two half hot channels on either side as the computational domain. The virtual flat boundaries of the outer half hot channels were treated as periodic surfaces to represent the complete heat exchanger. In applying the periodic boundary conditions the pack was assumed to contain infinite plates (neglecting the end effects), although the ends effects may be significant if the number of plates is less than 50 [9]. For the selected geometry, three-dimensional, steady state numerical simulations were carried out using a finite volume based commercial CFD package. GAMBIT was used as the preprocessor for geometry creation and mesh generation, while FLUENT 5/6 was used as the solver and postprocessor. The inputs to the simulation included the inlet velocities and temperatures of hot and cold fluids. The simulations predicted the heat transfer coefficient and pressure drop along with the velocity, pressure, and temperature distribution in the channels. The simulation results in terms of Nusselt number and friction factor f were validated with empirical correlations from the literature and data obtained from an experimental test facility on a small sized PHE.

---

2 Mathematical Model

For an incompressible and steady state flow through corrugated channels, the mass continuity, momentum (Navier-Stokes), and energy equations (in conservation form and tensorial notation) can respectively be written as:

$$\frac{\partial u_j}{\partial x_j} = 0 \tag{1}$$

$$\frac{\partial u_i u_j}{\partial x_j} = -\frac{1}{\rho}\frac{\partial p}{\partial x_i} + \frac{\partial}{\partial x_j}(\nu + \nu_t)\frac{\partial u_i}{\partial x_j} + B_j \tag{2}$$

$$\frac{\partial u_j T}{\partial x_j} = \frac{\partial}{\partial x_j}\left(\frac{\nu}{\sigma} + \frac{\nu_t}{\sigma_t}\right)\frac{\partial T}{\partial x_j} \tag{3}$$

The transport equations for k and epsilon in the realizable k-ε model are [10],

$$\frac{\partial(\rho k u_j)}{\partial x_j} = \frac{\partial}{\partial x_j}\left[\left(\mu + \frac{\mu_t}{\sigma_k}\right)\frac{\partial k}{\partial x_j}\right] + G_k + G_b - \rho\varepsilon - Y_M + S_k \tag{4}$$

$$\frac{\partial(\rho\varepsilon u_j)}{\partial x_j} = \frac{\partial}{\partial x_j}\left[\left(\mu + \frac{\mu_t}{\sigma_\varepsilon}\right)\frac{\partial\varepsilon}{\partial x_j}\right] + \rho C_1 S_\varepsilon - \rho C_2 \frac{\varepsilon^2}{k + \sqrt{\nu\varepsilon}}$$

$$+ C_{1\varepsilon}\frac{\varepsilon}{k}C_{3\varepsilon}G_b + S_\varepsilon \tag{5}$$

In these equations, G_k represents the generation of turbulence kinetic energy due to the mean velocity gradients, G_b is the generation of turbulence kinetic energy due to buoyancy, Y_M accounts for the effect of compressibility on turbulence, which was neglected in this study, σ_k and σ_ε are the turbulent Prandtl numbers for k and ε, respectively, and S_k and S_ε are the user defined source terms, which were not used in this study.

In the realizable k-ε model, the k equation is the same as that in the standard k-ε and RNG k-ε models with different constants. However, the ε equation is quite different from the other models, mainly due to the absence of the G_k term in the equation and the absence of singularity, even if k vanishes [10]. Both these features are in contrast with the traditional k-ε models. Turbulent (or eddy) viscosity is defined as

$$\mu_t = \rho C_\mu \frac{k^2}{\varepsilon}$$

where C_μ is a variable in the realizable k-ε model. It is computed in the numerical code itself as a function of mean strain and rotation rates, the angular velocity of system rotation, and the turbulence field (k and ε) [10]. It recovers a standard value of 0.09 for an inertial sublayer in an equilibrium boundary layer. This is
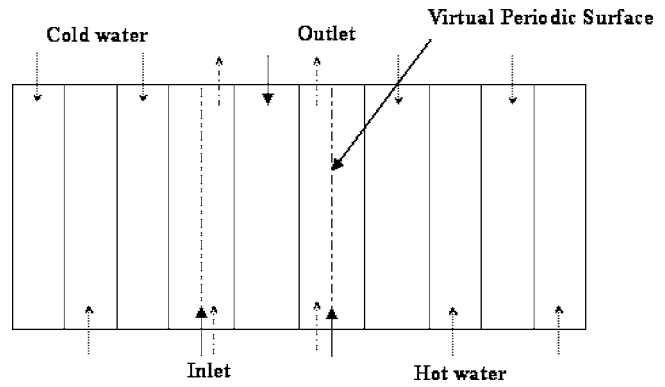

Fig. 1 Schematic diagram—periodic boundary condition

another difference from the standard k-ε and RNG k-ε models, where C_μ is taken as a constant.

3 Solution Methodology

The governing equations were solved using a commercial CFD package (Fluent 5/6) with the following simplifying assumptions:

1. Being a small PHE, there is no mal-distribution of flow and the flow is equally divided into all the channels. (This assumption was also confirmed experimentally by evaluating the maldistribution factor as discussed in Sec. 5.)
2. Heat transfer surface was assumed to be free from fouling.
3. Periodicity exists in the direction perpendicular to channels, implying an infinite pack. Although the actual pack may be much smaller, this assumption is necessary to keep the computational domain reasonable. Therefore, the computational domain was reduced to two halves of hot water channel and one cold-water channel.

The computational domain consisted of a cold channel formed by two corrugated plates and two halves of hot channel on either side, as shown in Figs. 1 and 2. The geometry consists of two corrugated plates and two imaginary flat plain surfaces, on outer sides of the corrugated plates. These virtual plain surfaces were defined as periodic surfaces. Thus periodic boundary conditions were applied to the hot water channel flow being split in the center. Only the heat transfer area of the plates was considered with the boundaries of the hot channels as flat periodic surfaces. A generally used chevron angle of 60° with the flow direction was assumed. Many earlier studies [e.g., [1,11]] have predicted the
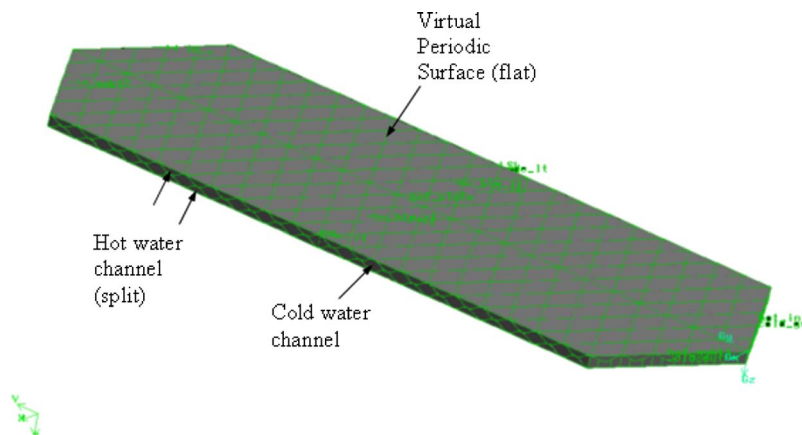

Fig. 2 Corrugated plate geometry with periodic boundaries

effect of chevron angles. In this approach, for varying the chevron angle, the whole geometry has to be created again, so it was not considered in this study.

The two corrugated plates were taken as double-sided walls or coupled, as these plates had fluid zones on both sides. The solver calculates the temperature of these walls from the temperature distribution of neighboring fluid zones. The gaskets were assumed to be adiabatic walls as there was no flow through it.

3.1 Boundary Conditions

3.1.1 Inlet Boundary Conditions. The velocity and temperature values were specified at the inlet of the channel. The direction of the inlet velocity was normal to the surface. It was assumed that flow is uniformly distributed at the entry of the heat transfer surface, after the distribution area (a reasonable assumption for well distributed flow). The inlet velocity was calculated from channel mass flow rate and channel inlet cross-sectional area. Percentage turbulence intensity and hydraulic diameter were also specified while solving the turbulence equation. The value of the hydraulic diameter was specified as twice the mean flow channel gap. Turbulence intensity of 1% was generally considered to be low, while 10% was considered to be high. For internal flows, the values at the inlets depend totally on the upstream history of flow. The values of turbulence intensity were estimated from an empirical correlation provided in Fluent [10] for fully developed duct flow, which were in the range 5% to 6%. These values were in agreement with the range specified by Fluent for complex flows. Turbulence kinetic energy and dissipation rates are then calculated by the code based on turbulence intensity, hydraulic diameter, and mean flow velocity.

3.1.2 Outlet Boundary Conditions. At the outlet, the pressure boundary condition was specified as a constant value equal to zero gauge pressure. Backflow total temperature, percentage turbulence intensity, and hydraulic diameter were also specified. The average of hot and cold fluid inlet temperatures was taken as backflow total temperature.

3.1.3 Periodic Boundary Conditions. The plain surfaces on both sides of the corrugated walls were grouped. A translational periodic boundary condition in the Z direction (normal to plane of plates) with zero pressure gradient was applied to these groups.

3.2 Working Fluid Properties.
Water was taken as the working fluid on both sides. Viscosity of water was taken as a second order polynomial function of the temperature. Other properties of water such as density and specific heat were assumed constant.

3.3 Geometry Creation and Meshing.
The chevron plates stacked together in a symmetric arrangement were assumed to bear sine wave corrugations. The corrugation pitch, amplitude, chevron angle, and number of repeat units specify the geometry of corrugated plate. The chevron plate used for experimentation had an amplitude, pitch, and chevron angle of 2.4 mm, 11.5 mm, and 60°, respectively. The corrugations were generated using a sinusoidal curve with the following equation:

$$y = 1.2 \sin\left(\frac{2\pi(x - 2.875)}{11.5}\right) + 1.2 \qquad (6)$$

The sine curve was translated through distance equal to pitch in the direction 60° to the X axis to form the top portion of unit cell. Then, the curve was reflected by 180°, rotated by 60°, and translated by the distance equal to the pitch to form the lower portion of the unit cell. The faces of the unit cell are formed from the edges. Initially, the unit cell geometry was repeated to form the corrugated plate. But, it resulted in multiple vertices, edges, and faces. So, a bottom-up approach was used for geometry creation. Vertices of unit cell were translated and surfaces were created.

To obtain identical meshing on the periodic surfaces, a surface was generated above each unit cell, making the total number of surfaces to be 300 (a single flat surface resulted in large values of skewness). Each surface was selected one by one and a link was formed between these surfaces during meshing. Three volumes were formed for meshing, one for the central channel and the other two for the outer two halves. For meshing, the two outer control volumes were again divided into 25 control volumes with a volume corresponding to each corrugation. The volumes formed were meshed using Tet/Hybrid T-Grid scheme with around 450,000 tetrahedral cells in all for the central channel. For the modeled periodic geometry the total number of cells was close to 880,000. By meshing the control volume with different interval sizes of 0.75, 0.9, 1, and 1.1, the grid independency study was performed. The variation in results was within 5% for pressure drop and average Nusselt number, when an interval size of 0.75 was used instead of 1. Therefore, final simulations were performed with an interval size of 1.

The nonequilibrium wall functions approach was used for near wall treatment as it does not require very fine mesh near the wall as in a near wall model, but provides reasonably good accuracy. The wall function approach used bridges the viscosity-affected region between the wall and the fully turbulent region. In most high-Reynolds-number flows, the wall function approach substantially saves computational resources. The wall functions approach is economical, robust, reasonably accurate, and a practical option for near wall treatments for industrial flow simulations. It takes variation of turbulent kinetic energy in the near wall into account. The nonequilibrium approach is recommended by Fluent [10] for complex flows where mean flow and turbulence change rapidly and depart from local equilibrium.

3.4 Turbulence Modeling.
As no single turbulence model is the best for all classes of problems, Fluent [10] provides choices that include the standard, RNG (renormalization group), and realizable k-ε models, the standard and SST (Shear stress Transport) k-ω models, the Reynolds stress model (RSM), and large eddy simulation (LES) models. The choice of turbulence model depends on the physics of flow, level of accuracy, established practice, available computational resources, etc. Different researchers have reported the use of different turbulence models for studies on plate heat exchangers, e.g., low Reynolds number and LES models [1], k-ω model [6,7], standard k-ε model [5], RNG k-ε model [4,12], etc. The realizable and RNG k-ε models have shown substantial improvements over the standard k-ε model where the flow features include strong streamline curvature, vortices, and rotation. The realizable model, although comparatively new, provides the best performance of all the k-ε model versions as recommended by Fluent [10] for several validations of separated flows and flows with complex secondary flow features.

In this study, initially, the results were obtained with first order discretization scheme for momentum, turbulence, and energy equation. The standard scheme was used for pressure discretization. The RNG k-ε model with standard wall functions for near wall treatment was used in turbulence viscous model. The pressure drop results were underpredicted by about 30% when compared with an empirical pressure drop correlation. The results were slightly improved (23% average underpredicted) when a second order discretization scheme was used for momentum, turbulence, and energy equation, and a PRESTO scheme was used for pressure discretization. By further modifying the near wall treatment to nonequilibrium wall functions, the pressure drop was underpredicted by 15% (average). Finally, the realizable k-ε turbulence model with nonequilibrium wall functions was used. The pressure drop was underpredicted by 10% (average) as discussed later in Sec. 7.

4 Experimentation

An experimental setup to study the heat transfer and pressure drop effects in a plate heat exchanger was developed [13,14] in the Refrigeration and Air-conditioning Laboratory, IIT Delhi (In-
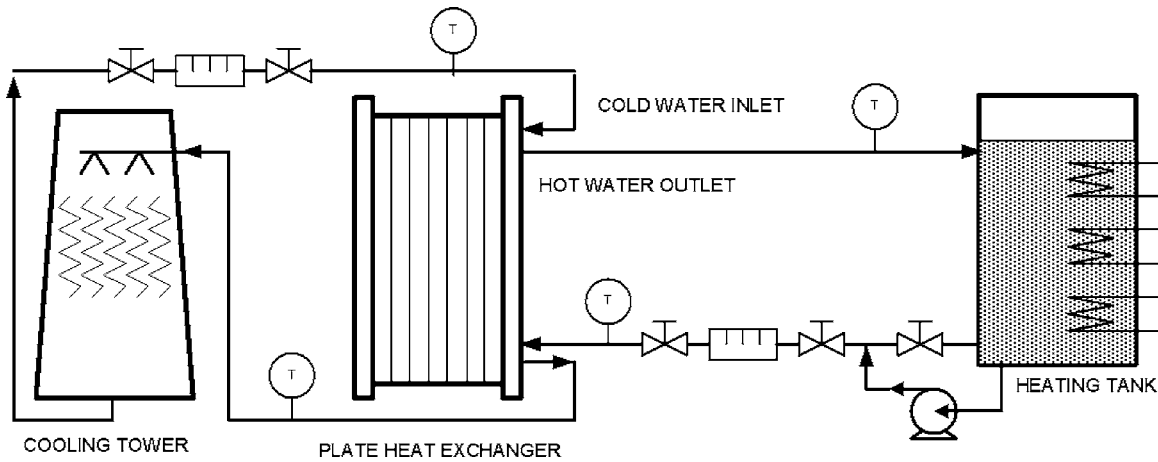
Fig. 3 Schematic diagram of the experimental test facility for PHE

dia). The experimental setup, as shown in Fig. 3, consisted of a commercial one-pass one-pass U-type counterflow plate heat exchanger (PHE). The PHE had 14 small size corrugated chevron stainless steel plates ($L_v=357$ mm, $L_w=100$ mm) with a corrugation angle of 60° with the vertical (flow direction). Different dimensions of the corrugated plate were measured on a coordinate measuring machine. Water was the working fluid on both the cold and hot sides. The hot water flowed through six channels in the upward direction, while cold fluid flowed in the downward direction through seven channels. Water was heated in a tank with four controlled heating elements of 1.5 kW each. The hot water and cold water were pumped respectively from the tank and the cooling tower to the PHE. Experiments were conducted for various heat loads, mass flow rates of water, and number of plates.

4.1 Instrumentation. Rotameters were used for the measurement of volumetric flow rates of both the hot and cold fluids, while differential U-tube mercury manometers were used for the measurement of overall pressure drop across the PHE on the cold and hot side (measurement uncertainty less than 130 Pa). The overall pressure drop includes the pressure drop in piping, ports, and channels. The inlet and outlet temperatures of the hot and cold fluids were measured using three-wire RTDs (measurement uncertainty of 0.1 °C). Based on the resolution of the measuring instruments, the root mean square (rms) uncertainty in Re, effectiveness, and friction factor were estimated to be 8.3%, 3.8%, and 15.8%, respectively. (Details are given in Joshi [14].) The average uncertainty in Nusselt number, based on the experimental correlation (Eq. (20) in Sec. 6.2) is 5.6%.

4.2 Data Analysis. The measured heat transfer and friction factor data obtained at steady state conditions were reduced to nondimensional form. The Reynolds number, Nusselt number, and friction factor were calculated based on the equivalent diameter as the characteristic length as follows:

$$\mathrm{Re} = \frac{U_c \times d_e \times \rho}{\mu} \tag{7}$$

$$\mathrm{Nu} = \frac{h \times d_e}{k} \tag{8}$$

$$f = \frac{\Delta P \times 2 \times d_e \times \rho}{4 \times G^2 \times L_v} \tag{9}$$

where $d_e=2b$ is the equivalent diameter given by twice the chan-

nel gap.

The heat lost by hot water and gained by cold water was calculated from the mass capacities of the fluids and the temperature difference between inlet and outlet.

$$Q = \dot{m} \times C_p \times \Delta T \tag{10}$$

The actual data showed energy balance on the hot and cold fluid sides to be within 7.5% for most of the readings. The difference can be attributed to heat losses to the surroundings and the measurement uncertainty. The overall heat transfer coefficient was calculated from the usual counterflow log mean temperature difference (LMTD) equation.

$$\mathrm{UA} = \frac{Q_c + Q_h}{2 \times \mathrm{LMTD}} \tag{11}$$

A standard Nusselt number correlation for turbulent flow [15,16] with two unknown coefficients was assumed, as given by:

$$\mathrm{Nu} = C \times \mathrm{Re}^a \times \mathrm{Pr}^{0.4} \tag{12}$$

The heat transfer coefficient on the hot side was obtained from the overall heat transfer coefficient by modified Wilson plot technique [17]. Although all data were typically in the turbulent flow regime (Re > 400), the data with constant cold fluid flow rate were used for regression analysis.

$$\frac{1}{\mathrm{UA}} = \frac{1}{C_1 \times \mathrm{Re}^a \times \mathrm{Pr}^{0.4} \times (Ak/d_e)} + C_2 \tag{13}$$

The three unknowns in the equation (a, C_1, and C_2) were evaluated following the nonlinear regression scheme suggested by Khartabil and Christensen [18]. The iterations were carried out numerically in EES Software [19].

5 Flow Maldistribution

The flow of the working fluid in PHEs is generally assumed to be uniformly distributed through each channel. But the farther channels have less fluid going though them as compared to the channels closer to the inlet port. Although according to Shah and Focke [9], this effect becomes significant for a large number of plates (50 or more), an experimental study was taken up to verify its significance for this study. This significance was checked on the basis of flow maldistribution parameter and theoretical nondimensional pressure drop [20,21] (for U arrangement) as follows:

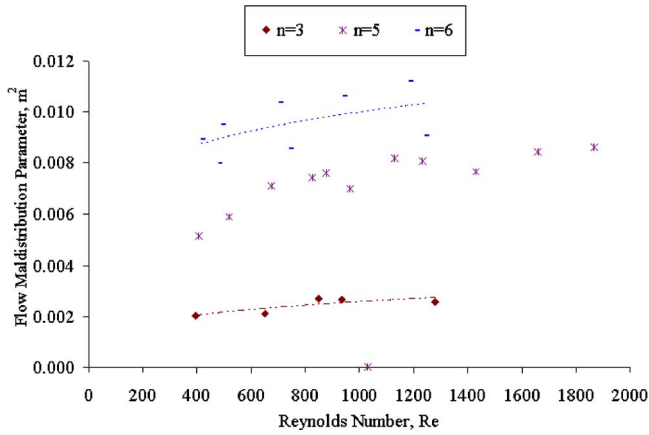$$m^2 = \left(\frac{n \times A_c}{A_p}\right) \times \frac{1}{\xi_c} \tag{14}$$

Fig. 4 Variation of experimental flow maldistribution parameter with Reynolds number

$$p_o - p_o^* = \left(\frac{m^2}{\tanh^2 m} \right) \left(\frac{A_p}{n \times A_c} \right)^2 \times \frac{\xi_c}{2} \qquad (15)$$

and the experimental nondimensional pressure drop is,

$$\Delta p^* = \frac{P - P^*}{\rho \times W_o^2} \qquad (16)$$

where channel friction coefficient, ξ_c, is given by

$$\xi_c = \frac{2 \times \Delta P_{ch}}{\rho \times U_c^2} \qquad (17)$$

The effect of flow maldistribution was studied by varying the total number of plates with the same channel mass flow rate. This means if the total number of plates is reduced to one third, by reducing total mass flow rate to one third, the channel mass flow rate can be kept constant. Various odd-even combinations of hot and cold fluid channels included 1-2, 3-4, 5-5, and 6-7, where the former is the number of channels on the hot side and the latter the number on the cold side.

The variation of the flow maldistribution parameter with Reynolds number for different number of channels is shown in Fig. 4. As the Reynolds number increases, the flow maldistribution parameter also increases. For the same Reynolds number, as the number of channels increases, the flow maldistribution increases, as expected. But, it can be seen that the values are too small (less than 0.01) to be of any significance for the PHE under consideration, indicating good flow distribution. Thus the assumption of no flow maldistribution in this case is justified.

6 Results and Discussion

Experiments were conducted with Reynolds number varying between 400 and 1300. The experiments with almost the same channel Reynolds number were repeated by varying the total number of channels. The total number of plates was varied from 4 to 14. Various odd-even combinations of hot and cold fluid channels included 1-2, 3-4, 5-5, and 6-7, where the former is the number of channels on the hot side and the latter the number on the cold side. The data were reduced to nondimensional numbers—friction factor and Nusselt number.

6.1 Friction Factor. The comparison of experimental and numerical friction factors for various channel Reynolds numbers is shown in Fig. 5. Theoretical friction factors using Kumar's empirical correlation [15] are also included in the figure.

$$f = \frac{k_p}{\mathrm{Re}^m} \qquad (18)$$

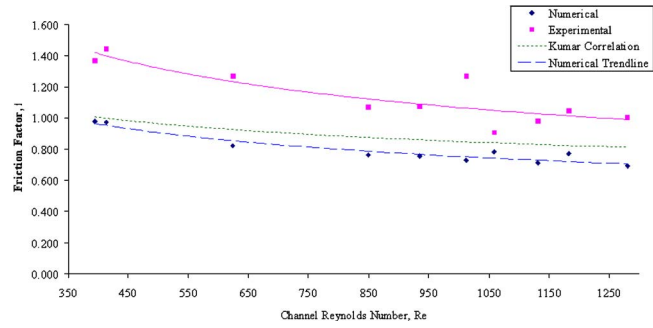where $k_p = 2.99$ and $m = 0.183$ are constants for the range consid-

Fig. 5 Comparison of experimental, numerical, and theoretical friction factors

ered, and Re is based on hydraulic diameter.

The experimental friction factor values are on average 23% higher than the theoretical friction factor with minimum disagreement of 8% and maximum disagreement of 33%. The experimental friction factors are much higher as they also include the pressure drops in the ports and the distribution area. The numerical friction factor is underpredicted by 2.5–14.5% (10% average) compared to the empirical correlation. This compares favorably with the numerical results of Ciofalo et al. [2], where the pressure drop was underpredicted by 20%–25%, and Sunden and Piazza [12], who reported underpredictions between 17% and 40%.

6.2 Nusselt Number. The variation of Nusselt number with Reynolds number is given in Fig. 6. The numerical simulation has been compared with the experimental data and the Hewitt et al. [16] correlation, which is based on data from Cooper and Usher [22] for small sized chevron plates.

$$\mathrm{Nu} = 0.4 \times \mathrm{Re}^{0.64} \times \mathrm{Pr}^{0.4} \qquad (19)$$

The trend-line for numerical results showed the Nusselt number varying with 0.62 power of the Reynolds number, which is comparable with the theoretically predicted dependence of 0.64 power of Reynolds number. The experimental data were reduced to get the following Nusselt number correlation as per the procedure outlined in Sec. 4.2.

$$\mathrm{Nu} = 0.448 \times \mathrm{Re}^{0.626} \times \mathrm{Pr}^{0.4} \qquad (20)$$

The same has also been plotted in Fig. 6 along with the numerical and the empirical correlation results. It is seen that the experimental results are almost overlapping the empirical correlation, but are higher than the numerical values. Numerical simulations underpredicted Nusselt number by 3% to 18% (13% average underprediction) when compared with empirical correlation. The underpredictions by CFD simulations have also been observed by others,
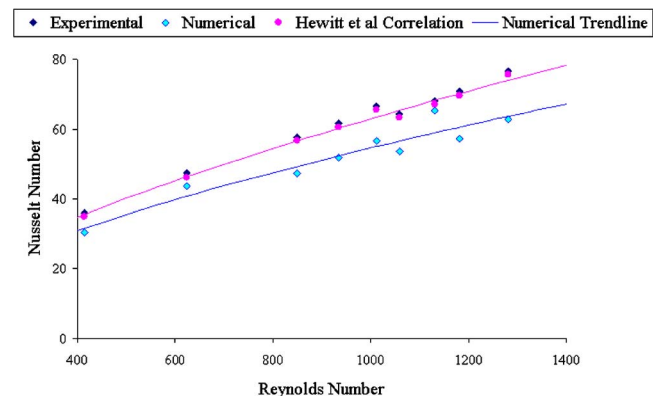

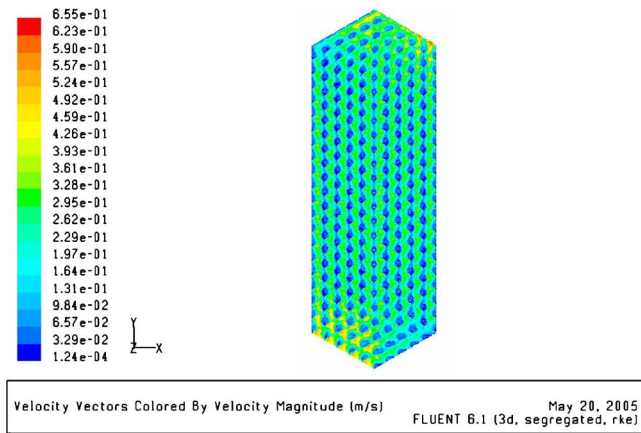**Fig. 6 Variation of Nusselt number with Reynolds number**

Fig. 7 Velocity vectors—at mid-section in hot channel

Fig. 9 Hot spots in cold channel

e.g., up to 25% [1,4,12] and up to 60% [7]. In addition to the selection of appropriate turbulence model, other reasons for underprediction could also be the exclusion of port and flow distribution areas in numerical modeling, but it needs further investigations.

6.3 Temperature and Velocity Distributions. The velocity vectors at the mid-section of the hot channel are shown in Fig. 7. The dark colored vectors are of negligible magnitude, representing the points of contact. Therefore, the dark color vectors are of negligible magnitude, while lighter colored vectors predominantly decide the flow direction. From the figure, it is seen that the velocity vectors describe a zig-zag pattern and fluid flow is mainly aligned along the main flow direction, as also observed by Ciofalo et al. [1] for large included angles. Swirl flow patterns in cross sections normal to furrows were also observed [23].

The contours of static temperature at the mid-section in the cold channel are shown in Fig. 8. The entry of cold fluid was from the top left corner and exit was from the bottom right corner whereas hot fluid was entering from the bottom left corner and leaving from the top right. In any longitudinal plane below mid-plane, the average temperatures on the left are higher than on the right, and above the plane it is vice versa due to entry effects of the hot and cold fluids.

From Fig. 8, hot spots are also seen in the cold channels. It is further discernible in Fig. 9 that the temperature contours are in a plane across the cold channel (as shown in Fig. 8 by the arrow). At the point of contact, as the surface area is less, the temperatures are higher as compared to central regions.

7 Conclusions

Numerical simulations of small sized plate heat exchangers using a new approach are reported in this paper. A realizable k-ε turbulence viscous model with nonequilibrium wall functions was found to give the best results. These were compared with experimentally obtained data and empirical correlations from the literature. It was found that the numerical friction factor was underpredicted by 2.5% to 14.5% compared to Kumar's correlation [15], while the experimental friction factor values are 8% to 33% higher than the correlation. The Nusselt number was underpredicted by 3% to 18% in comparison to the Hewitt et al. correlation [16]. One of the reasons for underprediction could be the exclusion of port and flow distribution areas in numerical modeling, but this needs further investigation. These numerical predictions of

Fig. 8 Contours of static temperature—at mid-section in cold channel

heat transfer and pressure drop with more realistic computational domain and boundary conditions compare favorably well with other approaches used in the literature.

Nomenclature

a = constant, exponent
A = heat transfer area of the plate, m^2
A_p = cross-sectional area of the port, m^2
A_c = cross-sectional area of a channel, m^2
b = mean flow channel gap, m
B_j = body force per unit mass, m/s^2
C, C_1, C_2 = constants
$C_{1\varepsilon}, C_{3\varepsilon}$ = constants in k-ε Eq. (5)
d_e = equivalent diameter of flow passages, m
D_h = hydraulic diameter of flow passages, m
f = Fanning friction factor, dimensionless
G_b = generation of turbulence kinetic energy due to buoyancy
G_k = generation of turbulence kinetic energy due to mean velocity gradients
h = heat transfer coefficient, W/m^{2}K
k = turbulence Energy, m^2/s^2 (Eqs. (4) and (5))
k = thermal conductivity, W/mK
L_w = plate width inside gaskets, m
L_v = vertical port distance, m
LMTD = log mean temperature difference, K
m^2 = Flow maldistribution parameter
n = number of channels for one fluid
N_p = number of flow passages in one pass on one fluid side of PHE
NTU = number of heat transfer units on one side, dimensionless
Nu = Nusselt number, dimensionless
p = pressure, Pa
ΔP = pressure drop in PHE, Pa
Q = heat transfer, W
Pr = Prandtl number, dimensionless
Re = Reynolds number, dimensionless
S_k, S_ε = source terms in Eqs. (4) and (5), respectively
T = temperature, °C, K
u_i, u_j = velocity vectors, m/s
U = overall heat transfer coefficient, W/m^{2}K
U_c = channel velocity, m/s
W_o = velocity at inlet port, m/s
x_i, x_j = length vectors, m
Y_M = dilatation dissipation term

Greek Symbols

ρ = fluid density, kg/m^3
β = chevron angle, deg
ε = dissipation, m^2/s^3 (Eqs. (4) and (5))
μ = fluid dynamic viscosity, Pas
ν = kinematic viscosity, m^2/s
$\sigma_k, \sigma_\varepsilon$ = turbulent Prandtl number for k and ε, respectively, dimensionless
ζ_c = channel frictional coefficient, dimensionless

Subscripts

c = cold
ch = channel
h = hot
i = inlet
o = outlet
t = turbulent

References

[1] Ciofalo, M., Stasiek, J., and Collins, M. W., 1996, "Investigation of Flow and Heat Transfer in Corrugated Passages-II. Numerical Simulations," Int. J. Heat Mass Transfer, **39**, pp. 165–192.

[2] Ciofalo, M., Piazza, I., and Stasiek, J., 2000, "Investigation of Flow and Heat Transfer in Corrugated-Undulated Passages," *Heat and Mass Transfer*, Springer-Verlag, New York, Vol. 36, pp. 449–462.

[3] Mehrabian, M. A., and Poulter, R., 2000, "Hydrodynamics and Thermal Characteristics of Corrugated Channels: Computational Approach," Appl. Math. Model., **24**, pp. 343–364.

[4] Sunden, B., 2004, "Advances in Numerical Modeling of Heat Exchanger Related Fluid Flow and Heat Transfer," Proc. XVII National and VI ISHMT/ASME Heat and Mass Transfer Conference, Kalpakkam, India, Jan. 5–7, pp. 136–146.

[5] Paras, S. V., Kanaris, A. G., Mouza, A. A., and Karabelas, A. J., 2002, "CFD Code Application to Flow Through Narrow Channels With Corrugated Walls," CHISA 2002, 15th International Congress of Chemical and Process Engineering. Prague, August.

[6] Kanaris, A. G., Mouza, A. A., and Paras, S. V., 2005, "Flow And Heat Transfer in Narrow Channels With Corrugated Walls—A CFD Code Application," Chem. Eng. Res. Des., **83**(A5), pp. 460–468.

[7] Pelletier, O., Stromer, F., and Carlson, A., 2005, "CFD Simulation of Heat Transfer in Compact Brazed Plate Heat Exchangers," ASHRAE Trans., **111**, pp. 846–854.

[8] Grijspeerdt, K., Hazarika, B., and Ucinic, D., 2003, "Application Of Computational Fluid Dynamics To Model The Hydrodynamics Of Plate Heat Exchangers For Milk Processing," J. Food. Eng., **57**, pp. 237–242.

[9] Shah, R. K., and Focke, W. W., 1988, "Plate Heat Exchangers and Their Design Theory," *Heat Exchanger Equipment Design*, R. K. Shah, E. C. Subbarao, R. A. Mashelkar (Eds.), Hemisphere, Washington, pp. 227–254.

[10] Fluent, 2003, FLUENT 6.1 User's Manual.

[11] Focke, W. W., Zachariades, J., and Olivier, I., 1985, "The Effect of Corrugation Inclination Angle on the Thermo-Hydraulic Performance of Plate Heat Exchangers," Int. J. Heat Mass Transfer, **28**(8), pp. 1469–1479.

[12] Sunden, B., and Piazza, I. D., 1998, "Numerical Analysis of Fluid Flow and Heat Transfer in Plate and Frame Heat Exchangers," HTD (Am. Soc. Mech. Eng.), **361**(3), pp. 287–293.

[13] Bhaduriya, R. M. S., 2002, "Simulation and Performance Study of Plate Heat Exchangers," M.Tech. thesis, Mechanical Engineering Department, IIT Delhi, India.

[14] Joshi, A. A., 2005, "Numerical and Experimental Study of Plate Heat Exchangers," M.Tech. thesis, Mechanical Engineering Department, IIT Delhi, India.

[15] Kakac, S., and Liu, H., 2002, *Heat Exchangers: Selection, Rating and Thermal Design*, CRC, Washington, DC, Chap. 10.

[16] Hewitt, G. F., Shires, G. L., and Bott, T. R., 1994, *Process Heat Transfer*, CRC, Boca Raton, FL, Chap. 8.

[17] Shah, R. K., 1990, "Assessment of Modified Wilson Plot Techniques for Obtaining Heat Exchanger Design Data," Heat Transfer 1990, Proceedings of the 9th International Heat Transfer Conference, Jerusalem, Israel, Vol. 5, pp. 51–56.

[18] Khartabil, H. F., and Christensen, R. N., 1992, "An Improved Scheme for Determining Heat Transfer Correlations From Heat Exchanger Regression Models With Three Unknowns," Exp. Therm. Fluid Sci., **5**, pp. 808–819.

[19] EES, Engineering Equation Solver, F-Chart Software, www.fchart.com/ees.shtml.

[20] Rao, B. P., and Das, S. K., 2004, "An Experimental Study on the Influence of Flow Maldistribution on the Pressure Drop Across a Plate Heat Exchanger," ASME J. Fluids Eng., **126**, pp. 680–691.

[21] Rao, B. P., Sunden, B., and Das, S. K., 2005, "An Experimental and Theoretical Investigation of the Influence of Flow Maldistribution on the Thermal Performance of Plate Heat Exchangers," Trans. ASME, Ser. C: J. Heat Transfer, **127**, pp. 332–343.

[22] Cooper, A., and Usher, J. D., 1990, "Friction Factor Correlations," *Hemisphere Handbook of Heat Exchanger Design*, G. F. Hewitt (Co. Ed.), Hemisphere, Washington DC, **3.7.4**.

[23] Ciofalo, M., Collins, M. W., and Stasiek, J., 1998, "Flow and Heat Transfer Predictions in Flow Passages of Air Preheaters: Assessment of Alternative Modeling Approaches," *Computer Simulations in Compact Heat Exchangers*, B. Sunden and M. Faghri (Eds.), Computational Mechanics Publications, Southampton, UK, Vol. 1, pp. 169–225.

Thermal Conductivity of Metal-Oxide Nanofluids: Particle Size Dependence and Effect of Laser Irradiation

Sang Hyun Kim

Sun Rock Choi

Dongsik Kim[1]
e-mail: dskim87@postech.ac.kr

Department of Mechanical Engineering,
POSTECH,
Pohang, 790-784 Korea

The thermal conductivity of water- and ethylene glycol-based nanofluids containing alumina, zinc-oxide, and titanium-dioxide nanoparticles is measured using the transient hot-wire method. Measurements are performed by varying the particle size and volume fraction, providing a set of consistent experimental data over a wide range of colloidal conditions. Emphasis is placed on the effect of the suspended particle size on the effective thermal conductivity. Also, the effect of laser-pulse irradiation, i.e., the particle size change by laser ablation, is examined for ZnO *nanofluids. The results show that the thermal-conductivity enhancement ratio relative to the base fluid increases linearly with decreasing the particle size but no existing empirical or theoretical correlation can explain the behavior. It is also demonstrated that high-power laser irradiation can lead to substantial enhancement in the effective thermal conductivity although only a small fraction of the particles are fragmented.* [DOI: 10.1115/1.2427071]

Keywords: nanofluid, thermal conductivity, particle size, laser ablation

1 Introduction

It has long been recognized since Maxwell first suggested his mixture theory [1] that suspending solid particles in liquids would substantially increase the effective thermal conductivity. Numerous investigations have been carried out concerning development of high thermal conductivity working fluids, as well as to understand the physical mechanisms of enhanced heat transfer by solid particles [2–11]. Particularly, recent advances in nanotechnology that enabled synthesis of nanoparticles in the size range under 100 nm accelerated the research on high-conductivity nanofluids. Effective thermal conductivities of various nanofluids were measured, most often as a function of particle concentration [2–8]. Some of the previous investigations reported considerably large enhancement of the thermal conductivity by addition of a small amount of solid suspensions. Lee et al. demonstrated that the thermal conductivity of metal oxide nanofluids is significantly higher than that of the base fluids [3]. More strikingly, Choi et al. [4] and Eastman et al. [5] reported anomalously increased thermal conductivities of the nanofluids containing carbon nanotubes and copper nanoparticles, respectively. However, those studies also indicated that no conventional mixing model can successfully explain the anomaly of the effective thermal conductivity. Furthermore, analysis of the measured thermal conductivity data reveals that the conventional mixing models, such as the Hamilton–Crosser model [12], have only a limited range of validity and fails to explain several important characteristics of the effective thermal conductivity. For example, the model does not consider the size of the suspended particles while experimental results indicate that the effective thermal conductivity increases significantly as the size is reduced.

Recently, several novel models for the effective thermal conductivity have been suggested. Theoretical models considering the interface effect were suggested to extend the Maxwell's mixing rule and the Hamilton–Crosser model [9,11]. Though the predic-

tion of those newly proposed models shows relatively good agreement with some of the measured data, they are not capable of predicting the nonlinear behavior of the effective thermal conductivity. Jang and Choi later proposed a new model based on the Brownian motion of the suspended particles [9] and demonstrate that the model can predict the size and temperature dependence of the effective thermal conductivity as well as the concentration dependence, unlike the conventional models. The work by Jang and Choi indeed provides good insights into the effective thermal conductivity of liquids containing solid suspensions. However, it is evident that additional studies should be performed to fully understand the physics underlying the enhanced heat conduction by nanoparticles. In particular, it should be pointed out that only a limited number of experimental data were used to confirm the model prediction of the size dependence of the nanofluid thermal conductivity in Ref. [9], as also noted by the authors. For instance, only one or two data points were used to determine the empirical proportionality parameter included in the model, which is obviously not enough to confirm the validity of the suggested model. It is also noted that the measured thermal conductivity data by the transient hot-wire technique, unlike the measurement of common liquids, show relatively large scatterings for nanofluids. This enlarged uncertainty is believed to be primarily due to the variation of the sample preparation process, i.e., particle size dispersion, stability, nonuniformity of the particle shape, etc., considering that the measurement technique generally produces reliable data. Accordingly, the need for further investigation is even more critical and one of the main objectives of the present work is to produce a consistent set of experimental data for a relatively wide range experimental parameters including the mean particle size. Lack of reliable experimental data is certainly one of the main reasons no universal theoretical or empirical model for the nanofluid thermal conductivity is yet available.

Since the size of the suspended particles in a nanofluid critically affects the effective thermal conductivity, particle fragmentation processes that can reduce the particle size can be employed to enhance the thermal conductivity of nanofluids. Among such processes, the laser ablation-based processes offer efficient means to

Table 1 Nanoparticle samples

	Al_2O_3	ZnO	TiO_2
Nominal mean particle diameter	38 nm[b]	10 nm[a] 30 nm[d] 60 nm[b]	10 nm[a] 34 nm[b] 70 nm[c]
Nominal density	3.6 g/cm^3	5.6 g/cm^3	3.95–4.2 g/cm^3
Morphology	Spherical	Elongated	Nearly spherical

[a]Meliorum Technology.
[b]Nanophase Technology Corporation.
[c]TAL materials, Inc.
[d]Advanced materials, Inc.

decrease the particle size. It has been known that high-power laser pulse irradiation onto liquid suspensions can result in substantial size reduction of the constituent nanoparticles [13–16]. According to the previous studies, the laser ablation process is not only a convenient way of changing the particle size but also an effective way to modify the shape and size distribution. Therefore, the laser fragmentation is expected to alter the thermal transport properties of a nanofluid significantly. Consequently, this work analyzes, for the first time to our knowledge, the behavior of thermal conductivity of nanofluids under UV pulsed laser irradiation.

In this work, the effective thermal conductivity of metal-oxide nanofluids is measured by the anodized transient hot-wire method. Water and ethylene glycol (EG)-based nanofluids containing alumina, zinc-oxide and titanium-dioxide particles are examined by varying the concentration up to 3% by volume. Emphasis is especially placed on the size effect. It is evident that reduction of the particle size strongly affects the nanoscale heat transfer mechanisms as it changes the motion of nanoparticles and possibly the atomic structures of the particle as well. The mean particle size is varied from 10 to 70 nm for ZnO and TiO_2 nanofluids. Since the thermal conductivity of Al_2O_3 nanofluid is relatively well known from previous studies [3], measurements are carried out for alumina nanofluids to compare the results with those from previous investigations. Finally, the effect of high-power laser treatment of ZnO/water nanofluid samples on the thermal conductivity is investigated. The results of the laser fragmentation process are analyzed by transmission electron microscope (TEM) and UV-visible absorption spectrum analyses.

2 Experiment

2.1 Nanofluid Preparation. Commercially available alumina (Al_2O_3), zinc-oxide (ZnO), and titanium-dioxide (TiO_2) nanoparticles were mixed with the base fluids (water and EG) to synthesize nanofluids by the two-step method. The manufactures and the specifications of the particles are listed in Table 1. Figure 1 displays the typical TEM images of the particles. As shown in Fig. 1, the shape of the ZnO particles is not spherical and therefore the mean diameter in Table 1 simply represents an effective value provided by the manufacturer. In the synthesis of the nanofluids, the suspension was sonicated in an ultrasonic bath for 1 h and then agitated for 10 h by a magnetic stirrer to prevent particle agglomeration and make the nanofluid homogeneous. Solium dodecyl sulfate (SDS) of 0.05 M was added as a surfactant in all cases. The surfactant concentration was chosen to be well above the critical micelle concentration 0.01 M. Addition of the surfactant obviously affect the thermal conductivity of the nanofluid and thus introduces ambiguities in the analysis. Nevertheless, it was unavoidable since the thermal conductivity decreased rapidly as the particle sedimentation takes place without the surfactant. With the surfactant, no change in the thermal conductivity was detected at least for the initial 5 h after synthesis of the nanofluid. The only exception is the 10 nm ZnO/EG nanofluid. In this case, no trial to stabilize the fluid was successful, including addition of different surfactants (sodium dodecyl sulfate, cetyltrim ethylammonium, octylphenoxy polyethoxy ethanol bromide) and variation of the pH level. Since 30 and 60 nm ZnO/EG nanofluids are stable, the instability of the 10 nm nanofluid must be related with increased surface area of the ZnO particles. Even for the stable nanofluids, there is a possibility that agglomeration and sedimentation of the particles decrease the thermal property over a long period of time. However, because the effect of this long-term stability is another issue of extensive investigation, it has not been analyzed in the present work. The thermal conductivity was always measured within several minutes after the end of the sample preparation process to ensure consistency of the measurement.

2.2 Thermal-Conductivity Measurement. The transient hot-wire method with an anodized tantalum wire has been employed to measure the thermal conductivity. Principles and details of the measurement technique can be found elsewhere [17–19]. In the present study, a tantalum wire of 25 μm in diameter and 54.0 mm in length was anodized for electrical insulation. A bare tantalum wire was electrically heated at an electrical potential of 50 V in a 0.01 wt% citric-acid solution to form an oxide layer on the surface [20]. Figure 2 shows the experimental setup for the measurement, where R_1 and R_2 represent 568.1 and 10 Ω standard resistors, respectively. The symbols R_p and R_v denote the hot wire and a variable resistor to balance the Wheatstone bridge circuit, respectively. The hot wire has been calibrated in a constant temperature bath and the measured resistance R can be expressed as a function of temperature T (in K) by

(a) Al_2O_3 (b) ZnO   (c) TiO_2
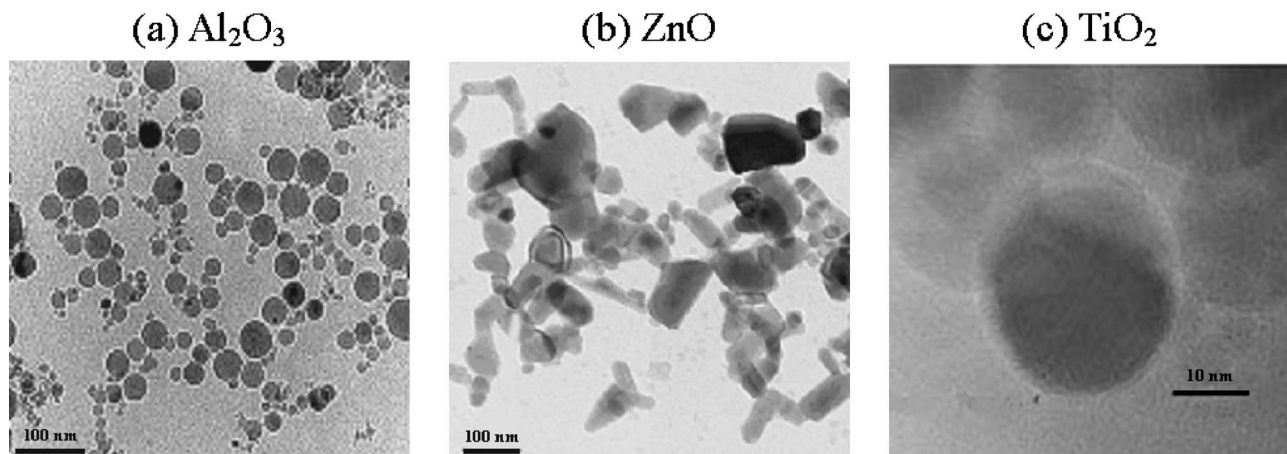
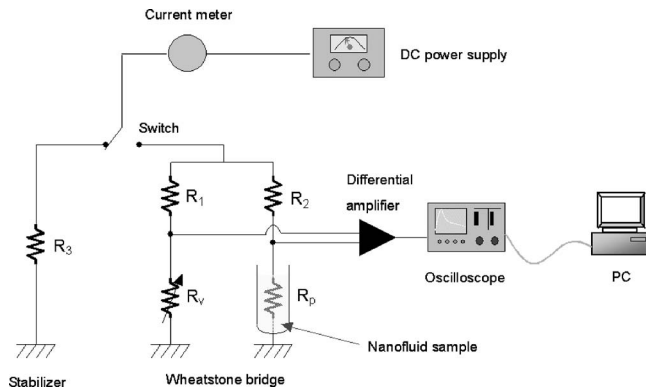**Fig. 1 Typical TEM images of nanoparticles**

Fig. 2 Schematic diagram of the experimental setup for thermal conductivity measurement

$$R = R_0[1 + \beta_1(T - 273.15) + \beta_2(T - 273.15)^2] \qquad (1)$$

where R_0 represents the resistance at $0\,^\circ\mathrm{C}$. The measured temperature coefficients of resistance β_1 and β_2 are 3.9092×10^{-3} and $-5.917 \times 10^{-7}\,\mathrm{K}^{-1}$, respectively. The electrical current was adjusted to cause about 2 K temperature rise for 1 s. The voltage signal from the Wheatstone bridge circuit is amplified by approximately 1000 times and a digital oscilloscope reads the signal at a rate of 2.5 kHz.

To confirm the experimental setup, the thermal conductivities of toluene, water, and ethylene glycol were measured as standard liquids. The results show that the measured thermal conductivities are 0.131, 0.607, and 0.252 W/m K at $20\,^\circ\mathrm{C}$ for toluene, deionized water, and ethylene glycol, respectively, exhibiting deviations from the literature values by 0.3%, 0.8%, and 0.1% [21]. Measurements were repeated ten times for a sample and the results were averaged to eliminate the electrical noise. Error analysis indicates that the standard deviation of the measurement is 0.3% based on total 30 measurements for the three standard liquids, with a maximum peak-to-peak fluctuation of 1.0%. These results demonstrate that the experimental setup used in the present study can produce a reliable thermal-conductivity data.
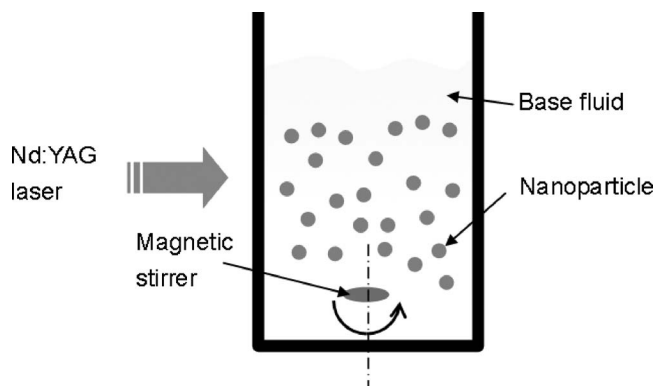
2.3 Laser Fragmentation Process. The laser fragmentation process is depicted in Fig. 3. A Q-switched Nd: yttrium-aluminum-garnet laser ($\lambda = 355$ nm, full width at half maximum 6 ns) was employed to ablate the particles suspended in the nanofluid. The quartz cuvette in Fig. 3 initially contains 60 nm ZnO particles at a volume concentration of 1%. Zinc oxide has been selected to analyze the effect of laser irradiation as it has a strong absorption peak in the UV spectral regime. The laser pulses having a fit-to-Gaussian spatial distribution of intensity and a spot size of 5 mm were incident on the liquid at a frequency of 10 Hz. The nanofluid was irradiated for 1 h, i.e., 36,000 pulses, at three different laser fluences 310, 460, and 610 mJ/cm^2. Though the degree of fragmentation is affected by the pulse number, the effect has been systematically analyzed in this work. To monitor the variation of the particle size in the nanofluid solution, the TEM images and the absorption spectrum were analyzed before and after the fragmentation process. The absorbance spectrum was measured by a UV-visible spectrometer (wavelength $\lambda = 250 - 800$ nm). Absorption spectrum generated by a colloidal solution is a complicated function which depends on various parameters including the wavelength, the relative index of refraction, and the size and shape of the particles. However, the average size of the particle can be correlated with the peak wavelength in the absorption spectrum. In general, the peak wavelength increases in proportion to the mean diameter of the suspended particles. Accordingly, to calibrate the absorbance data as a function of the mean diameter, the absorbance spectrum of the untreated ZnO nanofluids was measured for three different mean diameters 10, 30, and 60 nm. The typical TEM images of the ZnO nanoparticles and the results of the corresponding absorption spectrum measurements are displayed in Figs. 4 and 5. Figures 4 and 5 confirm that the absorption spectrum can certainly be used to monitor any "significant" variations in the mean particle size although it is not sensitive enough to elucidate the details of the size distribution.
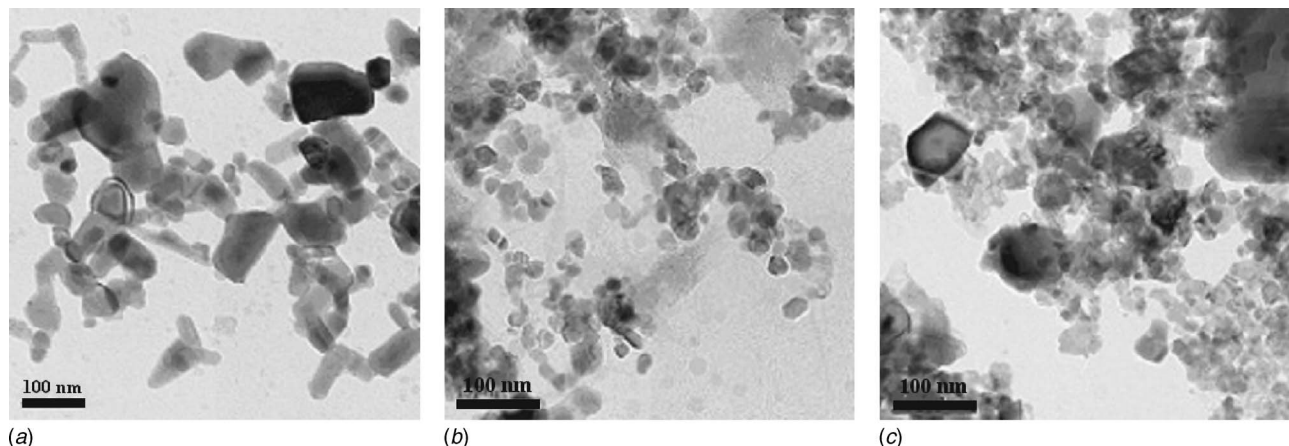

Fig. 3 Schematic diagram of the laser fragmentation process for nanofluid size reduction

Fig. 4 TEM images of ZnO/water nanofluids for average particle sizes of (a) 60, (b) 30, and (c) 10 nm
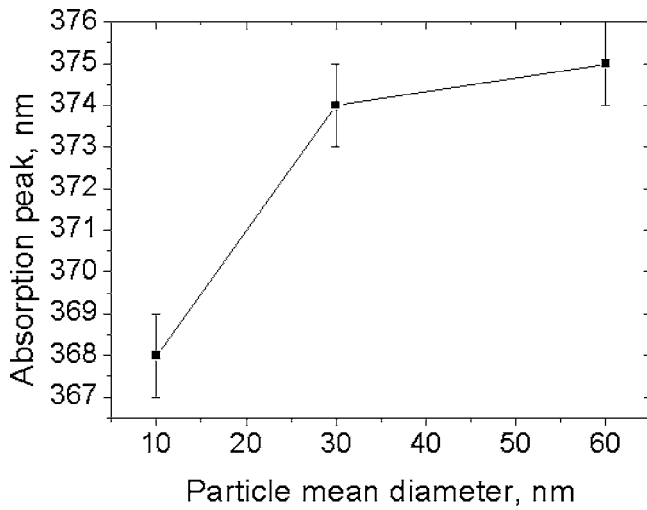
Fig. 5 Absorbance peak as a function of particle mean diameter

3 Results and Discussion

3.1 Thermal Conductivity of Nanofluids and Particle Size Dependence. The results of thermal-conductivity measurement for 38 nm-sized alumina nanofluids are summarized in Table 2 and Fig. 6. The lines in Fig. 6 are the results of linear curve fitting. These results show that the thermal conductivity of the nanofluids is linearly proportional to the particle concentration in the range of the measurement. Comparison of the measured data with those by Lee et al. [3] indicates that the two independently measured results are in good agreement. It is evident that this good agreement is owing to the fact that the nanoparticles used in both studies are from the same type of manufacturing process.

Tables 3 and 4 summarize the effective thermal conductivity of zinc-oxide and titanium-dioxide nanofluids, respectively. The thermal conductivity of the 10 nm ZnO/EG nanofluid was not measured as the colloidal stability was not good enough to quantify the property of the nanofluid, regardless of the surfactant addition and pH-level variation. The reason for this instability is unclear at this moment and requires further investigations. However, since

Table 2 Thermal conductivity of Al$_2$O$_3$/water and Al$_2$O$_3$/EG nanofluids compared with the previous research

	Volume fraction (%)	Thermal conductivity (W/m K)			
		Distilled water		Ethylene glycol	
		Present experiment	Lee et al.[a]	Present experiment	Lee et al.[a]
Al$_2$O$_3$ Nanofluids (38 nm)	0.3	0.613	-	-	-
	0.5	0.615	-	-	-
	0.8	0.618	-	-	-
	1	-	0.622	0.259	0.260
	1.5	0.630	-	-	-
	2	0.639	0.637	0.270	0.267
	3	0.656	0.653	0.279	0.277

[a]See Ref. [3].
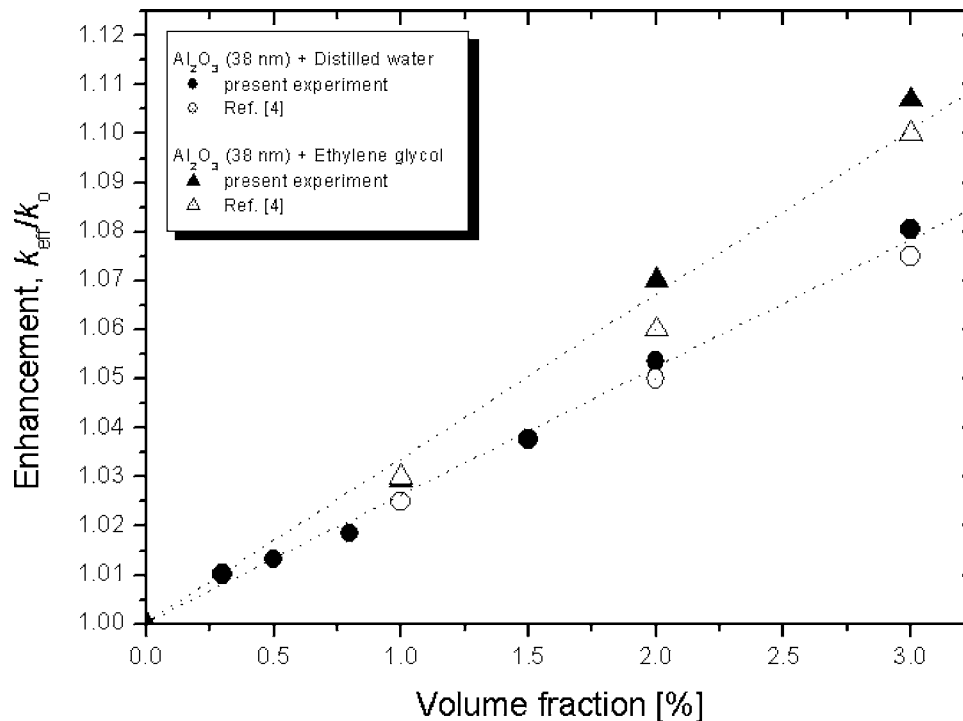
Fig. 6 Thermal-conductivity enhancement by Al$_2$O$_3$/water and by Al$_2$O$_3$/EG nanofluids as a function of volume fraction

Table 3 Thermal conductivity and thermal-conductivity ratio of ZnO/water and ZnO/EG nanofluids

	Average particle size (nm)	Volume fraction (%)	Distilled water		Ethylene glycol	
			Thermal conductivity (W/m K)	Thermal conductivity ratio	Thermal conductivity (W/m K)	Thermal conductivity ratio
ZnO nanofluids	10	1	0.637	1.049	-	-
		2	0.665	1.096	-	-
		3	0.693	1.142	-	-
	30	1	0.627	1.033	0.267	1.060
		2	0.650	1.071	0.284	1.127
		3	0.677	1.115	0.305	1.210
	60	1	0.618	1.018	0.260	1.032
		2	0.637	1.049	0.270	1.071
		3	0.651	1.073	0.279	1.107

analysis of the colloidal stability is beyond the scope of the present work, no attempt has been made to reveal the underlying physics. Tables 3 and 4 show that thermal-conductivity enhancement of approximately 20% and 15% relative to the base fluid is obtained at a volume concentration of 3% by ZnO and TiO$_2$ nanoparticles, respectively. The thermal-conductivity ratio, i.e., the thermal conductivity normalized by that of the base fluid, is displayed in Figs. 7 and 8. In the figures, the thermal conductivity is linearly proportional to the volume fraction. In both cases of ZnO and TiO$_2$ nanofluids, the maximum enhancement is observed when the smallest (10 nm-sized) particles are suspended in EG. The observation that EG gives larger enhancement than water as a base fluid is also found in Al$_2$O$_3$ nanofluids. Examination of Tables 3 and 4 and Figs. 7 and 8 discloses that the thermal conductivity of ZnO nanofluids is generally greater than that of TiO$_2$ nanofluids. Notable is that this particle dependence cannot be explained by the high thermal conductivity of ZnO (29 W/m K at 319.2 K [22]) relative to that of TiO$_2$ (8.37 W/m K at 298.2 K [22]). Comparison of the thermal conductivity of Al$_2$O$_3$ nanofluids with that of TiO$_2$ nanofluids gives an opposite trend. Though the thermal conductivity of Al$_2$O$_3$ (25.1 W/m K at 299.2 K [22]) is higher than that of TiO$_2$, the alumina nanofluid has a lower effective thermal conductivity. For example, according to Tables 2 and 4, the thermal conductivity of alumina/EG (38 nm) is 0.259 W/m K at 1% volume fraction while that of TiO$_2$/EG nanofluid is 0.259–0.262 for 34–70 nm in the mean diameter at the same concentration. These observations clearly indicate that the heat transfer enhancement by nanofluid cannot be explained by increased heat conduction inside the solid particles

only. The lines in Figs. 7 and 8 are the theoretical predictions by the Hamilton–Crosser model [12]

$$\frac{k_{\text{eff}}}{k_{\text{BF}}} = \frac{\xi + (n-1) - (n-1)(1-\xi)\phi}{\xi + (n-1) + (1-\xi)\phi} \tag{2}$$

where the empirical shape factor n is 3 and 6 for cylinder and sphere, respectively. It is apparent that the model is intrinsically incapable of representing the particle size dependence of the nanofluid. Considering that the TiO$_2$ particles are spherical as displayed in Fig. 1(c), Fig. 8 reveals that the Hamilton–Crosser model underestimates the thermal conductivity of TiO$_2$ nanofluids, particularly for those containing small-sized particles. Since the shape of the ZnO nanoparticle is irregular as depicted in Fig. 1(b), the prediction by the Hamilton–Crosser model cannot be directly compared with the experimental results. However, Fig. 7 indicates that the measured thermal conductivity is not remarkably different from the predictions of the conventional mixing rule.
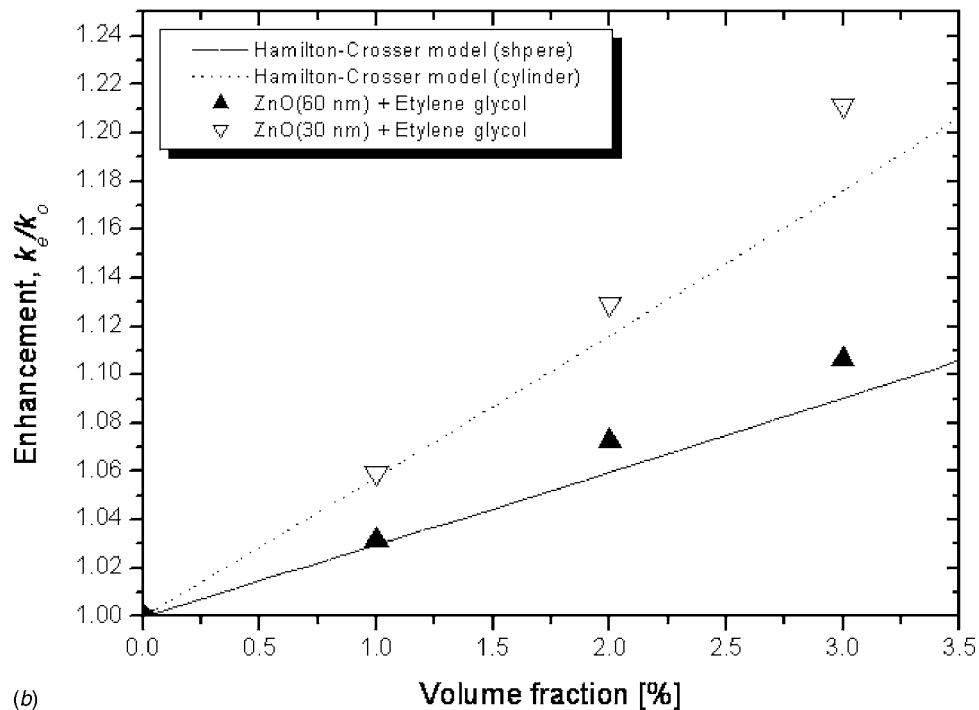
The results of thermal-conductivity measurement exhibit that the thermal conductivity of a nanofluid is strongly dependent on the size of the suspended particles and justifies the need for more advanced models for nanofluid thermal conductivity. Figures 9 and 10 depict the size dependence. In Figs. 9 and 10, solid lines are the results of linear curve fitting while the dashed lines are the predictions of a recently suggested theoretical model [9]. The theoretical model is based on the assumption that heat transfer enhancement by a nanofluid can be attributed to the Brownian motion of the particles

Table 4 Thermal conductivity and thermal-conductivity ratio of TiO$_2$/water and TiO$_2$/EG nanofluids

|	Average particle size (nm)	Volume fraction (%)	Distilled water		Ethylene glycol	
			Thermal conductivity (W/m K)	Thermal conductivity ratio	Thermal conductivity (W/m K)	Thermal conductivity ratio
TiO$_2$ nanofluids	10	1	0.627	1.033	0.266	1.051
		2	0.654	1.077	0.278	1.099
		3	0.676	1.114	0.292	1.154
	34	1	0.624	1.028	0.262	1.036
		2	0.645	1.063	0.273	1.079
		3	0.660	1.087	0.284	1.123
	70	1	0.619	1.020	0.259	1.024
		2	0.633	1.043	0.266	1.051
		3	0.646	1.064	0.272	1.075
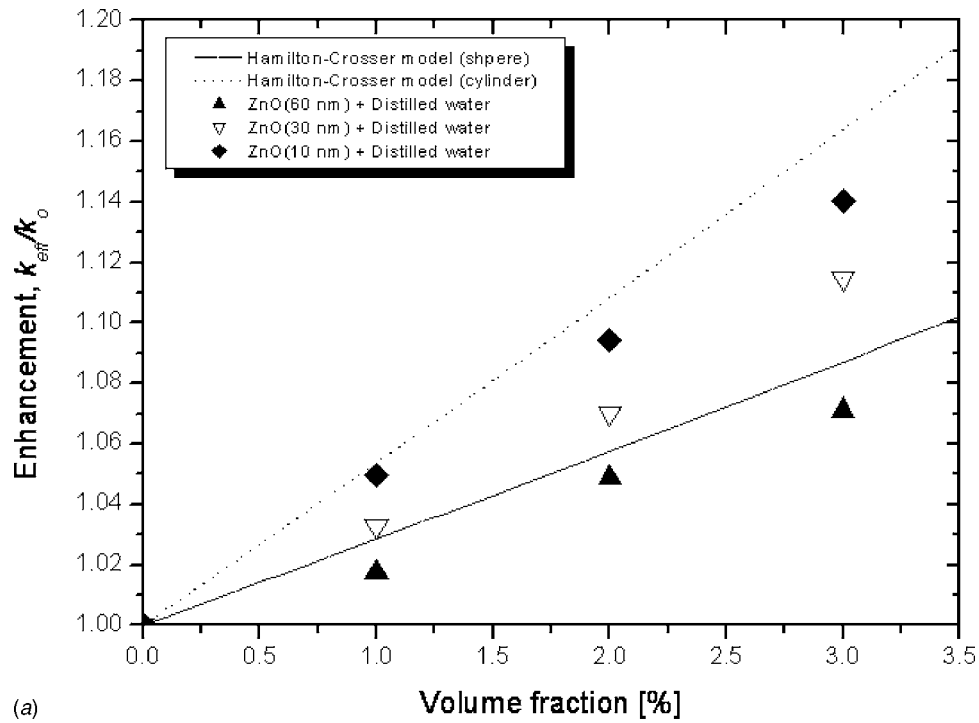
Fig. 7 Thermal-conductivity ratio: (*a*) ZnO/water and (*b*) ZnO/EG nanofluids

$$k_{eff} = k_{BF}(1 - \phi) + k_{particle}\phi + 3C_1 \frac{d_{BF}}{d_{particle}} k_{BF} \mathrm{Re}^2_{d_{particle}} \mathrm{Pr}\, \phi \quad (3)$$

where $\mathrm{Re}_{d_{particle}}$ and Pr are the Reynolds number characterizing the flow around the particle and the Prandtl number of the base fluid. In Eq. (3), C_1 is an empirical parameter determined by fitting the equation to the experimental data. Figures 9 and 10 evince that the measured size dependence is close to a linear relation while the model suggests relatively strong size dependence at small diameters. In Fig. 9(*b*), Eq. (3) appears well correlated with the experimental results, which is, however, because the correlation is fitted

to only two data points. Several factors, such as the irregularity of the particle shape/diameter and the instability of the nanofluid (role of the surfactant), might contribute to this discrepancy. It is noted again that no thermal conductivity degradation has been observed for the initial 5 h with addition of SDS but no long-term stability analysis has been executed in the present work. Also, other physical mechanisms might have induced the difference between measured and predicted thermal conductivities. However, the measured size dependence suggests an approximately linear correlation for "practically available" nanofluids, showing significant deviation from the prediction by Eq. (3). No existing corre-
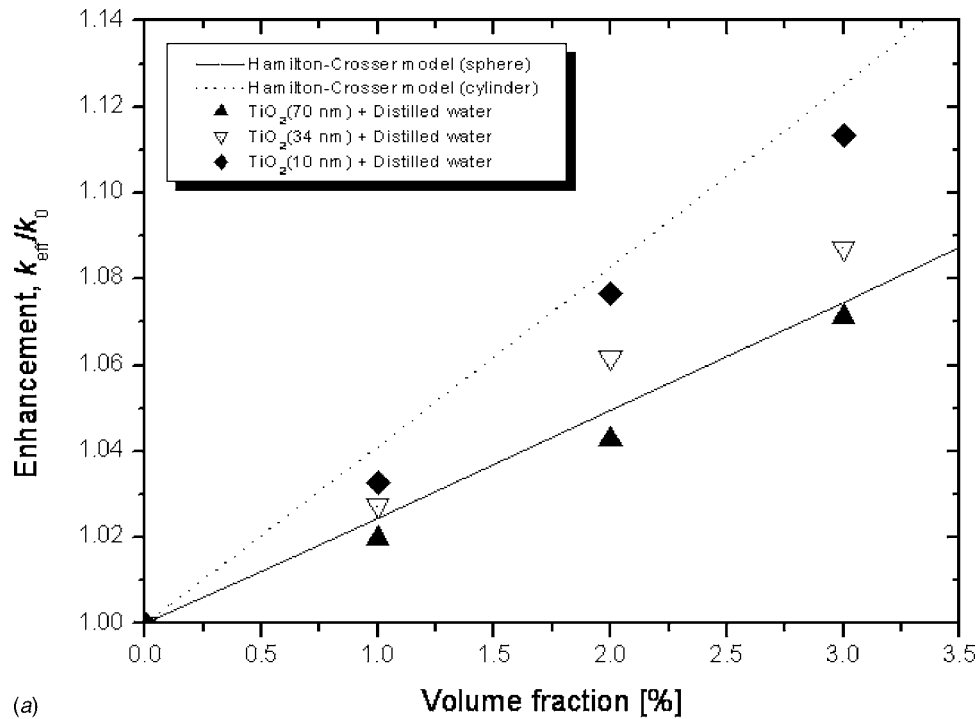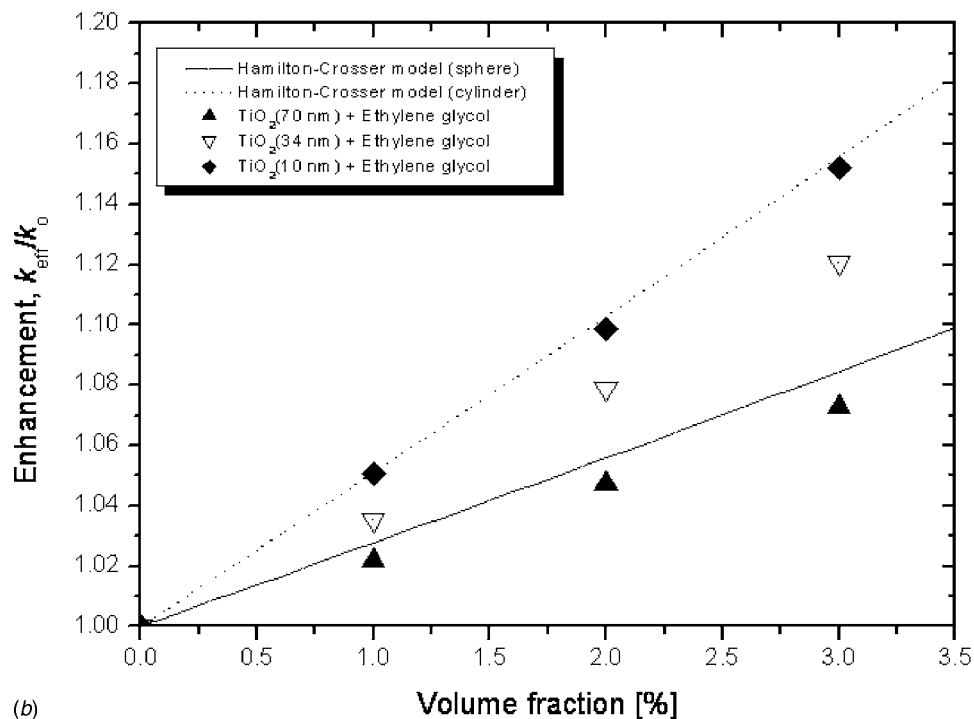
Fig. 8 Thermal-conductivity ratio: (a) TiO_2/water and (b) TiO_2/EG nanofluids

lation can explain this linear size dependence of the thermal conductivity.

3.2 Effect of Laser Irradiation on Nanofluid Thermal Conductivity. The apparent ablation threshold for ZnO particles in water was measured by monitoring the absorption spectrum and extinction coefficient change after approximately 1000 pulses. If the laser fluence incident on the glass cuvette is less than 300 ± 30 mJ/cm^2 (58 mJ/pulse), no significant change was observed in the absorbance spectrum and the extinction coefficient. Correspondingly, the nanofluid composed of 60 nm sized particles

was tested by the UV laser pulses at three different pulse energies 60, 90, and 120 mJ/pulse. The thermal conductivity of the laser-treated nanofluids was measured after 36,000 pulses, resulting in the measured values of 0.618, 0.624, and 0.626 W/m K at laser fluences 310, 460, and 610 mJ/cm^2, respectively. Compared to the thermal conductivity of the untreated 60 nm ZnO nanofluid 0.618 W/m K, it is clear that laser irradiation at a fluence above the ablation threshold increases the thermal conductivity by changing the size of the suspended particles. The thermal conductivity of the 60 nm-sized nanofluid processed at 610 mJ/cm^2 is
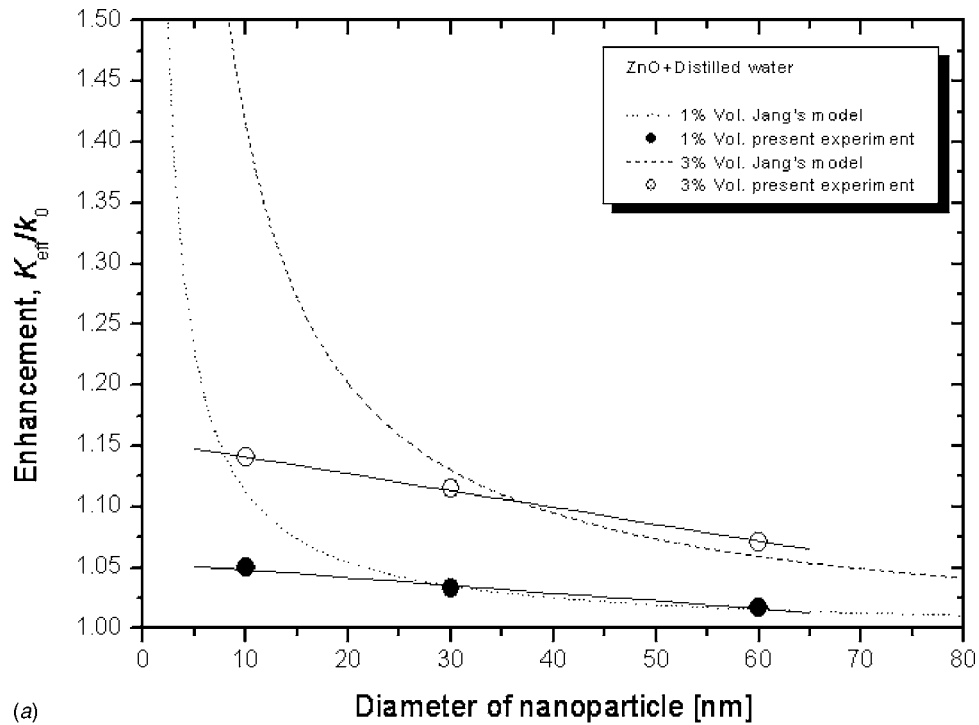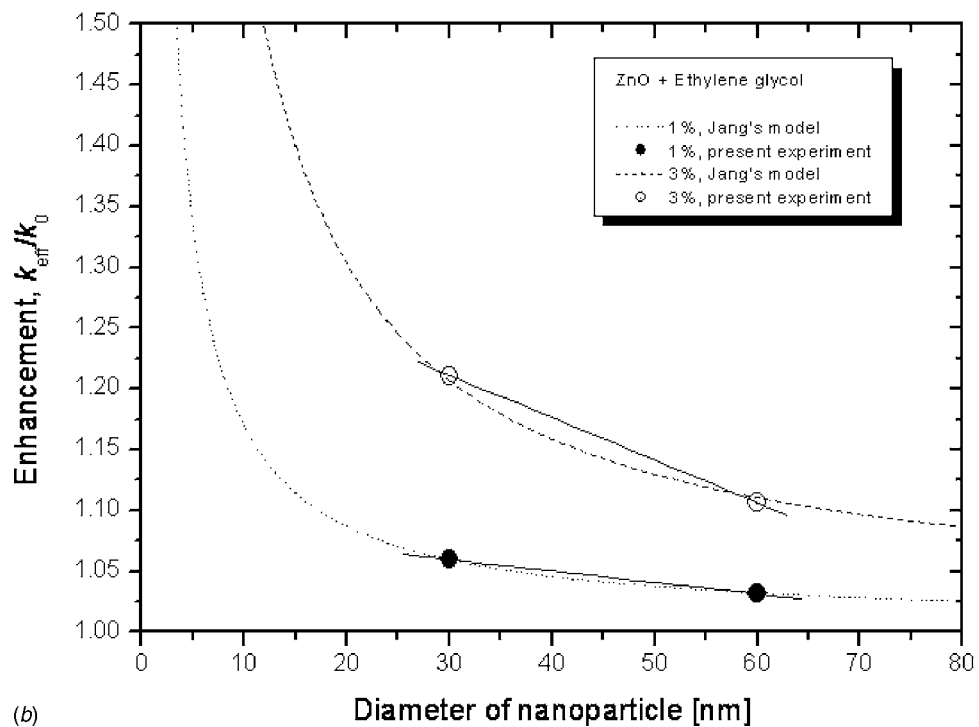
Fig. 9 Variation of thermal-conductivity ratio with particle diameter: (*a*) ZnO/water and (*b*) ZnO/EG nanofluids (comparison with a theoretical model (see Ref. [9])

close to that of the 30 nm-sized unprocessed nanofluid as depicted in Fig. 11. Notable is that the incident laser fluence is above the ablation threshold but not high enough to cause complete fragmentation of the suspended particles. At the tested laser fluence level, most of the particles are only partially ablated with a relatively low fragmentation efficiency. Our previous investigation on laser fragmentation of small particles indicated that the ablation threshold is substantially lower than that required for the same material in the bulk form but the particles are only partially frag-

mented unless the laser fluence is substantially higher than the threshold value [23]. The TEM analysis confirms this claim as well, clearly showing that the changes in the nanoparticles by laser irradiation are only partial. Figure 12 exhibits typical TEM images of the ZnO particles after the laser fragmentation process. Compared to the image in Fig. 4(*a*), Fig. 12(*a*) shows no significant change in the particle shape and size. On the other hand, Fig. 12(*b*) displays several small particles generated by the fragmentation process. If the majority of the particles went through the
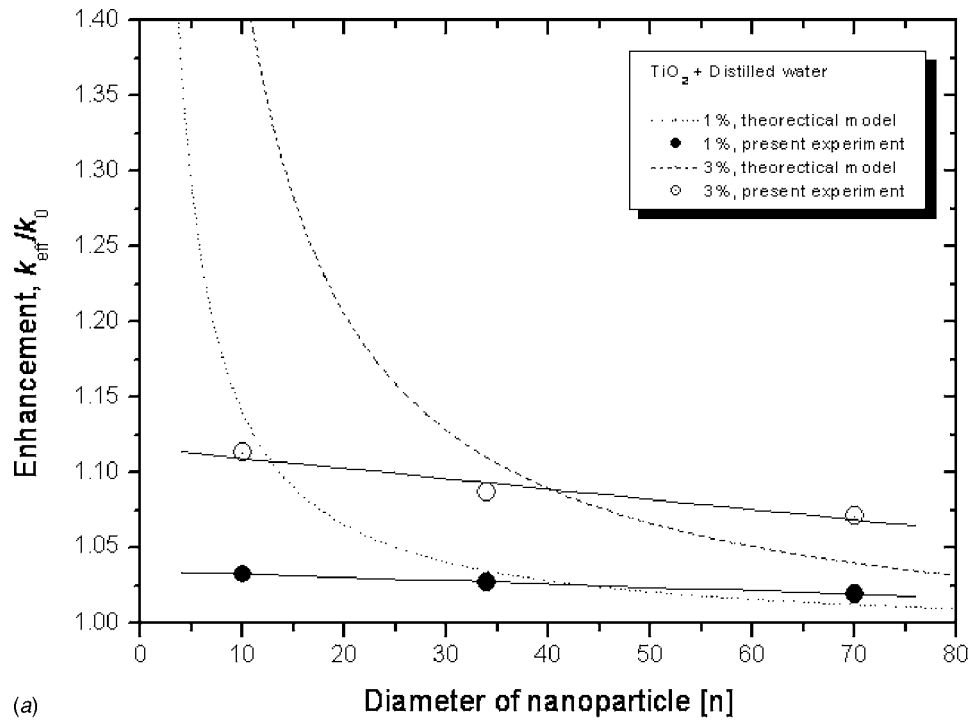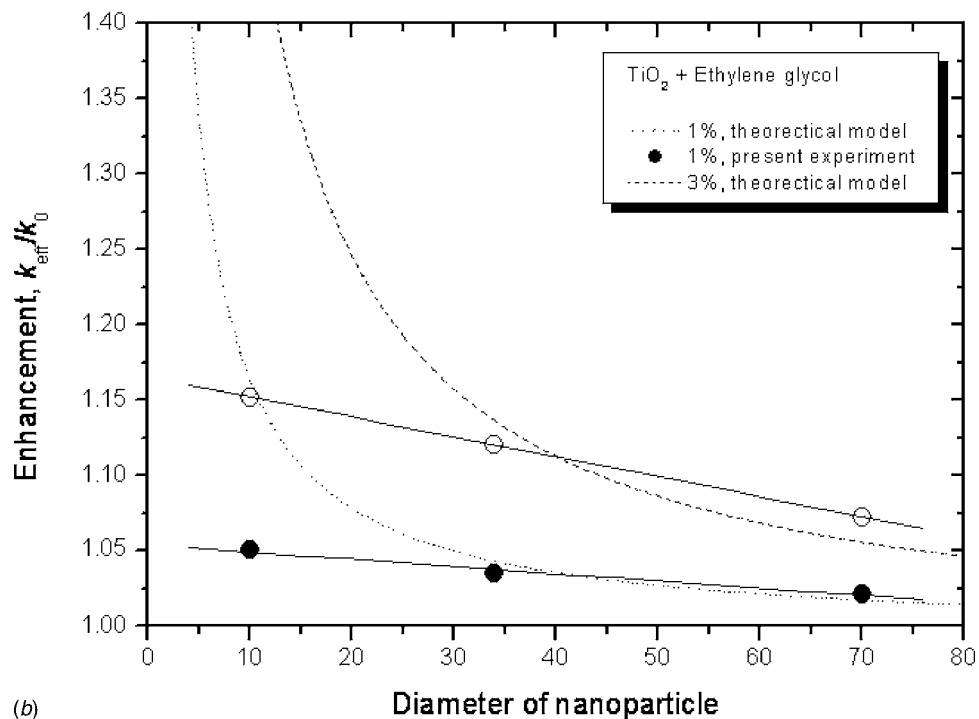
Fig. 10 Variation of thermal-conductivity ratio with particle diameter: (*a*) TiO$_2$/water and (*b*) TiO$_2$/EG nanofluids (comparison with a theoretical model (see Ref. [9])

fragmentation process, there would be a frequency shift in the absorbance peak as indicated in Fig. 5. However, the absorption spectrum analysis presents no change in the absorbance peak at all laser fluences, with the peak being always around 375±1 nm. Consequently, the enhancement of thermal transport is believed to be due to partial fragmentation of the particles. It is thus certain that size reduction, even though partial, can considerably increase the nanoscale mixing effects, leading to significant enhancement of the nanofluid thermal conductivity.

4 Conclusion

In this work, the thermal conductivity of several oxide nanofluids were experimentally analyzed over a wide range of experimental conditions and the results can be summarized as follows.

(1) The thermal conductivities of various water- and EG-based nanofluids containing ZnO, and TiO$_2$ nanofluids were measured, for the first time for some combinations, by varying the volume
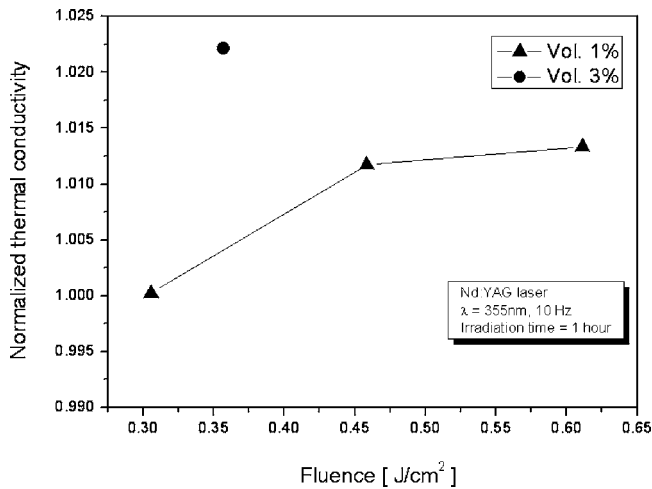
Fig. 11 Normalized thermal conductivity of 60 nm ZnO/water nanofluids after laser irradiation at different laser fluences (36,000 pulses) and two concentrations. The thermal conductivity has been normalized by the value before laser irradiation.

Fig. 12 TEM images of ZnO nanoparticles after laser irradiation at laser fluences (*a*) 310 and (*b*) 610 mJ/cm^2

fraction and the particle size, producing consistent experimental data to reveal the size dependence of the thermal conductivity of nanofluids.

(2) The measured thermal conductivity is inversely proportional to the mean diameter of the suspended particles and the dependence appears to be linear. This dependence cannot be explained by an existing theoretical correlation.

(3) The effect of high-power laser irradiation $\sim O(10^8 \text{ W/cm}^2)$ on the effective thermal conductivity of a nanofluid has been analyzed. The results demonstrate that high-power laser irradiation can result in significant increase in the effective thermal conductivity even though only a small fraction of the particles are fragmented.

Acknowledgment

Nomenclature

C_1 = proportionality coefficient
d = diameter (m)
k = thermal conductivity (W/m K)
n = empirical shape factor of particles
Pr = Prantdl number
R, R_0 = resistance of the hot wire (Ω)
R_1, R_2 = resistance of the standard resistor (Ω)
R_3 = equivalent resistance of the stabilizer circuit (Ω)
R_p = resistance of the hot wire (Ω)
R_v = resistance of a variable resistor (Ω)
$\text{Re}_{d_{particle}}$ = Reynolds number based on the nanoparticle
T = temperature (K)

Greek Symbols

β_1, β_2 = temperature coefficient of resistance (K^{-1})
ϕ = volume fraction
λ = wavelength (m)
ξ = thermal conductivity ratio $= k_{particle}/k_{BF}$

Subscripts

BF = base fluid
eff = effective
particle = nanoparticle

References

[1] Maxwell, J. C., 1881, *A Treatise on Electricity and Magnetism*, Vol. 1, 2nd ed., Clarendon Press, Oxford, p. 435.
[2] Masuda, H., Ebata, A., Teramae, K., and Hishinuma, N., 1993, "Alteration of Thermal Conductivity and Viscosity of Liquid by Dispersing Ultra-Fine Particles," Netsu Bussei, **4**, pp. 227–233.
[3] Lee, S., Choi, S. U. S., Li, S., and Eastman, J. A., 1999, "Measuring Thermal Conductivity of Fluids Containing Oxide Nanoparticles," ASME J. Heat Transfer, **121**, pp. 280–289.
[4] Choi, S. U. S., Zhang, Z. G., Yu, W., Lockwood, F. E., and Grulke, E. A., 2001, "Anomalous Thermal Conductivity Enhancement in Nanotube Suspensions," Appl. Phys. Lett., **79**, pp. 2252–2254.
[5] Eastman, A., Choi, S. U. S., Li, S., Yu, W., and Thompson, L. J., 2001, "Anomalously Increased Effective Thermal Conductivities of Ethylene Glycol-Based Nanofluids Containing Copper Nanoparticles," Appl. Phys. Lett., **78**, pp. 718–720.
[6] Xie, H., Wang, J., Xi, T., and Liu, Y., 2002, "Thermal Conductivity of Suspensions Containing Nanosized SiC Particles," Int. J. Thermophys., **23**, pp. 571–580.
[7] Xie, H., Lee, H., Youn, W., and Choi, M., 2003, "Nanofluids Containing Multiwalled Carbon Nanotubes and Their Enhanced Thermal Conductivities," J. Appl. Phys., **94**, pp. 4967–4971.
[8] Das, S. K., Putra, N., Thiesen, P., and Roetzel, W., 2003, "Temperature Dependence of Thermal Conductivity Enhancement for Nanofluids," ASME J. Heat Transfer, **125**, pp. 567–574.
[9] Jang, S. P., and Choi, S. U. S., 2004, "Role of Brownian Motion in the Enhanced Thermal Conductivity of Nanofluids," Appl. Phys. Lett., **84**, pp. 4316–4318.
[10] Xuan, Y., and Roetzel, W., 2000, "Conceptions for Heat Transfer Correlation of Nanofluids," Int. J. Heat Mass Transfer, **43**, pp. 3701–3707.
[11] Keblinski, P., Phillpot, S. R., Choi, S. U. S., and Eastman, J. A., 2002, "Mechanisms of Heat Flow in Suspensions of Nano-Sized Particles (Nanofluids)," Int. J. Heat Mass Transfer, **45**, pp. 855–863.
[12] Hamilton, R. L., and Crosser, O. K., 1962, "Thermal Conductivity of Heterogeneous Two-Component Systems," Ind. Eng. Chem. Fundam., **1**, pp. 187–191.
[13] Mafune, F., Kohno, J., Takeda, Y., and Kondow, T., 2002, "Growth of Gold Clusters into Nanoparticles in a Solution Following Laser-Induced Fragmentation," J. Phys. Chem. B, **106**, pp. 8555–8561.
[14] Takami, A., Kurita, H., and Koda, S., 1999, "Laser-Induced Size Reduction of Noble Metal Particles," J. Phys. Chem. B, **103**, pp. 1226–1232.
[15] Sugiyama, M., Okazaki, H., and Koda, S., 2002, "Size and Shape Transformation of TiO$_2$ Nanoparticles by Irradiation of 308-nm Laser Beam," Jpn. J. Appl. Phys., Part 1, **41**, pp. 4666–4674.
[16] Yeh, M., Yang, Y., Lee, Y., Lee, H., Yeh, Y., and Yeh, C., 1999, "Formation and Characteristics of Cu Colloids from CuO Powder by Laser Irradiation in 2-Propanol," J. Phys. Chem. B, **103**, pp. 6851–6857.
[17] Kestin, J., and Wakeham, A., 1978, "A Contribution to the Theory at the Transient Hot-Wire Technique for Thermal Conductivity Measurement," Physica A, **92**, pp. 102–116.
[18] Roder, H. M., 1981, "A Transient Hot Wire Thermal Conductivity Apparatus for Fluids," J. Res. Natl. Bur. Stand., **86**, pp. 457–493.
[19] John, A. I., Scott, A. C., Watson, J. T. R., and Ferguson, D., 1988, "Measurement of the Thermal Conductivity of Gases by the Transient Hot Wire Method," Philos. Trans. R. Soc. London, Ser. A, **A 325**, pp. 295–356.
[20] Duenas, S., Castan, E., and Barbolla, J., 1999, "Use of Anodic Tantalum Pentoxide for High-Density Capacitor Fabrication," J. Mater. Sci., **10**, pp. 379–384.
[21] Lide, D. R., 2000, *CRC Handbook of Chemistry and Physics*, 81st ed., CRC Press, Boca Raon, FL.
[22] Touloukian, Y. S., 1970, *Thermophysical Properties of Matter*, Vol. 2, IFI/Plenum, New York.
[23] Jang, D., Oh, B., and Kim, D., 2004, "Visualization of Microparticle Explosion and Flow Field in Nanoparticle Synthesis by Pulsed Laser Ablation," Appl. Phys. A: Mater. Sci. Process., **79**, pp. 1149–1151.

The Role of the Viscous Dissipation in Heated Microchannels

Gian Luca Morini
DIENCA-Università degli Studi di Bologna,
Viale Risorgimento 2,
40136 Bologna, Italy
e-mail: gianluca.morini@mail.ing.unibo.it

Marco Spiga
Dipartimento di Ingegneria Industriale,
Parco Area delle Scienze 181A,
43100 Parma, Italy

Many experimental works appeared in the last decade in the open literature dealing with forced convection through microchannels. The earliest experimental results on single-phase flows in microchannels evidenced that for channels having a hydraulic diameter less than 1 mm the conventional continuum models can no longer be considered as able to accurately predict pressure drop and convective heat transfer coefficients. This conclusion seemed to be valid for both gas and liquid flows. Sometimes the authors justified this conclusion by invoking new micro-effects, e.g., electrostatic interaction between the fluid and the walls or scaling effects (axial heat conduction, viscous forces, conjugate heat transfer, wall roughness, and so on). In this paper the role of the viscous dissipation in liquids flowing through heated microchannels will be analyzed by using the conventional theory. We will present a correlation between the Brinkman number and the Nusselt number for silicon ⟨100⟩ and ⟨110⟩ microchannels. It will be demonstrated that the fluid is of importance in establishing the exact limit of significance of the viscous dissipation in microchannels; a criterion to analyze the significance of the viscous effects will be presented. The role of the cross-section aspect ratio on the viscous dissipation will be highlighted. The main goal of this work is to demonstrate that the problem of heat transfer enhancement in microdevices cannot be solved by indefinitely reducing the microchannel dimensions because the viscous dissipation effects shall offset the gains of high heat transfer coefficients associated with a reduction in the channel size. [DOI: 10.1115/1.2430725]

Keywords: viscous dissipation, Brinkman number, microchannels, convective heat transfer, Nusselt number

Introduction

Micro-flow devices (MFDs) are downscaled devices like channels, nozzles, diffusers, pumps, mixers, heat pipes, sensors, transducers, and actuators, incorporated in complex systems for medical diagnosis and surgery, chemical analysis, biotechnology, and motor management. The development of micro-fluidic devices during the past 10 years has been particularly striking. Today, the research on MEMS (micro-electro-mechanical systems) is exploring different applications that involve the dynamics of fluids and the single- and two-phase forced convective heat transfer in microchannels. Recent advances in micro-fabrication techniques make it possible to build microchannels with very small hydraulic diameters ($100-0.1$ μm) in different ways. For example, the chemical etching is used to build microchannels on silicon wafers; in this case, the shape of the channels depends on a variety of factors such as the crystallographic nature of the silicon used. When a KOH-anisotropic etching technique is employed, the microchannels have a fixed cross-section that depends on the orientation of the silicon crystal planes; for instance, the microchannels etched in ⟨100⟩ or in ⟨110⟩ silicon shall have a trapezoidal cross-section (with an apex angle of 54.74 deg imposed by the crystallographic morphology of the silicon) or a rectangular cross-section, respectively (see Fig. 1). Many experimental and numerical studies on the pressure drop and the convective heat transfer in this kind of microchannel have appeared in the open literature and a complete review of these works is due to Morini [1]. The first work aimed at analyzing the convective heat transfer through trapezoidal and rectangular silicon heated microchannels

was made by Wu and Little [2]. They measured average Nusselt numbers higher than those predicted by the conventional correlations for fully developed laminar flows and for fully developed turbulent flows. In addition, in the fully developed laminar regime the Nusselt numbers seemed to depend on the Reynolds number. The authors evidenced that the very large relative roughness of the microchannels could improve heat transfer coefficients and proposed a correlation in order to predict the average Nusselt numbers in the turbulent regime. Choi et al. [3] confirmed that the Nusselt number depends on the Reynolds number and on the Prandtl number even in the laminar regime. The authors proposed two new correlations to predict the average Nusselt number both in laminar and turbulent regime. As highlighted in [1], the correlation proposed by Choi et al. [3] for microtubes is not in agreement with the one proposed by Wu and Little [2]. Yu et al. [4] investigated in particular the heat transfer in microtubes in the turbulent regime ($6000 < \text{Re} < 20,000$); they proposed a correlation for the average Nusselt number. Also in this case, the Nusselt numbers in the turbulent regime are larger than those predicted by means of the conventional theory but even the Yu's correlation seems to be in disagreement with those of Choi et al. and of Wu and Little. Wang and Peng [5] and Peng and Peterson [6] determined experimentally the average convective heat transfer coefficient through metallic microchannels. The variation of the Nusselt number with the Reynold number exhibited an unusual behavior: the Nusselt number evidenced a decrease with increasing the Reynolds number in the laminar regime. They compared their experimental data with the Sieder-Tate correlation and with the correlation for microchannels proposed by Wu and Little for the laminar regime; it was found that, for low values of the Reynolds number, the experimental data disagreed with the correlations used. Wang and Peng [5] proposed a correlation for the determination of the average Nusselt number through rectangular microchannels as a
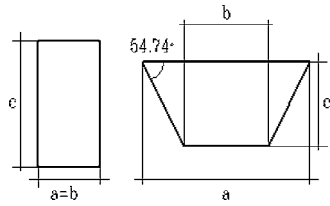
Fig. 1 Typical microchannel cross-sections obtained by chemical etching on ⟨100⟩ and ⟨110⟩ silicon wafers

function of Reynolds and Prandtl numbers for turbulent flows. This correlation proposes a modification of the Dittus-Boelter equation where the empirical coefficient 0.023 is replaced with 0.008 05; that means that in microchannels the experimental Nusselt numbers were lower than the predictions of the conventional theory for the same value of the Reynolds and Prandtl number. Nguyen et al. [7] proposed a correlation in order to predict the Nusselt number for water flow through trapezoidal microchannels in the laminar and in the turbulent regime; they correlated the Nusselt number to the Reynolds number. The experimental Nusselt numbers were larger than the predictions of the Dittus-Boelter correlation in the turbulent regime. Adams et al. [8] tested Gnielinski's correlation for the prediction of the Nusselt number in the turbulent regime for capillary tubes having a hydraulic diameter between 0.76 and 1.08 mm ($3200 < \mathrm{Re} < 23{,}000$) to complement the data provided by Yu et al. [4]. The experimental Nusselt numbers were usually higher than those predicted by Gnielinski's correlation. These results suggested a modification of Gnielinski's correlation, which has been corrected by means of a factor F depending on the Reynolds number and on the hydraulic diameter of the capillary tube. Wu and Cheng [9] investigated experimentally 13 different trapezoidal silicon microchannels (25.9–291 μm). They found that the laminar Nusselt number and apparent friction constant increase with the increase of surface roughness and surface hydrophilic property. The Nusselt number increases almost linearly with the Reynolds number at low Reynolds numbers ($\mathrm{Re} < 100$). Li et al. [10] investigated numerically a silicon micro heat sink with a geometry identical to that employed in the experimental work of Kawano et al. [11] and in the numerical investigations of Qu and Mudawar [12] and Fedorov and Viskanta [13]. The microchannels were rectangular with a hydraulic diameter of 87 μm and heated from below (90 W/cm^2). They proposed a correlation in order to calculate the mean Nusselt number as a function of the Reynolds and Prandtl numbers. Qu and Mudawar [12] investigated the heat transfer characteristics of the micro heat sink of Kawano et al. [11]. The three-dimensional conjugate heat transfer problem was solved numerically. The assumptions of constant solid and fluid properties, excluding water viscosity, were considered in the numerical model. Qu et al. [14] investigated the heat transfer characteristics of water flowing through trapezoidal silicon microchannels with a hydraulic diameter ranging from 62 to 169 μm. The experimental results were compared with the numerical predictions by considering the conjugate heat transfer between the solid and the fluid region. The assumptions of constant thermophysical properties and fully developed flow were used in the numerical analysis. They found that the measured Nusselt numbers were lower than the predicted numerical values. They concluded that the lower Nusselt numbers can be due to the effect of surface roughness of the microchannel walls also in the laminar regime; this conclusion contradicts common sense as other authors pointed out. Gao et al. [15] measured the axial distribution of the local Nusselt number inside rectangular microchannels with a fixed width of 25 mm and a height ranging from 1 to 0.1 mm. It was observed that, for microchannels having a height larger than 0.4 mm, the measured average Nusselt number agreed with the conventional correlations in the laminar regime. For microchannels less than 0.4 mm in height a signifi-

cant decrease in the Nusselt number was observed. On the contrary, the friction factor for any microchannel agreed with the conventional theory. The authors remarked that this is in contradiction with the Reynolds analogy, which at least predicts variations of the friction factor and of the Nusselt number in the same direction.

Lee et al. [16] conducted an experimental investigation in order to explore the validity of classical correlations for predicting the thermal behavior in single-phase flows through rectangular microchannels with a hydraulic diameter ranging between 318 and 903 μm. The authors concluded that the conventional theory can be employed in predicting heat transfer behavior, but the mismatch in the boundary and inlet conditions between the microchannel experiments and the conventional correlations sometimes precluded their use for predictions.

Grohmann [17] investigated experimentally the convective heat transfer for argon flowing in microtubes of 250 and 500 μm diameter. An enhancement of heat transfer has been evidenced with respect to the conventional predictions; the author explained the increase of the convective heat transfer coefficients with the increased influence of roughness in microtubes. A new correlation has been proposed in order to predict the Nusselt number in the laminar and turbulent regimes. In general, it is possible to observe that the new correlations proposed to predict the Nusselt number in microchannels disagree one with another and any correlation disagrees with the conventional prediction. In order to explain this behavior many researchers underlined that the Navier-Stokes equations are no longer adequate to study the flows through microchannels because the characteristic lengths of MFDs are sometimes of the same order of magnitude as the mean free path of the molecules of the flowing fluid: this occurs especially for gas flows. On the contrary, for liquids with a distance between the molecules much smaller than that for gases the continuum approach and the Navier-Stokes equations hold even in microchannels.

Herwig and Hausner [18] observed that in order to study the forced convection of liquids in the laminar regime a common theoretical basis for macro- and micro-flows can be used; nevertheless, certain effects can be of different importance for microsystems if compared with macro-systems. Herwig and Hausner [18] called these effects "scaling effects with respect to a standard macro-analysis." Guo and Li [19] remarked that, since different forces have different dependences with respect to length, the surface forces (like surface tensions, viscous forces, or electrostatic forces) become more important and even dominant as the scale is reduced. For this reason, it is possible to identify the following main "scaling effects" for single-phase flows in microchannels: (i) axial heat conduction (small Peclet number), (ii) conjugate heat transfer, (iii) temperature dependent properties, (iv) wall roughness (nonuniform wall roughness distribution), and (v) viscous dissipation (intense viscous forces).

Axial heat conduction and conjugate heat transfer in microchannels have been studied numerically by several authors. The effects of thermal conductivity of the solid region around the microchannels have been explored by Qu and Mudawar [12]; for the geometry investigated, the effects of the solid thermal conductivity on the average Nusselt number were so small that their results for a copper heat sink and a silicon heat sink were virtually identical. For the same geometry, Li et al. [10] observed that the magnitude of the heat flux due to axial heat conduction in the solid region depends on the Reynolds number. They concluded that for low fluid flow rates particular attention should be paid to the effects of this heat loss.

A large number of papers have been devoted to analyzing the effect of the thermophysical property variations with temperature [20–22]. The main conclusion of these works is that it is very important to consider the variation of the fluid viscosity in the analysis of micro-flows, especially at low Reynolds numbers, whereas quantities such as density, specific heat, and so on can be

considered independent of temperature. The role of surface roughness on fluid flow and heat transfer in microchannels has been emphasized by several authors both experimentally and theoretically [23–26]. Sabry [23], in order to explain the role of the surface roughness at the walls, stated that liquid flow is probably partially separated from the walls by a very thin gas blanket trapped by the roughness elements in microchannels. This gas blanket could influence the value assumed by the friction factor, the critical Reynolds number linked to the transition between laminar to turbulent regime, the Nusselt number, and it could explain the dependence of friction factor and Nusselt number on the Reynolds number even in the laminar regime.

The effect of the viscous forces in microchannels has been investigated by many authors. Tso and Mahulikar [27] presented a theoretical and experimental analysis of circular microchannels, taking into account the effect of the viscous dissipation by means of the Brinkman number. They found that the experimental data for laminar flow can be well connected by using the variation of the Brinkman number. In their experimental analysis the authors found very small values of the Brinkman number (of the order of 10^{-8}), too low to affect directly the water bulk temperature by means of the viscous dissipation. The author remarked that for microchannels the effect of the Brinkman number is related to the reduction of the dynamic viscosity between the inlet and the outlet of a microchannel due to the increase in the bulk temperature; this fact can reduce the Brinkman number at the exit by about 50% of its inlet value. The authors concluded that the axial variation of the Brinkman number affects the convective heat transfer in microchannels; they defined this effect as the secondary effect of the Brinkman number. The authors stated that the secondary effect of the Brinkman number can be used in order to explain the decrease in the Nusselt number when the Reynolds number increases in the laminar regime. However, the data used in order to correlate the Nusselt number with the Brinkman number were obtained under conditions in which the Reynolds number and the Prandtl number also varied. In this manner it becomes hard to distinguish the effect of the Brinkman number on the Nusselt number from the effects of the Reynolds number and the Prandtl number.

Tunc and Bayazitoglu [28] studied the effects of the viscous dissipation for rarefied gas flow in the slip-flow regime in circular and rectangular microchannels. They concluded that the Brinkman number plays an important role in the heat transfer through microdevices also for gas flows.

Xu et al. [29] investigated the viscous dissipation effects for liquid flows in microchannels; they stated that deviations from predictions using conventional theory that neglects viscous dissipation could be expected because viscous dissipation tends to be significant due to high velocity gradients existing in channels with small hydraulic diameters. They proposed a criterion to draw the limit of the significance of the viscous dissipation effects in microchannel flows.

More recently, Koo and Kleinstreuer [30] investigated the viscous dissipation effects on the temperature field and friction factor in circular and rectangular microchannels. They demonstrated that viscous dissipation is a strong function of the hydraulic diameter, the channel aspect ratio, and the Brinkman number. They concluded that ignoring viscous dissipation could affect accurate flow predictions in microchannels.

Morini [31,32] investigated the effect of the viscous heating for liquid flows through microchannels in order to demonstrate that the temperature variation due to the viscous heating could change the value of the Poiseuille number by means of the variation of the fluid viscosity with the temperature. A criterion in order to predict when the viscous dissipation effects can be neglected in microchannels was theoretically derived. In addition, Morini evidenced in [31] that the criterion to draw the limit of significance of viscous heating in microchannels proposed by Xu et al. [29] tends to underestimate the viscous dissipation effects.

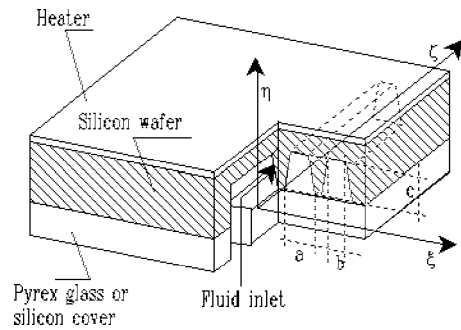The conclusions of Morini [31,32] about the importance of the

Fig. 2 Sketch of a silicon heat sink

viscous effects in microchannels are confirmed by the conclusions of Hetsroni et al. [33] in their critical review of the results on the convective heat transfer in microchannels that appeared in the last years in the open literature.

This paper is devoted to study theoretically the effects of the viscous heating on the convective heat transfer coefficient for liquid flows in microchannels. Since our main aim is to isolate this single aspect of the problem, in this paper the other scaling effects will not be taken into account.

Mathematical Model

Let us consider the silicon microchannel heat sink shown in Fig. 2; the microchannels obtained by chemical etching on the silicon wafer are in general closed by a Pyrex glass cover bonded to the substrate or by means of a silicon wafer. A liquid flows through the channels; due to the small size of the microchannels the flow is typically laminar. The microchannels have an axially unchanging cross-section with area equal to Ω and a wetted perimeter equal to Γ. A Cartesian system of coordinates ξ, η, ζ is assumed, with its origin in the left bottom corner of the inlet cross-section (see Fig. 2).

A fixed linear power q_w is imposed on the top of the silicon substrate while all the other outside walls of the unit cell are adiabatic. Some simplifying assumptions can be made before applying the conventional Navier-Stokes and energy equations to model the heat transfer process in a microchannel. The major assumptions can be summarized as follows:

1. The fluid is Newtonian, incompressible, and with a laminar fully developed profile of velocity $u(\xi, \eta)$ and a uniform inlet temperature θ_{in}.
2. The transport processes are considered to be steady-state and bi-dimensional (through the microchannel the velocity and the temperature profiles are considered as fully developed).
3. All the channel walls are rigid and nonporous.
4. Thermal radiation is neglected.
5. Axial thermal conduction (Pe$\gg$1), natural convection (Gr/Re$^2 \ll$1), and interior heat sources are neglected.
6. Solid and fluid thermophysical properties are assumed as constant with the temperature.

In silicon heat sinks, due to the high thermal conductivity of the silicon, the temperature gradient in the silicon substrate is very limited and the solid temperature field is close to an isothermal one: this fact has been demonstrated numerically by Fedorov and Viskanta [13], Qu and Mudawar [12], and Li et al. [10]. When a pyrex cover is used to close the heat sink, three walls of the microchannels work with a constant temperature; on the contrary, the pyrex side can be considered adiabatic. In general, the ratio between the thermal conductivity of the silicon and of the liquid assumes very high values, the same occurs for the ratio between the length and the hydraulic diameter of the microchannel. For these reasons the microchannels can be conveniently studied as

"long ducts" under a classical H1 thermal boundary condition with three sides having an imposed uniform temperature and one side (the pyrex side) as adiabatic; this situation is classified in the literature as a 3L/S version [34]. Conversely, when a silicon cover is used to close the microchannels, all the boundaries can be considered as isothermal; it is possible to use the H1 thermal boundary condition, with four sides having an imposed uniform temperature; this situation is classified in the literature as a 4 version [34]. The choice of the right thermal boundary conditions is a very important item in order to simulate correctly the heat transfer characteristics of microflows as pointed out by Lee et al. [16] by means of a comparison between experimental results and numerical predictions obtained by using different kind of thermal boundary conditions. The numerical results obtained by Lee et al. [16] confirmed that the H1 boundary condition (implemented in their commercial code using thin and highly conductive microchannel walls with no axial conduction) can be used as a computationally economical alternative to a full 3D conjugate analysis.

Under the mentioned hypotheses the conservation equations of momentum and energy can be written as follows:

$$\nabla^2 u = \frac{1}{\mu}\frac{dp}{d\zeta}$$

$$\nabla^2 \theta + \frac{\mu}{\lambda}(\nabla u \cdot \nabla u) = \frac{u(\xi, \eta)}{\alpha}\frac{\partial\theta}{\partial\zeta} \qquad (1)$$

In the fully developed thermal region of a heated duct the temperature profile continues to change with ζ but the "relative temperature shape" of the profile no longer changes. Resorting to the definition of a thermally fully developed region for the H1 boundary condition, it is possible to demonstrate that:

$$\frac{\partial\theta}{\partial\zeta} = \frac{\partial\theta_b}{\partial\zeta} = \frac{q_w + \mu\int_\Omega (\nabla u \cdot \nabla u)d\Omega}{\rho c_p W\Omega} \qquad (2)$$

where q_w is the power per unit length to the heated wall, W is the fluid average velocity, and Ω is the area of the cross-section.

It is suitable introducing the dimensionless quantities:

$$x = \frac{\xi}{D_h}; \quad y = \frac{\eta}{D_h}; \quad \Gamma^* = \frac{\Gamma}{D_h}; \quad \Omega^* = \frac{\Omega}{D_h^2}; \quad \nabla^* = D_h\nabla$$

$$V(x,y) = \frac{u}{W}; \quad p^* = -\frac{D_h^2}{\mu W}\frac{dp}{d\zeta}; \quad T = \frac{\lambda(\theta - \theta_{in})}{q_w}; \quad \text{Br} = \frac{\mu W^2}{q_w}$$
$$(3)$$

We point out that the Brinkman number used here is defined in a different form from its classical definition ($\text{Br}' = \mu W^2/q_w'' D_h$) in which the wall heat flux is used. Because the value of q_w'' depends on the geometry of the microchannels considered (in particular on its heated perimeter), in this paper the Brinkman number is referred to the linear heat flux q_w. It is possible to calculate Br' from Br as $\text{Br}' = \Gamma_h^* \text{Br}$ where Γ_h^* is the dimensionless heated perimeter of the microchannel.

Consequently, the dimensionless momentum and energy balance equations are readily obtained in the following form:

$$\nabla^{*2}V = -p^*$$

$$\nabla^{*2}T + \text{Br}(\nabla^*V \cdot \nabla^*V) = \frac{V(x,y)}{\Omega^*}(1 + \text{Br}\,\Phi^*) \qquad (4)$$

where the dimensionless viscous-energy-dissipation function Φ^* is defined as:

$$\Phi^* = \int_{\Omega^*}(\nabla^*V \cdot \nabla^*V)d\Omega^* \qquad (5)$$

The momentum balance equation is solved by using the no-slip boundary condition at the wall, which means considering negligible any rarefaction effect. For Newtonian liquid flows this assumption is always justified for hydraulic diameters of the microchannel greater than 1 μm.

The complete set of boundary conditions is thus:

$$V|_\Gamma = 0, \quad T|_\Gamma = 0 \quad \text{(4 version)}$$

$$V|_\Gamma = 0, \quad \left.\frac{\partial T}{\partial y}\right|_{\Gamma_b^*} = 0, \quad T|_{\Gamma^* - \Gamma_b^*} = 0 \quad \text{(3 version)} \qquad (6)$$

where Γ_b^* is the dimensionless length of the bottom boundary of the microchannels ($\Gamma_b^* = a/D_h$).

Flow and Thermal Characteristics. From the dimensionless velocity distribution $V(x,y)$ it is possible to derive the values assumed by the main flow parameters as a function of the microchannel aspect ratio. In particular, it is possible to determine the value of the Poiseuille number, defined as the product of the Fanning friction factor for fully developed flow (f) and the Reynolds number (Re), by means of the following relation:

$$f\text{Re} = -\frac{1}{2\Omega^*}\int_{\Omega^*}\nabla^*\cdot(\nabla^*V)d\Omega^* = \frac{p^*}{2} = \frac{2\Phi^*}{\Gamma^*} = \frac{\Phi^*}{2\Omega^*} \qquad (7)$$

Equation (7) states the link existing between the Poiseuille number and the viscous-energy dissipation function Φ^* (Eq. (5)) as demonstrated in [31].

From the dimensionless temperature distribution $T(x,y)$, the value of the bulk temperature can be computed:

$$T_b = \frac{1}{\Omega^*}\int_{\Omega^*}V(x,y)T(x,y)d\Omega^* \qquad (8)$$

The local Nusselt number along the walls of the microchannels can be calculated as follows:

$$\text{Nu}_l = -\frac{1}{T_b}(n \cdot \nabla^*T|_w) \qquad (9)$$

where n is the versor normal at the wall.

By averaging the local Nusselt number along the heated perimeter one can obtain the thermally fully developed mean Nusselt number:

$$\text{Nu} = \frac{1}{\Gamma_h^*}\int_{\Gamma_h^*}\text{Nu}_l\,d\Gamma^* = -\frac{1}{\Gamma_h^* T_b}\int_{\Gamma_h^*}n \cdot \nabla T\,d\Gamma^* = -\frac{1}{\Gamma_h^* T_b} \quad (10)$$

where Γ_h^* is the dimensionless heated perimeter ($\Gamma_h^* = \Gamma^*$ (4 version), $\Gamma_h^* = \Gamma^* - \Gamma_b^*$ (3 version)).
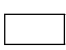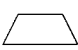
Numerical Accuracy. The problem described by Eq. (4) with the boundary condition given in Eq. (6) has been numerically solved by means of a code written by using the software package FlexPDE™ [35]. This package is devoted to the solution of systems of partial differential equations through a Rayleigh-Ritz-Galerkin finite element method. The numerical procedure implies an iterative refinement of the grid until the prescribed accuracy, correlated with the maximum local residual value R_k, is reached. The iterative procedure is stopped when the velocity field V and the temperature field T satisfy the following condition:

$$\max(R_k(V,N),R_k(T,N)) < \varepsilon \quad \forall\,k \in [1,N] \qquad (11)$$

where N denotes the number of triangular elements.

In order to determine the convergence error, the numerical results obtained by varying ε have been compared with the analytical values of the Poiseuille number (fRe) and of the Nusselt num-
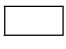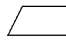
Table 1 The Poiseuille number (fRe) for fully developed flow through rectangular and trapezoidal microchannels

fRe			
β	Present results	Shah and London [36]	
0	24.000	24	24
0.01	23.677	-	23.597
0.05	22.477	22.47701	22.174
0.1	21.169	21.16888	20.737
0.2	19.071	19.07050	18.650
0.3	17.512	17.51209	17.244
0.4	16.368	16.36810	16.263
0.5	15.548	15.54806	15.565
0.6	14.980	14.97996	15.060
0.7	14.605	14.60538	14.690
0.8	14.378	14.37780	14.417
0.9	14.261	14.26098	14.215
1	14.227	14.22708	14.063
10/9	14.261	14.26098	13.940
5/4	14.378	14.37780	13.832
10/7	14.605	14.60538	13.745
5/3	14.980	14.97996	13.685
2	15.548	15.54806	13.654
2.5	16.368	16.36810	13.654
10/3	17.512	17.51209	13.679
5	19.071	19.07050	13.694
10	21.169	21.16888	13.622
∞	24.000	24	13.308

ber (Nu) obtained by Shah and London [36] and Morini [37], respectively, for rectangular channels with three or four walls heated in which viscous dissipation is neglected.

The Poiseuille numbers (fRe) for a fully developed flow through rectangular and trapezoidal microchannels are quoted in Table 1. Table 2 shows the average Nusselt numbers Nu_0 obtained by neglecting the viscous dissipation (Br=0) for rectangular and trapezoidal microchannels as a function of the aspect ratio. The cross-section aspect ratio is usually defined as the ratio between the height and the width of the channel. The definition of the

Table 2 Average Nusselt number (Nu_0) for negligible viscous heating (Br=0) for rectangular and trapezoidal mocrichannels with three or four sides heated, as a function of the aspect ratio

Nu₀						
β	Present results	Morini [37]		Present results	Morini [37]	
0	8.235	8.235	8.235	5.385	5.385	5.385
0.05	7.451	-	7.302	4.763	-	4.752
0.1	6.785	6.785	6.575	4.283	4.283	4.283
0.2	5.738	5.738	5.536	3.639	3.639	3.666
0.3	4.990	4.990	4.852	3.302	3.302	3.315
0.4	4.472	4.472	4.391	3.163	3.163	3.116
0.5	4.123	4.123	4.073	3.140	3.140	3.002
0.6	3.895	3.895	3.850	3.182	3.182	2.939
0.7	3.750	3.750	3.691	3.259	3.259	2.906
0.8	3.664	3.664	3.577	3.355	3.355	2.889
0.9	3.620	3.620	3.493	3.460	3.460	2.883
1	3.608	3.608	3.431	3.568	3.568	2.883
10/9	3.620	3.620	3.381	3.688	3.688	2.889
5/4	3.664	3.664	3.338	3.836	3.836	2.898
10/7	3.750	3.750	3.303	4.018	4.018	2.912
5/3	3.895	3.895	3.277	4.246	4.246	2.930
2	4.123	4.123	3.261	4.539	4.539	2.948
2.5	4.472	4.472	3.255	4.923	4.923	2.964
10/3	4.990	4.990	3.251	5.439	5.439	2.968
5	5.738	5.738	3.236	6.131	6.131	2.946
10	6.785	6.785	3.188	7.044	7.044	2.880
∞	8.235	8.235	3.093	8.235	8.235	2.765

aspect ratio is univocal for a rectangular cross-section; on the contrary, two different definitions of the aspect ratio are used in the literature for trapezoidal channels ($\gamma = c/a$ or $\beta = c/b$ with reference to the symbols in Fig. 1). In this work β is used; for trapezoidal channels β tends to infinity as the cross-section approaches the triangular shape.

For ε equal to 10^{-7}, the following maximum relative differences between the numerical and the analytical values of fRe and Nu have been found:

$$\Delta_{f\text{Re}} = 0.003\%, \quad \Delta_{\text{Nu}} = 0.005\% \qquad (12)$$

The estimates given for the convergence error on the main flow parameters for rectangular channels are considered reliable also for the numerical results obtained for the trapezoidal channels. By using the same value of ε (10^{-7}) for all the cross-sections considered, the required number of triangular elements (N) in order to satisfy the residual-based adaptive refinement criterion ranges between a minimum value of 70,000 (for the square channel) and a maximum value of 250,000 (for the trapezoidal channel with an aspect ratio $\beta = 0.02$).

Discussion of the Results

Significance of the Viscous Dissipation. Firstly, it is important to draw the limit of significance of the viscous dissipation in heated or cooled microchannels; in particular, in this section a criterion will be carried out in order to predict the range of the Brinkman number where the viscous dissipation effect cannot be neglected in the analysis of the heat transfer in microchannels.

In this investigation the entrance effects are neglected and the longitudinal temperature gradient along the microchannel (Eq. (2)) is considered as a constant. Numerical analyses of Tso and Mahulikar [27] and Koo and Kleinstreuer [30] confirmed that the entrance effects have a limited effect on the temperature distribution along the flow direction, in particular for low Reynolds numbers. By integrating Eq. (2) between the inlet and the outlet of a microchannel one can calculate the temperature difference between the extremes of the microchannel:

$$\Delta \theta_b = \frac{q_w}{\rho c_p W \Omega} L + \frac{\mu W^2 \Phi^*}{\rho c_p W \Omega} L = \Delta \theta_q + \Delta \theta_v \qquad (13)$$

where L is the microchannel length.

The bulk temperature difference between the inlet and the outlet of the channel is considered as a sum of two terms: (i) the temperature drop linked to the heat flux at the wall ($\Delta \theta_q$) and (ii) the temperature rise due to the viscous dissipation inside the fluid ($\Delta \theta_v$).

If one considers the ratio between these two contribution, it is possible to demonstrate that this ratio is linked to the Brinkman number and the Poiseuille number by means of the following relation:

$$\kappa = \frac{\Delta \theta_v}{\Delta \theta_q} = \text{Br } \Phi^* = 2 \text{ Br } \Omega^* f\text{Re} \qquad (14)$$

In order to draw the limit of the significance of the viscous dissipation effects in a microchannel one can impose that they are significant when this ratio is greater than a fixed value ($\kappa_{\text{lim}} = 1 - 5\%$); in this manner the following inequality on the Brinkman number can be made:

$$\text{Br} > \frac{\kappa_{\text{lim}}}{2\Omega^* f\text{Re}} \qquad (15)$$

If this inequality is satisfied, the effects of the viscous dissipation cannot be neglected.

For rectangular and trapezoidal channels the dimensionless area of the cross-section is a function of the aspect ratio (β) and of the apex angle (ϕ); it can be expressed as follows:
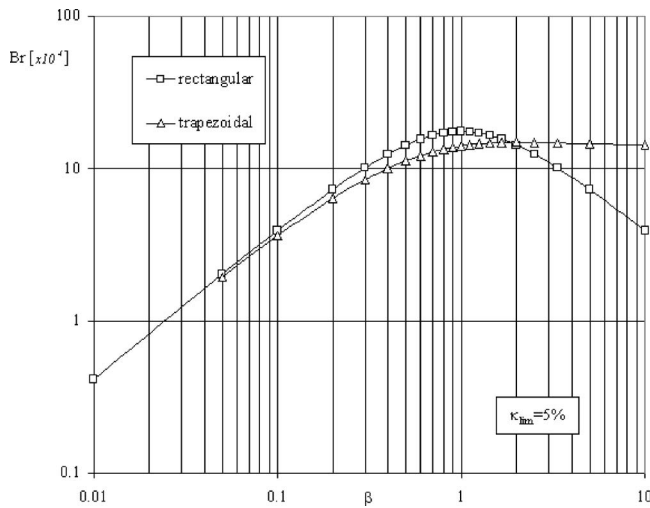
Fig. 3 Maximum value of the Brinkman number for which the viscous dissipation effects can be neglected for trapezoidal ($\phi=54.74$ deg) and rectangular ($\phi=90$ deg) microchannels as a function of the aspect ratio β

$$\Omega^* = \frac{\left[1 + \beta\left(\dfrac{1}{tg\phi} + \dfrac{1}{sen\phi}\right)\right]^2}{4\beta^2\left[\dfrac{1}{\beta} + \dfrac{1}{tg\phi}\right]} \qquad (16)$$

Figure 3 shows the maximum value of the Brinkman number for which the viscous dissipation effects can be neglected for microchannels having trapezoidal ($\phi=54.74$ deg) and rectangular ($\phi=90$ deg) cross-section, as a function of the aspect ratio β. A value of κ_{lim} equal to 5% is considered. It is evident that for shallow microchannels the effects of the viscous dissipation become important for lower Brinkman numbers.

In order to consider the applicability to the microchannels of the proposed criterion, the value of the minimum Reynolds number (linked to the minimum Brinkman number indicated in Eq. (15)) for which κ becomes equal to 5% is computed as a function of the hydraulic diameter for a rectangular microchannel having $\beta=3$. In Fig. 4 the minimum Reynolds number is shown for water and isopropanol as working fluids in rectangular and trapezoidal microchannels having an aspect ratio $\beta=3$. A constant wall heat
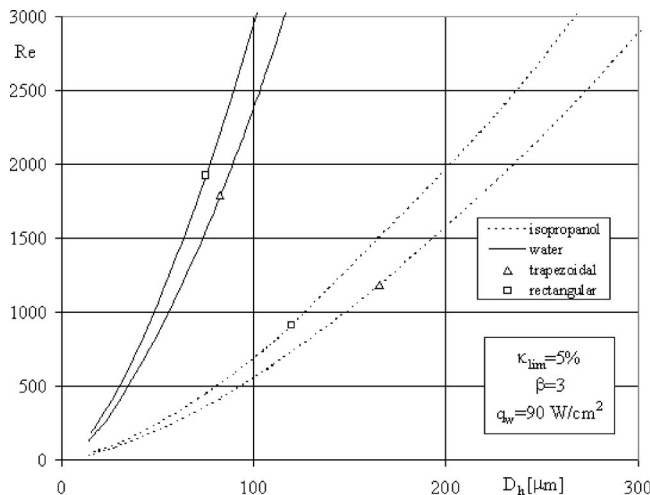
Fig. 4 Maximum Reynolds numbers for which the effects of the viscous dissipation can be neglected
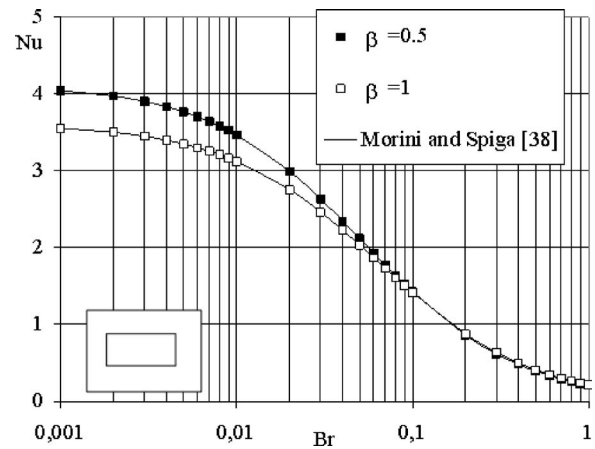
Fig. 5 Comparison between the numerical and the analytical values of the average fully developed Nusselt number for rectangular channels with $\beta=1$ and $\beta=0.5$ (four sides heated)

flux at the wall equal to 90 W/cm^2 is considered in agreement with the experimental and theoretical works of Kawano et al. [11], Fedorov and Viskanta [13], Qu and Mudawar [12], and Li et al. [10]. It is evident that the viscous effects are more important for isopropanol than for water as the physical intuition suggests. In addition, it is interesting to note that for water the viscous effects have to be considered only for microchannels having a hydraulic diameter less than 100 μm; when the hydraulic diameter decreases the minimum Reynolds number decreases and the viscous effects become important even if the Reynolds numbers are low (Re $<$ 500). In Fig. 4 the role of the cross-section shape is highlighted; it is possible to note that the viscous effects occur earlier in the trapezoidal microchannel for fixed values of the hydraulic diameter and aspect ratio.

Figure 4 proves that the viscous effects are typical scaling effects; in fact, they are negligible for high values of the hydraulic diameter but tend to become very important when hydraulic diameters less than 100–300 μm are considered.

Uniform Heat Flux Microchannels. The problem of the determination of the Nusselt number for a Newtonian incompressible fluid through a rectangular channel in fully developed laminar flow with viscous dissipation for H1 boundary condition and any combination of heated and adiabatic sides of the duct has been solved analytically by Morini and Spiga [38]. They used the integral transform technique in order to determine the velocity and the temperature inside the rectangular channels.

A comparison with the analytical results by Morini and Spiga [38] is made in order to verify the reliability of the numerical procedure adopted in this paper to study the effect of the viscous dissipation through silicon microchannels.

Figure 5 shows the comparison between the numerical results and the analytical values of the average fully developed Nusselt number for two rectangular channels with different values of the aspect ratio ($\beta=1$ and $\beta=0.5$). It is possible to note that the numerical results are in a good agreement with the analytical results of Morini and Spiga [38]; this comparison is considered as a benchmark for the numerical procedure followed in this paper.

In Fig. 6 the trends of the local Nusselt number along the perimeter of two trapezoidal microchannels having aspect ratio β equal to 1 (Fig. 6(a)) and 0.2 (Fig. 6(b)) with four heated sides are shown as a function of the Brinkman number. It is evident that the convective heat transfer coefficient presents strong variations along the perimeter of the microchannel; in particular, the value of the local Nusselt number approaches zero near the corners of the channels where the fluid tends to be stagnant. When the aspect ratio decreases the longer sides tend to be characterized by a more
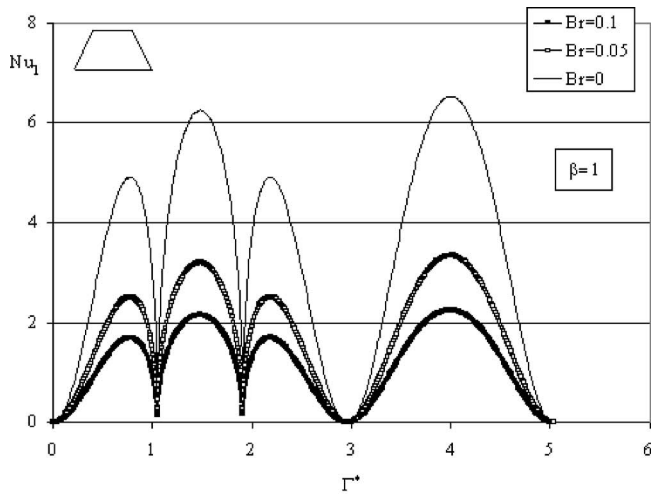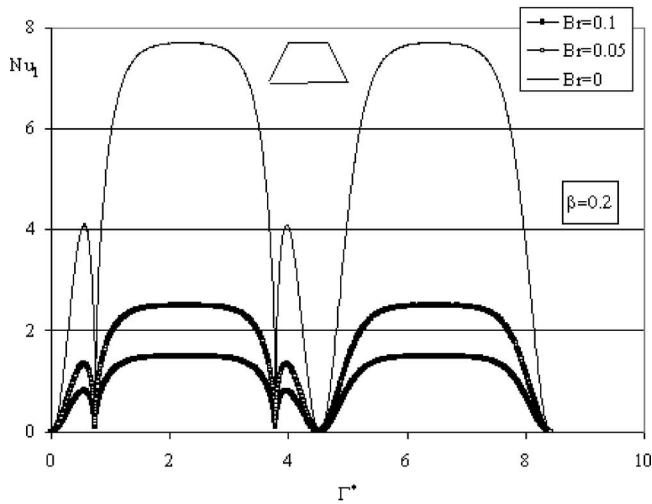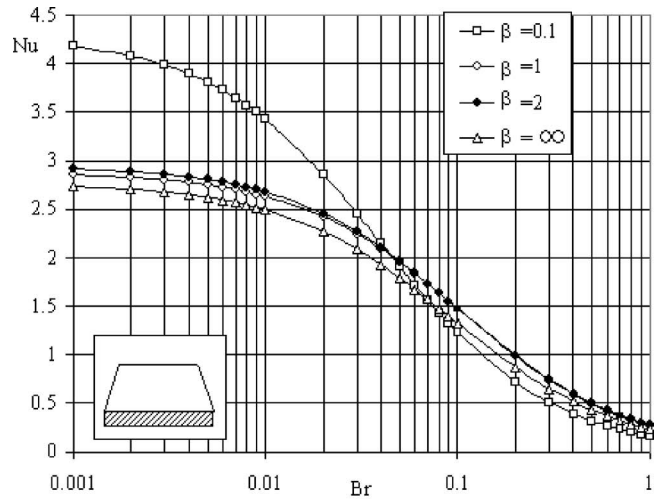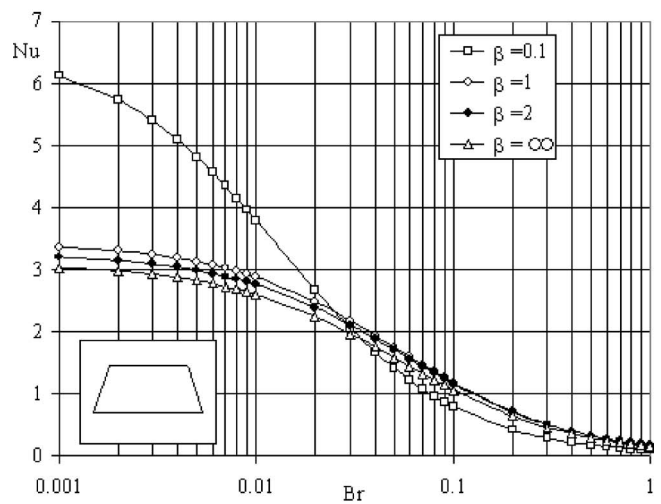
Fig. 6 Local Nusselt number along the perimeter of two trapezoidal microchannels with four heated sides for $\beta=1$ (a) and $\beta=0.2$ (b) as a function of the Brinkman number

Fig. 7 The average fully developed Nusselt number as a function of the Brinkman number for trapezoidal silicon microchannels with three (a) and four (b) sides heated

uniform value of the local convective heat transfer coefficient. Figure 6 puts in evidence the reduction of the local values of the Nusselt numbers when the Brinkman number increases; when the effect of the viscous forces is significant (Br>0.001) the local Nusselt numbers tend to decrease as an effect of the reduction of the temperature gradients at the walls due to the viscous internal heat production. In Figs. 7(a) and 7(b) the average fully developed Nusselt number is plotted as a function of the Brinkman number for trapezoidal silicon microchannels with three and four sides heated, respectively. Looking at Figs. 6 and 7 it is possible to note that in general the Nusselt number is higher for cross-sections having lower aspect ratios if the viscous dissipation is negligible (Br<0.001). For large Brinkman numbers this rule is reversed; in fact, for high Brinkman numbers the cross-sections with lower aspect ratios exhibit lower Nusselt numbers. For large Brinkman numbers the square microchannels have higher Nusselt numbers than the rectangular channels with very small aspect ratios. This confirms that the aspect ratio of the channels plays an important role in viscous dissipation as observed numerically by Koo and Kleinstreuer [30].

Morini and Spiga [38] demonstrated analytically that the link

between the average Nusselt number and Brinkman number can be expressed by means of this general relationship for circular and noncircular ducts:
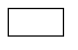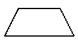
$$Nu = \frac{Nu_0}{1 + \sigma \, Br} \qquad (17)$$

where Nu_0 is the value of the Nusselt number when Br=0 (Nu_0 is quoted in Table 2 for the geometries considered in this paper) and σ is a parameter depending on the geometry of the channel cross-section and on the combination of heated and adiabatic sides of the channel.

In Table 3 the values assumed by σ for rectangular and trapezoidal microchannels having three and four sides heated, respectively, are listed. Using these data and Eq. (17) it is possible to calculate the value assumed by the fully developed Nusselt number as a function of the Brinkman number in KOH-etched silicon microchannels.

For the sake of completeness, it can be useful to remember that for circular microtubes with prescribed wall heat flux, the analytical value of σ is equal to $48\pi/11$ and the fully developed average Nusselt number (Nu_0) is equal to $48/11$ [39].

Table 3 Coeficients σ for rectangular and trapezoidal microchannels having three or four sides heated

β	σ			
	▭	⬭	▱ (bottom shaded)	▱ (shaded)
0.05	131.35	136.51	43.98	45.472
0.1	67.98	73.17	23.41	24.863
0.2	36.57	41.79	13.53	14.866
0.3	26.39	31.58	10.75	11.844
0.4	21.57	26.68	9.808	10.569
0.5	18.91	23.88	9.605	9.952
0.6	17.36	22.14	9.75	9.658
0.7	16.42	20.98	10.07	9.52
0.8	15.89	20.19	10.505	9.476
0.9	15.62	19.62	10.999	9.474
1	15.54	19.22	11.528	9.494
10/9	15.62	18.9	12.141	9.551
5/4	15.89	18.63	12.935	9.618
10/7	16.42	18.42	13.971	9.717
5/3	17.36	18.28	15.371	9.848
2	18.91	18.22	17.353	9.988
2.5	21.57	18.28	20.357	10.167
10/3	26.39	18.44	25.449	10.367
5	36.57	18.7	35.817	10.579
10	67.98	18.99	67.369	10.765
∞	–	19.15	–	10.864

(a)

(b)

Fig. 8 The average fully developed Nusselt number for microchannels with an uniform wall temperature with three (a) and four (b) sides heated as a function of the cross-section aspect ratio (β)

Uniform Wall Temperature Microchannels. In this section the temperature distribution in a silicon microchannel duct with a uniform temperature at the walls (T boundary condition) is obtained as a particular case of the solution for the H1 boundary condition. Considering Eqs. (13) and (14) the bulk temperature rise between the inlet and the outlet of a microchannel can be expressed as follows:

$$\Delta\theta_b = \Delta\theta_q(1 + \kappa) \tag{18}$$

It is possible to observe that the bulk temperature rise vanishes when κ is equal to -1. When this case occurs, the T boundary conditions is reached; in other words, there exists only one value of the Brinkman number compatible with the T boundary condition when viscous heating is taken into account:

$$Br_T = -\frac{1}{\Phi^*} = -\frac{1}{2\Omega^* f Re} \tag{19}$$

It is easy to demonstrate that Eq. (19) is consistent with the conclusion of Zanchini [39] for circular tubes, where $Br_T = -1/8\pi$. This analysis underlines that the T boundary condition can be considered as a particular case of an H1 thermal problem in which the heat flux at the wall is equal to the internal heat generation due to the viscous dissipation. The negative value of the Brinkman number Br_T remembers that, in the presence of the viscous dissipation, the uniform temperature at the walls can be maintained only by cooling the fluid (negative values of the heat flux at the wall). For trapezoidal and rectangular microchannels, the fully developed Nusselt number in the T boundary condition can be calculated by Eq. (17) by posing $Br = Br_T$. This fact underlines that for a microchannel with a uniform wall temperature for which the effects of the viscous dissipation are important, the fully developed Nusselt number becomes independent by the Brinkman number. By using Eqs. (17) and (19) it is worth noticing that:
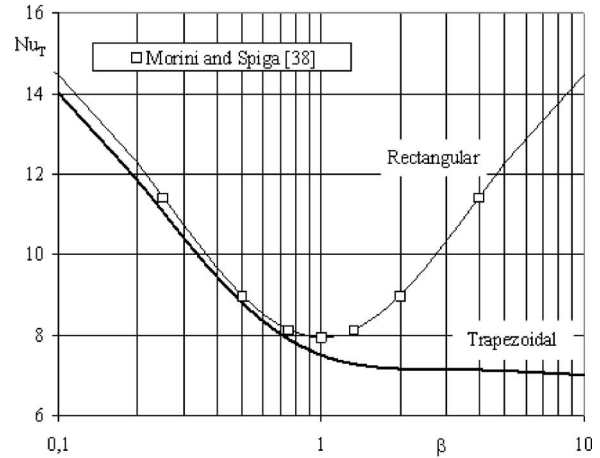
$$\frac{Nu_0}{Nu_T} = 1 - \frac{\sigma}{2\Omega^* f Re} \tag{20}$$

in which the average Nusselt number in the H1 thermal boundary condition obtained by neglecting the viscous dissipation (Nu_0) is related to the average Nusselt number in the T boundary condition with viscous dissipation (Nu_T) by means of the Poiseuille number ($f Re$) and the σ coefficient.

In Fig. 8 the values of the fully developed average Nusselt number in the T boundary condition with three sides heated (a) and with four sides heated (b) when the viscous dissipation is taken into account are shown as a function of the cross-section aspect ratio (β) for trapezoidal and rectangular microchannels. It is evident that for low aspect ratios the Nusselt numbers for rectangular and trapezoidal cross-sections tends to become equal. When the aspect ratio increases, the average Nusselt numbers for trapezoidal microchannels are lower than those for rectangular ones. In Fig. 8(b) a comparison between the numerical results obtained in the present work and the analytical values obtained by Morini and Spiga [38] by means of the technique of the finite integral transform for rectangular channels with four sides heated is made; the agreement is good and this fact can be considered an additional benchmark of the numerical results presented in this paper.
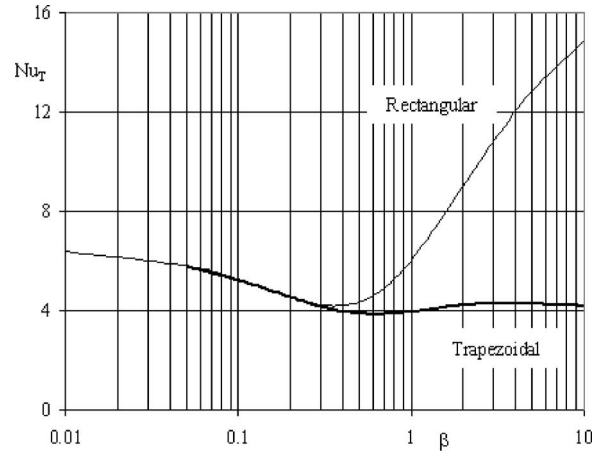
Area Goodness Factor Comparison. In order to compare the thermal performances of silicon micro-heat sinks with rectangular or trapezoidal microchannels it is possible to use the area goodness factor defined as follows:

$$\frac{j}{f} = \frac{Nu \, Pr^{-1/3}}{f Re} = \frac{1}{\Omega_{tot}^2}\left[\frac{Pr^{2/3} \, NTU \, \dot{m}^2}{2\rho\Delta p}\right] \tag{21}$$

This factor has been introduced by Shah and London [36] in order to compare different kinds of heat exchangers. A different perfor-

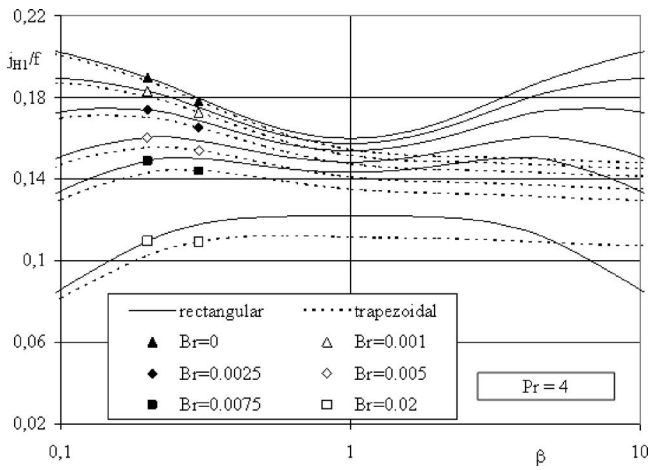**Fig. 9 The area goodness factor (j_{H1}/f) for rectangular and trapezoidal microchannels with four sides heated as a function of the aspect ratio**

Fig. 10 The area goodness factor (j_{H1}/f) for rectangular and trapezoidal microchannels with three sides heated as a function of the aspect ratio

mance evaluation technique has been introduced by Bejan [40] and used by Sekulic et al. [41] to compare the thermal performance of singly connected ducts by means of the evaluation of the entropy generation caused by finite temperature differences and by fluid friction. In this work the performances of silicon micro heat sinks are evaluated by using the area goodness factor (Eq. (21)).

From the first equality in Eq. (21) it is evident that this factor depends only on the Brinkman number for the fully developed laminar flow of a specified fluid. The second equality shows that the area goodness factor is inversely proportional to the square of the total flow area ($\Omega_{tot}=n\Omega$ with n equal to the number of microchannels) of the heat sink.

Since the dimensionless quantities j and f are independent of the scale of the geometry (D_h), the area goodness factor j/f for different microchannels represents the influence of the geometric factors on the pressure losses and the heat transfer.

In Fig. 9 the area goodness factor is shown as a function of the aspect ratio for rectangular and trapezoidal microchannels with four sides heated. It is evident that the rectangular microchannels give, in general, higher values of the area goodness factor; this fact means that the micro-heat sinks with rectangular microchannels are more compact than those with trapezoidal microchannels for a fixed value of the heat exchanged because they have a lower flow area.

If the viscous dissipation can be neglected ($Br\approx0$), when rectangular microchannels are employed very high (deep) or very low (shallow) values of the aspect ratio assure high values of the area goodness factor. On the contrary, for trapezoidal microchannels the j/f factor is maximum for low aspect ratio (shallow microchannels).

It is worth noting by Fig. 9 that when β is low the difference between the trapezoidal and rectangular geometries tends to vanish because the cross-sections tend to become similar to parallel plates. It is interesting to note that when the Brinkman number increases the area goodness factor reaches the maximum for intermediate values of the aspect ratio; the viscous effects tend to penalize the performances of the microchannel that are very shallow and/or very deep.

These conclusions are confirmed by Fig. 10 for microchannels with three sides heated. In this case for $Br=0$ the j/f factor is maximum for high values of the aspect ratio when rectangular microchannels are employed. For micro-heat sinks with trapezoidal microchannels, the j/f factor is always lower than for rectangular microchannels, but when the aspect ratio decreases this dif-
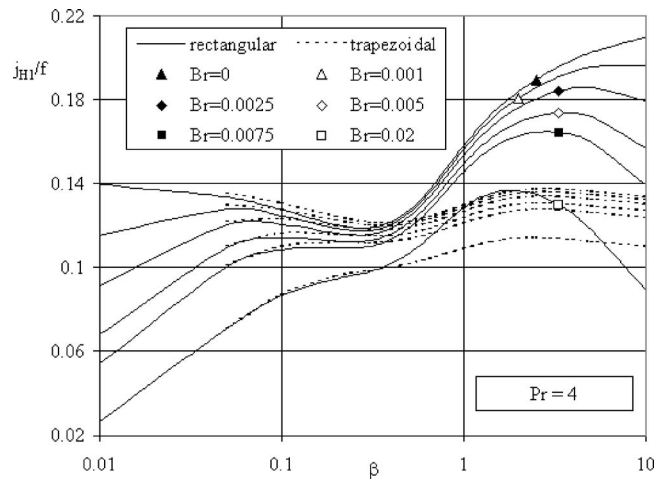
ference tends to vanish. In addition, Fig. 10 highlights that the dependence of the j/f factor on the aspect ratio is weak for trapezoidal cross-sections.

Finally, it is important to underline that the model presented here is valid under the hypothesis of thermophysical properties independent of the temperature. On the contrary, the variation with temperature, especially for the fluid viscosity, cannot be ignored, in particular for low Reynolds numbers when, for a prescribed wall heat flux, there is a strong temperature rise between the inlet and the outlet of the microchannel. Since the viscosity tends to decrease when the temperature increases, the viscous dissipation effects calculated by using the proposed constant properties model could be overestimated. For this reason in a future work the effect of the viscosity dependence on the temperature will be integrated in the model.

Conclusions

Often "unexpected experimental results" obtained by testing liquid flows through microchannels are associated to scaling effects and/or to the lack of accuracy in the experimental tests. In this work the effects of the viscous dissipation in heated microchannels are analyzed.

The main conclusions of this work can be summarized as follows:

- It has been shown that the fluid is of importance in establishing the exact limit of significance of viscous dissipation effects on the heat transfer coefficients. It has been demonstrated that for isopropanol viscous dissipation becomes important for microchannels having a hydraulic diameter less than 200 μm; on the contrary, for water this limit becomes 50 μm. A criterion to draw the limits of the significance of the viscous effects for any fluid has been suggested.

- It has been demonstrated that the aspect ratio of the microchannel, the Brinkman number, and the Reynolds number play an important role in determining the impact of the viscous dissipation on the Nusselt number. The viscous heating penalizes the heat transfer by reducing the value of the Nusselt number. A simple correlation between the Nusselt number and the Brinkman number has been proposed for the typical cross-sections of silicon microchannels.

- The area goodness factors for micro heat sinks with rectangular and trapezoidal microchannels have been computed as a function of the aspect ratio and of the Brinkman number in order to individuate the best geometry in terms of compact flow area. It has been demonstrated that the rectangular ge-

ometry guarantees higher j/f factors and that the Brinkman number influences the optimal value to assign to the aspect ratio.

In conclusion, it is important to stress that the numerical results presented in this paper demonstrate that the problem of enhancing the heat transfer in microdevices cannot be solved by indefinitely reducing the microchannel dimensions because the viscous dissipation effects shall offset the gains of high heat transfer coefficients associated with a reduction in the channel size.

Acknowledgment

Nomenclature

a, b = maximum and minimum width of the cross-section, m
Br = Brinkman number $(=\mu W^2/q_w)$
c_p = fluid specific heat, J kg^{-1} K^{-1}
c = height of the microchannel, m
D_h = hydraulic diameter of the duct $(=4\Gamma/\Omega)$, m
f = Fanning friction factor
h = convective heat transfer coefficient, W m^{-2} K^{-1}
j = Colburn number $(=\text{Nu Pr}^{-1/3}\text{Re}^{-1})$
L = microchannel length, m
$\dot{m}$ = mass flux, kg/s
Nu = Nusselt number $(=hD_h/\lambda)$
NTU = number of transfer units
p = pressure of the fluid in the duct, Pa
p^* = dimensionless pressure defined by Eq. (3)
Pe = Peclet number $(=\text{Re Pr})$
Pr = Prandtl number $(=\nu/\alpha)$
q_w = linear power (i.e., power per unit length), W m^{-1}
Re = Reynolds number $(=WD_h/\nu)$
T = dimensionless temperature defined by Eq. (3)
u = axial fluid velocity, m s^{-1}
V = dimensionless axial fluid velocity defined by Eq. (3)
W = fluid average velocity, m s^{-1}
x, y, z = dimensionless Cartesian coordinates
∇ = gradient operator

Greek Symbols

α = thermal diffusivity $(=\lambda/\rho c_p)$, m^2 s^{-1}
β = microchannel aspect ratio $(=c/b)$
ϕ = cross-section apex angle
Φ^* = dimensionless viscous-energy-dissipation function defined by Eq. (5)
Γ = wetted perimeter, m
Γ^* = dimensionless wetted perimeter defined by Eq. (3)
κ = parameter defined by Eq. (14)
λ = thermal conductivity, W m^{-1} K^{-1}
ν = kinematic viscosity, m^2 s^{-1}
μ = dynamic viscosity, kg m^{-1} s^{-1}
ρ = fluid density, kg m^{-3}
σ = parameter defined by Eq. (17)
θ = fluid temperature, K
Ω = cross-sectional area, m^2
Ω^* = dimensionless cross-sectional area defined by Eq. (3)
ξ, η, ζ = Cartesian coordinates, m

Subscripts

b = mixing cup (or bulk)
h = heated
in = inlet
l = local
tot = total
w = wall

References

[1] Morini, G. L., 2004, "Single-Phase Convective Heat Transfer in Microchannels: A Review of Experimental Results," Int. J. Therm. Sci., **43**, pp. 631–651.
[2] Wu, P., and Little, W. A., 1984, "Measurement of the Heat Transfer Characteristics of Gas Flow in Fine Channel Heat Exchangers Used for Microminiature Refrigerators," Cryogenics, **124**, pp. 415–420.
[3] Choi, S. B., Barron, R. F., and Warrington, R. O., 1991, "Fluid Flow and Heat Transfer in Microtubes," in Micromechanical Sensors, Actuators and Systems, ASME DSC 32, Atlanta, GA, pp. 123–134.
[4] Yu, D., Warrington, R. O., Barron, R., and Ameel, T., 1995, "An Experimental and Theoretical Investigation of Fluid Flow and Heat Transfer in Microtubes," Proc. ASME/JSME Thermal Eng. Joint Conf., Maui, pp. 523–530.
[5] Wang, B. X., and Peng, X. F., 1994, "Experimental Investigation on Liquid Forced-Convection Heat Transfer Through Microchannels," Int. J. Heat Mass Transfer, **37**(Suppl. 1), pp. 73–82.
[6] Peng, X. F., and Peterson, G. P., 1996, "Convective Heat Transfer and Flow Friction for Water Flow in Microchannel Structures," Int. J. Heat Mass Transfer, **39**, pp. 2599–2608.
[7] Nguyen, N. T., Bochnia, D., Kiehnscherrf, R., and Dözel, W., 1996, "Investigation of Forced Convection in Microfluid Systems," Sens. Actuators, A, **55**, pp. 49–55.
[8] Adams, T. M., Abdel-Khalik, S. I., Jeter, S. M., and Qureshi, Z. H., 1998, "An Experimental Investigation of Single-Phase Forced Convection in Microchannels," Int. J. Heat Mass Transfer, **41**, pp. 851–857.
[9] Wu, H. Y., and Cheng, P., 2003, "An Experimental Study of Convective Heat Transfer in Silicon Microchannels With Different Surface Conditions," Int. J. Heat Mass Transfer, **46**, pp. 2547–2556.
[10] Li, J., Peterson, G. P., and Cheng, P., 2004, "Three-Dimensional Analysis of Heat Transfer in a Micro-Heat Sink With Single Phase Flow," Int. J. Heat Mass Transfer, **47**, pp. 4215–4231.
[11] Kawano, K., Minakami, K., Iwasaki, H., and Ishizuka, M., 1998, "Development of Micro Channels Heat Exchanging, Application of Heat Transfer in Equipment, Systems and Education," ASME HTD-361, pp. 173–180.
[12] Qu, W., and Mudawar, I., 2002, "Analysis of Three-Dimensional Heat Transfer in Micro-Channel Heat Sinks," Int. J. Heat Mass Transfer, **45**, pp. 3973–3985.
[13] Fedorov, A. G., and Viskanta, R., 2000, "Three-Dimensional Conjugate Heat Transfer in the Microchannel Heat Sink for Electronic Packaging," Int. J. Heat Mass Transfer, **43**, pp. 399–415.
[14] Qu, W., Mala, G. M., and Li, D., 2000, "Heat Transfer for Water Flow in Trapezoidal Silicon Microchannels," Int. J. Heat Mass Transfer, **43**, pp. 3925–3936.
[15] Gao, P., Le Person, S., and Favre-Marinet, M., 2002, "Scale Effects on Hydrodynamics and Heat Transfer in Two-Dimensional Mini and Microchannels," Int. J. Therm. Sci., **41**, pp. 1017–1027.
[16] Lee, P. S., Garimella, S. V., and Liu, D., 2005, "Investigation of Heat Transfer in Rectangular Microchannels," Int. J. Heat Mass Transfer, **48**, pp. 1688–1704.
[17] Grohmann, S., 2005, "Measurements and Modeling of Single-Phase and Flow-Boiling Heat Transfer in Microtubes," Int. J. Heat Mass Transfer, **48**, pp. 4073–4089.
[18] Herwig, H., and Hausner, O., 2003, "Critical View on New Results in Micro-Fluid Mechanics: An Example," Int. J. Heat Mass Transfer, **46**, pp. 935–937.
[19] Guo, Z. Y., and Li, Z. X., 2003, "Size Effect on Single-Phase Channel Flow and Heat Transfer at Microscale," Int. J. Heat Fluid Flow, **24**, pp. 284–298.
[20] Richter, M., Woias, P., and Weiß, D., 1997, "Microchannels for Applications in Liquid Dosing and Flow-Rate Measurements," Sens. Actuators, A, **62**, pp. 480–483.
[21] Judy, J., Maynes, D., and Webb, B. W., 2002, "Characterization of Frictional Pressure Drop for Liquid Flows Through Microchannels," Int. J. Heat Mass Transfer, **45**, pp. 3477–3489.
[22] Toh, K., Chen, X., and Chai, J., 2002, "Numerical Computation of Fluid Flow and Heat Transfer in Microchannels," Int. J. Heat Mass Transfer, **45**, pp. 5133–5141.
[23] Sabry, M. N., 2000, "Scale Effects on Fluid Flow and Heat Transfer in Microchannels," IEEE Trans. Compon. Packag. Technol., **23**, pp. 562–567.
[24] Kandlikar, S. G., Joshi, S., and Tian, S., 2001, "Effect of Channel Roughness on Heat Transfer and Fluid Flow Characteristics at Low Reynolds Numbers in Small Diameter Tubes," *Proceedings of 35th National Heat Transfer Conference*, Anaheim, CA, Paper No. 12134.
[25] Celata, G. P., Cumo, M., Guglielmi, M., and Zummo, G., 2000, "Experimental Investigation of Hydraulic and Single Phase Heat Transfer in 0.130 mm Capillary Tube," *Proceedings of International Conference On Heat Transfer and Transport Phenomena in Microscale*, Banff, Canada, pp. 108–113.
[26] Croce, G., and D'Agaro, P., 2004, "Numerical Analysis of Roughness Effect on Microtube Heat Transfer," Superlattices Microstruct., **35**, pp. 601–616.
[27] Tso, C. P., and Mahulikar, S. P., 1998, "The Use of the Brinkman Number for Single Phase Forced Convective Heat Transfer in Microchannels," Int. J. Heat Mass Transfer, **41**, pp. 1759–1769.

[28] Tunc, G., and Bayazitoglu, Y., 2001, "Heat Transfer in Microtubes With Viscous Dissipation," Int. J. Heat Mass Transfer, **44**, pp. 2395–2403.

[29] Xu, B., Ooi, K. T., Mavriplis, C., and Zaghloul, M. E., 2003, "Evaluation of Viscous Dissipation in Liquid Flow in Microchannels," J. Micromech. Microeng., **13**, pp. 53–57.

[30] Koo, J., and Kleinstreuer, C., 2004, "Viscous Dissipation Effects in Microtubes and Microchannels," Int. J. Heat Mass Transfer, **47**, pp. 3159–2169.

[31] Morini, G. L., 2003, "Viscous Heating in Liquid Flows in Microchannels," Int. J. Heat Mass Transfer, **48**, pp. 3637–3647.

[32] Morini, G. L., 2005, "Viscous Dissipation as Scaling Effect for Liquid Flows in Microchannels," *Proc. 3rd ASME Int. Conf. Micro Minichannels ICMM05*, Toronto.

[33] Hetsroni, G., Mosyak, A., Pogrebnyak, E., and Yarin, L. P., 2005 "Flow and Heat Transfer in Microchannels," Int. J. Heat Mass Transfer, **48**, pp. 1982–1998.

[34] Shah, R. K., and London, A. L., 1974, "Thermal Boundary Conditions and Some Solutions for Laminar Duct Flow Forced Convection," ASME J. Heat Transfer, **96**, pp. 159–165.

[35] FLEXPDE™, 1999, Finite Element Software, PDE Solution Inc.

[36] Shah, R. K., and London, A. L., 1978, "Laminar Flow Forced Convection in Ducts," Adv. Heat Transfer, **14**, pp. 196–222.

[37] Morini, G. L., 2000, "Analytical Determination of the Temperature Distribution and Nusselt Numbers in Rectangular Ducts with Constant Axial Heat Flux," Int. J. Heat Mass Transfer, **43**, pp. 741–755.

[38] Morini, G. L., and Spiga, M., 1999, "Nusselt Numbers in Rectangular Ducts With Viscous Dissipation," ASME J. Heat Transfer, **121**, pp. 1083–1087.

[39] Zanchini, E., 1997, "Effect of Viscous Dissipation on the Asymptotic Behaviour of Laminar Forced Convection in Circular Tubes," Int. J. Heat Mass Transfer, **40**, pp. 169–178.

[40] Bejan, A., 1978, "General Criterion for Rating Heat-Exchanger Performance," Int. J. Heat Mass Transfer, **21**, pp. 655–658.

[41] Sekulic, D. P., Campo, A., and Morales, J. C., 1997, "Irreversibility Phenomena Associated With Heat Transfer and Fluid Friction in Laminar Flows Through Singly Connected Ducts," Int. J. Heat Mass Transfer, **40**, pp. 905–914.

Convection Heat Transfer in Microchannels With High Speed Gas Flow

Stephen E. Turner
Naval Undersea Warfare Center,
Newport, RI 02841
e-mail: turnerse@npt.nuwc.navy.mil

Yutaka Asako
Tokyo Metropolitan University,
Tokyo, 1920397, Japan
e-mail: asako@ecomp.metro-u.ac.jp

Mohammad Faghri[1]
University of Rhode Island,
Kingston, RI 02881
e-mail: faghri@egr.uri.edu

This paper presents an experimental investigation of convective heat transfer for laminar gas flow through a microchannel. A test stand was set up to impose thermal boundary conditions of constant temperature gradient along the microchannel length. Additionally, thin film temperature sensors were developed and used to directly measure the microchannel surface temperature. Heat transfer experiments were conducted with laminar nitrogen gas flow, in which the outlet Ma was between 0.10 and 0.42. The experimental measurements of inlet and outlet gas temperature and the microchannel wall temperature were used to validate a two-dimensional numerical model for gaseous flow in microchannel. The model was then used to determine local values of Ma, Re, and Nu. The numerical results show that after the entrance region, Nu approaches 8.23, the fully developed value of Nu for incompressible flow for constant wall heat flux if Nu is defined based on $(T_w - T_{ref})$ and plotted as a function of the new dimensionless axial length, $X^* = (x/2H)(\text{Ma}^2)/(\text{Re Pr})$. [DOI: 10.1115/1.2426358]

Keywords: experimental, heat transfer, microscale, sensors, thin films

Introduction

Flow and heat transfer through microchannels have been investigated during the last 20 years to determine if the small characteristic length causes deviation from continuum flow behavior. Early research by Tuckermann and Pease [1] showed that laminar flow of water through a microchannel heat exchanger could dissipate up to 790 W/cm^2, a heat flux that is generally achieved only with boiling liquids.

Peiyi and Little [2] fabricated counterflow heat exchangers in glass wafers. The flow loop consisted of parallel channels of height 89–97 μm and width 312–572 μm spaced 281–472 μm apart. For Reynolds numbers less than 2200, Peiyi and Little compared their measurements of Nusselt number with an empirical relation for fully developed laminar flow through smooth tubes with little agreement.

Choi et al. [3] conducted experiments to study convection heat transfer in constant temperature glass microtubes. For laminar flow, the measured Nusselt number was found to increase with increasing Reynolds number over the range 0.1–7.

Peng et al. [4] and Peng and Peterson [5] measured the heat transfer coefficient for the flow of water and methanol through microchannels of rectangular cross section with hydraulic diameters ranging from 0.133 to 0.343 mm. Their data for laminar flow with constant wall heat flux indicates that the Nusselt number increases as the Reynolds number increases.

Fulin and Scaringe [6] conducted an analysis of three heat exchangers etched into silicon wafers. Each heat exchanger consisted of a common inlet and outlet connected by 12 parallel microchannels of 1 mm width, 48 mm length, and 2 mm spacing. Experiments were conducted with water yielding Reynolds numbers between 800 and 3500. Nusselt numbers between 9 and 12 were reported by the researchers for laminar flow.

Jiang et al. [7] have fabricated resistance temperature sensors on the backside of a silicon microchannel wafer (phosphorous implantation). While the temperature sensors are external to the microchannel, they represent an integrated approach to local temperature measurement for microchannel systems.

Recently, microchannels have been fabricated for two phase flow experiments having a nearly constant heat flux boundary condition and local resistance temperature sensors [8]. A single boron resistor was ion implanted along the heated length of the microchannel on the outside surface of the silicon wafer. By measuring the current flowing through the entire resistor and the voltage drop across nine segments of the resistor, the local resistance could be calculated. The local temperature along the resistor was determined from calibration curves obtained for each resistor segment. The resistance temperature sensors were found to have an uncertainty of ±3 °C.

The influence of rarefaction on the Nusselt number has been studied by Hadjiconstantinou [9] and Hadjiconstantinou and Simek [10] for gas flow between parallel flat plates. Their analysis shows a decrease in Nu as Kn increases, for both constant wall heat flux and constant wall temperature boundary conditions.

There have been very few experimental efforts to measure the Nusselt number for gas flow through microchannels. In the experiments referenced above, the microchannel wall temperature was not measured directly and there was no capability for fluid temperature measurement along the microchannel. Further, the author is not aware of any experimental investigation of the influence of compressibility on Nusselt number for laminar internal flow. Neither has the author found any analytical treatment of combined friction and heat transfer for internal compressible flow.

Therefore, an experimental investigation was undertaken to benchmark the friction factor for laminar, compressible flow of gas through microchannels of rectangular cross section. A systematic set of experiments was conducted to independently show the influence of rarefaction, compressibility, and surface roughness on the friction factor for isothermal wall conditions. This work is reported by Turner et al. [11–13] and Asako et al. [14]. The present investigation is a continuation of this work which is focused on heat transfer for laminar gas flow through channels of constant cross-section area. The objectives were to: (1) develop temperature sensors for direct temperature measurement of the microchannel surface; (2) apply thermal boundary conditions
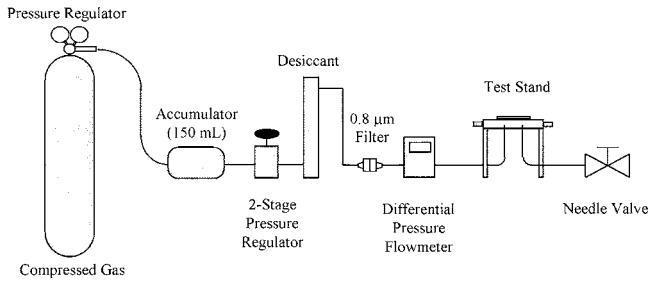
Fig. 1 Test stand for microchannel heat transfer experiment

which would result in the microchannel surface having a constant temperature gradient along the length; and (3) determine the effect of compressibility on the Nusselt number for gas flow in micro-channels.

Heat Transfer Experiment

To accomplish the objectives, a single microchannel of 981 μm width $\times$ 50.47 μm height $\times$ 25.0 mm length was fabricated on a silicon wafer. The channel width to height ratio was close to 20 so that the angled sidewalls could be neglected. The reported width was measured at the half-height of the channel. Nine thin-film resistance temperature sensors (RTDs) were deposited onto the surface of the microchannel (at the bottom of the etched silicon) for direct temperature measurement along the channel length. The microchannel has a smooth relative surface roughness, ε/H =0.00044, and the Knudsen number was within the range $0.0002 < \text{Kn} < 0.002$ for all the tests. In this way the test data was isolated from the effects of surface roughness or rarefaction, so that the influence of compressibility could be observed.

The two limiting heat transfer problems for internal flows are constant wall temperature and constant wall heat flux boundary condition. For the case of constant wall temperature, the fluid temperature asymptotically approaches the wall temperature. For constant wall heat flux, the fluid temperature increases with a constant temperature gradient along the channel length. As the hydraulic diameter of the channel decreases, the convection heat transfer coefficient (htc) increases. Preliminary calculations showed that for a microchannel with constant wall temperature and large htc, the fluid temperature becomes nearly equal to the wall temperature just downstream of the inlet. It was predicted that the exit fluid temperature would be equal to the wall temperature for all the laminar flow cases, so without local fluid temperature measurement capability, the experiment would yield little information. For the case of constant wall heat flux, both the wall and fluid temperatures are increasing along the channel length. The difference between the wall and bulk fluid temperature are expected to be dependent on the flow conditions and heat flux.

For fully developed incompressible flow, constant heat flux boundary conditions are manifested by a constant temperature gradient of both the wall temperature and the bulk gas temperature. In this investigation, constant wall heat flux boundary conditions were attempted by setting the microchannel wall temperature gradient to a constant along the axis.

A schematic of the test stand is shown in Fig. 1. Experiments were conducted with pressurized nitrogen at the inlet. A needle valve was placed downstream of the microchannel exit to raise the outlet pressure above atmospheric pressure. The manifold shown in Fig. 2 was built to interface the microchannel test section with the required instrumentation and to provide the desired thermal wall conditions.

The heat transfer manifold was fabricated from a low thermal conductivity plastic. The test section was placed with the glass side against the insulating manifold. A 12.5-mm-thick aluminum plate was held against the backside of the silicon and a 12.5-mm-thick acrylic plate covered the aluminum plate. The aluminum
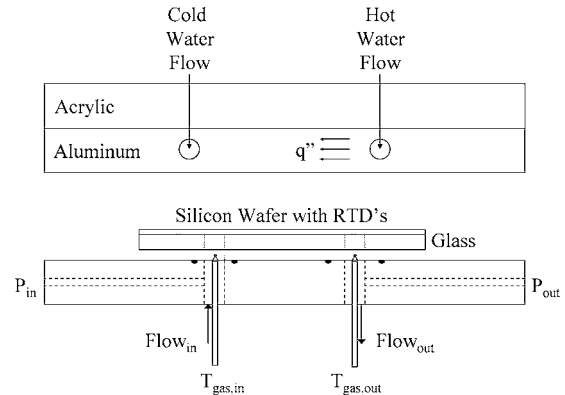

Fig. 2 Schematic of the heat transfer manifold, instrumentation, and boundary condition control

plate served as the wafer retainer and the temperature control for the microchannel. A temperature gradient was imposed in the aluminum plate by passing 18–20°C water through one channel and 90°C water through the other channel. A distance of 50.8 mm separates the parallel channels. The acrylic plate insulated the top side of the aluminum plate and the manifold insulated the bottom side of the test section. As a result, a linear temperature distribution was set up in the aluminum plate and the test section between the two water channels. There is close thermal contact between the silicon wafer and the aluminum plate, so the test section takes on the same temperature distribution as the aluminum plate.

Instrumentation. The gas pressure at the microchannel inlet and outlet was measured with Omega PX811 pressure transducers. The fluid temperature was measured at the microchannel inlet and outlet as shown in Fig. 2. The sensors were bare wire type-T thermocouples having a wire diameter of 25.4 μm and a junction diameter of approximately 76 μm. Each bare wire thermocouple was threaded through a 1.7-mm-diameter ceramic tube that has two holes in it. It was found that conduction losses through the wires away from the junction were significant compared to the heat convected to the junction from the heated gas flowing out of the microchannel. Therefore, a guard heater was mounted to the fitting underneath the manifold through which the ceramic tube passes. The guard heater raised the temperature of the thermocouple wires passing through the ceramic tubes, preventing conduction losses from the thermocouple junction.

Test Section Fabrication. The test section consists of a 100-mm-diameter silicon wafer, in which a single microchannel and 18 side channels were etched to a nominal depth of 50 μm. Thin-film resistors and leads were sputter deposited into the microchannel and side channels. Then a glass plate was anodically bonded to the silicon wafer. The thin-film leads extend past the edge of the glass where they are connected to data acquisition wires. A photo of a completed test section is shown in Fig. 3.

The microchannel and side channels were patterned onto a (100) silicon wafer using a standard photolithography process. The channels were wet etched into the silicon using KOH. The etching was followed by thermal oxidation in an 1100°C furnace to grow a thin layer of silicon dioxide on the bare silicon surfaces. A second photolithography process was conducted by spin coating a layer of polyimide liftoff resist (LOR) followed by positive photoresist. A second photomask, with the RTD pattern, was aligned with the first microchannel pattern and exposed to broadband ultraviolet (UV) light. After development and oxygen plasma cleaning, a 0.02-μm-thick (approximate) layer of chromium was sputtered onto the wafer, followed by a 0.9 μm layer of platinum 10% rhodium. The chromium layer was necessary to promote adhesion of the platinum alloy to the silicon dioxide surface. The liftoff process was conducted in an ultrasonic bath to remove all metal
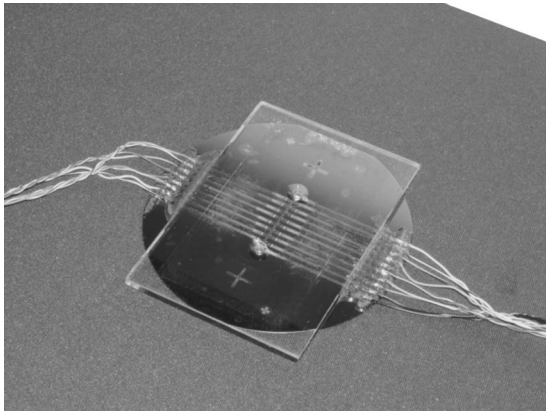
Fig. 3 Microchannel test section with nine thin film RTDs

except for the RTDs and leads. At this point in the fabrication process, the silicon wafer has channels etched to a depth of approximately 50 μm; the bottom of the channels has the thin film RTD pattern of less than 1 μm thickness. Figure 4 shows a cross-section view of test section, in which the thin film location is at the bottom of the etched channels. A top view shows the serpentine pattern of each RTD. The line width of each RTD in the microchannel is 100 μm and the penetration through the microchannel side wall is 150 μm for each side channel. Outside of the microchannel, the side channel line width is increased to 1000 μm to decrease the electrical resistance of the leads.

The next step in the fabrication process was to characterize the microchannel dimensions. This was accomplished with a Sloan Dektak IIA mechanical profiling machine. Prior to measuring the microchannel dimensions, the Dektak was calibrated with a 10 μm NIST traceable calibration standard. Then, ten cross-section scans were obtained to give the average channel depth, surface roughness, and width. After characterization of the microchannel, a glass plate was bonded to the silicon wafer. The 70 mm $\times$ 100 mm $\times$ 3.175 mm glass plate had two holes drilled through it (4.76 mm diameter, 30 mm apart) to mate with the inlet and exit ports of the microchannel. The glass plate was bonded to the silicon wafer using an anodic bonding process at an approximate temperature of 400°C and 3 kV. After bonding the glass plate, the test section was subjected to a thermal annealing process of 500°C for 10 h in a furnace. The purpose of the annealing step was to remove dislocations from the thin films, which had the effect of increasing the thermal coefficient of resistance (TCR) and stabilizing the RTDs.

The platinum alloy in the side channels extends past the edge of

the glass plate for connection with data acquisition wires. A 1 μm layer of copper was sputtered onto the platinum alloy to enable soldering of the wires to the thin film leads. The electrical continuity of each RTD was tested through the wires to verify the connections. The wires were secured to the silicon wafer with epoxy to prevent the soldered connection from snapping off. The side channels were also sealed with epoxy where they pass underneath the edge of the glass plate. A vacuum was applied to the microchannel ports to draw the epoxy into the side channels. The last step was a low temperature annealing process at 100–120°C for 10 h to stabilize the electrical connection at the interfaces of the platinum alloy and copper, and between the copper and solder.

RTD Calibration. Calibration was conducted on the heat transfer manifold. The plumbing was reconfigured so that the hot water from the circulation bath flowed through both ports in the aluminum plate. Since the aluminum and silicon have high thermal conductivity and the aluminum plate and test section are insulated all around, the temperature along the channel length was uniform. The RTDs were calibrated against three type-T thermocouples mounted on the back side of the silicon wafer at locations corresponding to the inlet, midchannel, and outlet. The thermocouples were the thin foil type with 12.5 μm thickness, and were made of special limits of error wire having an uncertainty of ±0.5°C. A conduction analysis indicated that for the calibration process, the maximum temperature difference through the thickness of the silicon (between the thermocouples and RTDs) would be 0.01°C. The calibration process consisted of setting the circulation bath temperature, waiting for steady conditions, and recording the resistance of each RTD and the three thermocouple temperatures.

The TCR for each RTD was determined by plotting the temperature against the RTD resistance, and calculating a best fit linear expression to the data. The TCR is calculated from the slope of the curve and the resistance at a reference temperature

$$\text{TCR} = \left(\frac{1}{R(T_{\text{ref}})}\right)\frac{R(T) - R(T_{\text{ref}})}{T - T_{\text{ref}}} \tag{1}$$

By rearranging Eq. (1), the resistance of an RTD is related to its temperature

$$R(T) = R(T_{\text{ref}})[1 + \text{TCR}(T - T_{\text{ref}})] \tag{2}$$

A calibration curve for RTD 1 is shown in Fig. 5. In this figure, the average temperature of the three thermocouples is plotted against the measured resistance of the RTD. The three thermocouple readings were all within 0.5°C of each other. The figure shows that the correlation coefficient, R^2, is nearly unity, which indicates that the TCR is a constant over the 30–90°C temperature range of the calibration. The TCR for each RTD is listed in Table 1 along with the resistance at the reference temperature of
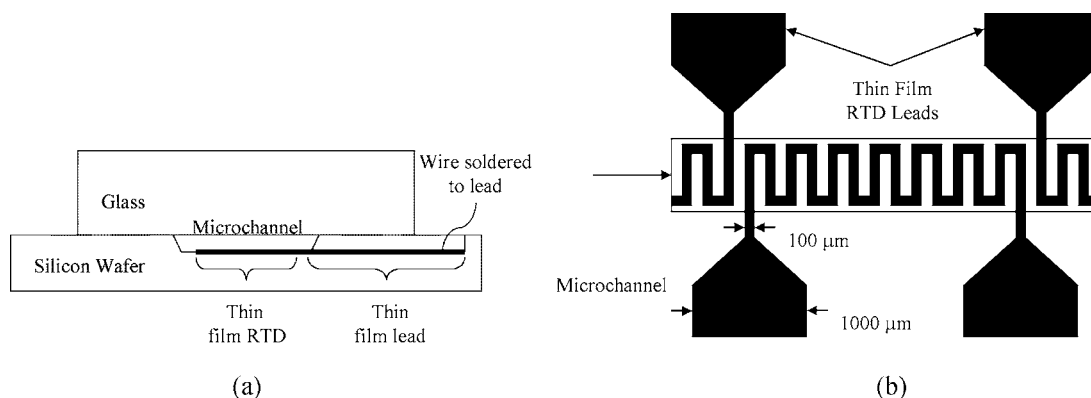

(a)

(b)

Fig. 4 Thin film RTD concept: (*a*) cross-section view showing the side leads sputtered at microchannel depth; and (*b*) top view showing the resistor pattern and the relative size of the resistors and leads
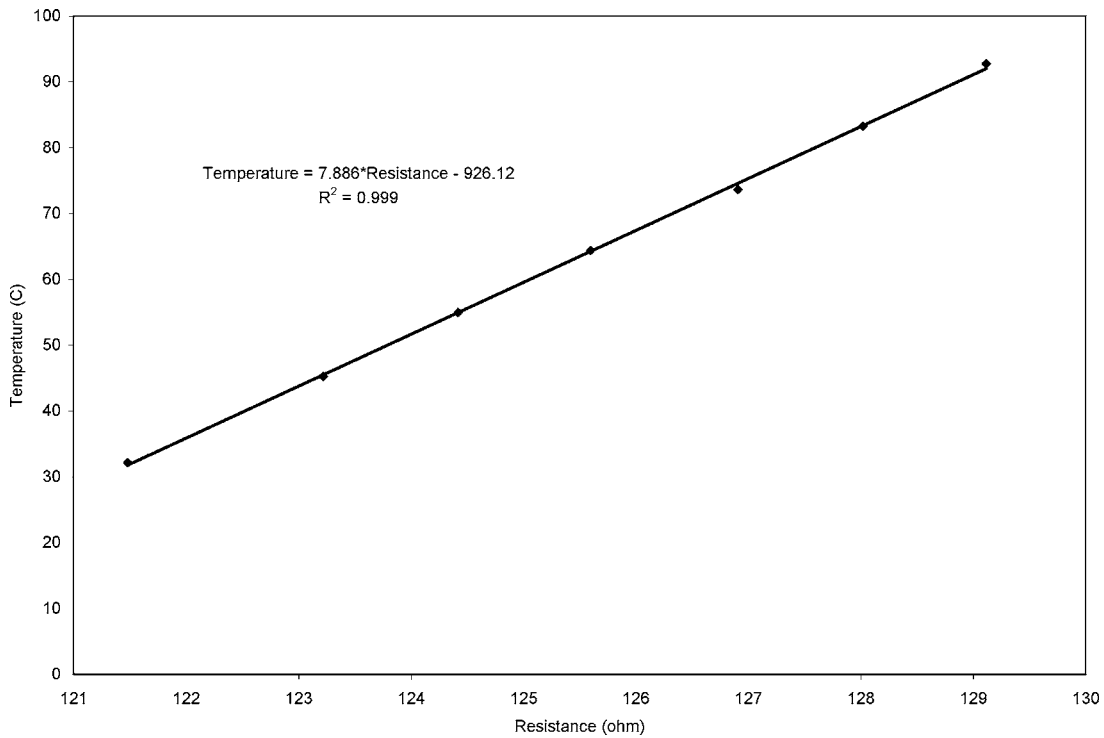
Fig. 5 Calibration data and linear curve fit for RTD 1

30°C, the location of the RTD with respect to the microchannel inlet, and the correlation coefficient.

Experimental Data

The thermal boundary conditions for the heat transfer experiments were set up by flowing hot water (90°C) and cold water (18–20°C) through the passages of an aluminum plate. The result was a constant temperature gradient in the microchannel test section. The dimensions of the microchannel test section with the thin film RTDs were 50.47 μm height $\times$981 μm width $\times$25.03 mm length. The center to center spacing of the RTDs was 3.20 mm and the average RTD thickness was 0.94 μm. The true length of the microchannel is measured as the minimum distance between the two holes in the glass cap. The center of the first thin film RTD is in the microchannel inlet port at the position $x=-0.225$ mm from the inlet.

Experiments were conducted by mounting the microchannel test section into the manifold, setting the hot and cold water temperatures, and setting the inlet gas pressure. A metering valve located downstream of the test section was adjusted until the desired downstream pressure was achieved. After steady conditions were established, the inlet and outlet pressure and temperature

were measured along with the flowrate and the resistance of each RTD. A typical wall temperature distribution measured by the thin film RTDs is shown in Fig. 6. A linear curve fit of the nine RTD measurements indicates that the wall temperature gradient was $dT_w/dx=820$°C/m. RTDs 2 and 3 have some minor deviation from the straight line, but overall $dT_w/dx=$ constant and the correlation coefficient, R^2, is very close to unity. With respect to measurement uncertainty, it is important to note that the wall temperature gradient is described by all nine RTDs rather than a small temperature difference measured between two adjacent RTDs. The gas temperature measured at the outlet is assumed to be the stagnation temperature and U is the cross-section averaged velocity

$$T_{stg} = T_{bulk} + \frac{U^2}{2C_p} \qquad (3)$$

The exit port of the microchannel has a cross-section area that is over 600 times greater than the microchannel cross-section area.

Fig. 6 Microchannel wall temperature measured by thin film RTDs

Table 1 RTD location and calibration

RTD	x (mm)	R (T_{ref})	TCR (1/C)	R^2
1	−0.225	121.199	1.044×10^{-3}	0.999
2	2.975	112.184	1.010×10^{-3}	0.999
3	6.175	114.269	1.004×10^{-3}	0.999
4	9.375	116.373	1.013×10^{-3}	0.999
5	12.575	114.883	0.992×10^{-3}	0.999
6	15.775	119.041	1.036×10^{-3}	1.000
7	18.975	119.119	1.011×10^{-3}	0.999
8	22.175	118.700	1.059×10^{-3}	0.999
9	25.375	120.565	1.113×10^{-3}	0.999

Table 2 Measured data for ten heat transfer tests

Ex. No.	P_{in} (kPa)	P_{out} (kPa)	$T_{gas,in}$ (K)	$T_{gas,out}$ (K)	$T_{w,in}$ (K)	$T_{w,out}$ (K)	Mass flow (kg/s)
1	234	101	308.1	341.7	322.2	342.7	4.912E-6
2	306	102	305.8	341.8	321.9	342.5	7.856E-6
3	312	196	307.5	342.0	322.7	343.0	5.921E-6
4	380	240	306.5	341.8	322.5	342.9	8.435E-6
5	448	288	305.5	341.3	322.4	342.7	1.113E-5
6	523	354	306.1	341.4	322.8	342.9	1.390E-5
7	589	439	305.4	341.2	322.7	343.0	1.461E-5
8	656	495	304.4	340.8	322.6	342.8	1.724E-5
9	525	425	306.4	342.0	322.9	343.3	9.529E-6
10	523	285	305.0	341.3	322.7	342.9	1.700E-5

Fig. 7 Velocity distribution for Test 9; both walls heated, $Re_{out}=915$, $Ma_{out}=0.12$

The thermocouple at the exit is positioned in the exit port where the gas velocity has effectively been reduced to zero.

After setting the wall temperature gradient with the hot and cold water, heat transfer tests were conducted at ten different gas flow conditions. It was found that the Mach number becomes large at the microchannel outlet when the exit was maintained at atmospheric pressure. A needle valve was installed downstream of the microchannel to control the microchannel outlet pressure. By controlling the inlet and outlet pressures, the Reynolds number, $Re=G^*D_h/\mu$, was varied independent of the Mach number. The mass flux, G, was determined by the volumetric flowrate, the density at the flowmeter, and the cross-section area of the microchannel, while the viscosity, μ, was evaluated at the local film temperature. For the ten flow conditions tested, the outlet Reynolds number was in the range $473<Re<1657$ and the outlet Mach number was in the range $0.12<Ma<0.42$. Summary data for each test are provided in Tables 2 and 3. For ease of comparison with analysis, the temperature is given in degrees Kelvin. The uncertainty of the temperature measurement at the inlet and outlet is 0.5 K.

Comparison of Experimental Data With a 2D Model. The thin film RTDs have enabled direct measurement of the microchannel wall temperature. Experiments were conducted at ten different flow conditions in which the volumetric flowrate, the inlet and outlet fluid temperature and pressure, and the microchannel wall temperature were measured. At the present time, it is not possible to measure the gas temperature within the microchannel, so measured fluid data are limited to the inlet and outlet. To better understand the gas temperature as is flows through the microchannel, a two-dimensional (2D) numerical model was developed. The model uses the experimental measurements of inlet fluid temperature and pressure, wall temperature, and the outlet fluid pressure and flowrate to predict the temperature profile of the fluid along the channel length. The model was validated by comparing the predicted fluid temperature at the microchannel outlet to the measured fluid temperature.

2D Compressible Model. The two-dimensional model is based on the arbitrary Lagrangian–Eulerian (ALE) method. The geom-etry is assumed to be flow between parallel flat plates. The 2D plane is divided into quadrilateral cells: 200 along the microchannel length and 20 through the height. Additional details of the 2D model formulation are available [15]. The velocity boundary conditions were zero velocity at the microchannel wall. Two sets of thermal boundary conditions were considered: both walls heated; and one wall heated, one wall insulated. The results for these two limiting boundary conditions provide a bound for the experimental data. The model input included the inlet temperature and pressure, the outlet pressure, mass flowrate, and the microchannel wall temperature to calculate the bulk and stagnation temperature along the microchannel length.

First the model was compared against data for Test 9, which had the lowest Mach number at the outlet (see Table 3). The velocity profiles are plotted in Fig. 7 for several cross sections along the microchannel length. At the inlet, the velocity profile is uniform in the y direction. The velocity vector includes a y direction component during the first 3 mm as the no slip boundary condition is imposed at the wall and the velocity becomes fully developed. The velocity profile remains fully developed along the entire microchannel length until reaching the outlet. A contour plot of the gas temperature is shown in Fig. 8 for the case of both walls heated. The gas temperature at the upper and lower walls takes on the prescribed temperature of the wall. The contours show that for a given distance, x, along the channel, the gas temperature is a minimum at the centerline where the velocity is a maximum. The difference between the wall temperature and the centerline temperature increases for x close to the outlet (as the velocity increases). The predicted bulk temperature and the stagnation temperature for Test 9 are plotted in Fig. 9 for the thermal boundary conditions of two sides heated. The measured wall temperature and the measured inlet and outlet gas temperatures are also plotted in the figure. At the entrance, the bulk and stagnation temperatures are the same since the velocity is small. As heat is transferred to the gas, the gas expands and accelerates along the microchannel length. The velocity increase causes some of the thermal energy to be converted to kinetic energy. At the channel outlet the difference between the stagnation temperature and the bulk temperature is 1.74 K. The difference between the predicted and measured stagnation temperature at the outlet is 0.35 K.

The two-dimensional model of Test 9 was also solved for the thermal boundary conditions of one side heated, one side insulated. A contour plot of the gas temperature is shown in Fig. 10. The upper wall is the insulated surface with $dT/dy=0$ and the lower wall has the prescribed temperature gradient, dT_w/dx =constant. From this contour plot it is seen that to support the conditions of one side heated, one side insulated, the temperature difference between the walls is on the order of 10 K. Although the thin film RTDs were not located on the glass surface of the microchannel, a thin foil thermocouple was positioned on the exter-

Table 3 Calculated parameters for ten heat transfer tests

Ex. No.	Re_{out}	Ma_{out}
1	473	0.26
2	756	0.42
3	569	0.16
4	811	0.19
5	1071	0.21
6	1336	0.21
7	1405	0.18
8	1657	0.19
9	915	0.12
10	1635	0.32
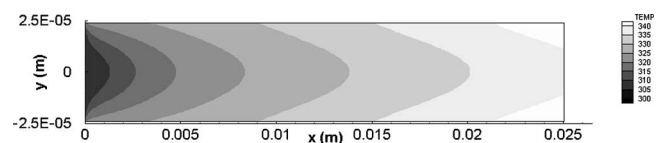
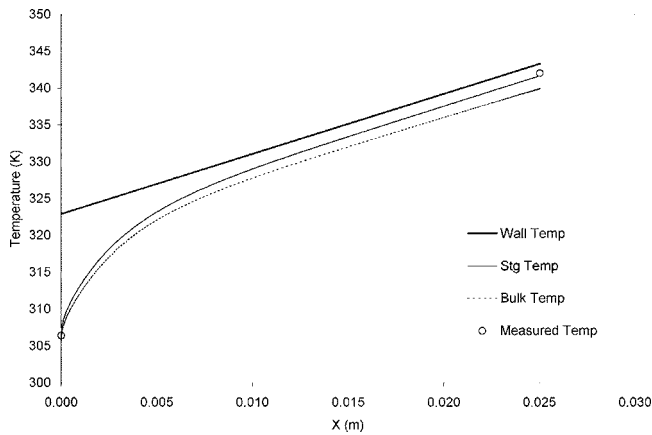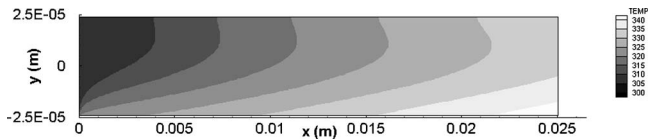**Fig. 8 Gas temperature contours for Test 9; both walls heated, $Re_{out}=915$, $Ma_{out}=0.12$**

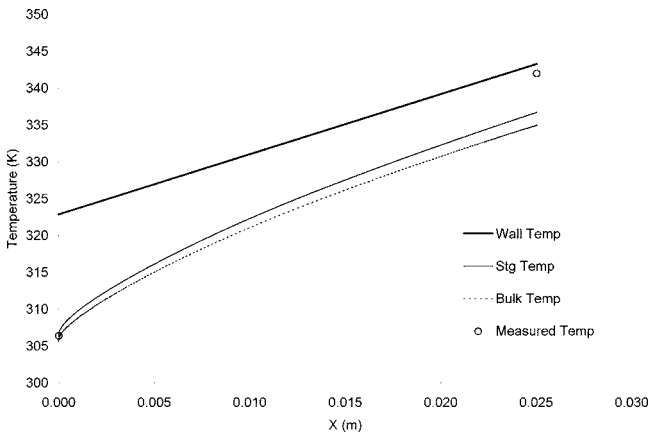**Fig. 9 Two-dimensional model prediction of stagnation and bulk temperatures for Test 9; both walls heated, $Re_{out}=915$, $Ma_{out}=0.12$**

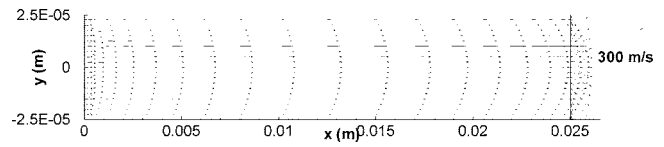**Fig. 12 Velocity profiles for Test 10; both sides heated, $Re_{out}=1635$, $Ma_{out}=0.32$**

nal surface of the glass at $x=12.5$ mm. The measured difference between the external surface of the glass and the silicon surface of the microchannel was 3.5 K. Since the glass has a low thermal conductivity and a thickness of 3.175 mm, the temperature of the glass surface of the microchannel is expected to be close to the silicon surface temperature. The predicted temperatures for Test 9 are shown in Fig. 11. For the one side heated case, the difference between the stagnation and bulk temperatures is still 1.74 K, however, the predicted stagnation temperature is 6.67 K below the measured total temperature. The analysis of both boundary condition cases indicates that the experiment is closely represented by the two sides heated boundary condition model.

The two-dimensional model was also compared to test data for the higher Mach number flow of test 10 (Ma=0.32). Velocity profiles are plotted at several cross sections along the microchannel length in Fig. 12. In this figure, the entrance length is seen to be about 3 mm since the y direction velocity is not present after x

=3 mm. The gas temperature contour for the case of two sides heated for Test 10 is shown in Fig. 13. This figure clearly illustrates the enhanced temperature gradient in the y direction due to the higher velocity. The gas temperature at the centerline of the channel is 15–20 K less than the wall temperature. The figure also previews the challenge of local gas temperature measurement. Precise control of the sensor location in the y direction will be necessary to resolve the temperature gradient. The predictions of bulk and stagnation temperature for the two sides heated case are presented in Fig. 14. For Test 10, the average velocity increases from 59 to 119 m/s along the channel. The model predicts the difference between the stagnation and bulk temperatures to be 11.4 K. The predicted stagnation temperature at the exit was found to be within 0.1 K of the measured temperature.

The model also predicts the temperature profile for the case of one side heated, one side insulated. A contour plot of the gas temperature is shown in Fig. 15. From this figure it is seen that for a given cross section the gas temperature at the insulated surface is 15–20 K less than at the heated surface. At the outlet this difference is greater than 20 K. At $x=12.5$ mm, the temperature measured on the external surface of the glass was 329.0 K. The microchannel wall temperature measured by the thin-film RTDs at $x=12.5$ mm was 332.8 K. This difference of 3.8 K is across the microchannel and the thickness of the glass. The temperature difference between the two surfaces of the microchannel is not 15–20 K.

The predicted bulk and stagnation temperatures are plotted in Fig. 16 along with the measured wall temperature and the gas temperature at the inlet and outlet. As the Mach number increases
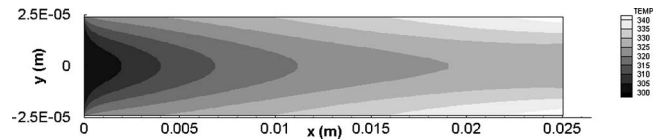

Fig. 10 Gas temperature contours for Test 9; one side heated, $Re_{out}=915$, $Ma_{out}=0.12$

Fig. 13 Gas temperature contour for Test 10; both sides heated, $Re_{out}=1635$, $Ma_{out}=0.32$

Fig. 11 Two-dimensional model prediction of stagnation and bulk temperatures for Test 9; one wall heated, one insulated, $Re_{out}=915$, $Ma_{out}=0.12$
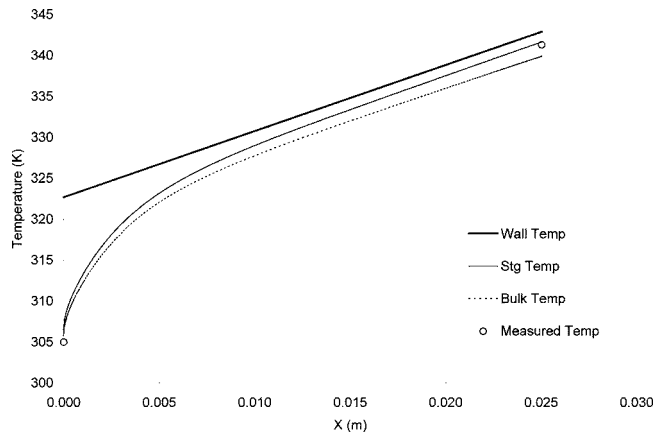

Fig. 14 Two-dimensional model prediction of stagnation temperature and bulk temperature for Test 10; two sides heated, $Re_{out}=1635$, $Ma_{out}=0.32$
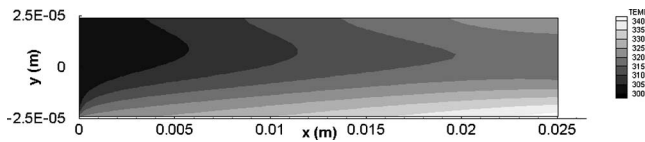
Fig. 15 Gas temperature contour for Test 10; one side heated, $Re_{out}=1635$, $Ma_{out}=0.32$

to 0.32 at the outlet, the difference between the stagnation and bulk temperatures grows to 11.2 K. However, the difference between the measured outlet temperature and the predicted stagnation temperature is 9.4 K. Comparison of the measurements with the two-dimensional model results for the higher Mach number case of Test 10 indicates that the two sides heated assumption is representative of the experiment, and does not support the one side heated, one side insulated assumption.

The two-dimensional model was solved for each of the ten experiments using both thermal boundary condition sets. Except for the first two experiments, application of the two sides heated boundary conditions resulted in prediction of the stagnation temperature within $1\,^{\circ}$C of the measured exit temperature. The model results for the one side heated, one side insulated consistently predict a lower stagnation temperature than was measured at the microchannel exit.

For Tests 1 and 2, the predicted stagnation temperature at the exit exceeds the wall temperature (see Figs. 17 and 18). These two tests have relatively high Ma at the exit. (0.44 and 0.28, respectively). Yet, in Test 10, which has Ma=0.34 at the outlet, the predicted stagnation temperature at the outlet is lower than the wall temperature. In Figs. 19 and 20, Ma is plotted against x for each of the ten tests. The gradient of Ma is larger at the exit for Tests 1 and 2 than it is for the other tests. However, at this time the authors are still investigating the reason why $T_{stg}>T_w$ at the exit for the model predictions but not for the experimental measurements.

Local Heat Transfer Quantities. In the previous section, the two-dimensional model results were validated by comparison with experimental measurements of the outlet stagnation temperature. The next step is to use the model to calculate the Nusselt number for the experiments. However, since heating along the microchannel caused not only the fluid temperature to increase, but also the flow velocity to increase, it appeared that the convection heat transfer coefficient, htc, must account for the heat transferred into kinetic energy. The heat transfer literature for high-velocity flows

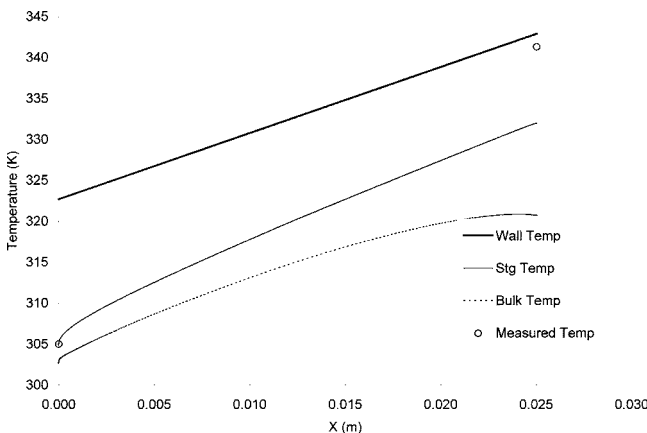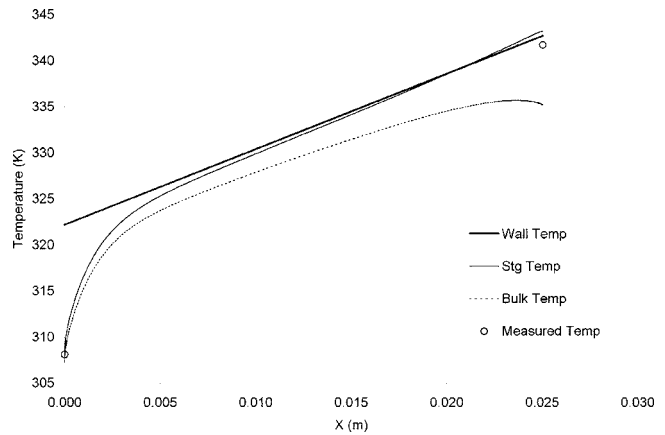**Fig. 17 Two-dimensional model prediction of stagnation and bulk temperatures for Test 1; two sides heated, $Re_{out}=473$, $Ma_{out}=0.26$**

on external surfaces ([13,14], pp. 370–387), suggests that if the bulk fluid temperature is replaced by the adiabatic wall temperature in the equation for heat flux, the Nusselt number correlations for incompressible flow can be used for compressible flow
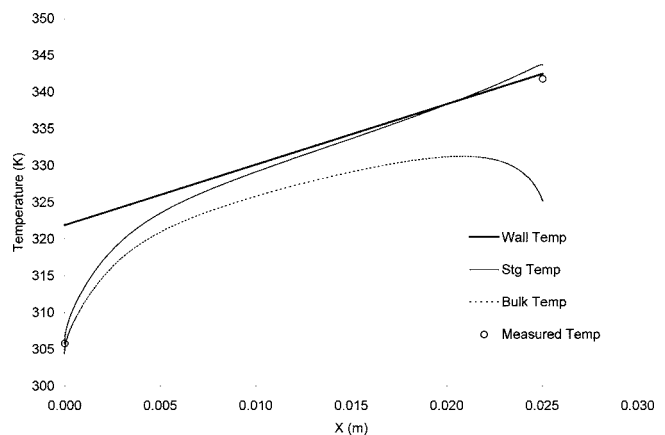

Fig. 18 Two-dimensional model prediction of stagnation and bulk temperatures for Test 2; two sides heated, $Re_{out}=756$, $Ma_{out}=0.42$
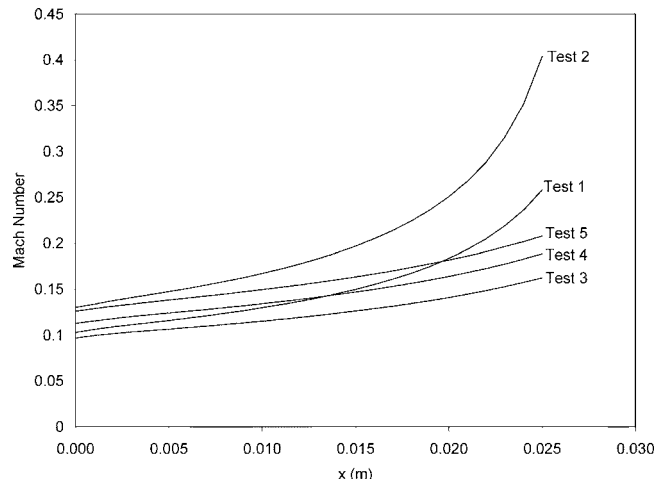

Fig. 16 Two-dimensional model prediction of stagnation temperature and bulk temperature for Test 10; one side heated, $Re_{out}=1635$, $Ma_{out}=0.32$

Fig. 19 Local Mach number for Tests 1–5
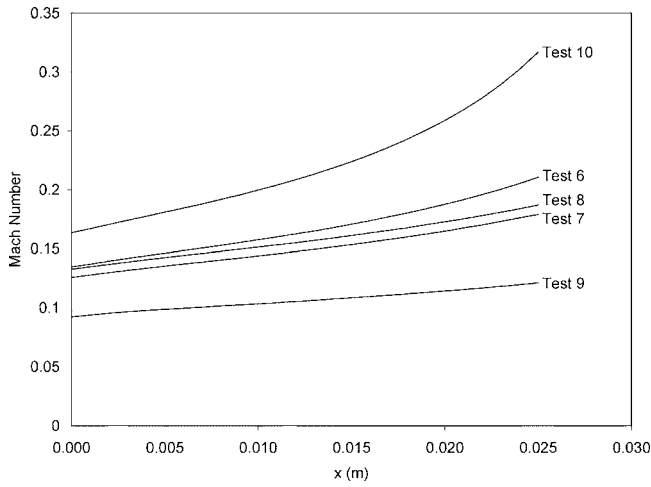
Fig. 20 Local Mach number for Tests 6–10

Fig. 21 Recovery factor plotted against X^* for two walls heated boundary conditions

$$\dot{q}'' = \text{htc}(T_w - T_{\text{aw}}) \tag{4}$$

where

$$T_{\text{aw}} = T_\infty + r_c \frac{U_\infty^2}{2C_p} \tag{5}$$

The adiabatic wall temperature in Eq. (5) is defined for external flow, in which T_∞ and U_∞ are independent of the wall conditions. T_{aw} is similar to the stagnation temperature except for the presence of the recovery factor, r_c. For external flow, numerical solution has shown that $r_c \approx (\text{Pr})^{1/2}$. It is proposed to apply Eq. (5) to internal flow by replacing T_{aw} with T_{ref}, T_∞ with T_{bulk}, and U_∞ with U, the cross-section averaged velocity. For internal gas flow with heat transfer, T_{bulk} and U change along the channel length

$$T_{\text{ref}} = T_{\text{bulk}} + r_c \frac{U^2}{2C_p} \tag{6}$$

Combining Eqs. (3) and (6), an expression for r_c is found

$$r_c = \frac{T_{\text{ref}} - T_{\text{bulk}}}{T_{\text{stg}} - T_{\text{bulk}}} \tag{7}$$

Using the new reference temperature, Eq. (4) is rewritten

$$\dot{q}'' = \text{htc}(T_w - T_{\text{ref}}) \tag{8}$$

A dimensionless parameter was sought to correlate the model results and a generalized Nusselt number for internal compressible flow. In a way similar to entrance length theory, a dimensionless quantity, X^* was defined

$$X^* = \left(\frac{x}{2H}\right)\left(\frac{\text{Ma}^2}{\text{Re Pr}}\right) \tag{9}$$

Local values of T_{ref} were calculated from Eq. (8) using htc defined from the fully developed value of Nu (8.235 for two walls at constant heat flux; 5.385 for one wall heated, one wall insulated). Then, local values of r_c were calculated from Eq. (7). For thermal boundary conditions of two sides heated, a correlation for r_c is proposed which is dependent on X^*

$$r_c = 0.674 - 0.427e^{-151.6X^*} \tag{10}$$

Figure 21 shows r_c plotted against X^* for each of the ten test conditions. As X^* increases, r_c approaches 0.674 and Nu approaches 8.23, the value of Nu for incompressible flow and uniform wall heat flux. The local Nu is plotted against X^* for each test case in Fig. 22. The figure shows that after the entrance region, the Nu approaches 8.23.
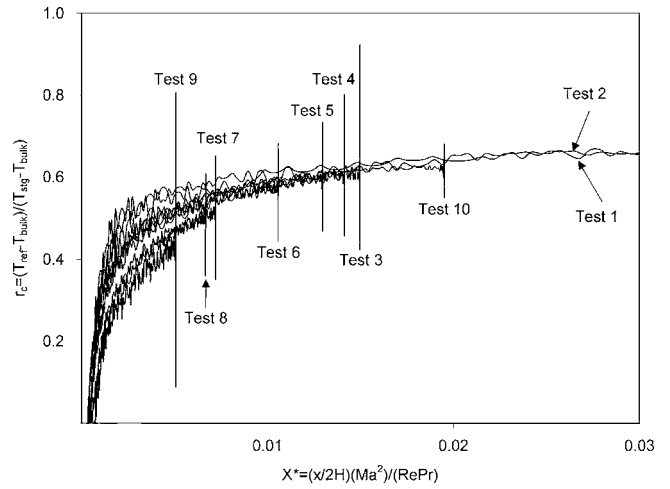
Although the experimental data are best represented by the model for two sides heated, the model results were also available for the case of one wall heated, one wall insulated. The Nusselt number for incompressible flow and one surface at constant heat flux, the other surface insulated, is 5.385. A correlation for the recovery factor was defined such that Nu approaches 5.385 as X^* increases

$$r_c = 0.578 - 0.578e^{-146.3X^*} \tag{11}$$

As X^* increases, r_c approaches 0.578 and Nu approaches 5.385. The local Nu is plotted against X^* for each of the ten cases in Fig. 23.

Discussion

In each of the ten experiments, gas entered the microchannel at a temperature that is 14–18 K lower than the wall temperature. In the thermal entrance region (approximately 0.005 m) the bulk and stagnation gas temperatures rise rapidly toward the wall temperature. After the entrance region the stagnation temperature of the gas increases at the same rate as the wall temperature. In general, an increase in the mass flow rate causes a decrease in the temperature difference, $T_w - T_{\text{stg}}$. High Ma at the outlet also causes a decrease in $T_w - T_{\text{stg}}$. Table 2 shows that in each experiment, the wall temperature was measured to be 322–323 K at the inlet and 343 K at the outlet, with $dT_w/dx = $ constant along the channel length. The mass flow, Re, and Ma were different for each test, but
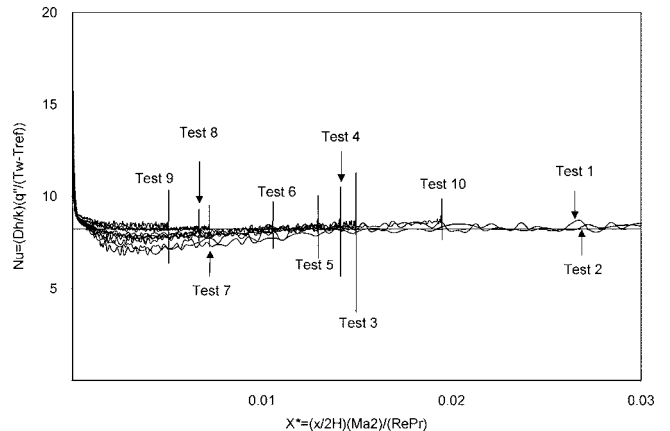

Fig. 22 Local Nu plotted against X^* for two wall heated boundary conditions
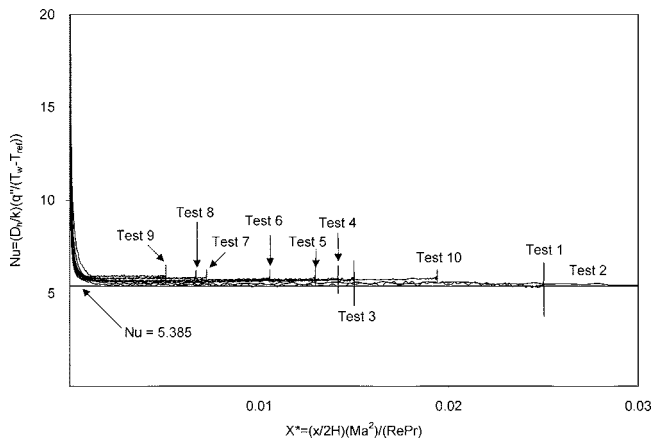
Fig. 23 Local Nu plotted against X^* for one wall heated, one wall insulated boundary conditions

the gas temperature measured at the outlet was consistently 341–342 K, just below the wall temperature. The computational model provides the gas temperature profile between the measurements at the inlet and the outlet.

The correlations developed for r_c and Nu will be useful to the microelectromechanical system (MEMS) designer for predicting the heat transfer for flow through channels with similar thermal boundary conditions. The two-dimensional model (or a one-dimensional model) can be set up to calculate local values of Re, Ma, and Nu along the length of the channel, if the inlet flow conditions and the wall temperature distribution is known [15–17].

Conclusions

The primary objective was to develop a sensor for direct measurement of the microchannel wall temperature. This objective was met and demonstrated for a series of heat transfer experiments. A microchannel test section was fabricated with nine thin-film RTDs located directly on the microchannel surface. The effort included development of the fabrication process and integrating the sensors into a microchannel test section.

A test stand was designed to conduct heat transfer tests with compressible gas flow through microchannels. The test stand imposes the thermal boundary conditions of constant temperature gradient in the wall. A series of ten heat transfer tests was conducted with laminar gas flow over a range of Ma<0.42. For incompressible flow, constant heat flux manifests itself in by constant temperature gradient in the wall. For compressible flow, the thermal boundary conditions of constant wall temperature gradient do not necessarily result in constant wall heat flux. Since the gas temperature measurement was limited to the inlet and outlet, a two-dimensional model was developed to determine local quantities of heat flux, Nu, Ma, and Re.

The model results were found to accurately predict the measured outlet temperature and confirmed the boundary condition assumption of two sides heated rather than one side heated, one side insulated. High speed convection heat transfer theory for external flow was applied to this internal flow and heat transfer scenario. A reference temperature was defined for the internal flow condition, which is analogous to the adiabatic wall temperature for external flow. Further, a dimensionless distance along the channel, X^*, was defined, such that a generalized expression for Nu could be developed. For the case of two walls heated and the case of one wall heated, one wall insulated, correlations for the recovery factor were determined so that the incompressible, fully developed value of Nu can be used to define heat transfer in compressible internal flow. For large X^*, the recovery factor approaches Pr.

Nomenclature

c = speed of sound in fluid $=(\gamma^* R^* T)^{1/2}$ (m/s)
C_p = specific heat at constant pressure (J/kg K)
D_h = hydraulic diameter (m)
G = mass flux $= \rho^* U$ (kg/m^2)
H = microchannel height (m)
f = friction factor
htc = convection heat transfer coefficient (W/m^2 K)
k = thermal conductivity (W/m K)
Kn = Knudsen number $=\lambda/H$
L = microchannel length (m)
Ma = Mach number $=U/c$
Nu = Nusselt number $=htc^* k/D_h$
P = pressure (kPa)
Pr = Prandtl number
r_c = recovery factor
R^2 = correlation coefficient for least squares curve fit
Re = Reynolds number $=G^* D_h/\mu$
RTD = resistance temperature device
T = temperature (K)
TCR = thermal coefficient of resistance
u = local velocity in x direction (m/s)
U = cross-section averaged velocity in x direction (m/s)
W = microchannel width (m)
x = axial distance from microchannel entrance (m)
X^* = dimensionless distance along the microchannel length $=(x/2H)(\text{Ma}^2)/(\text{Re Pr})$
q'' = heat flux (W/m^2)

Subscripts

aw = adiabatic wall
ref = reference
stg = stagnation
w = wall

Greek Symbols

ε = Height of surface roughness features (m)
λ = Mean free path of gas (m)
μ = viscosity
ρ = Density (kg/m^3)

References

[1] Tuckerman, D. B., and Pease, R. F. W., 1981, "High-Performance Heat Sinking For VLSI," IEEE Electron Device Lett., **EDL-2**, No. (5) pp. 126–129.
[2] Peiyi, W., and Little, W. H., 1984, "Measurement of Heat Transfer Characteristics for Gas Flow in Fine Channel Heat Exchangers Used for Microminiature Refrigerators," Cryogenics, **24**(8), pp. 415–420.
[3] Choi, S. B., Barron, R. F., and Warrington, R. O., 1991, "Fluid Flow and Heat Transfer in Micro Tubes," *Micro Mechanical Sensors, Actuators, and Systems, SAME*, DSC, Vol. 32, pp. 123–134.
[4] Peng, X. F., Wang, B. X., Peterson, G. P., and Ma, H. B., 1995, "Experimental Investigation of Heat Transfer in Flat Plates with Rectangular Microchannels," Int. J. Heat Mass Transfer, **38**(1), pp. 127–137.
[5] Peng, X. F., and Peterson, G. P., 1996, "Convective Heat Transfer and Flow Friction for Water Flow in Microchannel Structures," Int. J. Heat Mass Transfer, **39**(12), pp. 2599–2608.
[6] Fulin, G., and Scaringe, R., 1995, "Enhanced Heat Transfer in the Entrance Region of Microchannels," *30th IECEC Proceedings*, Orlando, FL, ASME, New York, 289–294.
[7] Jiang, L., Wong, M., and Zohar, Y., 1999, "A Micro-Channel Heat Sink with Integrated Temperature, Sensor for Phase Transition Study," *Proceedings 12th IEEE International Conference January 17–21*, IEEE Micro Electro Mechanical Systems, pp. 159–164. IEEE,
[8] Zhang, L., Koo, J-M., Jiang, L., Asheghi, M., Goodson, K., Santiago, J., and Kenny, T., 2002, "Measurement and Modeling of Two-Phase Flow in Microchannels with Nearly Constant Heat Flux Boundary Conditions," J. Microelectromech. Syst., **11**(1), pp. 12–19.
[9] Hadjiconstantinou, N. G., 2000, "Convective Heat Transfer in Micro and Nano Channels: Nusselt Number Beyond Slip Flow," *ASME: Proceedings of the International Mechanical Engineering Congress and Exposition*, Orlando, FL, November, ASME, New York, Vol. 366, No. 2, pp. 13–22.
[10] Hadjiconstantinou, N. G., and Simek, O., 2001, "Nusselt Number in Micro an

Nano Channels Under Conditions of Constant Wall Temperature," *ASME: Proceedings of the International Mechanical Engineering Congress and Exposition*, New York, November 11–16, ASME, New York.

[11] Turner, S. E., Lam, L. C., Faghri, M., and Gregory, O. J., 2004, "Experimental Investigation of Gas Flow in Microchannels," J. Heat Transfer, **126**(5), pp. 752–762.

[12] Turner, S. E., Sun, H., Faghri, M., and Gregory, O. J., 2001, "Compressible Gas Flow Through Smooth and Rough Microchannels," *ASME: Proceedings of the International Mechanical Engineering Congress and Exposition*, New York, November 15–17, ASME, New York.

[13] Turner, S. E., 2004, "Gas Flow and Heat Transfer in Microchannels: An Experimental Investigation of Compressibility, Rarefaction, and Surface Rough-

ness," Ph.D. dissertation, University of Rhode Island, Kingston, RI.

[14] Asako, Y., Pi, T., Turner, S. E., and Faghri, M., 2003, "Effect of Compressibility on Gaseous Flows in Microchannels," Int. J. Heat Mass Transfer, **46**, pp. 3041–3050.

[15] Asako, Y., and Toriyama, H., 2003, "Heat Transfer Characteristics of Gaseous Flows in Micro-Channels," *Proceedings 1st International Conference on Microchannels and Minichannels*, Rochester, New York, April 24–25.

[16] Shapiro, A. H., 1953, *The Dynamics and Thermodynamics of Compressible Fluid Flow*, Ronald, New York.

[17] Kays, W. M., and Crawford, M. E., 1993, *Convective Heat and Mass Transfer*, 3rd ed., McGraw-Hill, New York.

Mark R. Abel

Samuel Graham[1]
e-mail: sgraham@me.gatech.edu

George W. Woodruff School of Mechanical
Engineering,
Georgia Institute of Technology,
Atlanta, GA 30332-0405

Justin R. Serrano

Sean P. Kearney

Leslie M. Phinney

Engineering Sciences Center,
Sandia National Laboratories,
Albuquerque, NM 87185-0834

Raman Thermometry of Polysilicon Microelectro-mechanical Systems in the Presence of an Evolving Stress

In this work, the use of Raman Stokes peak location and linewidth broadening methods were evaluated for thermometry applications of polysilicon microheaters subjected to evolving thermal stresses. Calibrations were performed using the temperature dependence of each spectral characteristic separately, and the uncertainty of each method quantified. It was determined that the Stokes linewidth was independent of stress variation allowing for temperature determination, irrespective of stress state. However, the linewidth method is subject to greater uncertainty than the Stokes shift determination. The uncertainties for each method are observed to decrease with decreasing temperature and increasing integration times. The techniques were applied to mechanically constrained electrically active polysilicon microheaters. Results revealed temperatures in excess of $500°C$ could be achieved in these devices. Using the peak location method resulted in an underprediction of temperature due to the development of a relative compressive thermal stress with increasing power dissipation. [DOI: 10.1115/1.2409996]

Keywords: Raman spectroscopy, MEMS, thermometry, thermal stresses

Introduction

Motivation. Recent developments in microelectromechanical systems (MEMS) and nanomaterials have intensified the development of high spatial resolution thermometry techniques capable of yielding absolute temperatures. This has been especially true for thermal MEMS, a class of microdevices whose function relies on the control and manipulation of temperature for reliable operation. For example, devices such as polysilicon microheaters, thermal actuators, and microhotplates may easily reach temperatures in excess of $300°C$ [1–6]. In addition, recent research has shown the ability to perform localized chemical vapor deposition (CVD) of nanomaterials on microheaters which reach temperatures in excess of $800°C$ [7,8]. Heated atomic force microscopy devices have also been used as thermal switches in thermal dip pen nano-lithography and thermal data storage and possess small heated regions which are difficult to discern using techniques such as infrared spectroscopy [9–11]. In all of these cases, the critical dimensions for temperature measurements can be $10 \mu m$ or smaller. The combination of this size range and the calibration of thermal metrology technique over such broad temperatures make absolute temperature measurements challenging.

In general, temperature measurements in microdevices can be performed using both optical and electrical temperature sensors. Of the technologies which exist to measure temperature, optical methods are preferred due to their nonintrusiveness and potential for high spatial resolution. An excellent detailed review of these optical techniques is provided by Zhang [12].

Of the many techniques which exist, Raman spectroscopy has been demonstrated as an excellent candidate for measuring steady state temperatures in Si MEMS and semiconductor devices over broad temperature ranges because it provides high spatial resolution and an absolute temperature measurement that does not suffer

from uncertainty in surface optical properties, which plague other optical thermometers for MEMS. The Raman technique, which uses a visible light source to induce the light scattering process, can provide spatial resolutions of order $1 \mu m$ when considering far field diffraction limitations. Most measurements require photon collection times on the order of seconds, thus only steady-state temperature mapping is generally implemented when using micro-Raman spectrometers.

While Raman spectroscopy has yielded absolute temperature measurements in microdevices, the combined effects of temperature and stress has remained largely unexplored. For application to polycrystalline Si-based microdevices, residual stresses are often encountered due to the CVD growth process combined with the inhomogeneous multilayer films involved. These stresses are expected to evolve with temperature changes in the devices, which may affect the accuracy of Raman thermometry, depending on the methodology used.

In this work, an investigation of Raman thermometry using the Stokes peak location and linewidth (full width at half maximum (FWHM)) is presented. A detailed study was performed to calibrate and quantify the uncertainties of the two test methods as a function of temperature and stress. Based on these results, insight into the relative merits of each technique is given. Due to the insensitivity of the linewidth technique to stress evolution in silicon, a comparison between the two test methods was made to observe the effects of stress evolution in polysilicon microheaters on the Stokes peak location temperature measurements.

Raman Spectroscopy. The Raman effect is a result of the inelastic scattering of photons which exchange energy by interacting with the allowed atomic vibrations or rotations of the probed material. In the case of silicon, the photons scatter due to their interaction with quantized lattice vibrations (phonons). The result is a frequency shift of the scattered photon to longer wavelengths (Stokes shift, energy loss) or shorter wavelengths (anti-Stokes shift, energy gain) [12]. The temperature dependence of this frequency shift arises from the anharmonicity of the interatomic potentials in the Si-Si bonds. It is possible to obtain the temperature from the Raman spectra through the ratio of the Stokes to anti-

Stokes intensities, by the magnitude of the Raman Stokes frequency shift, or changes in the FWHM (or linewidth) of the Stokes signature. This increase in linewidth occurs with higher temperature due to increased optical phonon relaxation rates.

The method of using the Stokes to anti-Stokes intensities to determine temperature has been widely utilized [12–16]. The anti-Stokes intensity increases relative to the Stokes intensity with increasing temperature due to the increased population of phonons in available states. This method is inherently independent of stress and yields accurate temperature measurements in microdevices at low to moderate temperatures. In contrast to the ratio technique, methods which utilize only the Stokes spectral information yield much shorter integration times for mapping temperature due to the strong Stokes scattering effect. While solid state modeling has shown that the Stokes shift is a nonlinear function of temperature between 5 and 1400 K, a linear assumption for the relationship in SI is highly accurate between 300 and 1273 K [13,17]. Thus, the Stokes peak location method has no change in sensitivity over the typical range in which most silicon MEMS devices are probed. While the linear dependence of the Stokes shift to temperature is attractive for calibration purposes, the shift is also a linear function of stress. Thus as temperature changes, the stress in multilayer electronics and MEMS devices may also evolve with both effects being convoluted into the single Stokes peak location measurement. For silicon, the linear coefficient for the Stokes shift with stress (β) is on the order of 3.6 cm^{-1}/GPa while the temperature coefficient (C_{Stokes}) is on the order of 0.024 cm^{-1}/K [17]. If stress effects are ignored in performing Stokes shift temperature measurements, this implies that a change in residual stress of 10 MPa would result in 1.5 K error without consideration of other measurement uncertainties. Beyond using the Stokes peak position, the Stokes linewidth may also be used for temperature determination. However, very little research has been performed on the use of this technique for thermal metrology and the effect of stress on its accuracy.

In this current work, an analysis of both the Stokes peak shift and linewidth measurement is presented. This study includes an uncertainty analysis as well as measurements on unreleased polysilicon microheaters with appreciable residual stress. In doing so, the impact of residual stresses in temperature measurements and the viability of using only characteristics of the Stokes spectral band were analyzed.

Experiment

Sample Preparation. In this study, polysilicon MEMS microheaters were measured using Raman spectroscopy. The devices consisted of phosphorous doped polysilicon with dimensions of 10 μm wide × 200 μm long × 2.2 μm thick on 3.9 μm of plasma-enhanced CVD (PECVD) oxide which was supported by a 500-μm-thick silicon wafer (Fig. 1). Dopants were ion implanted with a final concentration of 10^{20} atoms/cm^3. Details of the device fabrication can be found elsewhere [18]. In order to introduce large stress variations in the beams, the devices were utilized without releasing them from the underlying PECVD oxide layer which constrained the deformation of the polysilicon heaters. The samples were annealed at 900°C to stabilize the polysilicon microstructure for 4 h before testing. This is annealing step was an additional processing step added to the procedure previously reported in Ref. [18]. Based on Raman spectroscopy a large residual compressive stress (~250 MPa) was present in the microheaters at room temperature.

Measurements. A Renishaw InVia Raman microscope with 180 deg backscattering geometry was used for all measurements in this study. With a spectrometer focal length of 250 mm and a diffraction grating with 3000 lines/mm, a spectral dispersion of 0.91 cm^{-1}/pixel is realized when a slit width of 65 μm is utilized. Because the minimal instrument-dependant linewidth of silicon is 3.5–4.0 cm^{-1} at room temperature, this resolution is sufficient to
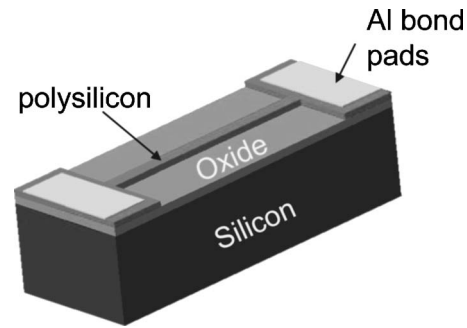

Fig. 1 Layout showing the sample used for temperature measurements in this study. The sample consists of a polysilicon microheater beam on a thick PECVD silicon dioxide on bulk silicon. Constraint in the movement of the microheater from the oxide layer is used to induce stress variations in the device.

detect Stokes peak shifts within ±0.057–0.1 cm^{-1} using peak fitting software. A slit width of 65 μm provides sufficient detection capabilities with maximum signal levels at the expense of some spectral resolution. The 488 nm Ar^+ laser beam was set to a sample power 45.4 μW as measured by a Newport Model 840-C optical power meter. This laser power ensured there was no Stokes peak shift due solely to laser heating. A 100× objective with a numerical aperture (NA) of 0.75 was used to focus the probe laser beam and collect the Raman signature of the polysilicon. This objective resulted in a spot size of 1.0 μm.

To calibrate the dependence of the Stokes response with temperature, Raman spectra were taken on a polysilicon film between room temperature and 1000°C using the method described in Ref. [18]. The sample was heated in a controlled environmental stage (Linkham THMS 1500) in increments of 100°C up to 1000°C. Twenty spectra were taken at each temperature step, and the mean Stokes peak frequency position and linewidth were found. Stokes peak position and linewidth data were plotted against temperature utilizing a linear and parabolic fit model, respectively.

To calibrate the effects of stress on the Stokes spectral response, polysilicon films were tested under four point bend loading at room temperature as described in Ref. [17]. From the Raman spectra taken during the bend tests, both the peak position and linewidth were determined as a function of stress between −300 and 300 MPa.

Once the calibrations were determined, an in-depth comparison of temperature measurements based on Stokes frequency and linewidth was performed. The measurements were performed on the center of a microheater as a function of device power dissipation. To power the microheater, a sense resistor of approximately 100 Ω was placed in series with the device to protect it from thermal run away effects and connected to a Keithley 2400 source meter. The dc power source was incremented in 1 V steps during measurements, from 0 to 15 V sourced. Twenty spectra with at least 2500 peak photoelectron counts were taken at each power setting and temperatures were calculated based on both line-position and linewidth estimates from the Raman spectra.

Results and Discussion

Experimental Results. The calibration of the Stokes peak location with temperature is shown in Fig. 2. The peak location of the Raman resonance associated with the triply degenerate first-order optical phonon in Si was approximated as a linear function of temperature across the entire tested range with a slope of $C_{Stokes} = -0.0232 \pm 0.0002$ cm^{-1}/°C. Following this linear fit, Eq. (1) can be used for a simple temperature calculation, based on a reference Stokes frequency, found at room temperature
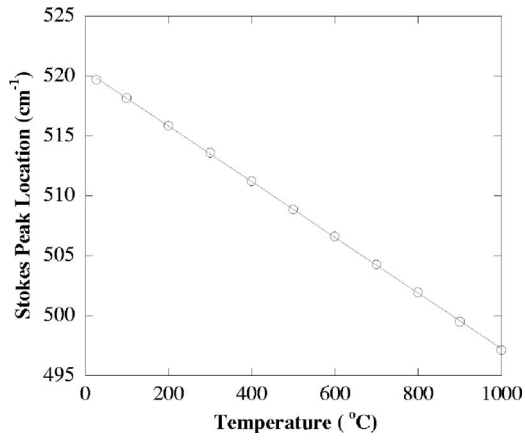
Fig. 2 Calibration of Stokes peak location for phosphorous doped polysilicon

$$T = T_{\text{ambient}} - \frac{\omega_{\text{ambient}} - \omega_{\text{measured}}}{C_{\text{Stokes}}} \qquad (1)$$

Here T is the device temperature; ω_{ambient} is the reference Stokes peak location at T_{ambient} (the reference temperature); and ω_{measured} is the Stokes peak location of spectra acquired from the powered device.

Upon investigation of the stress calibration data [17], it was determined that the linewidth was unaffected by applied stress for all polysilicon samples as well as a single-crystal silicon reference. As seen in Fig. 3, the linewidth data are scattered about its mean by roughly ±0.055 cm^{-1} across the entire stress range measured. This is well within the 2σ uncertainty of the roomtemperature linewidth data and implies that linewidth technique may be utilized: (1) for stress independent temperature measurements or (2) to determine the relative change in stress in devices when combined with stress-dependent methods like the Stokes peak location.

The temperature calibration of the Stokes linewidth is shown in Fig. 4 from room temperature to 1000°C. A parabolic fit to the calibration data in the form of Eq. (2) is shown, where Γ is the Stokes linewidth

$$\Gamma(T) = AT^2 + BT + C \qquad (2)$$

Parameters A, B, and C were found as 4.605E-6, 0.008011, and 4.258, respectively, from the data fit and used for the calculation of device temperature by solving the ensuing quadratic equation. Both line-positions and linewidth temperature calibrations yielded a correlation coefficient of greater than 0.99 using their respective fits.

Uncertainty Analysis. The uncertainty of the peak location and linewidth estimators are found in Tables 1 and 2, respectively. Based on these results, the linewidth temperature uncertainty is roughly a factor of 12 times greater than that of the Stokes peak position at room temperature for a single measurement and a factor of 8 times greater at 510°C. A clear trend favors the narrow peaks associated with a lower sample temperature and higher peak intensity for determining both Stokes peak location and linewidth. The data also show that within each measurement technique, the uncertainty is larger at higher temperatures than at lower temperatures. The larger uncertainty at elevated temperatures can be attributed to asymmetric peak broadening of the signal which makes peak fitting more difficult. By recording consecutive scans, both data uncertainties may be further reduced as a function of the number of measurements in a set, N, shown by Eq. (3)
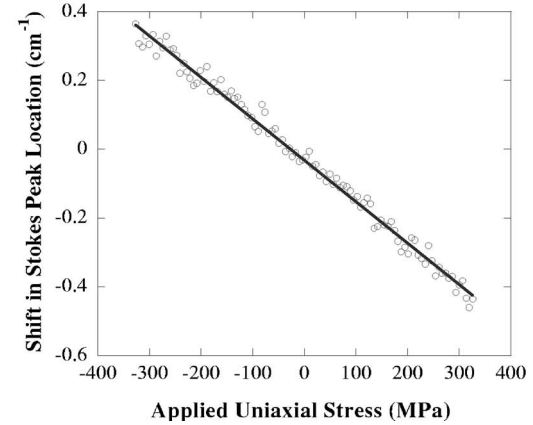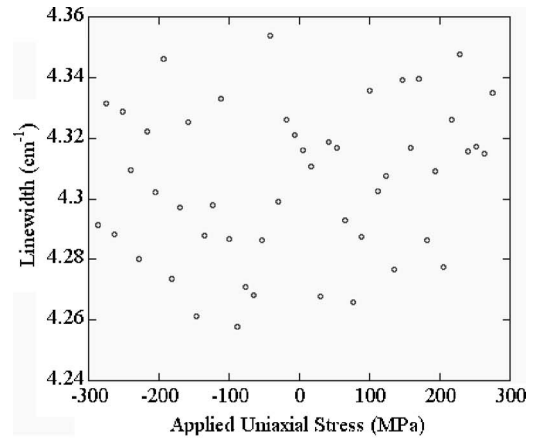

Fig. 3 Effect of stress on the linewidth of doped polysilicon (top). The scatter of the linewidth with stress is far less than the measurement uncertainty. The effect of stress on the Stokes peak location results in a linear shift with applied stress (bottom).
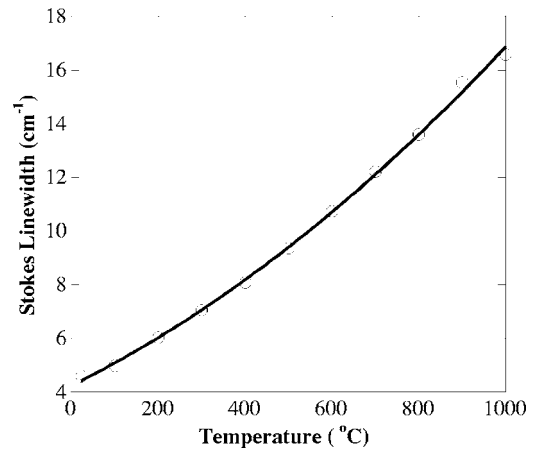
$$y = \frac{2\sigma}{\sqrt{N}} \qquad (3)$$

From these uncertainty data, there is a tradeoff between signal integration time and reduced uncertainty. Also, the use of the Stokes linewidth requires significantly more measurements in or-

Fig. 4 Linewidth calibration of phosphorous doped polysilicon which displays a quadratic behavior over the temperature range shown.

Table 1 Uncertainty of the Stokes peak position estimator for a single measurement

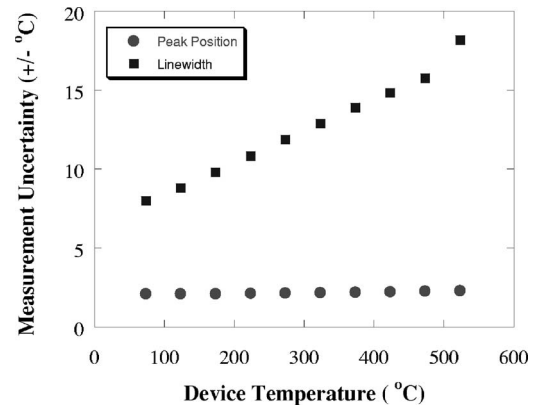| Sample temperature (°C)	Stokes frequency		
	Signal (photoelectron counts)	2σ (cm^{-1})	Contribution to temperature uncertainty (°C)
23	2500	0.0641	2.76
	5000	0.0617	2.65
	10,000	0.0266	1.14
510	2500	0.1317	5.67
	5000	0.1294	5.57
	10,000	0.0923	3.97

Fig. 5 Estimated measurement uncertainty as a function of temperature from all sources. The uncertainty is based on a vector summation of the individual contribution to uncertainty and then taking 20 samples to reduce the single measurement uncertainty according to Eq. (3).

der to reduce measurement uncertainty in any case.

To estimate total uncertainty of either the linewidth or peak location methods, the contributions from instrument drift, calibration fitting, and spectrum curve fitting were each considered. A more detailed description of the source of these uncertainties can be found in Ref. [19] and their values are summarized in Table 3. To calculate the uncertainty of the linewidth method, a relative change in linewidth was used to estimate the temperature with the reference value being the linewidth at room temperature (4.23 cm^{-1}). The uncertainty in determining the reference linewidth was determined from the statistical distribution of 20 experimental measurements. In a similar manner, the room temperature reference for Si ($\sim$520.5 cm^{-1}) and its uncertainty were determined as well. The uncertainty from the calibration curve fit was determined from the 95% confidence interval on the fitting parameters. For the peak location method, uncertainties due to stress evolution were not included. The effect of stress on the

measurement is accounted for by comparison with the linewidth data.

Figure 5 shows a plot of the total temperature uncertainty for the two techniques using a vector summation of the single measurement uncertainties followed by Eq. (3) with $N=20$ experimental realizations. The data show that the linewidth uncertainty increases much more rapidly with increasing temperature than peak location temperature measurements, ranging from ± 7 °C near room temperature to ± 18 °C at 500 °C. The quantification of these uncertainties as a function of temperature is applied to all measurements made in the subsequent sections.

Device Measurements. Raman Stokes peak position measurements of an unpowered micro-heater revealed a peak position of $\omega_{ambient}=521.4$ cm^{-1}. Using the calibration factor of $\beta=3.6$ cm^{-1}/GPa, the indicated a large compressive stress on the order of 250 MPa. Temperature measurements were made by measuring relative Stokes shifts from 521.4 cm^{-1} as opposed to an absolute value reference of 520.5 cm^{-1} which is known for bulk Si without stress. By making our measurements relative to 521.4 cm^{-1}, the superposition of any tensile or compressive stresses relative to the unpowered state can be readily observed. Figure 6 compares the peak-location and linewidth-based temperatures from the center of a microheater. Data show a linear increase with power up to temperatures on the order of 500 °C. Measurements by the two methods are within 8% of each other across the entire power dissipation range (0–552 mW). The maximum temperature difference between the two methods was found

Table 2 Uncertainty of the Stokes linewidth estimator for a single measurement

Sample temperature (°C)	Stokes linewidth		
	Signal (photoelectron counts)	2σ (cm^{-1})	Contribution to temperature uncertainty (°C)
23	2500	0.2704	32
	5000	0.2508	30
	10,000	0.1112	14
510	2500	0.5831	46
	5000	0.5234	41
	10,000	0.3547	28

Table 3 Contribution to single measurement temperature uncertainty from other sources

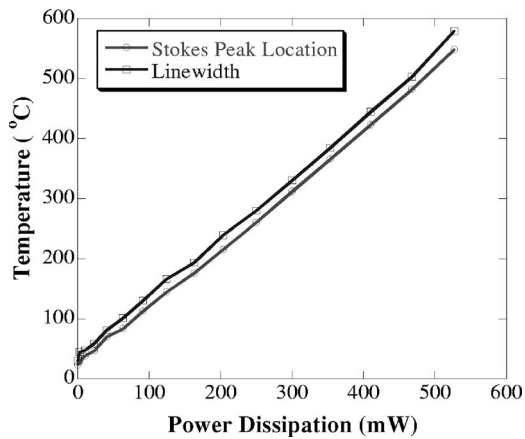| Source of uncertainty	Uncertainty type	Uncertainty (cm^{-1})	Equivalent temperature uncertainty
Accuracy of Stokes peak position	Precision	± 0.055 cm^{-1} at 300 K ± 0.095 cm^{-1} at 700 K	± 2.3 K at 300 K ± 4.1 K at 700 K
Reference uncertainty	Bias	± 0.22 cm^{-1} (peak location) ± 0.115 cm^{-1} (linewidth)	± 9 K ± 13 K
Calibration curve fit	Bias	± 0.01 cm^{-1} at 300 K (peak location) ± 0.1 cm^{-1} at 800 K (peak location) ± 0.114 cm^{-1} at 300 K (linewidth) ± 0.85 cm^{-1} at 800 K (linewidth)	± 0.43 K ± 4.3 K ± 13 K ± 66 K

Fig. 6 Temperature at the center of a microheater as a function of power dissipated. When comparing the Stokes and linewidth techniques, a thermally induced compressive stress was realized.
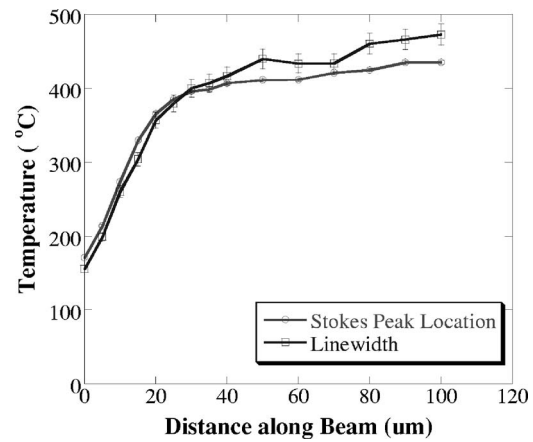

Fig. 7 Temperature distribution of a fixed–fixed microheater using half-symmetry. A comparison of the Stokes and linewidth calibration is seen, revealing good agreement near the bond pad (distance=0 μm) and a significant difference at the beam center (distance=100 μm). The measured temperature difference (33°C) is greater than the ±15°C uncertainty between the two measurements at 400°C. This difference suggests the presence of a compressive stress in the device.

to be 31°C at 552 mW. Based on Fig. 5, we expect the uncertainty of the linewidth method to be ±18°C and ±2.3°C for the peak position. Thus, the deviations between the methods are greater than the measurement uncertainty. The Stokes peak location method underestimated the temperature at the center of the microheater when compared to that of the linewidth. Recalling that the linewidth method is insensitive to stress, this difference in temperature may be attributed to changes in stress in the devices due to heating. The presence of a lower temperature from the Stokes peak-location method is indicative of a developing compressive stress in the polysilicon device relative to the unpowered state, consistent with the device deformation. The localized heating of the beam will cause thermal expansion in the polysilicon microheater which is constrained by the underlying thermal oxide. The constraints from the oxide layer (having a lower coefficient of thermal expansion relative to the polysilicon) places a compressive stress on the polysilicon relative to its stress state at zero power dissipation. Based on the Raman data, the maximum estimated superimposed compressive stress is approximately 200 MPa which is estimated by Eq. (4)

$$\sigma = (T_{\text{peak\_location}} - T_{\text{linewidth}}) \left(\frac{C_{\text{Stokes}}}{\beta} \right) \quad (4)$$

However, the maximum uncertainty in the linewidth measurement is ±18°C (Fig. 6) which results in an equivalent stress uncertainty of ±110 MPa which is very large. To reduce this uncertainty, the number of photoelectron counts (integration time) or the number of experimental measurements should be increased to improve temperature measurement accuracy of the linewidth measurement. By simply using N=40 realizations and a photoelectron count of 5000, the stress uncertainty will be reduced to ±30 MPa. While it is feasible to automate and analyze the collection of large Raman data sets, it remains difficult to determine the exact components of the stress tensor. In general, an assumption of the stress state (e.g., biaxial) must be made in order to estimate the stress levels. Assumptions of biaxial stress states are generally consistent with many multilayer thin-film MEMS devices. Complete determination of the stress tensor in a polycrystalline silicon sample cannot be made without such assumptions. Off-axis polarized Raman measurements may yield more details of the stress state when applied to single crystalline Si since this configuration can detect the breakup of the triply degenerate optical phonons which is stress state dependent [20].

To measure the spatial temperature distribution, power was dissipated in the device to yield an approximate temperature of 450°C at the beam center. Spectral measurements were repeated twice with N=20 realizations at each point along the beam from

the anchor pad (x=0) to the beam's center (x=100 μm). Measurements 5 μm apart were probed near the anchor pad where a large temperature gradient was expected. The spacing between measurement points was increased to 10 μm closer toward the beam center where greater temperature uniformity was seen. The analysis of the data gave insight into temperature and thermal stress behavior, both across the beam length for a given power and at the beam center as function of power.

Figure 7 shows a comparison of the temperature distribution using the two measurement techniques on a microheater dissipating 322.15 mW. The data indicate comparable temperatures between the two measurement techniques near the anchor pads where the temperatures are the lowest and the change in stress is the smallest. Moving toward the center of the beam, the differences between the two methods becomes very apparent being on the order of 33°C at the beam center. This difference is greater than the ±15°C uncertainty difference between the two measurement techniques. The temperature distribution shows the development of a superimposed compressive stress near the center of the beam in the region of maximum temperature. Again, this behavior is consistent with the constraints of deformation on the heated beam and clearly shows that the use of the Stokes peak location and linewidth methods can reveal both temperature and regions of stress evolution.

Conclusions

This work has shown the ability to use Raman spectroscopy for the measurement of absolute temperature in doped polysilicon MEMS devices by using both spectral frequency and linewidth. Both methods are rather straightforward in calibration without the need of knowing surface optical properties. The Stokes peak location and linewidth methods showed relatively good agreement for the devices measured in this study. However, the small differences (within 8% of each other) were consistent with the development of an evolving compressive stress due to constrained deformation in the heated beams. Such differences have been seen when devices are subjected to a developing tensile stress. In this case, the Stokes peak position temperature overpredicts the temperature in contrast to what is seen in this current study. It should be noted that the stress levels exhibited in the device configurations in the work are an extreme case when compared to thermal MEMS devices which exist as released structures, having more

freedom to expand under thermal loading (e.g., thermal actuators, microhotplates, etc.). Overall, the peak location method has a lower uncertainty than the linewidth measurement procedure and should be sufficient for mapping devices where changes in stress are small. In regions of large temperature changes, however, comparisons with the two methods can reveal both some aspects of the nature of the stress as well as improved temperature accuracy. The present method clearly shows that the evolution of stress can affect the Stokes peak location method while providing insight into the development of compressive stresses. The uncertainties of the methods can be reduced by using longer integration times and/or collecting a large number of data points. The integration times needed to obtain a higher photoelectron count will depend on the allowable laser energy used during measurements. Higher laser energies will result in larger photoelectron counts/unit time but at the risk of device heating when using laser energies which are above the band gap of the device. The need for low laser powers for small Si structures makes this method generally applicable for steady-state measurements due to the longer integration times needed to reach 2500 or more signal intensity. Reduction in uncertainty is paramount to make more definitive claims of apparent stress in MEMS devices. Currently, complete Raman mapping of devices such as the one shown in this study can be performed in 1.5 h with a 2 μm spatial increment between measurements.

Acknowledgment

Nomenclature

C_{Stokes} = linear calibration coefficient relating the shift in Stokes peak location to temperature

T_{ambient} = reference ambient temperature of the device under zero power dissipation

$T_{\text{peak\_location}}$ = temperature measured by the Stokes peak location method

$T_{\text{linewidth}}$ = temperature measured by the change in Stokes linewidth

β = linear calibration coefficient relating the shift in Stokes peak location to stress

ω_{ambient} = Stokes peak location at the reference ambient temperature

ω_{measured} = Stokes peak location of device under thermal loading

Γ = polynomial function describing Stokes linewidth as a function of temperature

References

[1] Baker, M. S., Plass, R. A., and Headley, T. J., 2004, "Final Report: Compliant Thermo-Mechanical MEMS Actuators," Sandia National Laboratories Sand Rep. No. SAND2004-6635, pp. 1–38.

[2] Dumitrescu, M., Cobianu, C., Lungu, D., Dascalu, D., Pascu, A., Kolev, S., and van den Berg, A., 1999, "Thermal Simulation of Surface Micromachined Polysilicon Hot Plates of Low Power Consumption," Sens. Actuators, A, **76**(1–3), pp. 51–56.

[3] Graebner, J. E., Pau, S., and Gammel, P. L., 2002, "All-Optical Excitation and Detection of Microelectrical-Mechanical Systems," Appl. Phys. Lett., **81**(19), pp. 3531–3533.

[4] Que, L., Park, J. S., and Gianchandani, Y. B., 2001, "Bent-Beam Electrothermal Actuators—Part I: Single Beam and Cascaded Devices," J. Microelectromech. Syst., **10**(2), pp. 247–254.

[5] Serrano, J. R., Phinney, L. M., and Brooks, C. F., 2005, "Laser-Induced Damage of Polycrystalline Silicon Optically Powered MEMS Actuators," *Proceedings of ASME InterPACK2005*, San Francisco, July 17–22, Paper No. IPACK2005-73322.

[6] Mitzner, K. D., Sternhagen, J., and Galipeau, D. W., 2003, "Development of a Micromachined Hazardous Gas Sensor Array," Sens. Actuators, A, **93**(1–3), pp. 92–99.

[7] Sunden, E. O., Wright, T. L., Lee, J., King, W. P., and Graham, S., 2006, "Room-Temperature Chemical Vapor Deposition and Mass Detection on a Heated Atomic Force Microscope Cantilever," Appl. Phys. Lett., **88**(3), pp. 033107–033109.

[8] Englander, O., Christensen, D., and Lin, L., 2003, "Local Synthesis of Silicon Nanowires and Carbon Nanotubes on Microbridges," Appl. Phys. Lett., **82**(26), pp. 4797–4799.

[9] King, W. P., Kenny, T. W., Goodson, K. E., Cross, G. L. W., Despont, M., Durig, U., Rothuizen, H., Binnig, G., and Vettiger, P., 2001, "Atomic Force Microscope Cantilevers for Combined Thermomechanical Data Writing and Reading," Appl. Phys. Lett., **78**(9), pp. 1300–1302.

[10] King, W. P., Kenny, T. W., Goodson, K. E., Cross, G. L. W., Despont, M., Durig, U. T., Rothuizen, H., Binnig, G., and Vettiger, P., 2002, "Design of Atomic Force Microscope Cantilevers for Combined Thermomechanical Writing and Thermal Reading in Array Operation," J. Microelectromech. Syst., **11**(6), pp. 765–774.

[11] Sheehan, P. E., Whitman, L. J., King, W. P., and Nelson, B. A., 2004, "Nanoscale Deposition of Solid Inks Via Thermal Dip Pen Nanolithography," Appl. Phys. Lett., **85**(9), pp. 1589–1591.

[12] Zhang, Z. M., 2000, "Surface Temperature Measurements Using Optical Techniques," *Annual Review of Heat Transfer*, C.-L. Tien, ed., Begell House, Inc., New York, pp. 351–411.

[13] Cui, J. B., Amtmann, K., Ristein, J., and Ley, L., 1998, "Noncontact Temperature Measurements of Diamond by Raman Scattering Spectroscopy," J. Appl. Phys., **83**(12), pp. 7929–7933.

[14] Gu, X. J., 1996, "Simultaneous Measurements of Stokes and Anti-Stokes Raman Spectra for Thermal Characterization of Diode Laser Facet," J. Raman Spectrosc., **27**(1), pp. 83–85.

[15] Lo, H. W., and Compaan, A., 1980, "Raman Measurements of Temperature During CW Laser Heating of Silicon," J. Appl. Phys., **51**(3), pp. 1565–1568.

[16] Pangilinan, G. I., and Gupta, Y. M., 1997, "Temperature Determination in Shocked Condensed Materials Using Raman Scattering," Appl. Phys. Lett., **70**(8), pp. 967–969.

[17] Abel, M., Wright, T., Sunden, E., Graham, S., King, W., and Lance, M. L., 2005, "Thermal Metrology of Silicon Microstructures Using Raman Spectroscopy," *Proceedings of IEEE Semi-Therm 21*, San Jose, CA, March 15–17, pp. 235–242.

[18] Abel, M., and Graham, S., 2005, "Thermometry of Polycrystalline Silicon Structures Using Raman Spectroscopy," *Proceedings of ASME InterPACK2005*, San Francisco, July 17–22, Paper No. IPACK2005-73088.

[19] Kearney, S. P., Phinney, L. M., and Baker, M. S., 2006, "Spatially Resolved Temperature Mapping of Electrothermal Actuators by Surface Raman Scattering," J. Microelectromech. Syst., **15**(2), pp. 314–321.

[20] Loechelt, G. H., Cave, N. G., and Menendez, J., 1995, "Measuring the Tensor Nature of Stress in Silicon Using Polarized Off-Axis Raman Spectroscopy," Appl. Phys. Lett., **66**(26), pp. 3639–3641.

Nonstationary Heat Conduction in Complex-Shape Laminated Plates

Alexander N. Shupikov
Professor, Chief Research Associate
e-mail: shupikov@ipmach.kharkov.ua

Natalia V. Smetankina
Senior Research Associate

Yevgeny V. Svet
Junior Research Associate

A.N. Podgorny Institute for Mechanical
Engineering Problems,
National Academy of Sciences of Ukraine,
2/10 Dm. Pozharsky Street,
Kharkov 61046, Ukraine

Based on the immersion method, an analytical solution has been obtained for the problem of nonstationary heat conduction in laminated plates of complex plan shape when they are heated with interlayer film heat sources. The temperature distribution over the thickness of each layer is represented in the form of an expansion in a system of the orthonormal Legendre polynomials and, in the plate plane, it is represented as trigonometric series expansions. Temperature fields were investigated in a five-layer plate for conditions of convective heat exchange with the environment. The method suggested can be applied for designing heating systems and determining temperature stresses in laminated glazing for different vehicles [DOI: 10.1115/1.2427073]

1 Introduction

In modern engineering, the problem of valid identification of the thermal condition of structural components is a topical one [1,2]. Its successful solution affects the reliability and effectiveness of operation of elements of different structures, which are often made of dissimilar materials. Analyzing the temperature fields in laminated plates and shells is a challenging mathematical problem because the layers possess essentially different thermophysical properties, and the conditions on layer interfaces have to be described taking into account internal heat sources.

A review of the literature has shown that the majority of publications deal with analyzing laminated structures under stationary heating conditions. Khdeir [3] investigated bending of simply supported nonsymmetric-structure laminated plates under the effect of temperature, which is distributed piecewise linearly over the pack. The systems of equations of thermal elasticity of the first-order theory with shear, and of the classical theory are solved using the state–space approach and Levy's method. Verijenko et al. [4] and Barut et al. [5] applied the hypothesis on piecewise-linear distribution of temperature over the thickness of a laminated pack to investigate stationary temperature fields in laminated composite shells and panels.

For the case of nonstationary thermal affects, laminated plates and shells are also considered at a known distribution of temperature fields. To investigate stresses in laminated rectangular simply supported plates, Savoia and Reddy [6] used a polynomial and exponential distribution of temperature over the layer thickness. The top and bottom surfaces of the layer were subject to uniform heating. The thermal elasticity equations were solved using the Navier method.

Oguamanam et al. [7] studied the response of laminated symmetric cross-ply cylindrical panels that were suddenly exposed to a heat flux. The temperature distribution is constant over thickness, and exponential in time.

Note that, to solve nonstationary heat conduction problems, methods based on applying techniques of discretization of an area or contour are used, e.g., the finite difference method [8], the finite element method (FEM) [7,9], or the boundary element method [10,11]. Since the solution of nonstationary heat conduction problems is mathematically involved, the analytical solutions are most

often obtained for one-dimensional heat transfer problems [12–14]. Lu et al. [15] obtained the analytical solution of the nonstationary heat conduction problem in a multi-dimensional composite cylinder slab by using the Laplace transform and separation of variables. Padovan [16], and Ootao et al. [17,18], obtained analytical solutions of the nonstationary heat conduction problem for laminated rectangular strips and plates at specified temperature distributions at the top and bottom of the plate. Nusier and Newaz [19] solved the nonstationary heat conduction problem for the case of N concentric cylinders. For the radial coordinate, they expanded the temperature function into a series of Bessel functions of the first and second kind. Therefore, a topical problem is developing methods of investigating processes of nonstationary heat conduction in structures of noncanonical plan shape taking into account their inhomogeneous structure, which allow representing the problem solution in analytical form.

Earlier the authors suggested a method of solving the stationary heat conduction problem for a laminated plate whose contour was made up of straight lines and arcs of circus. The method is based on representing the temperature distribution in each layer by a system of the Legendre polynomials. In this paper, the method has been generalized for the case of the problem of nonstationary heat conduction in laminated complex-shape plates; and an analytical solution of the problem has been obtained without invoking the hypothesis on temperature distribution over the layer thickness.

2 Mathematical Statement

A laminated plate is considered, which is assembled of I layers of constant thickness h_i $(i=\overline{1,I})$ (Fig. 1). We shall denote the plate top and bottom, the layer interfaces, and the side surfaces of layers as Ω_t, Ω_b, Ω_i $(i=\overline{1,I-1})$ and Ω_L^i $(i=\overline{1,I})$, respectively. The plate is referred to as the Cartesian system of coordinates, which is related to the external surface of the first layer and, on the coordinate plane, it occupies area Ω_t bound by contour $L:x_L=x(s)$, $y_L=y(s)$ (where s is arc current length). Convective heat transfer occurs on the top, bottom, and side surfaces of the plate.

The heat conduction equation and the boundary conditions for a laminated plate are obtained from the variational heat balance equation [20]

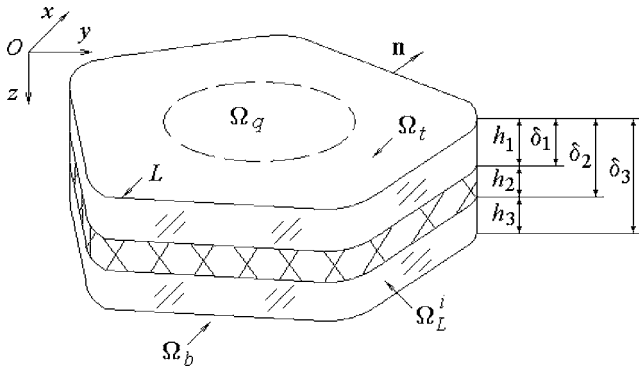**Fig. 1 Laminated plate**

$$\delta[\chi_i(T)] = \delta\left\langle \sum_{i=1}^{I}\left(\frac{1}{2}\int\int\int_{V_i}\left\{k_i\left[\left(\frac{\partial T^i}{\partial x}\right)^2 + \left(\frac{\partial T^i}{\partial y}\right)^2 + \left(\frac{\partial T^i}{\partial z}\right)^2\right]\right.\right.\right.$$

$$\left. -2q^iT^i + 2\rho_i c_i T^i\frac{\partial T^i}{\partial \tau}\right\}dv + \frac{1-\delta_{iI}}{2}\int\int_{\Omega_i}(T^i - T^{i+1})^2 ds$$

$$+\frac{1}{2}\int\int_{\Omega_L^i}H_L^i(T^i - T_L^i)^2 ds + (1 - \delta_{il})\int\int_{\Omega_{qi}^i}q_\Omega^i T^i ds$$

$$\left.+\frac{1}{2}\int\int_{\Omega_t}H_1(T^1 - T_t)^2 ds + \frac{1}{2}\int\int_{\Omega_b}H_I(T^I - T_b)^2 ds\right\rangle$$

$$(1)$$

were $T^i = T^i(x,y,z,\tau)$ is temperature; k_i is thermal conductivity of the ith layer material; ρ_i is density of the layer material; c_i is specific heat of the ith layer; H_L^i, H_t, and H_b are convective heat transfer coefficients for the side, top, and bottom surfaces of the plate, respectively; T_L^i, T_t, and T_b are environment temperatures at the boundary of the side, top, and bottom surfaces; $q^i(x,y,\tau)$ is intensity of the ith inner heat source; $q_\Omega^i(x,y,\tau)$ is intensity of the ith film heat source located on the interface of adjacent layers; Ω_q^i is the area occupied by the ith film heat source; δ_{iI} is the Kronecker symbol; and τ is time.

Further transformations of Eq. (1), taking into account Gauss formulas, allow obtaining the heat conduction equation

$$\frac{\partial T}{\partial \tau} = \nu_i\Delta T^i + \frac{q^i}{c_i\rho_i}, \quad \Delta = \frac{\partial^2}{\partial x^2} + \frac{\partial^2}{\partial y^2} + \frac{\partial^2}{\partial z^2}, \quad i = \overline{1,I} \quad (2)$$

the boundary conditions on the external surfaces

$$-k_1\frac{\partial T^1}{\partial z} + H_1(T^1 - T_t) = 0, \quad (x,y,z) \in \Omega_t \quad (3)$$

$$k_I\frac{\partial T^I}{\partial z} + H_I(T^I - T_b) = 0, \quad (x,y,z) \in \Omega_b \quad (4)$$

on the layer interfaces

$$k_i\frac{\partial T^i}{\partial z} - k_{i+1}\frac{\partial T^{i+1}}{\partial z} + q_\Omega^i = 0, \quad T^i = T^{i+1}, \quad z = t_i, \quad t_i = \sum_{j=1}^{i}h_j,$$

$$i = \overline{1, I-1} \quad (5)$$

and on the side surface of the plate

$$k_i\frac{\partial T^i}{\partial \mathbf{n}} + H_L^i(T^i - T_L^i) = 0, \quad (x,y,z) \in \Omega_L^i, \quad i = \overline{1,I} \quad (6)$$

In Eq. (2), $\nu_i = k_i/(\rho_i c_i)$ is thermal diffusivity of the ith layer. In condition (6), $\mathbf{n} = \mathbf{n}(x,y)$ denotes the external normal to the side surface.

The distribution of temperatures in the layers and on the side surface, as well as the density of inner heat sources, is represented as [21]

$$T^i(x,y,z,\tau) = \sum_{r=0}^{R}T_r^i(x,y,\tau)f_r^i(z), \quad (x,y) \in \Omega \quad (7)$$

$$T_L^i(x,y,z,\tau) = \sum_{r=0}^{R}T_{Lr}^i(x,y,\tau)f_r^i(z), \quad (x,y) \in L \quad (8)$$

$$q^i(x,y,z,\tau) = \sum_{r=0}^{R}q_r^i(x,y,\tau)f_r^i(z), \quad (x,y) \in \Omega_q^i \quad (9)$$

where $f_r^i(z)$ is the Legendre polynomial of the rth degree

$$f_0^i = \frac{1}{\sqrt{h_i}}, \quad f_1^i = \frac{\sqrt{3}}{\sqrt{h_i}}(2\bar{z}_i - 1), \quad f_2^i = \frac{\sqrt{5}}{\sqrt{h_i}}(6\bar{z}_i^2 - 6\bar{z}_i + 1)$$

$$f_3^i = \frac{\sqrt{7}}{\sqrt{h_i}}(20\bar{z}_i^3 - 30\bar{z}_i^2 + 12\bar{z}_i - 1), \dots ; \quad \bar{z} = \frac{z - t_{i-1}}{h_i}; \quad i = \overline{1,I}$$

With account of expansion (7), conditions (3)–(5) form a system of linear algebraic equations that allows us to represent coefficients T_2^i and T_3^i in terms of coefficients T_0^j and T_1^j $(j = \overline{1,I})$

$$T_2^i = \sum_{j=1}^{I}(\chi_{j11}^iT_0^j + \chi_{j21}^iT_1^j) + \psi_1^i, \quad T_3^i = \sum_{j=1}^{I}(\chi_{j12}^iT_0^j + \chi_{j22}^iT_1^j)$$

$$+ \psi_2^i, \quad i = \overline{1,I} \quad (10)$$

where χ_{j11}^i, χ_{j12}^i, χ_{j21}^i, χ_{j22}^i, ψ_1^i and ψ_2^i are constants.

Expressions (10) allow writing expansion (7) as

$$T^i(x,y,z,\tau) = \sum_{j=1}^{I}[(\delta_{ij}f_0^i + \chi_{j11}^if_2^i + \chi_{j12}^if_3^i)T_0^j + (\delta_{ij}f_1^i + \chi_{j21}^if_2^i$$

$$+ \chi_{j22}^if_3^i)T_1^j] + \psi_1^if_2^i + \psi_2^if_3^i \quad (11)$$

So, temperature as expression (11) satisfies the boundary conditions on the external surfaces Eqs. (3) and (4), and on the layer interfaces Eq. (5). Taking into account Eq. (11), heat conduction Eq. (2) takes the form

$$\sum_{j=1}^{I}\left\{\left[\chi_{jk}^{31}I + \sum_{i=1}^{I}\chi_{ijk}^{11}\left(\frac{\partial^2}{\partial x^2} + \frac{\partial^2}{\partial y^2}\right)\right]T_0^j + \left[\chi_{jk}^{41}I + \sum_{i=1}^{I}\chi_{ijk}^{21}\left(\frac{\partial^2}{\partial x^2}\right.\right.\right.$$

$$\left.\left.+ \frac{\partial^2}{\partial y^2}\right)\right]T_1^j\right\} + \left(\frac{\partial^2}{\partial x^2} + \frac{\partial^2}{\partial y^2}\right)\sum_{i=1}^{I}\chi_{ik}^{51} + \chi_k^{61}I$$

$$-\sum_{j=1}^{I}\left[\left(\sum_{i=1}^{I}\chi_{ijk}^{11}\frac{\rho_ic_i}{k_i}\right)\frac{\partial T_0^j}{\partial \tau} + \left(\sum_{i=1}^{I}\chi_{ijk}^{21}\frac{\rho_ic_i}{k_i}\right)\frac{\partial T_1^j}{\partial \tau}\right] + \frac{q_0^k}{k_k}$$

$$+\sum_{i=1}^{I}\left(\chi_{k11}^i\frac{q_2^i}{k_i} + \chi_{k12}^i\frac{q_3^i}{k_i}\right) = 0$$

$$\sum_{j=1}^{I}\left\{\left[\chi_{jk}^{32}I+\sum_{i=1}^{I}\chi_{ijk}^{12}\left(\frac{\partial^2}{\partial x^2}+\frac{\partial^2}{\partial y^2}\right)\right]T_0^j+\left[\chi_{jk}^{42}I+\sum_{i=1}^{I}\chi_{ijk}^{22}\left(\frac{\partial^2}{\partial x^2}\right.\right.\right.$$

$$\left.\left.+\frac{\partial^2}{\partial y^2}\right)\right]T_1^j\right\}+\left(\frac{\partial^2}{\partial x^2}+\frac{\partial^2}{\partial y^2}\right)\sum_{i=1}^{I}\chi_{ik}^{52}+\chi_k^{62}I$$

$$-\sum_{j=1}^{I}\left[\left(\sum_{i=1}^{I}\chi_{ijk}^{12}\frac{\rho_i c_i}{k_i}\right)\frac{\partial T_0^j}{\partial\tau}+\left(\sum_{i=1}^{I}\chi_{ijk}^{22}\frac{\rho_i c_i}{k_i}\right)\frac{\partial T_1^j}{\partial\tau}\right]+\frac{q_1^k}{k_k}$$

$$+\sum_{i=1}^{I}\left(\chi_{k21}^i\frac{q_2^i}{k_i}+\chi_{k22}^i\frac{q_3^i}{k_i}\right)=0,\quad k=\overline{1,I}\qquad(12)$$

and the boundary condition on the side surface of the ith layer Eq. (6) takes the form

$$\sum_{j=1}^{I}\left[\left(\sum_{i=1}^{I}\chi_{ijk}^{11}k_i\right)\frac{\partial T_0^j}{\partial n}+\left(\sum_{i=1}^{I}\chi_{ijk}^{21}k_i\right)\frac{\partial T_1^j}{\partial n}+\left(\sum_{i=1}^{I}\chi_{ijk}^{11}H_L^i\right)T_0^j\right.$$

$$\left.+\left(\sum_{i=1}^{I}\chi_{ijk}^{21}H_L^i\right)T_1^j\right]+\sum_{i=1}^{I}\frac{\partial\chi_{ik}^{51}}{\partial n}k_i+\sum_{i=1}^{I}\chi_{ik}^{51}H_L^i-H_L^k T_{L1}^k=0$$

$$\sum_{j=1}^{I}\left[\left(\sum_{i=1}^{I}\chi_{ijk}^{12}k_i\right)\frac{\partial T_0^j}{\partial n}+\left(\sum_{i=1}^{I}\chi_{ijk}^{22}k_i\right)\frac{\partial T_1^j}{\partial n}+\left(\sum_{i=1}^{I}\chi_{ijk}^{12}H_L^i\right)T_0^j\right.$$

$$\left.+\left(\sum_{i=1}^{I}\chi_{ijk}^{22}H_L^i\right)T_1^j\right]+\sum_{i=1}^{I}\frac{\partial\chi_{ik}^{52}}{\partial n}k_i+\sum_{i=1}^{I}\chi_{ik}^{52}H_L^i-H_L^k T_{L2}^k$$

$$=0,\quad k=\overline{1,I}\qquad(13)$$

where

$$\chi_{ijk}^{\vartheta1}=\int_{\delta_{i-1}}^{\delta_i}\chi_{\vartheta ij}\chi_{1ik}dz,\quad\chi_{ijk}^{\vartheta2}=\int_{\delta_{i-1}}^{\delta_i}\chi_{\vartheta ij}\chi_{2ik}dz,\quad\vartheta=1,4$$

$$\chi_{ik}^{\vartheta1}=\int_{\delta_{i-1}}^{\delta_i}\chi_{\vartheta i}\chi_{1ik}dz,\quad\chi_{ik}^{\vartheta2}=\int_{\delta_{i-1}}^{\delta_i}\chi_{\vartheta i}\chi_{2ik}dz,\quad\vartheta=5,6$$

$$\chi_{1ij}=\delta_{ij}f_0^i+\chi_{j11}^i f_2^i+\chi_{j12}^i f_3^i,\quad\chi_{2ij}=\delta_{ij}f_0^i+\chi_{j21}^i f_2^i+\chi_{j22}^i f_3^i$$

$$\chi_{3ij}=\chi_{j11}^i\frac{12\sqrt5}{h_i^2}f_0^i+\chi_{j12}^i\frac{20\sqrt{21}}{h_i^2}f_1^i,\quad\chi_{4ij}=\chi_{j21}^i\frac{12\sqrt5}{h_i^2}f_0^i$$

$$+\chi_{j22}^i\frac{20\sqrt{21}}{h_i^2}f_1^i$$

$$\chi_{5i}=\psi_1^i f_2^i+\psi_2^i f_3^i,\quad\chi_{6i}=\psi_1^i\frac{12\sqrt5}{h_i^2}f_0^i+\psi_2^i\frac{20\sqrt{21}}{h_i^2}f_1^i$$

To solve systems (12) and (13), a method was used, which is similar to the immersion method [22]. It allows for representing the problem solution in analytical form. The initial arbitrary plan-shaped laminated plate is immersed into an auxiliary enveloping laminated plate with the same composition of layers. The shape of the enveloping plate is selected so that one can obtain a simple analytical solution. In this paper, the enveloping plate is a rectangular one with null conditions on the side surface (Fig. 2).

The convective heat transfer conditions on the top and bottom surfaces of the auxiliary plate coincide with the heat transfer conditions of the initial plate. To ensure meeting of actual boundary conditions (6) on the side surface of the initial plate, compensating sources $q_i^{\text{comp}}(x,y,z,\tau)$, $(x,y,z)\in\Omega_L^i$ are attached to the auxiliary plate over the trace of side surface Ω_L^i. The functions of compensating sources are represented as expansions similar to (9) $q_i^{\text{comp}}(x,y,z,\tau)$
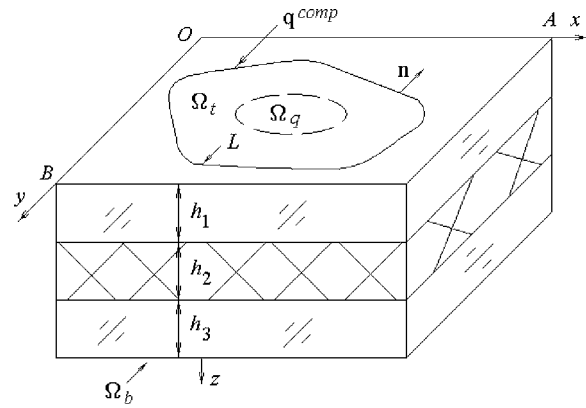

Fig. 2   Auxiliary plate

$$q_i^{\text{comp}}(x,y,z,\tau)=\sum_{r=0}^{R}q_{ir}^{\text{comp}}(x,y,\tau)f_r^i(z)$$

and they are included in heat conduction Eq. (12) as integral relationships

$$q_r^i(x,y,\tau)=\int_0^{s^*}q_{ir}^{\text{comp}}(x_L,y_L,\tau)\delta(x-x_L,y-y_L)ds,\quad r=0,1,2,3$$
$$(14)$$

where $\delta(x-x_L,y-y_L)$ is the two-dimensional Dirac delta function, and s^* is length of contour L of the initial plate.

The boundary conditions on side surface Ω_L^i, which the analytical solution should satisfy on account of the relationships (14), yield a system of integral equations for determining the intensities of compensating sources

$$\mathbf{B}^L\mathbf{T}[\mathbf{F}(x,y,\tau)]=\mathbf{C}^L,\quad x,y\in L\qquad(15)$$

where

$$B_{2k-12j-1}^L=\left(\sum_{i=1}^{I}\chi_{ijk}^{11}k_i\right)\frac{\partial}{\partial n}+\sum_{i=1}^{I}\chi_{ijk}^{11}H_L^i$$

$$B_{2k-12j}^L=\left(\sum_{i=1}^{I}\chi_{ijk}^{21}k_i\right)\frac{\partial}{\partial n}+\sum_{i=1}^{I}\chi_{ijk}^{21}H_L^i$$

$$B_{2k2j-1}^L=\left(\sum_{i=1}^{I}\chi_{ijk}^{12}k_i\right)\frac{\partial}{\partial n}+\sum_{i=1}^{I}\chi_{ijk}^{12}H_L^i$$

$$B_{2k2j}^L=\left(\sum_{i=1}^{I}\chi_{ijk}^{22}k_i\right)\frac{\partial}{\partial n}+\sum_{i=1}^{I}\chi_{ijk}^{22}H_L^i$$

$$C_{2k-1}^L=-\left[\left(\sum_{i=1}^{I}\frac{\partial\chi_{ik}^{51}}{\partial n}k_i\right)+\sum_{i=1}^{I}\chi_{ik}^{51}H_L^i-H_L^k T_{L1}^k\right]$$

$$C_{2k}^L=-\left[\left(\sum_{i=1}^{I}\frac{\partial\chi_{ik}^{52}}{\partial n}k_i\right)+\sum_{i=1}^{I}\chi_{ik}^{52}H_L^i-H_L^k T_{L2}^k\right]$$

$$\mathbf{T}=(T_0^1,T_1^1,\dots,T_0^j,T_1^j,\dots,T_0^I,T_1^I)^T$$

$$F_{2k-1}=\frac{q_0^k}{k_k}+\sum_{i=1}^{I}\left(\chi_{k11}^i\frac{q_2^i}{k_i}+\chi_{k12}^i\frac{q_3^i}{k_i}\right)$$

$$F_{2k} = \frac{q_1^k}{k_k} + \sum_{i=1}^{I}\left(\chi_{k21}^i \frac{q_2^i}{k_i} + \chi_{k22}^i \frac{q_3^i}{k_i}\right), \quad k=\overline{1,I}, \; j=\overline{1,I}$$

Further, $T_0^i(x,y,\tau)$, $T_1^i(x,y,\tau)$, and $q_r^i(x,y,\tau)$ are expanded into trigonometric series in functions satisfying the boundary conditions of the enveloping rectangular plate

$$T_0^i(x,y,\tau) = \sum_{m=1}^{M}\sum_{n=1}^{N} T_{0mn}^i(\tau)\sin\frac{m\pi x}{A}\sin\frac{n\pi y}{B}$$

$$T_1^i(x,y,\tau) = \sum_{m=1}^{M}\sum_{n=1}^{N} T_{1mn}^i(\tau)\sin\frac{m\pi x}{A}\sin\frac{n\pi y}{B}$$

$$q_r^i(x,y,\tau) = \sum_{m=1}^{M}\sum_{n=1}^{N} q_{rmn}^i(\tau)\sin\frac{m\pi x}{A}\sin\frac{n\pi y}{B}$$

where A and B are lengths of the sides of the enveloping rectangular plate in the direction of axes Ox and Oy. This makes it possible to reduce the heat conduction problem to integrating a system of ordinary differential equations

$$\mathbf{M}\dot{\mathbf{T}}_{mn} + \boldsymbol{\Lambda}\mathbf{T}_{mn} = \mathbf{F}_{mn} \tag{16}$$

with initial conditions

$$\mathbf{T}_{mn} = \mathbf{T}_{mn}^0, \quad t=0 \tag{17}$$

Here $\mathbf{T}_{mn}$, $\mathbf{T}_{mn}^0$, and $\mathbf{F}_{mn}$ are vectors with the following components

$$\mathbf{T}_{mn} = \left(T_{0mn}^1, T_{1mn}^1, \ldots, T_{0mn}^I, T_{1mn}^I\right)^T$$

$$\mathbf{T}_{mn}^0 = \left(T_{0mn}^{01}, T_{1mn}^{01}, \ldots, T_{0mn}^{0I}, T_{1mn}^{0I}\right)^T$$

$$\mathbf{F}_{mn} = \left(F_{1mn}, \ldots, F_{2Imn}\right)^T$$

$$F_{2k-1\,mn} = \frac{q_{0mn}^k}{k_k} + \sum_{i=1}^{I}\left(\chi_{k11}^i \frac{q_{2mn}^i}{k_i} + \chi_{k12}^i \frac{q_{3mn}^i}{k_i}\right)$$

$$F_{2kmn} = \frac{q_{1mn}^k}{k_k} + \sum_{i=1}^{I}\left(\chi_{k21}^i \frac{q_{2mn}^i}{k_i} + \chi_{k22}^i \frac{q_{3mn}^i}{k_i}\right), \quad k=\overline{1,I}$$

$\mathbf{M}$ and $\boldsymbol{\Lambda}$ are square matrices with elements of the form

$$M_{2k-1\;2j-1} = \sum_{i=1}^{I} \chi_{ijk}^{11}\frac{\rho_i c_i}{k_i}, \quad M_{2k-1\;2j} = \sum_{i=1}^{I} \chi_{ijk}^{21}\frac{\rho_i c_i}{k_i}$$

$$M_{2k\;2j-1} = \sum_{i=1}^{I} \chi_{ijk}^{12}\frac{\rho_i c_i}{k_i}, \quad M_{2k\;2j} = \sum_{i=1}^{I} \chi_{ijk}^{22}\frac{\rho_i c_i}{k_i}$$

$$\Lambda_{2k-1\;2j-1} = \chi_{jk}^{31} + L_{mn}\sum_{i=1}^{I} \chi_{ijk}^{11}, \quad \Lambda_{2k-1\;2j} = \chi_{jk}^{41} + L_{mn}\sum_{i=1}^{I} \chi_{ijk}^{21}$$

$$\Lambda_{2k\;2j-1} = \chi_{jk}^{32} + L_{mn}\sum_{i=1}^{I} \chi_{ijk}^{12}, \quad \Lambda_{2k\;2j} = \chi_{jk}^{42} + L_{mn}\sum_{i=1}^{I} \chi_{ijk}^{22},$$

$$k=\overline{1,I}, \; j=\overline{1,I}$$

Systems (15) and (16) are integrated over the time interval $[0,\tau^*]$. This interval is divided into κ equal interval intervals with length $\Delta\tau$, so that $\tau^* = \kappa\Delta\tau$. At such time of discretization, by applying the method of solution expansion into Taylor's series [23], the form of solution of system (16) at each time step can be represented as recurrent relationships

$$\mathbf{T}_{mn}^{\kappa+1} = \widetilde{\mathbf{A}}\mathbf{T}_{mn}^{\kappa} + \widetilde{\mathbf{B}}\mathbf{F}_{mn}^{\kappa+1} \tag{18}$$

where κ is the current number of the time interval; and $\widetilde{\mathbf{A}}$ and $\widetilde{\mathbf{B}}$ are square matrices obtained by numeric transformations of matrices $\mathbf{M}$ and $\boldsymbol{\Lambda}$ Eq. (16).

Besides, functions T_0^i and q_r^i, included in the boundary conditions of the initial plate, are expanded into a series over the trace of contour L [22]

$$T_0^{i\kappa+1}(s) = \sum_{\mu=0}^{\mu^*}\sum_{\alpha=1,2} T_{0\alpha\mu}^{i\kappa+1}d_{\alpha\mu}(s), \quad T_0^{i\kappa+1}(s) = \sum_{\mu=0}^{\mu^*}\sum_{\alpha=1,2} T_{0\alpha\mu}^{i\kappa+1}d_{\alpha\mu}(s) \tag{19}$$

$$q_r^{i\kappa+1}(s) = \sum_{\mu=0}^{\mu^*}\sum_{\alpha=1,2} q_{r\alpha\mu}^{i\kappa+1}d_{\alpha\mu}(s) \tag{20}$$

where

$$d_{1\mu} = \sin[\mu\gamma(s)], \quad d_{2\mu} = \cos[\mu\gamma(s)]$$

$$\gamma(s) = 2\pi\int_0^s d\widetilde{s} \Big/ \int_0^{s^*} d\widetilde{s}, \quad 0 \le \gamma(s) \le 2\pi$$

With account of transformations (18)–(20), the solution of the system of integral Eqs. (15) at each time step is reduced to solving a system of linear algebraic equations with respect to the coefficients of expanding into a series the functions of compensating sources $q_{r\mu\alpha}^i$

$$\sum_{\mu=0}^{\mu^*}\sum_{\alpha=1,2}\sum_{\zeta=1}^{2I} \Gamma_{\xi\zeta\eta\beta\mu\alpha}F_{\mu\alpha}^{\xi} + \frac{F_{\mu\alpha}^{\xi}}{2} = V_{\xi\eta\beta}, \quad \xi=\overline{1,2I},$$

$$\eta=\overline{0,\eta^*}, \quad \beta=1,2$$

Here

$$F_{\mu\alpha}^{\xi} = \sum_{j=1}^{l}\frac{1}{k_j}(\chi_{i\gamma 1}^j q_{1\mu\alpha}^{j\kappa+1} + \chi_{i\gamma 2}^j q_{2\mu\alpha}^{j\kappa+1}) + \frac{1}{k_i}q_{\gamma-1\mu\alpha}^{i\kappa+1},$$

$$\gamma=1,2, \quad i=\overline{1,I}, \quad \begin{cases}\gamma=1, & \xi=2i-1 \\ \gamma=2, & \xi=2i\end{cases}$$

$$\Gamma_{\xi\zeta\eta\beta\mu\alpha} = (M_{\xi\zeta}^1\Theta_{\mu\alpha}^1 + M_{\xi\zeta}^2\Theta_{\mu\alpha}^2)\Theta_{\eta\beta}, \quad V_{\xi\eta\beta} = V_{\xi\eta\beta}^2 - V_{\xi\eta\beta}^1$$

$$V_{\xi\eta\beta}^1 = \sum_{\mu=0}^{\mu^*}\sum_{\alpha=1,2}(\Lambda_\xi^1\Theta_{\mu\alpha}^1 + \Lambda_\xi^2\Theta_{\mu\alpha}^2)\Theta_{\eta\beta}, \quad V_{\xi\eta\beta}^2 = \Lambda_\xi^3\Theta_{\eta\beta}$$

$$M_{2k-1\;2j-1}^1 = \sum_{i=1}^{I} k_i\chi_{ijk}^{11}, \quad M_{2k-1\;2j}^1 = \sum_{i=1}^{1} k_i\chi_{ijk}^{21}$$

$$M_{2k\;2j-1}^1 = \sum_{i=1}^{I} k_i\chi_{ijk}^{12}, \quad M_{2k\;2j}^1 = \sum_{i=1}^{1} k_i\chi_{ijk}^{22}$$

$$M_{2k-1\;2j-1}^2 = \sum_{i=1}^{I} H_L^i\chi_{ijk}^{11}, \quad M_{2k-1\;2j}^2 = \sum_{i=1}^{1} H_L^i\chi_{ijk}^{21}$$

$$M_{2k\;2j-1}^2 = \sum_{i=1}^{I} H_L^i\chi_{ijk}^{12}, \quad M_{2k\;2j}^2 = \sum_{i=1}^{1} H_L^i\chi_{ijk}^{22}$$

$$\Lambda_{2k-1}^1 = \sum_{i=1}^{I} k_i\chi_{ik}^{51}, \quad \Lambda_{2k}^1 = \sum_{i=1}^{I} k_i\chi_{ik}^{52}$$
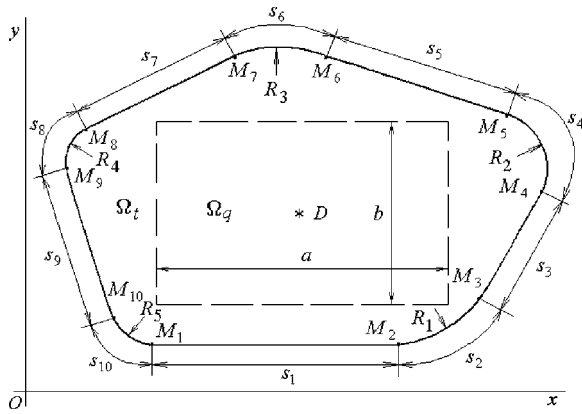
Fig. 3   Plan shape of plate

Fig. 4   Temperature distribution over plate thickness 1—1 s, 2—10 s, 3—10^2 s, 4—10^3 s, 5—10^5 s, 6 — solution of stationary problem, 7 — solution obtained by FEM at the point of time $\tau = 10^2$ s, and 8 — solution obtained by FEM at the point of time $\tau = 10^4$ s

$$\Lambda^2_{2k-1} = \sum_{i=1}^{I} H^i_L \chi^{51}_{ik}, \quad \Lambda^2_{2k} = \sum_{i=1}^{I} H^i_L \chi^{52}_{ik}$$

$$\Lambda^3_{2k-1} = H^k_L T^k_{L1}, \quad \Lambda^3_{2k} = H^k_L T^k_{L2}$$

$$\Theta^1_{\mu\alpha} = \frac{4}{AB} \sum_{m=1}^{M} \sum_{n=1}^{N} \int_0^{s^*} \frac{\partial \sin \dfrac{m\pi x}{A} \sin \dfrac{n\pi y}{B}}{\partial \mathbf{n}} d_{\mu\alpha} \, ds$$

$$\Theta^2_{\mu\alpha} = \frac{4}{AB} \sum_{m=1}^{M} \sum_{n=1}^{N} \int_0^{s^*} \sin \frac{m\pi x}{A} \sin \frac{n\pi y}{B} d_{\mu\alpha} \, ds$$

$$\Theta_{\eta\beta} = \frac{1}{\lambda_\eta} \sum_{m=1}^{M} \sum_{m=1}^{N} \int_0^{s^*} \sin \frac{m\pi x}{A} \sin \frac{n\pi y}{B} d_{\beta\eta} \, ds,$$

$$\lambda_\eta = \begin{cases} 2\pi, & \eta = 0 \\ \pi, & \eta \neq 0 \end{cases}$$

The values of temperatures in the layers of plates (Eq. (11)) are found after the intensities of compensating sources have been computed (Eq. (20)).

3   Numerical Examples

The validity of the method suggested is illustrated by example of the problem on the thermal state of a five-layer plate. The plate contour consists of K sections of straight lines and mating therewith K arcs of circles ($K = 5$). The analysis schematic of the plate is shown in Fig. 3. The location of the heat source is shown with a dashed line.

Contour sections s_{2k-1}, which are sections of straight lines (Fig. 3), are specified by the following equations

$$x = x_{2k-1} + (S - S_{2(k-1)})\cos \alpha_{2k-1}$$

$$y = y_{2k-1} + (S - S_{2(k-1)})\sin \alpha_{2k-1}, \quad k = \overline{1,K} \tag{21}$$

where point $M_{2k-1}(x_{2k-1}, y_{2k-1})$ is the origin of the $(2k-1)$th straight section.

Contour sections s_{2k}, which are arcs of circles (Fig. 3), are specified by relationships

$$x = x_{2k} + R_k \left[\sin\left(\frac{S - S_{2k-1}}{R_k} + \alpha_{2k-1} \right) - \sin \alpha_{2k-1} \right]$$
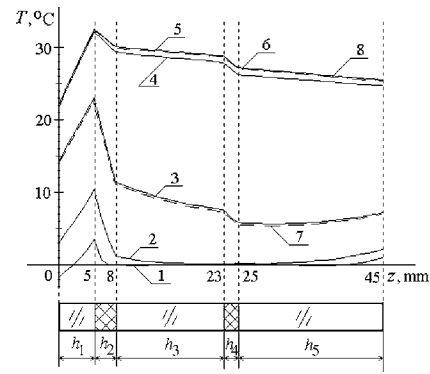
$$y = y_{2k} + R_k \left[\cos\left(\frac{S - S_{2k-1}}{R_k} + \alpha_{2k-1} \right) - \cos \alpha_{2k-1} \right], \quad k = \overline{1,K} \tag{22}$$

where point $M_{2k}(x_{2k}, y_{2k})$ is the end of the $(2k-1)$th straight section. Besides, the following designations are accepted in formulas (21) and (22)

$$S_k = \sum_{i=1}^{k} s_i, \quad S_0 = 0$$

α_{2k-1} is the angle between the $(2k-1)$th straight section on the contour and the positive direction of axis Ox, and S is the length of the contour section from the origin of reference [point $M_1(x_1, y_1)$] to current point $M(x, y)$ on the given contour section.

The plate has the following characteristics: $s_1 = 0.5$ m, $s_3 = 0.23$ m, $s_5 = 0.44$ m, $s_7 = 0.34$ m, $s_9 = 0.31$ m; $R_1 = 0.25$ m, $R_2 = 0.12$ m, $R_3 = 0.27$ m, $R_4 = 0.08$ m, $R_5 = 0.11$ m; $\alpha_1 = 0$ deg, $\alpha_3 = 60$ deg, $\alpha_5 = 160$ deg, $\alpha_7 = 205$ deg, $\alpha_9 = 285$ deg; $h_1 = 5 \times 10^{-3}$ m, $h_2 = 3 \times 10^{-3}$ m, $h_3 = 1.5 \times 10^{-2}$ m, $h_4 = 2 \times 10^{-3}$ m, $h_5 = 2 \times 10^{-2}$ m; $k_i = 1.61$ W/(m$^\circ$C), $c_i = 0.75 \times 10^3$ J/(kg$^\circ$C), $\rho_i = 2.5 \times 10^3$ kg/m^3 ($i = 1,3,5$); and $k_i = 0.17$ W/(m$^\circ$C), $c_i = 1.5 \times 10^3$ J/(kg$^\circ$C), $\rho_i = 1.2 \times 10^3$ kg/m^3 ($i = 2,4$).

The film heat source is located between the first and second layers, occupies area Ω_q with dimensions $a = 0.64$ m and $b = 0.4$ m, and its power $q^1 = 3.5 \times 10^3$ W/m^2.

The convective heat transfer coefficients, the environment, and initial temperatures are as follows: $H_1 = 80$ W/(m$^2 {}^\circ$C), $H_1 = 25$ W/(m$^2 {}^\circ$C), $T_t = -20\,^\circ$C, $T_b = 20\,^\circ$C, and $T^{0i} = 0\,^\circ$C, $I = \overline{1, I}$.

The condition of heat insulation is satisfied on the plate's side surface

$$\frac{\partial T^i}{\partial \mathbf{n}} = 0$$

As numerical analysis of the solution has shown, the first four terms in series (7)–(9) can be taken into account to provide sufficient accuracy of the problem solution. A comparison of the solution with results obtained by using FEM for plates with a canonical plan shape was carried out earlier in Ref. [21].

Figure 4 shows the temperature distribution over plate thickness in point D (see Fig. 3) obtained by the proposed method and FEM for different points of time. Point D is located in the middle of area Ω_q occupied by the heat source, and its coordinates are ($x_1 + c, y_1 + d$), where $c = 0.3$ m, and $d = 0.325$ m. Figure 4 also shows a similar temperature distribution obtained when solving the stationary heat conduction problem. It is evident that, by the point of
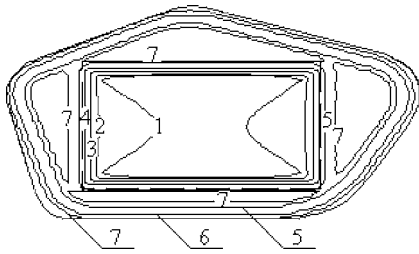
Fig. 5 Temperature distribution on surface Ω_t at the point of time $\tau=10^2$ s: 1—+14.3°C, 2—+14.2°C, 3—+12°C, 4—0°C, 5—−13°C, 6—−13.5°C, and 7—−14.1°C
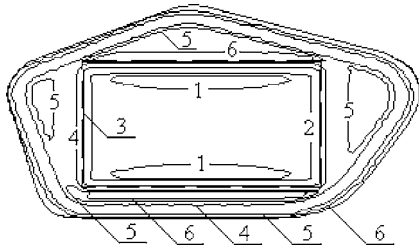

Fig. 6 Temperature distribution on surface Ω_1 (surface with heat source) at the point of time $\tau=10^2$ s: 1—+23°C, 2—+22°C, 3—0°C, 4—−12°C, 5—−12.7°C, and 6—−12.9°C
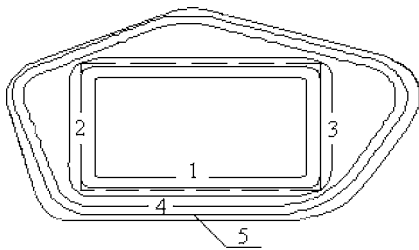

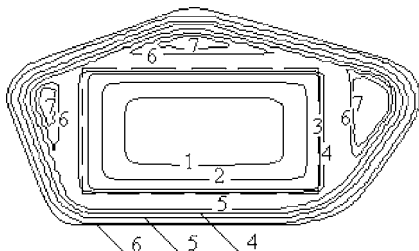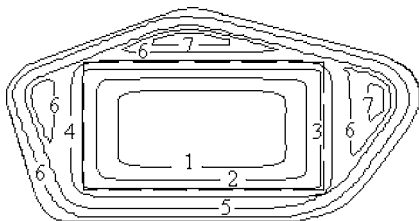**Fig. 7 Temperature distribution on surface Ω_b at the point of time $\tau=10^2$ s: 1—+7.1°C, 2—+6°C, 3—+5.5°C, 4—+5°C, and 5—+4.1°C**

Fig. 8 Temperature distribution on surface Ω_t at the point of time $\tau=10^4$ s: 1—+22°C, 2—+21°C, 3—0°C, 4—−10°C, 5—−14°C, 6—−15.2°C, and 7—−15.3°C

Fig. 9 Temperature distribution on surface Ω_1 (surface with heat source) at the point of time $\tau=10^4$ s: 1—+32.4°C, 2—+31°C, 3—0°C, 4—−13°C, 5—−13.2°C, 6—−14°C, and 7—−14.1°C
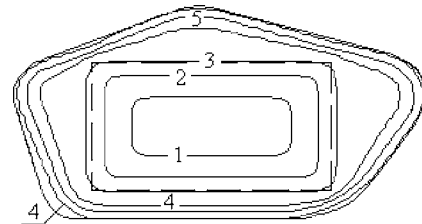
Fig. 10 Temperature distribution on surface Ω_b at the point of time $\tau=10^4$ s: 1—+25.4°C, 2—+22°C, 3—+9°C, 4—+5°C, and 5—+4°C

time $\tau=10^4$ s, the temperature field acquires a stationary character. The maximum variance in solutions of the stationary and nonstationary problems was within 0.3%, which confirms the accuracy of the method developed and the validity of results obtained.

Figures 5–7 show the temperature fields on the plate surfaces at the point of time $\tau=10^2$ s when the temperature drop between layers is at a maximum. Figures 8–10 show the temperature fields on the plate surfaces at the point of time $\tau=10^4$ s. The external surface of the first layer Ω_t (Figs. 5 and 8) and the surfaces containing heat source Ω_1 (Figs. 6 and 9), exhibit a sharp change in temperature close to the edge of the area occupied by the heat generating film. Such differentials can result in significant temperature stresses in plate layers. The temperature on the external surface of the fifth layer Ω_b (Figs. 7 and 10) is only positive.

4 Conclusions

An analytical method of solving nonstationary heat conduction problems for laminated plates has been developed. It allows us to describe the heat condition of plates with a noncanonical plan shape for different boundary condition options on the contour and face surfaces of the plate.

The results of analyzing temperature fields can be used for solving problems in thermal elasticity of laminated plates. Selecting adequately the shape, power, and dimensions of the heat source makes it possible to ensure the required values of stresses in layers.

The approach suggested can be applied for designing heating systems and determining temperature stresses in laminated glazing for different vehicles.

References

[1] Goldstein, R. J. et al., 2005, "Heat Transfer—A Review of 2002 Literature," Int. J. Heat Mass Transfer, **48**(5), pp. 819–927.
[2] Goldstein, R. J. et al., 2006, "Heat Transfer—A Review of 2003 Literature," Int. J. Heat Mass Transfer, **49**(3–4), pp. 451–534.
[3] Khdeir, A. A., 1997, "On the Thermal Response of Antisymmetric Angle-Ply Laminated Plates," ASME J. Appl. Mech., **64**(1), pp. 229–233.
[4] Verijenko, V. E., Tauchert, T. R., and Tabakov, P. Y., 1999, "Refined Theory of Laminated Anisotropic Shells for the Solution of Thermal Stress Problems," J. Therm. Stresses, **22**(1), pp. 75–100.
[5] Barut, A., Madenci, E., and Tessler, A., 2000, "Non-Linear Analysis of Composite Panels Under Non-Uniform Temperature Distribution," Int. J. Solids Struct., **37**(27), pp. 3681–3713.
[6] Savoia, M., and Reddy, J. N., 1995, "Three-Dimensional Thermal Analysis of Laminated Composite Plate," Int. J. Solids Struct., **32**(5), pp. 539–608.
[7] Oguamanam, D. C. D., Hansen, J. S., and Heppler, G. R., 2004, "Nonlinear Transient Response of Thermally Loaded Laminated Panels," ASME J. Appl. Mech., **71**(1), pp. 49–56.
[8] Kim, J., Moon, T. J., and Howell, J. R., 2003, "Transient Thermal Modeling of In-Situ Curing During Tape Winding of Composite Cylinders," J. Heat Transfer, **125**(1), pp. 137–146.
[9] Phongthanapanich, S., and Dechaumphai, P., 2004, "Evaluation of Combined Delaunay Triangulation and Remeshing for Finite Element Analysis of Conductive Heat Transfer," Trans. Can. Soc. Mech. Eng., **27**(4), pp. 319–339.
[10] Davey, K., and Hinduja, S., 1989, "An Improved Procedure for Solving Transient Heat Conduction Problems Using the Boundary Element Method," Int. J. Numer. Methods Eng., **28**(12), pp. 2293–2306.
[11] Hematiyan, M. R., and Karami, G., 2003, "A Boundary Element Formulation for Inverse Analysis of Solidification Problems Using Pseudo Heat Source Method," Comput. Mech., **31**(3/4), pp. 262–271.

[12] Van der Tempel, L., 2002, "Transient Heat Conduction in a Heat Generating Layer Between Two Semi-Infinite Media," J. Heat Transfer, **124**(2), pp. 299–306.

[13] Cai, R., and Zhang, N., 2003, "Explicit Analytical Solutions of Linear and Nonlinear Interior Heat and Mass Transfer Equation Sets for Drying Process," J. Heat Transfer, **125**(1), pp. 175–178.

[14] Monde, M., Arima, H., and Mitsutake, Y., 2003, "Estimation of Surface Temperature and Heat Flux Using Inverse Solution for One-Dimensional Heat Conduction," J. Heat Transfer, **125**(2), pp. 213–223.

[15] Lu, X., Tervola, P., and Viljanena, M., 2006, "Transient Analytical Solution to Heat Conduction in Multi-Dimensional Composite Cylinder Slab," Int. J. Heat Mass Transfer, **49**(5–6), pp. 1107–1114.

[16] Padovan, J., 1975, "Thermoelasticity of Anisotropic Generally Laminated Slabs Subject to Spatially Periodic Thermal Loads," ASME J. Appl. Mech., **42**(2), pp. 341–346.

[17] Ootao, Y., Tanigawa, Y., and Hatachi, S., 2001, "Transient Thermal Stresses of Angle-Ply Laminated Strip Due to Nonuniform Heat Supply in the Width Direction," Trans. Jpn. Soc. Mech. Eng., Ser. A, **44**(2), pp. 222–230.

[18] Ootao, Y., and Tanigawa, Y., 2001, "Control of Transient Thermoelastic Displacement of a Two-Layered Composite Plate Constructed of Isotropic Elastic and Piezoelectric Layers Due to Nonuniform Heating," Arch. Appl. Mech., **71**(4–5), pp. 207–220.

[19] Nusier, S. Q., and Newaz, G. M., 1998, "Transient Residual Stresses in Thermal Barrier Coatings: Analytical and Numerical Results," ASME J. Appl. Mech., **65**(2), pp. 346–353.

[20] Altenbakh, I., Gabbert, U., Dankert, J., Köppler, H., Koczyk, S., Sacharov, A. S., Kislookij, V. N., and Kiričevskij, V. V., 1982, *Die Methode der Finiten Elemente in der Festkörpermechanik*, VEB Fachbuchverlag, Leipzig, Chap. 2.

[21] Kantor, B. Ya., Smetankina, N. V., and Shupikov, A. N., 2001, "Analysis of Non-Stationary Temperature Fields in Laminated Strips and Plates," Int. J. Solids Struct., **38**(48/49), pp. 8673–8684.

[22] Shupikov, A. N., and Smetankina, N. V., 2001, "Non-Stationary Vibration of Multilayer Plates of an Uncanonical Form. The Elastic Immersion Method," Int. J. Solids Struct., **38**(14), pp. 2271–2290.

[23] Shupikov, A. N., and Ugrimov, S. V., 1999, "Vibrations of Multilayer Plates Under the Effect of Impulse Loads. Three-Dimensional Theory," Int. J. Solids Struct., **36**(22), pp. 3391–3402.

Modeling of Radiation Heat Transfer in the Drawing of an Optical Fiber With Multilayer Structure

Chunming Chen

Yogesh Jaluria
e-mail: jaluria@jove.rutgers.edu

Department of Mechanical and Aerospace
Engineering,
Rutgers, The State University of New Jersey,
New Brunswick, NJ 08903

A numerical model is developed to study the radiative heat transfer in a furnace for optical fiber drawing with a core-cladding structure in the fiber. The focus is on the effect of the difference in composition and thus the radiation properties in the two regions on radiative transport. The zonal method is applied to calculate the radiative heat transfer within the neck-down region of the preform. The radiative heat transfer between the preform and the furnace is computed by an enclosure analysis. A parallel computational scheme for determining the direct exchange areas is also studied. The radiation model is verified by comparisons with benchmark problems. Numerical results for a pure silica preform, a GeO_2-doped silica core with a pure silica cladding preform, and a pure silica core with a B_2O_3-doped silica cladding preform are presented. Radiation properties for these are obtained from the literatures and a three-band model is developed to represent the values. It is found that radiative heat flux on the surface of the preform is strongly affected by the differences in the absorption coefficient due to doping. However, changes of about 1% in the refractive index have only a small effect on radiative heat transfer. The basic approach is outlined in order to form the basis for simulating optical fiber drawing processes, which typically involve fibers and preforms with a core and a cladding. Furthermore, the approach can apply to estimate the multi-layer fiber drawing, which is of interest in the fabrication of specialty fibers that have been finding uses in a variety of practical applications. The model can be extended to other similar processes, which involve multiple regions with different radiation properties. The main interest in this study is on the approximate representation of radiation properties and on the modeling of the transport process. [DOI: 10.1115/1.2430723]

Keywords: radiation, heat transfer, multi-layer, cylinder, zonal method

1 Introduction

The manufacture of silica optical fibers typically begins with doped silica preforms, which usually consist of two concentric cylinders called the core and the cladding that the core has a higher refractive index. In a draw tower, the preform is pulled through a high-temperature cylindrical furnace. When the preform is heated beyond its softening point of about 1900 K for silica, it can be drawn into a fiber of diameter around 125 μm by an applied axial tension. The region where the diameter of the preform decreases significantly is called the neck-down region. A schematic diagram of the fiber drawing process is shown as Fig. 1. During this drawing process, the radiative heat transfer is known to be the dominant mode of energy transport [1]. Therefore a rigorous study on the radiative transport is essential for an accurate simulation of the process.

The radiative transport in the furnace for the drawing of pure silica fibers has been investigated by a number of researchers (Paek and Runk [2], Myers [1], Lee and Jaluria [3–5], Kaminski [6], Yin and Jaluria [7,8], and Wei et al. [9]). Paek and Runk [2] approximated the radiative heat flux absorbed in the preform from the measured temperature distribution at the furnace. Myers [1] first presented a two-band model for the absorption coefficient of silica glass. He decoupled the temperature of the furnace from that of the preform and determined the temperature of the furnace and

the radiative heat flux leaving the furnace by the method of Usiskin and Siegel [10]. Lee and Jaluria [3–5] considered the furnace, the preform, the top, and the bottom disks as an enclosure and solved for the radiation heat transfer within this enclosure. All these early studies used the optically thick assumption for radiation absorption in the glass. However, this approximation cannot be applied to the lower neck-down region, since the diameter of the preform becomes very small as it approaches the fiber diameter. Besides the optically thick approximation, Kaminski [6] employed the $P1$ approximation for calculating the radiative heat flux in the upper neck-down region, which can often be treated as an optically thick region. In order to achieve accurate results within the whole neck-down region, Yin and Jaluria [7,8] used the zonal method to investigate the radiative transport. A comparison with the results from the optically thick approximation showed that the zonal method was more accurate for considering radial temperature variations and the small-diameter lower neck-down region. Recently, the discrete ordinates method was used by Wei et al. [9] to study the spectral radiative transfer and the transient temperature field in a semitransparent glass rod. They also revealed that the effects of the absorption coefficient in the short wavelength region ($\lambda < 3 \ \mu$m) on the radiative heat transfer could not be neglected.

However, all these studies neglected the difference in the radiative properties between the core and the cladding, even though they may have considerable effect on the radiative transfer between the furnace and the preform. For optical communication purposes, the core always has a slightly higher (0.1–1.0%) refractive index than that of the cladding. In order to change the refrac-
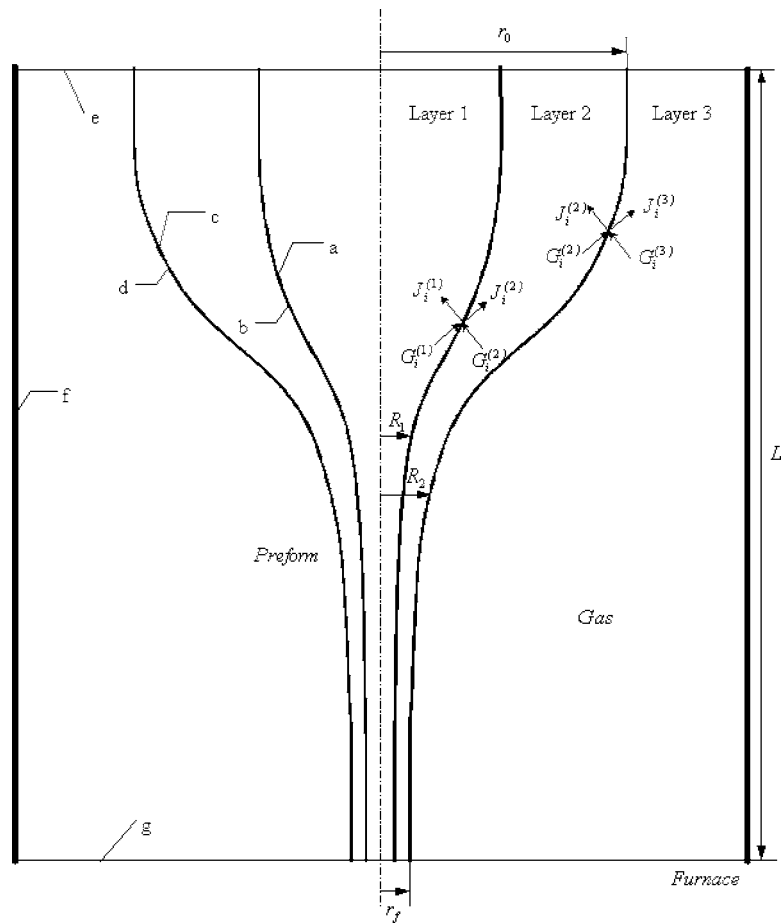
Fig. 1   Schematic diagram of a double-layer silica fiber drawing, indicating the radiosities and irradiations on the interfaces

tive index of silica, chemicals called "dopants" are added into pure silica. For example, GeO_2, P_2O_5, TiO_2, and Al_2O_3 are often used to increase the refractive index; F and B_2O_3 are used to reduce the refractive index [11]. Three typical refractive index profiles in optical fibers are shown in Fig. 2 [12]. The transmission characteristics of optical fiber are also significantly affected by dopants. The absorption loss comes from three sources: intrinsic ultraviolet absorption, intrinsic infrared absorption, and extrinsic impurity absorption. Intrinsic infrared absorption spectra of GeO_2, and B_2O_3 doped fused silica and pure silica were measured in the $1.8-25$ μm wavelength region by Izawa et al. [13,14]. The spectrum of 10 wt % GeO_2-doped fused silica is found to be very close to that of pure silica, except that the absorption peaks slightly shift to longer wavelength in the $3-25$ μm wavelength region. In the shorter $1.8-3.0$ μm wavelength region, the absorption loss mechanism of pure silica is also dominant in GeO_2-doped fuse silica core fiber. However the intrinsic infrared absorption spectrum is significantly affected by doping with B_2O_3. Strong variations, from pure silica absorption bands, are observed at 3.7, 7.4, 12.4, 13.9, and 15.3 μm in 5 wt % B_2O_3 doped silica and the absorption loss in $1.8-3.0$ μm increases by several orders of magnitude in $B_2O_3-GeO_2$-doped silica core fiber. The intrinsic ultraviolet absorption spectra of GeO_2, and B_2O_3-doped fused silica are obtained by Shibata [13]. Strong increases in absorption loss are found due to these two dopants, GeO_2, and B_2O_3, in the 0.2–0.5 wavelength region. Extrinsic absorption usually comes from OH ions or other impurities introduced in the fiber fabrication process. The OH content of the above measured fibers is about 50 ppb and gives only a slight absorption loss about 2.7 μm [13,14].

Since the absorption coefficient and refractive index of the doped silica preform are significantly affected by the dopants, it is of particular interest to investigate the effects of different doping materials and their amounts on the radiative heat transfer within the neck-down region for doped silica preforms. Yin and Jaluria [8] briefly studied a simpler case of thermal transport in a double-layer preform without neck-down. They found that the temperature of the preform increases slightly due to 1% difference in the refractive index between the core and the cladding. But the effects of a difference in the absorption coefficients (even 50%) were found to be negligible. However, it is necessary to extend the investigation to the neck-down region to quantify the relation between the dopants and the radiative heat transfer, because the temperature distribution and radiative heat flux are strongly dependent on the neck-down profile.

In this paper, only the radiation heat transfer in the optical fiber drawing process is considered. Further study will couple all three kinds of heat transfer, namely radiation, conduction, and convection, for complete modeling of the multi-layer fiber. The zonal method is applied to study radiation transport within the neck-down region of a double-layer doped silica preform. The preform is considered as a participating medium without scattering. The core and the cladding, which have been doped with various materials, are treated as two separate layers bounded by a diffuse interface. The radiative heat transfer for two different doped silica preforms is studied here; one is GeO_2-doped silica core with pure silica cladding, the other is pure silica core with B_2O_3-doped silica cladding. Three-band models for the absorption coefficients of pure silica, GeO_2-doped silica and B_2O_3-doped silica are developed from Izawa's results [13,14]. The radiative heat fluxes at
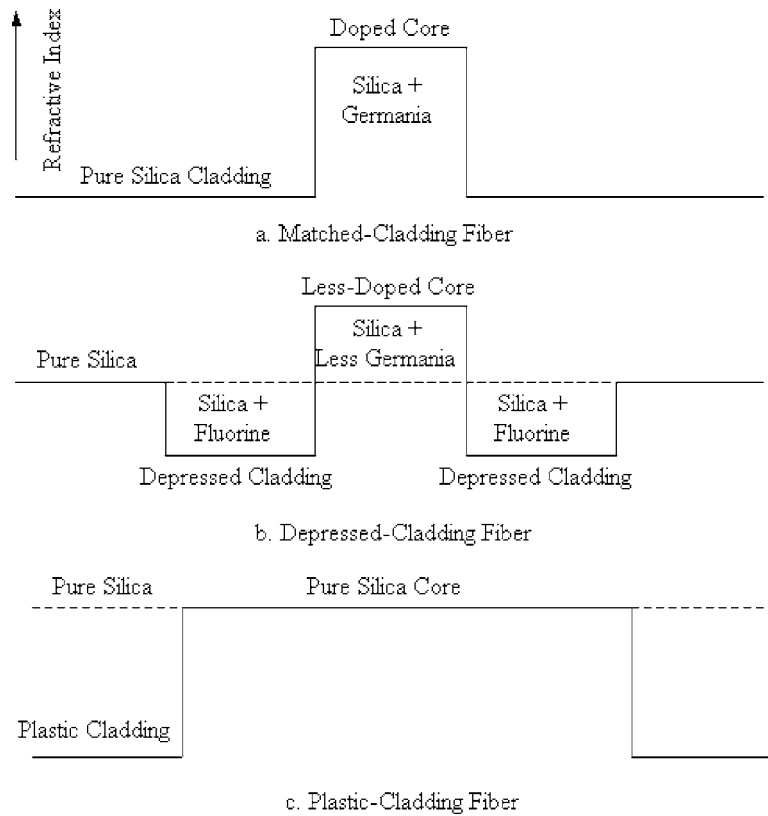
Fig. 2 Refractive-index profile of: (*a*) matched-cladding; and (*b*) depressed-cladding single-mode fibers and (*c*) plastic-cladding silica multimode fibers (adapted from Hecht [12])

the interfaces are calculated for prescribed temperature distributions in the preform. The effects of dopants GeO_2 and B_2O_3 on the radiative heat flux are investigated.

2 Analysis and Numerical Approach

The radiative transport inside a cylindrical furnace is considered here. The surface of the furnace is assumed to be diffuse and gray. The openings of the top and the bottom are considered to be black and at the ambient temperature. The inner and outer surfaces of the preform are assumed to be diffuse, an assumption that has been used by Yin and Jaluria [7]. They found that the error caused by the diffuse surface assumption is not significant by comparing the emissivity of a glass rod for both specular and diffuse surfaces. The preform is a semi-transparent participating medium in two layers, the core and the cladding, made of pure silica or various doped silica. The refractive index of the core is usually slightly higher than that of the cladding by 0.1–1.0%. The refractive index of pure fused silica is taken as 1.42 [15]. The infrared absorption spectra of pure and doped silica glass were measured by Izawa et al. [13,14], as shown as Fig. 3. For simplicity, three-band models are adapted in the study from Izawa's data to approximate the absorption coefficients of pure and doped silica glass. The average absorption coefficient in a particular wavelength interval is given by

$$\bar{a} = -\ln\left[\int_{\lambda_1}^{\lambda_2} e^{-a_\lambda(\lambda)} d\lambda \Big/ (\lambda_2 - \lambda_1)\right] \quad (1)$$

For pure fused silica with low OH content, the band absorption models developed as

$$a = 0, \text{ for } \lambda < 0.15 \ \mu m \quad (2)$$

$$a = 0.0059 \text{ cm}^{-1}, \text{ for } 0.15 \ \mu m \leq \lambda < 3.0 \ \mu m \quad (3)$$

$$a = 0.8455 \text{ cm}^{-1}, \text{ for } 3.0 \ \mu m \leq \lambda < 4.8 \ \mu m \quad (4)$$

$$a = 345.0 \text{ cm}^{-1}, \text{ for } 4.8 \ \mu m \leq \lambda < 8.0 \ \mu m \quad (5)$$

For B_2O_3 doped silica

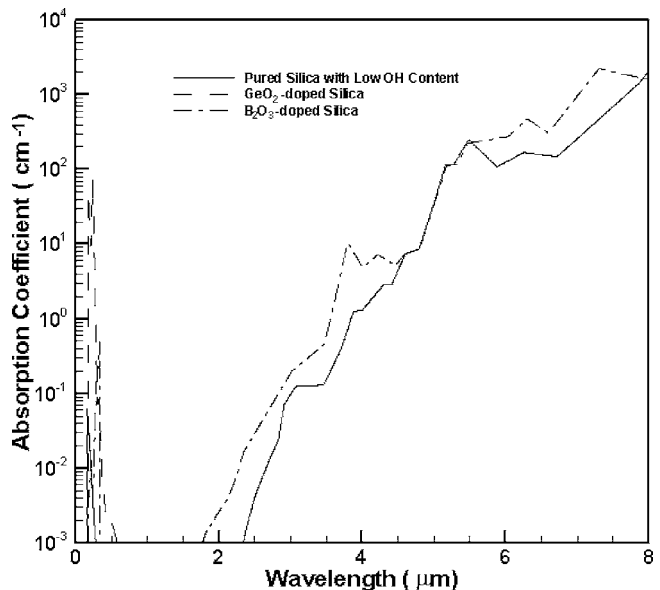$$a = 0, \text{ for } \lambda < 0.15 \ \mu m \quad (6)$$

Fig. 3 Measured absorption coefficients of pure fused silica with low OH content, GeO$_2$-doped silica and B$_2$O$_3$-doped silica [13,14]

$$a = 0.0192 \text{ cm}^{-1}, \text{ for } 0.15 \ \mu\text{m} \leq \lambda < 3.0 \ \mu\text{m} \qquad (7)$$

$$a = 1.466 \text{ cm}^{-1}, \text{ for } 3.0 \ \mu\text{m} \leq \lambda < 4.8 \ \mu\text{m} \qquad (8)$$

$$a = 759.0 \text{ cm}^{-1}, \text{ for } 4.8 \ \mu\text{m} \leq \lambda < 8.0 \ \mu\text{m} \qquad (9)$$

For GeO$_2$ doped silica

$$a = 0, \text{ for } \lambda < 0.15 \ \mu\text{m} \qquad (10)$$

$$a = 0.0445 \text{ cm}^{-1}, \text{ for } 0.15 \ \mu\text{m} \leq \lambda < 3.0 \ \mu\text{m} \qquad (11)$$

$$a = 0.8455 \text{ cm}^{-1}, \text{ for } 3.0 \ \mu\text{m} \leq \lambda < 4.8 \ \mu\text{m} \qquad (12)$$

$$a = 345.0 \text{ cm}^{-1}, \text{ for } 4.8 \ \mu\text{m} \leq \lambda < 8.0 \ \mu\text{m} \qquad (13)$$

Wei et al. [9] showed that the effect of the absorption coefficient in the short-wavelength region ($\lambda < 3.0 \ \mu$m) on the temperature and heat flux is considerable since about 60% of the overall emissive power is concentrated in this region at usual operating temperatures of 2000 K. Therefore, the absorption coefficients in the short-wavelength region should not be neglected although they are quite small. In the $4.8 \ \mu\text{m} \leq \lambda < 8.0 \ \mu$m wavelength region, the absorption coefficients are very large in the range $9.0–2077 \text{ cm}^{-1}$. Accurate average absorption coefficients are not obtained numerically in this interval. Two approximate average absorption coefficients are given here by $\bar{a} = \int_{\lambda_1}^{\lambda_2} a(\lambda) d\lambda / (\lambda_2 - \lambda_1)$.

In the earlier studies, Myers' two-band model [1] has been used to approximate the absorption coefficient of pure silica perform as

$$a = 0, \text{ for } \lambda < 3.0 \ \mu\text{m} \qquad (14)$$

$$a = 4.0 \text{ cm}^{-1}, \text{ for } 3.0 \ \mu\text{m} \leq \lambda < 4.8 \ \mu\text{m} \qquad (15)$$

$$a = 150.0 \text{ cm}^{-1}, \text{ for } 4.8 \ \mu\text{m} \leq \lambda < 8.0 \ \mu\text{m} \qquad (16)$$

However, he did not give the concentration of OH or of other impurities. From Myers's model, the transmission of 1-cm-thick plates consisting of fused silica is 1.83% in the 3.0–4.8 μm wavelength region; the transmission of 1-cm-thick plates consisting of fused silica from Izawa's data is 23–42.93%. Obviously Myers' results show a strong absorption band in this wavelength region, which could come from high OH content or other impurities [13,14]. The three-band model is more appropriate for approximating the absorption coefficients of low-OH silica preform. Due to lack of detailed composition and optical properties of realistic preforms, new three-band models from Izawa's data are used here to investigate the effects of dopants on radiative transport in optical fiber drawing.

A schematic diagram of radiosity and irradiation on the interfaces is shown in Fig. 1. There are three enclosures: the core (layer 1), the cladding (layer 2), and the inert gas (layer 3). The zonal method is applied to calculate the radiation transfer inside the preform. The radiation exchange between the furnace and outer surface of the preform is computed by an enclosure analysis. The interfaces $(a), (b), (c), (d)$ and the internal side of the top (e), the furnace (f), and the bottom (g) are divided into axisymmetric surface ring elements. The volume of the perform is divided into axisymmetric volume ring elements. From the enclosure theory, the outgoing and incoming heat fluxes at every surface element can be obtained for each absorbing band. The incoming heat fluxes at ith surface element are given as

$$G_{i,\lambda}^{(l)} = \frac{1}{A_i^{(l)}} \left(\sum_{j=1}^{N_s^{(l)}} (\overline{S_j S_i})_\lambda^{(l)} J_{j,\lambda}^{(l)} + \sum_{j=1}^{N_g^{(l)}} (\overline{G_j S_i})_\lambda^{(l)} n^{(l)2} \sigma T_j^{(l)4} f_{i,\lambda} \right) \quad (l=1,2)$$

$$(17)$$

$$G_{i,\lambda}^{(3)} = \sum_{j=1}^{N_s^{(3)}} F_{i-j} J_{i,\lambda}^{(3)} \qquad (18)$$

where, the superscript 1, 2, 3 denote layer 1, 2, 3 of Fig. 1; the subscript, λ, denotes a particular absorption band and the subscripts i and j denote the surface or volume ring elements.

The outgoing heat fluxes at ith surface element are obtained as follows

$$J_{i,\lambda}^{(1)} = \tau_b G_{i,\lambda}^{(2)} + \rho_a G_{i,\lambda}^{(1)} \qquad (19)$$

for ith element on the surface a

$$J_{i,\lambda}^{(2)} = \tau_a G_{i,\lambda}^{(1)} + \rho_b G_{i,\lambda}^{(2)} \qquad (20)$$

for ith element on the surfaces b

$$J_{i,\lambda}^{(2)} = \tau_d G_{i,\lambda}^{(3)} + \rho_c G_{i,\lambda}^{(2)} \qquad (21)$$

for ith element on the surfaces c

$$J_{i,\lambda}^{(3)} = \tau_c G_{i,\lambda}^{(2)} + \rho_d G_{i,\lambda}^{(3)} \qquad (22)$$

for ith element on the surface d

$$J_{i,\lambda}^{(3)} = \varepsilon_i \sigma T_i^{(3)4} f_{i,\lambda} + (1 - \varepsilon_i) G_{i,\lambda}^{(3)} \qquad (23)$$

for ith element on the surfaces e, f, g.

The reflectivity of the interface is given by Richmond [15] as

$$\rho_a = \hat{\rho}\left(\frac{n_1}{n_2}\right), \rho_c = \hat{\rho}(n_2)$$

$$\hat{\rho}(n) = 1 - \frac{1}{n^2}\left[\frac{1}{2} - \frac{(3n+1)(n-1)}{6(n+1)^2} - \frac{n^2(n^2-1)^2}{(n^2+1)^3} \ln\left(\frac{n-1}{n+1}\right) \right.$$
$$\left. + \frac{2n^3(n^2+2n-1)}{(n^2+1)(n^4-1)} - \frac{8n^4(n^4+1)}{(n^2+1)(n^4-1)^2} \ln(n) \right] \qquad (24)$$

The relationship between the transmissivities of the inner and outer surfaces is given by Siegel and Spuckler [16] as

$$\tau_d = n_2^2 \tau_c, \ \tau_b = (n_1/n_2)^2 \tau_a \qquad (25)$$

The view factor $F_{i,j}$ and the direct exchange areas $(\overline{SS})_\lambda^{(l)}, (\overline{SG})_\lambda^{(l)}$ are defined as given by Modest [17] as

$$(\overline{S_i S_j})_\lambda^{(l)} = \int_{A_i^{(l)}} \int_{A_j^{(l)}} \exp(-a_\lambda^{(l)} S_{ij}^{(l)}) \frac{\cos \theta_i^{(l)} \cos \theta_j^{(l)}}{\pi S_{ij}^{(l)2}} dA_i^{(l)} dA_j^{(l)}$$

$$(26)$$

$$(\overline{S_i G_j})_\lambda^{(l)} = \int_{A_i^{(l)}} \int_{V_j^{(l)}} a_\lambda^{(l)} \exp(-a_\lambda^{(l)} S_{ij}^{(l)}) \frac{\cos \theta_i^{(l)}}{\pi S_{ij}^{(l)2}} dA_i^{(l)} dV_j^{(l)} \quad (27)$$

The view factors are computed using the approach given by Lee and Jaluria [3]. The surface–surface, surface–volume, and volume–volume direct exchange areas need to be determined for the core and the cladding, respectively. The expressions for direct exchange areas are given as

$$(\overline{S_i S_j})_\lambda^{(l)} = \int_{z_{i \ \text{min}}}^{z_{i \ \text{max}}} \int_{z_{j \ \text{min}}}^{z_{j \ \text{max}}} \int_{\phi_{j \ \text{min}}}^{\phi_{j \ \text{max}}} F_{SS}(z_i, z_j, \phi_j) d\phi_j \, dz_j \, dz_i \quad (28)$$

$$(\overline{S_i G_j})_\lambda^{(l)}$$
$$= \int_{z_{i \ \text{min}}}^{z_{i \ \text{max}}} \int_{z_{j \ \text{min}}}^{z_{j \ \text{max}}} \int_{r_{j \ \text{min}}}^{r_{j \ \text{max}}} \int_{\phi_{j \ \text{min}}}^{\phi_{j \ \text{max}}} F_{SG}(z_i, z_j, r_j, \phi_j) d\phi_j \, dr_j \, dz_j \, dz_i$$

$$(29)$$

where ϕ_j is the azimuthal angle of the ring element j. Because of the blocking effect, only the part of the ring element j, whose azimuthal angle is between the minimum azimuthal angle $\phi_{j \ \text{min}}$

Table 1 Limiting values for $\cos \phi_{j\,\min}$ and $\cos \phi_{j\,\max}$

	$\cos \theta_i \geq 0$	$\cos \theta_i \leq 0$
$\cos \theta_j \geq 0$	$\cos \phi_{j\,\min} = \min(\Gamma_1, 1)$	$\cos \phi_{j\,\min} = \min(\chi_i, \Gamma_1, 1)$
	$\cos \phi_{j\,\max} = \max(\chi_i, \chi_j, \Gamma_2, -1)$	$\cos \phi_{j\,\max} = \max(\chi_j, \Gamma_2, -1)$
$\cos \theta_j \leq 0$	$\cos \phi_{j\,\min} = \min(\chi_j, \Gamma_1, 1)$	$\cos \phi_{j\,\min} = \min(\chi_i, \chi_j, \Gamma_1, 1)$
	$\cos \phi_{j\,\max} = \max(\chi_i, \Gamma_2, -1)$	$\cos \phi_{j\,\max} = \max(\Gamma_2, -1)$

and the maximum azimuthal angle $\phi_{j\,\max}$, can be viewed from one point on the ring element i. The detailed expressions for F_{SS}, F_{SG} are given by Yin [8]. The limiting azimuthal angles in the core are determined by a method similar to that used by Yin and Jaluria [7]. The limiting azimuthal angles in the cladding are obtained by Modest's method [18], as given in Table 1, with

$$\chi_i = \frac{r_i}{r_j} + \frac{z_j - z_i}{r_j}\tan\theta_i \tag{30}$$

$$\Gamma_1 = \max\left[\frac{R_1^2(z)(z_j - z_i)^2 - r_i^2(z_j - z)^2 - r_j^2(z - z_i)^2}{2 r_i r_j (z - z_i)(z_j - z)}\right]_{z \in (z_i, z_j)} \tag{31}$$

$$\Gamma_2 = \min\left[\frac{R_1^2(z)(z_j - z_i)^2 - r_i^2(z_j - z)^2 - r_j^2(z - z_i)^2}{2 r_i r_j (z - z_i)(z_j - z)}\right]_{z \in (z_i, z_j)} \tag{32}$$

where R_1 is the local radius of the inner body and R_2 is the local radius of the outer body. The direct exchange areas in Eqs. (12)–(14) are calculated using Gaussian quadrature. The radiative heat flux at ith surface ring element for a particular absorption band is computed using the following equation

$$q_{i,\lambda}^{(l)} = J_{i,\lambda}^{(l)} - G_{i,\lambda}^{(l)} \tag{33}$$

3 Parallel Computation of the Direct Exchange Areas

Since the computation for the direct exchange areas is very time consuming, parallelization for this computation is desirable and is employed here. The parallel code is modified with the message-passing interface (MPI). The calculation for every process does not require parallel communication since each processor has all the data about the geometry and radiation properties. The performance of this parallel code is evaluated by calculating with the efficiency as [19]

$$E(n,p) = \frac{T_\sigma(n)}{p T_\pi(n,p)} \tag{34}$$

where T_σ is the runtime of the serial solution; T_π is the runtime of the parallel solution with p processes; and n denotes the size of input. A parallel computation of direct exchange areas for Myer's two-band model is performed on the MPHASE cluster at Rutgers University. It has 44 dual CPU rack-mount AMD MP 1.6 GHz from Aspen Systems. A comparison of the predicted speedup and the actual speedup is shown in Fig. 4 and the parallel efficiency is found to be about 0.7, as seen in Fig. 5.

4 Validation

Validation of the computational procedure for view factors and direct exchange areas in the core has been done in earlier studies by Lee and Jaluria [3] and Yin and Jaluria [7]. In this paper, two benchmark problems of radiation heat transfer between two concentric cylinders, containing nonparticipating or participating medium, are used to validate the radiation model. First, the direct exchange areas for two finite concentric cylinders enclosing non-participating medium are calculated and compared with the ana-
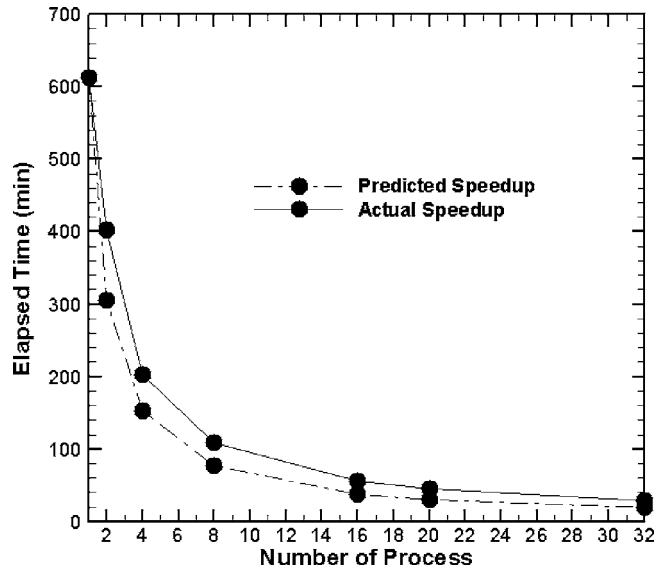

Fig. 4 Comparison of ideal speedup and actual speedup in parallel computation of the direct exchange areas

lytical results given by Siegel and Howell [20]. The calculated and analytical results are tabulated in Table 2, which shows very good agreement.

Another case of a gray gas at radiative equilibrium between the infinite concentric cylinders is also investigated and compared with the numerical results of Loyalka [21]. His results, which agree very well with the Monte Carlo results of Perlmutter and Howell [22], can be considered as benchmark data for comparison. The length of these concentric cylinders is set at 20 times its diameter. The temperature of the inner surface (T_1) is 1000 K and the temperature of the outer surface (T_2) is 2000 K. Both the inner cylinder and the outer cylinder are assumed to be black bodies. The nondimensional radiative heat flux, $\psi = q(\tau_1)/(J_1 - J_2)$, at the inner surface is shown in Fig. 6. A 10×50 grid is used. It can be seen that the radiative heat transfer decreases as the optical thickness or as the radius ratio r_1/r_2 increases. The calculated results agree fairly well with Loyalka's results.
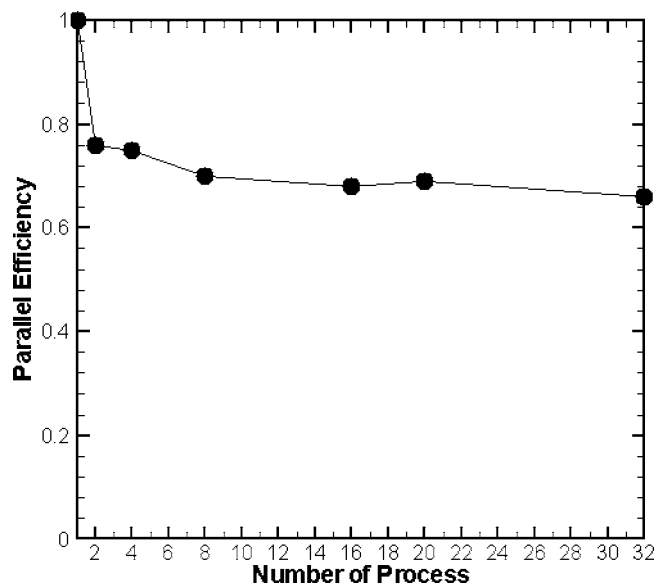

Fig. 5 Plot of parallel processing efficiency versus number of processes

Table 2 Calculated and analytical values for the direct exchange areas for two finite concentric cylinders containing nonparticipating medium

	Calculated	Analytical		Calculated	Analytical
$\overline{S_1 S_0}$	1.749×10^{-4}	1.746×10^{-4}	$\overline{S_2 S_0}$	3.742×10^{-4}	3.757×10^{-4}
$\overline{S_1 S_1}$	0.0	0.0	$\overline{S_2 S_1}$	1.221×10^{-4}	1.221×10^{-4}
$\overline{S_1 S_2}$	1.221×10^{-4}	1.221×10^{-4}	$\overline{S_2 S_2}$	6.883×10^{-4}	6.883×10^{-4}
$\overline{S_1 S_3}$	1.749×10^{-4}	1.746×10^{-4}	$\overline{S_2 S_3}$	3.742×10^{-4}	3.742×10^{-4}
$\dfrac{\sum\limits_{j=0}^{3} \overline{S_1 S_j}}{A_1}$	1.001	1.0	$\dfrac{\sum\limits_{j=0}^{3} \overline{S_2 S_j}}{A_2}$	0.997	1.0

Two relations for the view factors and the direct exchange areas obtained from energy conservation are given as

$$\sum_{j=1}^{N_s^{(3)}} F_{i-j} = 1 \qquad (35)$$

$$\frac{1}{A_i}\left(\sum_{j=1}^{N_s^{(l)}} (\overline{S_j S_i})_\lambda^{(l)} + \sum_{j=1}^{N_s^{(l)}} (\overline{G_j S_i})_\lambda^{(l)} \right) = 1 \quad (l=1,2,3) \qquad (36)$$

Both summations of view factors for the elements on the surface d and of the direct exchange areas calculated for the case of pure silica preform are satisfied with Eqs. (35) and (36), respectively. The errors are found to be within 0.5%.

5 Results and Discussion

During the optical fiber drawing process, the profile of the neck-down regions varies due to the furnace temperature distribution. In order to investigate the radiative heat transfer within the neck-down region, two sample profiles are studied here, as shown in Fig. 7. One of the sample neck-down profiles was obtained numerically by Yin [8], which can be expressed as an eighth-order polynomial given as

$$\log_{10} R = -1.181331 \times 10^6 z^8 + 1.564007 \times 10^6 z^7 - 8.320225$$
$$\times 10^5 z^6 + 2.206848 \times 10^5 z^5 - 2.856596 \times 10^4 z^4$$
$$+ 1.33958 \times 10^3 z^3 - 1.81201 \times 10 z^2 - 5.541218$$
$$\times 10^{-2} z + 2.602491 \qquad (37)$$

The other sample profile is given as a cosinusoidal function (Lee [3])

$$\text{for } z \leq z_0, \quad R_2 = r_0 \qquad (38)$$

$$\text{for } z_0 < z < z_f, \quad R_2 = \frac{r_0 + r_f}{2} + \frac{|r_0 - r_f|}{2}\cos\left(\pi\frac{z - z_0}{z_0 - z_f}\right) \quad (39)$$

$$\text{for } z \geq z_f, \quad R_2 = r_f \qquad (40)$$

Two furnace temperature distributions are studied given by the following

$$\text{TF1:} \quad T_F = 2500 - 2000\left(\frac{z}{L} - 0.5\right)^2 \qquad (41)$$

$$\text{TF2:} \quad T_F = 2000 \qquad (42)$$

For the interior region of the preform, two temperature distributions are considered. One is taken as uniform at $T_f = 1000$ K (TP1) and the other with the axial and radial temperature variations given by
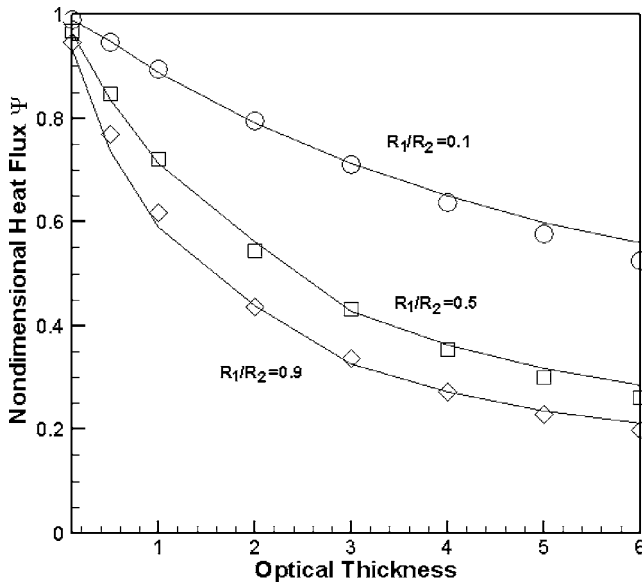

Fig. 6 Nondimensional radiative heat transfer between two infinite concentric cylinders at radiative equilibrium. Symbols represent benchmark data [20].
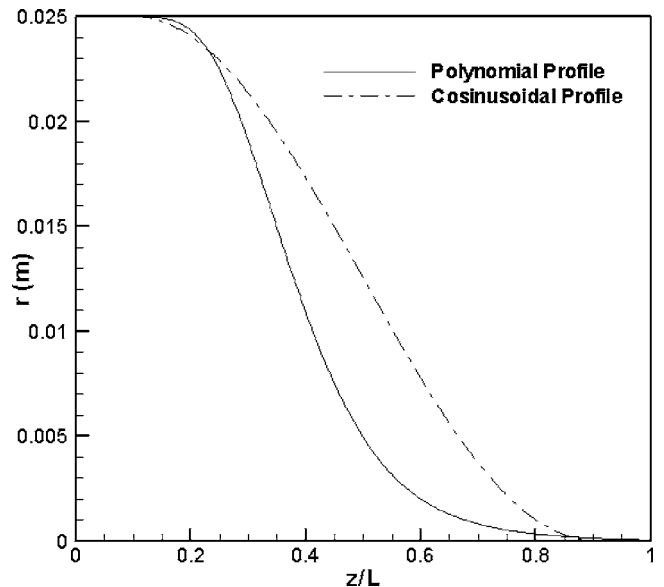

Fig. 7 Neck-down profiles considered

Table 3 Optical thickness at beginning and end of the preform for various materials

Materials	Absorption coefficient (m^{-1})	Optical thickness at the preform end $(D=0.05 \text{ m})$	Optical thickness at the fiber end $(D=1.25\times10^{-4} \text{ m})$
Silica with high OH content (Myer's model)	400	20	0.05
	15,000	750	1.875
Silica with low OH content	0.59	0.03	0.00007
	84.55	4.2	0.01
	34,500	1725	4.3
Boron doped silica	1.92	0.098	0.00024
	146.6	7.33	0.018
	75,900	3795	9.48
Germania doped silica	4.45	0.2225	0.00056
	84.55	4.2	0.01
	34,500	1725	4.3

TP2: $\quad T_f = 1000 \times \left(1 + 0.5 \times \sqrt{\dfrac{z}{L}} \right) \times \left[1 + 0.2 \times \left(\dfrac{r}{R} \right)^2 \right.$

$$\left. \times \left(1 - \dfrac{z}{L} \right)^2 \right] \qquad (43)$$

The diameters of the preform and the fiber are taken as 5 cm and 125 μm, respectively, while the diameter of the furnace is taken as 7 cm. The length of the preform and the furnace are taken as 30 cm. The furnace is divided into 80 uniform surface elements. The nonuniform grid scheme developed by Lee [4] is employed for the preform. In the axial direction, the preform is divided into 30 subdivisions. Every subdivision consists of four volume elements in the core and five volume elements in the cladding. In order to achieve grid independence, a finer mesh of 60×10 is also used for the core and cladding. No significant difference between the results from the two grid scheme is found. Therefore, a grid of 30×4 is taken for the core and a grid of 30×5 is taken for the cladding in this paper. The optical thickness of the preform decreases drastically from the preform to the fiber and varies with doping as shown as Table 3. Various points for Gaussian quadrature are selected to evaluate the integrations for direct exchange areas based on the magnitude of optical thickness.

In this paper, the radiative heat fluxes are computed using the polynomial profile given by Eq. (37), a parabolic temperature distribution of the furnace (TF1) and prescribed preform temperature (TP2), if the profile, the furnace temperature and the preform temperature are not mentioned. The results are shown as a nondimensional radiative heat flux, given by

$$Q = \frac{q}{\sigma(T_{F0}^4 - T_{f0}^4)} \qquad (44)$$

where $T_{F0} = 2000$ K and $T_{f0} = 1000$ K.

5.1 Comparison With Results From Myer's Two-Band Model. Figure 8 shows the nondimensional radiative heat flux at the outer surface of the preform, using both the present three-band model and Myers's two-band model to approximate the absorption coefficient for a pure silica preform. The preform temperature is taken as TP1. In the wavelength region 0.15 μm $\leq \lambda < 3.0$ μm, the absorption coefficient is as small as 0.0059 cm^{-1}. However, considerable radiative heat flux in the upper preform is obtained for the first absorption band. That is because over 60% of emissive power from the furnace surface, which is at a temperature between 2000 K and 2500 K, lies in this wavelength interval. The absorption coefficient in the second absorption band given by Myers's model is higher than that from the new three-band model, which might be due to high OH content or other impurities. It is worth mentioning that the OH ion in silica glass causes a strong absorption band at 2.72 μm [13]. As expected, a significantly

stronger absorption, using Myer's two-band model, is observed in the second absorption band than that using the three-band model. The optical thicknesses in the third absorption band for these two models are very large, as shown in Table 3, from 1725 to 4.3 for the new three-band model and from 750 to 1.87 for Myers's two-band model. Since most of the preform can be treated as optically thick for the third absorption band and almost all the radiation energy in the third absorption band is absorbed by the preform, the radiative heat fluxes from both the models are found to be very close. Comparison of the total radiation from all these absorption bands using the two models shows that the radiative heat flux is larger at the upper neck-down region and smaller at the lower neck-down region from the prediction of the three-band model. Clearly, it is important to model the radiation properties accurately inorder to obtain an accurate simulation of the fiber drawing process.

5.2 Effect of Furnace Temperature Distribution. The furnace temperature distribution is a critical operating condition for the optical fiber drawing process. Two typical furnace temperature profiles, TF1 and TF2, are given by Eq. (41) and (42). The neck-down profile is taken to be a polynomial function, as given by Eq. (37). The preform temperature is taken as TP1. Figure 9 shows the
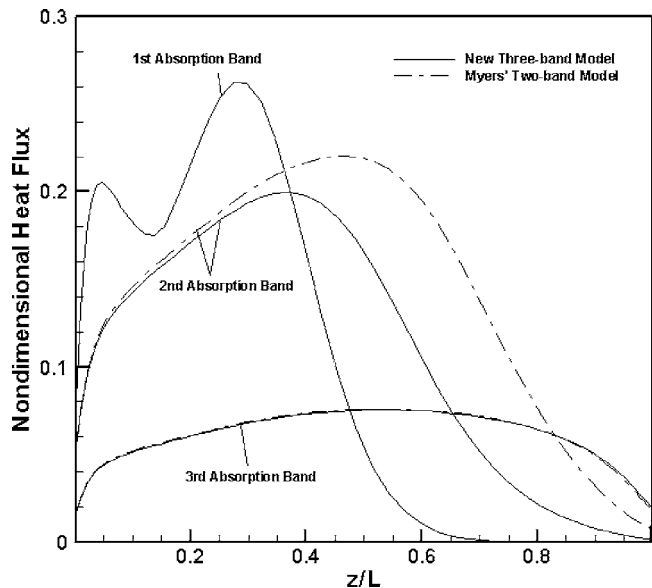

Fig. 8 Comparison of nondimensional radiative heat flux calculated using the three-band model and Myers's two-band model
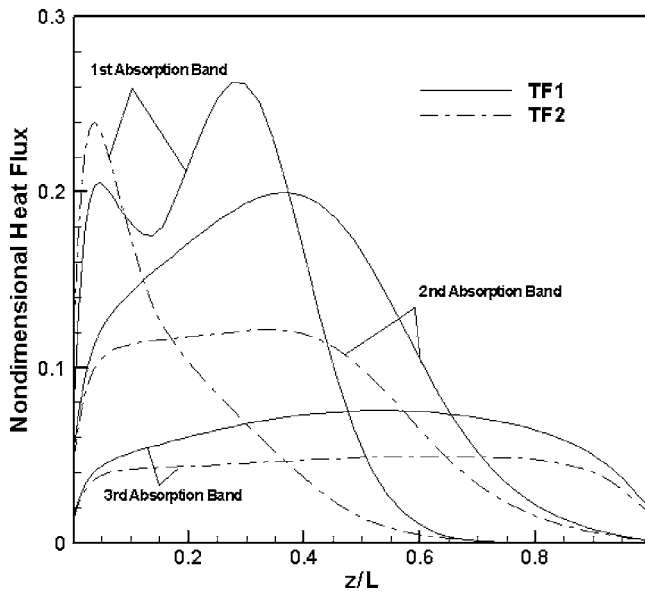
Fig. 9 Effects of the furnace temperature distribution

Fig. 11 Results for different the preform temperature distributions

radiative heat fluxes at the outer surface of the preform for three absorption bands for the two cases. As expected, the radiative heat fluxes for all three absorption bands are strongly affected by the furnace temperature distribution. It can be seen that the radiative heat flux has a peak near the entrance when the furnace temperature is uniform, TF2, and the peak moves close to the middle when the furnace temperature profile is taken to be parabolic, TF1.

5.3 Effect of Neck-Down Profile. Two neck-down profiles, defined by the polynomial function of Eq. (37) and the cosinusoidal function of Eqs. (38)–(40), were shown in Fig. 7. The preform temperature is taken as TP1. Radiative heat fluxes at the outer surface of the preform for the three absorption bands for these two different profiles are obtained, as shown in Fig. 10. The heat flux for the first absorption band at the upper neck-down region $0 < z/L < 0.4$ is larger with the polynomial profile because the absorption is weak in this absorption band and the internal reflection is the major factor. For the second absorption band, the heat fluxes

Fig. 10 Effect of the neck-down profile

at lower neck-down region $0.4 < z/L < 1$ drop as a result of decrease in the optical thickness. Since most of the preform is optically thick for the third band, the heat fluxes for the third absorption band barely change with these two neck-down profiles.

5.4 Effect of Preform Temperature Distribution. The radiative heat fluxes for the two preform temperature distributions, TP1 and TP2, are shown in Fig. 11. TP1 is taken as a uniform temperature of 1000 K. For TP2, the temperature is increased axially from 1000 K to 1500 K at the centerline. The temperature difference between the surface and the centerline is decreased from the inlet to the outlet. The maximum temperature difference in the radial direction is set at the inlet, where the surface temperature is 20% higher than the centerline temperature. At the outer surface, the radiative heat flux for TP1 is significantly larger than that for TP2 because of lower preform temperature. At the inner surface, the radiative heat flux for TP1 is slightly smaller in the upper neck-down region and becomes larger in the lower neck-down region than that for TP2. That is because the temperature in the cladding for TP2 is much higher than that in the core in the upper neck-down region and the temperature gradually becomes uniform in the lower neck-down region. These results indicate the application and validity of the present model for arbitrary temperature distributions in the preform. This is obviously the case in actual fiber drawing where the temperature distribution results from the heat transfer and glass flow mechanisms.

5.5 Effect of Absorption Coefficient. Doping changes the absorption coefficients in the core and the cladding and it is important to quantify the effects on the radiation heat transfer. The effects of the difference in the absorption coefficients due to two typical dopants GeO_2 and B_2O_3 are considered here. The diameters of the core and the cladding are taken as 62.5 μm and 125 μm, respectively. The difference in the refractive index is neglected. The refractive index of doped silica is taken as 1.42 as pure silica. Figure 12 shows the radiative heat fluxes on the interfaces for pure silica core and B_2O_3-doped silica cladding preform, GeO_2-doped silica core and pure silica cladding preform, and pure silica preform. Since both dopants, B_2O_3 and GeO_2, give rise to greater absorption in the preform, the radiative heat fluxes at the outer surface of the doped preforms are larger than that of pure silica preform. On the interface between the core and the cladding, absorption is stronger for GeO_2-doped silica core/pure silica clad-
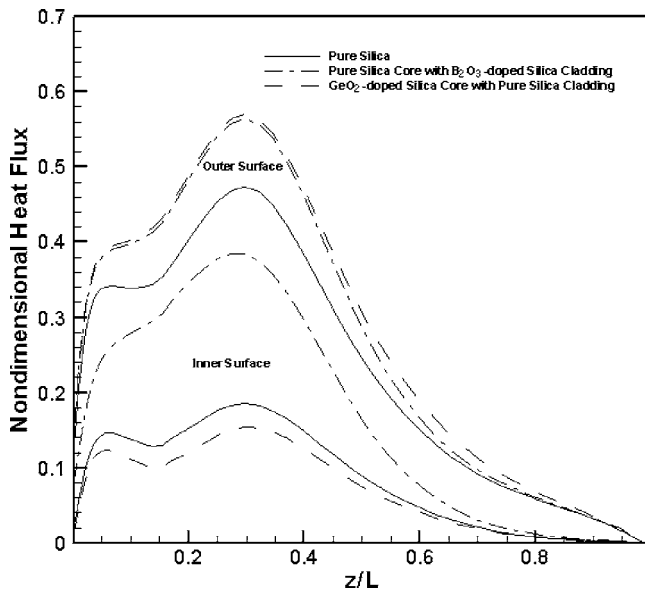
Fig. 12 Comparisons among radiative heat fluxes for pure Silica core with B_2O_3-doped silica cladding, for GeO_2-doped silica core with pure silica cladding, and for pure silica preforms

Fig. 13 Effect of refractive index on radiative heat flux for GeO_2-doped silica core with pure silica cladding preform

ding preform and a lot weaker for pure silica core/B_2O_3-doped silica cladding preform because the transmissivity of pure silica cladding is much higher than that of B_2O_3-doped silica cladding. Both the doped silica preforms absorb more energy by radiation than pure silica preform during the optical fiber drawing process and thus require smaller draw tension for the same drawing speed. The differences in the absorption coefficients of the core and the cladding will lead to significant difference in the temperature of these two layers.

5.6 Effect of Refractive Index. Doping also affects the refractive index in the core and the cladding. In order to investigate the effect of the refractive index, two kinds of preforms are studied here, pure silica core with B_2O_3-doped silica cladding preform and GeO_2-doped silica core with pure silica cladding preform. The geometry of the preform is the same as above. The refractive index of pure silica is taken as 1.42. The absorption coefficients in the core and cladding for both preforms are assumed to be unchanged with various concentrations of dopants. For the first case, the core is GeO_2-doped silica and the cladding is pure silica. The refractive index of the core (n_1) increases from 1.42 by 1%, 10%, and 20%, and the refractive index of the cladding (n_2) remains at 1.42. The results are shown in Fig. 13. The core absorbs larger radiation energy with increasing n_1/n_2 as a result of increasing internal reflections in the core. Although the total absorbed radiation energy is also increased in the preform, the amount of the radiation energy absorbed by the cladding only has a slight change. The effect of higher refractive index in the core is to increase the temperature of the core, which will cause the preform to soften faster. For the second case, the core is pure silica and the cladding is B_2O_3-doped silica. The refractive index of the core (n_1) remains 1.42, and the refractive index of the cladding (n_2) decreases from 1.42 by 1%, 10%, and 20%. The results are shown in Fig. 14. The fact that the cladding with decreasing n_2 absorbs less radiation energy is due to decreasing internal reflection in the cladding. Although the amount of radiation energy absorbed by the core increases slightly as n_1/n_2 increases, the total radiation energy absorbed by the preform is decreased and the temperature of the cladding will drop.

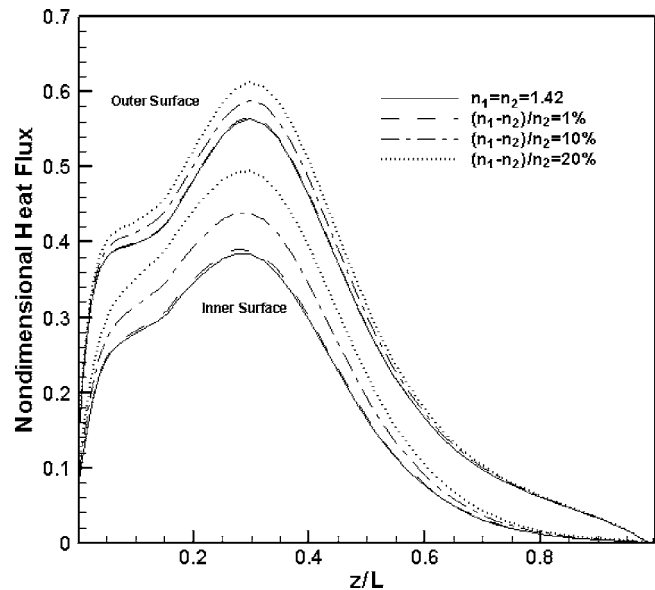**5.7 Effect of Geometry.** Since the transmissivity of glass also

depends on the dimension of the core and the cladding, two common types of preforms are studied to investigate the effect of geometry on the radiative heat transfer. For graded-index fibers, the common diameter of the core is 50 μm or 62.5 μm, and the diameter of the cladding is 125 μm [12]. For the GeO_2-doped silica core with pure silica cladding preform, the results for these two geometries are shown in Fig. 15. Lower radiative heat fluxes are on the outer and the inner interfaces for the case of 50-μm-diameter core because both the absorption by the preform and the transmissivity of the cladding decrease. For the pure silica core with B_2O_3-doped silica cladding preform, the radiative heat fluxes are obtained as shown in Fig. 16. Higher radiative heat flux at the outer surface and lower radiative heat flux at the inner surface are observed for the case of 50-μm-diameter core. This is
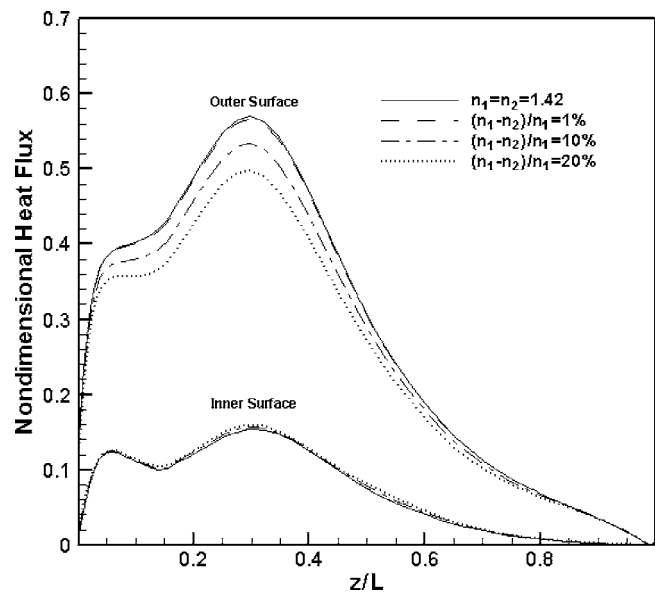

Fig. 14 Effect of refractive index on radiative heat flux for pure silica core with B_2O_3-doped silica cladding preform
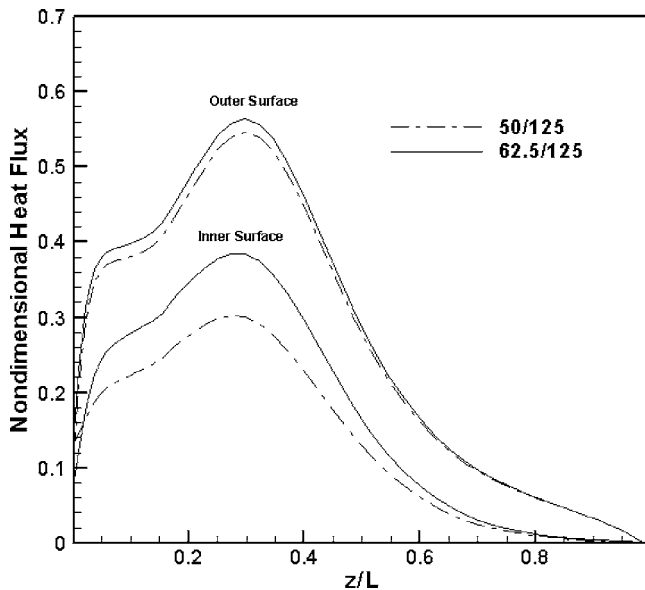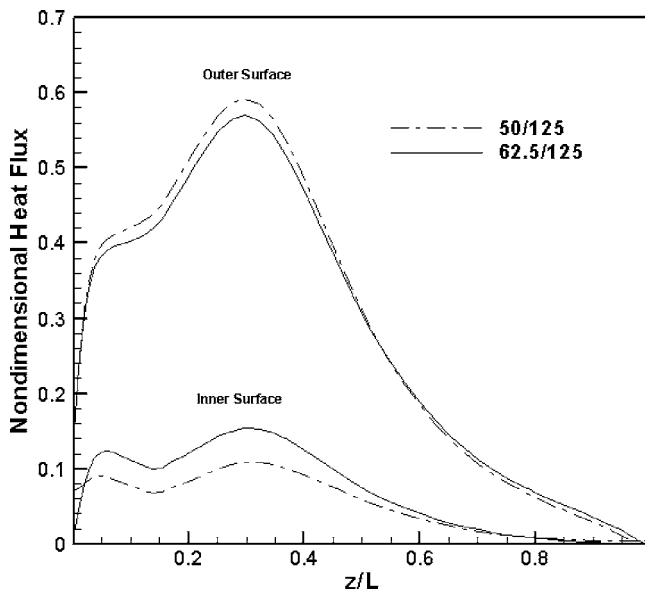
Fig. 15 Effect of geometry on radiative heat flux for GeO$_2$-doped silica core with pure silica cladding preform; the diameter of the core is 50 μm or 62.5 μm and the diameter of the cladding is 125 μm

expected from the fact that the effective absorption coefficient of the preform is larger and the transmissivity of the cladding is smaller.

6 Conclusions

The zonal method has been used to calculate the radiation heat transfer within the neck-down region of a double-layer optical fiber drawing. The core and the cladding are treated as separate layers bounded by a diffuse interface. Three-band models of the absorption coefficients for pure silica, GeO$_2$-doped silica, and B$_2$O$_3$-doped silica, are developed from Izawa's data, including the bandwidths of 0.15–3.0, 3.0–4.8, and 4.8–8.0 μm. The computa-

Fig. 16 Effect of geometry on radiative heat flux for pure silica core with B$_2$O$_3$-doped silica cladding preform; the diameter of the core is 50 μm or 62.5 μm and the diameter of the cladding is 125 μm

tion of direct exchange areas is parallelized. The radiation model is validated by comparisons with two simpler problems. The calculated direct exchange areas for the finite concentric cylinder enclosing a nonparticipating medium agrees well with analytical results. Also the comparison of the radiative heat flux for the case of a gray gas at radiative equilibrium between infinite concentric cylinders shows good agreement.

The effects of various furnace temperature, the profiles of the neck-down region, and dopants on radiative heat flux are investigated. The profile of radiative heat flux is strongly affected by various furnace temperature distributions and the profiles of the neck-down region. The results also show that radiative heat flux increases significantly for double-layer fibers of combinations of pure silica and doped silica because of the increase in absorption coefficients. The proportion of radiation absorbed in the core and the cladding also varies with doping and the geometries of the preform. The study on the changes in refractive index indicates that the radiative heat flux increases as the refractive index in the core becomes larger and decreases as the refractive index in cladding becomes smaller. However a 1% difference in refractive index has a slight effect on radiative transfer. Since the radiation heat transfer is the dominant mode of heat transfer in the optical fiber drawing process, the effects of dopants will ultimately cause a significant difference in the temperature distribution of the core and cladding. Therefore, the changes in the radiation properties, especially the absorption coefficients, due to doping are critical in the analysis of thermal transport in optical fiber drawing process. The paper presents the quantitative effects of the property changes due to doping and composition variations, as well as an approach to model the overall radiation heat transfer in the system.

Nomenclature

A = area, m^2
a = absorption coefficient of glass, cm^{-1}
E = parallel efficiency
F_{i-j} = view factor between surface ring element i and j
f = fraction of black body emissive power for an absorption band
G = irradiation, W/m^2
$\overline{G_jS_i}$ = direct exchange area between surface ring element i and volume ring element j
J = radiosity, W/m^2
L = height of furnace, m
N_s = number of surface ring elements
N_g = number of volume ring elements
n = refractive index
p = number of process
q = radiative heat flux
R = radius of preform, fiber, furnace, m
S_{ij} = distance between surface or volume ring elements i and j
$\overline{S_jS_i}$ = direct exchange area between surface ring element i and j
T = temperature, K
T_σ = runtime of the serial solution
T_π = runtime of the parallel solution

Greek Symbols

ε = emissivity

θ_i = angle between the direction normal to surface ring element i and vector connecting surface ring element i and j

λ = wavelength

ρ = reflectivity

σ = Stenfan–Boltzmann constant, 5.67051×10^{-8} W/(m^2 K^4)

ϕ_i = azimuthal angle

Superscripts

1 = core

2 = cladding

3 = gas

Subscripts

f = fiber

i = surface or volume ring element i

j = surface or volume ring element j

λ = spectral

References

[1] Myers, M. R., 1989, "A Model for Unsteady Analysis of Preform Drawing," AIChE J., **35**(4), pp. 592–602.

[2] Paek, U. C., and Runk, R. B., 1978, "Physical Behavior of the Neck-down Region during Furnace Drawing of Silica Fibers," J. Appl. Phys., **49**, pp. 4417–4422.

[3] Lee, S.H.-K., and Jaluria, Y., 1995, "The Effects of Geometry and Temperature Variations on the Radiative Transport during Optical Fiber Drawing," J. Mater. Process. Manuf. Sci., **3**, pp. 317–331.

[4] Lee, S.H.-K., and Jaluria, Y., 1995, "Effects of Streamwise Convergence in Radius on the Laminar Forced Convection in Axisymmetric Ducts," Numer. Heat Transfer, Part A, **28**, pp. 19–38.

[5] Lee, S.H.-K., and Jaluria, Y., 1996, "Effects of Variable Properties and Viscous Dissipation During Optical Fiber Drawing," ASME J. Heat Transfer, **118**, pp. 350–358.

[6] Kaminski, D. A., 1995, "Thermal Transport in Optical Fiber Manufacturing," *Proceedings of the 1st International Symposium on Radiative Heat Transfer*, M. Pinar Menguc, ed., Kusadasi, Turkey, August, Begell House, New York, pp. 667–681.

[7] Yin, Z., and Jaluria, Y., 1997, "Zonal Method to Model Radiative Transport in an Optical Fiber Drawing Furnace," ASME J. Heat Transfer, **119**(3), pp. 597–603.

[8] Yin, Z., 1997, "Numerical Investigation of Thermal Transport in Optical Fiber Drawing Processes," Ph.D. thesis, Rutgers University, New Brunswick, NJ.

[9] Wei, Z., Lee, K.-M., Tchikanda, S. W., Zhou, Z., and Hong, S.-P., 2003, "Effects of Radiative Transfer Modeling on Transient Temperature Distribution in Semitransparent Glass Rod," ASME J. Heat Transfer, **125**, pp. 635–643.

[10] Usiskin, C. M., and Siegel, R., 1960, "Thermal Radiation From a Cylindrical Enclosure With Specified Wall Heat Flux," ASME J. Heat Transfer, **82**(4), pp. 369–374.

[11] Murata, H., 1996, *Handbook of Optical Fibers and Cables*, 2nd ed., Marcel Dekker, New York.

[12] Hecht, J., 2002, *Understanding Fiber Optics*, 4th ed., Prentice Hall, Upper Saddle River, NJ.

[13] Izawa, T., and Sudo, S., 1987, *Optical Fibers: Materials and Fabrication*, KTK Scientific Publishers, Tokyo, Japan.

[14] Izawa, T., Shibata, N., and Takeda, A., 1977, "Optical Attenuation in Pure and Doped Fused Silica in the IR Wavelength Region," Appl. Phys. Lett., **31**(1), pp. 33–35.

[15] Richmond, J. C., 1963, "Radiation of Emittance to Other Optical Properties," J. Res. Natl. Bur. Stand., Sect. C, **67C**(3), pp. 217–226.

[16] Siegel, R., and Spuckler, C. M., 1992, "Effect of Index of Refraction on Radiation Characteristics in a Heated Absorbing, Emitting and Scattering Layer," ASME J. Heat Transfer, **114**, pp. 781–784.

[17] Modest, M. F., 1993, *Radiative Heat Transfer*, McGraw-Hill, New York.

[18] Modest, M. F., 1998, "Radiative Shape Factors Between Differential Ring Elements on Concentric Axisymmetric Bodies," Int. J. Thermophys., **2**, pp. 86–88.

[19] Pacheco, P. S., 1997, *Parallel Programming with MPI*, Morgan Kaufmann, San Francisco, CA.

[20] Siegel, R., and Howell, J. R., 2002, *Thermal Radiation Heat Transfer*, Taylor & Francis, New York.

[21] Loyalka, S. K., 1969, "Radiative Heat Transfer Between Parallel Plates and Concentric Cylinders," Int. J. Heat Mass Transfer, **12**, pp. 1513–1517.

[22] Perlmutter, M., and Howell, J. R., 1964, "Radiant Transfer Through a Gray Gas-Between Concentric Cylinders Using Monte Carlo," J. Heat Transfer, Vol. **86C**, pp. 169–179.

Finite Element Simulation for Short Pulse Light Radiative Transfer in Homogeneous and Nonhomogeneous Media

W. An
e-mail: anwei@hit.edu.cn

L. M. Ruan[1]
e-mail: ruanlm@hit.edu.cn

H. P. Tan

H. Qi

Y. M. Lew

School of Energy Science and Engineering,
Harbin Institute of Technology,
150001 Harbin, P.R.C.

With the rapid progress on ultrashort pulse laser, the transient radiative transfer in absorbing and scattering media has attracted increasing attention. The temporal radiative signals from a medium irradiated by ultrashort pulses offer more useful information which reflects the internal structure and properties of media than that by the continuous light sources. In the present research, a finite element model, which is based on the discrete ordinates method and least-squares variational principle, is developed to simulate short-pulse light radiative transfer in homogeneous and nonhomogeneous media. The numerical formulations and detailed steps are given. The present models are verified by two benchmark cases, and several transient radiative transfer cases in two-layer and three-layer nonhomogeneous media are investigated and analyzed. The results indicate that the reflected signals can imply the break of optical properties profile and their location. Moreover, the investigation for uniqueness of temporal reflected and transmitted signals indicate that neither of these two kinds of signals can be solely taken as experimental measurements to predict the optical properties of medium. They should be measured simultaneously in the optical imaging application. The ability of the present model to deal with multi-dimensional problems is proved by the two cases in the two-dimensional enclosure. [DOI: 10.1115/1.2430720]

Keywords: transient radiative transfer, finite element, absorbing and scattering media, micro-scale, non-intrusive diagnostics

1 Introduction

In most studies, radiative transfer can be taken as a steady-state process. The transient term of radiative transfer equation (RTE) can be neglected. However, recent rapid advances in the ultrashort-pulse laser have opened up many emerging areas. Applications span a broad range from material processing, particle detection and sizing, remote sensing, to biomedical engineering, etc. There has been increasing attention paid to the transient radiative transfer in absorbing and scattering media, because the transient effects of radiation cannot be neglected in these applications. A booming application in this domain is optical tomography (OT), which is able to detect tumors and other abnormalities hidden in biological tissues by utilizing the short-pulsed near infrared laser. With several advantages over established imaging methods such as ultrasound, X-ray computed tomography, and magnetic resonance imaging, the short-pulse near infrared laser is believed to be a safer and cheaper alternative for traditional imaging techniques. In fact, it has been proved that near infrared light passed relatively easier through such structures as the skull, brain, and breast due to less absorption and scattering. Furthermore, the temporal radiative signals convey the additional information which is often not available in large pulse width or continuous wave lasers.

In this technique, the short-pulse laser irradiated to the surface of biologic tissue is absorbed and scattered by the media. Transmitted and reflected optical signals are measured and compared with the results of forward calculation. Then, an inverse analysis is used to reconstruct the medium internal structure or properties. A detailed depiction of this technique can be found in the literature [1]. In order to obtain optical information of biologic tissue, the accurate forward calculation is essentially important for inverse analysis and estimates [2]. However, the diffusion optical tomography (DOT) is perhaps the most widely studied optical imaging technique and commercial imaging systems based on DOT have been developed in recent years. This model is constructed on the basis of diffusion approximation equation for radiative transport [3]. Although in many cases it is indeed a good approximation for describing light propagation in biological tissues, several researchers [4–6] have reported the limits of this approximation theoretically and experimentally. A restriction that is often mentioned is that of high albedo (weak absorption or albedo near one). However, Brewster and Yamada's work [5] indicate that the albedo criterion for application of diffusion theory to time-dependent scattering may be much less restrictive than what is usually reported. Even then, Elaloufi et al. [6] have shown that the diffusion approximation fails to describe both short- and long-time radiation transport in optically thin slabs. Moreover, their research also reveals that the diffusion approximation fails for short times, even in the optically thick slabs. As a result, alternatives to the diffusion approximation need to be formulated for accurately predicting transient transport in optically thin and heterogeneous media. Therefore, the simulation of transient radiative transfer has received considerable concern over the past 5 years. Several numerical strategies have been developed, which include the discrete ordinate method (DOM) [7,8], finite volume method (FVM) [9,10], integral equation (IE) models [2,11], and Monte Carlo method (MCM) [12,13]. However, little information about the finite element method (FEM) for transient radiative transfer was reported until recently [14].

As pointed out by Pontaza and Reddy [15], the spatial discretization of the RTE by the FEM allows for the modeling of irregular boundaries in two and three dimensions, the continuous represen-
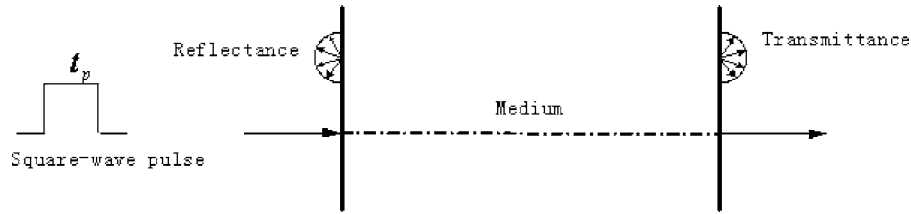
Fig. 1 The physical model of transient radiative transfer

tation of spatially varying properties, and the ability to easily perform *h*- and *p*-type refinements. Therefore, the FEM of radiation heat transfer has been investigated by many researchers recently. The standard Galerkin finite element method (GFEM) has been developed and integrated with DOM to simulate the radiation transfer by Liu [16]. This model can solve anisotropic scattering conveniently and need no complex integration and visibility judgment. The accuracy of this model in absorbing and anisotropic scattering media is investigated by An et al. [17]. The least squares finite element method (LSFEM) [15] and discontinue finite element method (DFEM) [18] are also presented to analyze the radiative transfer. However, all of these finite element methods are used to simulate the steady radiative heat transfer. Although in the previous work [14], the transient diffuse radiation in the participating media has been solved by the LSFEM, the radiative transfer result from the short-pulse irradiation was not investigated. In fact, the consideration for the interactive effect of collimated light with the absorbing and scattering media can provide more practical simulation for optical imaging techniques. Moreover, although the propagation of pulse light in the multi-layer nonhomogeneous media has already been extensively studied by Lu and Hsu [19,20], some significant phenomena and conclusive information have not been clarified. Therefore, the objectives of the present work are not only to extend the FEM to simulate the propagation of pulse light, but also to devote and supply significant parameter analysis and the uniqueness investigation for the inversion of optical imaging.

Due to the hyperbolic wave equation coupled with the in-scattering integral term, the simulation of the transient radiative transfer is anything but a simple task. Additionally, the rapid-changed pulse irradiation is also a substantial challenge in the stability and accuracy of numerical methods. Therefore, a least-squares strategy was employed to eliminate the unrealistic oscillations in the present study. The least-squares finite element formulations for the steady-state radiative transfer were first presented by Pontaza and Reddy [15]. In their study, the space-angle coupled and decoupled least-squares finite element models were proposed to simulate the radiative transfer in one-dimensional absorbing and scattering media. However, the space-angle coupled model is difficult to extend to multidimensional problems. Therefore, the present paper employs the space-angled decoupled model. Furthermore, a method based on DOM+ISW [21] for solid angle discretization is adopted to deal with the irradiative direction of collimated light.

In the following sections, detailed mathematic formulation and computational steps are given first. The present model is verified by two benchmark solutions. Then, several transient radiative problems in two-layer or three-layer nonhomogeneous media are investigated. The reflected and transmitted temporal signals are analyzed. The effect of albedo in the optically think media is also investigated. Finally, two two-dimensional (2D) transient radiative problems are also simulated to show the ability of the present model to deal with multi-dimensional problems.

2 Mathematic Formulation

2.1 Transient Radiative Transfer Equation. For the participating media, the transient radiative transfer equation (TRTE) in the Cartesian coordinate system can be written as

$$\frac{\partial I(r,\Omega,t)}{C\,\partial t} + \frac{\partial I(r,\Omega,t)}{\partial s} = -(\kappa_a + \sigma_s)I(r,\Omega,t) + \kappa_a I_b(r,t)$$

$$+ \frac{\sigma_s}{4\pi}\int_{\Omega'=4\pi} I(r,\Omega',t)\Phi(\Omega',\Omega)d\Omega' \tag{1}$$

where $I(r,\Omega,t)$ is radiative intensity, which is a function of position r, direction Ω, and time t; $I_b(r,t)$; is the radiative intensity of black body; C is propagation speed of radiation transport in the medium; and κ_a and σ_s are the absorption and scattering coefficient, respectively (see Fig. 1). The $\Phi(\Omega',\Omega)$ is the scattering phase function between incoming direction Ω' and scattering direction Ω. The second term on the left hand side of the equation represents the gradient of radiative intensity in the direction Ω. The three terms on the right side of the equation represent the change in intensity due to absorption and outgoing scattering, emission, and incoming scattering, respectively. When considered the gray diffuse reflection boundary, the radiative boundary condition can be written as follows.

$$I(r_w,\Omega,t) = \varepsilon_w I_b(r_w,t) + \frac{1-\varepsilon_w}{\pi}\int_{n\cdot\Omega'<0} I(r_w,\Omega',t)$$

$$\times |n\cdot\Omega'|d\Omega' \quad (n\cdot\Omega>0) \tag{2}$$

where $I(r_w,\Omega,t)$ is the intensity leaving the boundary; $I(r_w,\Omega',t)$ is the intensity arriving at the boundary; ε_w is the wall emissivity; and n is the unit out-normal vector on the wall. If we consider the transient radiative transfer with incident collimated irradiation, the radiative intensity can be separated into two parts [22]

$$I(r,\Omega,t) = I_c(r,\Omega,t) + I_d(r,\Omega,t) \tag{3}$$

where $I_c(r,\Omega,t)$ is the attenuated intensity of the collimated light; $I_d(r,\Omega,t)$ and is the diffuse intensity, which is the scattered radiation into direction Ω. The $I_c(r,\Omega,t)$ can be obtained by solving the TRTE for the collimated beam. In the Ω direction, it can be expressed as

$$I_c(r,\Omega,t) = I_{in}e^{-\beta l}[H(l^*-l) - H(l^*-l_p^*-l)]\delta(\Omega-\Omega_0) \tag{4}$$

where I_{in} is the initial intensity of incident radiation; the radiative spreading distance in the medium l^* is defined as $l^*=C\cdot t$; the l_p^* is defined as $l_p^*=C\cdot t_p$; t_p is the width of pulse; H and δ represent Heaviside step function and delta function respectively; l is the distance between incident location and r; Ω_0 is the direction of the incident light; and β is the extinct coefficient.

2.2 Least-Squares Finite Element Formulations. To solve the TRTE numerically, the angular dependence has to be removed

first. Similar to the conventional DOM, the angular integration over 4π solid angles is replaced by summing up the function on a finite number of discrete ordinate directions. For specific ordinate direction m, its direction cosines along the coordinates x, y, and z can be denoted as μ_m, η_m, and ξ_m.

Then, the TRTE of m direction can be written as

$$\frac{\partial I^m}{C \partial t} + \mu_m \frac{\partial I^m}{\partial x} + \eta_m \frac{\partial I^m}{\partial y} + \xi_m \frac{\partial I^m}{\partial z} + BI^m = S \qquad (5)$$

where the simplified coefficients B and S are defined as

$$B = \kappa_a + \sigma_s - \frac{\sigma_s}{4\pi} \Phi^{mm} w_m \qquad (6a)$$

$$S = \kappa_a I_b + \frac{\sigma_s}{4\pi} \sum_{m'=1, m' \neq m}^{M} I^{m'} \Phi^{m'm} w_{m'} + S' \qquad (6b)$$

In Eq. (6b) M is the number of discrete directions; and the source term S' can be expressed as

$$S' = \frac{\sigma_s}{4\pi} I_{in} e^{-\beta s} [H(l^* - l) - H(l^* - l_p^* - l)] \Phi(\mathbf{\Omega}_0, \mathbf{\Omega}) \qquad (7)$$

Equation (5) is a hyperbolic partial difference equation with respect to I^m which can be solved by using the finite element method. The weighted residual method applied to Eq. (5) provides

$$\int_V \left(\frac{\partial I^m}{C \partial t} + \mu_m \frac{\partial I^m}{\partial x} + \eta_m \frac{\partial I^m}{\partial y} + \xi_m \frac{\partial I^m}{\partial z} + BI^m - S \right) W_l \, dV = 0 \quad (8)$$

where V is the domain of solution. By using the least-squares finite element method, Eq. (8) can be rewritten in matrix form as

$$[K][I_{n+1}^m] = [K'][I_n^m] + [R] \qquad (9)$$

where $[K]$ is the stiffness matrix; $[R]$ is the right side term; and I_{n+1}^m is the radiative intensity in m direction at the $(n+1)$th instant. It can be solved through the value of I_n^m. A detailed process and the mathematic formulation of LSFEM for transient radiative transfer can be found in the literature [14]. It is worth mentioning that the stiffness matrix generated from the LSFEM is symmetric and positive-definite (SPD), whereas that generated from the Galerkin finite element method is unsymmetric. Consequently, storing the stiffness matrix for the LSFEM is inexpensive and some fast, robust iterative solutions for SPD matrix systems can be employed. By solving Eq. (9), the radiative intensity in the m direction can be acquired. Similarly, we can write out the equations and obtain the radiative intensity in each discrete direction.

2.3 Discretization of Solid Angle. For solid angle discretization, several strategies have been developed in the last three decades. The Sn-type discretization and azimuthal discretization are two of the most widely used strategies. In our previous research [14], the Sn-type discretization, which is always employed in the DOM, was introduced in the finite element model. However, the traditional Sn-type discretization cannot deal with the collimated radiative transfer due to the limited direction of the solid angle. Certainly, some novel quadrature scheme such as the double cyclic triangles (DCT) quadrature, which was employed by Sakami et al. [23], can be used to replace the Sn quadrature. But it is obvious that the DCT quadrature scheme is still not flexible enough to deal with arbitrary direction incident. Although the azimuthal discretization which is always associated with the FVM is competent to deal with the collimated radiative problem, previous research shows this discretization can increase the ray effect [24]. Therefore, a method based on the discrete ordinate scheme with infinity small weight (DOM+ISW) [21] is adopted in the present simulation. A sole, adjunctive direction with an infinitely small weight is used to simulate the arbitrary direction of incident radiative intensity. In the present model, the direction of the colli-

mated light is numbered as $M+1$; and the weight of the direction is set to 10^{-10}. The direction cosines μ_{M+1}, η_{M+1} and ξ_{M+1} can be set as 1.0, 0.0, and 0.0 precisely if the incident direction is parallel to the x axis.

Compared with the other method, the DOM+ISW method is very simple and doesn't damage the moment condition of the Sn discretization. It can be applied to any cases where the conventional DOM is applicable. Its detailed process and study of accuracy can be found in the literature [21]. In the following subsection, the angle discretization employs the Sn-type quadrature scheme based on the DOM+ISW method except for the special announcement.

2.4 Treatment of Incident Pulse. Certainly, the collimated radiative intensity on the sole direction I_c^{M+1} can also be obtained by the numerical simulation of FEM. However, the numerical simulation for the I_c^{M+1} can lead to two different kinds of errors: the wiggle and numerical diffusion [25], which affect the results of FEM seriously. The other available technique is to utilize the analytical solving technique for the incident pulse. That means the transport of diffuse radiation I_d is still solved by the numerical simulation of FEM, whereas the spread of collimated light is obtained by the precise analytical solving method. For the square-wave pulse, the radiative intensity of collimated light can be written as

$$\boldsymbol{I}_c^{M+1} = \boldsymbol{I}_{in} e^{-\beta l} [H(l^* - l) - H(l^* - l_p^* - l)] \qquad (10)$$

If the temporal shape of pulse is the Gaussian type and has a temporal duration t_p at the full width half maximum (FWHM), it can be written as

$$\boldsymbol{I}_c^{M+1} = I_{in} e^{-\beta l} \cdot f(t_p) \qquad (11)$$

where $f(t_p)$ is the shape function of temporal pulse about t_p. The detailed investigation and comparison for the different strategies to deal with the steep incident pulse can be found in the literature [25].

2.5 Solution Method. The spatial discretization and computational processes in each discrete direction are the same, and the radiative intensity in each direction is solved independently. The boundary condition expressed in Eq. (2) should be imposed upon Eq. (9) as the inflow boundary condition. Due to the dependence of both source terms and boundary conditions on the radiative intensities, global iterations are necessary at each time step. At the outset, the source terms S in Eq. (6b) and irradiation should be computed by the initial intensity. Then the matrix K, K', and right hand term R in Eq. (9) are computed. Equation (9) is solved for each direction. In each time step, the computational results replace the previous ones and the iterative procedure will continue until the convergence is met. The radiative intensities of nodes are saved and taken as known conditions in the next time step. The above processes are repeated until the defined end time. The solver of the discretized equations is based on the preconditioned conjugate gradients arithmetic.

3 Results and Discussion

Based on the above theories, a computer code is implemented. In order to evaluate the accuracy of the present model, two benchmark cases are investigated first. In all of the cases, the numerical solution was considered to be convergent when the relative error of radiative intensity is less than 0.01%. All computations are realized in a Personal Computer with AMD2100+CPU. The grid-independent checks for all results have already been verified in the present research. It is found that there is very little difference (about 0.1%) between 50 nodes and 100 nodes for the following cases. Therefore, the effect of spatial mesh can be ignored. All computations of the present paper employed the Crank–Nicolson time scheme because it has little numerical diffusion.

3.1 Homogeneous Media With Continuous Light Irradiation. In the first case of a one-dimensional cold media, the optical thickness is 1.0 and the albedo is 0.5. Only the isotropic scattering is considered. The wall is black and at a cold temperature (0 K). A continuous incident light whose radiative intensity is I_0 irradiates on the left wall at the initial time $t=0$. The dimensionless radiative heat flux Q and incident radiation G in the media are, respectively, defined as

$$Q(x,t) = \frac{1}{I_0} \int_{4\pi} I(x,\Omega,t)\cos(s,n)d\Omega \quad G(x,t) = \frac{1}{I_0} \int_{4\pi} I(x,\Omega,t)d\Omega$$
(12)

where s represents the direction of the radiative intensity I; and n is the direction of coordinate axis x. Tan and Hsu [2] investigated this case by IE models and their results are believed to be the very precise benchmark. Therefore, the results of the present FEM are compared with those of IE to evaluate the accuracy of the present model. The spatial domain is discretized into 100 uniform linear elements and the solid angle discretization adopts the S_{20}. With the Galerkin time difference scheme, the time step is taken as $\Delta l^* = C \cdot \Delta t = 0.01$. The results of six different instants are shown in Figs. 2(a) and 2(b).

As shown in Fig. 2, the results of FEM and IE are in good agreement. The maximum relative error is about 2.2%.

3.2 Two-Layer Nonhomogeneous Media With Short Pulse Light Irradiation. As shown in Fig. 3, the short pulse light with pulse width $l_p^* = 3.0 \times 10^{-4}$ m irradiates on the surface of the two-layer isotropic scattering media. In this case, the optical thicknesses of the two-layer media are all 0.5. The albedoes of the two-layer media are 0.1 and 0.9, respectively. Two different situations, which the short pulse collimated light irradiated on the left wall and the right wall, respectively, were investigated using the reverse Monte Carlo Method by Lu and Hsu [19]. The present model employs 100 uniform linear elements for the spatial discretization and the S_{20} for the solid angle discretization. The time step is taken as $\Delta l^* = 10^{-5}$ m.

It can be observed from Fig. 4 that the reflected signals produced by the left-incidence light and the right-incidence light are obviously different. Due to scattering by the back media, the "local minimum" [19] or called "dual peak" phenomenon [20] can be observed at the $l^* = 10^{-3}$ m instant in the reflected signal produced by the left-incident light. An obvious bend (or slope change) can also be found at the same instant from the result produced by the right-incident light. Therefore, as pointed out by Lu and Hsu [19], the reflected signal contains considerable useful information which could be used to infer the structure and properties of media. In addition, it is not difficult to find that using l^* as the x coordination can easily infer the information of location where a break of optical properties in medium happens. As shown in Fig. 4, the results of FEM and reverse Monte Carlo method (RMC) are in good agreement. The maximum relative error is about 3.0%.

Although Lu and Hsu [19] proposed the local minimum phenomenon and gave the condition that this phenomenon can be produced, the relationship between the structure of media and this phenomenon was not analyzed in their work. The present research will reveal this relationship in some nonhomogeneous cases.

The schematic diagrams of structure in the two-layer nonhomogeneous media are shown in Fig. 5. The locations of the interface are 0.2, 0.5, and 0.8 m, respectively, in the three cases. Their optical properties are shown in Table 1. It can be easily found that the optical thicknesses and albedos of two-layer media are equivalent in the three cases. Therefore, it may be inappropriate using the optical thickness and albedo to describe the nonhomogeneous media in the transient radiative transfer. The geometric information should be provided at the same time. The present cases employ 50 uniform linear elements for the spatial discretization and the S_{20} for the solid angle discretization. The time step is taken as
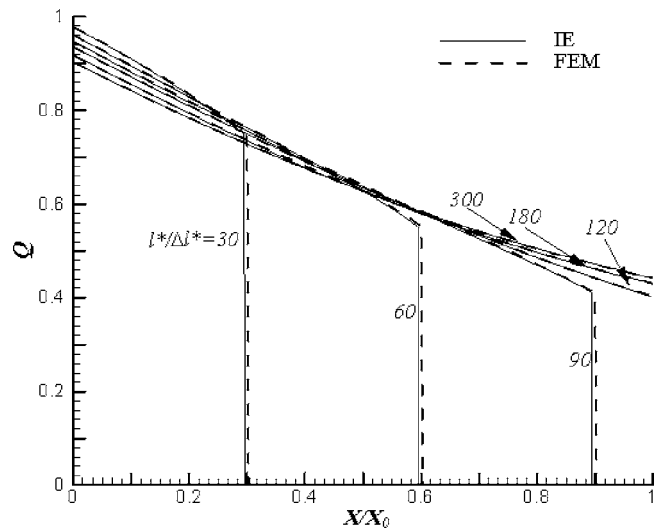
(a)
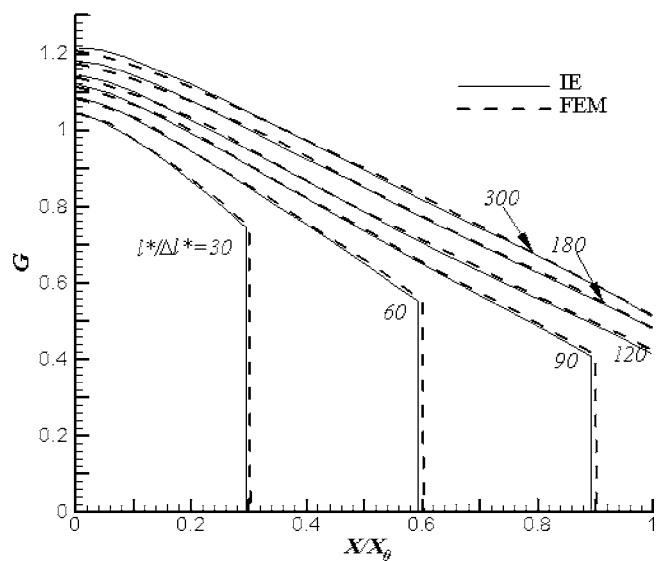
(b)

Fig. 2 The dimensionless heat flux and incident radiation in one-dimensional slab at different time: (a) the dimensionless heat flux; and (b) the dimensionless incident radiation. The optical thickness is 1.0 and the albedo is 0.5.

$\Delta l^* = C \cdot \Delta t = 10^{-2}$ m. The width of pulse is $l_p^* = 0.3$ m in these cases. The results of reflectance and transmittance are shown in Fig. 6. As shown in Fig. 6(a), the instant at which the local minimum took place varied with the location of interface. Accordingly, one can infer the internal structure of the multi-layer media from this variation. From Fig. 6(b), one can hardly find an obvious sign
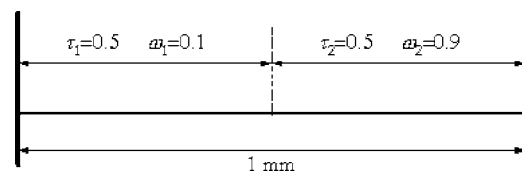

Fig. 3 The structural and optical properties of the two-layer media: the optical thicknesses of the two-layer media are all 0.5; their albedoes are 0.1 and 0.9, respectively
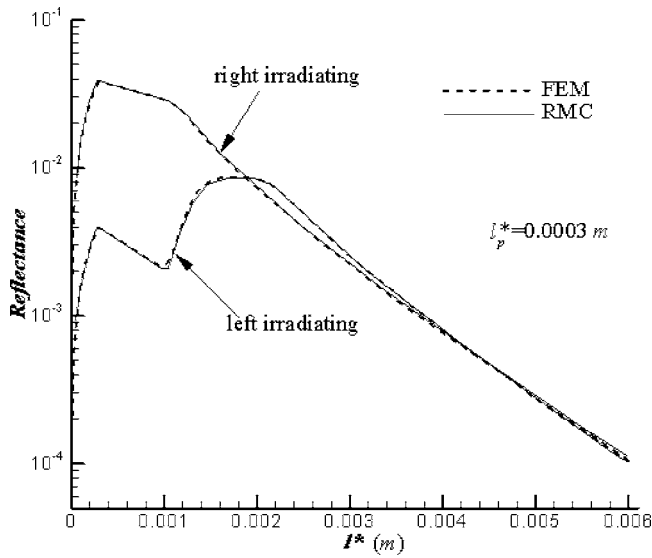
Fig. 4 The reflectance in the two-layer inhomogenous media: the results of the left-incident and right-incident light

about the structure and properties of media, although they are different for the three cases. Therefore, the reflected signals may play a very significant role in the inversion of optical imaging.

Lu and Hsu [19] believe the "local minimum" can be produced when the following two conditions are met: the normalized pulse width is less than one and the preceding layer scattering coefficient is less than that of the following layer. However, the following cases will indicate that the above conditions are not sufficient conditions for this phenomenon.

The optical properties of three cases are listed in Table 2. Their structures are similar to Case 1. The computational conditions such as the spatial, solid angle meshes, and the time step are the same as the above cases. As shown in Fig. 7, a local minimum can obviously be observed in the reflectance of Case 4. However, with the increase of optical thickness, it becomes very obscure in the result of Case 5. In the result of Case 6, the local minimum disappears completely. This can be explained as follows: a majority of the scattering energy produced by the second layer is absorbed
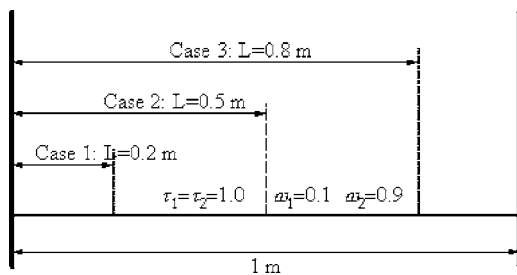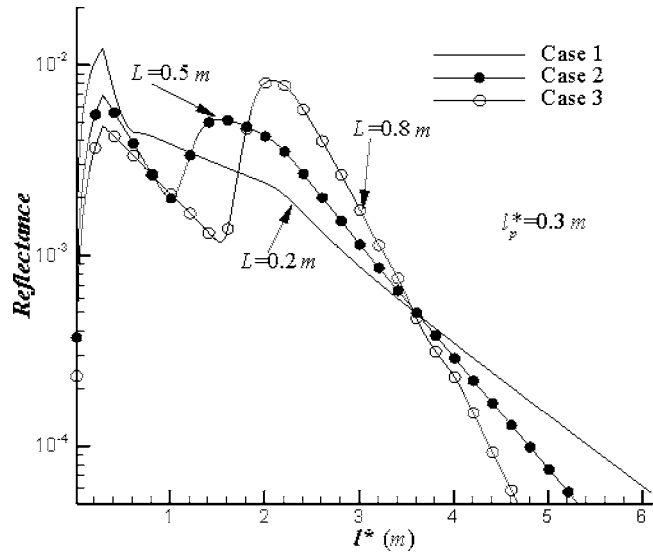

Fig. 5 The schematic diagram for Cases 1–3: the locations of the interface are 0.2, 0.5, and 0.8 m, respectively. The optical thicknesses and albedos of two-layer media are equivalent in the three cases.
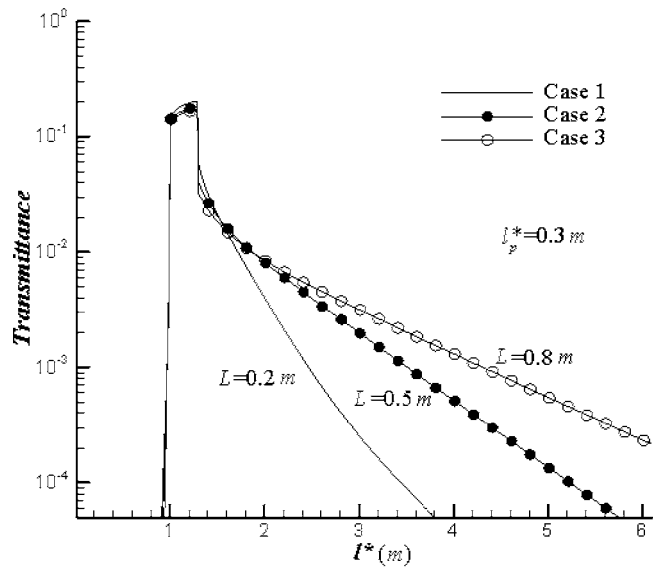

(a)

(b)

Fig. 6 The reflectance and transmittance in the two-layer media for Cases 1–3: (a) the reflectance; and (b) the transmittance

by the first layer in the process of reflecting to the front surface, where the remnants are less than the scattering energy produced by the first layer. In fact, a short enough pulse is necessary in order to obtain high spatial resolution. But the "dual peak" phenomenon is a special phenomenon that can only occur under a special condition. We believe that it might not appear under the majority of optically thick conditions that are prevalent in the biologic tissue. However, as shown in Fig. 7, the reflected signals can still imply the occurrence and location of the break of optical

Table 1 The structural and optical parameters of two-layer media for Cases 1–3[a]

Case	L	κ_{a1}	σ_{s1}	κ_{a2}	σ_{s2}
1	0.2	4.5	0.5	0.125	1.125
2	0.5	1.8	0.2	0.2	1.8
3	0.8	1.125	0.125	0.5	4.5

[a]The unit of length is m, the unit of absorbing and scattering coefficient is m^{-1}.

Table 2 The optical parameters of two-layer media for Case 4 to 6[a]

Case	τ_{1+2}	κ_{a1}	σ_{s1}	κ_{a2}	σ_{s2}
4	1.0	2.25	0.25	0.0625	0.5625
5	2.0	4.5	0.5	0.125	1.125
6	4.0	9.0	1.0	0.25	2.25

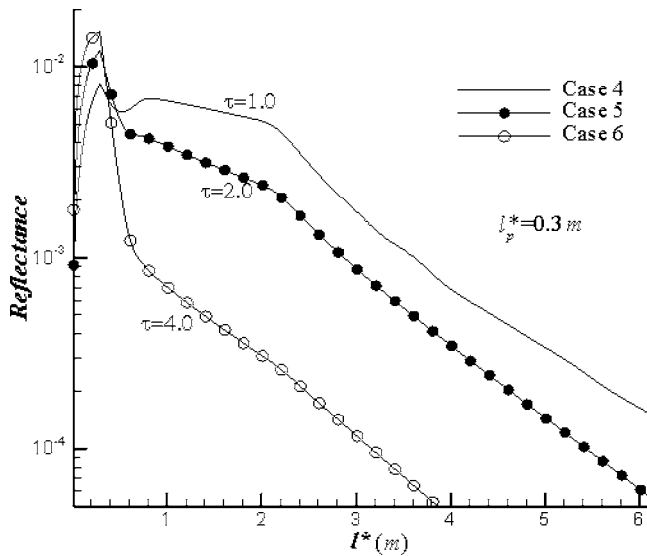[a]The unit of absorbing and scattering coefficient is m^{-1}.

Fig. 7 The reflectance in the two-layer media for Cases 4–6: the "dual peak" phenomenon can be observed in Case 4, but cannot be founded in Cases 5 and 6

properties even if the local minimum does not happen. Accordingly, as long as an obvious bend can be observed from the result of a reflected signal, a break of optical property exists determinately.

3.3 Three-Layer Nonhomogeneous Media With Short Pulse Light Irradiation. The analysis of uniqueness for the result is very important in solving the inverse problem. The present cases do service for this objective. The transient radiation in three-layer nonhomogeneous media is investigated in the present research. The schematic diagram and the optical properties of the media are shown in Fig. 8. The absorbing and scattering coefficients of the two side layers are 0.25 m^{-1} and 2.25 m^{-1}, respectively. The absorbing and scattering coefficients of the middle layer are 18.0 m^{-1} and 2.0 m^{-1} in Case 1. They become 8.0 m^{-1} and 2.0 m^{-1} in Case 2. The present model employs 50 uniform linear elements for the spatial discretization and the S_{20} for the solid angle discretization. The time step is taken as $\Delta l^* = 10^{-2}$ m. The width of pulse is $l_p^* = 0.1$ m in these cases. The reflectance and transmittance of the three cases are shown in Fig. 9. It can be observed from Fig. 9(a) that the reflected signals are very close in the majority of time for the two cases. Although the optical properties of the middle layer are drastically different, the difference between the reflectance of the two cases reached 20% only at the longer instant. However, the transmitted signals of the two cases are obviously different. This means that the reflected signal alone cannot provide sufficient information for effective inversion under some situations. A similar status can also occur in the transmitted signal under some situations such as Cases A11 and A14 in Ref. [19] in which the distribution of scattering coefficients of those
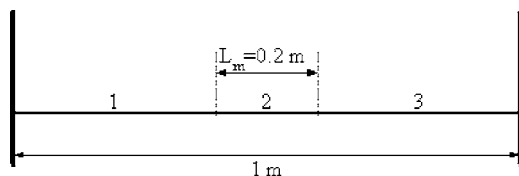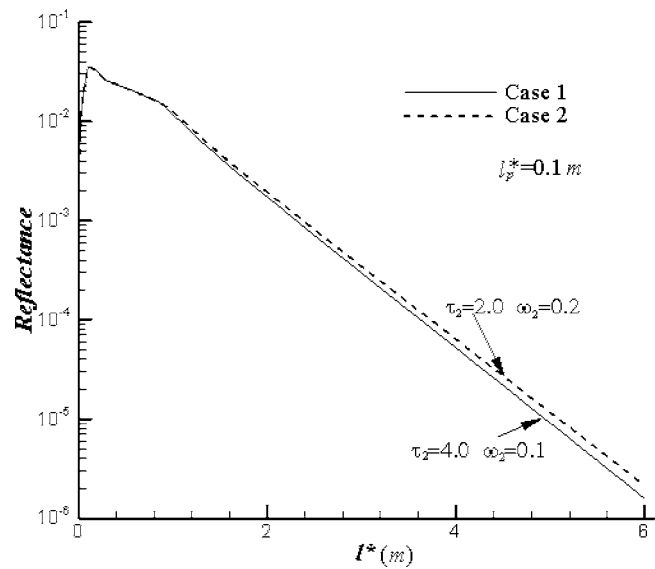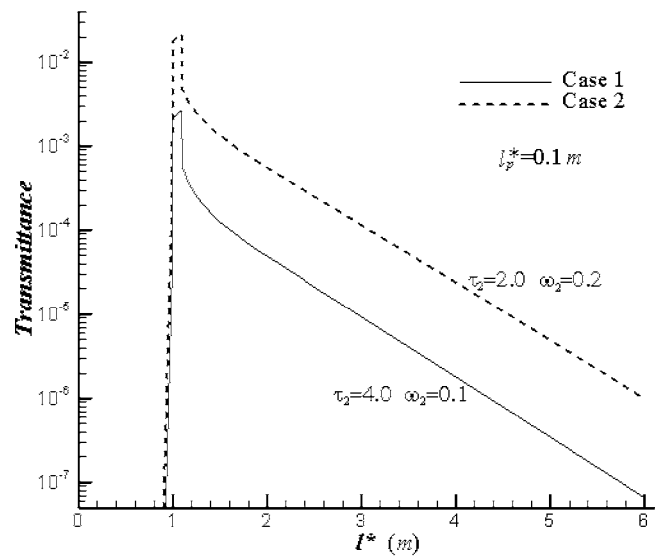

Fig. 8 The schematic diagram for the three-layer media: the absorbing and scattering coefficient of the two side layers are 0.25 m⁻¹ and 2.25 m⁻¹, that of the middle layer are 18.0 m⁻¹ and 2.0 m⁻¹ in Case 1. They become 8.0 m⁻¹ and 2.0 m⁻¹ in Case 2.

(a)

(b)

Fig. 9 The reflectance and transmittance in the three-layer media: (a) the reflectance; and (b) the transmittance. The reflected signals are very close in the majority of time for the two cases. The transmitted signals are obviously different.

cases is reversed, whereas their transmittance curves are very close. This illuminates that the transmitted signal cannot precisely and apparently respond to the changes of the optical properties. In a word, none of the reflected and transmitted signals can be solely taken as experimental measurements to predict the optical properties of the medium. These two kinds of signals should be measured simultaneously in the optical imaging application. Moreover, the time of sampling should be extended to a comprehensive distribution.

3.4 Effect of Albedo in the Optically Thick Media. Brewster and Yamada [5] first proposed that the albedo criterion for application of diffusion theory to time-dependent scattering may be much less restrictive than what is usually reported. The author investigated the temporal reflectance in a semi-infinite optically thick slab by the MCM and diffusion approximation model. To validate their conclusion, a similar case is designed to investigate the effect of albedo in the optically thick media by the LSFEM. In
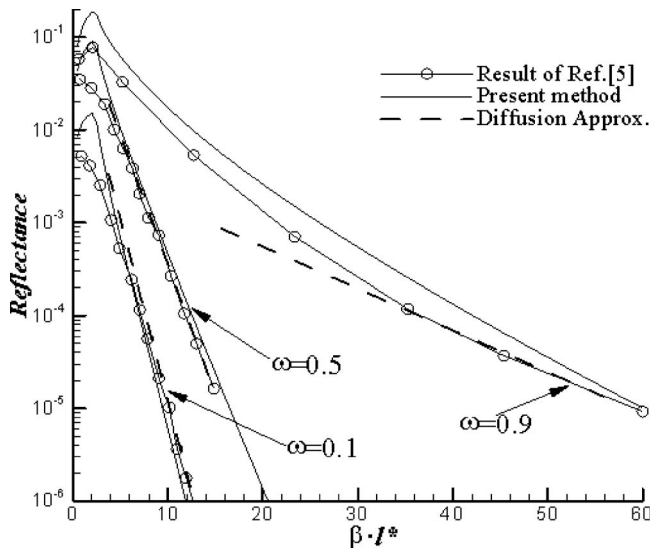
Fig. 10 Effect of albedo in the optically thick media: the albedos are 0.9, 0.5, and 0.1, respectively

this case, the isotropic scattering media is considered. The optical thickness is set to 500 to approximate the semi-infinite optically thick media. The results of different albedo are compared with that of Ref. [5].

It can be seen from Fig. 10 that the results of LSFEM agree with that of Monte Carlo and diffusion approximation at $\omega=0.1$ and $\omega=0.5$. For the situation of $\omega=0.9$, the result of LSFEM has similar declining trade with that of the MCM. A probable cause of disagreement can be attributed to the limited optical thickness for the present case. Therefore, as pointed by Brewster [5], we can get the same conclusion that the albedo criterion for application of diffusion theory is not necessary.

3.5 Two-Dimensional Homogeneous Media With Short Pulse Light Irradiation. The transient radiative transfer in two-dimensional isotropic and anisotropic scattering media is analyzed. In this case, the medium is contained in a rectangular enclosure with the optical thickness $\tau_x=\tau_y=10$ and the albedo is 0.998. The left wall is irradiated by a collimated beam whose temporal pulse shape is a square wave. The width of pulse is l_p^* =0.1 m. The linear scattering phase function is considered as

$$\Phi(\Omega',\Omega) = 1 + a(\mu\mu' + \eta\eta' + \xi\xi') \quad (13)$$

Positive and negative values of the coefficient a correspond to forward and backward scattering phase functions, respectively. The space and solid angle discretization employ 20×20 quadrangle elements and the S_8 scheme, respectively. The time step is taken as $\Delta l^*=0.02$ m. As shown in Fig. 11, the results of FEM and DOM [23] are in good agreement. The maximum relative error is about 3.0%. This indicates that the present model can simulate the transient radiative transfer in the multidimensional anisotropic scattering media accurately and effectively.

3.6 Two-Dimensional Nonhomogeneous Media With Short Pulse Light Irradiation. As shown in the Fig. 12, a two-dimensional (2D) square inhomogeneous media is considered in this case. The width of the square is 1.0 m. The absorbing and isotropic scattering coefficients of background media are 0.01 m^{-1} and 1.99 m^{-1}, respectively. There is a square core with 0.2 m width at the center of the background media. The absorbing and scattering coefficients of the core are 0.05 m^{-1} and 9.95 m^{-1}, respectively. With the time width l_p^*=0.1 m, a bundle of pulse light irradiates on the center of the left boundary of the square media. The spatial width of pulse light d_p is 0.1 m. The reflected and
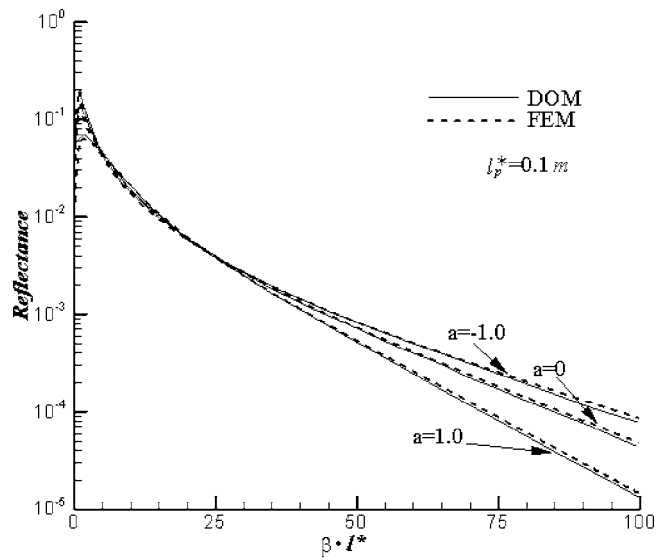
(a)
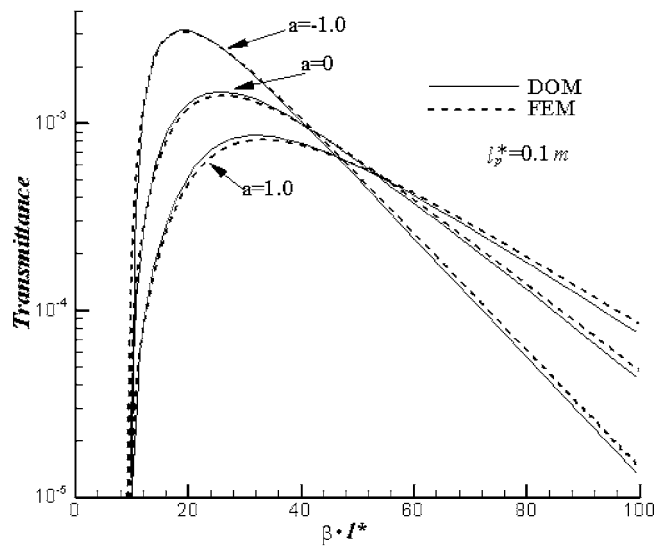
(b)

Fig. 11 The reflectance and transmittance in the two dimensional homogeneous media: (a) the reflectance; and (b) the transmittance. The optical thickness $\tau_x=\tau_y=10$ and the albedo is 0.998.

transmitted signals of different boundary location are simulated by the present method. In the simulation, the spatial discretization employs 40×40 uniform quadrilateral mesh. The solid angle discretization is the S_{12} scheme. The time step is $\Delta l^*=C\cdot\Delta t$ =0.02 m. The reflected signals on the left boundary are shown in Fig. 13(a). The transmitted signals on the top and right boundary are shown in Figs. 13(b) and 13(c).

From Fig. 13(a), it can be found that the instants of each point on the left boundary at which the reflected signals begin appearing is different. The farther a point is away from the incident source, the later it is to obtain the reflected signals. The reflected signal at point 1 is the most intensive. The "dual peak" phenomenon can be observed from all of the reflected signals at the left boundary. With the increase of distance from the source, the intensity of the second peak at point 2-4 gradually becomes weaker. After the point $l^*=2.2$ m, the declining speed of reflectance at each point is nearly the same.

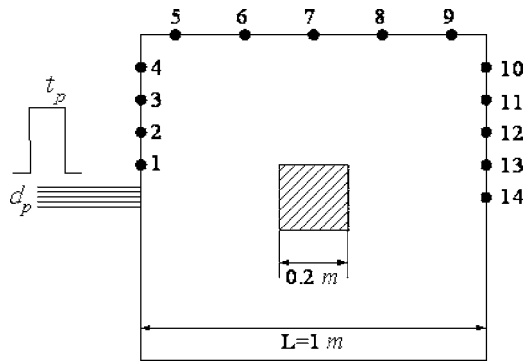The results of transmitted signal at the top boundary are shown

Fig. 12 The schematic diagram for the two-dimensional inhomogeneous media: the absorbing and isotropic scattering coefficients of background media are 0.01 m⁻¹ and 1.99 m⁻¹, respectively; they become 0.05 m⁻¹ and 9.95 m⁻¹ in the center core

in Fig. 13(b). It is similar to the reflected signals at the left boundary that the farther a point is away from the incident source, the later it is to obtain the radiative signals. But compared with the reflected signals of the left side, the variation of the signal intensity at different points on the top side is peculiar. Although the instant of point 7 at which the scattering signals begin appearing is later than that of points 5 and 6, its transmittance is more intensive. Moreover, the dual peak phenomenon doesn't occur at points 8 and 9. Therefore, point 7 is the critical point. A probable explain is that at this critical point, the increase of transmittance evoked by the incident pulse is immersed, before it begins to decline, by the scattering energy produced by the high scattering core. At points 8 and 9, the increase of transmittance can be attributed to the scattering energy produced by the core. Therefore, the dual peak doesn't occur at points 8 and 9.

It can be found in Fig. 13(c) that the dual peak phenomenon doesn't occur on the right boundary. The instants of each point at which the transmitted signals begin appearing are very close. But the peak value of transmittance is gradually decreased with the
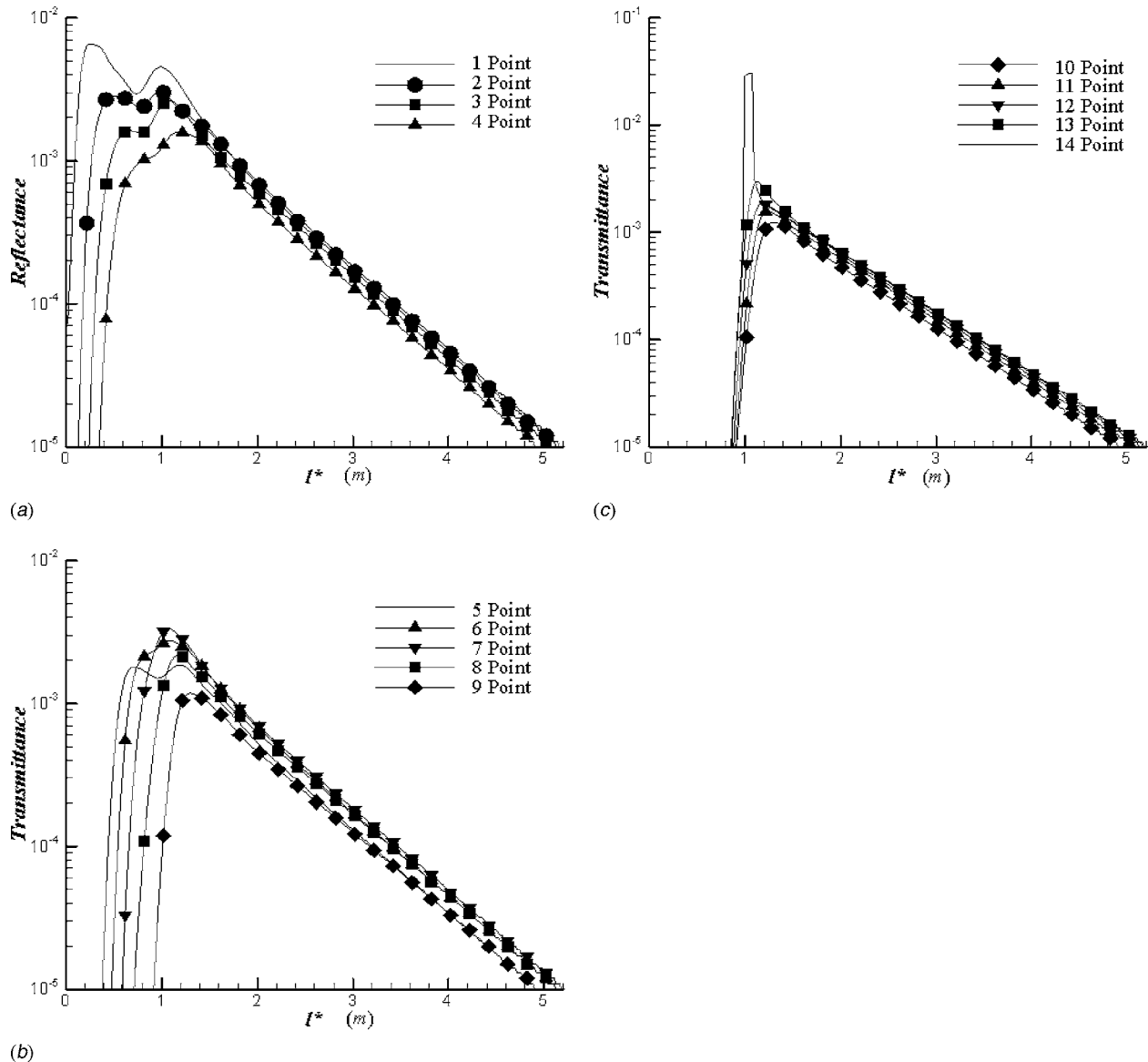

(a)

(c)

(b)

Fig. 13 The detected signals on the boundary of 2D inhomogeneous media: (a) the reflectance at points 1–4; (b) the transmittance at points 5–9, and (c) the transmittance at points 10–14

increasing distance away from the incident source. Similarly, after the point $l^*=2.2$ m, the declining speed of transmittance at each point is nearly the same.

4 Conclusion

In the present research, a finite element model is developed to simulate the interactive effect between the pulse light and the participating media. The model is based on least-squares variational principles and discrete ordinary method. A novel solid angle discretization based on the DOM+ISW method is proposed to simulate the arbitrary direction of the incident pulse light. The least-squares strategy in the space discretization not only produces a smooth result but also leads to a symmetric positive definite coefficient matrix which can be stored inexpensively and efficiently. Verified by some benchmark cases, the results of LSFEM show a good agreement with that of IE and RMC. Several results in the two-layer or three-layer nonhomogeneous media indicate that the reflected signals imply significant information about the media. The reflected signals can denote the break of optical properties as well as the information about the internal structure. Therefore, the reflected signals should be taken as important data in the inversion of optical imaging. The investigation into the uniqueness of the result indicates that none of the reflected and transmitted signals can solely be taken as experimental measurements to predict the optical properties of the medium. These two kinds of signals should be measured simultaneously in the optical imaging application. Moreover, the time of sampling should be extended to a comprehensive distribution. In addition, the case of optically thick media indicates that the albedo criterion for application of diffusion theory is not necessary. The last case in the two-dimensional enclosure proves the ability of the present model to deal with multi-dimensional problems.

Acknowledgment

Nomenclature

B = modified extinction coefficient, Eq. (6a)
C = propagation speed of radiation transport in the medium
G = dimensionless incident radiation, Eq. (12)
H = the Heaviside function
I = radiative intensity, W/(m^2 sr)
K,K' = stiffness matrix of finite element
M = number of discrete directions
Q = dimensionless radiative heat flux, Eq. (12)
S = modified source function, Eq. (6b)
R = right side term of finite element
V = the domain of solution
W_l = the weight function of finite element
a = the coefficient in Eq. (13)
d_p = spatial width of pulse light
l = distance
l^* = the radiative spreading distance in the medium, m
l_p^* = the product of time and the width of pulse, m
Δl^* = the product of the time step and the speed of light, m
$\boldsymbol{n}_w$ = unit normal vector of boundary surface
$\boldsymbol{r}$ = the location
$s_{m'}$ = unit vector in the direction, m'
t = the time, s
$w_{m'}$ = angular weight of solid angle, m'

x,y,z = coordinate directions
Ω = solid angle, sr
Φ = scattering phase function
ε = emissivity
κ_a = absorption coefficient, m^{-1}
σ_s = scattering coefficient, m^{-1}
β = extinct coefficient
ω = scattering albedo
τ = optical thickness
μ,η,ξ = direction cosines
δ = the Delta function

Subscripts

b = blackbody
c = collimated
d = diffuse
n = time step
p = pulse
w = wall

Superscript

m,m' = indices for ordinate directions

References

[1] Gibson, A. P., Hebden, J. C., and Arridge, S. R., 2005, "Recent Advances in Diffuse Optical Imaging," Phys. Med. Biol., **50**, pp. R1–R43.
[2] Tan, Z. M., and Hsu, P. F., 2001, "An Integral Formulation of Transient Radiative Transfer," ASME J. Heat Transfer, **123**, pp. 466–475.
[3] Arridge, S. R., Schweiger, M., Hiraoka, M., and Delpy, D. T., 1993, "A Finite Element Approach to Modelling Photon Transport in Tissue," Med. Phys., **20**, pp. 299–309.
[4] Firbank, M., Arridge, S. R., Schweiger, M., and Delpy, D. T., 1996, "An Investigation of Light Transport Through Scattering Bodies with Non-Scattering Regions," Phys. Med. Biol., **41**, pp. 767–783.
[5] Brewster, M. Q., and Yamada, Y., 1995, "Optical Properties of Thick, Turbid Media from Picosecond Time-Resolved Light Scattering Measurements," Int. J. Heat Mass Transfer, **38**(14), pp. 2569–2581.
[6] Elaloufi, R., Carminati, R., and Greffet, J. J., 2002, "Time-Dependent Transport Through Scattering Media: From Radiative Transfer to Diffusion," J. Opt. A, Pure Appl. Opt., **4**(5), pp. 103–108.
[7] Guo, Z., and Kumar, S., 2000, "Discrete-Ordinates Solution of Short-Pulsed Laser Transport in Two-Dimensional Turbid Media," Appl. Opt., **39**(24), pp. 4411–4417.
[8] Sakami, M., Mitra, K., and Vo-Dinh, T., 2002, "Analysis of Short-Pulse Laser Photon Transport Through Tissues for Optical Tomography," Opt. Lett., **27**(5), pp. 336–338.
[9] Chai, J. C., 2003, "One-Dimensional Transient Radiation Heat Transfer Modeling Using a Finite-Volume Method," Numer. Heat Transfer, Part B, **44**, pp. 187–208.
[10] Chai, J. C., 2004, "Transient Radiative Transfer in Irregular Two-Dimensional Geometries," J. Quant. Spectrosc. Radiat. Transf., **84**, pp. 281–294.
[11] Wu, C. Y., 2000, "Propagation of Scattered Radiation in a Participating Planar Medium With Pulse Irradiation," J. Quant. Spectrosc. Radiat. Transf., **64**, pp. 537–548.
[12] Hsu, P. F., 2001, "Effects of Multiple Scattering and Reflective Boundary on the Transient Radiative Transfer Process," Int. J. Therm. Sci., **40**, pp. 539–549.
[13] Lu, X. D., and Hsu, P. F., 2004, "Reverse Monte Carlo Method for Transient Radiative Transfer in Participating Media," ASME J. Heat Transfer, **126**, pp. 621–627.
[14] An, W., Ruan, L. M., Tan, H. P., and Qi, H., 2005, "Least Squares Finite Element Analysis for Transient Radiative Transfer in Absorbing and Scattering Media," ASME J. Heat Transfer, **128**, pp. 499–503.
[15] Pontaza, J. P., and Reddy, J. N., 2005, "Least-Squares Finite Element Formulations for One-Dimensional Radiative Transfer," J. Quant. Spectrosc. Radiat. Transf., **95**(3), pp. 387–406.
[16] Liu, L. H., 2004, "Finite Element Simulation of Radiative Heat Transfer in Absorbing and Scattering Media," AIAA J., **18**(4), pp. 555–557.
[17] An, W., Ruan, L. M., Qi, H., and Liu, L. H., 2005, "Finite Element Method for Radiative Heat Transfer in Absorbing and Anisotropic Scattering Media," J. Quant. Spectrosc. Radiat. Transf., **96**(3–4), pp. 409–422.
[18] Cui, X., and Li, B. Q., 2005, "Discontinuous Finite Element Solution of 2D Radiative Transfer With and Without Axisymmetry," J. Quant. Spectrosc. Radiat. Transf., **96**(3–4), pp. 383–407.
[19] Lu, X. D., and Hsu, P. F., 2005, "Reverse Monte Carlo Simulations of Light Pulse Propagation in Non-Homogeneous Media," J. Quant. Spectrosc. Radiat. Transf., **93**, pp. 349–367.
[20] Hsu, P. F., and Lu, X. D., 2005, "Temporal Reflectance from a Light Pulse Irradiated Medium Embedded With Highly Scattering Cores," *Proceedings EUROTHERM Seminar 82, Numerical Heat Transfer, 2*, Gliwice-Cracow, Po-

land, September 13–16, pp. 323–332.

[21] Li, H. S., Zhou, H. C., Lu, J. D., and Zheng, C. G., 1995, "Computation of 2D Pinhole Image-Formation Process of Large-Scale Furnaces Using the Discrete Ordinates Method," J. Quant. Spectrosc. Radiat. Transf., **78**, pp. 437–453.

[22] Modest, M. F., 1993, *Radiative Heat Transfer*, McGraw-Hill, New York.

[23] Sakami, M., Mitra, K., and Hsu, P. F., 2002, "Analysis of Light Pulse Through Two-Dimensional Scattering and Absorbing Media," J. Quant. Spectrosc. Radiat. Transf., **73**, pp. 169–179.

[24] Chai, J. C., Lee, H. S., and Partankar, S. V., 1993, "Ray Effect and False Scattering in the Discrete Ordinates Method," Numer. Heat Transfer, Part B, **24**(2), pp. 373–389.

[25] Ruan, L. M., An, W., Xie, M., and Tan, H. P., 2006, "Simulation of Short-Pulse Light Radiative Transfer in Participating Media by Least Squares Finite Element Method," *Proceedings EUROTHERM Seminar 78, Computational Radiative Transfer in Participating Media, 2*, Poitiers-Futuroscope, France, April 5–7, pp. 115–123.

A Boundary Element Method for Evaluation of the Effective Thermal Conductivity of Packed Beds

Jianhua Zhou[1]

Aibing Yu

School of Materials Science and Engineering,
The University of New South Wales,
Sydney, NSW 2052, Australia

Yuwen Zhang[2]

Department of Mechanical and Aerospace
Engineering,
University of Missouri-Columbia,
Columbia, MO 65211
e-mail: zhangyu@missouri.edu

The problem of evaluating the effective thermal conductivity of random packed beds is of great interest to a wide-range of engineers and scientists. This study presents a boundary element model (BEM) for the prediction of the effective thermal conductivity of a two-dimensional packed bed. The model accounts for four heat transfer mechanisms: (1) conduction through the solid; (2) conduction through the contact area between particles; (3) radiation between solid surfaces; and (4) conduction through the fluid phase. The radiation heat exchange between solid surfaces is simulated by the net-radiation method. Two regular packing configurations, square array and hexagonal array, are chosen as illustrative examples. The comparison between the results obtained by the present model and the existing predictions are made and the agreement is very good. The proposed BEM model provides a new tool for evaluating the effective thermal conductivity of the packed beds. [DOI: 10.1115/1.2430721]

1 Introduction

Heat transfer through a packed bed is of great interest in numerous industrial thermal systems, such as catalytic reactors [1], drying processes [2], processes involving transpiration cooling [3], high-performance cryogenic insulation [4], etc. Knowing the thermal properties of these materials, especially the effective thermal conductivity, is essential to allow correct design of these thermal systems. Many theoretical models for predicting the effective thermal conductivity of a packed bed have been reported. Most of the existing models are based on the so-called "unit cell method" [5–16], in which some unit cell is regarded as representative for the whole bed. Three heat transfer modes—conduction, convection and radiation—are arranged in series and/or in parallel in the unit cell. The unidirectional heat flow that leads to easy computation is usually assumed. For example, Yagi and Kunni [5] proposed a correlating formula for the effective thermal conductivity based on a unit cell, in which a portion of the heat is conducted by the solid, a portion by the fluid, and the rest of heat by a multilayer system consisting successively of a layer of the solid and a layer of the fluid. Zehner and Schlunder [6] presented an analytical expression by choosing a cylindrical unit cell, in which heat is transferred by conduction through two parallel paths: conduction through the gas-filled voids in the outer cylinder and conduction through the solid and gas phases in the inner cylinder. The unit cell method can give satisfactory predictions only when the constituent thermal conductivities are of the similar magnitude [17,18].

In recent years, a new method based on particle-size scale is receiving more and more attention [19–21]. In this method, the geometrical details between two touching deformed particles are considered to a more or less extent, and a representative temperature—usually the temperature at each particle center—in the packed bed can be calculated. The constriction resistance to heat flow between two touching particles is calculated first by

some methods, and then a linear system of simultaneous equations is established based on the thermal equilibrium requirement for each particle. These equations can be solved to obtain the temperatures at all particle centers. The effective thermal conductivity is finally determined according to the particle-center temperature distribution. For instance, Argento and Bouvard [19] calculated the constriction resistance between two touching spheres by using the finite element method and then established a linear system of simultaneous equations. Cheng et al. [20] employed the Voronoi polyhedron to represent the structure of random packing composed of monosized spheres. Based on this structure, they obtained the integral expressions of heat flux between two spheres and a linear system of simultaneous equations was established.

Theoretically, the temperature field in the whole packed bed can be obtained by solving the conduction differential equations in the solid and liquid phases with a continuous temperature and heat flux boundary condition at the solid–fluid interfaces [22]. The effective thermal conductivity can then be determined by the temperature field. This approach is subparticle scale in nature, which is expected to be able to give the most "exact" solutions since almost no assumption is introduced in the whole solution process. However, the irregular geometries at the solid–solid and solid–fluid interfaces necessitate very high computer time and storage. Among the existing numerical methods, the finite difference method (FDM) is not convenient for the establishing of such a model due to its poor adaptability to complex geometry. The finite element method (FEM) appears to be a suitable candidate since the grid-generation in FEM is flexible, but it is still a domain-based numerical method that requires discretizing the space everywhere inside the entire computation domain. Particularly, an extremely fine mesh is needed near the point of contact between particles. Accordingly, a very large computer memory is required to store the space-discretizing information. Therefore, both FDM and FEM are not appropriate to establish such a subparticle scale model.

The boundary element method (BEM) [23–27] converts the partial differential equation into boundary integral equation and thus is referred to as the "boundary-only method." Although the particle number is usually very large in a simulation, the computational cost is expected to be acceptable since only boundary discretization is required. Furthermore, the BEM has very strong

---

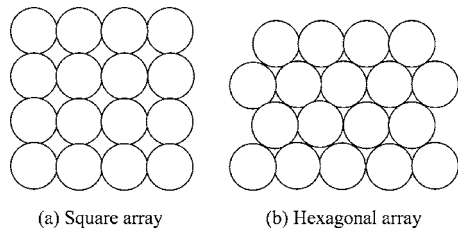(a) Square array   (b) Hexagonal array

Fig. 1 Two-dimensional regular packing structure

adaptability to complex geometry involved in the packed bed. The unknowns in the BEM simulation are the temperatures and heat fluxes on the domain boundary, which allows us to combine the BEM with the thermal radiation in an efficient way because radiation is also a surface behavior for the case where the solid phase is opaque and the fluid phase is nonparticipating. The foregoing advantages of BEM make it an ideal tool to analyze the combined conduction/radiation heat transfer in a packed bed.

This study develops a boundary element method for the prediction of the effective thermal conductivity of a two-dimensional packed bed. The boundary element formulation, net-radiation method, and the iterative solution procedure for the coupled conductive/radiative heat transfer are described in detail for two regular packing configurations—square array and hexagonal array. The predicted results are compared with the existing theoretical predictions and good agreement is found.

2 Mathematical Formulation

2.1 Physical Model and Boundary Discretization. Figure 1 illustrates two regular packing structures, namely square array and hexagonal array (alternatively, the terms "in-line arrangement" and "staggered arrangement" have also been used, for example, in Ref. [14]) that will be studied. Figure 2 shows the Cartesian coordinate system and the discretization of the boundaries for a square array including 20 particles. In our real simulation, however, packed beds can include hundreds of particles in order to obtain physically meaningful results.

The whole packed bed is bounded by two horizontal plates and two vertical plates and some external compression loads are exerted on the bounding plates. As a result, all the particles in the packed bed are subject to deformation at the particle–particle contact point. Although the particle–particle contact areas can be calculated by the theory of contact mechanics [28], the details of contact mechanics will not be considered in this study for simplicity. It is worth noting that, in Fig. 2, the sizes of all the particle–particle contact areas, as well as the bounding plate–particle contact areas, are depicted in an exaggerated way for clarity (in practice, the ratios of contact size to particle size are usually very small, e.g., 0.01). Since the thermal conductivity of the solid phase is different from that of the fluid phase, the entire packed bed domain will be divided into two subregions: solid and fluid. In addition, the boundary of the solid region can be further divided into external boundary and internal boundaries due to the presence of the fluid-filled voids.

The heat transfer occurring in the fluid-filled voids immediately adjacent to the bounding plates (e.g., the void 3-4-5-6-7-3 in Fig. 2) is not considered in the heat transfer computation, which may cause the so-called "wall effect." In this study, the wall effects are removed by increasing the number of particles, as is usually done in previous studies [19,20]. All the external boundary nodes of the solid region are subject to a zero heat flux boundary condition except those nodes located at the top or bottom bounding plates where a constant temperature boundary condition is applied (T_t at top bounding plate and T_b at bottom bounding plate).

For the case shown in Fig. 2, the boundary of the solid phase is discretized into 196 constant boundary elements (100 elements on the external boundary and 96 elements over the 12 internal boundaries). The boundary nodes, where the unknown values (temperature or heat flux) are to be solved, are located at the middle of each boundary element. In addition, special care is given to the numbering of the boundary nodes. As shown in Fig. 2, for the external boundary of the solid region, the numbering scheme is defined in the counterclockwise direction, whereas for the internal boundaries the numbering scheme is defined in the clockwise direction. For the boundary of the fluid region or "fluid-filled voids," the numbering scheme is defined in the same direction as that of the internal boundary of the solid region. To capture the drastic temperature variation near the particle–particle contact point, fine mesh is generated in the vicinity of contact point and coarse mesh is generated elsewhere (this feature is not shown in Fig. 2 for the clearness of the figure).

2.2 Boundary Element Scheme. It is assumed that the solid and fluid phases in the packed bed are homogeneous and isotropic media. The two-dimensional steady heat conduction in the solid and fluid phases of the packed beds in Cartesian coordinates are described by the Laplace equations
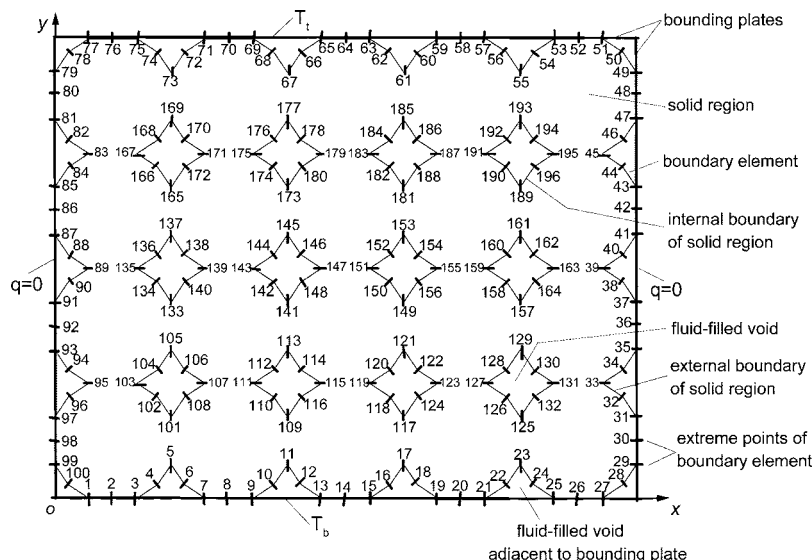

Fig. 2 Coordinate system and discretization of the boundaries

$$\frac{\partial^2 T_s}{\partial x^2} + \frac{\partial^2 T_s}{\partial y^2} = 0 \quad \text{in } \Omega_s \tag{1}$$

$$\frac{\partial^2 T_f}{\partial x^2} + \frac{\partial^2 T_f}{\partial y^2} = 0 \quad \text{in } \Omega_f \tag{2}$$

where Ω_s and Ω_f are solid and fluid regions, respectively.

The boundary conditions of the problem are as follows

$$T_s = T_t \quad \text{on } \Gamma_{et} \tag{3}$$

$$T_s = T_b \quad \text{on } \Gamma_{eb} \tag{4}$$

$$-k_s \frac{\partial T_s}{\partial n_s} = 0 \quad \text{on } \Gamma_{er} \tag{5}$$

$$T_s = T_f \quad \text{on } \Gamma_i \tag{6}$$

$$k_s \frac{\partial T_s}{\partial n_s} = -k_f \frac{\partial T_f}{\partial n_f} - q_r'' \quad \text{on } \Gamma_i \tag{7}$$

where Γ_{et} is the external boundary of solid region located at the top bounding plate; Γ_{eb} is the external boundary of solid region located at the bottom bounding plate; Γ_{er} is the rest part of the external boundary of solid region excluding Γ_{et} and Γ_{eb} (the total external boundary of the solid region is $\Gamma_e = \Gamma_{et} + \Gamma_{eb} + \Gamma_{er}$); Γ_i is the internal boundary of the solid region (the internal boundary of the solid region is composed of many sub-boundaries, which constitute the solid–fluid interface; and Γ_i represents the sum of all these sub-boundaries); and q_r'' is the radiative heat flux on the internal boundaries of the solid region. Equations (6) and (7) fulfill the requirement of the continuous temperature and heat flux condition at the solid–fluid interface. In the numerical solution procedure, iteration between solutions of solid and liquid phase is needed in order to satisfy Eqs. (6) and (7).

The boundary element method will be briefly described using the solid phase as an example. When the solid phase is the present computational domain, and the normal temperature derivatives on the solid–fluid interface, $\partial T_s / \partial n_s$, are obtained from the solution of the fluid phase. Therefore, the boundary condition in Eq. (7) can be written as

$$\frac{\partial T_s}{\partial n_s} = \bar{q}_s \quad \text{on } \Gamma_i \tag{8}$$

where $\bar{q}_s$ is the normal temperature derivative on the solid–fluid interface

$$\bar{q}_s = -\frac{k_f}{k_s} \frac{\partial T_f}{\partial n_f} - \frac{q_r''}{k_s} \tag{9}$$

Equations (1), (3)–(5), and (8) form the closed mathematical description for the BEM simulation in the solid region. It can be seen that essential boundary conditions are imposed on $\Gamma_{et} + \Gamma_{eb}$, whereas natural boundary conditions are exerted on $\Gamma_{er} + \Gamma_i$. The mathematical description for the BEM simulation in the solid region can be rewritten in a more compact form as follows

$$\nabla^2 T_s = 0 \quad \text{in } \Omega_s \tag{10}$$

$$T_s = \bar{T}_s \quad \text{in } \Gamma_{et} + \Gamma_{eb} \tag{11}$$

$$\frac{\partial T_s}{\partial n_s} = \bar{q}_s \quad \text{in } \Gamma_{er} + \Gamma_i \tag{12}$$

where ∇^2 is the Laplace operator.

Applying a weighted residual formulation to Eq. (10) yields

$$\int_{\Omega_s} (\nabla^2 T_s) T^* d\Omega = \int_{\Gamma_{er}+\Gamma_i} (q_s - \bar{q}_s) T^* d\Gamma + \int_{\Gamma_{et}+\Gamma_{eb}} (\bar{T}_s - T_s) q^* d\Gamma \tag{13}$$

where $q_s = \partial T_s / \partial n_s$; $q^* = \partial T^* / \partial n_s$; and T^* is the weighting function, which is the fundamental solution to the Laplace equation subject to a concentrated unit heat source, and is given by (for a two-dimensional problem)

$$T^* = \frac{1}{2\pi} \ln\left(\frac{1}{r}\right) \tag{14}$$

where r is the distance from a "source point" i (i.e., the point of application of the concentrated unit heat source) to any field point.

Integrating the left-hand side of Eq. (13) by parts twice gives

$$\int_{\Omega_s} T_s (\nabla^2 T^*) d\Omega = -\int_{\Gamma_{er}+\Gamma_i} \bar{q}_s T^* d\Gamma - \int_{\Gamma_{et}+\Gamma_{eb}} q_s T^* d\Gamma$$
$$+ \int_{\Gamma_{er}+\Gamma_i} T_s q^* d\Gamma + \int_{\Gamma_{et}+\Gamma_{eb}} \bar{T}_s q^* d\Gamma$$
$$= -\int_{\Gamma_s} q_s T^* d\Gamma + \int_{\Gamma_s} T_s q^* d\Gamma \tag{15}$$

where Γ_s is the total boundary of the solid region, $\Gamma_s = \Gamma_{et} + \Gamma_{eb} + \Gamma_{er} + \Gamma_i$.

The properties of the fundamental solution T^* lead to the following integral expression

$$T_s^i + \int_{\Gamma_{er}+\Gamma_i} T_s q^* d\Gamma + \int_{\Gamma_{et}+\Gamma_{eb}} \bar{T}_s q^* d\Gamma$$
$$= \int_{\Gamma_{er}+\Gamma_i} \bar{q}_s T^* d\Gamma + \int_{\Gamma_{et}+\Gamma_{eb}} q_s T^* d\Gamma \tag{16}$$

Equation (16) is valid for any point inside the domain Ω_s. If we take the point i to the boundary, the boundary integration equation, which only involves boundary integration, is obtained as follows

$$c_i T_s^i + \int_{\Gamma_{er}+\Gamma_i} T_s q^* d\Gamma + \int_{\Gamma_{et}+\Gamma_{eb}} \bar{T}_s q^* d\Gamma$$
$$= \int_{\Gamma_{er}+\Gamma_i} \bar{q}_s T^* d\Gamma + \int_{\Gamma_{et}+\Gamma_{eb}} q_s T^* d\Gamma \tag{17}$$

where the coefficient c_i is a function of the solid angle of the boundary at point i. c_i takes the value of 0.5 on a smooth boundary, which is the case in this study since the constant boundary elements are adopted.

If we discretize the boundary into a series of elements, a linear system of equations will result. After solving these equations, the unknowns on the boundary can be obtained. Once all the normal derivatives and temperatures on the boundary are known, the temperature at any points inside the region Ω_s can be computed using Eq. (16).

The effective thermal conductivities of the packed bed are computed by

$$k_e = \frac{Q}{A \cdot \dfrac{(T_t - T_b)}{H}} \tag{18}$$

After the temperatures on the internal boundary of the solid region are obtained, the BEM simulation is performed in each fluid-filled void. It should be pointed out that, in these regions, special attention should be paid to the calculation of the normal to the boundary since the boundary-node numbering scheme is de-
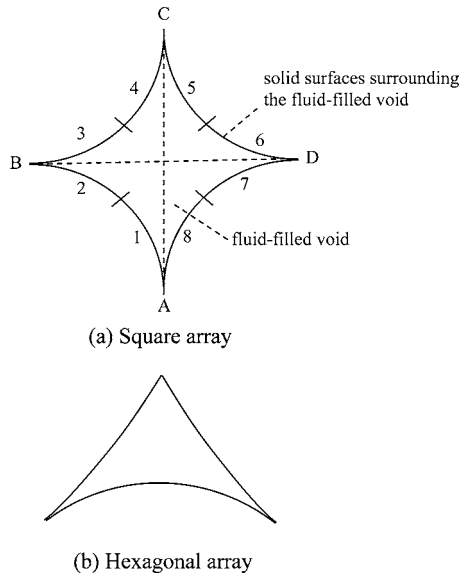
(a) Square array

(b) Hexagonal array

Fig. 3   Geometries of the fluid-filled voids

fined in the clockwise direction, which is in contrast to that of the solid region. On the whole, the BEM simulation in the fluid-filled voids region is similar to that in the solid region and will not be given here.

2.3   Radiation Heat Transfer. Radiation becomes important at high temperatures. The present BEM model takes the radiation between solid surfaces into account. It is assumed that the solid phase is opaque and its surface is diffuse and gray. The fluid in the voids is considered a nonparticipating medium. The radiation heat exchange occurs among the solid surfaces surrounding the fluid-filled voids. For two-dimensional packed beds, the solid surfaces surrounding a fluid-filled void usually constitute a closed cavity and therefore the radiation problem becomes one occurring in a closed cavity. Figure 3 shows the two geometries of the fluid-filled voids for the two regular packings depicted in Fig. 1. For random packing, the problem will become more complicated because the solid surfaces surrounding a fluid-filled void may not form a closed cavity (there are openings on the boundary). This means that the radiation rays can travel from the one fluid region to another, which is considered a long range effect [29]. The extension of the present work to random packing structures is underway.

To illustrate the key features of the present radiation model, the case shown in Fig. 3(a) will be considered. The boundary of the fluid-filled void is composed of four convex solid surfaces and there are eight boundary elements on the boundary. For simplicity, it is assumed that the enclosure (i.e., the fluid-filled void) is composed of four radiation surfaces (i.e., surfaces AB, BC, CD, and DA) disregarding how many boundary elements there are on the boundary in the BEM simulation. With this assumption, the view factors between the four surfaces can be calculated by Hottel's crossed-string method [30] with considerable ease. For instance, the view factor from surface AB to BC is calculated by

$$F_{AB-BC} = \frac{\overline{AB} + \overline{BC} - \overline{AC}}{2\overline{AB}} \tag{19}$$

where $\overline{AB}$, $\overline{BC}$ are, respectively, the path lengths of the curves AB and BC; and $\overline{AC}$ is the length of the line joining the points A and C. The view factor from surface AB to CD is computed by

$$F_{AB-CD} = \frac{\overline{AC} + \overline{BC} - \overline{BC} - \overline{DA}}{2\overline{AB}} \tag{20}$$

where $\overline{DA}$ is the path length of the curve DA; and $\overline{BD}$ is the length of the line joining the points B and D. Since four surfaces of the void are all convex, the view factor between a surface and itself is zero.

The radiative heat exchange between the solid surfaces is computed by using the net-radiation method [30]. By applying this method, the following system of equations can be obtained

$$J_i - (1 - \varepsilon_i)\sum_j F_{ij}J_j = \varepsilon_i \sigma T_i^4 \tag{21}$$

where ε_i is the emissivity of surface i.

In Eq. (21), T_i is calculated in the following way. Once the BEM simulation is performed in the solid region, all the temperatures on the solid boundary surrounding a fluid-filled void are known. The temperatures of the surfaces AB, BC, CD, and DA are taken as the arithmetic mean of the temperatures of the boundary elements on that surface. For instance, the temperature of surface AB is calculated by

$$T_{AB} = \frac{T_1 + T_2}{2} \tag{22}$$

where T_1 and T_2 are the temperatures of the boundary elements 1 and 2 in Fig. 3.

After all the outgoing radiative flux, J_i, are obtained from Eq. (21), the net heat loss of each surface is

$$q_i'' = J_i - \sum_j F_{ij}J_j \tag{23}$$

where a positive q'' means a certain amount of heat should be supplied to the surface in order to maintain the present temperature of this surface. Conversely, a negative q'' implies a certain amount of heat should be removed from the surface in order to maintain its temperature. It is worth noting that q_r'' in Eq. (7) is identical to q'' in Eq. (23).

2.4   Iteration Solution Procedure. Due to the presence of a nonlinear radiative boundary condition, it is necessary to perform an iterative solution procedure in order to obtain the solution of Eqs. (1)–(7). The iteration solution procedure is as follows:

1. Make an initial guess for the normal temperature derivatives on the solid–fluid interface;
2. Perform the boundary element simulation in the solid region;
3. After step 2, the temperatures on the solid–fluid interface are known. The radiative heat flux q_r'' can thus be calculated by the net-radiation method; the conductive heat flux $-k_f \partial T_f/\partial n_f$ at the solid–fluid interface can be computed by performing boundary element simulation in the fluid-filled voids;
4. Using the most recently obtained value of the combined heat flux (i.e., $-k_f \partial T_f/\partial n_f - q_r''$, obtained by step 3) as the input heat flux on the solid–fluid interface, go back to step 2 and perform the boundary element simulation in the solid region again; and
5. Repeat the foregoing solution process until the changes of the combined heat flux on the solid–fluid interface (i.e., $-k_f \partial T_f/\partial n_f - q_r''$) become smaller than a prescribed minor tolerance (e.g., 10^{-6}).

3   Results and Discussion

A BEM computer code has been developed based on the model described in the preceding section. For simplicity, it is assumed that the deformations at all contact points are identical [31]. For the square array and hexagonal array packings, the void fraction is
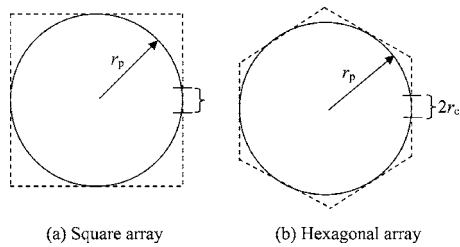
Fig. 4 Calculation of void fraction

Fig. 5 Effect of particle number on the effective thermal conductivity

found to be a function of the ratio of contact radius to particle radius. Because of the periodicity of the packing structure, the void fractions for these two packing systems can be obtained from the unit cells as illustrated Fig. 4, where r_c and r_p are the contact radius and particle radius, respectively. The void fraction for the square array packing is calculated by

$$\phi = 1 - \frac{\gamma\sqrt{1-\gamma^2} + \frac{\pi}{4} - \arcsin\gamma}{1-\gamma^2} \qquad (24)$$

where γ is the ratio of contact radius to particle radius, $\gamma = r_c/r_p$. The void fraction for the hexagonal array packing is computed by

$$\phi = 1 - \frac{\sqrt{3}\cdot\left(\gamma\sqrt{1-\gamma^2} + \frac{\pi}{6} - \arcsin\gamma\right)}{1-\gamma^2} \qquad (25)$$

The relationship between the ratio of contact radius to particle radius and the void fraction can be seen more clearly in Table 1. For the same deformation, the hexagonal array is a more closed packing than the square array. The void fraction corresponding to the case $\gamma=0.01$ is very close to that of point contact, therefore the simulation case $\gamma=0.01$ can be approximately regarded as the case of point contact.

As stated earlier, heat transfer occurring in the fluid-filled voids immediately adjacent to the bounding plates is not considered, so something should be done first to remove the "wall effects." Figure 5 shows the effect of particle number on the effective thermal conductivity. Similar results are obtained for other r_c/r_p and k_s/k_f values. It is seen that, to obtain stable calculating results, 20 particles are sufficient for square array packing and 120 particles are required for hexagonal array packing. This is because the wall effect for the hexagonal array is more notable than that for the square array packing. It is should be pointed out that, in this study, all the calculations are performed on a personal computer (Intel Pentium® IV 2.4 GHz with 256 MB memory). For the square array packing including 20 particles, one numerical case costs about 30 min of CPU time; for the hexagonal array packing including 120 particles, the CPU time is about 200 min.

One of the advantages of the present BEM method is that the temperature at any point within the packed bed can be determined accurately according to the calculated boundary values using Eq.

(16). Figures 6 and 7 show the temperature distributions in local regions (to be more representative, these local regions are deliberately chosen to be located at the whole-bed center) for square array and hexagonal array. It is seen that the isotherm lines are much denser in the vicinity of the particle-to-particle contact area. This indicates that the heat flux constriction effect due to particle contact can be well captured by the present boundary element model. In addition, the symmetry of these temperature distributions agrees well with the regular packing features of the two packed beds.

Figure 8 presents a comparison of the results obtained by the present model with those obtained by previous models (radiation is not considered in Fig. 8). The maximum and minimum values of the thermal conductivity of a solid–fluid two phase packing system are also shown in this figure. According to Ref. [22], the maximum thermal conductivity of a two-phase packing system is attained when the media are arranged in alternate layers separated by planes parallel to the direction of heat flow; the minimum conductivity of such a system is attained when the media are separated by planes running perpendicular to the direction of heat flow. As can be seen from Fig. 8, all the previous models underestimate the effective thermal conductivity when the solid/fluid thermal conductivity ratio is high. This is in good agreement with the conclusions made in Refs. [17,18]. Since almost no assumption is made during the model formulation and solution process, the results obtained by the present BEM model might be the closest to the "exact solution" under the simulation condition.

Radiation is known to be an important mechanism of heat transfer in packed beds, particularly at high temperatures. The models that have been proposed to describe simultaneous radiation and conduction can be classified into three types: unit cell models [7–9], pseudo-homogeneous models [32,33], and the ray tracing method [34,35]. No matter which method is used, the contribution of radiation to heat transfer is usually expressed as an equivalent conductivity–radiative conductivity

$$k_r = 4Fd_p\sigma T_m^3 \qquad (26)$$

where d_p is the particle diameter; and F is the radiation exchange factor. Many analytical expressions have been proposed to calculate this parameter, as summarized in Table 2.

As Vortmeyer [29] pointed out, the radiation contribution in packed beds depends not only on the void fraction and emissivity of the solid surface, but also on the solid thermal conductivity. To date, only Schotte's model [8] considers the influence of the solid conductivity on the radiation contribution. In Schotte's model, the radiative conductivity k_r is obtained by the following two steps

$$k_r^0 = 4Fd_p\sigma T_m^3 \qquad (27)$$

Table 1 Relationship between the void fraction and ratio of contact radius to particle radius

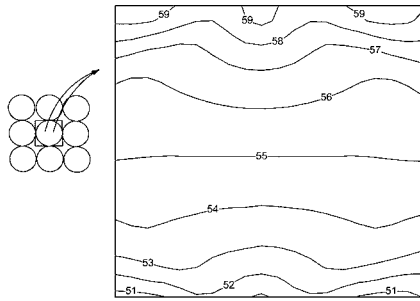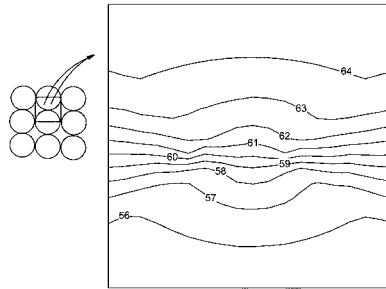| Ratio of contact radius to particle radius $\gamma=r_c/r_p$	Void fraction ϕ	
	Square array	Hexagonal array
0.3	0.1573	0.0386
0.2	0.1874	0.0650
0.1	0.2073	0.0851
0.05	0.2127	0.0910
0.01	0.2145	0.0930
Point contact	0.2146	0.0931

(a) Temperature distribution in a local region near the particle-center

(b) Temperature distribution in a local region near the particle-to-particle contact point

Fig. 6 The temperature distributions in local regions for the case of square array (20 particles are used for simulation)

$$k_r = \frac{1 - \phi}{\dfrac{1}{k_s} + \dfrac{1}{k_r^0}} + \phi k_r^0 \qquad (28)$$

The radiation exchange factor in Eq. (27) is $F = \varepsilon$.

Once the radiative conductivity is known, the effective of thermal conductivity k_e of the packed bed can be calculated as the sum of the effective conductivity without radiation contribution k_c and the radiative conductivity k_r

$$k_e = k_c + k_r \qquad (29)$$

In this study, the radiative conductivity is obtained using the following procedure. The effective thermal conductivity at real temperature level k_e is first calculated using the combined conduction/radiation BEM model. Then, the pure conduction BEM model is employed to compute the effective conductivity without radiation contributions k_c. Finally, the radiative conductivity k_r is obtained by: $k_r = k_e - k_c$.

Figure 9 shows a comparison of the results with the previous theoretical predictions when the radiation contribution is considered. As is seen, there are large variations among the results ob-
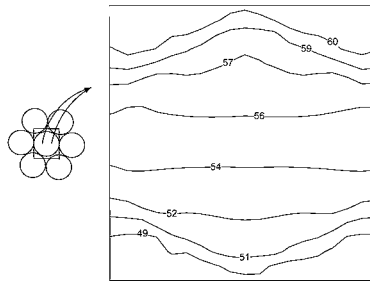
(a) Temperature distribution in a local region near the particle-center
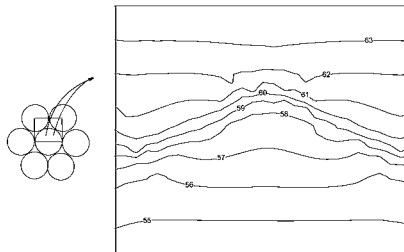
(b) Temperature distribution in a local region near the contact points of three particles

Fig. 7 The temperature distributions in local regions for the case of hexagonal array (120 particles are used for simulation)
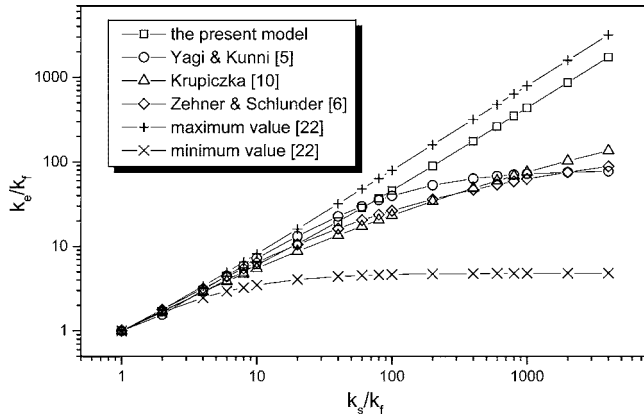
Fig. 8 Comparison of the present model with previous theoretical models (square array, r_p=2.5 mm, r_c/r_p=0.1, T_m=55°C)

Fig. 9 Comparison of the calculating results with the previous predictions when radiation contribution is considered (square array, r_p=2.5 mm, r_c/r_p=0.1, k_f=0.029, ε=0.9)

tained by different thermal radiation models. The k_r values predicted by the present model fall in the range of the previous ones. Since only Schotte's model [8] considers the influence of the solid conductivity on the radiation contribution, the present results are closer to those obtained by Schotte's model. It is also observed from Fig. 9 that the radiative conductivity increases with increasing solid conductivity. When the solid conductivity exceeds some value, further increase of radiative conductivity becomes less significant (see Fig. 9, k_s/k_f increases from 600 to 2000). This can be explained as follows. When the solid conductivity is low, the heat conduction in solids dominates the heat transfer process, so even a small increase of solid conductivity can give rise to the increase of radiative conductivity. However, when the solid conductivity is high, the total energy transfer process is dominated by radiation, so further increase of solid conductivity cannot lead to a pronounced increase of the radiative conductivity.

Figure 10 shows the ratio k_e/k_f plotted against the ratio k_s/k_f with γ (the ratio of contact radius to particle radius) as a parameter. It is plotted for the bed mean temperature 55°C, where the radiation contribution can be safely neglected. It is seen that the ratio k_e/k_f increases with the increase of k_s/k_f. For the same value of γ, the effective thermal conductivity for the hexagonal array packing is higher than that for the square array packing since the hexagonal array is a more closed packing when the same deformation is considered.

The radiation contribution depends on the bed mean temperature as well as the particle size. Figure 11 shows the effects of bed
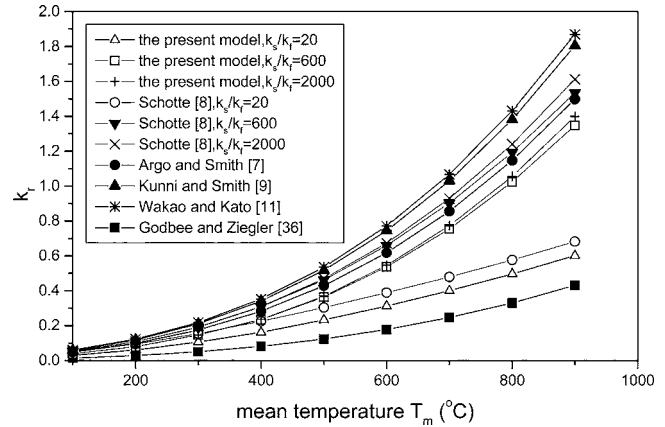
mean temperature and particle size on the effective thermal conductivity. The effective thermal conductivity increases with the increasing mean temperature and particle size, indicating that the radiation contribution becomes more significant for higher mean temperature and larger particle radius. This is in good agreement with the experimental observation of Yagi and Kunni [5]. In addition, when the ratio of contact radius to particle radius is low (e.g., r_c/r_p=0.01, this means a small contact deformation), the effective thermal conductivity increases more quickly as the mean temperature increases. This result arises from the fact that, when the contact deformation is small, more solid surface can be used for radiation heat exchange. Furthermore, it is observed that, for closed packing of small-size particles (e.g., curve 4 in Fig. 11), the values of k_e/k_f are nearly constant, which indicates that thermal radiation can be neglected in such cases. The effective thermal conductivity for the square array can exceed that for the hexagonal array when the mean temperature is high. This suggests that the effective thermal conductivity of hexagonal array packing is not necessarily larger than that of square array packing when the radiation is the main heat transfer mechanism, depending on the mean temperature of packed beds.

Figure 12 presents the effect of the solid surface emissivity on the effective thermal conductivity. As expected, the effective thermal conductivity of the packed bed goes up as the surface emissivity increases. The influence of the surface emissivity is more notable for the case of square array. This is because under the

Table 2 Analytical expressions for radiation exchange factor

Investigator	Radiation exchange factor, F
Argo and Smith[a]	$\dfrac{1}{2/\varepsilon-1}$
Kunni and Smith[b]	$\left(1+\dfrac{\phi}{1-\phi}\dfrac{1-\varepsilon}{2\varepsilon}\right)^{-1}$
Wakao and Kato[c]	$\dfrac{2}{2/\varepsilon-0.264}$
Schotte[d]	ε
Godbee and Ziegler[e]	$\dfrac{\epsilon\phi}{1-\phi}$

[a]See Ref. [7].
[b]See Ref. [9].
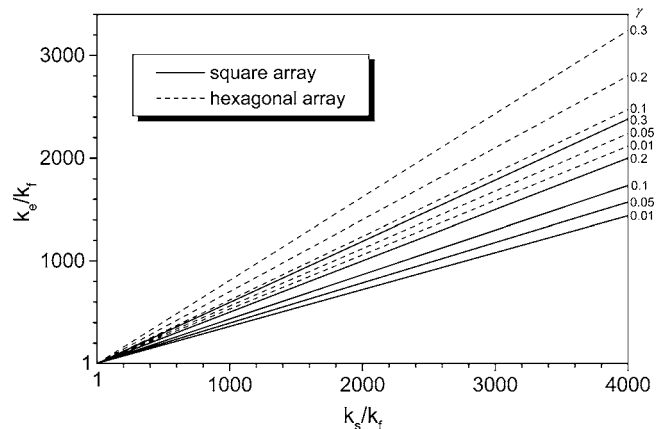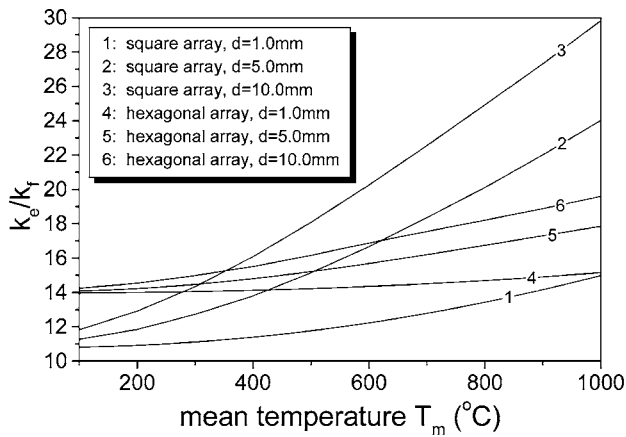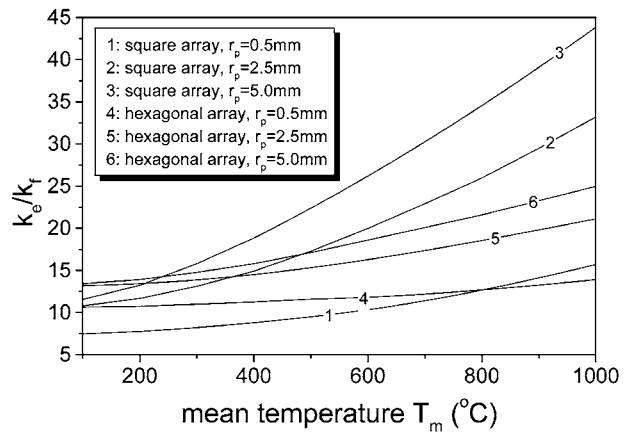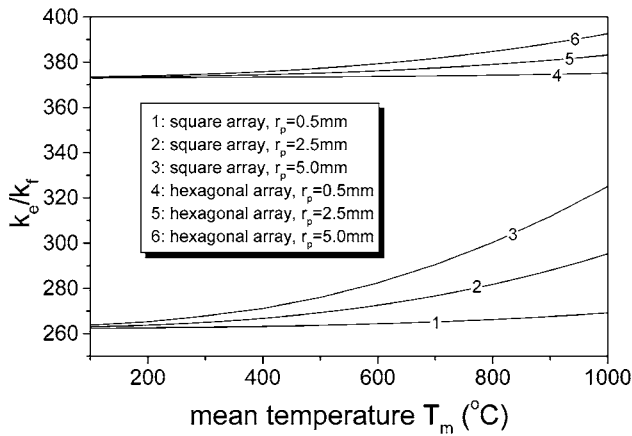[c]See Ref. [11].
[d]See Ref. [8].
[e]See Ref. [36].

Fig. 10 The effective thermal conductivity for the square array and hexagonal array packings (T_m=55°C)
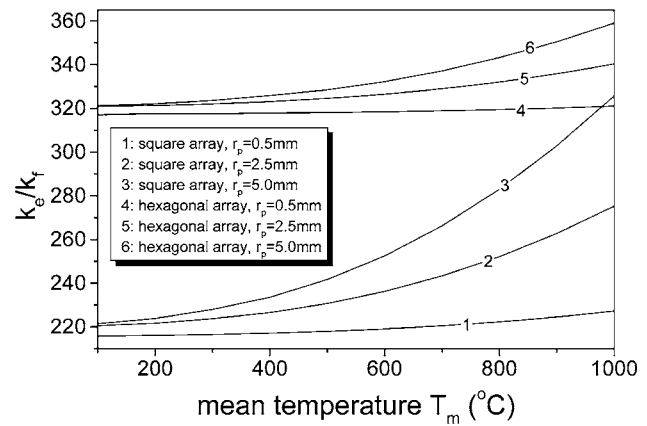
Fig. 11 The effects of mean temperature and particle size on the effective thermal conductivity ($\varepsilon = 0.9$)

same particle deformation ratio ($r_c/r_p = 0.1$) the void fraction of the square array is much higher than that of the hexagonal array and, this in turn, leads to a stronger radiative exchange effect.
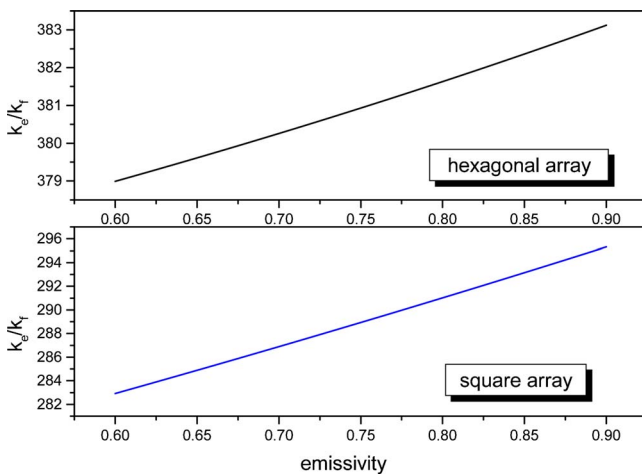

Fig. 12 The effect of solid surface emissivity on the effective thermal conductivity: ($r_p = 2.5$ mm, $r_c/r_p = 0.1$, $k_s/k_f = 600$, $T_m = 1000\,°C$)

4 Conclusions

A boundary element model is developed to predict the effective thermal conductivity of two-dimensional packing structures. The radiation heat exchange between solid surfaces is calculated by the net-radiation method. The problem is a coupled conductive/radiative heat transfer problem and was solved using an iterative procedure. The effective thermal conductivity of the packed bed can then be computed by using the temperature field. The proposed model is tested for two regular packing configurations: square array and hexagonal array. The comparison between the calculated results and the previous predictions are made to verify the coupled conduction/radiation model proposed in this study, and good agreements are obtained. The effective thermal conductivities for various solid/fluid conductivity ratios under different contact deformation are given. The effects of mean temperature, particle size, and surface emissivity on the effective thermal conductivity are examined. The numerical scheme formulated in this study is quite general in nature, and can be directly applied to random packing including multi-sized particles as long as the packing structure has been detected.

Nomenclature

A = total area of the packed bed in a direction perpendicular to the heat flow (m^2)

d_p = particle diameter (m)

F = radiation exchange factor

F_{AB-BC} = view factor from surface AB to surface BC

F_{ij} = view factor from surface i to surface j

H = distance between the top and bottom bounding plates (m)

J = outgoing radiative heat flux (W/m^2)

k = thermal conductivity (W/(m °C))

k_c = effective thermal conductivity without radiation contribution (W/(m °C))

k_e = effective thermal conductivity of the packed bed (W/(m °C))

n = outward normal

q'' = heat flux (W/m^2)

q = normal temperature derivative on the solid–fluid interface (°C/m)

Q = sum of the heat transfer rate at the boundary elements located at top bounding plate (W)

r = distance from a source point to any field point (m)

r_c = particle-to-particle contact radius (m)

r_p = particle radius (m)

T = temperature (°C)

T^* = fundamental solution to the Laplace equation subject to a concentrated unit heat source (°C)

T_m = bed mean temperature, $T=(T_t+T_b)/2$ (°C)

x, y = Cartesian coordinates (m)

Greek Symbols

Γ = boundary

Ω = region

γ = ratio of contact radius to particle radius, $\gamma = r_c/r_p$

ε = emissivity of solid surface

σ = Stefan–Boltzmann constant, 5.669×10^{-8} W/(m^2 K^4)

ϕ = void fraction of the packed bed

Subscripts

b = bottom

c = contact

e = external

f = fluid

i = surface i or internal

j = surface j

p = particle

r = radiative

s = solid

t = top

References

[1] Fogler, H. S., 1999, *Elements of Chemical Reaction Engineering*, 3rd ed., Prentice-Hall, Englewood Cliffs, NJ.

[2] Whitaker, S., 1980, "Heat and Mass Transfer in Granular Porous Media," *Advances in Drying*, Vol. 1, Hemisphere, New York, pp. 23–61.

[3] Cho, H. H., and Eckert, E. R. G., 1994, "Transition from Transpiration to Film Cooling," Int. J. Heat Mass Transfer, **37**, pp. 3–8.

[4] Tien, C. L., and Cunnington, G. R., 1973, "Cryogenic Insulation Heat Transfer," *Advances in Heat Transfer*, Vol. 9, Hemisphere, New York, pp. 349–417.

[5] Yagi, S., and Kunni, D., 1957, "Studies on Effective Thermal Conductivities in Packed Beds," AIChE J., **3**(3), pp. 373–381.

[6] Zehner, P., and Schlunder, E. U., 1970, "Thermal Conductivity of Granular Materials at Moderate Temperatures (in German)," Chem.-Ing.-Tech., **42**, pp. 933–941.

[7] Argo, W. B., and Smith, J. M., 1953, "Heat Transfer in Packed Beds," Chem. Eng. Prog., **49**(8), pp. 443–451.

[8] Schotte, W., 1960, "Thermal Conductivity of Packed Beds," AIChE J., **6**(1), pp. 63–67.

[9] Kunni, D., and Smith, J. M., 1960, "Heat Transfer Characteristic of Porous Rocks," AIChE J., **6**(1), pp. 71–78.

[10] Krupiczka, R., 1967, "Analysis of Thermal Conductivity in Granular Materials," Int. Chem. Eng., **7**(1), pp. 122–144.

[11] Wakao, N., and Kato, K., 1969, "Effective Thermal Conductivity of Packed Beds," J. Chem. Eng. Jpn., **2**(1), pp. 24–33.

[12] Nozad, I., Carbonell, R. G., and Whitaker, S., 1985, "Heat Conduction in Multiphase Systems—I: Theory and Experiment for Two-Phase Systems," Chem. Eng. Sci., **40**(5), pp. 843–855.

[13] Shonnard, D. R., and Whitaker, S., 1989, "The Effective Thermal Conductivity for a Point Contact Porous Medium: An Experimental Study," Int. J. Heat Mass Transfer, **32**(3), pp. 503–512.

[14] Sahraoui, M., and Kaviany, M., 1993, "Slip and No-slip Temperature Boundary Conditions at Interface of Porous, Plain Media: Conduction," Int. J. Heat Mass Transfer, **36**(4), pp. 1019–1033.

[15] Hsu, C. T., Cheng, P., and Wong, K. W., 1995, "A Lumped-Parameter Model for Stagnant Thermal Conductivity of Spatially Periodic Porous Media," ASME J. Heat Transfer, **117**, pp. 264–269.

[16] Buonanno, G., Carotenuto, A., Giovinco, G., and Massarotti, N., 2003, "Experimental and Theoretical Modeling of the Effective Thermal Conductivity of Rough Steel Spheroid Packed Beds," ASME J. Heat Transfer, **125**, pp. 693–702.

[17] Crane, R. A., and Vachon, R. I., 1977, "A Prediction of the Bounds on the Effective Thermal Conductivity of Granular Materials," Int. J. Heat Mass Transfer, **20**(7), pp. 711–723.

[18] Prasad, V., Kladias, N., Bandyopadhaya, A., and Tian, Q., 1989, "Evaluation of Correlations for Stagnant Thermal Conductivity of Liquid-Saturated Porous Beds of Spheres," Int. J. Heat Mass Transfer, **32**(9), pp. 1793–1796.

[19] Argento, C., and Bouvard, D., 1996, "Modeling the Effective Thermal Conductivity of Random Packing of Spheres through Densification," Int. J. Heat Mass Transfer, **39**(7), pp. 1343–1350.

[20] Cheng, G. J., Yu, A. B., and Zulli, P., 1999, "Evaluation of Effective Thermal Conductivity from the Structure of a Packed Bed," Chem. Eng. Sci., **54**, pp. 4199–4209.

[21] Vargas, W. L., and McCarthy, J. J., 2001, "Heat Conduction in Granular Materials," AIChE J., **47**(5), pp. 1052–1059.

[22] Deissler, R. G., and Boegli, J. S., 1958, "An Investigation of Effective Thermal Conductivities of Powders in Various Gases," Trans. ASME, **80**, pp. 1417–1425.

[23] Brebbia, C. A., 1978, *The Boundary Element Method for Engineers*, Wiley, New York.

[24] Brebbia, C. A., Telles, J. C. F., and Wrobel, L. C., 1984, *Boundary Element Techniques*, Springer, Berlin, Germany.

[25] Beer, G., and Watson, J. O., 1992, *Introduction to Finite and Boundary Element Methods for Engineers*, Wiley, New York.

[26] Banerjee, P. K., 1994, *Boundary Element Methods in Engineering*, 2nd ed., McGraw-Hill, London.

[27] Wrobel, L. C., 2002, *Boundary Element Method* (Vol. 1, Applications in Thermo-Fluids and Acoustics), Wiley, New York.

[28] Johnson, K. L., 1985, *Contact Mechanics*, Cambridge University Press, Cambridge, MA.

[29] Vortmeyer, D., 1978, "Radiation in Packed Solids," *Proceedings of the 6th International Heat Transfer Conference*, Vol. 6, U. Grigul et al., eds., Toronto, August 7–11, Hemisphere, Washington, DC, pp. 525–539.

[30] Siegel, R., and Howell, J. R., 2002, *Thermal Radiation Heat Transfer*, 4th ed., Hemisphere, Washington, DC.

[31] Siu, W. W. M., and Lee, S. H.-K., 2000, "Effective Conductivity Computation of a Packed Bed Using Constriction Resistance and Contact Angle Effects," Int. J. Heat Mass Transfer, **43**, pp. 3917–3924.

[32] Larkin, B. K., and Churchill, S. W., 1959, "Heat Transfer by Radiation through Porous Insulations," AIChE J., **5**(4), pp. 467–474.

[33] Chen, J. C., and Churchill, S. W., 1963, "Radiant Heat Transfer in Packed Beds," AIChE J., **9**(1), pp. 35–41.

[34] Yang, Y. S., Howell, J. R., and Klein, D. E., 1983, "Radiative Heat Transfer through a Randomly Packed Bed of Spheres by the Monte Carlo Method," ASME J. Heat Transfer, **105**, pp. 325–332.

[35] Argento, C., and Bouvard, D., 1996, "A Ray Tracing Method for Evaluating the Radiative Heat Transfer in Porous Media," Int. J. Heat Mass Transfer, **39**(15), pp. 3175–3180.

[36] Godbee, H. W., and Ziegler, T. W., 1966, "Thermal Conductivities of MgO, Al$_2$O$_3$, and ZrO$_2$ Powders to 850 °C. II. Theoretical," J. Appl. Phys., **37**(1), pp. 56–65.

The Effects of Film Thickness, Light Polarization, and Light Intensity on the Light Transmission Characteristics of Thermochromic Liquid Crystals

Timothy B. Roth

Ann M. Anderson[1]
e-mail: andersoa@union.edu

Department of Mechanical Engineering,
Union College,
Schenectady, NY 12302

Thermochromic liquid crystal materials change their crystalline structure and optical properties with temperature, making them useful in temperature measurement applications. This paper presents the results of a study to develop a temperature measurement system that uses light transmission through thermochromic liquid crystals instead of light reflection. We painted Hallcrest R25C10W sprayable liquid crystals on a clear surface and placed it in a spectrophotometer. The amount of light transmitted at monochromatic wavelengths from 400 nm to 700 nm was measured for temperatures from 25°C to 55°C under conditions of nonpolarized, linearly polarized, and cross-polarized light, for three light intensity levels, and three liquid crystal layer thicknesses. As the temperature was increased the amount of light transmitted through the liquid crystal layer increased. When the liquid crystals are in their active range the transmission spectra exhibit an s-curve shape and the percent of light transmitted through the liquid crystals at a fixed temperature increases with increasing wavelength. We detected significant changes in the transmission spectra for temperatures from 27°C to 48°C, whereas when used with reflected light the thermochromic liquid crystals are useful over a significantly smaller range. As the thickness of the thermochromic liquid crystal layer increases or as the incoming light intensity decreases, the amount of light transmitted through the liquid crystals decreases. We also investigated the effects of temperature overheat on the transmission spectra and found that heating the thermochromic liquid crystals above their active range increases the amount of light transmission. However, when the liquid crystals are cooled below their active range they return to their original state. We have analyzed the spectrophotometer data in a number of ways including: (a) total amount of light transmitted, (b) amount of red, green, and blue light transmitted; and (c) spectral curve shape characteristics (peak transmission, inflection wavelength and wavelength for peak transmission) all as a function of temperature. A linear relationship exists between temperature and all of these variables which we believe can be exploited for the development of a charge coupled light camera based light transmission system for temperature measurement. [DOI: 10.1115/1.2430724]

Keywords: thermochromic liquid crystals, temperature measurement, light transmission

Introduction

The goal of the work presented here is to develop a system that uses light transmission to measure temperature with thermochromic liquid crystals (TLCs). Thermochromic liquid crystals are materials that change their crystalline structure and thus their optical properties with temperature. The liquid crystal phase occurs between a highly ordered crystalline phase at low temperature and a highly disordered liquid phase at higher temperature. In the active temperature range, the crystals align to form a helical structure. The pitch of this helix is a function of temperature. As the pitch changes, so does the wavelength of light that is reflected or transmitted. The temperature range over which the TLCs behave this way is called the active range. The event temperature occurs at the low end of the range and the clearing point temperature occurs at the high end of the range.

Light reflection is the current method used in thermochromic liquid crystal temperature measurement (see for example Bakrania and Anderson [1] or Hay and Hollingsworth [2]). TLCs must be calibrated to relate color to temperature. In a calibration experiment, the surface of a temperature controlled material is painted black, and then coated with TLCs. A light source is used to illuminate the TLC surface and the reflected light is captured by a digital or charge coupled device (CCD) camera. The TLC surface is heated over a range of temperatures, corresponding to the active range of the TLCs, and the CCD camera records images of the surface at every temperature. The images are then analyzed using digital image processing techniques. Hay and Hollingsworth [2] suggest using the hue of the color displayed by the liquid crystals to determine the temperature. Hue is calculated from the red, green, and blue intensity values and represents the dominant wavelength of color.

The main disadvantage of the reflection technique is that the calibration is very sensitive to lighting effects. This includes: how

much light, the lighting type, and the viewing angle [3,4]. One often needs to calibrate the surface in the same environment where the temperature measurement is to be made. In addition, while the TLCs display color over the entire active range, the range over which one can obtain a useful calibration is generally only 25–50% of the active range [2].

Several investigators have reported that liquid crystals exhibit hysteresis when heated above their clearing point temperature [1,5,6]. Under hysteresis conditions the intensity of the color is greatly reduced and the calibration curve changes. However, once the TLCs are cooled below the event temperature they generally return to their original behavior. Smith et al. [7] provide an excellent review on the use of reflected light from TLCs to measure temperature.

Although the light transmission characteristics of liquid crystals have been measured as a function of applied voltage for liquid crystal display applications (see for example Birecki and Kahn [8]), very little work has been done to characterize the light transmission characteristics of thermochromic liquid crystals. Diankov et al. [9] report measurements of the amount of light transmitted through polymer stabilized and polymer dispersed cholesteric liquid crystals. They used monochromatic light with cross polarization. They observed a modulation in the intensity of transmitted monochromatic light with temperature change and report that this activity occurs over a wide range (outside the active range) of the liquid crystals. They conclude that it would be possible to develop an "on–off" type temperature sensor. In a further study, Pavlova et al. [10] compare the color of transmitted light to the color of reflected light through the same polymer dispersed cholesteric liquid crystals. The results show a larger change in color of the reflected light from which they conclude light reflection techniques are best. However, they do not address any of the issues described above and they present very little information about the actual spectra of transmitted light.

In this paper we present detailed data on the light transmission characteristics of thermochromic liquid crystals. We have examined the effects of light polarization type (nonpolarized, linear polarized, and linear cross polarized), light intensity level and the thickness of the liquid crystal layer. We extend previous work by presenting detailed information on the light transmission behavior of the liquid crystals. We also show that there is a linear relationship between temperature and the spectral transmission characteristics and that this relationship is applicable over a wide range of temperatures.

Methods and Materials

We used Hallcrest R25C10W sprayable thermochromic liquid crystals in this study. In this formulation, the liquid crystal material is first microencapsulated by a polymer coating which results in microcapsules with diameters in the $10–15 \ \mu$m range. The resulting slurry is then combined with a water soluble aqueous binder to form a sprayable material. These crystals have a published event temperature of $25\,°$C (red start) and a bandwidth of $10\,°$C.

Surface Preparation. We prepared four TLC test surfaces. The TLCs were applied to the outer surface of a standard 1 cm path length polystyrene cuvette which was modified to connect to a circulating water bath.

Surface 1 was used to test polarizing light conditions and overheat effects. In preparing this surface we diluted the TLCs with water in a 1:1 ratio and stirred the mixture for 15–30 min. We then used an airbrush to spray the TLCs onto one side of the cuvette (the remaining three sides were covered to prevent TLC material from getting on the surface and to protect the surface from getting scratched during cuvette preparation). The surface was dried with a heat gun between the application of each coat to
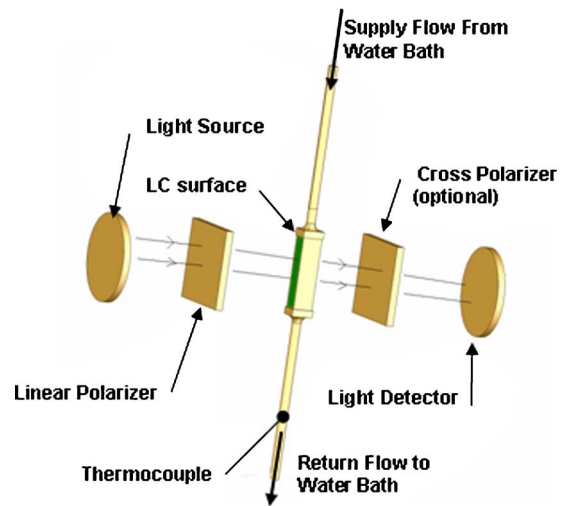

Fig. 1 Schematic of test setup used in light transmission tests

ensure that each layer of TLC material dried completely. Approximately ten coats of TLC material were painted onto the cuvette. We estimated the thickness of this surface to be approximately 0.05 mm.

Surface 2 was used for light reflection tests. This cuvette was airbrush painted with flat black paint before applying the TLC material as described above.

When testing Surfaces 1 and 2 we used a thermocouple ($\pm 1\,°$C) located approximately 25 cm downstream of the cuvette to measure the temperature of the water going through the cuvette. A one-dimensional heat transfer analysis accounting for the convection from the water to the liquid crystal surface and convection to the ambient air estimates a maximum temperature difference between the thermocouple and the liquid crystal surface of $0.2\,°$C (at a water temperature of $27\,°$C) to $1\,°$C at ($50\,°$C). Since the goal of this part of the work was to measure the transmission characteristics as a function of temperature and not to specifically develop a direct calibration the thermocouple temperature measurement was deemed sufficient.

Surfaces 3 and 4 were used to study the effect of TLC thickness and light intensity. We embedded calibrated thermocouples in one side of the cuvette and then poured diluted TLC material over the thermocouples to form a thicker TLC surface. After allowing the surfaces to dry we measured the layer thickness using a microscope and a set of calipers. The thickness (± 0.03 mm) of Surface 3 was approximately 0.24 mm. Surface 4 was approximately 0.40 mm thick. For Surfaces 3 and 4 we used the embedded calibrated thermocouples as our temperature reference ($\pm 0.1\,°$C).

Light Transmission Measurements. Figure 1 shows the temperature control system and spectrophotometer set up used for the transmission tests. The cuvettes were placed in the spectrophotometer sample holder and attached to a constant temperature water bath using Tygon tubing. The bath circulated water through the inside of the cuvette during testing.

All of the transmission tests were performed using a Perkin Elmer Lambda 900 ultraviolet visible near-infrared (UV/VIS/NIR) spectrophotometer. We measured a baseline transmission spectrum on the unpainted side of each cuvette at $25\,°$C to account for absorption due to optics, the polarizing film, the cuvette surface and the water. We measured a less than 1% variation in transmission through the "non-TLC" materials from 25 to $55\,°$C. A comparison of the transmission spectra for different sides of the same cuvette showed a maximum variation in transmission of 0.3%. Repeated testing on the same surface showed a maximum variation in transmission level of 0.2% and of 0.35% if reposition-
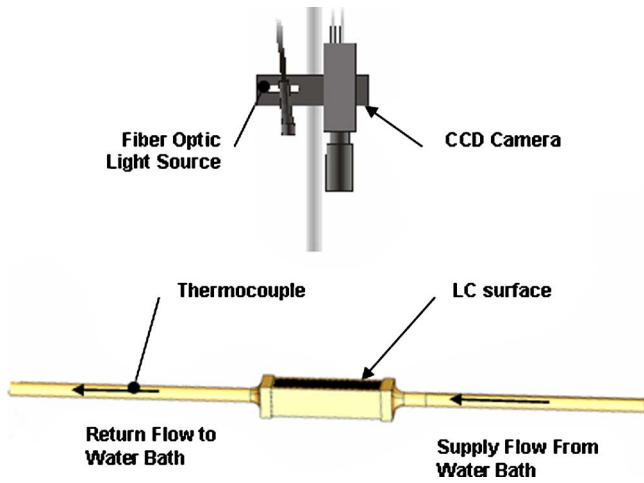
Fig. 2   Schematic of test setup used in light reflection tests

Fig. 3   Transmission spectra for Surface 1 under linear polarized lighting conditions

ing of the cuvette was included.

Transmission spectra were measured every $1-2°C$ for temperatures from $25°C$ to $55°C$. The system was stabilized at each temperature set point to ensure steady state conditions. Measurements were made for wavelengths from 400 nm to 700 nm using a 1 nm data interval, a 0.2 s integration time, a scan speed of 250 nm/min, and slit size of 2 nm. Transmission spectra measurements of the TLC material were repeatable to within a 1% transmission level.

For testing linear polarized (LP) light conditions we placed a polarizing film in the light entry beam path (see Fig. 1) and measured the baseline spectra with the filter in place as described above. For the linear cross polarized (LCP) light tests we placed a second polarizing film in the receiving end of the spectrophotometer optics as shown in Fig. 1. The second film was placed at an angle to minimize transmission through the system without the cuvette in place. This setup yielded approximately 0.5% transmission. We placed an identical polarizing film in a reference cell which allowed us to cancel the absorption effects of the second polarizing film. To study the effect of light intensity level we placed a neutral density filter in the incoming beam path. We used a Thermo Oriel 50490 filter (84–86% transmission in the visible range) and a 50510 filter (49–56% transmission in the visible range). The baseline spectra for these tests did not include the neutral density filters because the intention was to change the incoming light intensity.

Temperature overheat effects were studied under LP and LCP lighting conditions. To do this, we heated the TLCs from $25°C$ to $65°C$ then cooled them back down to $25°C$. Spectra were taken at $35°C$ and $45°C$ during both the heating and the cooling phase to determine the effect of overheating.

Light Reflection Measurements. For the light reflection tests, the Surface 2 cuvette was connected to the temperature control system and mounted horizontally as shown in Fig. 2. We used a Sony XC-003 CCD camera connected to a National Instruments IMAQ PCI-1408 image processing board to acquire images of the surface as it was heated with the hot water control system. A Fostec model 20760 fiber optic light illuminated the TLC surface. Both the camera and the fiber optic light were fitted with polarizing lenses to eliminate reflections on the lenses of the camera and the light source. Images of the surface were acquired in $1°C$ intervals from $25°C$ to $45°C$.

Uncertainty Estimates. The uncertainty in the measurements of light transmission is less than 1% transmission based on repeatability measurements. The uncertainty in the temperature measurement is $±1°C$ on Surfaces 1 and 2 and $±0.1°C$ on Surfaces 3
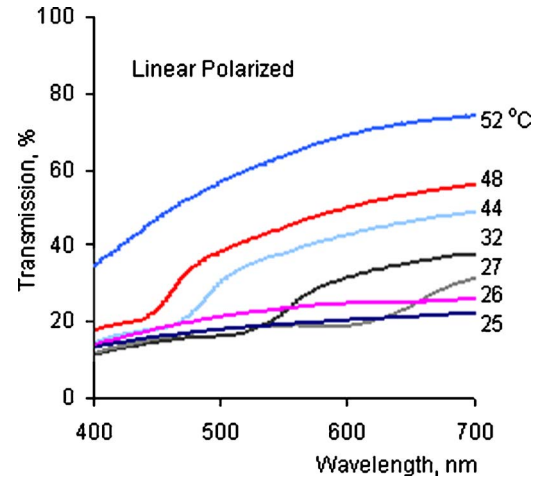
and 4. The calculated values of total, red, green, and blue intensities have uncertainty values less than 0.2 a.u. and the uncertainty in inflection point wavelength is less than 2 nm. All values are quoted at 95% confidence.

Results

Transmission Spectra/Light Polarization Effects. Figure 3 shows transmission spectra for linear polarized light through Surface 1 at temperatures from $25°C$ to $52°C$. We found no difference between the transmission spectra for nonpolarized and polarized lighting conditions because all baseline spectra included the polarizing filters. For a fixed temperature the transmission increases with increasing wavelength. As temperature is increased from $25°C$ to $26°C$ the transmission level increases for all wavelengths. Then, from $26°C$ to $27°C$, the transmission decreases for wavelengths less than about 660 nm and increases for wavelengths above this. From $27°C$ to $52°C$ the transmission level increases for all wavelengths as temperature is increased. The lowest transmission levels (10–15%) occur at the lower end of the active range at $25°C$ and the highest (35–70%) occur at $52°C$ (above the active range). Between $27°C$ and $48°C$ the spectra exhibit an "in-pattern," s-curve shape. For a given temperature, as wavelength increases from 400 nm the spectrum is relatively flat until a "critical" wavelength is reached. For example at $32°C$ this critical wavelength occurs at about 525 nm. At this point the slope of the spectrum increases. Each spectrum passes through an inflection point and then the slope decreases. This region of high slope or "transmission deficit" shifts to lower wavelengths as temperature increases (i.e., at $48°C$ the critical wavelength is about 440 nm). At small wavelengths, the effect of temperature (from $25°C$ to $48°C$) on transmission level is small (a change from 12% to 17% transmission at 400 nm) while at large wavelengths it is more significant (22–56% transmission at 700 nm). More of the higher wavelength (red) light is transmitted for all temperatures. This may in part be due to scattering effects (i.e., more light is scattered at small wavelengths).

Figure 4 plots transmission spectra for linear cross polarized light. (Recall that the polarizing films were aligned for minimum transmission.) When the cuvette with TLC surface is placed in the spectrophotometer it polarizes the light and allows for some light to be transmitted. At $25°C$ the transmission level increases with wavelength and transmits 13–18% of the light (compared to 0.5% when the surface is not in place). There is a region of temperatures ($27-48°C$) for which the spectra exhibit an "in-pattern" shape. At these temperatures the TLCs start to polarize or "twist" the incoming light and allow more light to pass through the second polar-
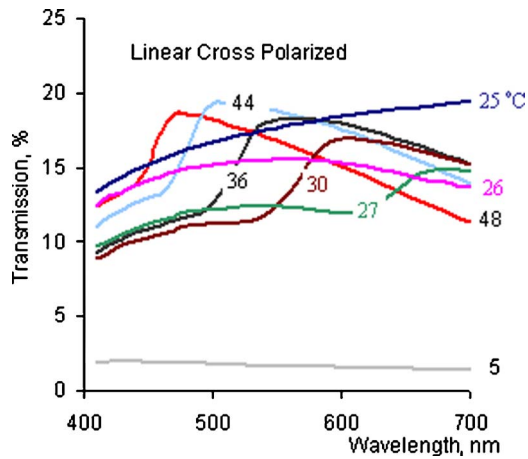
Fig. 4 Transmission spectra for Surface 1 under linear cross polarized lighting conditions

izer. For a fixed temperature, the transmission increases slightly with wavelength from 400 nm until a critical wavelength is reached. At this point the slope of the curve increases (as it did for LP light). However, under LCP lighting conditions at a fixed temperature, the transmission level increases with wavelength, reaches a maximum, and then decreases. For example, at 36°C the transmission level increases to ~18% at 550 nm and then decreases with increasing wavelength. Above 48°C, which is outside the active range, the crystals transmit very little light (note that the 52°C spectra levels are around 0.5%). If we compare the LP and LCP spectra at a given temperature we find that the inflection points are similar but that the LCP transmission levels are lower, particularly so at higher wavelengths.

Reflection Data. We also measured the amount of reflected light from the TLCs as a function of temperature using the setup described above. The images were analyzed using the MATLAB image processing toolbox and the red, green, and blue (RGB) components are plotted in Fig. 5. The figure shows that the red component peaks at about 29°C, the green at 33°C, and the blue at 45°C. If we compare the reflection and transmission data, we find that the transmission deficit wavelength range for a given temperature corresponds to the reflected RGB data. For example, the transmission deficit region for the 32°C spectra lies in the
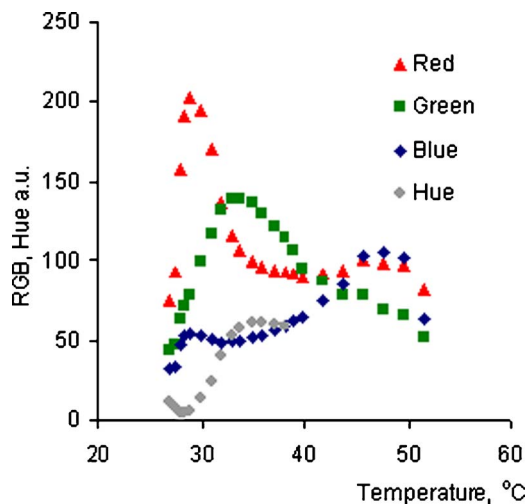
490–580 nm region which implies that the crystals are reflecting in the green range. From Fig. 5 we see that this is near the peak range of the green signal. Likewise, the transmission deficit occurs in the 600–700 nm range for 30°C which is near the red peak in the reflected data. Hue was calculated and is also plotted in Fig. 5. Hue is monotonic only between 28°C and 35°C which yields a 7°C calibration range.

Effects of Temperature Overheat. Figure 6 plots the results of temperature overheat on the transmission spectra under LP lighting conditions. Spectra at 35°C and 45°C on heating from 25°C and on cooling from 65°C are plotted for the LP lighting conditions. The spectra exhibit hysteresis. On cooling from 65°C there is increased transmission between 450 nm and 550 nm for the 35°C spectrum and between 400 nm and 500 nm for the 45°C spectrum. The effect of overheat is to reduce the transmission deficit region of the spectra. This corresponds to results seen in reflection tests. Bakrania and Anderson [1] report that the RGB signals are lowered upon overheat. After overheating, the liquid crystals transmit more light and thus reflect less, leading to the lowered RGB values.

Effects of TLC Layer Thickness. Figure 7 plots spectra for

Fig. 6 Temperature overheat effects under linear polarized lighting conditions show that the overheated TLCs transmit more light at low wavelengths

Fig. 5 RGB values for reflected light conditions for Surface 2. These data show a red peak at 29°C, a green peak at 34°C, and a blue peak at 45°C.
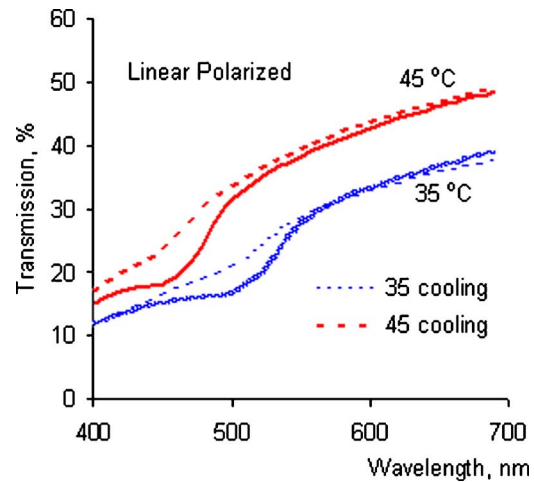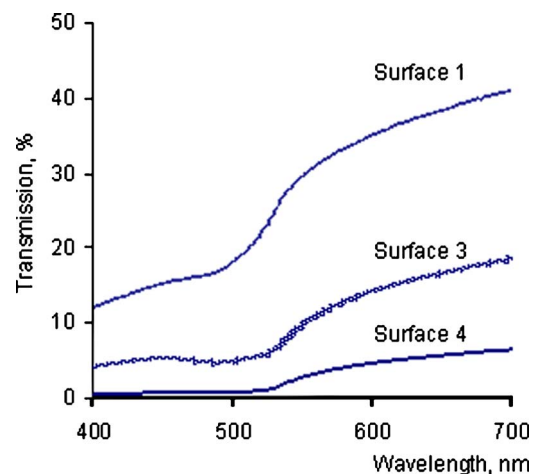

Fig. 7 A comparison of the transmission spectra at 36°C for Surfaces 1, 3, and 4 shows decreasing transmission with increasing layer thickness
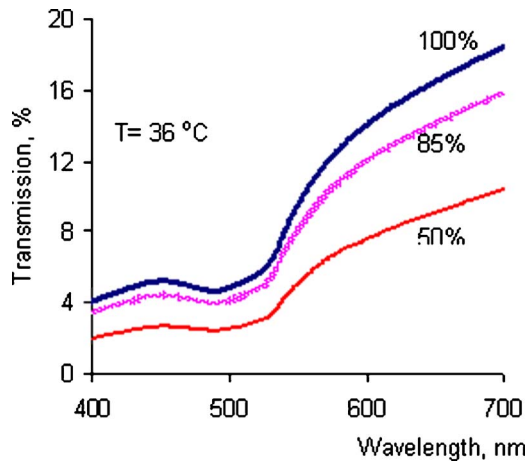
Fig. 8 A comparison of the transmission spectra at 36°C for Surface 3 under three different light intensity levels. The shapes of the spectra are similar.
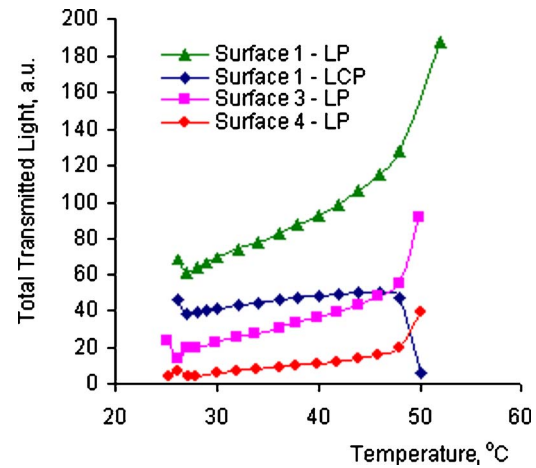

Fig. 9 Total intensity of transmitted light as a function of temperature for Surfaces 1, 3, and 4 for linear polarized and linear and cross-polarized lighting conditions

Surfaces 1, 3, and 4 at 36°C. Surface 1 is the thinnest (~0.05 mm) and Surface 4 is the thickest (~0.4 mm). As expected, the amount of light transmitted through the surface decreases with increasing thickness. The shape of the spectra are comparable, with similar inflection points. However they do not scale. The ratio of the Surface 3 to Surface 4 transmission level is a function of both wavelength and temperature.

Effects of Light Intensity. We measured the effects of light intensity using a set of neutral density filters placed in the beam of the incoming light. The filters passed ~85% and ~50% of the light over a wavelength range from 400 nm to 700 nm. Figure 8 plots the transmission spectra at 36°C from 400 nm to 700 nm for 100%, 85%, and 50% light transmission. As expected, as the light level decreases the amount of light transmission decreases. The shape of the spectra are similar and scale on the intensity level.

Data Analysis

The goal of this work is to investigate the effect of temperature on the light transmission spectra so that we can develop a technique that will use some measure of transmission to calibrate the TLCs as a function of temperature. We are looking for a measure that is dependent on temperature, insensitive to lighting conditions, preferably linear, and is applicable over a large temperature range. This section reviews some of the measurements derived from the transmission spectra. We looked at total transmission levels, bandwidth transmission levels, and several shape characteristics of spectra.

We calculated the total transmission as a function of temperature for wavelengths from 400 to 700 nm. The calculation was performed by summing the transmission percent value (a number between 0 and 1) at every wavelength. Figure 9 plots the total transmission for Surface 1 under both LP and LCP lighting conditions and for Surfaces 3 and 4 under LP lighting conditions as a function of temperature. All three surfaces exhibit a linear relationship between total transmitted light and temperature for temperatures between 27°C and 48°C. This temperature range corresponds to that for which the spectra show in-pattern behavior. The LP data have a higher slope (indicating higher sensitivity) and are more linear ($R^2 = 0.995$ for LP versus $R^2 = 0.948$ for LCP). This linear section spans a range that is three times that found for hue in the reflection tests. The three LP tests show a large increase in transmission at 50°C which is outside the active range. The LCP results show a large decrease at this temperature because the TLCs no longer polarize the light and the cross polarizer cuts out all light.

Next we separated each spectrum into its red, green, and blue components as a CCD camera would. We multiplied the liquid crystal transmission spectra by the RGB spectral response characteristics of a Sony X003 CCD camera, and calculated total transmission in the blue range (approximately 400–480 nm), the green range (approximately 481–580 nm), and the red range (approximately 581–700 nm). These results are plotted in Fig. 10 for Surface 3. There is a linear region between 30°C and 48°C with the green component showing the highest slope. Figure 11 shows the normalized green component versus temperature for Surfaces 1, 3, and 4. The green component was normalized by the green value at 30°C so that we could compare the sensitivities. Although the transmission levels are larger for the thinnest surface (Surface 1) the sensitivity of this value to temperature is much higher for the thickest surface (Surface 4) which shows a factor of 7.6 increase over the 18°C temperature range (versus a factor of 3.5 for Surface 3 and of 2.4 for Surface 1).

We also looked at factors that describe the shape of the spectra. We characterized three things: (1) the inflection point wavelength (both LP and LCP); (2) the wavelength at which maximum transmission occurs (for the LCP data only); and (3) the maximum transmission level (for the LCP data only). These data quantify the leftward shift of the "in-pattern" spectra that occurs with increas-
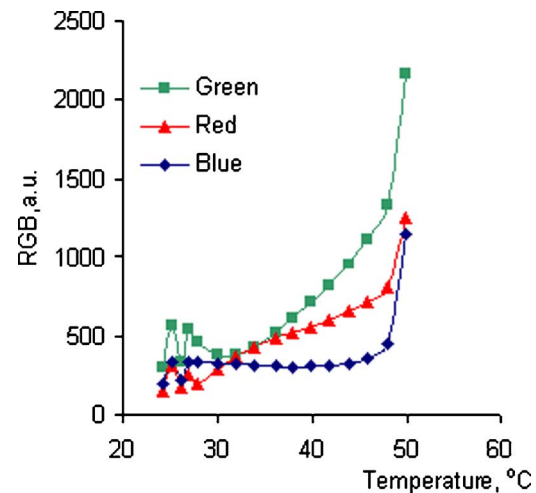

Fig. 10 Intensity of red, green, and blue transmitted light as a function of temperature for Surface 3 under linear polarized lighting conditions
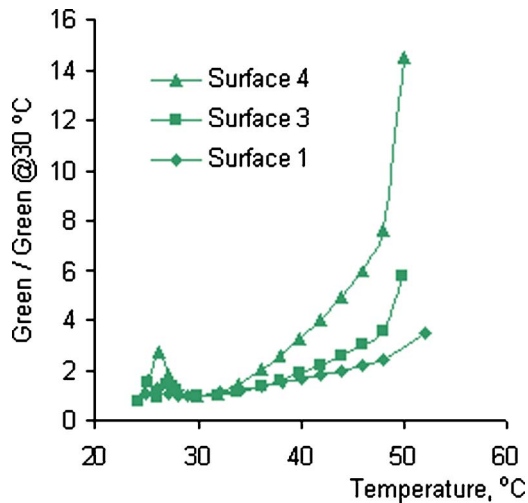
Fig. 11 The normalized green signal for Surfaces 1, 3, and 4 shows a larger relative change in the signal for the thicker surface

ing temperature. The uncertainty in our ability to estimate the inflection point wavelength is less than 2 nm. The results are plotted in Fig. 12 for Surface 1. The LP inflection wavelengths are slightly higher than the LCP values. The inflection point wavelength decreases with temperature (due to the leftward shift in the spectra as temperature increases) and the relationship is fairly linear between 32 °C and 48 °C where the wavelength decreases from 550 nm to 450 nm. The wavelength for maximum transmission also decreases with temperature. The wavelength decreases from 675 nm to 475 nm over the 27–38 °C range. There is only a small increase in the maximum transmission value (from 15% to 20%) over the range of temperatures.

Figure 13 plots the inflection point data for Surfaces 3 and 4 under LP lighting conditions and with reduced intensity for Surface 3. The data show that the inflection point is not dependent on surface thickness or on light intensity.

Discussion

The most encouraging finding from this study is that there is a large temperature range for which characteristics of the transmission spectra are linearly sensitive to temperature change. The reflection data in Fig. 5 show only a 7 °C range over which we
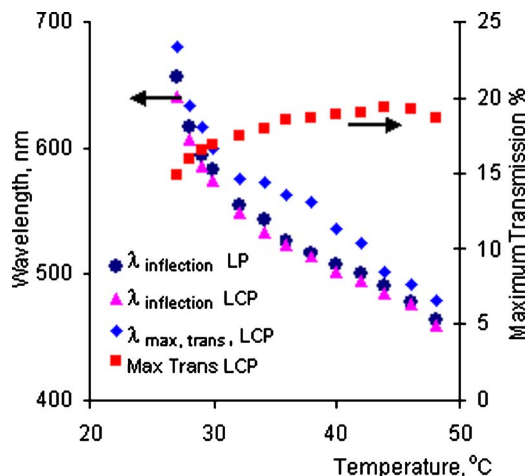

Fig. 12 Characteristics of the spectral shape as a function of temperature for Surface 1
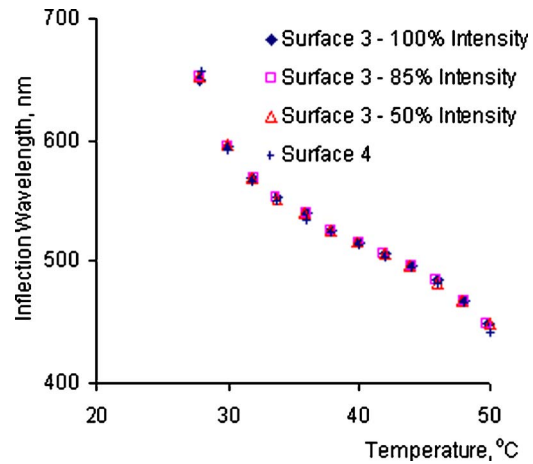

Fig. 13 Inflection point wavelength for three light intensity levels on Surface 3 and 100% light on Surface 4

could calibrate the liquid crystals. Figures 9 and 10 show that total transmission (intensity), red intensity, and green intensity are linear over a 20 °C range for the LP lighting conditions. In addition, the characteristics of our "in pattern" spectra plotted in Figs. 12 and 13 show significant, linear sensitivity to changes in temperature. Linear cross-polarized light spectra reveal information about the polarizing effect of the crystals but the intensity levels do not change significantly with temperature. The spectral shape characteristics of LCP transmission are interesting and could possibly be used to measure temperature.

The advantage of using the spectral shape characteristics of inflection point wavelength and maximum transmission wavelength is that they are not sensitive to the incoming light intensity or the thickness of the TLC layer, however they are not easily measured with a CCD camera. The advantage of measuring the overall transmission (intensity) levels is that these are measurements that are easily recorded by a CCD camera. However, the levels will be a function of the light intensity of the source and we may need to address the sort of lighting problems found in reflection tests (angle of light, intensity of light). Preliminary results with a CCD camera show that we can normalize out the effect of light intensity using transmission data from outside the TLC active range.

Overall, for the particular liquid crystal formulation studied here, we find that a measure of light transmission intensity for linearly polarized (or even unpolarized) light through a relatively thick liquid crystal surface is the best measure of temperature. We can use total, red, or green intensity. For the liquid crystals used here (which have a red start temperature) the change in blue intensity appears to be insignificant and is unsuitable as a temperature indicator because there is very little change in the spectra with temperature for wavelengths less than 450 nm as evidenced in the data of Fig. 10.

Figure 11 illustrates the effect of TLC layer thickness. The overall transmission level is lower for the thick surface and more sensitive to temperature. This suggests that the use of more liquid crystal material will improve the technique. However, this may lead to measurement errors if significant temperature gradients exist across the liquid crystal layer. Estimates for the tests of the thick layer used in this study indicate that the temperature difference across the layer is less than 0.2 °C under worst case conditions. However, in actual applications with high heat transfer rates, this will be larger.

Spatial and temporal resolution are also important characteristics of a temperature measurement system. Although not directly addressed in this study, we expect spatial resolution for the transmission technique to be similar to that seen in reflection methods.

The temporal resolution will depend on the thickness of the TLC required for a measurable signal change. Initial results indicate that the transmission technique may require thicker surfaces which will decrease temporal resolution.

The lighting configuration inherent in a light transmission measurement offers both advantages and disadvantages, depending on the particular application and its optical accessibility. We envision the use of a sensor that integrates the TLC material with the light source, which could then be mounted directly on a surface of interest or the system can use behind-surface lighting. However, depending on the particular application, this may not be practical.

The TLCs used in this study were optimized for use in light reflection temperature measurement methods. They show promising behavior for a transmission based measurement system but future work will concentrate on the development of TLC formulations that are optimized for transmission response. Further development of the light transmission technique will lead to an alternate method for liquid crystal thermography that will complement the existing technique and offer more flexibility in lighting configurations.

Conclusion

This work is the first to report detailed information on the effect of temperature on the light transmission characteristics of thermochromic liquid crystals. We have found that there are significant, measurable changes in the amount and pattern of light transmitted through thermochromic liquid crystals as a function of temperature. We believe these findings can be used to develop a light transmission based calibration system that will complement and may even offer advantages over the standard light reflection techniques. These advantages include a larger calibration range and less sensitivity to lighting effects. The specific issues under consideration in the development of a CCD based system include accounting for the effect of light source intensity, determining the best type of light source (all of our tests have been conducted with monochromatic light), and the issue of implementing a light transmission set up in an actual experiment.

References

[1] Bakrania, S., and Anderson, A. M., 2002, "A Transient Technique for Calibrating ThermoChromic Liquid Crystals: The Effects of Surface Preparation, Lighting and Overheat," *Proceedings of IMECE'02:2002 ASME International Mechanical Engineering Congress & Exposition*, November 2000, New Orleans.

[2] Hay, J. L., and Hollingsworth, D. K., 1996, "A Comparison of Trichromic Systems for Use in the Calibration of Polymer-Dispersed Thermochromic Liquid Crystals," Exp. Therm. Fluid Sci., **12**, pp. 1–12.

[3] Farina, D. J., Hacker, J., Moffat, R. J., and Eaton, J. K., 1994, "Illuminant Invariant Liquid Calibration of Thermochromic Liquid Crystals," Exp. Therm. Fluid Sci., **9**, pp. 1–12.

[4] Wiberg, R., and Lior, N., 2004, "Errors In Thermochromic Liquid Crystal Thermometry," Rev. Sci. Instrum., **75**(9), pp. 2985–2994.

[5] Birrell, D. C., and Eaton, J. K., 1998, "Liquid Crystal Temperature Measurement for Real-Time Control," *Applications of Digital Image Processing XXI*, A. G. Tescher, ed., Proc. SPIE **3460**, 58–66.

[6] Baughn, J. W., Anderson, M. R., Mayhew, J. E., and Wolf, J. D., 1999, "Hysteresis of Thermochromic Liquid Crystal Temperature Measurement Based in Hue," J. Heat Transfer, **212**, pp. 1067–1072.

[7] Smith, C. R., Sabatino, D. R., and Praisner, T. J., 2001, "Temperature Sensing With Thermochromic Liquid Crystals," Exp. Fluids, **30**, pp. 190–201.

[8] Birecki, H., and Kahn, F. J., 1980, "The Optics of Twisted Nematic Liquid Crystal Displays," J. Appl. Phys., **51**(4), pp. 1950–1954.

[9] Diankov, G., Naradikian, H., and Angelov, T., 2003, "Polymer-Stabilized Liquid Crystal Indicator Used In Thermometry," J. Mater. Sci.: Mater. Electron., **14**(10), pp. 831–832.

[10] Pavlova, P., Avramov, L., Naradikian, H., Angelov, T., and Petrov, A. G., 2005, "Temperature Dependence of Chromaticity in Polymer-Dispersed Cholesteric Liquid Crystal: Reflection and Transmission Characteristics," J. Optoelectron. Adv. Mater., **7**(1), pp. 285–288.

Gligor H. Kanevce
Senior Professor and Academician
Macedonian Academy of Sciences and Arts,
Skopje, Macedonia
e-mail: kanevce@osi.net.mk

Ljubica P. Kanevce
Senior Professor
e-mail: kanevce@osi.net.mk

Vangelce B. Mitrevski
Assistant Professor
e-mail: elbo@mt.net.mk

Faculty of Technical Sciences,
St. Kliment Ohridski University,
Bitola, Macedonia

George S. Dulikravich[1]
Professor, Chairperson
Fellow ASME
Department of Mechanical and Materials
Engineering,
Florida International University,
10555 West Flagler St., EC 3474,
Miami, FL 33174
e-mail: dulikrav@fiu.edu

Helcio R. B. Orlande
Senior Professor, Chairperson
Mem. ASME
Department of Mechanical Engineering,
Federal University of Rio de Janeiro,
COPPE/UFRJ, Brazil
e-mail: horlande@aol.com

Inverse Approaches to Drying of Thin Bodies With Significant Shrinkage Effects

This paper deals with the application of inverse concepts to the drying of bodies that undergo changes in their dimensions. Simultaneous estimation is performed of moisture diffusivity, together with the thermal conductivity, heat capacity, density, and phase conversion factor of a drying body, as well as the heat and mass transfer coefficients and the relative humidity of drying air. This was accomplished by using only temperature measurements. A mathematical model of the drying process of shrinking bodies has been developed where the moisture content and temperature fields in the drying body are expressed by a system of two coupled partial differential equations. The shrinkage effect was incorporated through the experimentally obtained changes of the specific volume of the drying body in an experimental convective dryer. The proposed method was applied to the process of drying potatoes. For the estimation of the unknown parameters, the transient readings of a single temperature sensor located in the midplane of the potato slice, exposed to convective drying, have been used. The Levenberg–Marquardt method and a hybrid optimization method of minimization of the least-squares norm are used to solve the present parameter estimation problem. Analyses of the sensitivity coefficients and of the determinant of the information matrix are presented as well.
[DOI: 10.1115/1.2427072]

Keywords: inverse approach, drying, thermophysical properties, heat and mass transfer coefficients

Introduction

There are several methods for describing the direct problem of complex simultaneous heat and moisture transport processes within a drying material. In the approach proposed by Luikov [1] the moisture and temperature fields in the drying body are expressed by a system of two coupled partial differential equations. The system of equations incorporates coefficients that must be determined experimentally.

All the coefficients, except for the moisture diffusivity, can be relatively easily determined by experiments [2,3]. A number of methods for the experimental determination of the moisture diffusivity exist such as: sorption kinetics methods, permeation methods, concentration-distance methods, drying methods, radiotracer methods, and methods based on the techniques of electron spin resonance and nuclear magnetic resonance, but there is no standard method. The adoption of a generalized method for moisture diffusivity estimation would be of great importance.

We have recently analyzed a method for moisture diffusivity estimation by the temperature response of a drying body [4–11].

The main idea of this method is to make use of the interrelation between the heat and mass transport processes within the drying body and from its surface to the surroundings. Then, the moisture diffusivity can be estimated on the basis of an accurate and easy to perform single thermocouple temperature measurement by using an inverse approach.

The objective of this paper is an analysis of the possibility of the simultaneous estimation of the moisture diffusivity, together with other thermophysical properties of vegetables, as well as the heat and mass transfer coefficients. The method requires a single drying experiment and a single temperature measurement probe. As a representative drying vegetable product, thin slices of potato have been chosen. An analysis of the influence of the drying air velocity, temperature and relative humidity, drying body dimensions, and drying time on the moisture diffusivity estimation, enables the design of appropriate experiments to be conducted as well. In order to realize this analysis, the sensitivity coefficients and the determinant of the information matrix were calculated for the characteristic drying regimes and drying body dimensions.

Physical Problem and Mathematical Formulation

The physical problem involves a single slice of a potato of thickness $2L$ initially at uniform temperature and uniform moisture content (Fig. 1). The surfaces of the drying body are in contact with the drying air, thus resulting in a convective boundary condition for both the temperature and the moisture content. The
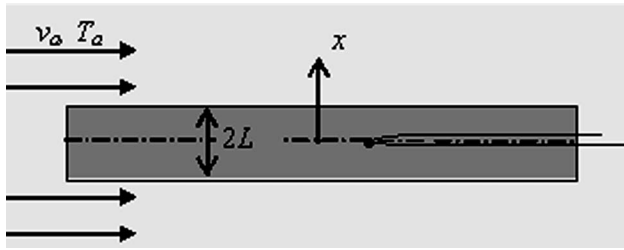

Fig. 1   Scheme of the drying experiment

problem is symmetrical relative to the midplane of the slice. The thickness of the body changes during the drying from $2L_0$ to $2L_f$.

In the case of an infinite flat plate the unsteady temperature, $T(x,t)$, and moisture content, $X(x,t)$, fields in the drying body are expressed by the following system of coupled nonlinear partial differential equations for energy and moisture transport

$$c\rho_s \frac{\partial T}{\partial t} = \frac{\partial}{\partial x}\left(k\frac{\partial T}{\partial x}\right) + \varepsilon \Delta H \frac{\partial(\rho_s X)}{\partial t} \tag{1}$$

$$\frac{\partial(\rho_s X)}{\partial t} = \frac{\partial}{\partial x}\left(D\rho_s \frac{\partial X}{\partial x} + D\rho_s \delta \frac{\partial T}{\partial x}\right) \tag{2}$$

Here, t, x, c, k, ΔH, ε, δ, D, and ρ_s are time, normal distance from the midplane of the plate, specific heat, thermal conductivity, latent heat of vaporization, ratio of water evaporation rate to the reduction rate of the moisture content, thermogradient coefficient, moisture diffusivity, and density of dry solid, respectively.

From the experimental and numerical examinations of the transient moisture and temperature profiles [12] it was concluded that for practical calculations, the influence of any thermodiffusion is small and can be ignored. Consequently, $\delta=0$ was utilized in this paper.

The shrinkage effect of the drying body was incorporated through the changes of the specific volume of the drying body. There are several models for describing the changes of the specific volume of the body during drying. In this paper, linear relationship between the specific volume, ν_s, and the moisture content, X, has been used

$$\nu_s = \frac{1}{\rho_s} = \frac{V}{m_s} = \frac{1 + \beta' X}{\rho_{b0}} \tag{3}$$

Here, m_s is the mass of the dry material of the drying body, V is the volume of the drying body, ρ_{b0} is the density of a fully dried body, and β' is the shrinkage coefficient.

Substituting the above expression for $\rho_s(=1/\nu_s)$ into Eqs. (1) and (2) and rearranging with $\delta=0$, results in

$$\frac{\partial T}{\partial t} = \frac{k}{\rho_s c}\frac{\partial^2 T}{\partial x^2} + \frac{\varepsilon \Delta H}{c}\frac{\rho_s}{\rho_{b0}}\frac{\partial X}{\partial t} \tag{4}$$

$$\frac{\partial X}{\partial t} = D\frac{\rho_{b0}}{\rho_s}\frac{\partial^2 X}{\partial x^2} + \frac{\rho_{b0}}{\rho_s^2}\frac{\partial(D\rho_s)}{\partial x}\frac{\partial X}{\partial x} \tag{5}$$

The problem of the moving boundaries due to the changes of the dimensions of the body during the drying was resolved by introducing the dimensionless coordinate

$$\psi = \frac{x}{L(t)} \tag{6}$$

Consequently, the resulting system of equations for the temperature and moisture content prediction becomes

$$\frac{\partial T}{\partial t} = \frac{k}{\rho_s c}\frac{1}{L^2}\frac{\partial^2 T}{\partial \psi^2} + \frac{\psi}{L}\frac{dL}{dt}\frac{\partial T}{\partial \psi} + \frac{\varepsilon \Delta H}{c}\frac{\rho_s}{\rho_{b0}}\left(\frac{\partial X}{\partial t} - \frac{\psi}{L}\frac{dL}{dt}\frac{\partial X}{\partial \psi}\right) \tag{7}$$

$$\frac{\partial X}{\partial t} = D\frac{\rho_{b0}}{\rho_s}\frac{1}{L^2}\frac{\partial^2 X}{\partial \psi^2} + \left[\frac{\rho_{b0}}{\rho_s^2}\frac{1}{L^2}\frac{\partial(D\rho_s)}{\partial \psi} + \frac{\psi}{L}\frac{dL}{dt}\right]\frac{\partial X}{\partial \psi} \tag{8}$$

The initial conditions are

$$t=0: \quad T(\psi,0) = T_0, \quad X(\psi,0) = X_0 \tag{9}$$

The temperature and the moisture content boundary conditions on the surfaces of the drying body in contact with the drying air are

$$-k\frac{1}{L}\left(\frac{\partial T}{\partial \psi}\right)_{\psi=1} + j_q - \Delta H(1-\varepsilon)j_m = 0$$

$$D\rho_s\frac{1}{L}\left(\frac{\partial X}{\partial \psi}\right)_{\psi=1} + j_m = 0 \tag{10}$$

The convective heat flux, $j_q(t)$, and mass flux, $j_m(t)$, on these surfaces are

$$j_q = h(T_a - T_{x=L})$$

$$j_m = h_D(C_{x=L} - C_a) \tag{11}$$

where h is the heat transfer coefficient, and h_D is the mass transfer coefficient, T_a is the temperature of the drying air, and $T_{x=L}$ is the temperature on the surfaces of the drying body. The water vapor concentration in the drying air, C_a, is calculated from

$$C_a = \frac{\varphi p_s(T_a)}{R_w T_{k,a}} \tag{12}$$

where φ is the relative humidity of the drying air and p_s is the saturation pressure. The water vapor concentration of the air in equilibrium with the surface of the body exposed to convection is calculated from

$$C_{x=L} = \frac{a(T_{x=L}, X_{x=L})p_s(T_{x=L})}{R_w T_{k,x=L}} \tag{13}$$

The water activity, a, or the equilibrium relative humidity of the air in contact with the convection surface at temperature $T_{x=L}$ and moisture content $X_{x=L}$ are calculated from experimental water sorption isotherms.

The boundary conditions on the midplane of the drying slice are

$$\left(\frac{\partial T}{\partial \psi}\right)_{\psi=0} = 0, \quad \left(\frac{\partial X}{\partial \psi}\right)_{\psi=0} = 0 \tag{14}$$

Problem defined by Eqs. (7)–(14) is referred to as a direct problem when initial and boundary conditions as well as all the parameters appearing in the formulation are known. The objective of the direct problem is to determine the temperature and moisture content fields in the drying body.

In order to approximate the solution of Eqs. (7) and (8), an explicit numerical procedure has been used.

The Drying Body Properties

In this paper, application of the proposed method for the estimation of the thermophysical properties of vegetables has been analyzed. As a representative vegetable product, a potato was chosen.

Heat capacity of food materials can be taken as equal to the sum of the heat capacity of solid matter and water absorbed by that solid

$$c = c_s + c_w X \tag{15}$$

Although the heat capacity of solid matter, c_s, and water, c_w, are functions of the temperature, constant values have been most widely used.

From Ref. [12] it was also concluded that for practical calculations the system of the two simultaneous partial differential equations could be used by treating the thermal conductivity, k, and the phase conversion factor, ε, as constants.

Moisture diffusivity of foods is a function of the temperature and the moisture content as well. The moisture diffusivity dependence of the moisture content for a potato is not clearly expressed [[13], p. 216], and it is very often considered as an Arrhenius-type temperature function [14,15]

$$D = D_0 \exp[-E_0/(RT_k)] \tag{16}$$

with constant values of the Arrhenius factor, D_0, and the activation energy for moisture diffusion, E_0.

The variation in water activity with change in moisture content of samples at a specified temperature is defined by sorption isotherms. There are many different models for describing the sorption isotherms of foods [3]. In recent years, the most widely accepted and efficient model for sorption isotherms of foods has been the Guggenheim–Anderson–de Boer (GAB) model

$$X = \frac{X_m C K a}{(1 - Ka)(1 - Ka + CKa)} \tag{17}$$

The monolayer moisture, X_m, and the adsorption constants C and K are related as Arrhenius type equations with the Arrhenius factors X_{m0}, C_0, and K_0, and the energy terms ΔH_X, ΔH_C, and ΔH_K, respectively.

Inverse Approach

The inverse problem in this paper is solved as a parameters estimation approach. The estimation methodology used is based on the minimization of the ordinary least square norm

$$E(\mathbf{P}) = [\mathbf{Y} - \mathbf{T}(\mathbf{P})]^{\mathrm{T}}[\mathbf{Y} - \mathbf{T}(\mathbf{P})] \tag{18}$$

Here, $\mathbf{Y}^{\mathrm{T}} = [Y_1, Y_2, \ldots, Y_{\mathrm{imax}}]$ is the vector of measured temperatures, $\mathbf{T}^{\mathrm{T}} = [T_1(\mathbf{P}), T_2(\mathbf{P}), \ldots, T_{\mathrm{imax}}(\mathbf{P})]$ is the vector of estimated temperatures at time t_i $(i=1,2,\ldots,\mathrm{imax})$, $\mathbf{P}^{\mathrm{T}} = [P_1, P_2, \ldots P_N]$ is the vector of unknown parameters, imax is the total number of measurements, and N is the total number of unknown parameters $(\mathrm{imax} \geq N)$.

A hybrid optimization algorithm OPTRAN [16] and the Levenberg–Marquardt method [17–19] have been utilized for the minimization of $E(\mathbf{P})$ representing the solution of the present parameter estimation problem.

The Levenberg–Marquardt method is a quite stable, powerful, and straightforward gradient search minimization algorithm that has been applied to a variety of inverse problems. It belongs to a general class of damped least square methods. The solution for vector $\mathbf{P}$ is achieved using the following iterative procedure

$$\mathbf{P}^{r+1} = \mathbf{P}^r + [(\mathbf{J}^r)^{\mathrm{T}}\mathbf{J}^r + \mu^r\mathbf{I}]^{-1}(\mathbf{J}^r)^{\mathrm{T}}[\mathbf{Y} - \mathbf{T}(\mathbf{P}^r)] \tag{19}$$

where r is the number of iterations, $\mathbf{I}$ is identity matrix, μ is the damping parameter, and $\mathbf{J}$ is the sensitivity matrix defined as

$$\mathbf{J} = \begin{bmatrix} \dfrac{\partial T_1}{\partial P_1} & \cdots & \dfrac{\partial T_1}{\partial P_N} \\ \vdots & & \\ \dfrac{\partial T_{\mathrm{imax}}}{\partial P_1} & \cdots & \dfrac{\partial T_{\mathrm{imax}}}{\partial P_N} \end{bmatrix} \tag{20}$$

Near the initial guess, the problem is generally ill conditioned so that large damping parameters are chosen thus making the term $\mu\mathbf{I}$ large as compared to term $\mathbf{J}^{\mathrm{T}}\mathbf{J}$. The term $\mu\mathbf{I}$ damps instabilities due to the ill-conditioned character of the problem. So, the matrix $\mathbf{J}^{\mathrm{T}}\mathbf{J}$ is not required to be nonsingular at the beginning of the iterations and the procedure tends towards a slow-convergent steepest descent method. As the iteration process approaches the converged solution, the damping parameter decreases, and the Levenberg–Marquardt method tends towards a Gauss method. In

fact, this method is a compromise between the steepest descent and Gauss method by choosing μ so as to follow the Gauss method to as large an extent as possible, while retaining a bias towards the steepest descent direction to prevent instabilities. The presented iterative procedure terminates if the norm of gradient of $E(\mathbf{P})$ is sufficiently small, if the ratio of the norm of the gradient of $E(\mathbf{P})$ to $E(\mathbf{P})$ is small enough, or if the changes in the vector of parameters are very small.

An alternative to the Levenberg–Marquardt algorithm, especially when searching for a global optimum of a function with possible multiple minima, is the hybrid optimization program OPTRAN [16]. OPTRAN incorporates six of the most popular optimization algorithms: the Davidon–Fletcher–Powell gradient search [20], sequential quadratic programming algorithm [21], Pshenichny–Danilin quasi-Newtonian algorithm [22], a modified Nelder–Mead simplex algorithm [23], a genetic algorithm [24], and a differential evolution algorithm [25]. Each algorithm provides a unique approach to optimization with varying degrees of convergence, reliability, and robustness at different stages during the iterative optimization procedure. The hybrid optimizer OPTRAN includes a set of rules and switching criteria to automatically switch back and forth among the different algorithms as the iterative process proceeds in order to avoid local minima and accelerate convergence towards a global minimum.

The population matrix was updated every iteration with new designs and ranked according to the value of the objective function, in this case the ordinary least square norm. As the optimization process proceeded, the population evolved towards its global minimum. The optimization problem was completed when one of several stopping criteria was achieved: the maximum number of iterations or objective function evaluations was exceeded, the best design in the population was equivalent to a target design, or the optimization program tried all six algorithms, but failed to produce a nonnegligible decrease in the objective function. The last criterion usually indicated that a global minimum had been found.

Parameters Estimation Analysis

For the inverse problem of interest here, the moisture diffusivity parameters, together with other thermophysical properties of the potato as well as the heat and mass transfer coefficients and the relative humidity of the drying air, are treated as unknown parameters.

Thus, in the inverse problem the analyzed vector of the unknown parameters was

$$\mathbf{P}^{\mathrm{T}} = [D_0, E_0, \rho_s, c_s, k, \varepsilon, h, h_D, \varphi] \tag{21}$$

For the simultaneous estimation of these unknown parameters, the transient reading of a single temperature sensor located at the position $x=0$, has been considered.

The possibility of the simultaneous estimation of the temperature-dependent moisture diffusivity together with the other thermophysical properties of the potato as well as the heat and mass transfer coefficients and the relative humidity of the drying air depends on the boundary conditions and dimensions of the drying sample. An analysis of the influence of the drying air parameters and dimensions of the drying sample needed for the design of the appropriate experiment have been conducted in this paper. In order to perform this analysis, the sensitivity coefficients have been calculated.

The sensitivity coefficients analysis has been carried out for an infinite flat plate model of a slice of potato with initial moisture content of $X(x,0)=5.00$ kg/kg and initial temperature $T(x,0) =20.0\,°C$. The drying air bulk temperature, T_a, was varied between 40 and 80 °C, the convection heat transfer coefficient between 27 and 33 W m^{-2} K^{-1}, and the initial thickness, $2L_0$, of the potato slice between 2 and 6 mm.

From the sensitivity coefficients analysis the following experimental parameters were chosen: $T_a=60\,°C$, $2L_0=3$ mm, $h =30$ W m^{-2} K^{-1}, $h_D=3.36 \times 10^{-2}$ m s^{-1}, and $\varphi=0.09$. Figure 2
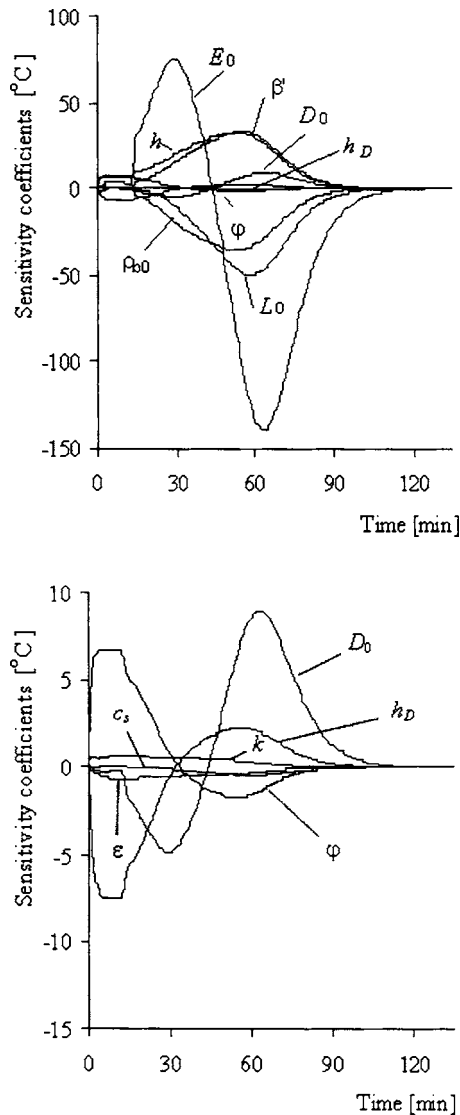
Fig. 2 Relative sensitivity coefficients for temperature

Fig. 3 Scheme of the experimental arrangement

shows the relative sensitivity coefficients $P_j \partial T_i / \partial P_j$, $i = 1, 2, \ldots, \text{imax}$, for temperature with respect to the unknown parameters, for this case.

It can be seen that the relative sensitivity coefficients with respect to the phase conversion factor, ε, and the thermal conductivity, k, are very small. This indicates that ε and k cannot be estimated in this case. This also indicates that the influence of the phase conversion factor and the thermal conductivity on the transient moisture content and temperature profiles is very small in this case. This can be explained by the very small heat transfer Biot number ($\text{Bi} = hL/k \leqslant hL_0/k = 0.11$) and consequently very small temperature gradients inside the body during the drying process. For these reasons, the phase conversion factor and the thermal conductivity were treated as known quantities for the examination described below.

The heat capacity of wet potato was taken as equal to the sum of the heat capacity of solid matter and absorbed water, Eq. (15). Since the heat capacity of the solid matter, c_s, presents only a few percent of the overall heat capacity of the potato, the relative sensitivity coefficients with respect to the heat capacity of solid matter is also very small. Consequently, the value of the heat capacity of the solid matter was also taken as known.

The relative sensitivity coefficients with respect to the density of the fully dried body, ρ_{b0}, and the shrinkage coefficient, β', are
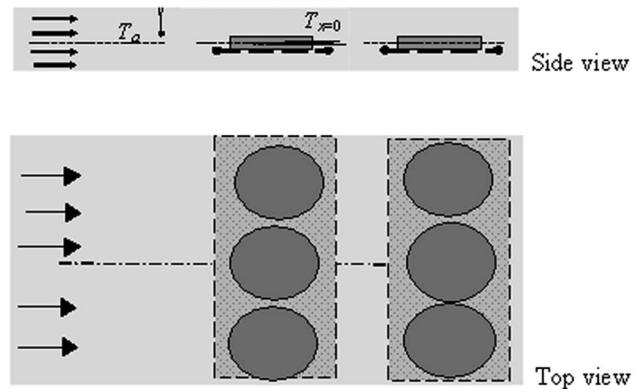
relatively high. Despite this, because the shrinkage effect of the drying body was incorporated through the changes of the specific volume of the drying body, these parameters were determined by separate experiments.

The relative sensitivity coefficients with respect to the initial potato slice thickness are high as well, but the initial slice thickness was measured with sufficient accuracy, so it is also taken as a known parameter.

It can be seen that the temperature sensitivity coefficient with respect to the convection mass transfer coefficient h_D is very small relative to the temperature sensitivity coefficient with respect to the convection heat transfer coefficient, h. The very high mass transfer Biot number and the very small heat transfer Biot number can explain this. To overcome this problem, in this paper the mass transfer coefficient was related to the heat transfer coefficient through the analogy between the heat and mass transfer processes in the boundary layer over a drying body [10]

$$ h_D = 0.95 \frac{D_a}{k_a} h \tag{22} $$

where D_a and k_a are the moisture diffusivity and thermal conductivity in the air, respectively. The obtained relation is very close to the well-known Lewis relation. By using the above relation between the heat and mass transfer coefficients, they can be estimated simultaneously, so that only the heat transfer coefficient is regarded as an unknown parameter.

Experiment

Real experiments have been conducted to investigate the applicability of the method to food processing, when involving drying of thin flat samples. The experiments have been conducted on the experimental setup that is designed to imitate an industrial convective dryer.

Drying of approximately three millimetres thick potato slices have been examined. The slices have been in contact with the drying air from the top and the bottom surfaces. Two shelves, (Fig. 3), each holding three moist potato slices have been introduced into the rectangular experimental channel of dimensions 25×200 mm. A microthermocouple was inserted in the midplane, ($x=0$), of each of the three slices on the first shelf. An arithmetical mean of the readings from the three thermocouples was used as a transient temperature reading, ($T_{x=0}$), for the estimation of the unknown parameters. The potato slices on the second shelf were weighed every ten minutes in order to obtain the volume-averaged moisture content change during drying. The temperature of the drying air, T_a, has been recorded as well. The initial moisture content, X_0, and the initial potato slices thickness, $2L_0$, were measured for each of the experiments.

The change of the specific volume of the drying body was determined by a separate experiment. The cylindrical potato slices
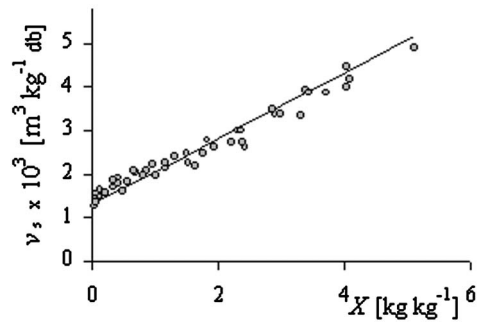
Fig. 4 Change of the specific volume during the drying of potato slices

Fig. 5 Determinant of the information matrix

with diameter of approximately 40 mm and thickness of approximately 3 mm have been placed on the second shelf and dried until the equilibrium moisture content has been reached. The dimensions and the mass of the slices were measured every 10 min. The initial moisture content and the initial potato slices thicknesses were measured as well. The experiment was repeated for different temperatures and speed of the drying air. The drying air temperature was varied between 50 and 70°C, and the drying air speed between 1.0 and 3.0 m s^{-1}.

The relative errors of the measurements were estimated between 0.1% and 1.0% for the mass and 0.3–2.5% for the dimensions of the slices. Microthermocouples were calibrated, relative to each other, within 0.2°C in the range of 20–80°C.

Results and Discussion

From the parameters estimation analysis it was concluded that the moisture diffusivity parameters, D_0 and E_0, the convection heat and mass transfer coefficients, h and h_D, and the relative humidity of the drying air, φ, will be treated as unknown parameters in this paper. All other quantities appearing in the direct problem formulation were taken as known.

Our experimental results for the changes of the specific volume of drying potato slices, (Fig. 4), confirm the expression (3) with $\rho_{b0}=755$ kg m^{-3} and the shrinkage coefficient $\beta'=0.57$. The heat capacity was calculated from Eq. (15). The following values, proposed in Ref. [26] for potatoes, were used: $c_s=1381$ J kg^{-1} K^{-1} and $c_w=4187$ J kg^{-1} K^{-1}. A mean value of $k=0.40$ W m^{-1} K^{-1} from the results obtained in Ref. [27] for the thermal conductivity of potato was utilized in this paper. The influence of the phase conversion factor ($0 \leqslant \varepsilon \leqslant 1$) on the transient moisture content and temperature profiles is very small. A mean value of $\varepsilon=0.5$ was used in the paper. For the GAB isotherm equation parameters the Gane experimental results for potatoes ([3], p. 45) were used in this paper ($C_0=6.609 \times 10^{-1}$; $\Delta H_C=528.4$ kJ kg^{-1}; $K_0=0.606$; $\Delta H_K=53.33$ kJ kg^{-1}; $\Delta H_X=123.6$ kJ kg^{-1}), except for X_{m0}. The value of $X_{m0}=3.8 \times 10^{-2}$ was obtained from our experimental results.

A number of drying experiments with similar experimental conditions, ($T_a=56.6$–59.5°C, $2L_0=2.36$–3.14 mm, $X_0=3.70$–4.83 kg/kg, and $T_0=14.9$–17.7°C), have been carried out.

The experimental drying time was estimated from the determinant of the information matrix. Figure 5 presents the transient
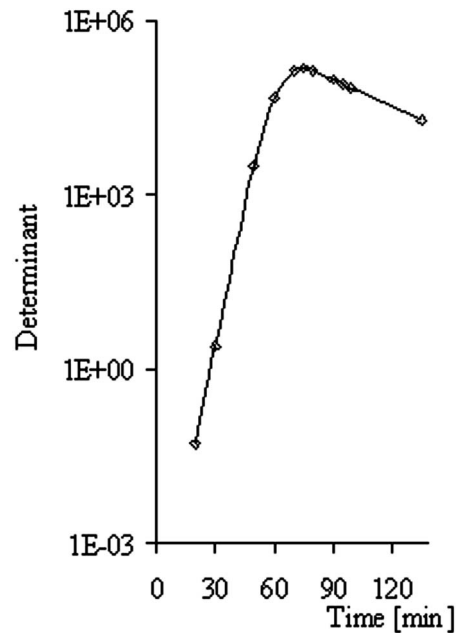
variation of the determinant of the information matrix if D_0, E_0, h, h_D, and φ are simultaneously considered as unknown. Elements of this determinant of the information matrix were defined [19] for a large, but fixed number of transient temperature measurements (451 in this case).

The maximum determinant value corresponds to the drying time when near equilibrium moisture content and temperature profiles have been reached.

The relative temperature sensitivity coefficients with respect to the moisture diffusivity parameters, D_0 and E_0, are almost linearly dependent, (Fig. 2). Despite this, we were able to obtain results using the OPTRAN [16] and the Levenberg–Marquardt algorithm [18]. Table 1 shows the computationally obtained parameters and rms error for experiment $E1$: $T_a=58.13$°C, $2L_0=3.14$ mm, $X_0=4.80$ kg/kg, and $T_0=17.53$°C. The rms changes and the convergence of the estimated values of the unknown parameters to the final values during the iterative process of the Levenberg–Marquardt method, for experiment $E1$ are shown in Fig. 6.

In Fig. 7 the estimated moisture diffusivities are compared with the results published by other authors that used different methods.

In Fig. 8 the experimental transient temperature reading, $T_{x=0}$, and the experimental volume-averaged moisture content change during drying are compared with numerical solutions for the estimated parameters. Very good agreements were obtained. The temperature changes during the weighing of the slices on the second shelf (every 10 min the second shelf together with the slices was taken outside the channel for 15 s to be weighed) can be seen in Fig. 8.

In Fig. 9, the experimental transient temperature reading, $T_{x=0}$, and the experimental volume-averaged moisture content changes during drying are compared with the numerical solutions with the estimated parameters in the cases when the shrinkage effect was

Table 1 Estimated parameters and rms error

	$D_0 \cdot 10^3$ (m s^{-1})	E_0 (kJ mol^{-1})	h (W m^{-2} K^{-1})	$h_D \cdot 10^2$ (m s^{-1})	φ (–)	rms (°C)
Initial guess	0.25	35	25	2.8	0.125	4.93
Estimated values	7.985	43.3	31.08	3.48	0.0899	0.55
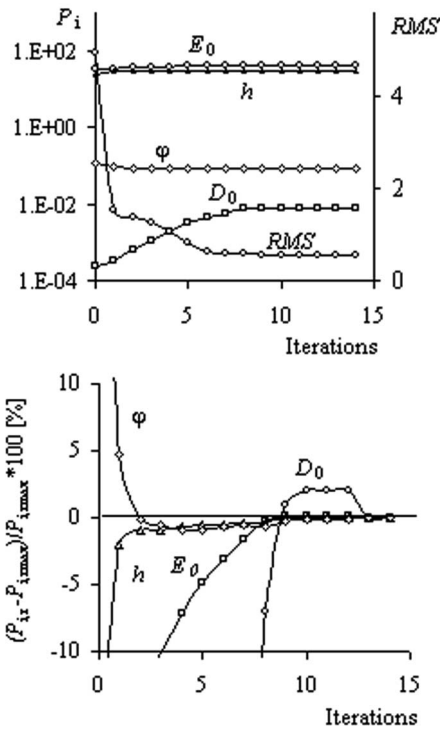
Fig. 6 Convergence history of rms errors and estimated parameters

Fig. 8 Time-variations during drying: The midplane temperature, $T_{x=0}$, the temperature of the drying air, T_a, and the volume-averaged moisture content, X: (a) the first shelf, and (b) the second shelf

incorporated and when it was not incorporated. It is very clear that the shrinkage effect cannot be ignored in the calculations of the drying processes of potato slices.

Conclusions

The inverse problem of simultaneous estimation of thermophysical properties and the boundary condition parameters of drying thin slices of vegetables by using only temperature measurements has been analysed. For this, a mathematical model of drying of shrinking bodies has been developed. As a representative vegetable product, a slice of a potato has been chosen.

It can be concluded that in the convective drying experiment it is possible, based on a single thermocouple temperature response,
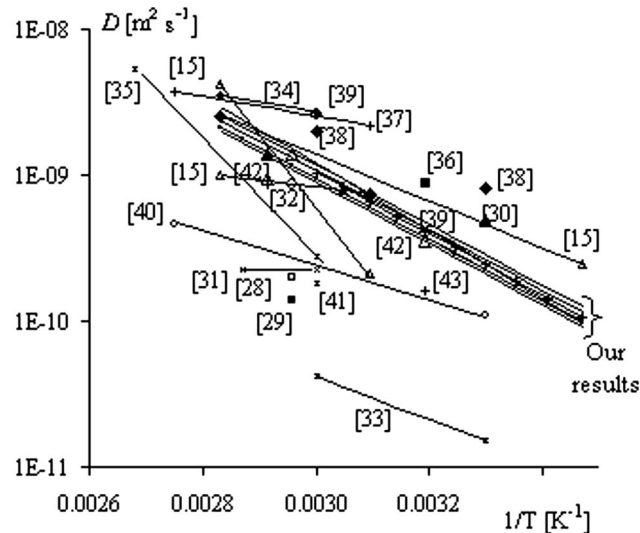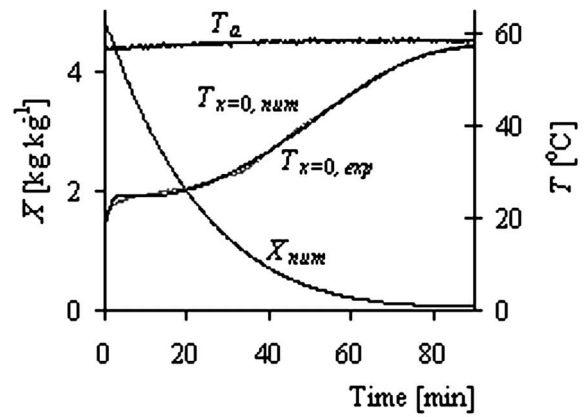
to estimate simultaneously the two moisture diffusivity parameters, the convection heat and mass transfer coefficients, and the relative humidity of the drying air.

Estimated moisture diffusivities compare well with the values obtained by other authors who utilized different methods.

Very good agreement between the experimental and numerical temperature and volume-averaged moisture content changes during drying has been obtained.

Since the relative temperature sensitivity coefficients with respect to the moisture diffusivity parameters in the Arrhenius-type

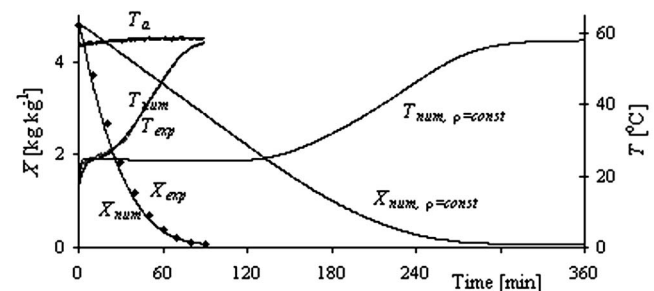Fig. 7 Moisture diffusivity of potatoes (see [28–43])

Fig. 9 Changes during drying with shrinkage effect and without shrinkage effect: The midplane temperature, $T_{x=0}$ and the volume-averaged moisture content, X

function are linearly dependent, other models for describing the moisture content and temperature-dependent moisture diffusivity could be analyzed in the future.

Nomenclature

a = water activity
c = heat capacity (dry basis), $J\,K^{-1}\,kg^{-1}$ db
C = concentration of water vapor, $kg\,m^{-3}$
D = moisture diffusivity, $m^2\,s^{-1}$
D_0 = Arrhenius factor, $m^2\,s^{-1}$
E_0 = activation energy $J\,kg^{-1}$
E = ordinary least square norm $(°C)^2$
h = heat transfer coefficient, $W\,m^{-2}\,K^{-1}$
h_D = mass transfer coefficient, $m\,s^{-1}$
ΔH = latent heat of vaporization, $J\,kg^{-1}$
$\mathbf{I}$ = identity matrix
j_m = mass flux, $kg\,m^{-2}\,s^{-1}$
j_q = heat flux, $W\,m^{-2}$
$\mathbf{J}$ = sensitivity matrix
k = thermal conductivity, $W\,m^{-1}\,K^{-1}$
L = flat plate thickness, m
m = mass, kg
p_s = saturation pressure, Pa
$\mathbf{P}$ = vector of unknown parameter
R = absolute gas constant, $J\,K^{-1}\,mol^{-1}$
R_w = specific gas constant, $J\,K^{-1}\,kg^{-1}$
t = time, s
T = temperature, °C
T_k = temperature, K
$\mathbf{T}$ = vector of estimated temperature, °C
v = specific volume, $m^3\,kg^{-1}$
V = volume, m^3
x = distance from the midplane, m
X = moisture content (dry basis), $kg\,kg^{-1}$ db
$\mathbf{Y}$ = vector of measured temperature, °C

Greek Symbols

β' = shrinkage coefficient, -
δ = thermo-gradient coefficient, K^{-1}
ε = phase conversion factor
μ = damping parameter
ρ = density, $kg\,m^{-3}$
φ = relative humidity
ψ = dimensionless coordinate

Subscripts

a = drying air
$b0$ = fully dried body
f = final
m = monolayer
w = water
s = dry solid

Superscripts

r = number of iterations
T = transposed

References

[1] Luikov, A. V., 1972, *Teplomassoobmen*, Energia, Moscow.
[2] Karathanos, V. T., Maroulis, Z. B., Marinos-Kouris, D., and Saravacos, D. G., 1996, "Higrothermal and Quality Properties Applicable to Drying," Drying Technol., **14**, pp. 1403–1418.
[3] Rahman, S., 1995, *Food Properties Handbook*, CRC Press, Boca Raton.
[4] Dantas, L. B., Orlande, H. R. B., and Cotta, R. M., 2001, "Estimation of Dimensionless Parameters of Luikov's System for Heat and Mass Transfer in Capillary Porous Media," Int. J. Therm. Sci., **41**, pp. 217–227.
[5] Dantas, L. B., Orlande, H. R. B., Cotta, R. M., and Lobo, P. D. C., 2000, "Parameter Estimation in Moist Capillary Porous Media by Using Temperature Measurements," *Inverse Problems in Engineering Mechanics II*, M. Tanaka and G. S. Dulikravich, eds., Elsevier, Amsterdam, pp. 53–62.

[6] Dantas, L. B., Orlande, H. R. B., and Cotta, R. M., 2002, "Effects of Lateral Heat Losses on the Parameter Estimation Problem in Moist Capillary Porous Media," *Inverse Problems in Engineering Mechanics III*, M. Tanaka and G. S. Dulikravich, eds., Elsevier, Amsterdam, pp. 13–22.
[7] Kanevce, G. H., Kanevce, L. P., and Dulikravich, G. S., 2000, "Moisture Diffusivity Estimation by Temperature Response of a Drying Body," *Inverse Problems in Engineering Mechanics II*, M. Tanaka and G. S. Dulikravich, eds., Elsevier, Amsterdam, pp. 43–52.
[8] Kanevce, G. H., Kanevce, L. P., and Dulikravich, G. S., 2000, "Influence of Boundary Conditions on Moisture Diffusivity Estimation by Temperature Response of a Drying Body," *Proc. 34th ASME National Heat Transfer Conf.*, Pittsburgh, PA, ASME paper No. NHTC2000-12296.
[9] Kanevce, G. H., Kanevce, L. P., and Dulikravich, G. S., 2002, "Simultaneous Estimation of Thermophysical Properties and Heat and Mass Transfer Coefficients of a Drying Body," *Inverse Problems in Engineering Mechanics III*, M. Tanaka and G. S. Dulikravich, eds., Elsevier, Amsterdam, pp. 3–12.
[10] Kanevce, G. H., Kanevce, L. P., and Dulikravich, G. S., 2003, "An Inverse Method for Drying at High Mass Transfer Biot Number," *Proc. HT03 ASME Summer Heat Transfer Conference*, Las Vegas, NV, ASME Paper No. HT20003-40146.
[11] Kanevce, G. H., Kanevce, L. P., Mitrevski, V. B., and Dulikravich, G. S., 2000, "Moisture Diffusivity Estimation From Temperature Measurements: Influence of Measurement Accuracy," *Proc. 12th Int. Drying Symposium (IDS'2000)*, P. J. A. M. Kerkhof, W. J. Coumans, G. D. Mooiweer, eds., Noordwijkerhout, The Netherlands, Paper No. 337.
[12] Kanevce, G. H., 1998, "Numerical Study of Drying," *Proc. 11th International Drying Symposium (IDS '98)*, Halkidiki, Greece, Vol. A, pp. 256–263.
[13] Saravacos, G. D., and Maroulis, Z. B., 2001, *Transport Properties of Foods*, Marcel Dekker, New York.
[14] Rovedo, C., Suarez, C., and Viollaz, P., 1998, "Analysis of Moisture Profiles, Mass Biot Number and Driving Forces During Drying of Potato Slabs," J. Food. Eng., **36**, pp. 211–231.
[15] Zogzas, N. P., and Maroulis, Z. B., 1996, "Effective Moisture Diffusivity Estimation From Drying Data: A Comparison Between Various Methods of Analysis," Drying Technol., **14**(7&8), pp. 1543–1573.
[16] Dulikravich, G. S., Martin, T. J., Dennis, B. H., and Foster, N. F., 1999, "Multidisciplinary Hybrid Constrained GA Optimization," *Evolutionary Algorithms in Engineering and Computer Science: Recent Advances and Industrial Applications (EUROGEN'99)*, K. Miettinen, M. M. Makela, P. Neittaanmaki and J. Periaux, eds., Wiley, Jyvaskyla, Finland, pp. 231–260.
[17] Beck, J. V., and Arnold, K. J., 1977, *Parameter Estimation in Engineering and Science*, Wiley, New York.
[18] Marquardt, D. W., 1963, "An Algorithm for Least Squares Estimation of Nonlinear Parameters," J. Soc. Ind. Appl. Math., **11**, pp. 431–441.
[19] Ozisik, M. N., and Orlande, H. R. B., 2000, *Inverse Heat Transfer: Fundamentals and Applications*, Taylor and Francis, New York.
[20] Fletcher, R., and Powell, M. J. D., 1963, "A Rapidly Convergent Descent Method for Minimization," Comput. J., **6**, pp. 163–168.
[21] Rao, S., 1996, *Engineering Optimization: Theory and Practice*, 3rd ed. J. Wiley Interscience, New York.
[22] Pshenichny, B. N., 1969, *Numerical Methods in Extremal Problems*, Mir, Moscow.
[23] Nelder, J. A., and Mead, R., 1965, "A Simplex Method for Function Minimization," Comput. J., **7**, pp. 308–313.
[24] Goldberg, D. E., 1989, *Genetic Algorithms in Search, Optimization and Machine Learning*, Addison-Wesley, Cambridge, MA.
[25] Storn, R., 1997, "Differential Evolution—A Simple and Efficient Heuristic for Global Optimization Over Continuous Spaces," J. Global Optim., **11**(4), pp. 341–359.
[26] Niesteruk, R., 1996, "Changes at Thermal Properties of Fruits and Vegetables During Drying," Drying Technol., **14**, pp. 415–422.
[27] Donsi, G., Ferrari, G., and Nigro, R., 1996, "Experimental Determination of Thermal Conductivity of Apple and Potato of Different Moisture Contents," J. Food. Eng., **30**, pp. 263–268.
[28] Aguilera, J. M., Chirife, J., Flink, J. M., and Karel, M., 1975, "Computer Simulation of Nonenzymatic Browing During Potato Dehydration," Lebensm.-Wiss. Technol., **8**, pp. 128–133.
[29] Chirife, J., 1983, "Fundamentals of the Drying Mechanism During Air Dehydration of Foods," *Advances in Drying*, A. S. Mujumdar, ed., Hemisphere, New York, pp. 73–102.
[30] Frias, A., Clemente, G., Rossello, C., and Mulet, A., 2003, "Kinetics of Fluidized Bed Drying of Potato," *Proc. Symposium EUDrying 03*, Heraklion, Crete, Greece, pp. 224–230.
[31] Gekas, V., and Lamberg, I., 1991, "Determination of Diffusion Coefficients in Volume-Changing Systems—Application in the Case of Potato Drying," J. Food. Eng., **14**, pp. 317–326.
[32] Islam, M. N., and Flink, J. M., 1982, "Dehydration of Potato II. Osmotic Concentration and Its Effects on Air Drying Behaviour," J. Food Technol., **17**, pp. 373–385.
[33] Khraisheh, M. A. M., Cooper, T. J. R., and Magee, T. R. A., 1997, "Transport Mechanisms of Moisture During Air Drying Processes," Trans. IChemE, Part C, **75** Part C, pp. 34–40.
[34] Kiranoudis, C. T., Maroulis, Z. B., and Marinos-Kouris, D., 1992, "Model Selection in Air Drying of Foods," Drying Technol., **10**(4), pp. 1097–1106.
[35] Kiranoudis, C. T., Maroulis, Z. B., and Marinos-Kouris, D., 1995, "Heat and Mass Transfer Model Building in Drying With Multiresponse Data," Int. J. Heat Mass Transfer, **38**(3), pp. 463–480.

[36] Magee, T. R. A., and Wilkinson, C. P. D., 1992, "Influence of Process Variables on the Drying of Potato Slices," Int. J. Food Sci. Technol., **27**, pp. 541–549.

[37] Maroulis, Z. B., Kiranoudis, C. T., and Marinos-Kouris, D., 1995, "Heat and Mass Transfer in Air Drying of Foods," J. Food. Eng., **26**(1), pp. 113–130.

[38] McLaughlin, C. P., and Magee, T. R. A., 1999, "The Effects of Air temperature, Sphere Diameter and Puffing With CO_2 on the Drying of Potato Spheres," Drying Technol., **17**(1&2), pp. 119–136.

[39] McMinn, W. A. M., and Magee, T. R. A., 1996, "Air Drying Kinetics of Potato Cylinders," Drying Technol., **14**(9), pp. 2025–2040.

[40] Mulet, A., 1994, "Drying Modelling and Water Diffusivity in Carrots and Potatoes," J. Food. Eng., **22**, pp. 329–348.

[41] Rovedo, C., Suarez, C., and Viollaz, P., 1995, "Drying of Foods: Evaluation of Drying Model," J. Food. Eng., **26**, pp. 1–12.

[42] Wang, N., and Brennan, J. G., 1992, "Effect of Water Binding on the Drying Behaviour of Potato," *Proc. 8th Int. Drying Symposium*, Montreal, Quebec, Canada, pp. 1350–1359.

[43] Yusheng, Z., and Poulsen, K. P., 1988, "Diffusion in Potato Drying," J. Food. Eng., **7**, pp. 249–262.

On the Use of the Fully Compressible Navier-Stokes Equations for the Steady-State Solution of Natural Convection Problems in Closed Cavities

Sandip Mazumder
Mem. ASME
Department of Mechanical Engineering,
The Ohio State University,
E410 Scott Laboratory,
201 W. 19th Avenue,
Columbus, OH 43210
e-mail: mazumder.2@osu.edu

The steady-state compressible form of the Navier-Stokes equations, along with no-slip boundary conditions on walls, represents a boundary value problem. In closed heated cavities, these equations are incapable of preserving the initial mass of the cavity and predicting the pressure rise. A simple strategy to adjust the reference pressure in the system is presented and demonstrated. The strategy is similar to solving the transient form of the governing equations, but completely eliminates truncation errors associated with temporal discretization of the transient terms. Results exhibit good agreement with previous reports. Additional results are shown to highlight differences between the fully compressible formulation and the Boussinesq approximation.
[DOI: 10.1115/1.2430726]

1 Introduction

Natural convection problems in closed cavities are unique. In such problems, the steady-state solution, assuming that it exists, is strongly dependent upon the initial mass (which translates to initial temperature and pressure in the case of a gas) in the cavity. This simple fact defies the general notion that at steady state initial conditions are forgotten. The observation also raises the question as to how steady state should be dealt with in analysis.

The Boussinesq approximation has found prolific usage in the solution of natural convection problems [1,2]. The Boussinesq approximation is only valid for "small" changes in temperature,

and its use cannot be justified for scenarios in which the temperature variations are "large," such as in closed furnaces and burners, since variable density (or compressibility) effects can become significant. In such a scenario, the fully compressible form of the governing equations must be used. This general case is the central focus of this short note.

In pressure-based approaches, such as the SIMPLE genre of algorithms [3,4], steady-state solution is generally obtained by directly solving the steady-state conservation equations, i.e., conservation equations without the time derivatives. In this technical brief, it is shown that solution of the steady-state fully compressible conservation equations (i.e., without the Boussinesq approximation) always results in physically inconsistent results if the computational domain is completely bounded by walls and there are no inflow/outflow boundaries. The inconsistency is a result of the fact that when the steady-state continuity equation is solved, the mass fluxes balance, but the initial mass in the cavity is not necessarily preserved since the density is allowed to change with temperature. A simple correction strategy is developed to address this inconsistency. The use of this correction strategy is finally demonstrated by solving a natural convection problem in a closed cavity using the SIMPLE algorithm and the fully compressible (i.e., without the Boussinesq approximation) steady-state conservation equations. Results, with and without the Boussinesq approximation, are compared for different Rayleigh numbers. It is found that although the average Nusselt numbers differ marginally, the local Nusselt numbers predicted by the two formulations differ significantly when the driving temperature differential is large, i.e., when compressibility effects are important.

2 Analysis and Results

The governing equations are the conservations of mass, momentum and energy. At steady state, they are written as [5]

$$\nabla \circ (\rho \mathbf{U}) = 0 \tag{1}$$

$$\nabla \circ (\rho \mathbf{U}\mathbf{U}) = -\nabla p + \nabla \circ (\mu \nabla \mathbf{U}) + \rho \mathbf{g} \tag{2}$$

$$\nabla \circ (\rho c_p \mathbf{U}T) = \nabla \circ (k_c \nabla T) \tag{3}$$

where $\mathbf{U}$ is the fluid velocity vector; p is the pressure; T is the temperature; and $\mathbf{g}$ is the gravity vector. The density, dynamic viscosity, thermal conductivity, and specific heat capacity of the fluid are denoted by ρ, μ, k_c, and c_p, respectively. In writing Eq. (2), it has been assumed that the fluid in question is Newtonian. In writing Eq. (3), it has been assumed that the specific heat capacity is independent of temperature, in addition to assumptions of the absence of radiation, external work, and viscous dissipation.

Let us now consider a natural convection problem in a closed cavity with a vertical hot wall at temperature T_h, a vertical cold wall at temperature T_c, and adiabatic horizontal walls. Let us also assume that initially the gas inside has the same temperature as the cold wall, and is at rest. As the gas inside becomes heated by conduction from the hot wall, both its average temperature and average pressure will increase, such that its average density remains more or less unchanged. While the increase in temperature

is caused by heat transfer, the increase in pressure is caused by the fact that since the total volume and mass of the system are both unchanged, the thermodynamic pressure must rise to keep the average density unchanged and preserve the mass in the cavity.

The solution of the steady state continuity and momentum equations (Eqs. (1) and (2)) does not provide the thermodynamic pressure of the system. The pressure distribution calculated is the hydrodynamic pressure distribution, and is essentially a pressure distribution that is consistent with the fluid flow pattern. This pressure must be added to a prescribed reference value to obtain the total thermodynamic pressure. The reference pressure is not known a priori, and can only be obtained by enforcing that the initial mass of the system remains unchanged. Unfortunately, the steady-state equations represent boundary value problems and do not have the mechanism in place to preserve the effect of initial conditions. Thus, the solution obtained by solving Eqs. (1)–(3) will be self-consistent, but physically inconsistent. Heat transfer will heat the system and lower the average density since the thermodynamic pressure increase cannot be calculated using the steady-state equations. The result will be loss of mass from what was initially present in the closed cavity. One approach to circumvent this problem is to additionally enforce that the total initial mass in the system is preserved. This idea will be used shortly to develop a strategy for self-consistent calculation of the reference pressure in the system.

An enormous volume of literature that reports numerical simulation of natural convection in closed cavities exists (Ref. [2] and the work cited therein). The preceding discussion raises the obvious question: Are all these published results of dubious credibility? A discussion of this critical issue is warranted at this juncture. First of all, the vast majority of natural convection calculations that have been reported in the literature have been performed after invoking the Boussinesq approximation. In the Boussinesq form of the governing equations, it is assumed that the density is a constant in all terms except in the body force term of the momentum equation. If the density is constant, the initial mass within the system is automatically preserved even if the system is heated. Thus, the Boussinesq form of the steady-state equations will result in both self-consistent and physically consistent results. It is also worth noting that the vast majority of results reported in the literature are computed and presented in nondimensional form, thereby allowing one to choose a small temperature difference (and adjust other parameters to get the desired Rayleigh number) so that compressibility effects are truly negligible and the Boussinesq approximation itself is valid.

Strategy for Correction of Reference Pressure. For steady-state calculations, a strategy for correction of the reference pressure can be developed by enforcing that the total mass within the closed cavity remains unchanged. The correction strategy is described here in the context of the SIMPLE algorithm. Assuming that the fluid inside is a gas that obeys the ideal gas law, the initial mass in the system is calculated as

$$m_{\text{init}} = \sum_{i=1}^{N_C} \left(\frac{p_i V_i}{R T_i} \right)_{\text{init}} \qquad (4)$$

where N_C is the total number of finite volumes (or cells) used in the computation; p_i, V_i, and T_i the pressure, volume, and temperature, respectively of the ith cell; and R is the characteristic gas constant. At any outer loop iteration of the SIMPLE algorithm, k, the total mass in the system must be equal to the initial mass, and thus

$$m_{\text{init}} = m_k = \sum_{i=1}^{N_C} \left(\frac{p_i V_i}{R T_i} \right)_k = \sum_{i=1}^{N_C} \left[\frac{(p_0 + p_i^H) V_i}{R T_i} \right]_k \qquad (5)$$

where the pressure has been additionally split into a reference pressure, p_0, which is invariant in space and a hydrodynamic pressure, p_i^H, that varies from cell to cell. Equation (5) may be rear-
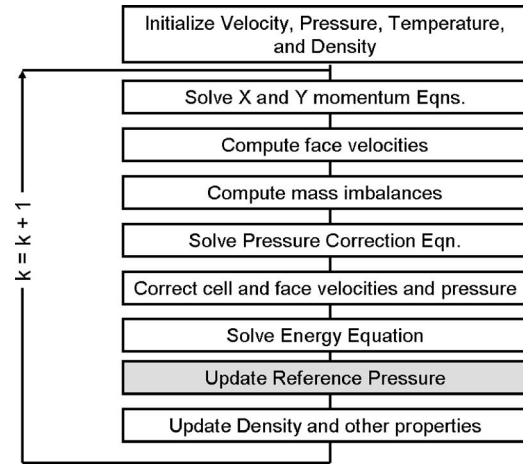
ranged to recalculate the reference pressure at each outer iteration of the SIMPLE algorithm

$$[p_0]_k = \left[m_{\text{init}} - \sum_{i=1}^{N_C} \left(\frac{p_i^H V_i}{R T_i} \right)_k \right] \bigg/ \sum_{i=1}^{N_C} \left(\frac{V_i}{R T_i} \right)_k \qquad (6)$$

The correction of the reference pressure must be performed at the end of each outer loop iteration prior to calculation of the density. The overall SIMPLE algorithm, after inclusion of this correction step, is depicted in Fig. 1.

The correction scheme, just described, stems from the realization that one of the solutions to the problem discussed here is to solve the unsteady form of the governing equations. This will automatically preserve the initial mass in the cavity. Unfortunately, solution of the unsteady equations gives rise to an additional truncation error due to temporal discretization and is, therefore, not always desirable for cases when the steady state solution is sought. In essence, the correction scheme introduced here is equivalent to pseudo-time marching the continuity equation alone, but without introducing any additional temporal discretization error.

Sample Calculations. The fully compressible formulation, after the necessary consistency corrections just described, was used to compute natural convection in a closed square cavity. In addition, computations were also performed using the Boussinesq approximation. Four different Rayleigh numbers were considered, and the parameters chosen for the computations are shown in Table 1. The hot wall temperature, T_h, was computed from the

Fig. 1 Flowchart of the SIMPLE algorithm with the proposed modification to update the reference pressure highlighted in gray

Table 1 Parameters used for sample calculations in the current study

Parameter	Value or definition
Dynamic viscosity, μ	2×10^{-5} kg m^{-1} s^{-1}
Thermal conductivity, k_c	0.026 W m^{-1} K^{-1}
Specific heat capacity, c_p	1012 J kg^{-1} K^{-1}
Initial pressure in cavity	$=p_0=1$ bar
Temperature of cold wall, T_c	300 K
Initial density in cavity	$=\rho_0=p_0/RT_c$
Size of cavity, $L \times H$	2 cm $\times$ 2 cm
Prandtl number, Pr	$=\mu c_p/k_c=0.77$
Grashof number, Gr$_L$	$=2g(T_h-T_c)L^3 / (T_h+T_c)(\mu/\rho_0)^2$
Rayleigh number, Ra$_L$	Gr$_L \times$ Pr
Temperature of hot wall, T_h	obtained by inverting expression for Ra$_L$ (see Table 2)

Table 2 Predicted average Nusselt numbers at the hot wall with and without the Boussinesq approximation, and comparison against previously reported numerical results

Ra_L	T_h	Nu_{av} [a]	Nu_{av}, current study, with Boussinesq	Nu_{av}, current study, without Boussinesq
10^4	314.8	2.24	2.25	2.25
3×10^4	346.7	3.14	3.16	3.16
10^5	490.5	4.51	4.57	4.57
3×10^5	1865.9	unavailable	6.34	6.38

[a]From Ref. [8].

prescribed Rayleigh numbers by inverting the relationship shown in Table 1. All computations were performed using the finite volume method [3,4] on a 100×100 uniform co-located mesh. The same calculations were also performed on a 40×40 uniform co-located mesh, and the calculated average Nusselt numbers were found to be within 1.2% of the finer mesh results. Thus, the results obtained using the 100×100 mesh are presented here. The advection terms were treated using the first order upwind difference scheme, while the diffusion terms were treated using the central

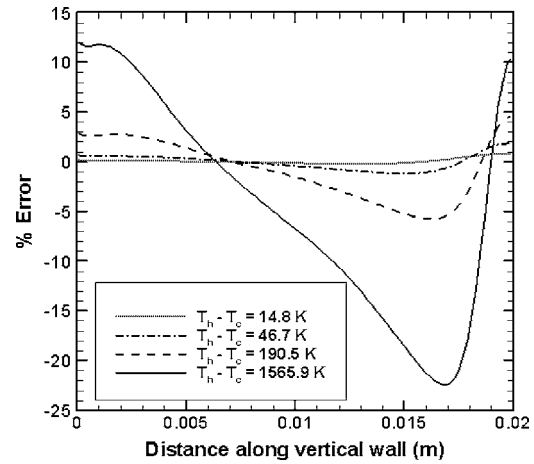**Fig. 2 Error in local Nusselt numbers at the hot wall, defined as $(Nu_{compressible} - Nu_{Boussinesq}) \times 100 / Nu_{compressible}$**
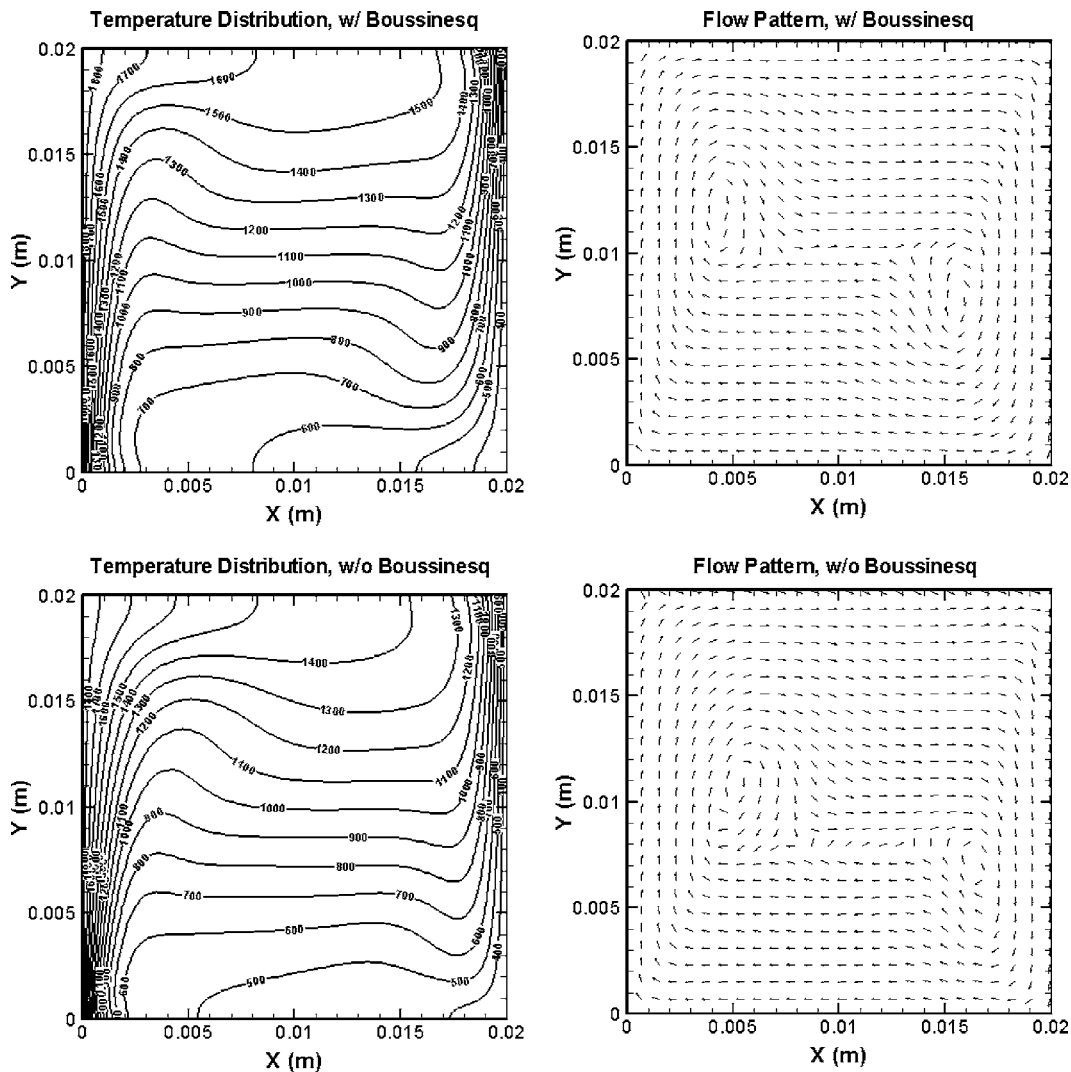

Fig. 3 Predicted temperature and flow distributions with and without the Boussinesq approximation for $Ra_L = 3 \times 10^5$ ($T_h - T_c = 1565.9$ K). The velocity vectors have been set to uniform size and plotted at intervals of four grid points to better depict the flow pattern.
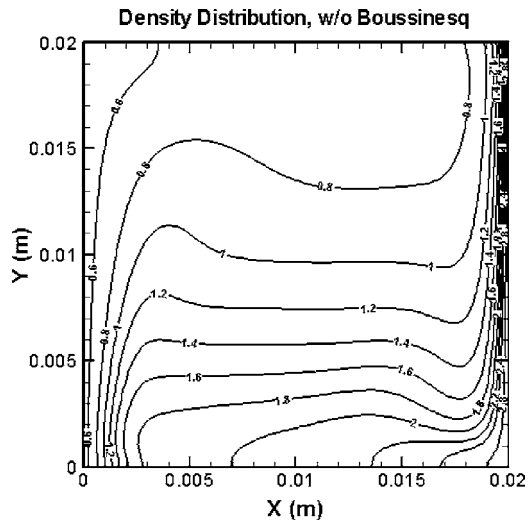
Fig. 4 Density distributions without the Boussinesq approximation for $Ra_L = 3 \times 10^5$ ($T_h - T_c = 1565.9$ K)

difference scheme [3,4]. The pressure weighted interpolation method [6,7] was used to address checkerboard pressure oscillations associated with the solution of the Navier–Stokes equations on a co-located mesh. The core SIMPLE algorithm was used. Depending on the Rayleigh number, it took between 300 and 1500 outer iterations for all residuals to decrease by ten orders of magnitude.

Average Nusselt numbers predicted by the two formulations, as well as previously reported benchmark numerical results [8] are shown in Table 2. First, it is seen that the results agree almost perfectly with previously reported results, thereby validating the current code. Second, the average Nusselt numbers predicted by the two formulations are almost identical except for marginal differences in the very last case ($Ra_L = 3 \times 10^5$) in which the temperature differential ($T_h - T_c$) is very large. This is a surprising result in light of the fact that for $T_h - T_c$ exceeding 1500 K, one would expect the Boussinesq approximation to fail and the Nusselt numbers predicted by the two formulations to be dramatically different. The matter was further investigated by probing the local Nusselt numbers. Figure 2 shows errors in the local Nusselt numbers predicted by the two formulations. The local Nusselt numbers predicted by the two formulations, in strong contrast to the average values, appear to be significantly different. The errors are positive in some locations, and negative in others, which explains the remarkable closeness of the average values. The continuity equation, under the Boussinesq approximation, is essentially a volume conservation equation. In the fully compressible formulation, it is truly a mass conservation equation. Thus, the local velocities predicted by the two approaches are different, especially when the spatial variation in density is significant (Fig. 3). On the other hand, the average density is the same in both cases, since the initial mass is preserved. Thus, the average recirculation velocity, which is primarily buoyancy driven, is comparable in the two cases, and helps explain why the average Nusselt numbers are similar, while the local values are significantly different. It is also worth noting in Fig. 3 that the flow and temperature distributions predicted by the Boussinesq form of the equations are always diagonally symmetric, while the expansion of the hot gas near the left hot wall pushes the fluid toward the right cold wall in the fully compressible formulation, thereby destroying the symmetry. For the same case, the density distribution without the Boussinesq approximation (fully compressible formulation) is also shown in Fig. 4, and clearly indicates a strong variation around a value of 1.165, which is the mean density within the cavity.

3 Summary and Conclusions

The steady-state compressible form of the Navier–Stokes equation, along with appropriate boundary conditions, represents a boundary value problem. When used for solution of natural convection problems in closed cavities, it is incapable of preserving the initial mass in the cavity, and yields wrong solutions. Such problems do not occur in the Boussinesq formulation since the fluid is treated as incompressible as far as mass conservation is concerned, and thus, the initial mass in the system is automatically preserved. A strategy to preserve the mass within the cavity was developed and demonstrated, and involves a simple algebraic calculation to update the reference pressure in the system at each iteration. Natural convection calculations were performed in a square cavity for different Rayleigh numbers (which was changed by changing the temperature differential between hot and cold walls) with and without the Boussinesq approximation. It was found that the Boussinesq approximation predicts average Nusselt numbers remarkably well even when compressibility effects are strong. Whether this is a mere coincidence or not will require further systematic studies. On the other hand, as the temperature differential was increased, local Nusselt numbers predicted by the Boussinesq approximation began to differ significantly from those predicted by the compressible formulation.

Nomenclature

c_p = specific heat capacity of fluid (J kg^{-1} K^{-1})
$\mathbf{g}$ = gravity vector (m s^{-2})
g = acceleration due to gravity (=9.81 m s^{-2})
k = iteration index
k_c = thermal conductivity of fluid (W m^{-1} K^{-1})
N_C = number of cells (or finite volumes)
p = pressure (Pa)
p_0 = reference pressure (Pa)
p_i = absolute pressure at ith cell (Pa)
R = characteristic gas constant (=286 J kg^{-1} K^{-1} for air)
Ra_L = Rayleigh number based on L, the distance between hot and cold wall
T = temperature (K)
T_i = temperature at ith cell (K)
T_h = temperature of hot wall (K)
T_c = temperature of cold wall (K)
$\mathbf{U}$ = fluid velocity vector (m/s)
V_i = volume of ith cell (m^3)
X, Y = space variables (m)

Greek Symbols

μ = dynamic viscosity (kg m^{-1} s^{-1})
ρ = mixture density (kg m^{-3})

References

[1] Jaluria, Y., 1980, *Natural Convection Heat and Mass Transfer*, Pergamon, New York.
[2] Leong, W. H., Hollands, K. G. T., and Brunger, A. P., 2005, "Experimental Nusselt Numbers for a Cubical-Cavity Benchmark Problem in Natural Convection," Int. J. Heat Mass Transfer, Vol. **42**, pp. 1979–1989.
[3] Patankar, S. V., 1980, *Numerical Heat Transfer and Fluid Flow*, Hemisphere, Washington, D.C.
[4] Ferziger, J., and Peric, M., 1999, *Computational Methods for Fluid Dynamics*, 2nd ed., Springer, Berlin.
[5] Whitaker, S., 1983, *Fundamental Principles of Heat Transfer*, Krieger, Melbourne, FL.
[6] Rhie, C. M., and Chow, W. L., 1983, "A Numerical Study of the Turbulent Flow Past an Isolated Airfoil with Trailing Edge Separation," AIAA J., **21**, pp. 1525–1532.
[7] Miller, T. F., and Schmidt, F. W., 1988, "Use of a Pressure Weighted Interpolation Method for the Solution of Incompressible Navier-Stokes Equations with Non-Staggered Grid System," Numer. Heat Transfer, **14**, pp. 213–233.
[8] Le Quere, P., 1991, "Accurate Solutions to the Square Thermally Driven Cavity at High Rayleigh Number," Comput. Fluids, **20**(1), pp. 29–41.

A Mathematical Model Predicting the Minimum Meniscus Radius in Mixed Particles

P. Cheng
Graduate Research Assistant

H. B. Ma[1]
Associate Professor
e-mail: mah@missouri.edu

Department of Mechanical and Aerospace Engineering,
University of Missouri–Columbia,
Columbia, MO 65211

The minimum meniscus radius occurring in the heat pipe determines the maximum capillary heat transport. The accurate prediction of minimum meniscus radii plays a key role in designing a highly efficient heat pipe cooling device. In the current investigation, a mathematical model predicting the minimum meniscus radius occurring in the sintered particles is developed. If the particle size distribution is given, the model can be used to predict the minimum meniscus radii in sintered particles.
[DOI: 10.1115/1.2430727]

Introduction

A sintered particle wick has been widely used in high heat flux heat pipes [1–3]. Researchers have developed a number of theoretical models determining the porosity of sintered particles. This property depends on the particle shape, particle size, surface condition, and packing method [4]. The boundary condition and metallurgy process could also determine this property. To simplify the problem, many researchers [5–8] have only focused on the loose packing spherical particles with either one uniform or two different radii. One typical approach is using the high-speed computer and statistical physics to simulate the particle system [6–8]. In addition to the porosity, another important parameter for a heat pipe is the minimum meniscus radius. While the minimum meniscus radius is directly related to the porosity, this property occurring in the sintered particles has not been extensively studied. A number of heat pipe textbooks [2,3,9] have indicated that this property for the sintered particles with a uniform size is equal to 0.41*r*, where *r* is the particle radius. All of these heat pipe textbooks cited the reference written by Ferell and Alleavitch [10], who actually did not conduct the investigation, and they cited it from Luikov's work [11] and Luikov found this value using uniform spherical particles and the radius of a circle inscribed among four adjacent particles [11]. Clearly, it is necessary to conduct an investigation to determine the minimum meniscus radius occurring in the sintered particles.

The current investigation presents a mathematical model predicting the minimum meniscus radius of sintered particles. What the system consists of, in particular mixed particles with different radii, makes the distribution of particles very complicated. This paper analyzes the possible structures in the uniform spherical particle system to obtain the minimum meniscus radius for this case. Then using this information, a mathematical expression predicting the minimum meniscus radius for mixed particles is presented.

Mathematical Model

When heat is applied to the evaporating region of a heat pipe, the heat will travel through the solid wall of the container to reach the working fluid. Provided that the heat pipe has not reached the boiling limit, heat will pass through the sintered particles saturated with working fluid and reach the top surface of the working fluid in the wick. The heat will then pass through a thin-film region consisting of three regions: the nonevaporating thin-film region, the evaporating thin-film region, and the meniscus thin-film region [1]. The evaporation in the thin-film region makes the liquid–vapor interface recede into the sintered particles. When the heat input in the evaporator increases, the liquid–vapor interface will further recede and cause the meniscus radius to become smaller. The decrease in the meniscus radius increases the capillary pressure to overcome the increase of pressure drop occurring in the flow path of the working fluid. When the increase of heat input has resulted in a minimum meniscus radius, the heat pipe has reached the capillary limit. Clearly, the minimum meniscus radius is a key in designing a high-heat flux heat pipe.

If heat is added to the sintered porous medium fabricated from the perfectly spherical particles, the heat is transferred through the sintered particles filled with the working fluid, reaching the top surface where the liquid–vapor–solid interface exists. There, by utilizing the thin-film evaporation, the heat is removed. In order to avoid the boiling limit, the thickness of sintered particles in the evaporating section is very thin; in particular, for a high heat flux heat pipe [1]. Clearly, the meniscus radius variation occurring in the top layer of sintered particles will be directly related to the heat transport through the heat pipe and the minimum meniscus radius occurring in the top layer of sintered particles will determine the maximum capillary heat transport capability of a heat pipe. The minimum meniscus radius is directly related to the maximum capillary pressure, i.e.

$$\Delta p_{c,\max} = \frac{2\sigma}{r_{c,e}} \qquad (1)$$

The minimum meniscus radius, $r_{c,e}$, in Eq. (1) is defined by

$$r_{c,e} = \frac{2A_{\text{gap}}}{P_{\text{gap}}} \qquad (2)$$

where A_{gap} is the minimum area trapped by particles and P_{gap} is the perimeter of the trapped area.

To simplify the problem, two assumptions are made, i.e., (1) the whole system is in a stable state; and (2) the particles are spherical. In the stage of pouring particles, the system of these particles (as shown in Fig. 1) may be unstable and the properties will be different from those in a stable system. During the transition from the unstable system to the stable system, symmetric structures need more energy for a new structure because the symmetric structures obtained the maximum energy during the pouring process. In other words, once the symmetric structures during the pouring process are formed, it is not easy for them to be restructured during the sintering process. Based on this assumption, only symmetric structures shown in Fig. 2 are formed. The second assumption is related to the shape of sintered particles. When the particles are sintered, they could be combined or "melt" into each other by the diffusion and their shapes are not perfectly spherical any more. This might result in the variation of relative positions of these particles.

For a structure to be stable, the following conditions should be satisfied, i.e.
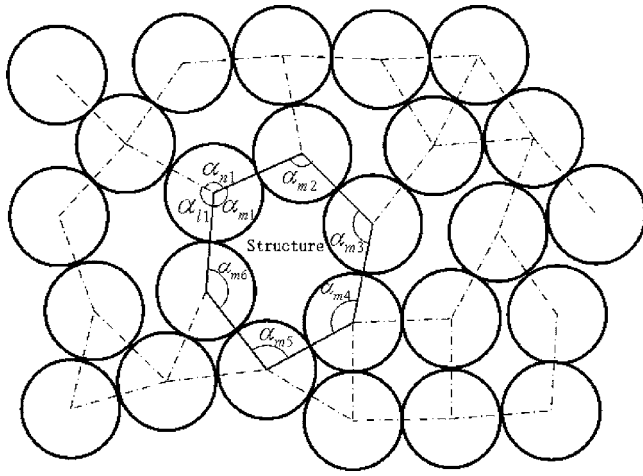

Fig. 1   Structures in one layer of particles

$$\sum_{x=1}^{N} \alpha_{mx} = (N-2)\pi \tag{3}$$

$$\sum_{y=1}^{M} \alpha_{yx} = 2\pi \tag{4}$$

where Eq. (3) comes from one structure and Eq. (4) from one particle. If all particles are uniform and have the same radius, it is found that not all of the symmetric structures satisfy the requirements shown in Eqs. (3) and (4), and only the triangular, rectangular, and hexagonal structures could exist in the system. Therefore, it can be concluded that the sintered particles investigated here consist of only these three structures. It is noticed that there are several structures around one particle as shown in Fig. 3. List all possible arrangements of these structures and consider that each group of those structures has the same possibility. The percentage of each structure could be determined. Use A, B, C to represent triangular, rectangular, and hexagonal structures, respectively. Table 1 lists all the possible groups of structures and the number of arrangements for each group. From Table 1, it could be found that the percentages for the triangular, rectangular, and hexagonal structures are 45%, 28%, and 27%, respectively. Using Eq.
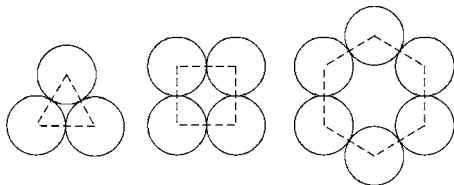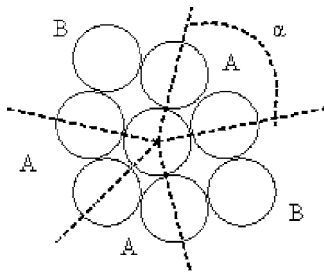

Fig. 2   Some stable structures

Fig. 3   Angles and structures around one particle

Table 1   Possible groups and arrangements

Group	6A	4B	3C	3A+2B	2A+2C	4A+1C	1A+2B +1C	Total
Arrangements	1	1	1	2	2	1	2	10

(2) the minimum meniscus radii for these structures can be found as $0.103r$, $0.273r$, and $0.654r$, for the triangular, rectangular, and hexagonal structures, respectively. The average minimum meniscus for the sintered particles with a uniform radius can be found by

$$r_{c,e} = 2\frac{A_{\text{gap},A} \cdot 45\% + A_{\text{gap},B} \cdot 28\% + A_{\text{gap},C} \cdot 27\%}{P_{\text{gap},A} \cdot 45\% + P_{\text{gap},B} \cdot 28\% + P_{\text{gap},C} \cdot 27\%} = 0.443r \tag{5}$$

where r is the particle radius. The minimum meniscus radius of $0.443r$ derived here agrees well with $0.41r$ cited by Ferrell and Alleavitch [10], which has been accepted by most heat pipe textbooks [2,3,9].

If the size of sintered particles is not uniform, the method described above obviously cannot be used to predict the minimum meniscus radius. To solve this problem, draw a long line linking any two particles, as shown in Fig. 4. The line will pass through all of the possible structures, which could be represented by the angles and their relative edges, as shown in Fig. 4. This can transform a two-dimensional (2D) problem into one dimensional.

Considering such a "long-enough" line, it could be found that the number of particles along it is determined by the structures. More structures need more particles to be included. The straight line starts from the center of one particle in one structure and ends at the center of one particle in another structure. The angle, θ, between the long line and the center connecting line of the first two particles, as shown in Fig. 4, is called the start angle, which would also influence the number of particles along the long line. However, the start angle and structures are independent of each other. With the variation of start angle, there exists a minimum number, N_0, of particles near the long line, which is directly determined by the structures and could be used to represent the structures. Hence, the number of particles along this long line is a function of start angle θ and N_0, which can be expressed as

$$N = F(N_0, \theta) = f(\theta)N_0 \tag{6}$$

In Fig. 4 there is another interconnected line connecting the center of particles which are near the straight line. As discussed above, this interconnected line contains all of the possible angles and edges of structures with their percentage. Angles formed on one side of the straight line are indicated by $\alpha_1, \alpha_2, \alpha_3, \ldots, \alpha_{l-1}$, and α_l and those formed on another side of the straight line by $\beta_1, \beta_2, \beta_3, \ldots, \beta_{m-1}$, and β_m.

The total length of the straight line can be found as

$$L = \sum_{n=1}^{N} \left[R_0 \cos\theta + R_n \cos\left(\theta - \sum \alpha_l + \sum \beta_m\right)\right]$$

$$= \sqrt{M_1^2 + M_2^2}\cos(\theta + \varphi) \tag{7}$$

where

$$M_1 = R_0 + \sum_{n=1}^{N}\left[R_n \cos\left(-\sum \alpha_l + \sum \beta_m\right)\right] \tag{8}$$

$$M_2 = \sum_{n=1}^{N}\left[R_n \sin\left(-\sum \alpha_l + \sum \beta_m\right)\right] \tag{9}$$

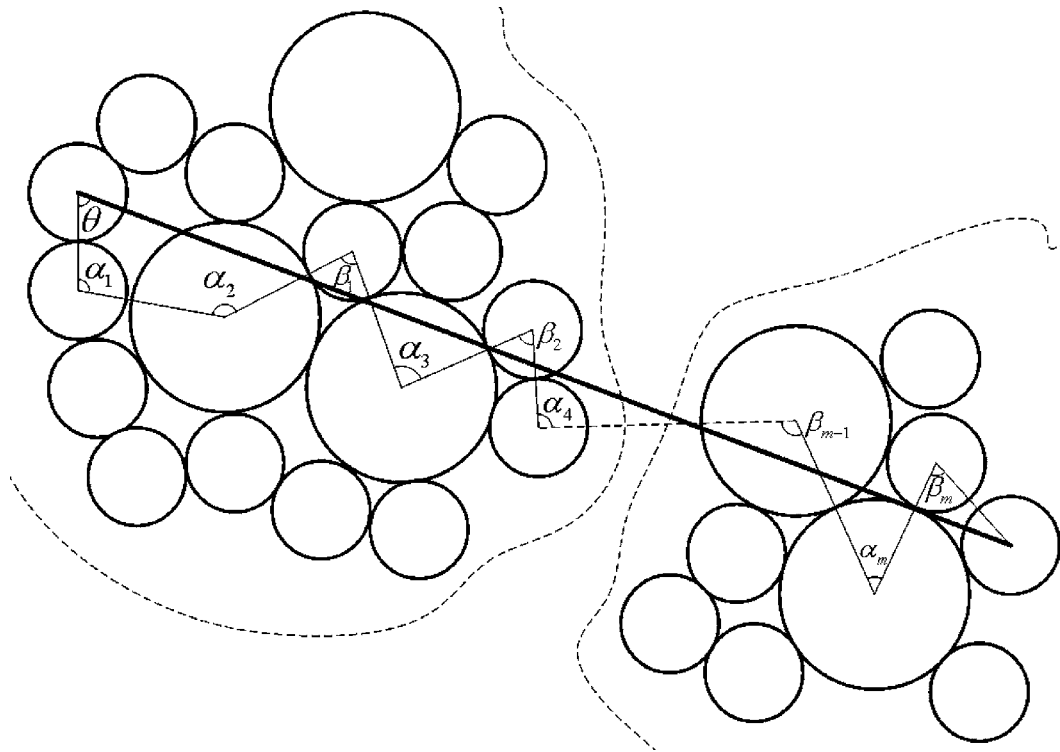$$\cos\varphi = M_1/\sqrt{M_1^2 + M_2^2}$$

Fig. 4 Possible structures in one layer of mixed particles

$$\sin \varphi = M_2/\sqrt{M_1^2 + M_2^2} \qquad (10)$$

Considering Eq. (6), the length of the straight line could be expressed as

$$L = \sqrt{f(\theta)N_0 \left[\sum X_i R_i^2 + g(R,\alpha,\beta)/N \right]} \cos(\theta + \varphi) \qquad (11)$$

where $g(R,\alpha,\beta)$, the sum of $N(N-1)$ terms, is the function of edges and angles.

Imagine one layer of particles placed on a large rectangle surface and each side long enough, where the area of the minimum gaps trapped by particles is equal to the difference between the rectangle area and the total area of all of the particles. The total length of perimeters of all the minimum gaps trapped by particles in the rectangle is equal to the total length of perimeters of all the particles. Then, the minimum meniscus radius can be found as

$$r_{c,e} = 2A_{\text{gap}}/P_{\text{gap}} = \frac{L_1 L_2 - \pi N_0^2 f(\theta) f(\pi/2 - \theta) \sum (Y_j r_j^2)}{\pi N_0^2 f(\theta) f(\pi/2 - \theta) \sum (Y_j r_j)} \qquad (12)$$

Equation (12) can be used to calculate the minimum meniscus radius occurring in the sintered particles with different sizes.

For example, when the sintered particles consist of two kinds of particles with diameters of 100 μm and 50 μm, respectively, with these given particle sizes, the total length of the straight line could be simplified as

$$L \approx k f(\theta) N_0 \sqrt{\sum X_i R_i^2} \qquad (13)$$

where the constant k considers the angle effect. Then Eq. (12) can be expressed as

$$r_{c,e} = \frac{k^2 \sum (X_i R_i^2) - \pi \sum (Y_j r_j^2)}{\pi \sum (Y_j r_j)} \qquad (14)$$

The constant k can be determined from the sintered particles with the uniform size, which can be found as

$$k^2 = 1.1333 \qquad (15)$$

Figure 5 illustrates the minimum meniscus radius variation for mixed particles with diameters of 100 μm and 50 μm. As shown, the predicted minimum meniscus radius is smaller than the average one, which can directly answer the question why the sintered mixed particles can produce a higher capillary pumping capability in a heat pipe.

Conclusions

A mathematical model predicting the minimum meniscus radius occurring in the sintered particles with different sizes is developed. For uniform-size particles, the minimum meniscus radius is found to be equal to $0.443r$. When the sintered particles are mixed with different sizes, the minimum meniscus radius can be predicted by
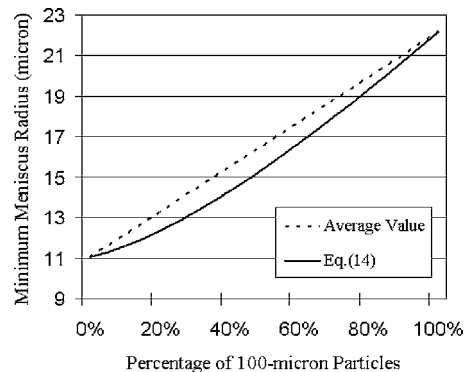

Fig. 5 Minimum meniscus radius predicted by Eq. (14)

$$r_{c,e} = 2A_{\text{gap}}/P_{\text{gap}} = \frac{k^2 \sum (X_i R_i^2) - \pi \sum (Y_j r_j^2)}{\pi \sum (Y_j r_j)}$$

The investigation conducted here can result in a better understanding of heat transfer mechanisms occurring in a high-heat-flux heat pipe.

Nomenclature

A_{gap} = area of the gap
E = potential energy
k = constant
L = length of the line
M = number of angles around one particle
N = number of the edges in one structure in Eq. (2); number of particles
$\Delta p_{c,\max}$ = maximum capillary pressure drop
P_{gap} = perimeter of the gap
r = radius of particle
$r_{c,e}$ = effective porous radius
R = edge length of structure
S = total area
X = percentage of the edge of the structure
Y = percentage of particle

Greek Symbols

α = structure angles in Eqs. (2) and (3); angles upward
β = angles downward
θ = start angle

σ = surface tension

Subscripts

i = structure edges
j = particle radius
l = upward angles
m = structure in Eq. (2); downward angles
n = particles along the line
x = angles in one structure
y = angles around one paritcle

References

[1] Hanlon, M. A., and Ma, H. B., 2003, "Evaporation Heat Transfer in Sintered Porous Media," ASME J. Heat Transfer, Vol. **125**, August, pp. 644–653.
[2] Peterson, G. P., 1994, *An Introduction to Heat Pipe*, Wiley, New York.
[3] Faghri, A., 1995, *Heat Pipe Science and Technology*, Taylor & Francis, New York.
[4] Harr, M. E., 1977, *Mechanics of Particulate media: A Probabilistic Approach*, McGraw-Hill, New York, Chap. 1.
[5] Graton, L. C., and Fraser, H. J., 1935, "Systematic Packing of Spheres With Particular Relation to Porosity and Permeability," J. Geol., **43**(8), pp. 785–909.
[6] Rodriguez, J., Allibert, C. H., and Chaix, J. M., 1986, "A Computer Method for Random Packing of Spheres of Unequal Size," Powder Technol., **47**, pp. 25–33.
[7] Yang, R. Y., Zou, R. P., and Yu, A. B., 2003, "Effect of Material Properties on the Packing of Fine Particles," J. Appl. Phys., **94**, pp. 3025–3034.
[8] Kurashige, M., Mishima, M., and Imai, K., 1999, "Simulated Effective Thermal Conductivity of Sintered, Randomly Packed Sphere and Statistical Structure of Packing," J. Therm. Stresses, **22**, pp. 713–733.
[9] Chi, S. W., 1976, *Heat Pipe Theory and Practice*, McGraw-Hill, New York.
[10] Ferrell, J. K., and Alleavitch, J., 1970, "Vaporization Heat Transfer in Capillary Wick Structures," Chem. Eng. Prog., Symp. Ser., **66**(102), pp. 82–91.
[11] Luikov, A. V., 1980, "Heat and Mass Transfer," *Transport Phenomena in Capillary-Porous Bodies*, Mir, Moscow, Chap. 5.

Analysis of Solid–Liquid Phase Change Under Pulsed Heating

Shankar Krishnan

Jayathi Y. Murthy

Suresh V. Garimella
e-mail: sureshg@purdue.edu

Cooling Technologies Research Center,
School of Mechanical Engineering,
Purdue University,
West Lafayette, IN 47907-2088

Solid/liquid phase change occurring in a rectangular container with and without metal foams subjected to periodic pulsed heating is investigated. Natural convection in the melt is considered. Volume-averaged mass and momentum equations are employed, with the Brinkman–Forchheimer extension to Darcy's law used to model the porous resistance. A local thermal nonequilibrium model, assuming equilibrium melting at the pore scale, is employed for energy transport through the metal foams and the interstitial phase change material (PCM). Separate volume-averaged energy equations for the foam and the PCM are written and are closed using a heat transfer coefficient. The enthalpy method is employed to account for phase change. The governing equations for the PCM without foam are derived from the porous medium equations. The governing equations are solved implicitly using a finite volume method on a fixed grid. The coupled effect of pulse width and natural convection in the melt is found to have a profound effect on the overall melting behavior. The influence of pulse width, Stefan number, and Rayleigh number on the temporal evolution of the melt front location and the melting rate for both the cases with and without metal foams is investigated.
[DOI: 10.1115/1.2430728]

Keywords: heat transfer, phase change, porous media, natural convection, nonequilibrium, enhancement

Introduction

Solid–liquid phase change [1,2] and cyclic melting and freezing are frequently encountered in latent heat storage systems and have attracted considerable attention for thermal energy storage applications [1]. In these applications, energy is stored in the form of latent heat of fusion during melting, and is recovered during freezing. Detailed reviews of melting and freezing phenomena can be found in Refs. [2–4]. In many electronics applications, periodic thermal transients may occur; examples include electronic power steering controllers, power semiconductors for motor drives and antilock braking controllers.

Though there is extensive literature on solid–liquid phase change [5,6], periodic pulse heating of phase change materials for electronics cooling has received less attention. Periodic melting and freezing in latent heat storage systems for space applications have been studied, and details of the system performance for these applications are available in Refs. [7,8]. However, the frequency of pulses investigated in these applications is usually very low.

A few studies have considered transient phase change for electronics cooling. Lu [9] reported a study of phase-change cooling with emphasis on suppressing the junction temperature rise due to a single high-power pulse. This study also provided design guidelines for high-power electronic packages. Evans et al. [10] analyzed power electronic packages and provided design guidelines relating the materials, geometry, power input, and junction temperature for steady-state conditions and transient pulses. Pal and Joshi [11] investigated numerically the melting of a phase change material (PCM) under transient variations in the power input for passive thermal control of electronic modules.

Commonly used PCMs such as paraffins have very low thermal diffusivity and are not suitable for transient thermal management applications. In order to improve their effective thermal conductivity and enhance heat transfer rates, internal fins or metal foams have been introduced into the PCM [12–14]. Vesligaj and Amon [15] investigated passive thermal control of portable electronics using PCMs with thermal conductivity enhancers under unsteady thermal workloads. Alawadhi and Amon [16] also studied phase change inside enclosures with metal fins to enhance heat transfer for transient applications. Baker et al. [17] performed an analysis of the thermal control performance of a nonmetallic PCM with metallic fins under periodic heating. They reported significant temperature suppression in periodic heat generating systems with little or no weight penalties for space applications. Similarly, Pal and Joshi considered thermal control of heat sources using metal foams [18]. Harris et al. [19] presented an approximate theoretical model to analyze the phase change process in a porous medium. Assuming equilibrium melting at the pore scale, a parametric study based on a semi-heuristic conduction model was formulated. The conditions for the existence of local thermal equilibrium were explored.

The objective of the present work is to investigate the problem of solid–liquid phase change occurring in a rectangular enclosure under pulsed heating from one side. The effect of incorporating metal foams in the enclosure is considered. The difference in response time between systems with and without metal foam has important implications for the thermal management of transient energy pulses [20]. If the time scale of the energy pulse is short compared to the response time of the heat sinking system, local overheating is possible. The presence of a metal foam decreases the response time substantially, and thus PCM systems with metal foams perform significantly better than those without metal foams. The objective of the present study is to investigate the influence of pulse width, Stefan number, and Rayleigh number on the temporal evolution of the melt front location (melting rate) and heat transfer from the active wall with and without metal foams. This work is a follow up to previous studies on metal foams by the authors [13,14], in which a constant heat input was provided to the domain with and without metal foams being present.

Mathematical Model

A schematic diagram of the problem under investigation is shown in Fig. 1. The square domain of side H encloses the metal foam and PCM. The vertical wall on the right is maintained at a constant temperature T_C. The top and bottom walls are adiabatic. The metal foam and the PCM are at equilibrium at temperature T_C^*, initially. At time $\tau = 0$, a rectangular pulsed temperature condition as shown in Fig. 1 is applied to the vertical wall on the left. The applied temperature alternates between the hot wall temperature, $T_H > T_{\text{melt}}$, and the cold wall temperature, $T_C < T_{\text{melt}}$. The thermophysical properties of the solid metal foam and the PCM are assumed to be constant over the range of temperatures considered. The liquid PCM is assumed to be incompressible, Newtonian, and subject to the Boussinesq approximation. Volume change due to phase change is ignored, as are thermal dispersion effects. Using the dimensionless variables

Fig. 1 Schematic diagram of the problem under investigation

Fig. 2 Predicted temporal evolution of melt volume fraction for two different Rayleigh numbers $(Ra=10^6, 10^8)$, Ste=1, Pr =50, and $\tau_w=0.01$
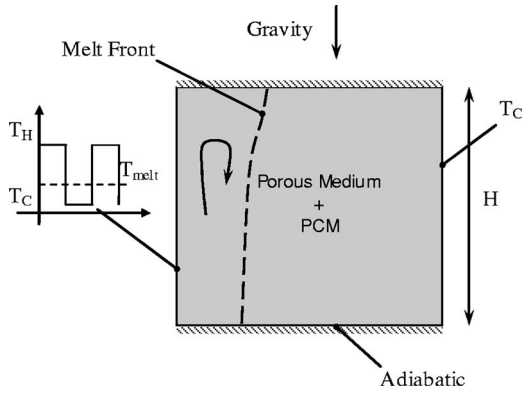
$$\xi = \frac{x}{H}; \quad \eta = \frac{y}{H}; \quad \tau = \frac{t\alpha_f}{H^2}; \quad U = \frac{uH}{\alpha_f}; \quad P = \frac{pH^2}{\rho_f \nu_f \alpha_f}$$

$$T_s^* = \frac{(T_m - T_c)}{(T_H - T_C)}; \quad T_f^* = \frac{(T_f - T_C)}{(T_H - T_C)}; \quad T^* = \frac{(T - T_C)}{(T_H - T_C)}$$

the dimensionless equations governing the conservation of mass, momentum and energy are

$$\nabla \cdot \mathbf{U} = 0 \tag{1}$$

$$\frac{1}{\text{Pr}}\left(\frac{1}{\varphi}\frac{\partial \mathbf{U}}{\partial \tau} + \frac{1}{\varphi^2}(\mathbf{U} \cdot \nabla)\mathbf{U}\right) = -\nabla P + \frac{1}{\varphi}\nabla^2 \mathbf{U} - \left(\frac{1}{\text{Da}^2} + \frac{F}{\text{Pr} \cdot \text{Da}}|\mathbf{U}|\right)\mathbf{U}$$
$$+ \text{Ra}\, T_f^* \frac{\mathbf{g}}{|\mathbf{g}|} \tag{2}$$

$$(1-\varepsilon)\Omega\frac{\partial T_m^*}{\partial \tau} = (1-\varepsilon)\lambda\nabla^2 T_m^* - \text{Nu}_i(T_m^* - T_f^*) \tag{3}$$

$$\frac{\partial T_f^*}{\partial \tau} + (\mathbf{U} \cdot \nabla)T_f^* = \varepsilon\nabla^2 T_f^* - \frac{\varepsilon}{\text{Ste}}\frac{\partial \gamma}{\partial \tau} - \text{Nu}_i(T_f^* - T_m^*) \tag{4}$$

In the above equations, F is the inertial coefficient; γ is the fraction of liquid in the PCM $(\gamma = V_l/V_f)$; and φ is the fraction of liquid PCM in the given volume $(\varphi = \gamma\varepsilon)$. The energy equations are closed using a heat exchange term. Details of the mathematical model can be found in Refs. [13,14]. A detailed discussion of the numerical methods employed for solving Eqs. (1)–(4), as well as code validation, and grid- and time-step independence are also available in Refs. [13,14] and are not repeated here. A nonuniform grid of 102×102 is employed for all the computations.

The inertial coefficient, F, for flow through metal foams is 0.068 [21]. The melting point of the PCM is maintained constant at $T_{\text{melt}}^* = 0.3$ for the calculations presented below. For metal foams, a constant porosity of 0.8 is used for all the computations. For organic PCMs (Pr > 25) undergoing phase change in porous enclosures, the velocities encountered are small ($\sim O(10^{-3})$ m/s or less) for $\text{Ra Da}^2 \le 10^4$. As the system is expected to be largely conduction dominated, it is critical to establish the diffusion limit for the interstitial heat transfer coefficients. The interstitial Nusselt number based on the pore diameter used for all the calculations is 5.9, based on the expression of Morgan [22] for flow over cylinders at the conduction limit. The details of the calculations and the effect of different interstitial Nusselt numbers on the heat transfer characteristics of metal foam-integrated PCM enclosures are available in Ref. [14]. For the periodic heat input studied here, two different pulse widths τ_w are chosen corresponding to: (i) the time for natural convection to just set in ($\tau_w \sim 9\,\text{Ra}^{-1/2}/\text{Ste}$) [5]; and (ii) the time for the entire PCM to melt completely.
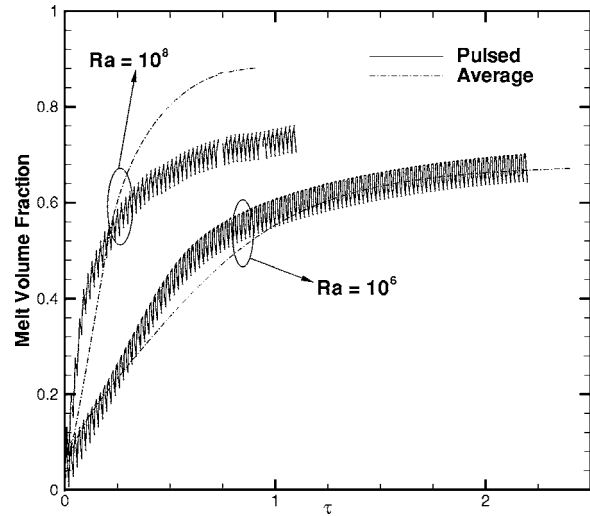
Results and Discussion

Melting of a pure phase change material (without foam) is first considered, followed by an investigation of the effects of the presence of a foam. The Prandtl number of the PCM material is 50, and the nondimensional melting temperature is fixed at 0.3. Further, the solid- and liquid-phase thermophysical properties of the PCM are assumed to be equal and constant. For the pure materials, the nondimensional pulse widths (τ_w) analyzed are 0.01 and 0.22. For a constant left wall temperature (T_H^*), the melting process in a rectangular enclosure follows a sequence of four regimes, each characterized by a unique Nusselt number [5,14]: (1) conduction $(\text{Nu} \sim ((\text{Ste}_H\tau)^{-1/2}))$; (2) mixed conduction plus convection $(\text{Nu} \sim ((\text{Ste}_H\tau)^{-1/2} + \text{Ra}(\text{Ste}_H\tau)^{3/2}))$; (3) convection $(\text{Nu} \sim \text{Ra}^{1/4})$, and (4) shrinking solid regimes. Here, $\text{Ste}_H = C_{pf}(T_H - T_{\text{melt}})/\Delta H$, and is based on the temperature difference $(T_H - T_{\text{melt}})$ and the PCM's specific heat, C_{pf}, which is assumed to be the same for both solid and fluid phases. Detailed discussions of the four regimes are given in Refs. [5,14]. It should be noted that the Nusselt number is time dependent in the conduction and conduction-plus-convection regime, but is time invariant during the quasi-steady convection regime. For boundary temperatures oscillating above and below the melting temperature of the PCM, melting occurs during the hot period followed by solidification during the cold period. If the pulse width is shorter than the "steady-state" time required for melting, then the melting process will not evolve through all the four different regimes.

Figure 2 shows the predicted PCM melt volume fraction at two different Rayleigh numbers, for a pulse width of 0.01. The Stefan number in the plots in this work is based on the melting period, i.e., $\text{Ste}_H = C_{pf}(T_H - T_{\text{melt}})/\Delta H$. The phase change process for Ra $= 10^6$ and 10^8 reaches a periodic steady-state over a nondimensional time of approximately 2 and 0.5, respectively. The time for convection to set in during the melting process is given by $9\,\text{Ra}^{-0.5}/\text{Ste}$ [5]; this time scale is derived assuming that the initial temperature of the domain is at the melting point.

For cases in which $\tau_w < 9\,\text{Ra}^{-0.5}/\text{Ste}$, i.e., for Ra $= 10^6$, the process is expected to be conduction dominated. For oscillating boundary conditions with high-frequency pulsing, the boundary layer response in conduction-dominated flow is confined to a thin region adjacent to the surface. The thickness of the region over which the pulse is felt is $\sim (\alpha_{ef}/f)^{1/2}$ in which f is the frequency of the pulses and $\alpha_{ef} = k/(\rho(C_p)_{ef})$ where $(C_p)_{ef} \sim \Delta H/\Delta T$. In non-
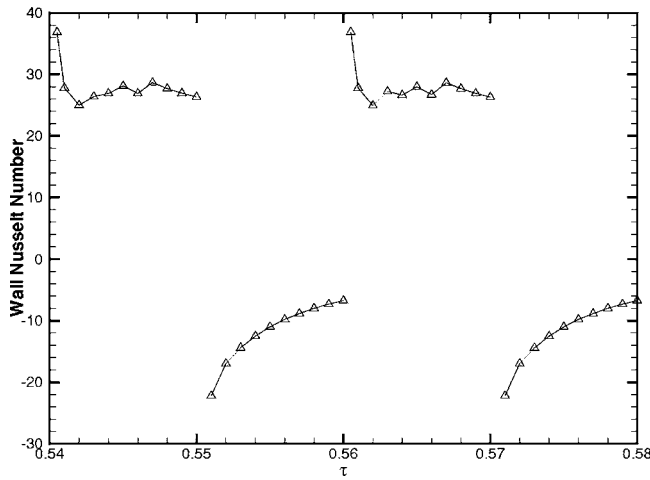
Fig. 3   Predicted wall Nusselt number for a Ra=10⁸, Ste=1.0, Pr=50, and τ_w=0.01 at periodic steady state

Fig. 4   Temporal evolution of predicted melt volume fraction for two different Stefan numbers (0.1 and 1.0) and for Ra=10⁸, Pr=50, and τ_w=0.01

dimensional terms, this length scale may be written as $(\alpha \mathrm{Ste}/f)^{1/2}/H$, where Ste takes appropriate values during the hot and cold periods. Since both the melting and solidification processes are conduction dominated for Ra=10^6, it is expected that an average amount of energy, corresponding approximately to a steady boundary temperature of $(T_H^*+T_C^*)/2$, enters the domain in each cycle. This "averaged" behavior is best illustrated by comparing the low-Ra behavior with the transient response of an enclosure with the left wall raised to $(T_H^*+T_C^*)/2$ at τ=0 and held at this constant temperature. The melt volume fraction for this case is shown in Fig. 2 and is labeled "average." The pulsed case at Ra=10^6 follows the "average" case closely.

In contrast, for Ra=10^8, the pulse width $\tau_w > 9\ \mathrm{Ra}^{-0.5}/\mathrm{Ste}$ and the phase change process enters a quasi-steady convection regime in which the melt volume fraction scales as $\mathrm{Ra}^{0.25}\mathrm{Ste}\ \tau$. As seen in Fig. 2, the correspondence between the net heat input into the domain in the pulsed case and that for a fixed average boundary temperature ("average" case) is no longer present when there is significant convection. It should be noted that for the average cases, the actual Rayleigh and Stefan numbers take half the values of the equivalent pulsed cases.

Figure 3 shows the predicted wall Nusselt number once a periodic steady state is achieved for Ra=10^8, Ste=1.0, and τ_w=0.01. The wall Nusselt number is calculated using the expression

$$\mathrm{Nu} = \frac{hH}{k_f} = (-1)\int_0^1 \left(\frac{\partial T^*}{\partial \xi}\right)_{\xi=0} d\eta \qquad (5)$$

The heat extraction period in each pulse is denoted by negative Nusselt numbers. At τ=0, the Nusselt number is theoretically infinite, and this is also true at the instant when the left wall temperature changes from hot to cold (this is represented in the plots as a break in the Nusselt number curves). As the melting process evolves, as discussed before, it follows a sequence of distinct regimes characterized by unique Nusselt numbers. It should be noted that the Nusselt number curves (at a periodic steady state) during the hot periods of the pulsed boundary temperature are very similar to those for a constant boundary temperature as discussed in Ref. [14] for Ra=10^8 and Ste=1.0. When the temperature on the left wall changes from T_H^* to T_C^*, solid begins to grow from the left wall (at the rate of $\tau^{1/2}$ where $\mathrm{Nu} \propto \tau^{-1/2}$ [3]) until the beginning of the next period, at which time the cycle is repeated.

The effect of Stefan number is brought out in Fig. 4 for Ra=10^8. Here again, the pulse width τ_w is 0.01. If the imposed temperature boundary conditions were constant and not pulsed, the Stefan number would be inversely proportional to the time taken
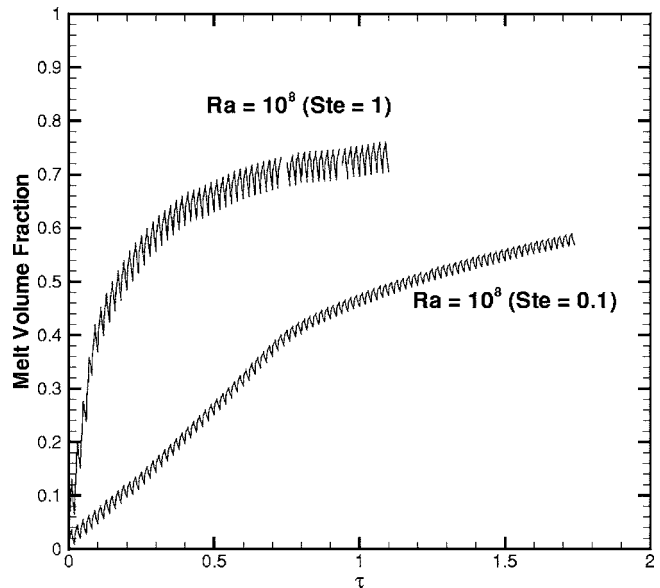
to reach steady state, i.e., $\tau_{ss} \propto \mathrm{Ste}^{-1}$. With an oscillating temperature boundary condition, the change in Stefan number affects the average melt volume fraction for a given cycle (in both the hot and cold periods) and also the total dimensionless time to reach a periodic steady state. It may be recalled that the process is conduction dominated during both the melting and resolidification periods for Ste=0.1. The same is not true for Ste=1.0 in this case, natural convection is established during the melting period. Thus it can be seen that there is a strong dependence of the melt volume fraction on the Stefan number.

Figure 5 shows the effect of pulse width variation from τ_w=0.01 and 0.22, for Ra=10^8, and Ste=1.0. For a nondimensional pulse width τ_w=0.22, the phase change process establishes a steady state even before the end of the pulse. This can be clearly seen in Fig. 5. It should be noted that the pulse width affects the total melted material during a given cycle and also the system periodic steady-state time scale.
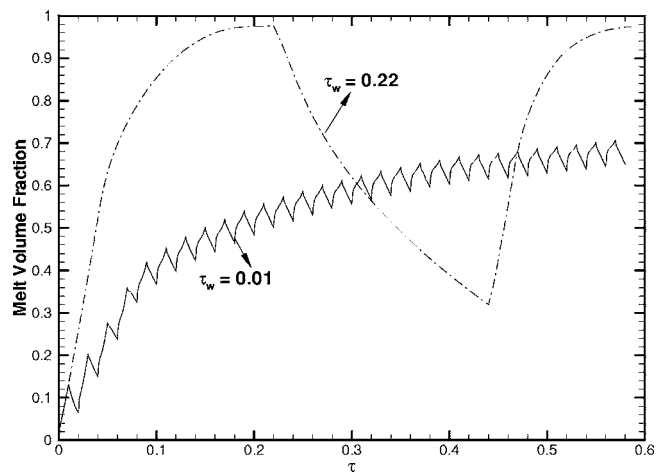

Fig. 5   Predicted temporal evolution of the melt volume fraction for Ra=10⁸, Ste=1.0, Pr=50, and two different pulse widths (τ_w=0.01 and 0.22)
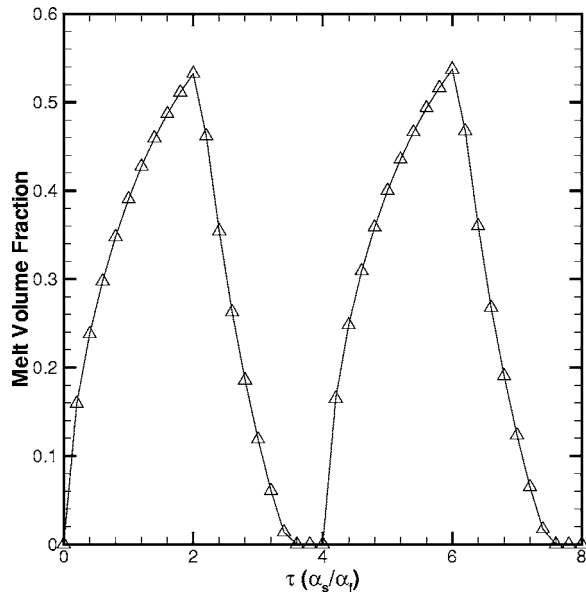
Fig. 6 Predicted melt volume fraction for Ra=10⁶, Pr=50, Da =10⁻², Ste=1.0, and τ_w=0.002

Fig. 7 Predicted wall Nusselt number for Ra=10⁶, Pr=50, Da =10⁻², Ste=1.0, and τ_w=0.002

Metal Foams. Metal foams impregnated with PCMs are considered next. The porosity of the metal foam is held constant at 0.8 with a pore size (d/H) of 0.0135. The ratio of the average ligament diameter of the foam to the mean cell size is 0.1875, with the average ligament diameter being 0.36 mm. The ratio of the metal foam-to-PCM thermal conductivity (λ) is 1000, while the ratio of thermal capacitances (Ω) is unity. The nondimensional melting temperature of the PCM is fixed at 0.3. The metal foam–PCM system steady state is dictated by the time for heat exchange between the metal foam and the PCM, $(1-\varepsilon)\Omega/\mathrm{Nu}_i$ [14]. As long as the heat exchange time is short compared to the response times of the two phases (PCM and metal foam), the two phases develop together in a coupled manner and the time to steady state is determined by the faster phase [14]. Therefore, it is expected that the time to reach steady state for the foam–PCM system is dictated by the metal foam response time ($\sim\Omega/\lambda$) due to the short heat exchange time between the two phases. A detailed discussion of the foam–PCM composite time scales and the effect of interstitial Nusselt number and temperature fields on the heat transfer characteristics for a constant temperature boundary condition can be found in Ref. [14]. The response time for the metal foam–PCM composite is faster by $O(10^{-3})$ than the PCM-only case discussed earlier. After initial computational experiments with constant temperature boundary conditions (not discussed here), it was found that the metal foam–PCM system reached a steady state at a dimensionless time of 0.008. Hence, the pulse widths employed in the following discussions, 0.002 and 0.008, are much shorter than for the PCM-only cases discussed before.

Figure 6 shows the melt volume fraction as a function of $\tau(\alpha_s/\alpha_f)$ for Ra=10⁶, τ_w=0.002, Ste=1, ε=0.8, Pr=50, Da =10⁻², and interstitial Nusselt number of 5.9. Since metal foam is the dominating scale, the dimensionless time is renormalized in terms of thermal diffusivity of the foam α_s. When $\mathrm{Nu}_i > (1-\varepsilon)\lambda$, the interphase heat exchange time is shorter than the diffusion time for metal foam (which is the fast-response phase) and the system steady state is dictated by the metal foam time scale. In the presence of the foam during the melting period, convective flow in the melt is impeded due to low values of the parameter Ra Da²(=100). Conduction-dominated profiles result, limiting the maximum possible melt volume fraction to $(1-T^*_{\mathrm{melt}})$ [14], i.e., both the temperature profile in the metal foam and the PCM are
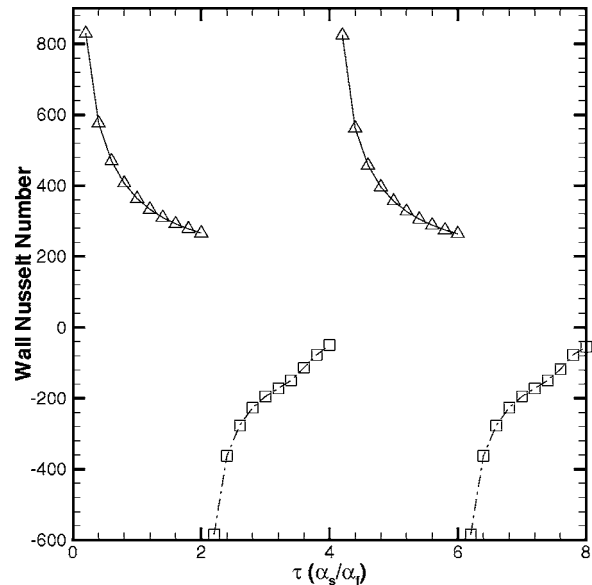
straight lines and the melt volume fraction is thus the region $T^* > T^*_{\mathrm{melt}}$. As expected for $\tau_w < \Omega/\lambda$, the melt volume fraction is less than $(1-T^*_{\mathrm{melt}})$. During the cold pulse period, the system steady state again is dictated by the metal foam, and the PCM foam cools off before the end of the pulse, i.e., the system reaches a periodic steady state much faster than the no-foam case discussed, by almost $O(10^{-2})$.

Figure 7 shows the Nusselt number at the hot wall for the case considered in Figure 6. The Nusselt number is defined as

$$\mathrm{Nu}_{\mathrm{total}} = \mathrm{Nu}_m + \mathrm{Nu}_f = -(1-\varepsilon)\lambda \int_0^1 \left(\frac{\partial T_m^*}{\partial \xi}\right)_{\xi=0} d\eta$$

$$-\varepsilon \int_0^1 \left(\frac{\partial T_f^*}{\partial \xi}\right)_{\xi=0} d\eta \qquad (6)$$

It should be noted that in Fig. 6, that the x axis is plotted in terms of $\tau(\alpha_s/\alpha_f)$. Initially, the heat transfer from the wall is large, but it drops rapidly as both the metal and PCM heat up. In the presence of foam, heat transfer is conduction dominated, and at steady state, the dimensionless temperature gradient at the wall for both metal foam and PCM is unity. Hence, for a constant temperature boundary condition, the Nusselt number asymptotes (drops) to $\mathrm{Nu}_{\mathrm{total}} \sim \varepsilon + (1-\varepsilon)\lambda$ at steady state. Since $\tau_w < \tau_{\mathrm{ss}}$, $\mathrm{Nu}_{\mathrm{total}}$ is higher than $\varepsilon + (1-\varepsilon)\lambda$. It can be seen from Fig. 7 that $\mathrm{Nu}_{\mathrm{total}} \to 0$ as the cold part of the cycle progresses, since the left and right walls are both subjected to T_C^* during this period. It should be noted that the Nusselt number for the case with foam is higher by an order of magnitude compared to the no-foam case discussed earlier.

The pulses of longer duration, in which the pulse width is chosen such that the phase change process reaches a steady state before the end of the hot period, are considered next. Figure 8 shows the melt volume fraction as a function of $\tau(\alpha_s/\alpha_f)$ for Ra =10⁶, τ_w=0.008, Ste=1, ε=0.8, Pr=50, Da=10⁻², and interstitial Nusselt number of 5.9. Since the process is conduction dominated, the system reaches a periodic steady state as discussed for the previous case. The increase in pulse width increases the amount of melted PCM during the hot period. As discussed before, the melt volume fraction asymptotes to $(1-T^*_{\mathrm{melt}})$. During the cold pulse period, the PCM-foam system cools off before the end of the
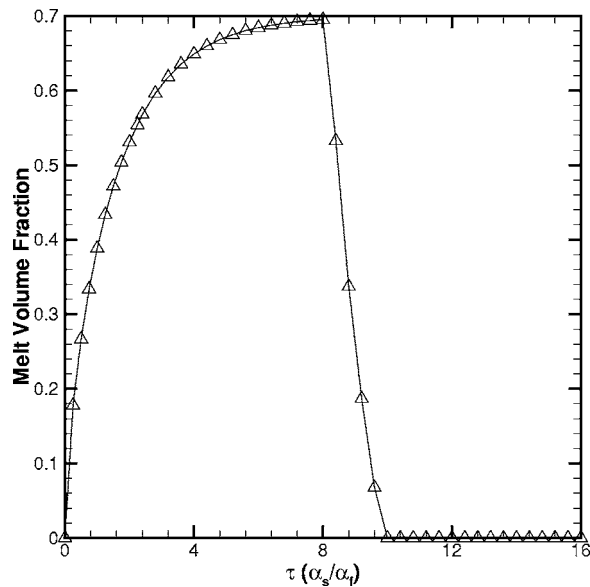
Fig. 8 Predicted melt volume fraction for Ra=10^6, Pr = 50, Da=10^{-2}, Ste=1.0, and τ_w=0.008

pulse.

When the Rayleigh number is increased from 10^6 to 10^8 (results not shown), the melt volume fraction at periodic steady state increases from 0.7 to 0.74; however, the overall behavior is similar to that for Ra=10^6 as discussed above. Similarly, a decrease in Stefan number from 1.0 to 0.1 with Ra=10^6 (results not shown) decreases the rate of melting due to the thermal inertia associated with phase change and the concomitant relative increase in the latent heat of fusion.

Conclusions

Solid/liquid phase change occurring in a rectangular container with and without metal foams under periodic pulsed heating is investigated. For the case of a pure PCM without a metal foam, the combined effect of pulse width and natural convection in the melt is found to have a profound effect on the overall melting behavior. For a pulse width $\tau_w < \text{Ra}^{-0.25}/\text{Ste}$, the phase change process exhibits an averaged behavior corresponding to steady wall heating at the mean wall temperature. For $\tau_w > \text{Ra}^{-0.25}/\text{Ste}$, natural convection effects becomes important and averaged behavior is not recovered.

For the metal foam–PCM composite case investigated, the heat transfer process is conduction dominated, irrespective of the pulse width value. The response time for the metal foam–PCM composite is faster by $O(10^{-3})$ than the PCM-only case. Since this time scale is relatively short, a periodic steady state is established rapidly in PCM-impregnated metal foams.

Acknowledgment

Nomenclature

C_p = isobaric specific heat, J kg^{-1} K^{-1}
Da = Darcy number ($K^{1/2}/H$)
d = mean pore diameter (m)
f = frequency (s^{-1})
F = inertial coefficient
g = gravity vector (ms^{-2})

H = height of the enclosure (m)
h_v = volumetric heat transfer coefficient (W m^{-3} K^{-1})
K = permeability (m^2)
k = thermal conductivity (W m^{-1} K^{-1})
k_e = equivalent thermal conductivity (W m^{-1} K^{-1})
Nu$_i$ = interstitial Nusselt number ($h_v H^2/k_f$)
Nu$_{i,d}$ = interstitial Nusselt number based on pore diameter
P = pressure (N m^{-2})
Pr = Prandtl number (ν_f/α_f)
Ra = Rayleigh number ($g\beta H^3(T_H-T_C)/(\alpha_f\nu_f)$)
Ste = Stefan number ($(C_p)_f(T_H-T_C)/\Delta H$)
T = temperature (K)
t = time (s)
U = velocity vector (ms^{-1})
V = volume (m^3)
u,v = velocity in x and y directions (ms^{-1})
x,y = Cartesian coordinates

Greek Symbols

α = thermal diffusivity (m^2 s^{-1})
β = coefficient of thermal expansion (K^{-1})
ΔH = enthalpy of freezing/melting (J kg^{-1})
ε = Porosity
γ = fraction of liquid melt in the PCM
η = dimensionless y coordinate
φ = fraction of liquid PCM (=$\varepsilon\gamma$)
λ = conductivity ratio of foam and PCM (k_m/k_f)
μ = dynamic viscosity (N s m^{-2})
ρ = density (kg m^{-3})
τ = dimensionless time
ν = kinematic viscosity (m^2 s^{-1})
ξ = dimensionless x coordinate
Ω = volumetric heat capacity ratio of foam and PCM ($(\rho C_p)_m/(\rho C_p)_f$)

Subscripts

C = cold
d = diameter
ef = effective fluid property
f = PCM
H = hot; height of enclosure
l = liquid
p = pore or particle
m = metal foam
s = solid (PCM)
ss = steady state
w = pulse width

Superscripts

$*$ = dimensionless quantity

References

[1] Humphries, W. R., and Griggs, E. L., 1974, *A Design Handbook of Phase Change Thermal Control and Energy Storage Devices*, NASA, Greenbelt, MD.
[2] Yao, L. S., and Prusa, J., 1989, "Melting and Freezing," Adv. Heat Transfer, **19**, pp. 1–95.
[3] Alexiades, V., and Solomon, A. D., 1993, *Mathematical Modeling of Melting and Freezing Processes*, Hemisphere, Washington, D.C.
[4] Viskanta, R., 1991, "Phase Change Heat Transfer in Porous Media," *Proceedings of 3rd International Symposium on Cold Region Heat Transfer*, Fairbanks, AK, June 11–14, pp. 1–24.
[5] Jany, P., and Bejan, A., 1988, "Scaling of Melting with Natural Convection in an Enclosure," Int. J. Heat Mass Transfer, **31**, pp. 1221–1235.
[6] Gau, C., and Viskanta, R., 1986, "Melting and Solidification of a Pure Metal on a Vertical Wall," ASME J. Heat Transfer, **108**, pp. 174–181.
[7] Hasan, M., Majumdar, A. S., and Weber, M. E., 1991, "Cyclic Melting and Freezing," Chem. Eng. Sci., **46**, pp. 1573–1587.

[8] Yimer, B., 1997, "Phase Change Heat Transfer During Cyclic Heating and Cooling with Internal Radiation and Temperature Dependent Properties," *Proceedings of National Heat Transfer Conference*, Baltimore, August 8–12, ASME, New York, HTD-Vol. 342, pp. 141–146.

[9] Lu, T. J., 2000, "Thermal Management of High Power Electronics with Phase Change Cooling," Int. J. Heat Mass Transfer, **43**, pp. 2245–2256.

[10] Evans, A. G., He, M. Y., Hutchinson, J. W., and Shaw, M., 2001, "Temperature Distribution in Advanced Power Electronics Systems and the Effect of Phase Change Materials on Temperature Suppression During Power Pulses," ASME J. Electron. Packag., **123**, pp. 211–217.

[11] Pal, D., and Joshi, Y., 1997, "Application of Phase Change Materials to Thermal Control of Electronic Modules: A Computational Study," ASME J. Electron. Packag., **119**, pp. 40–50.

[12] Shatikian, V., Dubovsky, V., Ziskind, G., and Letan, R., 2003, "Simulation of PCM Melting and Solidification in a Partitioned Storage Unit," ASME Paper No. HT2003-47167.

[13] Krishnan, S., Murthy, J. Y., and Garimella, S. V., 2004, "A Two-Temperature Model for Analysis of Passive Thermal Control Systems," ASME J. Heat Transfer, **126**, pp. 628–637.

[14] Krishnan, S., Murthy, J. Y., and Garimella, S. V., 2005, "A Two-Temperature Model for Solid-Liquid Phase Change in Metal Foams," ASME J. Heat Transfer, **127**, pp. 995–1004.

[15] Vesligaj, M. J., and Amon, C. H., 1999, "Transient Thermal Management of Temperature Fluctuations during Time Varying Workloads on Portable Electronics," IEEE Trans. Compon. Packag. Technol., **22**, pp. 541–550.

[16] Alawadhi, E. M., and Amon, C. H., 2000, "Performance Analysis of an Enhanced PCM Thermal Control Unit," *Proceedings of ITherm 2000*, Las Vegas, NV, May 24–26, pp. 283–289.

[17] Baker, K. W., Jang, J. H., and Yu, J. S., 1995, "Thermal Control of Phase Change Package with Periodic Pulse Heating—A Case Study," *Proceedings of ASME/JSME Thermal Engineering Conference*, Maui, HI, March 19–24, ASME, New York, 4, pp. 463–469.

[18] Pal, D., and Joshi, Y., 1999, "Thermal Control of Horizontal Mounted Heat Sources using Phase Change Materials," Adv. Electron. Packag., **26**, pp. 1625-1630.

[19] Harris, K. T., Haji-Sheikh, A., and Agwu Nnanna, A. G., 2001, "Phase-Change Phenomena in Porous Media—A Non-Local Thermal Equilibrium Model," Int. J. Heat Mass Transfer, **44**, pp. 1619–1625.

[20] Krishnan, S., and Garimella, S. V., 2004, "Analysis of a Phase Change Energy Storage System for Pulsed Power Dissipation," IEEE Trans. Compon. Packag. Technol., **27**(1), pp. 191–199.

[21] Hwang, J. J., Hwang, G. J., Yeh, R. H., and Chao, C. H., 2002, "Measurement of Interstitial Convective Heat Transfer Coefficient and Frictional Drag for Flow Across Metal Foams," ASME J. Heat Transfer, **124**, pp. 120–129.

[22] Morgan, V. T., 1975, "The Overall Convective Heat Transfer from Smooth Circular Cylinders," Adv. Heat Transfer, **11**, pp. 199–264.

Analysis of Heat Transfer Inside Flexible Thin-Film Channels With Nonuniform Height Distributions

A.-R. A. Khaled

Thermal Engineering and Desalination Technology Department,
King AbdulAziz University,
P.O. Box 80204,
Jeddah 21589, Saudi Arabia
e-mail: akhaled4@yahoo.com

Heat transfer inside flexible thin-film channels having nonuniform height distributions is analyzed in this work. The terminology "flexible thin film channel" is referred to a thin-film channel having two plates separated by soft elastic seals. The fluidic volume enclosed between the plates can expand due to any increase in the fluid pressure. This expansion which is determined from the height (distance between the plates) distribution is related to the pressure drop and the seals stiffness by applications of force or moment balance laws on the mobile plate. The seals stiffness parameter (S), Peclet number (Pe), dimensionless inlet height (H_i), and the aspect ratio (ε) are found to be the controlling parameters. It is found that flexible thin-film channels with flexible plates produce additional cooling over the cooling effect for those having inflexible plates. The heated plate temperature when plates are flexible is lower than that for the other case by more than 14.8% when Pe $\varepsilon < 1.0$ and $H_i = 3.0$ Moreover, the cooling effect of flexible thin-film channels is found to increase relative to rigid thin-film channels as the S and Pe ε decrease. Finally, it is recommended to treat flexible thin-film channels as rigid ones when $S_A > 3.45$ (inflexible plates case) or $S_B > 10$ (flexible plates case).
[DOI: 10.1115/1.2430729]

Keywords: flexible thin film channel, heat transfer, seals, convection, stiffness

1 Introduction

Various engineering applications utilize fluidic thin-film channels such as heat pipes and microchannel heat sinks. For example, microchannel heat sinks are found to be feasible for removing the excessive heating [1–3] associated with electronic devices. However the rapid development in electronics and microelectromechanical systems (MEMS) applications requires further removal of heats. As such, new technologies were developed in order to enhance heat transfer. For example, the use of porous medium in cooling of electronic devices is found to enhance heat transfer [4]. However, it creates a substantial increase in the pressure drop. Furthermore, Bowers and Mudawar [5] have shown that two phase flow is capable of removing maximum heat fluxes generated by electronic packages however; the cooling system may become unstable near certain conditions.

Recently, Khaled and Vafai [6,7] have provided new solutions for enhancing heat transfer by utilizing "flexible thin film channels." The flexible thin film channel is composed of two plates which are separated from each other by soft seals (Fig. 1). The terminology "soft seals" is used in this work to refer to elastic seals (e.g., made from elastic polymers) having elastic modulus

coefficients lower than 2 MPa. Therefore, the volume between the plates where the coolant flows through expands due to any increase in the coolant pressure. Khaled and Vafai [7] demonstrated that significant cooling can be achieved due to the expansion of flexible thin-film channels compared to the cooling effect produced by rigid channels. The height of the flexible thin film channel is referred to as the distance between its plates (Fig. 1) which is usually between 10 μm and 1 mm. It is worth noting that Khaled and Vafai [6,7] considered flexible thin-film channels that expand uniformly along the flow direction. In contrast, they may encounter nonuniform expansions in many situations.

In this work, heat transfer inside flexible thin-film channels with nonuniform height profile (see Fig. 1) is analyzed. Two cases are considered: Case A: flexible thin-film channels with inflexible plates, and Case B: flexible thin-film channels with one flexible plate. For both cases, the height distribution is related to the total pressure drop in the coolant. The relation is obtained by applying the force or moment balance laws on the mobile plate accounting for the elastic forces and moments exerted by the seals. The governing momentum and energy equations are properly nondimensionalized and solved numerically in order to explore the dynamic and thermal behaviors of flexible thin film channels.

2 Problem Formulation

Consider a two-dimensional flexible thin-film channel that has small heights $h(x)$ compared to its length B. The x axis is taken along the coolant flow direction while the y axis is taken along its height as shown in Fig. 1. The width of the thin film channel, D, is assumed to be large enough such that two-dimensional flow between the plates is assumed. The height is considered to have the following generic form

$$\frac{h(x)}{h_e} = \left[\left(\frac{h_i}{h_e} \right)^{1/n} - \left[\left(\frac{h_i}{h_e} \right)^{1/n} - 1 \right] \left(\frac{x}{B} \right) \right]^n \tag{1}$$

where n, h_e, and h_i are the power-law index, exit, and inlet heights, respectively. When $n = 1.0$, the inclination angle of the upper plate is uniform. This is the case when the upper plate is inflexible. However, the upper plate deflects with different slops due to variations in the pressure when it is flexible which is the case when $n \neq 1.0$. Later on, the relation between the height profile, seals stiffness, and the total pressure drop will be derived for $n = 1.0$ and $n = 0.25$. The case when $n = 0.25$ represents the height profile when the upper plate stiffness (due bending around the z axis) is negligible compared to the seals stiffness.

The fluid is assumed to be Newtonian and the flow inside the flexible thin-film channel is considered to be laminar with negligible convective momentum terms. Therefore, the velocity field, Reynolds equation, and the energy equation are [6]

$$u(x,y) = \frac{[h(x)]^2}{2\mu} \frac{dP}{dx} \left\{ \left[\frac{y}{h(x)} \right]^2 - \left[\frac{y}{h(x)} \right] \right\} \tag{2}$$

$$\nu(x,y) = -\frac{[h(x)]^3}{2\mu} \frac{d^2P}{dx^2} \left\{ \frac{1}{3} \left[\frac{y}{h(x)} \right]^3 - \frac{1}{2} \left[\frac{y}{h(x)} \right]^2 \right\} + \frac{[h(x)]^2}{2\mu} \frac{dP}{dx} \left\{ \frac{1}{2} \left[\frac{y}{h(x)} \right]^2 \frac{dh}{dx} \right\} \tag{3}$$

$$\frac{d}{dx} \left\{ [h(x)]^3 \frac{dP}{dx} \right\} = 0 \tag{4}$$

$$\rho c_p \left(u \frac{\partial T}{\partial x} + \nu \frac{\partial T}{\partial y} \right) = k \frac{\partial^2 T}{\partial y^2} \tag{5}$$

where T, u, ν, ρ, P, μ, and k are the fluid's temperature, axial velocity, normal velocity, fluid's density, pressure, fluid's dynamic viscosity, fluid's specific heat, and the fluid's thermal conductivity, respectively.
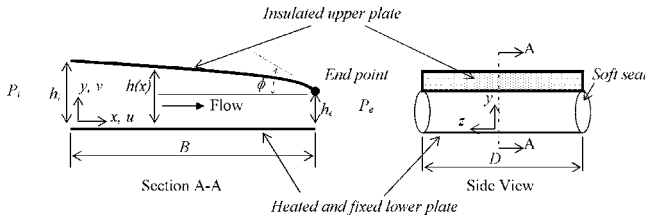
Fig. 1 Side and front sectional views for a flexible thin film channel

The following dimensionless variables are utilized

$$X = \frac{x}{B} \tag{6a}$$

$$\eta = \frac{Yh_e}{h(x)} \tag{6b}$$

$$U = \frac{u}{u_o} \tag{6c}$$

$$V = \frac{v}{u_o(h_e/B)} \tag{6d}$$

$$\theta = \frac{T - T_i}{qh_e/k} \tag{6e}$$

where q, u_0, and T_i are the applied heat flux at the lower plate, reference velocity, and the inlet temperature, respectively. Therefore, Eqs. (2), (3), and (5) and the solution of Eq. (3) can be reduced to the following

$$\frac{P(X) - P_e}{P_i - P_e} = \frac{1}{[H_i^{(1-3)/n} - 1]}\{-1 + [H_i^{1/n} - (H_i^{1/n} - 1)X]^{1-3n}\} \tag{7}$$

$$U(X,Y) = 6(1 - 3n)\frac{(H_i^{1/n} - 1)}{(H_i^{(1-3n)/n} - 1)H}(\eta - \eta^2) \tag{8}$$

$$V(X,Y) = 6n(1 - 3n)\frac{(H_i^{1/n} - 1)(H_i - 1)^{1/n}}{(H_i^{(1-3n)/n} - 1)H^{1/n}}(\eta^3 - \eta^2) \tag{9}$$

$$6(1 - 3n)\frac{(H_i^{1/n} - 1)}{(H_i^{(1-3n)/n} - 1)}H(\eta - \eta^2)\frac{\partial\theta}{\partial X} = \frac{1}{\text{Pe}\,\varepsilon}\frac{\partial^2\theta}{\partial\eta^2} \tag{10}$$

where P_i and P_e are the pressures at the inlet and exit, respectively. The Peclet number Pe, aspect ratio ε, H, and H_i are defined as follows

$$\text{Pe} = \frac{\rho c_p u_o h_i}{k} \tag{11a}$$

$$\varepsilon = \frac{h_e}{B} \tag{11b}$$

$$H = \frac{h}{h_e} \tag{11c}$$

$$H_i = \frac{h_i}{h_e} \tag{11d}$$

where $u_0 = (P_i - P_e)h_e^2/(12\mu B)$. The dimensionless wall shear stress is equal to

$$\tau^* = \frac{-\mu\lfloor(\partial u/\partial y)|_{y=0}\rfloor_{\text{AVG}}}{(P_i - P_e)\varepsilon} = \frac{1}{2}\left(\frac{1 - 3n}{1 - 2n}\right)\left(\frac{H_i^{(1-2n)/n} - 1}{H_i^{(1-3n)/n} - 1}\right) \tag{12}$$

2.1 Case A: Flexible Thin Film Channels With Inflexible Plates ($n = 1.0$). The dimensionless height for this case varies with X according to the following relation

$$H(X) = H_i - (H_i - 1)X \tag{13}$$

The dimensionless inlet height H_i is related to the total pressure drop $(P_i - P_e)$ by applying the balance of moments around the upper plate end point (Fig. 1) accounting for elastic forces [8] exerted by seals. This reveals the following equation

$$-D\int_0^B (P - P_e)(B - x)dx = K_m\phi \cong \tan\phi = (H_i - 1)\varepsilon \tag{14}$$

where K_m and ϕ are the seals stiffness and the inclination angle of the upper plate, respectively. The solution of Eq. (14) prescribes the following relation

$$S_A \equiv \frac{K_m\varepsilon}{[DB(P_i - P_e)]B} = \frac{H_i^2}{(H_i^2 - 1)(H_i - 1)^2}\left[\frac{H_i}{2} + \frac{1}{H_i} - \frac{1}{2}\right. $$
$$\left. - \frac{\ln(H_i)}{(H_i - 1)}\right] \tag{15}$$

where S_A is the dimensionless stiffness parameter for this case.

2.2 Case B: Flexible Thin-Film Channels Having Flexible Upper Plates ($n = 0.25$). The dimensionless height for this is expressed by the following relation

$$H(X) = 1 + (H_i - 1)\left(\frac{P - P_e}{P_i - P_e}\right) \tag{16a}$$

$$S_B \equiv \frac{Kh_e}{P_i - P_e} = \frac{1}{H_i - 1} \tag{16b}$$

where K and S_B are the seals stiffness per unit plate surface area and the corresponding dimensionless stiffness parameter, respectively. It is assumed in this equation that the pressure is linearly proportional to the deflection of the upper plate with a constant of proportionality equal to K. This is valid as long as the upper plate stiffness is negligible compared to the seals stiffness [9]. Solving Eq. (4) for P and substituting P in Eq. (16) results in the following height profile

$$H(X) = \sqrt[4]{H_i^4 - [H_i^4 - 1]X} \tag{17}$$

Note that Eq. (17) is similar to Eq. (1) when $n = 0.25$.

2.3 Thermal Boundary Conditions. Uniform wall heat flux is assumed at the lower plate while the upper plate is considered to be insulated. The upper plate can be, for example, a rigid glass plate or a flexible plastic plate. Thus, the imposed boundary conditions are

$$\theta(X,0) = 0, \qquad \frac{\partial\theta}{\partial\eta}\bigg|_{x,\eta=0} = -H(X)$$

$$\frac{\partial\theta}{\partial\eta}\bigg|_{X,\eta=1} = -\varepsilon^2 H(X)(H(X) - 1) \quad \frac{\partial\theta}{\partial X}\bigg|_{X,\eta=1} \cong 0 \tag{18}$$

The mean bulk temperature is equal to

$$\theta_m(X) \equiv \int_0^1 U(X,\eta)\theta(X,\eta)d\eta \bigg/ \int_0^1 U(X,\eta)d\eta$$

$$= \frac{(H_i^{(1-3n)/n} - 1)}{(H_i^{1/n} - 1)(1 - 3n)}\left(\frac{X}{\text{Pe}\,\varepsilon}\right) \tag{19}$$

For low values of Pe ε, the thermal entrance region can be neglected, thus the average dimensionless lower plate temperature $(\theta_W)_{\text{AVG}}$ is approximated by the following
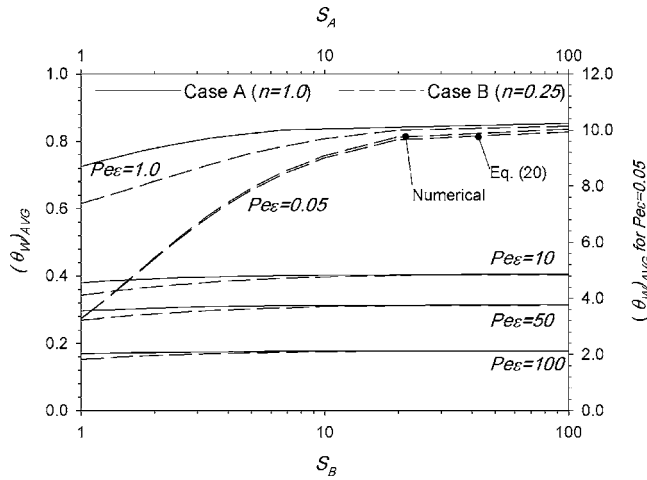
Fig. 2 Variation of the dimensionless average lower plate temperature $(\theta_W)_{\mathrm{AVG}}$ with the dimensionless stiffness parameters S_A and S_B

Fig. 3 Variation of λ_{MAX} and f_{MAX} with the inlet dimensionless height H_i

$$(\theta_W)_{\mathrm{AVG}} = \int_0^1 \theta(X,0)dX = 0.372\frac{(H_i^{(n+1)/n}-1)}{(n+1)(H_i^{1/n}-1)}$$

$$+ \frac{H_i^{(1-3n)/n}-1}{2(H_i^{1/n}-1)(1-3n)\mathrm{Pe}\,\varepsilon} \quad (20)$$

Define λ_{MAX} and f_{MAX} as the maximum ratio of $(\theta_W)_{\mathrm{AVG}}$ and τ^* to $(\theta_W)_{\mathrm{AVG}}$ and τ^* when S tends to infinity (rigid thin film channels), respectively. They are equal to

$$\lambda_{\mathrm{MAX}} \equiv \frac{H_i^{(1-3n)/n}-1}{(H_i^{1/n}-1)(1-3n)} \quad (21a)$$

$$f_{\mathrm{MAX}} = \left(\frac{1-3n}{1-2n}\right)\left(\frac{H_i^{(1-2n)/n}-1}{H_i^{(1-3n)/n}-1}\right) \quad (21b)$$

3 Numerical Methods

Equation (10) was descritized using three points central differencing in the η direction and two points backward differencing in the X direction. The resulting tridiagonal system of algebraic equations at $X=\Delta X(\Delta X=\Delta\eta=0.005)$ was then solved using Thomas algorithm [9]. The same procedure was repeated for subsequent X values until $X=1.0$. Excellent agreement was found between the numerical results and the results of Eq. (20) as shown in Fig. 2. The maximum relative error was found to be 0.4% at Pe $\varepsilon=0.05$. Minimum and maximum values of Pe ε are taken to be Pe $\varepsilon=1.0$ and Pe $\varepsilon=50$, respectively. A flexible thin-film channel with $h_e=100$ μm and $B=3$ mm has Pe $\varepsilon=1.0$ when $u_0=0.03$ m/s (water as coolant). Minimum S_A and S_B values are selected to be 1.0. This corresponds to $K_m=29.2$ N μm($D=1$ mm) and $K=1080$ kN/m^3. For seals with square crosssection, the seals stiffness per unit plate area is approximated by $K\equiv 2E/D$, where E is the seals elastic modulus. Thus, $K=2\times 10^6$ kN/m^3 when $E=1$ MPa for rubber seals while it is equal to $K=2000$ kN/m^3 when $E=1$ kPa for soft seals.

4 Discussion of the Results

Equations (15) and (17) predict that H_i decreases as the S_A and S_B increase. It can also be proposed based on these equations that flexible thin-film channels may be treated as rigid thin-film channels when $S_A>3.45$ or $S_B>10$. These values result in $H_i<1.10$. The effects of S_A and S_B on $(\theta_W)_{\mathrm{AVG}}$ are illustrated in Fig. 2. As the supporting seals become softer (when S decreases), the value
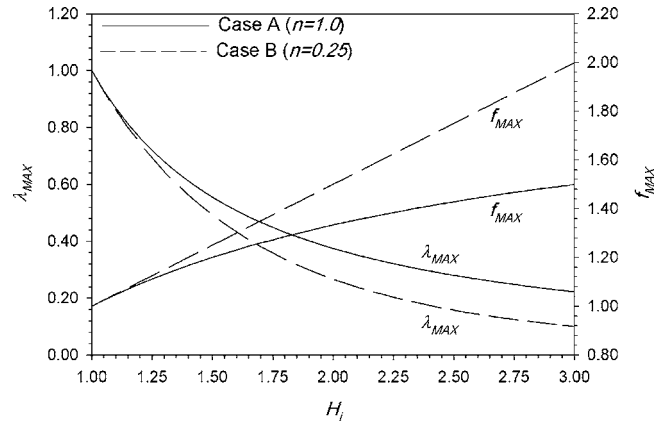
of $(\theta_W)_{\mathrm{AVG}}$ decreases. This reduction becomes apparent when $S_A<3.45$ and Pe $\varepsilon<5.0$. For example, Fig. 2 shows that flexible thin-film channels with inflexible plates (Case A) having $S_A=1.0$ produce 16% reduction in $(\theta_W)_{\mathrm{AVG}}$ at Pe $\varepsilon=1.0$ relative to $(\theta_W)_{\mathrm{AVG}}$ produced by rigid thin-film channels ($S_A\rightarrow\infty$). The cooling effect increases as both S_A and Pe ε decrease. Figure 2 also shows that the maximum percentage reduction in $(\theta_W)_{\mathrm{AVG}}$ relative to that for rigid thin films ($S_B\rightarrow\infty$) is 29% for Case B when $S_B=$Pe $\varepsilon=1.0$. As such flexible thin-film channels of Cases A or B are preferred to be utilized at lower values of Pe ε. It can be depicted from Fig. 3 that the maximum reduction in $(\theta_W)_{\mathrm{AVG}}$ associated with Case B is lower than that for Case A by 55% (when $H_i=3.0$ where $(\lambda_{\mathrm{MAX}})_A=0.22; (\lambda_{\mathrm{MAX}})_B=0.1$), while the maximum increase in wall shear stress for Case B is greater than that for Case A by 44%. The former percentage is greater than the latter one which demonstrates the superiority of flexible thin-film channels with flexible plates over those with inflexible plates. Finally, Correlation (22) is generated for design purposes to relate $(\theta_W)_{\mathrm{AVG}}$ to H_i, n, and Pe ε for the following range: $1.0<H_i<3.0, 1.0<\mathrm{Pe}\,\varepsilon<50$ and $0.25<n<2.0$

$$(\theta_W)_{\mathrm{AVG}} = \frac{0.14\ln^{-0.324}H_i^{-1.972}+0.864n^{0.0741}(\mathrm{Pe}\,\varepsilon)^{0.0184}}{[4.143(\mathrm{Pe}\,\varepsilon)^{1.463}-2.240H_i^{-1.980}]^{0.251}} \quad (22)$$

The maximum percentage error between the results of the correlation and the numerical results is about 10%. When $H_i=1.5, 2.0$, and 3.0, the additional cooling effect produced by Case B relative to Case A which is measured by $[(\theta_W)_{\mathrm{AVG}}]_A-[(\theta_W)_{\mathrm{AVG}}]_B/[(\theta_W)_{\mathrm{AVG}}]_A$ is 2.7%, 6.4%, and 14.8%, respectively, when Pe $\varepsilon=1.0$.

5 Conclusions

Heat transfer inside flexible thin-film channels having nonuniform height distributions was analyzed in this work. The concentration of this work was on two different cases which have a strong physical basis: Case A: flexible thin-film channels having inflexible plates while the flexible thin-film channels falling under Case B have flexible upper plates. The expansion of the analyzed systems which is determined from the height profile was related to the pressure drop and the seals stiffness by the application of force or moment balance laws on the mobile plate. The governing momentum and energy equations were properly nondimensionalized and reduced to simpler forms for small Reynolds numbers. The reduced equations were then solved numerically using an implicit method. It was found that flexible thin-film channels with flexible plates enhances heat transfer better than those with inflexible plates especially as the stiffness parameter, Peclet number, and

aspect ratio decrease. Finally, It is recommended to treat flexible thin-film channels as rigid thin film channels when $S_A > 3.45$ or $S_B > 10$.

Nomenclature

B = flexible thin film channel's length
c_p = fluid's specific heat
D = flexible thin film channel's width
E = seals modulus of elasticity
H = dimensionless flexible thin film channel height
H_i = dimensionless flexible thin film channel inlet height
h = flexible thin film channel height
h_i = flexible thin film channel inlet height
h_e = flexible thin film channel exit height
K_m = effective seals stiffness (Case A)
K = seals stiffness (Case B)
k = fluid's thermal conductivity
Pe = Peclet number
P = fluid's pressure
P_i = inlet pressure
P_e = exit pressure
q = applied heat flux
S_A = dimensionless stiffness parameter (Case A)
S_B = dimensionless stiffness parameter (Case B)
T, T_i = temperature in fluid and the inlet temperature
U, u = dimensionless and dimensional axial velocities
u_0 = reference speed
V, v = dimensionless and dimensional normal velocities
X, x = dimensionless and dimensional axial coordinates
y = dimensional normal coordinate

Greek Symbols

ε = aspect ratio
μ = fluid's dynamic viscosity
θ, θ_m = dimensionless temperature and dimensionless mean bulk temperature
$(\theta_W)_{\text{AVG}}$ = average dimensionless lower plate temperature
ρ = fluid's density
η = dimensionless y coordinate

References

[1] Tuckerman, D. B., and Pease, D. B., 1981, "High-Performance Heat Sinking for VLSI," IEEE Electron Device Lett., **EDL-2**, pp. 126–129.
[2] Missaggia, L. J., Walpole, J. N., Liau, Z. L., and Philips, R. J., 1989, "Micro-channel Heat Sinks for Two Dimensional High-Power-Density Diode Laser Arrays," IEEE J. Quantum Electron., **25**, pp. 1988–1992.
[3] Vafai, K., and Zhu, L., 1999, "Analysis of a Two-Layered Micro Channel Heat Sink Concept in Electronic Cooling," Int. J. Heat Mass Transfer, **42**, pp. 2287–2297.
[4] Hadim, A., 1994, "Forced Convection in a Porous Channel With Localized Heat Sources," ASME J. Heat Transfer, **116**, pp. 465–472.
[5] Bowers, M. B., and Mudawar, I., 1994, "Two-Phase Electronic Cooling Using Mini-Channel and Microchannel Heat Sink," ASME J. Electron. Packag., **116**, pp. 290–305.
[6] Khaled, A.-R. A., and Vafai, K., 2002, "Flow and Heat Transfer Inside Thin Films Supported by Soft Seals in the Presence of Internal and External Pressure Pulsations," Int. J. Heat Mass Transfer, **45**, pp. 5107–5115.
[7] Khaled, A.-R. A., and Vafai, K., 2005, "Analysis of Flexible Microchannel Heat Sinks," Int. J. Heat Mass Transfer, **48**, pp. 1739–1746.
[8] Norton, R. L., 1998, *Machine Design: An Integrated Approach*, 2nd ed. Prentice-Hall, Englewood Cliffs, NJ.
[9] Blottner, F. G., 1970, "Finite-Difference Methods of Solution of the Boundary-Layer Equations," AIAA J., **8**, pp. 193–205.